

Dissertation

Effective Damping of Vibrations of Plan-asymmetric Buildings

ausgeführt zum Zwecke der Erlangung des akademischen Grades
eines Doktors der technischen Wissenschaften unter der Leitung von

Em.o. Univ.Prof. Dip.-Ing. Dr.techn. Dr.h.c. Franz Ziegler

E2063

Institut für Hochbau und Technologie

Zentrum für Allgemeine Mechanik und Baudynamik

eingereicht an der Technischen Universität Wien

Fakultät für Bauingenieurwesen

von

Dipl. Ing. FU Chuan

1080 Wien Pfeilgasse 4-6

Matr.Nr. 0127106

Erstgutachter: Em.o. Univ.Prof. Dip.-Ing. Dr.techn. Dr.h.c. Franz Ziegler, TU-wien

Zweitgutachter: o. Univ.Prof. Dip.-Ing. Dr.techn. Hans Irschik, J-K Universität, Linz

Wien, April 2008

Vorwort

Die vorliegende Arbeit entstand während meiner Tätigkeit als Doktorandin am Zentrum für Allgemeine Mechanik und Baudynamik der Technischen Universität Wien. Mein besonderer Dank gebührt Herrn Em.O.Univ.Prof. Dip.-Ing. Dr.techn. Dr.h.c. Franz Ziegler, ehemals Vorstand des Instituts für Allgemeine Mechanik, für die Anregung auf dem interessanten Gebiet der Schwingungstilgung zu dissertieren und für wertvolle Hinweise und Diskussionen im Laufe der Entstehung dieser Arbeit.

Herrn o.Univ.Prof. Dipl.-Ing. Dr.techn. Hans Irschik, Vorstand des Instituts für Technische Mechanik der Johannes Kepler Universität in Linz, möchte ich für die Zweitbegutachtung dieser Dissertation recht herzlich danken.

Ein besonderer Dank gebührt auch Herrn AO.Univ.Prof. Dipl.-Ing. Dr.techn. Rudolf Heuer, Herrn Univ.Do. Dipl.-Ing. Dr.techn. Piotr Borejko und Herrn Univ.Ass. PhD. Peter Rosko, vom Zentrum für Allgemeine Mechanik und Baudynamik der Technischen Universität Wien für die Unterstützung beim Anfertigen dieser Arbeit.

Kurzfassung

Die vorliegende Dissertation „Effektive Schwingungsdämpfung von planmäßig asymmetrischen Gebäuden“ untersucht den Einfluß passiver Tilger in asymmetrischen Gebäuden bei Erdbebenbelastung, wobei insbesondere gekoppelte Torsions- und Biegeschwingungen untersucht werden. Da der Massenmittelpunkt C_M nicht mit dem Steifigkeitsmittelpunkt C_S der Geschoßdecken übereinstimmt, verursacht die seismische Erregung in einer Richtung eine dreidimensionale Schwingung (schiefe Biegeschwingung und Torsion). Die dynamische Schwingungstilgerung dissipiert Energie, um strukturelle Beschädigung oder Unannehmlichkeit der Bewohner zu minimieren, mit Gas-Flüssigkeitskombitilgern (tuned liquid column gas dampers-TLCGDs) und/ oder mit Gas-Flüssigkeitskombi-Torsionstilgern (torsional tuned liquid column gas dampers-TTLCGDs), mit Gasfeder Wirkung. Es wurden theoretische Studien durchgeführt. Die Zielsetzung dieser Arbeit war, die optimale Installation und die optimalen Parameter von Gas-Flüssigkeitskombitilgern und Gas-Flüssigkeitskombi-Torsionstilgern für seismische Anwendungen festzustellen. Sie können in verschiedenen Positionen in den vorgewählten Geschoßdecken installiert werden, dennoch ist eine optimale Position von der Lage des modalen Geschwindigkeitspols abhängig. Wenn die Geschwindigkeitspole außerhalb der Geschoßdecke (mäßige Asymmetrie) liegen, dann ist die ideale Position des U-förmigen Gas-Flüssigkeitskombitilgers durch den größtmöglichen normalen Abstand zu diesem Geschwindigkeitspol gegeben. Wenn der modale Geschwindigkeitspol innerhalb der Geschoßdecke (starke Asymmetrie) liegt, dann wird eine neue Konstruktion vorgeschlagen: der horizontale Abschnitt des Rohr-Systems wird gebogen, so dass der Gas-Flüssigkeitskombi-Torsionstilger den Geschwindigkeitspol umschließt. Die optimale Eigenfrequenz und der lineare Dämpfungskoeffizient des Gas-Flüssigkeitskombitilgers werden mittels geometrischer Transformation in Analogie zum klassischen Feder-Masse-Tilger (tuned mass dampers -TMDs) abgeleitet. Anschließend führt eine Feinabstimmung mit einem im Zustandsraum definierten Gütekriterium zu einer weiteren Verbesserung der Tilgerwirkung. Eine besondere robuste Dämpfung in einem vergrößerter Frequenzfenster wird durch die Aufteilung in kleine, parallele wirkende Gas-Flüssigkeitskombitilger erreicht. Numerische Beispiele haben bereits gezeigt, dass eine wirkungsvolle Methode zur effektiven Dämpfung von Translations- und Torsionsschwingungen vorgelegt wird.

Abstract

The purpose of this dissertation is to reduce lateral flexural and torsional vibrations of asymmetric buildings under the influence of earthquakes by means of passive absorbers. Since the centre of mass C_M and the centre of stiffness C_S of the floors do not coincide, even the uni-directional seismic excitation causes a three dimensional vibration (oblique bending and torsion). Dynamic vibration absorbers dissipate energy to avoid structural damage or discomfort of the occupants. As to tuned liquid column gas damper (TLCGD) and torsional tuned liquid column gas damper (TTLCGD), theoretical studies have been carried out to reduce translational and torsional vibrations of asymmetric structures. The objective of this study was to determine optimum installation and the optimum parameters for TLCGDs and TTLCGDs for seismic applications. They could be installed on any position of the selected floor. Nevertheless, an optimal position is highly dependent on the position of the center of velocity C_V in order to minimize vibration. If such a center falls outside of the floor (moderate asymmetry), the ideal position of the trace of the mid-plane of the U-shaped TLCGD requires its normal distance from this center maximum. If the modal center lies within the floor plan (strong asymmetry), the TTLCGD has its horizontal curved piping section enclosing the center. The optimal natural frequency and equivalent linear damping coefficient of TLCGD or TTLCGD are derived by means of geometrical transformation in analogy to the classical tuned mass damper (TMD) or torsional tuned mass damper (TTMD), respectively. Improvements of the performance in MDOF structures are achieved by considering the neighbouring modes in the state space rendering the optimal parameters modified. A special robust damping to increase frequency window is reached by the smaller, parallel action of TLCGD-units. Numerical examples have already shown that an effective method is presented for controlling the translational and torsional response of asymmetric structures.

Contents

1 INTRODUCTION	1
1.1 OVERVIEW OF PASSIVE DEVICES	1
1.1.1 THE TUNED MECHANICAL DAMPER, TMD	1
1.1.2 THE TUNED LIQUID COLUMN DAMPER, TLCD AND ITS EXTENSION TO INCLUDE A GAS-SPRING, TLCGD	1
1.2 MOTIVATION OF THE RESEARCH	3
1.3 LITERATURE REVIEW	3
1.4 OVERVIEW OF THE DISSERTATION	4
2 SINGLE-STOREY MODERATELY PLAN-ASYMMETRIC SPACE FRAME WITH TLCGDS	6
2.1 INTRODUCTION	6
2.2 EQUATION OF MOTION FOR SINGLE-STOREY MODERATELY ASYMMETRIC SPACE FRAME	6
2.2.1 EFFECTIVE MASS AND STIFFNESS OF A COLUMN	9
2.2.2 INFLUENCE OF THE NORMAL FORCE ON THE STIFFNESS MATRIX: GEOMETRIC CORRECTION	9
2.2.3 NATURAL MODES OF THE MAIN STRUCTURE	10
2.3 POSITION OF THE MODAL CENTER OF VELOCITY C_v	11
2.4 THE EQUATION OF RELATIVE MOTION OF THE FLUID IN A TLCGD	12
2.5 THE NATURAL FREQUENCY OF TLCGD IN RELATION TO THE LINEAR FREQUENCY OF THE MATHEMATICAL PENDULUM	17
2.6 CONTROL FORCES OF TLCGD	18
2.7 CONTROL OF SDOF MAIN STRUCTURE BY A SINGLE TLCGD WHEN COMPARED TO AN EQUIVALENT TMD	21
2.7.1 ANALOGY BETWEEN TMD AND TLCGD WHEN ATTACHED TO SDOF-MAIN STRUCTURE	22
2.8 CONTROL OF SINGLE-STOREY MODERATELY PLAN-ASYMMETRIC SPACE FRAME BY A SINGLE TLCGD WHEN COMPARED TO AN EQUIVALENT TMD	23
2.8.1 TMD ATTACHED TO SPACE FRAME	23
2.8.2 TLCGD ATTACHED TO SPACE FRAME	25
2.8.3 ANALOGY BETWEEN TMD AND TLCGD WHEN ATTACHED TO 3DOF-MAIN SYSTEM	27
2.9 DYNAMIC MAGNIFICATION FACTOR	27

2.9.1 STEADY STATE VIBRATION OF THE LIGHTLY DAMPED MAIN STRUCTURE WITHOUT TLCGD	28
2.9.2 STEADY STATE VIBRATION OF THE MAIN STRUCTURE WITH TLCGD ATTACHED PARALLEL TO Y-DIRECTION	28
2.10 NUMERICAL EXAMPLE	29
2.10.1 STATIC DIMENSIONING AND A STATIC SAFETY CRITERION OF THE COLUMNS	29
2.10.2 NATURAL MODES OF THE MAIN STRUCTURE	30
2.10.3 POSITION OF THE CENTER OF VELOCITY CV FOR THE MODES NUMBERED J=1,2,3	31
2.10.4 THE LINEARIZED EQUATION OF MOTION FOR TLCGD	32
2.10.5 THE LINEARIZED CONTROL FORCES FOR TLCGD ACTING ON THE FLOOR APPLYING THE SUBSTRUCTURE SYNTHESIS	32
2.10.6 TLCGD DESIGN, DEN HARTOG' OPTIMIZATION	33
2.10.7 OPTIMIZATION OF SINGLE-STOREY SPACE FRAME WITH 3 TLCGDS IN THE STATE SPACE DOMAIN	36
2.10.8 TLCGD3 ALTERNATIVELY INSTALLED ON THE SHORT SIDE OF THE FLOOR AND ORIENTED PARALLEL TO THE Z-DIRECTION	47
2.10.9 ORIGINAL STRUCTURE WITH THE DEAD FLUID-MASS OF TLCGD INCLUDED	56
2.10.10 DIMENSIONING OF THE PIPE	57
2.10.11 OBLIQUE SEISMIC EXCITATION BY THE STRONG MOTION PHASE OF THE EL CENTRO EARTHQUAKE (1940)	58
2.10.12 KANAI-TAJIMI MODEL OF THE GROUND ACCELERATION: SOIL AMPLIFICATION	64

3. SINGLE-STOREY STRONGLY PLAN-ASYMMETRIC SPACE FRAME WITH TTLCGDS AND TLCGDS **73**

3.1 INTRODUCTION	73
3.2 EQUATION OF MOTION FOR SINGLE-STOREY STRONGLY ASYMMETRIC SPACE FRAME	73
3.3 TORSIONAL TUNED LIQUID COLUMN DAMPER, TTLCGD	75
3.4 EQUATION OF MOTION OF TTLCGD	76
3.4.1 EQUATION OF MOTION OF TTLCGD (THE VERTICAL SEGMENT, A (Y _A , Z _A , 0), $\beta = \pi/2$)	76
3.4.2 EQUATION OF MOTION OF TTLCGD (THE INCLINED SEGMENT PARALLEL TO Z-AXIS, A (Y _A , 0, 0), $\pi/4 \leq \beta < \pi/2$)	78
3.4.3 EQUATION OF MOTION OF TTLCGD (THE INCLINED SEGMENT PARALLEL TO Y-AXIS, A (0, Z _A , 0), $\pi/4 \leq \beta < \pi/2$)	79
3.5 FORCES AND MOMENTS OF TTLCGD	79
3.5.1 FORCES AND MOMENTS (THE VERTICAL SEGMENT, A (Y _A , Z _A , 0), $\beta = \pi/2$)	79
3.5.2 FORCES AND MOMENTS (THE INCLINED SEGMENT PARALLEL TO Z-AXIS, A (Y _A , 0, 0), $\pi/4 \leq \beta < \pi/2$)	81

3.5.3 FORCES AND MOMENTS (THE INCLINED SEGMENT PARALLEL TO Y-AXIS, A (0, Z _A , 0), $\pi/4 \leq \beta < \pi/2$)	82
3.6 CONTROL OF SINGLE-STOREY STRONGLY PLAN-ASYMMETRIC SPACE FRAME BY A SINGLE TTLCGD ($\beta = \pi/2$) WHEN COMPARED TO AN EQUIVALENT TTMD	82
3.6.1 TORSIONAL TUNED MECHANICAL DAMPER, TTMD	82
3.6.2 TTLCGD ATTACHED TO SPACE FRAME (THE VERTICAL SEGMENT, A (Y _A , Z _A , 0), $\beta = \pi/2$)	83
3.6.3 ANALOGY BETWEEN TTMD AND TTLCGD ($\beta = \pi/2$) WHEN ATTACHED TO 3DOF-MAIN SYSTEM	84
3.7 CONTROL OF SINGLE-STOREY STRONGLY PLAN-ASYMMETRIC SPACE FRAME BY A SINGLE TTLCGD ($\pi/4 \leq \beta < \pi/2$) WHEN COMPARED TO AN EQUIVALENT TTMD	85
3.7.1 TTMD ATTACHED TO SPACE FRAME, A POINT MASS IN Y-AXIS	85
3.7.2 TTLCGD ATTACHED TO SPACE FRAME (THE INCLINED SEGMENT PARALLEL TO Z-AXIS, A (Y _A , 0, 0), $\pi/4 \leq \beta < \pi/2$)	86
3.7.3 ANALOGY BETWEEN TTMD AND TTLCGD ($\pi/4 \leq \beta < \pi/2$) WHEN ATTACHED TO 3DOF-MAIN SYSTEM	87
3.8 NUMERICAL EXAMPLE	88
3.8.1 STATIC DIMENSIONING AND A STATIC SAFETY CRITERION OF THE COLUMNS	88
3.8.2 NATURAL MODES OF THE MAIN STRUCTURE	88
3.8.3 POSITION OF THE MODAL CENTERS OF VELOCITY C _v	89
3.8.4 TTLCGD AND TLCGD DESIGN, DEN HARTOG' OPTIMIZATION	90
3.8.5 OPTIMIZATION OF THE TTLCGD-, TLCGD-MAIN STRUCTURE SYSTEM IN THE STATE SPACE DOMAIN	93
3.8.6 OBLIQUE SEISMIC EXCITATION BY THE STRONG MOTION PHASE OF THE EL CENTRO EARTHQUAKE (1940)	102
3.8.7 KANAI-TAJIMI MODEL OF THE GROUND ACCELERATION: SOIL AMPLIFICATION	108
3.9 SINGLE-STOREY SYMMETRIC SPACE FRAME	114

4. MULTI-STOREY MODERATELY PLAN-ASYMMETRIC SPACE FRAME WITH TLCGDS **114**

4.1 INTRODUCTION	114
4.2 EQUATION OF MOTION FOR MULTI-STOREY MODERATELY ASYMMETRIC SPACE FRAME	115
4.2.1 EQUATION OF MOTION FOR TWO-STOREY MODERATELY ASYMMETRIC SPACE FRAME	115
4.2.2 EQUATION OF MOTION FOR N-STOREY MODERATELY ASYMMETRIC SPACE FRAME	119
4.3 CONTROL OF N-STOREY MODERATELY PLAN-ASYMMETRIC SPACE FRAME BY A SINGLE TLCGD WHEN COMPARED TO AN EQUIVALENT TMD	120

4.3.1 TMD ATTACHED ON THE I-TH FLOOR	120
4.3.2 TLCGD ATTACHED ON THE I-TH FLOOR	121
4.3.3 ANALOGY BETWEEN TMD AND TLCGD WHEN ATTACHED TO N-STOREY SPACE FRAME	122
4.4 TWO-STOREY MODERATELY ASYMMETRIC SPACE FRAME: NUMERICAL EXAMPLE	122
4.4.1 STATIC DIMENSIONING AND A STATIC SAFETY CRITERION OF THE COLUMNS	123
4.4.2 NATURAL MODES OF THE MAIN STRUCTURE	123
4.4.3 POSITION OF THE MODAL CENTERS OF VELOCITY C_v	125
4.4.4 TLCGD DESIGN, DEN HARTOG' OPTIMIZATION	125
4.4.5 OPTIMIZATION OF THE TWO-STOREY SPACE FRAME WITH 3TLCGDS IN THE STATE SPACE DOMAIN	128
4.5 THREE-STOREY MODERATELY ASYMMETRIC SPACE FRAME: NUMERICAL EXAMPLE	136
4.5.1 STATIC DIMENSIONING AND A STATIC SAFETY CRITERION OF THE COLUMNS	137
4.5.2 NATURAL MODES OF THE MAIN STRUCTURE	137
4.5.3 POSITION OF THE MODAL CENTERS OF VELOCITY C_v	143
4.5.4 TLCGD DESIGN, DEN HARTOG' OPTIMIZATION	143
4.5.5 OPTIMIZATION OF THE THREE-STOREY SPACE FRAME WITH 3 TLCGDS IN THE STATE SPACE DOMAIN	146
4.6 FOUR-STOREY MODERATELY ASYMMETRIC SPACE FRAME: NUMERICAL EXAMPLE	155
4.6.1 STATIC DIMENSIONING AND A STATIC SAFETY CRITERION OF THE COLUMNS	155
4.6.2 NATURAL MODES OF THE MAIN STRUCTURE	156
4.6.3 POSITION OF THE MODAL CENTERS OF VELOCITY C_v	157
4.6.4 TLCGD DESIGN, DEN HARTOG' OPTIMIZATION	158
4.6.5 OPTIMIZATION OF THE FOUR-STOREY SPACE FRAME WITH 4 TLCGDS IN THE STATE SPACE DOMAIN	161
4.6.6 TLCGD4 ALTERNATIVELY INSTALLED ON THE SECOND FLOOR	170
4.6.7 FORCING BY THE NS-EL CENTRO SEISMOGRAM UNDER VARYING ANGLES OF ATTACK	180

5 MULTI-STOREY STRONGLY PLAN-ASYMMETRIC SPACE FRAME WITH TTLCGDS AND TLCGDS **185**

5.1 INTRODUCTION	185
5.2 EQUATION OF MOTION FOR MULTI-STOREY STRONGLY ASYMMETRIC SPACE FRAME	186
5.3 CONTROL OF N-STOREY STRONGLY PLAN-ASYMMETRIC SPACE FRAME BY A SINGLE TTLCGD ($\beta = \pi/2$) WHEN COMPARED TO AN EQUIVALENT TTMD	186
5.3.1 TTMD ATTACHED TO SPACE FRAME	186

5.3.2 TTLCGD ATTACHED TO SPACE FRAME (THE VERTICAL SEGMENT, A ($Y_A, Z_A, 0$), $\beta = \pi/2$)	187
5.3.3 ANALOGY BETWEEN TTMD AND TTLCGD WHEN ATTACHED TO N-STOREY SPACE FRAME	188
5.4 TWO-STOREY STRONGLY ASYMMETRIC SPACE FRAME: NUMERICAL EXAMPLE	188
5.4.1 STATIC DIMENSIONING AND A STATIC SAFETY CRITERION OF THE COLUMNS	189
5.4.2 NATURAL MODES OF THE MAIN STRUCTURE	189
5.4.3 POSITION OF THE MODAL CENTERS OF VELOCITY C_v	190
5.4.4 TTLCGD AND TLCGD DESIGN, DEN HARTOG' OPTIMIZATION	190
5.4.5 OPTIMIZATION OF THE TTLCGD-, TLCGD-STRUCTURE SYSTEM IN THE STATE SPACE DOMAIN	192
5.5 THREE-STOREY STRONGLY ASYMMETRIC SPACE FRAME: NUMERICAL EXAMPLE	201
5.5.1 STATIC DIMENSIONING AND A STATIC SAFETY CRITERION OF THE COLUMNS	201
5.5.2 NATURAL MODES OF THE MAIN STRUCTURE	202
5.5.3 POSITION OF THE MODAL CENTERS OF VELOCITY C_V	203
5.5.4 TTLCGD AND TLCGD DESIGN, DEN HARTOG' OPTIMIZATION	203
5.5.5 OPTIMIZATION OF THE TTLCGD-, TLCGD-STRUCTURE SYSTEM IN THE STATE SPACE DOMAIN	205
5.6 FOUR-STOREY STRONGLY ASYMMETRIC SPACE FRAME: NUMERICAL EXAMPLE	214
5.6.1 STATIC DIMENSIONING AND A STATIC SAFETY CRITERION OF THE COLUMNS	214
5.6.2 NATURAL MODES OF THE MAIN STRUCTURE	215
5.6.3 POSITION OF THE MODAL CENTERS OF VELOCITY	216
5.6.4 TTLCGD AND TLCGD DESIGN, DEN HARTOG' OPTIMIZATION	217
5.6.5 OPTIMIZATION OF THE TTLCGD-, TLCGD-MAINSTRUCTURE SYSTEM IN THE STATE SPACE DOMAIN	219
5.6.6 FORCING BY THE NS-EL CENTRO SEISMOGRAM UNDER VARYING ANGLES OF ATTACK	227
<u>6 THIRTY-STOREY MODERATELY ASYMMETRIC STRUCTURE</u>	<u>233</u>
6.1 INSTALLATION OF THE TLCGD	233
6.2 TLCGD DESIGN, DEN HARTOG' OPTIMIZATION	234
6.3 SMALLER TLCGD-UNITS IN PARALLEL ACTION, FINE-TUNING IN STATE SPACE	237
6.4 FORCING OF THE 30 STOREY MODERATELY ASYMMETRIC BUILDING BY THE NS-EL CENTRO SEISMOGRAM UNDER VARYING ANGLES OF ATTACK	238
<u>7 CONCLUSIONS</u>	<u>249</u>

Notation

a	the length of the structural floor
\bar{a}	absolute acceleration of fluid
\bar{a}_g	guiding acceleration
\bar{a}_c	the Coriolis acceleration
\bar{a}'	relative acceleration
A_p	area enclosed by TTLCD
A_B	cross sectional area of horizontal TLCD section
A_H	cross sectional area of inclined TLCD section
\underline{A}	system matrix
b	the width of the structural floor
B	horizontal width of TLCD
\underline{B}	system (TLCD) input matrix
C_A	damping coefficient of TLCD
\underline{C}	damping matrix of structure
C_M	the mass center of the moving frame
C_S	the stiffness center of the moving frame
C_V	the center of velocity
C_f	the instant position of the fluid center of mass
\vec{D}_{C_M}	angular momentum vector with respect to C_M
\vec{D}_A	angular momentum vector with respect to A
DMF	dynamic magnification factor of structure response
e_y, e_z	the eccentricity
$\vec{e}_x, \vec{e}_y, \vec{e}_z, \vec{e}_t'$	cartesian unit vectors, unit vector in tagential direction
\underline{E}_N	the influence matrix of the ground excitation
f_A	the natural frequency of TLCD (Hz)
F_{Ay}, F_{Az}	TLCD interation forces
F_{Ay}^*, F_{Az}^*	TMD interation forces
F_c	buckling force
f	external force, e.g. wind
G	dead load
g	acceleration of gravity
H	length of inclined TLCD section
H_a	effective height
I_x	the mass moment of inertia of structure
I_{fx}	the axial moment of inertia of the fluid mass
\vec{I}	momentum vector, identity vector
J	performance index
k_y, k_z	the stiffness of column in y - or z - direction
\bar{k}_y, \bar{k}_z	the corrected stiffness of column in y - and z -directions
k'_y, k'_z	the stiffness of extra column in y - or z - direction
k_G	the geometric stiffness of c-c beam
$\underline{K}, \underline{K}', \underline{K}^*$	stiffness matrix, corrected stiffness matrix conjugate

l, l_c	stiffness matrix of structure the length of the beam, buckling length
\underline{L}	position matrix
L_0	length of the mathematical pendulum
L_1	length dependent on the cross sectional area
L_{eff}	length of liquid column, effective length
m_S	mass of the homogenous rigid floor
m_k	the modal mass
m_1	the additional point mass
\vec{M}_{C_M}	interaction moment with respect to C_M
\vec{M}_A	interaction moment with respect to A
\vec{M}_p	the additional moment from gravity force
$\underline{M}, \underline{M}^*$	mass matrix, conjugate mass matrix of the structure
m_f, m_A^*	fluid mass, conjugate mass
N	number of floor
N_{sd}	calculating combined load
O	the coordinate origin of the moving frame
p_1, p_2, p_0	pressure, pressure difference
\underline{P}	solution of Lyapunov equation
\vec{P}	the control force vector
Q_k	live load
q_j, \vec{q}	modal coordinate, modal vector
\vec{r}	position vector
\vec{r}'	relative position vector
r_f	the radius of inertia for fluid mass
r_S	the radius of inertia with respect to the mass center C_M
\vec{r}_S	static influence vector
\vec{R}	the resultant of the external forces
\underline{R}	TLCD parameter matrix
s'	coordinate of relative streamline
\underline{S}	weighing matrix
t	time (s)
u	relative liquid displacement
\dot{u}	relative flow velocity
u_T	rotation about x-axis
U_0	the amplitude of the fluid
v	the floor displacement in y-direction
\vec{v}	velocity vector
\vec{v}_g	guiding velocity
v'	relative velocity vector
V_0	gas volume inside TLCD
\ddot{v}_g	the seismic ground acceleration in y-direction

\ddot{v}_t	the absolute acceleration in y -direction
w	the floor displacement in z -direction
\ddot{w}_g	the seismic ground acceleration in z -direction
\ddot{w}_t	the absolute acceleration in z -direction
w_f	total floor displacement
\bar{x}	the displacement vector in the mass center
$\ddot{\bar{x}}_g$	the seismic ground acceleration vector
\bar{z}	state space vector
β	TLCD opening angle
θ	rotation angle about x -axis (rad)
ζ_S, ζ_A	damping ratio of structure/absorber
δ	tuning ratio
δ_L	the head loss coefficient
δ_{ij}	Kronecker symbol
$\bar{\phi}_n$	modal shape vector
ϕ	modal matrix
γ	the general angle of TLCD to y -direction
$\kappa, \kappa_1, \bar{\kappa}, \bar{\kappa}_1, \bar{\kappa}_2, \bar{\kappa}_3$	geometry factors of TLCD
$\kappa_{T0}, \kappa_T, \kappa_{Ty}, \kappa_{Tz}, \bar{\kappa}_T, \bar{\kappa}_{Ty}, \bar{\kappa}_{Tz}, \bar{\kappa}_{T3}$	geometry factors of TTLCD
μ	absorber-structure mass ratio
μ^*	conjugate absorber-structure mass ratio
ρ	mass density of fluid
ω	the circular forcing frequency
ω_n	undamped natural frequency of structure
ω_A	undamped circular frequency of TLCD
ω_S	the natural frequency of the main structure
ω_S^*	conjugate natural frequency of the main structure
ω_A^*	circular frequency of TMD
Ω	diagonal matrix with the structural circular frequency

1 Introduction

This chapter begins with an overview of tuned mechanical damper (TMD) and tuned liquid column damper (TLCD). A brief literature review in the area of TLCD is made. The motivation of the present research is presented in the next section and the organization of the dissertation is finally laid out in detail.

1.1 Overview of passive devices

Passive devices protect a structure by increasing its energy dissipation capacity. A supplemental damping system works by absorbing a portion of the input energy to a structure thereby reducing energy dissipation demands and preventing damage to the primary structure. This effect is achieved either by conversion of kinetic energy to heat or through the transfer of energy among vibration modes. The first method utilizes devices that operate on principles such as frictional sliding, yielding of metals, phase transformation in metals, and deformation of viscoelastic solids or fluids, examples include metallic yield dampers, friction dampers, viscoelastic dampers, viscous fluid dampers, etc. The second method of energy dissipation incorporates dynamic vibration absorbers, such as tuned mechanical damper (TMD), tuned liquid damper (TLD) and tuned liquid column damper (TLCD). The following Sections are conceptually concerned with TMD and TLCD.

1.1.1 The tuned mechanical damper, TMD

The tuned mechanical damper is the most commonly used passive device, which consists of a mass attached to the building through a spring and a dashpot. Alternatively, a pendulum-type mechanical damper is used in high-rise buildings, e.g. in the Taipei 101 tower. In order to be effective, its parameters need to be optimally tuned to the building dynamic characteristics, thus imparting indirect damping through modification of the combined structural system.

Den Hartog¹ derived expressions for the optimum damping coefficient and the tuning ratio (i.e., ratio of the absorber frequency to the natural frequency of the undamped single-degree-of-freedom (SDOF)-primary system) for the coupled SDOF-TMD system subjected to harmonic excitation. The optimum absorber parameters that minimize the displacement response of the primary system were found to be simple functions of the mass ratio (ratio of mass of SDOF-structure and damper).

1.1.2 The tuned liquid column damper, TLCD and its extension to include a gas-spring, TLCGD

TLCD is an effective passive energy absorbing device that has been proposed for controlling vibrations of structures under different dynamic loading conditions, see e.g. Sakai². Such a TLCD consists of a rigid, U-shaped tube of rectangular, oval or circular cross-section that is smoothly integrated into a building and partially filled with a liquid, preferably water. Similar to the TMD, the vibration decreasing capability is based on an energy transfer from the supporting host structure to the TLCD, thereby including a relative flow of the water column. Finally, the energy is dissipated by viscous and turbulent fluid damping. TLCDS provide many advantages, when compared to TMD, such as low cost, no moving mechanical parts, relatively easy installation in new buildings or in retrofitting existing structures, simple maintenance requirements. Indeed, a TLCD may not cause additional cost or weight if a water tank used for water supply and fire fighting is incorporated into design of a TLCD. Furthermore, they can be combined with active control mechanisms to function as hybrid systems.

Hochrainer³ invented the gas-spring effect. Applications of the TLCD with a sealed piping

system, tuned liquid column gas damper (TLCGD), to tall buildings or slender bridges, see Hochrainer and Ziegler⁴, Reiterer⁵, Reiterer and Ziegler⁶, can effectively reduce steady state vibrations, equally well as a direct increase of the modal structural damping. In the passive mode, a sealed piping system with gas pressure in the equilibrium state properly adjusted extends the frequency range of application even of large sized TLCGD up to about 5 Hz and limits the maximum speed of the fluid-gas interface.

The experimental and theoretical work by Kwok⁷ and further studies on TLCD in recent years have demonstrated its high effectiveness in suppressing wind induced structural vibration. To reduce transient vibration peaks in the initial period of the strong motion phase of an earthquake, a novel active control by pressurising gas above the liquid column-ATLCD is required as the cheap counterpart to the ATMD. Hochrainer³ invented such an ATLCD. A semi-active MR-TLCD control system using magnetorheological fluid was recently proposed to counteract the vibrations of wind-excited tall buildings⁸.

Under the earthquake loads, plan-asymmetric buildings with irregular distributions of mass and/or stiffness are likely to undergo torsional responses coupled with the lateral vibrations. In this dissertation, TLCGD instead of TMD are used to mitigate bending and torsional vibrations of tall buildings. Active control is outside of the scope of this dissertation.

In this study, the passive action of TLCGD is considered and the coupled torsional response of plan-asymmetric structures is investigated. The dynamic model of a building is established by assigning three-degrees-of-freedom to each floor in a first attempt of condensation of a large system, second attempt is by modal truncation. Each floor is represented as a rigid diaphragm that is horizontally obliquely displaced and rotated about the vertical axis during earthquake or wind induced vibrations. Thus it has three degrees-of-freedom. These modal expansion displacements and the small rotation combine approximately to a rotation about the floor's center of velocity. If such a center falls outside of the floor, translations dominate and the ideal position of the trace of the mid-plane of the U-shaped TLCGD requires its normal distance from this center maximum. If the modal center lies within the floor plan, the novel torsional tuned liquid column gas damper (TTLCGD) with its horizontal curved piping section enclosing the center for best efficiency becomes superior. The plane TLCGD and TTLCGD are applied in numerical studies in a total of eight different small scale building models and a 30-storey high-rise eccentric structure⁹.

Tuning of the TLCGD is performed in several steps. At first, the linearized model is tuned with respect to a selected mode of the structure using the analogy to TMD tuning³ with the properly transformed Den Hartog's optimal parameters taken into account¹. In a second step, improvements of the performance in MDOF structures are achieved by considering the neighbouring modes as well, in a state space optimization with the Den Hartog parameters as starting values. Such a fine-tuning renders the optimal parameters modified. Final adjustments are easily performed in the course of *in-situ* testing by adjusting the equilibrium gas pressure in TLCGD.

1.2 Motivation of the research

Through intensive research and development in recent years, TLCD has been accepted as an effective vibration control device for new and in retrofit for existing civil engineering structures to enhance their reliability in suppressing horizontal vibrations forced by earthquakes, wind-gusts and traffic loads, and there are relatively fewer studies in literature on the suppression of torsional vibrations of tall buildings by using TLCD. However, a real building usually possesses a large number of degrees of freedom and is actually asymmetric to some degree even with a nominally symmetric plan. It will undergo coupled vibrations simultaneously under purely translational excitations. The earthquakes acting on tall buildings are analytically expressed as 3-D model. Meanwhile, here the 3-D responses of tall buildings may be coupled due to the eccentricities between the stiffness and mass centers of the buildings. Therefore, reducing the large earthquake-induced coupled torsional vibration

naturally becomes a critical consideration in the design of earthquake-sensitive tall buildings. In these cases, when torsional responses of the buildings dominate, extensive analytical and numerical work has been done to present the calculation method and optimize the parameters of TLCGD systems. The low frequency modes are often prominent in the responses of tall buildings and high-rise structures, and controlling only the first mode is not sufficient for the expected effectiveness. Therefore, the approach for reducing the multi-modal responses of tall buildings with multiple TLCGDs is presented here. The numerical examples show that the spatially placed TLCGDs system can reduce lateral-torsional responses significantly with fairly small mass ratios assigned.

1.3 Literature review

In recent years, there has been an increasing interest in the application of TLCD to the problem of vibration suppression in civil structures. Since Sakai and his co-authors² developed the idea of TLCD in 1989 for the purpose of structural vibration suppression, many successors had employed it in many civil engineering applications to verify its control effectiveness. Some references discuss the determination of optimal parameters, such as the optimal frequency tuning ratio and optimal head loss coefficient.

The investigations conducted by Haroun *et al.*¹⁰ showed that the TLCD could reduce lateral vibration of a structure effectively if the parameters of the TLCD were properly selected. Aiming at improving the robustness of TLCD, multiple tuned liquid column damper (MTLCD), which consists of a series of TLCDs with distributed natural frequencies, has been studied by Gao *et al.*¹¹ for reducing lateral vibration of a structure. Xue *et al.*¹² demonstrated that the TLCD could also reduce torsional vibrations of a structure under time-harmonic excitation, and Shum and Xu^{13,14} theoretically and experimentally investigated the effectiveness of TLCD in reducing torsional vibration of a structure. TLCD is thus believed to be an effective device in controlling the lateral or torsional vibration of a building structure. However, there is little information on whether and how TLCDs can most effectively reduce the coupled lateral and torsional vibration of a building structure.

Huo *et al.*⁹ proposed the vibration control methodology of TLCD on eccentric structures, modelled as torsional coupled multi-storey shear structures, excited by multi-dimensional ground motions. The equations of motion of the multi-storey eccentric structure with two TLCDs set in orthogonal directions subjected to multi-dimensional earthquake excitation, are derived. The main parameters such as frequency of TLCD, frequency of structure and eccentric distance are investigated. A 30-storey high-rise eccentric structure under three different types of earthquake records as numerical example is analyzed using TLCD control method. Li *et al.*¹⁵ proposed the TLCD semi-active control of eccentric structures excited by multi-dimensional ground motions as well. This semi-active control strategy is established and implemented based on Artificial Neural Network (ANN). The numerical example of five-storey eccentric structure has shown that it is an effective method presented for controlling the coupled torsion.

The TTLCD is a type of damper that can effectively control the torsional response of structures. The results of free vibration and forced vibration simulations show that TTLCD is effective on the control of structural torsional response, for a first attempt see e.g. Hochrainer³. In a later publication Huo *et al.*¹⁶ presented the optimal parameters of TTLCD for vibration control of offshore platforms based on the stochastic vibration theory. The torsional vibration and torsionally coupled vibration of platform structures are controlled by use of TTLCD. To make frequency tuning more accessible, the sealed TTLCD is proposed in this dissertation, exhibiting the gas-spring effect, TTLCGD.

1.4 Overview of the Dissertation

This dissertation consists of seven chapters, focusing mainly on the coupled lateral and torsional vibration control of asymmetric buildings by means of TLCGD and TTLCGD of various designs.

Chapter 2 provides a theoretical investigation on the performance of TLCGDs for mitigating the coupled lateral and torsional vibrations of single-storey moderately plan-asymmetric space frames which can be modeled as a three degree-of-freedom structure. The biaxial horizontal earthquakes are applied at the rigid foundation as a single-point-excitation. The equation of relative fluid motion in TLCGD is derived using a generalized Bernoulli equation of relative streamlines in a moving frame, see Ziegler¹⁷, page 483. The interaction forces and moments between absorber and structure are determined. Then, the optimum TLCGD parameters are derived by employing Den Hartog's procedure followed by fine-tuning in a state space optimization. Finally, a numerical example is given in order to illustrate the effectiveness of TLCGD in suppressing the time-harmonic excitation and the earthquake response under varying angles of attack as well.

The control performance of TTLCGD over coupled torsional response of single-storey strongly plan-asymmetric space frames excited by ground motions is investigated in Chapter 3. Strong asymmetry renders several modal centers of velocity within the floor plan. Based on the equation of motion for TTLCGD-structure system, the optimal control parameters of TTLCGD are given through the analogy between TTMD and TTLCGD as derived the first time in this dissertation under general conditions. A numerical study shows that the TTLCGD is an effective torsional response control device.

In Chapter 4, in order to enhance the understanding of TLCGD performance and its behavior in the mitigation of coupled torsional motion of tall building, multi-storey moderately plan-asymmetric space frames are studied. Three numerical examples of a multi-storey moderately plan-asymmetric space frame show that TLCGD is very effective to suppress coupled lateral and torsional vibrations under either time-harmonic excitation or earthquake ground motion.

Chapter 5 deals with the optimum parameters of TTLCGD for multi-storey strongly plan-asymmetric space frames under horizontal earthquake excitations. Theoretical development and numerical results show that TTLCGD is adequate for reducing both translations and rotation under earthquakes from any incident angle-of-attack.

In Chapter 6 a 30-storey moderately asymmetric structure described in literature under either time-harmonic excitation or earthquake ground motion is investigated. The author performed a model reduction to 12 degrees of freedom using the method of modal truncation and TLCGDs are installed to mitigate the first three modes.

Finally, Chapter 7 summarizes the results drawn from the research presented in this dissertation.

The studies reported in this dissertation are intended to provide insight into the behavior of TLCGD and TTLCGD and their potential applications to large-scale structures using smaller units in parallel action. This work is expected to accelerate the implementation of these dampers in the areas of vibration mitigation in tall buildings.

References

- [1] DenHartog J.P., Mechanical vibrations. 4th edn, McGraw-Hill, New York, 1956.
- [2] Sakai F., Takaeda S., Tamaki T., Tuned liquid column damper-new type device for suppression of building vibration. In: Proc. Int. Conf. on High-rise Buildings, Nanjing, China, 1989, 926-931.
- [3] Hochrainer M.J., Control of vibrations of civil engineering structures with special emphasis on tall buildings. Dissertation (in English), TU-Wien, A-1040 Vienna, Austria, 2001.
- [4] Hochrainer M.J., Ziegler F., Control of tall building vibrations by sealed tuned liquid column dampers, Structural Control and Health Monitoring. 2006; 6, 13, 980-1002.
- [5] Reiterer M., Damping of vibration-prone civil engineering structures with emphasis on bridges. Dissertation (in German), TU-Wien, A-1040 Vienna, Austria, 2004.
- [6] Reiterer M., Ziegler F., Control of pedestrian-induced vibrations of long-span bridges, Structural Control and

Health Monitoring. 2006; 13, 6, 1003-1027.

[7] Kwok K.C.S., Xu Y.L., Samali B., Control of wind-induced vibrations of tall structures by optimized tuned liquid column dampers, *Computational mechanics*. 1991, 249-254.

[8] Ni Y.Q., Ying Z.G., Wang J.Y., Ko J.M., Spencer B.F., Stochastic optimal control of wind-excited tall buildings using semi-active MR-TLCDs, *Probabilistic Engineering Mechanics*. 2004; 19, 3, 269-277.

[9] Huo L.S., Li H.N., Sun L., Parameter study of TLCD control system excited by multi-dimensional ground motions, *Earthquake Engineering and engineering vibration*. 2001; 21, 4, 147-153.

[10] Haroun M.A., Pires J.A., Won A.Y.J., Suppression of environmentally-induced vibrations in tall buildings by hybrid liquid column dampers, *The Structural Design of Tall Buildings*. 1996; 5, 1, 45-54.

[11] H.Gao, K.S.C. Kwok, B. Samali, Characteristics of multiple tuned liquid column dampers in suppressing structural vibration, *Engineering Structures*. 1993; 21, 1, 216-331.

[12] Xue S.D., Ko J.M., Xu Y.L., Tuned liquid column dampers for suppressing pitching motion of structures, *Engineering Structures*. 2000; 22, 11, 1538-1551.

[13] Shum K.M., Xu Y.L., Multiple-tuned liquid column dampers for torsional vibration control of structures: experimental investigation, *Earthquake Engineering and Structural Dynamics*. 2002; 31, 4, 977-991.

[14] Shum K.M., Xu Y.L., Multiple-tuned liquid column dampers for torsional vibration control of structures: theoretical investigation, *Earthquake Engineering and Structural Dynamics*. 2003; 32, 2, 309-328.

[15] Li H.N., Huo L.S., TLCD semi-active control of eccentric structures using neural networks, 15th ASCE Engineering Mechanics Conference June 2-5, 2003, Columbia University, New York, NY.

[16] Huo L.S., Li H.N., Torsionally coupled response control of offshore platform structures using circular tuned liquid column dampers, *China Ocean Engineering*. 2004; 18, 2, 173-183.

[17] Ziegler F., *Mechanics of Solids and Fluids*, correct reprint of second edition, Springer, New York, 1998.

2 Single-storey Moderately Plan-asymmetric Space Frame with TLCGDs

2.1 Introduction

In this chapter, we investigate how to reduce lateral oblique flexural and torsional vibrations of a single-storey moderately asymmetric structure e.g. caused by earthquakes, by means of plane U-shaped TLCGD. The modal displacements and rotation combine to a sufficiently small rotation about the floor's center of velocity. We define moderate asymmetry if the modal centers of velocity are outside of the floor plan. Since the centre of mass C_M and the centre of stiffness C_S do not coincide for an asymmetric structure, even the uni-directional seismic excitation in general causes a three dimensional in-plane motion of the floor. A model of TLCGD for reducing coupled lateral and torsional motions of such a single-storey mass asymmetric structure is developed. The coupled equations of motion of the TLCGD-main structure are derived considering the floor and damper interaction. Such a substructure model constitutes a theoretical basis of this dissertation and will be used for further studies on the performance and the control effectiveness of TLCGD. The installation of TLCGD on moderately asymmetric structures should be a successful means for reducing the effects of dynamic excitations. In principle, the TLCGD can be set at any position of the selected floor. However, the ideal position of the midplane of the U-shaped TLCGD requires its normal distance from center of velocity maximum. The analogy between TMD and TLCGD when attached to main SDOF-structure under the horizontal base acceleration has been established by Hochrainer¹, see also Hochrainer and Ziegler². It is repeated in Section 2.6 for sake of completeness and it becomes a basic procedure for a more general analogy between TMD and TLCGD when attached to the 3DOF-space frame structure. We also present a numerical example to illustrate that multiple properly tuned TLCGDs in controlling multiple modes considerably increase the effective structural damping and thus reduce the ductility demands in the response to strong ground motions.

2.2 Equation of motion for single-storey moderately asymmetric space frame

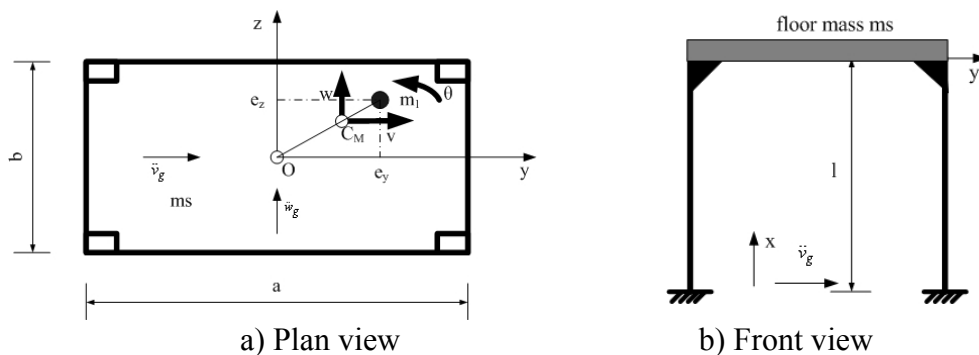


Fig. 2.1: Single-storey moderately asymmetric space frame.

The simplest model is analyzed here: a single-storey shear-type space frame has e.g., a rectangular base of length a and width b , as shown in Fig. 2.1. It consists of a homogenous floor of mass m_S , which is supported by four symmetrically arranged clamped-clamped “massless” and inextensible elastic columns of height l in each corner. The columns have the same anisotropic stiffness k_y and k_z in y - and z -directions. An additional point mass m_1 is

attached off-center on the rigid floor, e_y , e_z denote the eccentricity. Let \ddot{v}_g , \ddot{w}_g denote the free-field horizontal components of a seismic ground acceleration in y -, z -directions, while soil-structure interaction is neglected. The lateral displacements of C_M are denoted v and w , and θ is the rotational angle about the vertical x -axis. The origin O of the Cartesian coordinates happens to be the center of stiffness C_S in this doubly symmetric arrangement of the columns.

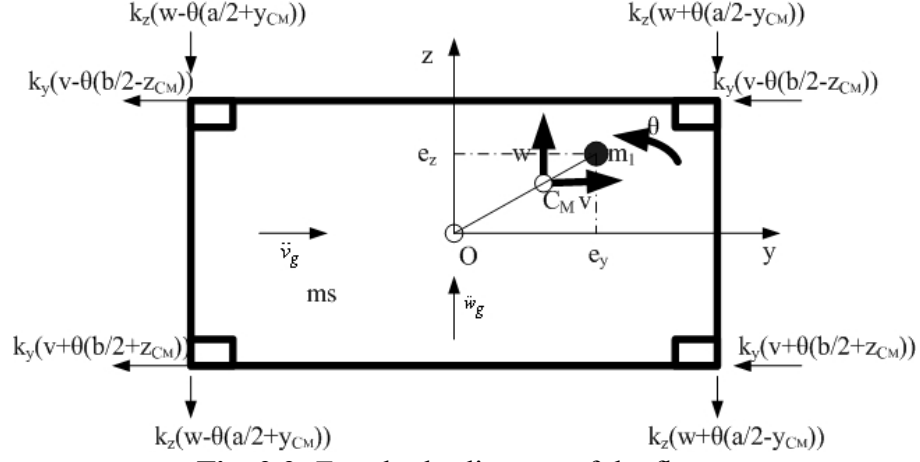


Fig. 2.2: Free-body-diagram of the floor.

The free-body-diagram of single-storey structure under ground excitation as indicated in Fig.2.2 is subjected to the basic laws of conservation of momentum and conservation of angular momentum about the vertical x -axis, see Ziegler³, page 400-411. The coordinates of the center of mass C_M with respect to point O are given by considering the static mass-moments, Fig. 2.2,

$$y_{C_M} = \frac{m_1}{m_S + m_1} e_y, \quad z_{C_M} = \frac{m_1}{m_S + m_1} e_z.$$

(i) Conservation of momentum in the y - z plane:

$$\begin{aligned} (m_S + m_1) \vec{a}_{C_M} &= \vec{R}, \quad \vec{a}_{C_M} = \ddot{v}_t \vec{e}_y + \ddot{w}_t \vec{e}_z, \\ \ddot{v}_t &= \ddot{v}_g + \ddot{v}, \quad \ddot{w}_t = \ddot{w}_g + \ddot{w}, \end{aligned}$$

where \ddot{v}_t and \ddot{w}_t are the absolute accelerations in y - and z -directions, respectively and \vec{R} is the resultant of the external forces, $|\theta| \ll 1$,

$$\vec{R} = -4 \left[k_y (v + z_{C_M} \theta) \vec{e}_y + k_z (w - y_{C_M} \theta) \vec{e}_z \right].$$

Thus, neglecting structural damping, in y - and z -directions we have respectively,

$$(m_S + m_1) \ddot{v} + 4k_y v + 4k_y z_{C_M} \theta = -(m_S + m_1) \ddot{v}_g, \quad (2.1a)$$

$$(m_S + m_1) \ddot{w} + 4k_z w - 4k_z y_{C_M} \theta = -(m_S + m_1) \ddot{w}_g. \quad (2.1b)$$

(ii) Conservation of angular momentum with respect to the center of mass C_M :

$$\frac{d\vec{D}_{C_M}}{dt} = \vec{M}_{C_M}, \quad \vec{D}_{C_M} = D_{C_M} \vec{e}_x, \quad \vec{M}_{C_M} = M_{C_M} \vec{e}_x, \quad D_{C_M} = I_x \dot{\theta}.$$

According to Fig. 2.2, the axial moment of the external forces becomes

$$M_{C_M} = -4k_y z_{C_M} v + 4k_z y_{C_M} w - 4 \left\{ k_y \left[\left(\frac{b}{2} \right)^2 + z_{C_M}^2 \right] + k_z \left[\left(\frac{a}{2} \right)^2 + y_{C_M}^2 \right] \right\} \theta,$$

$$I_x \ddot{\theta} + (k_y b^2 + k_z a^2 + 4k_y z_{C_M}^2 + 4k_z y_{C_M}^2) \theta + 4k_y z_{C_M} v - 4k_z y_{C_M} w = 0, \quad (2.1c)$$

where the mass moment of inertia about the vertical x -axis of the rectangular floor with point mass m_1 is, Fig. 2.2,

$$I_x = m_S (a^2 + b^2) / 12 + m_S (y_{C_M}^2 + z_{C_M}^2) + m_1 \left[(e_y - y_{C_M})^2 + (e_z - z_{C_M})^2 \right] = (m_S + m_1) r_S^2,$$

where r_S denotes the radius of inertia with respect to the center of mass C_M .

The three coupled equations of undamped motion namely Eqs. (2.1a)- (2.1c) are put in the matrix form,

$$\underline{\underline{M}} \ddot{\underline{\underline{x}}} + \underline{\underline{K}} \underline{\underline{x}} = -\underline{\underline{M}} \ddot{\underline{\underline{x}}}_g, \quad \underline{\underline{x}}^T = [v \quad w \quad u_T], \quad \ddot{\underline{\underline{x}}}_g^T = [\ddot{v}_g \quad \ddot{w}_g \quad 0], \quad u_T = \theta r_S, \quad (2.2)$$

where $\underline{\underline{M}}$ and $\underline{\underline{K}}$ are the mass and stiffness matrices of the structure with dimension 3×3 , both are positive definite; $\underline{\underline{x}}$ means the displacement vector in the center of mass of the structure; $\ddot{\underline{\underline{x}}}_g$ denotes the given seismic ground acceleration vector.

The diagonal mass- and the symmetric stiffness matrix of the 3-DOF (degree-of-freedom) structure are deduced from Eqs. (2.1a)- (2.1c) by inspection

$$\underline{\underline{M}} = (m_S + m_1) \begin{bmatrix} 1 & 0 & 0 \\ 0 & 1 & 0 \\ 0 & 0 & 1 \end{bmatrix}, \quad (2.3)$$

$$\underline{\underline{K}} = 4 \begin{bmatrix} k_y & 0 & k_y z_{C_M} / r_S \\ 0 & k_z & -k_z y_{C_M} / r_S \\ k_y z_{C_M} / r_S & -k_z y_{C_M} / r_S & (k_y b^2 + k_z a^2 + 4k_y z_{C_M}^2 + 4k_z y_{C_M}^2) / 4r_S^2 \end{bmatrix}. \quad (2.4)$$

(i) Control of stiffness matrix by direct method, see e.g. Chopra⁴, page 376 and Fig.2.3:

1) $v=1, w=0, u_T = \theta r_S = 0$, 2) $v=0, w=1, u_T = \theta r_S = 0$, 3) $v=0, w=0, u_T = \theta r_S = 1$

$$\begin{aligned} k_{yy} &= 4k_y & k_{yz} &= 0 & k_{y\theta} &= 4k_y z_{C_M} / r_S \\ k_{zy} &= 0 & k_{zz} &= 4k_z & k_{z\theta} &= -4k_z y_{C_M} / r_S \\ k_{\theta y} &= 4k_y z_{C_M} / r_S & k_{\theta z} &= -4k_z y_{C_M} / r_S & k_{\theta\theta} &= (k_y b^2 + k_z a^2 + 4k_y z_{C_M}^2 + 4k_z y_{C_M}^2) / r_S^2 \end{aligned}$$

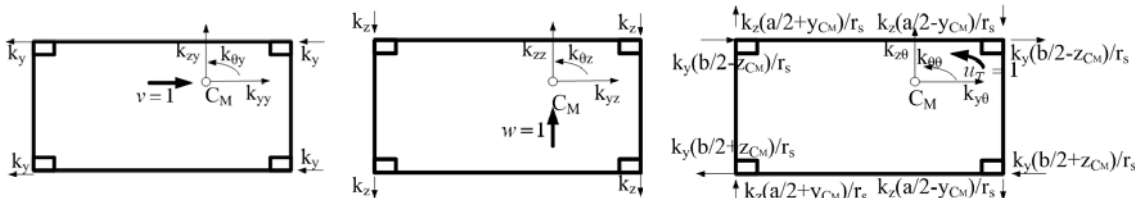


Fig. 2.3: Evaluation of stiffness matrix of single-storey moderately asymmetric space frame: restoring forces indicated.

(ii) Control of the mass matrix by the direct “stiffness method”, see Fig.2.4:

$$\begin{aligned} 1) \quad \ddot{v} &= 1, \ddot{w} = 0, \ddot{u}_T = \ddot{\theta} r_S = 0, & 2) \quad \ddot{v} &= 0, \ddot{w} = 1, \ddot{u}_T = \ddot{\theta} r_S = 0, & 3) \quad \ddot{v} &= 0, \ddot{w} = 0, \ddot{u}_T = \ddot{\theta} r_S = 1 \\ m_{yy} &= m_S + m_1 & m_{zz} &= m_S + m_1 & m_{\theta\theta} &= m_S + m_1 \end{aligned}$$

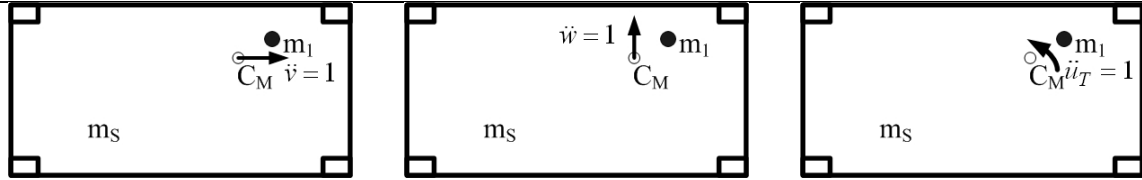


Fig. 2.4: Direct evaluation of mass matrix of single-storey moderately asymmetric space frame: inertial forces indicated.

2.2.1 Effective mass and stiffness of a column

If we consider the mass per unit of length ρA , as well as the stiffness EI of the column both to be constant (for convenience of integration), an approximation of the equation of motion of the flexural vibration in the first natural mode can be determined. An admissible Ritz approximation can be always given affined to a proper static deformation. Hence, see Ziegler³, page 611,

$$w(\xi, t) = q(t)\varphi(\xi), \quad (2.5)$$

where $\varphi(\xi)$ suffices to choose the Hermite shape function for the cc-beam, unit displacement of $x=l$ is 1,

$$H_3(\xi) = -2\xi^3 + 3\xi^2, \quad 0 \leq \xi = x/l \leq 1. \quad (2.6)$$

The kinetic energy becomes simply

$$T = \frac{1}{2} \int_0^1 \dot{w}^2 \rho A l d\xi = \frac{\dot{q}^2}{2} \rho A l \int_0^1 H_3^2(\xi) d\xi = \frac{\bar{m}_1 \dot{q}^2}{2}. \quad (2.7)$$

Thus, the kinetic energy is equivalent to that of a single equivalent mass \bar{m}_1

$$\bar{m}_1 = \int_0^1 H_3^2(\xi) \rho A l d\xi = \frac{13}{35} m_c, \quad m_c = \rho A l, \quad (2.8)$$

where m_c is the mass of column.

The potential energy of the slender column (rigid in shear) is approximated by

$$V = U = \frac{1}{2} \int_0^1 \frac{EI}{l^3} \left(\frac{\partial^2 w}{\partial \xi^2} \right)^2 d\xi = \frac{EI}{2l^3} q^2 \int_0^1 \left(\frac{d^2 H_3}{d\xi^2} \right)^2 d\xi = \frac{kq^2}{2}. \quad (2.9)$$

The effective static stiffness of the cc-column becomes

$$k = \frac{EI}{l^3} \int_0^1 \left(\frac{d^2 H_3}{d\xi^2} \right)^2 d\xi = \frac{12EI}{l^3}. \quad (2.10)$$

The moment of inertia I for standard profiles is listed by Robert⁵.

2.2.2 Influence of the normal force on the stiffness matrix: geometric correction

If a slender column is subjected to a large compressive force, its lateral stiffness is significantly reduced. The geometric correction of stiffness of c-c beam is $k_G = 6N/5l$, where $N < 0$ is the compressive axial force, l is the length of the beam. If the lateral load is less than 0.3 of the critical buckling load, the linear geometric stiffness correction is applicable, see e.g. Clough-Penzien⁶, page 167 and Ziegler³, page 604. A numerical example is studied in Section 2.9.1.

Assuming that additional point mass m_1 is attached on number 1 column, the column has the corrected stiffness \bar{k}_{y1} and \bar{k}_{z1} in y - and z -directions, and other columns have the

same corrected stiffness $\bar{k}_{y2} = \bar{k}_{y3} = \bar{k}_{y4}$ and $\bar{k}_{z2} = \bar{k}_{z3} = \bar{k}_{z4}$ in y - and z -directions, the corrected stiffness matrix can be derived as

$$\begin{aligned}
 k'_{11} &= \bar{k}_{y1} + 3\bar{k}_{y2}, \quad k'_{12} = k'_{21} = 0, \quad k'_{13} = k'_{31} = \left[(\bar{k}_{y1} + 3\bar{k}_{y2})z_{C_M} + (\bar{k}_{y2} - \bar{k}_{y1})b/2 \right] / r_S, \\
 k'_{22} &= \bar{k}_{z1} + 3\bar{k}_{z2}, \quad k'_{23} = k'_{32} = - \left[(\bar{k}_{z1} + 3\bar{k}_{z2})y_{C_M} - (\bar{k}_{z1} - \bar{k}_{z2})a/2 \right] / r_S, \\
 k'_{33} &= \left[(\bar{k}_{y1} + 3\bar{k}_{y2})(b^2/4 + z_{C_M}^2) + (\bar{k}_{z1} + 3\bar{k}_{z2})(a^2/4 + y_{C_M}^2) + (\bar{k}_{y2} - \bar{k}_{y1})bz_{C_M} \right. \\
 &\quad \left. + (\bar{k}_{z2} - \bar{k}_{z1})ay_{C_M} \right] / r_S^2
 \end{aligned} \tag{2.11}$$

i) Position of the center of stiffness

The center of stiffness C_S coincides with the origin O in the floor without considering the geometric correction as the columns have the same anisotropic stiffness. The distance between center of stiffness and center of mass is increased by considering the geometric correction and the rotational response of the structure becomes more prominent. The coordinate of the center of stiffness can be calculated by means of the static stiffness-moments, see Fig.2.5,

$$y_{C_S} = \frac{(\bar{k}_{z1} - \bar{k}_{z2})a/2}{\bar{k}_{z1} + 3\bar{k}_{z2}} < 0, \quad z_{C_S} = \frac{(\bar{k}_{y1} - \bar{k}_{y2})b/2}{\bar{k}_{y1} + 3\bar{k}_{y2}} < 0. \tag{2.12}$$

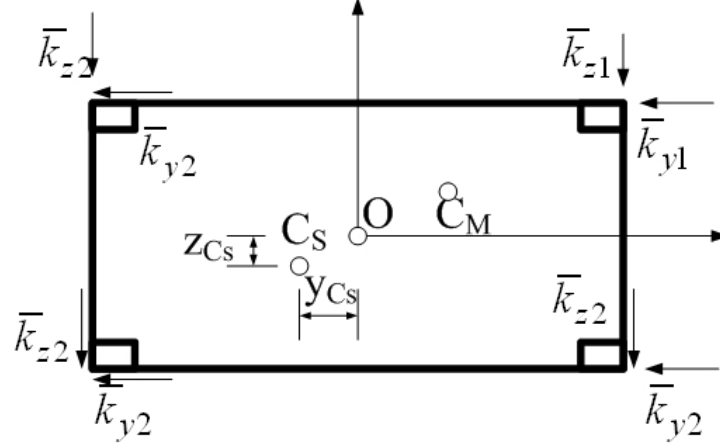


Fig. 2.5: Position of the center of stiffness.

2.2.3 Natural modes of the main structure

The solution of the eigenvalue problem associated with the homogenous Equation (2.2) when considering the corrected stiffness matrix provides the natural circular frequencies ω_n and mode shapes $\vec{\phi}_n$, $n=1,2,3$ of the undamped main system. Consequently, the undamped free vibration is time-harmonic, see e.g. Chopra⁴, page 404,

$$\vec{x}(t) = \vec{\phi}_n A_n \cos \omega_n t. \tag{2.13}$$

After substituting Eq. (2.13) into the homogenous Eq. (2.2), the time-reduced equations result, $\left[\underline{\mathbf{K}}' - \omega_n^2 \underline{\mathbf{M}} \right] \vec{\phi}_n = \vec{0}$. The characteristic equation becomes,

$$\det \left[\underline{\mathbf{K}}' - \omega_n^2 \underline{\mathbf{M}} \right] = 0. \tag{2.14}$$

The three eigenvalues ω_n^2 can be assembled into a diagonal matrix Ω^2

$$\underline{\Omega}^2 = \begin{bmatrix} \omega_1^2 & 0 & 0 \\ 0 & \omega_2^2 & 0 \\ 0 & 0 & \omega_3^2 \end{bmatrix}. \quad (2.15)$$

The orthogonal eigenvectors $\vec{\phi}_n$ corresponding to the natural frequencies ω_n can be assembled into the modal matrix $\underline{\phi}$

$$\underline{\phi} = \begin{bmatrix} \phi_{11} & \phi_{12} & \phi_{13} \\ \phi_{21} & \phi_{22} & \phi_{23} \\ \phi_{31} & \phi_{32} & \phi_{33} \end{bmatrix}. \quad (2.16)$$

$\vec{\phi}_n$ are normalized to either putting $\max|\phi_{ji}|=1$, rendering the modal mass by scalar product $m_k = \vec{\phi}_j^T \underline{M} \vec{\phi}_j$, or ortho-normalized by requiring $m_k = \vec{\phi}_j^T \underline{M} \vec{\phi}_j = 1$.

The numerical solution is a standard solution in Matlab 7.0⁷, performed numerically by calling the function *eig*.

2.3 Position of the modal center of velocity C_V

The point of a rigid body in-plane motion that instantly has zero velocity is called the center of velocity C_V , the acceleration of C_V is generally nonzero. The velocity of any point P of the body can be calculated using the equation $\vec{v}_P = \vec{v}_{C_M} + \hat{\theta} \hat{r}_{PC_M}$, where \hat{r}_{PC_M} is the positively rotated orthogonal vector to \vec{r}_{PC_M} , $\hat{r}_{PC_M} = \vec{e}_x \times \vec{r}_{PC_M}$. If $P=C_V$, its material position with respect to point C_M is defined, see e.g. Ziegler³, page19,

$$\vec{v}_{C_V} = \vec{v}_{C_M} + \hat{\theta} \hat{r}_{C_V C_M} = 0. \quad (2.17a)$$

With respect to small displacements and small rotation, Eq. (2.17a) is multiplied by the time differential to render

$$\delta r_{C_M} + \delta \theta \hat{r}_{C_V C_M} = 0. \quad (2.17b)$$

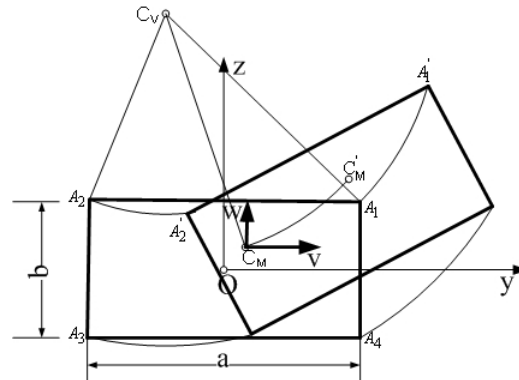


Fig. 2.6: Moderately asymmetric space-frame. Position of the center of velocity is outside floor plan. Small displacements and small rotation $|\theta| \ll 1$ of the floor are understood, exaggerated in the figure.

The centers of mass and stiffness are distant points in the floor of the space frame. Consequently, the modal shapes are defined by rotations of the floor about the modally resulting centers of velocity, a general position of the floor is shown in Fig.2.6. The position vector of the center of velocity C_V is $\vec{r}_{C_V}^T = [y_{C_V} \quad z_{C_V}]$ and the displacement of C_V for

sufficiently small motions is zero. The material vector $\vec{r}_{C_V C_M}^T = [y_{C_V} - y_{C_M} \quad z_{C_V} - z_{C_M}]$, with the rotated material vector $\hat{\vec{r}}_{C_V C_M}^T = [-(z_{C_V} - z_{C_M}) \quad y_{C_V} - y_{C_M}]$, (see Fig.2.6). The coordinates of the center of velocity can be derived under such conditions, putting $\delta\theta \doteq \theta$, $\delta v \doteq v$, $\delta w \doteq w$,

$$y_{C_V} = y_{C_M} - \frac{1}{\theta} w, \quad z_{C_V} = z_{C_M} + \frac{1}{\theta} v. \quad (2.18a)$$

In terms of the components of the modal vector $\vec{\phi}_j$,

$$y_{C_V j} = y_{C_M} - \frac{r_S}{\phi_{j3}} \phi_{j2}, \quad z_{C_V j} = z_{C_M} + \frac{r_S}{\phi_{j3}} \phi_{j1}, \quad \phi_{j3} \neq 0. \quad (2.18b)$$

2.4 The equation of relative motion of the fluid in a TLCDG

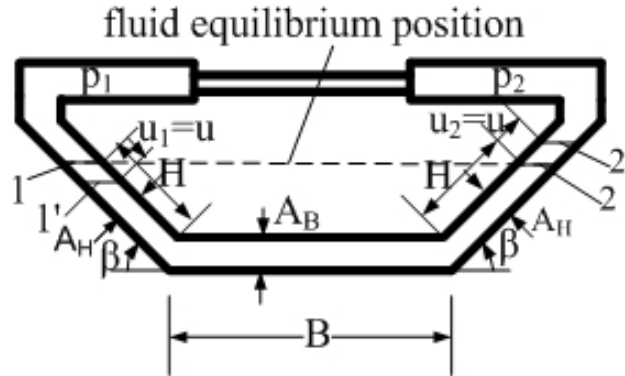


Fig. 2.7: U-shaped tuned liquid column gas damper.

A TLCDG with geometry shown in Fig. 2.7 is a symmetric, U- or V-shaped rigid piping system consisting of one horizontal and two inclined ($\frac{\pi}{4} \leq \beta \leq \frac{\pi}{2}$), partially water-filled pipe sections. Let ρ , B , H , denote the liquid density, $\rho=1000 \text{ kg/m}^3$ for water, the horizontal length of the liquid column, and the length of the liquid column in the inclined pipe sections at rest, respectively. Furthermore A_B , A_H denote the cross-sectional areas of the liquid column assumed to be constant of the horizontal and inclined pipe sections, respectively. The relative motion of the liquid column is described by the displacement $u_1 = u_2 = u(t)$. It is important to emphasize that $u(s', t)$ is a relative displacement of the liquid with respect to the moving frame. Since the ends of the piping system might be closed and filled with gas, an internal gas pressure can build up on either side of the liquid path, denoted p_1 and p_2 with a reference pressure p_0 in equilibrium, see Hochrainer¹ and Hochrainer, Ziegler².

Figure 2.8 shows a model of the single-storey moderately asymmetric structure (for the main system see Section 2.2) equipped with a TLCDG, with its trace under the general angle γ to the y -direction. The position coordinate of the reference point A of the TLCDG is $(y_A, z_A, 0)$.

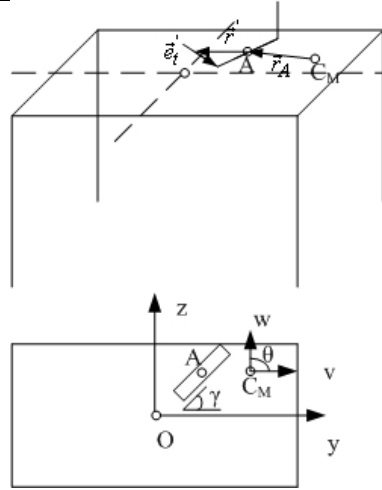


Fig. 2.8: Model of single-storey asymmetric space frame with a single TLCGD, reference configuration. C_M is the center of mass of the main system (without TLCGD). The mass of the piping system is considered in the course of fine-tuning.

The motion of TLCGD during lateral and torsional vibrations is shown in Figs. 2.8 and 2.9. The liquid motion in TLCGD can be classified as two types: i) the global motion of the liquid with the main structure; and ii) its relative flow, assuming the piping system to be rigid. The generalized non-stationary Bernoulli equation can be used to derive the equation of relative fluid motion, see e.g. Ziegler³, page 483. The generalized Bernoulli equation of the ideal fluid-flow takes on the form

$$\int_1^{2'} \bar{a} \cdot \bar{e}'_t ds' = -g(x_2 - x_1) - \frac{1}{\rho}(p_2 - p_1), \quad (2.19)$$

where x_1 , x_2 and g denote the geodesic height of the free surface 1' and 2' and the constant of gravity $g = 9.81 \text{ m/s}^2$; \bar{a} and \bar{e}'_t denote the absolute acceleration of a fluid particle and the relative streamline's tangential direction, respectively.

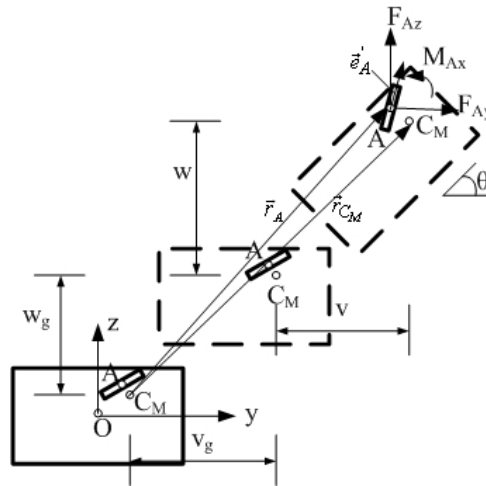


Fig. 2.9: TLCGD under general in-plane acceleration of the floor: \dot{v}_i , \dot{w}_i and $\ddot{\theta}$. Resulting force components F_{Ay} , F_{Az} and moment M_{Ax} , indicated in the instant configuration.

The position of a liquid particle against the center of mass of the main system C_M is described by $\bar{r} = \bar{r}_A + \bar{r}'$, where \bar{r}' denotes the relative position of a fluid particle with respect to point A . The relative position vector \bar{r}' is decomposed into its horizontal and

vertical components, $\vec{r}' = \vec{r}'_{y'z'} + \vec{r}'_x$. \vec{r}_A is the in-plane position vector of point A against origin C_M , see e.g. Ziegler³, page 497. The velocity \vec{v} can be derived straightforwardly by differentiating \vec{r} with respect to time

$$\vec{v} = \frac{d\vec{r}_A}{dt} + \frac{d\vec{r}'}{dt} = \vec{v}_A + \frac{d\vec{r}'}{dt}, \quad (2.20)$$

$$\frac{d\vec{r}'}{dt} = \dot{\theta} \hat{e}_x \times \vec{r}' + \frac{d'\vec{r}'}{dt} = \dot{\theta} \hat{r}'_{y'z'} + \dot{\vec{u}}. \quad (2.21)$$

Here we define $\dot{\vec{u}} = \dot{u}(s', t) \vec{e}'_t$, see Fig. 2.7, as the relative velocity of the fluid particle with respect to the moving reference frame. $\vec{v}_g = \vec{v}_A + \dot{\theta} \hat{r}'_{y'z'}$ denotes the guiding velocity, $\vec{v}_A = \vec{v}_{C_M} + \dot{\theta} \hat{r}_{AC_M}$, see Fig. 2.9. A second differentiation with respect to time renders an expression for the acceleration

$$\vec{a} = \vec{a}_A + \ddot{\theta} \hat{r}'_{y'z'} - \dot{\theta}^2 \vec{r}'_{y'z'} + 2\dot{\theta} \hat{e}_x \times \dot{\vec{u}} + \frac{d'\dot{\vec{u}}}{dt} = \vec{a}_g + \vec{a}_c + \vec{a}', \quad (2.22)$$

with the guiding acceleration $\vec{a}_g = \vec{a}_A + \ddot{\theta} \hat{r}'_{y'z'} - \dot{\theta}^2 \vec{r}'_{y'z'}$ and the Coriolis acceleration $\vec{a}_c = 2\dot{\theta} \hat{e}_x \times \dot{\vec{u}}$, the latter is perpendicular to the relative velocity $\dot{\vec{u}}$. The relative acceleration $\vec{a}' = \frac{d'\dot{\vec{u}}}{dt}$ is the relative rate of the relative velocity and with respect to the moving frame can

be expressed as $\vec{a}' \cdot \vec{e}'_t = \frac{\partial' \dot{u}}{\partial t} + \frac{\partial}{\partial s'} \left(\frac{\dot{u}^2}{2} \right)$, see again Ziegler³, page 498.

Projecting absolute acceleration, Eq. (2.22), along the relative streamline's tangent \vec{e}'_t yields

$$\vec{a} \cdot \vec{e}'_t = \vec{a}_g \cdot \vec{e}'_t + \underbrace{\vec{a}_c \cdot \vec{e}'_t}_0 + \vec{a}' \cdot \vec{e}'_t = \vec{a}_A \cdot \vec{e}'_t - \dot{\theta}^2 \vec{r}'_{y'z'} \cdot \vec{e}'_t + \frac{\partial' \dot{u}}{\partial t} + \frac{\partial}{\partial s'} \left(\frac{\dot{u}^2}{2} \right). \quad (2.23)$$

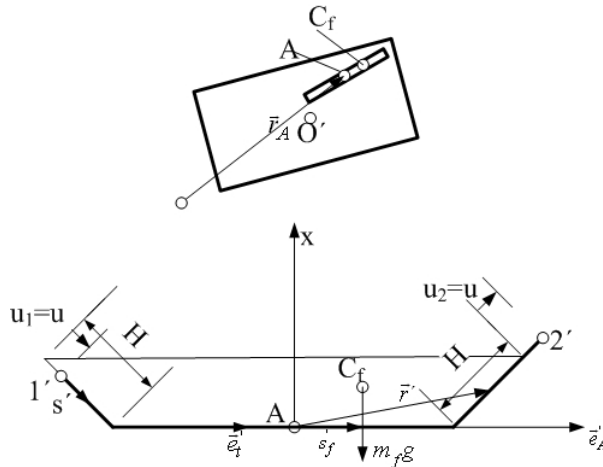


Fig. 2.10: TLCGD in general horizontal motion. Instant position of the fluid center of mass C_f is shown.

The absolute acceleration of the reference point $A (y_A, z_A, 0)$ is given by, Fig. 2.7,
 $\vec{a}_A = a_y \vec{e}_y + a_z \vec{e}_z = \vec{a}_{C_M} + \ddot{\theta} \hat{r}_{AC_M} - \dot{\theta}^2 \vec{r}_{AC_M}$, $\vec{r}_{AC_M} = (y_A - y_{C_M}) \vec{e}_y + (z_A - z_{C_M}) \vec{e}_z$,
 $\hat{r}_{AC_M} = -(z_A - z_{C_M}) \vec{e}_y + (y_A - y_{C_M}) \vec{e}_z$, thus,

$$a_y = \ddot{v}_g + \ddot{v} - (z_A - z_{C_M})\ddot{\theta} - (y_A - y_{C_M})\dot{\theta}^2, a_z = \ddot{w}_g + \ddot{w} + (y_A - y_{C_M})\ddot{\theta} - (z_A - z_{C_M})\dot{\theta}^2 \quad (2.24)$$

where the seismic ground acceleration, a common time function is understood, is \ddot{v}_g in y -direction, \ddot{w}_g in z -direction. \ddot{v} , \ddot{w} and $\ddot{\theta}$ are the acceleration of the floor's center of mass in y - and z -directions and the angular acceleration of the floor, respectively. \vec{a}_A projected in \vec{e}'_A -direction is

$$\vec{a}_A \cdot \vec{e}'_A = a_y \cos(\gamma + \theta) + a_z \sin(\gamma + \theta). \quad (2.25)$$

For the inclined segments, Fig. 2.10: $0 \leq s' \leq H - u_1$: $\vec{e}'_A \cdot \vec{e}'_t = \cos \beta$,

$$0 \leq s' \leq H + u_2$$
: $\vec{e}'_A \cdot \vec{e}'_t = \cos \beta$.

For the horizontal segment, Fig. 2.10: $0 \leq s' \leq B$: $\vec{e}'_A \cdot \vec{e}'_t = 1$.

Using $u_1 = u_2 = u(t)$ and the continuity equation $\dot{u}(s', t) A(s') = \text{const.}$, the integral term, see Eq. (2.19), becomes

$$\int_1^2 \vec{a}_A \cdot \vec{e}'_t ds' = [(H - u) \cos \beta + B + (H + u) \cos \beta] (\vec{a}_A \cdot \vec{e}'_A) = (B + 2H \cos \beta) (\vec{a}_A \cdot \vec{e}'_A), \quad (2.26)$$

For the inclined segments:

$$0 \leq s' \leq H - u_1: \vec{r}'_{y'z'} = -\left[\frac{B}{2} + (H - u_1) \cos \beta - s' \cos \beta\right] \vec{e}'_A,$$

$$\vec{r}'_{y'z'} \cdot \vec{e}'_t = -\left[\frac{B}{2} + (H - u_1) \cos \beta - s' \cos \beta\right] \cos \beta, \quad (2.27)$$

$$0 \leq s' \leq H + u_2: \vec{r}'_{y'z'} = \left(\frac{B}{2} + s' \cos \beta\right) \vec{e}'_A, \quad \vec{r}'_{y'z'} \cdot \vec{e}'_t = \left(\frac{B}{2} + s' \cos \beta\right) \cos \beta. \quad (2.28)$$

For the horizontal segment: $0 \leq s' \leq B$:

$$\vec{r}'_{y'z'} = -\left(\frac{B}{2} - s'\right) \vec{e}'_A, \quad \vec{r}'_{y'z'} \cdot \vec{e}'_t = -\left(\frac{B}{2} - s'\right). \quad (2.29)$$

Substituting $u_1 = u_2 = u(t)$, the integral terms become

$$-\dot{\theta}^2 \int_1^2 \vec{r}'_{y'z'} \cdot \vec{e}'_t ds' = -\dot{\theta}^2 u (B \cos \beta + 2H \cos^2 \beta), \quad (2.30)$$

$$\int_1^2 \frac{\partial}{\partial s'} \left(\frac{\dot{u}^2}{2} \right) ds' = \frac{1}{2} (\dot{u}_2^2 - \dot{u}_1^2) = 0 \quad (\text{symmetry}), \quad (2.31)$$

$$\int_1^2 \frac{\partial \dot{u}}{\partial t} ds' = \ddot{u} (H - u_1) + \ddot{u} B \frac{A_H}{A_B} + \ddot{u} (H + u_2) = \left(2H + B \frac{A_H}{A_B} \right) \ddot{u}, \quad (2.32)$$

$$x_2 - x_1 = (H + u_2) \sin \beta - (H - u_1) \sin \beta = 2u \sin \beta. \quad (2.33)$$

If the piping system is not sealed, then the air pressure at the free surface is approximately equal to the ambient pressure $p_1 = p_2 = p_0$, Figure 2.7 and the pressure difference vanishes. If the piping system is sealed, the gas inside the air chamber is quasi-statically compressed, see Ziegler³, page 88 by the liquid surface in sufficiently slow motion (piston theory). Hence, the pressure difference $p_2 - p_1$ in Eq. (2.19) in the range of linearized gas compression, i.e. if the maximum fluid-stroke is limited by $\max|u| \leq H_a/3$, changes the undamped natural circular frequency of the TLCDG defined in Equation (2.34a), Hochrainer¹ and Hochrainer, Ziegler². Thus, $p_2 - p_1 \approx 2np_0u/H_a$, $1 \leq n \leq 1.4$. n is the

polytropic index, which is determined by the type of quasi-static state-change of the gas. For an adiabatic process of any two atomic gas $n=1.4$ whereas for the isothermal (slow) process $n=1.0$, Ziegler³, page 88. Any other polytropic process is in between those two extreme situations. H_a denotes the effective height of the gas volume at rest $V_0 = A_H H_a$.

Finally, the experimentally observed averaged turbulent damping $\delta_L |\dot{u}| \dot{u}$ must be added, see Hochrainer¹, where $\delta_L = \frac{\lambda}{2L_{eff}}$ is the head loss coefficient. Substitution of Eqs. (2.26)-

(2.33) into Eq. (2.19), adding the turbulent pressure loss and considering the linearized gas compression yield the nonlinear and parametrically forced ($\beta < \pi/2$) equation of motion of the relative fluid motion in the TLCGD,

$$\ddot{u} + \delta_L |\dot{u}| \dot{u} + \omega_A^2 \left(1 - \kappa_1 \frac{\dot{\theta}^2}{\omega_A^2} \right) u = -\kappa (\vec{a}_A \cdot \vec{e}'_A) \quad (2.34)$$

$$\kappa = \frac{B + 2H \cos \beta}{L_{eff}}, \quad \kappa_1 = \kappa \cos \beta, \quad L_{eff} = 2H + \frac{A_H}{A_B} B,$$

$$\omega_A = \sqrt{\frac{2g \sin \beta}{L_{eff}}} \quad (\text{"open TLCD", no gas-spring}),$$

$$\omega_A = \sqrt{\frac{2g}{L_{eff}} \left(\sin \beta + \frac{h_0}{H_a} \right)}, \quad h_0 = np_0 / \rho g \quad (\text{linearized gas-spring}), \quad 1 \leq n \leq 1.4. \quad (2.34a)$$

L_{eff} can be considered as the length of an equivalent uniform liquid column with constant cross sectional area A_H rendering the same natural circular frequency ω_A of the TLCD; κ , κ_1 are geometry dependent coupling factors linking the floor acceleration and the TLCGD excitation, respectively. Furthermore, p_0 , ρ and g denote the gas pressure in equilibrium, the liquid density, e.g. water $\rho = 1000 \text{ kg/m}^3$ and the gravity constant. The TLCGD are ideally suited to extend the frequency range of civil engineering applications by properly adjusting the equilibrium gas-pressure p_0 .

The stiffness of TLCGD, $\omega_A^2 \left(1 - \kappa_1 \frac{\dot{\theta}^2}{\omega_A^2} \right)$ turns out to be timevariant for $\beta < \pi/2$, i.e. unwanted parametric forcing is present due to rotation about the vertical x -axis. For small rotations $|\theta| \ll 1$, $\cos \theta \doteq 1$, $\sin \theta \doteq \theta$, $\tan \theta \doteq \theta$, the right hand side of Eq. (2.34) becomes approximately $\kappa a_y \left(1 + \frac{a_z}{a_y} \theta \right)$ for the TLCGD oriented parallel to the y -direction.

In the course of the tuning procedure, an equivalent linearized damping coefficient $C_A = 2m_f \zeta_A \omega_A$ might be used to replace the nonlinear turbulent damping term, where $\zeta_A = 4U_0 \delta_L / 3\pi$ is the linear damping ratio proportional to the amplitude U_0 of a time harmonic relative fluid flow for details of equivalent linearization. It is achieved by Hochrainer¹, page 74. Approximately, we put $U_0 = \max |u|$ in any motion. If the damping coefficient ζ_A exceeds the cut-off value of parametric resonance, the influence of parametric excitation becomes negligible, see Reiterer⁸, page 77 and Reiterer, Ziegler⁹.

Ziegler¹⁰ pointed out the speed limitation of the fluid-gas interface to keep the interface intact and thus to allow the application of the piston theory, based on Lindner-Silvester and Schneider¹¹,

$$\max |\dot{u}| = 2\pi f \max |u| < 10m/s. \quad (2.35)$$

Substituting the acceleration components, Eq. (2.24) into Eq. (2.34), and further linearizing the forcing term yield the simplified and linearized equation of motion for the relative fluid flow in the TLCGD in proper form for tuning and to be compared to the equivalent TMD-equation,

$$\ddot{u} + 2\zeta_A \omega_A \dot{u} + \omega_A^2 u = -\kappa \left\{ \left[\ddot{v}_g + \ddot{v} - (z_A - z_{C_M}) \ddot{\theta} \right] \cos \gamma + \left[\ddot{w}_g + \ddot{w} + (y_A - y_{C_M}) \ddot{\theta} \right] \sin \gamma \right\}. \quad (2.36)$$

We can see that the left-hand terms in Eq. (2.36) are corresponding to the vibrational terms of the relative liquid motion and the right-hand terms in Eq. (2.36) can be regarded as the linearized portions of the generalized external forces causing the motion of the liquid.

2.5 The natural frequency of TLCGD in relation to the linear frequency of the mathematical pendulum

The frequency of the mathematical pendulum (rigid massless rod with a point-mass, attached at a pivot point) for small angular motion is approximately constant and solely

depends on its length L_0 , $f_A = \sqrt{\frac{g/\pi^2}{4L_0}}$ (Hz). Thus, its length is related to a given frequency

by a hyperbola, Fig. 2.11,

$$L_0 = (g/\pi^2) / (4f_A^2). \quad (2.37)$$

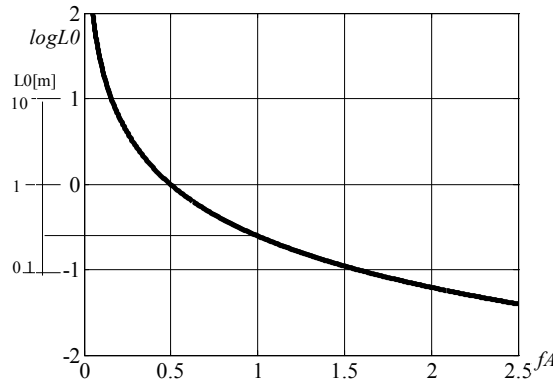


Fig. 2.11: Relation of length and frequency of the mathematical pendulum, $f_A = 1\text{Hz}$, $L_0 = 0.25\text{m}$.

The natural frequency of the open TLCD, i.e. without a gas-spring is, Eq. (2.34a),

$$f_A = \frac{\omega_A}{2\pi} = \sqrt{\frac{(g/\pi^2)}{4(L_{eff}/2)}} \sin \beta \text{ (Hz)}. \text{ If TLCD and the pendulum have the same frequency, we}$$

can write the relation $L_{eff} = 2L_0 \sin \beta$. The natural frequency of the TLCD is thus practically limited to frequencies below 0.5 Hz. The length of a pendulum that would have a frequency of 0.5 Hz is about $L_0 = 1\text{m}$ and thus the effective length of the equivalent TLCD is just $L_{eff} = 1.4\text{m}$ for $\beta = \pi/4$.

Taking into account Eq. (2.34a), the frequency of a TLCGD, with linearized gas-spring effect is rewritten as

$$f_A = \frac{\omega_A}{2\pi} = \sqrt{\frac{(g/\pi^2)}{4(L_{eff}/2)} \left(\sin \beta + \frac{h_0}{H_a} \right)}.$$

If the TLCGD and the mathematical pendulum have the same frequency, we can determine the parameters of the gas-spring, crucial for frequency tuning, in terms of the effective liquid column length L_{eff} as

$$h_0/H_a = L_{eff}/2L_0 - \sin \beta. \quad (2.38)$$

Equation (2.38) determines the gas volume $A_H H_a$ if for some reasons the equilibrium pressure p_0 and thus h_0 is assigned. In some applications the atmosphere pressure is a suitable choice.

2.6 Control forces of TLCGD

To couple the TLCGD with the main structure it becomes important to know the interface reactions. Assuming that the dead weight of a rigid piping system has been added to the corresponding floor mass, only the interaction forces between the massless, rigid, liquid filled piping system and the supporting floor are considered. F_{Ay} , F_{Az} and M_{Ax} the control forces in y , z and θ directions are derived by conservation of momentum and angular momentum of the moving fluid.

(i) Instant coordinates of center of fluid mass C_f , conservation of momentum $\vec{R} = m_f \vec{a}_f$.

The instant position of C_f with respect to reference point A is given by $\vec{r}'_f + x_f \vec{e}_x$, $\vec{r}'_f = s'_f \vec{e}'_A$,

see again Fig. 2.10. Hence, $\vec{r}_f = \vec{r}_A + \vec{r}'_f + x_f \vec{e}_x$,

$$\frac{d\vec{r}'_f}{dt} = \dot{s}'_f \vec{e}'_A + s'_f \dot{\theta} \hat{e}'_A, \quad \vec{v}_f = \frac{d\vec{r}_f}{dt} = \vec{v}_A + \dot{s}'_f \vec{e}'_A + s'_f \dot{\theta} \hat{e}'_A + \dot{x}_f \vec{e}_x, \quad (2.39)$$

$$\vec{a}_f = \frac{d\vec{v}_f}{dt} = \vec{a}_A + (\ddot{s}'_f - s'_f \dot{\theta}^2) \vec{e}'_A + (2\dot{s}'_f \dot{\theta} + s'_f \ddot{\theta}) \hat{e}'_A + \ddot{x}_f \vec{e}_x, \quad (2.40)$$

and by means of the static fluid mass-moments

$$\begin{aligned} m_f s'_f &= \rho A_H (H+u) \left(\frac{B}{2} + \frac{H+u}{2} \cos \beta \right) - \rho A_H (H-u) \left(\frac{B}{2} + \frac{H-u}{2} \cos \beta \right), \\ &= \rho A_H u (B + 2H \cos \beta) \end{aligned} \quad (2.41)$$

$$m_f x_f = \rho A_H (H+u) \frac{H+u}{2} \sin \beta + \rho A_H (H-u) \frac{H-u}{2} \sin \beta = \rho A_H (H^2 + u^2) \sin \beta. \quad (2.42)$$

Hence, we define

$$s'_f = \frac{B + 2H \cos \beta}{L_1} u = \bar{\kappa} u, \quad \dot{s}'_f = \bar{\kappa} \dot{u}, \quad \ddot{s}'_f = \bar{\kappa} \ddot{u},$$

$$x_f = \frac{(H^2 + u^2) \sin \beta}{L_1} = \bar{\kappa}_2 \frac{1}{2H} (H^2 + u^2), \quad \dot{x}_f = \bar{\kappa}_2 \frac{1}{H} u \dot{u}, \quad \ddot{x}_f = \bar{\kappa}_2 \frac{1}{H} (\dot{u}^2 + u \ddot{u}). \quad (2.43)$$

with the following two geometry coefficients and the total fluid mass,

$$\bar{\kappa} = \kappa L_{eff} / L_1, \quad \bar{\kappa}_2 = (2H/L_1) \sin \beta, \quad m_f = \rho \int_{l'}^{l''} A(s') ds' = \rho A_H L_1, \quad L_1 = 2H + \frac{A_B}{A_H} B. \quad (2.44)$$

L_1 equals L_{eff} in the case of $A_H = A_B$.

Substituting Eq. (2.43) into Eq. (2.40) confirms, after multiplication with m_f the result, Eq. (2.45).

$$\vec{R} = m_f \vec{a}_A + m_f \bar{\kappa}_2 \frac{1}{H} (\dot{u}^2 + u\ddot{u}) \vec{e}_x + m_f \bar{\kappa} (\ddot{u} - u\dot{\theta}^2) \vec{e}'_A + m_f \bar{\kappa} (2\dot{u}\dot{\theta} + u\ddot{\theta}) \hat{\vec{e}}'_A, \quad (2.45)$$

where

$$\vec{a}_A = [a_y \cos(\gamma + \theta) + a_z \sin(\gamma + \theta)] \vec{e}'_A + [-a_y \sin(\gamma + \theta) + a_z \cos(\gamma + \theta)] \hat{\vec{e}}'_A. \quad (2.46)$$

It must be mentioned, that static dead weight loading of fluid mass is not included in the unwanted vertical reaction force component F_{Ax} . However, when working with framed structures, this vertical force is generally negligible. Equation (2.45) renders the components of the control forces acting on the piping system, Fig. 2.9,

$$F_A \vec{e}'_A = m_f [a_y \cos(\gamma + \theta) + a_z \sin(\gamma + \theta)] + m_f (\bar{\kappa} \ddot{u} - \bar{\kappa} u \dot{\theta}^2), \quad (2.47)$$

$$F_A \hat{\vec{e}}'_A = m_f [-a_y \sin(\gamma + \theta) + a_z \cos(\gamma + \theta)] + m_f (2\bar{\kappa} \dot{u} \dot{\theta} + \bar{\kappa} u \ddot{\theta}), \quad (2.48)$$

and when rotated

$$F_{Ay} = m_f [a_y + (\bar{\kappa} \ddot{u} - \bar{\kappa} u \dot{\theta}^2) \cos(\gamma + \theta) - (2\bar{\kappa} \dot{u} \dot{\theta} + \bar{\kappa} u \ddot{\theta}) \sin(\gamma + \theta)], \quad (2.49)$$

$$F_{Az} = m_f [a_z + (\bar{\kappa} \ddot{u} - \bar{\kappa} u \dot{\theta}^2) \sin(\gamma + \theta) + (2\bar{\kappa} \dot{u} \dot{\theta} + \bar{\kappa} u \ddot{\theta}) \cos(\gamma + \theta)]. \quad (2.50)$$

Equations (2.49) and (2.50) are simplified under the condition $|\theta| \ll 1$ and the essential linear parts become

$$F_{Ay} = m_f [\ddot{v}_g + \ddot{v} - (z_A - z_{C_M}) \ddot{\theta}] + \bar{\kappa} m_f \ddot{u} \cos \gamma, \quad (2.51)$$

$$F_{Az} = m_f [\ddot{w}_g + \ddot{w} + (y_A - y_{C_M}) \ddot{\theta}] + \bar{\kappa} m_f \ddot{u} \sin \gamma. \quad (2.52)$$

(ii) Use of the law of conservation of the angular momentum of the fluid body, see Ziegler³, page 405.

The resultant of the acting moments can be calculated by, with respect to the accelerated point of reference A ,

$$\frac{d\vec{D}_A}{dt} + m_f (\vec{r}'_f + x_f \vec{e}_x) \times \vec{a}_A = \vec{M}_A, \quad \frac{d\vec{D}_A}{dt} = \frac{d'\vec{D}_A}{dt} + \dot{\theta} (\vec{e}_x \times \vec{D}_A), \quad (2.53)$$

relative angular momentum

$$\vec{D}_A = \int_{m_f} (\vec{r}' \times \vec{v}') dm_f = \int_{m_f} [\vec{r}' \times (\dot{\theta} \hat{\vec{r}}'_{y'z'} + \dot{\vec{u}})] dm_f \quad (2.54)$$

$$= \rho \left[\dot{\theta} \int_{1'}^{2'} A(s') (\vec{r}' \times \hat{\vec{r}}'_{y'z'}) ds' + \int_{1'}^{2'} A(s') \dot{u}(s', t) (\vec{r}' \times \vec{e}'_t(s')) ds' \right]$$

$$0 \leq s' \leq H - u_1: \quad \vec{r}' \times \vec{e}'_t = -\frac{B}{2} \sin \beta \hat{\vec{e}}'_A, \quad 0 \leq s' \leq H + u_2: \quad \vec{r}' \times \vec{e}'_t = -\frac{B}{2} \sin \beta \hat{\vec{e}}'_A,$$

$$0 \leq s' \leq B: \quad \vec{r}' \times \vec{e}'_t = 0$$

$$\rho \int_{1'}^{2'} A(s') \dot{u}(s', t) (\vec{r}' \times \vec{e}'_t(s')) ds' = -\bar{\kappa}_2 m_f \frac{B}{2} \dot{u} \hat{\vec{e}}'_A \quad (2.55)$$

$$\begin{aligned}
 \rho \dot{\theta} \int_1^{2'} A(s') |\vec{r}'_{y'z'}|^2 ds' &= \rho \dot{\theta} A_H \int_0^{H-u} \left[-\left(\frac{B}{2} + (H-u_1) \cos \beta - s' \cos \beta \right) \right]^2 ds' \\
 + \rho \dot{\theta} A_B \int_0^B \left[-\left(\frac{B}{2} - s' \right) \right]^2 ds' &+ \rho \dot{\theta} A_H \int_0^{H+u} \left(\frac{B}{2} + s' \cos \beta \right)^2 ds' \quad , \\
 = \rho \dot{\theta} A_H \left[\frac{A_B}{A_H} \frac{B^3}{12} + \frac{B^2}{2} H + B(H^2 + u^2) \cos \beta + \left(\frac{2}{3} H^3 + 2Hu^2 \right) \cos^2 \beta \right]
 \end{aligned} \quad (2.56)$$

$$0 \leq s' \leq H - u_1 :$$

$$\vec{r}'_x \times \hat{r}'_{y'z'} = -\left[(H - u_1) \sin \beta - s' \sin \beta \right] \left[-\left(\frac{B}{2} + (H - u_1) \cos \beta - s' \cos \beta \right) \right] \vec{e}'_A,$$

$$0 \leq s' \leq H + u_2 : \quad \vec{r}'_x \times \hat{r}'_{y'z'} = -(s' \sin \beta) \left(\frac{B}{2} + s' \cos \beta \right) \vec{e}'_A,$$

$$\rho \dot{\theta} \int_1^{2'} A(s') (\vec{r}'_x \times \hat{r}'_{y'z'}) ds' = -\rho \dot{\theta} A_H \left[HBu \sin \beta + \left(\frac{2}{3} u^3 + 2H^2 u \right) \sin \beta \cos \beta \right] \vec{e}'_A, \quad (2.57)$$

$$\begin{aligned}
 \vec{D}_A &= m_f \left\{ -\left[\frac{HB}{L_1} + \left(\frac{2}{3} \frac{u^2}{L_1} + 2 \frac{H^2}{L_1} \right) \cos \beta \right] u \dot{\theta} \sin \beta \vec{e}'_A - \bar{\kappa}_2 \frac{B}{2} \dot{u} \hat{e}'_A \right. \\
 &\left. + \left[\frac{A_B}{A_H} \frac{B^3}{12L_1} + \frac{B^2}{2L_1} H + B \left(\frac{H^2}{L_1} + \frac{u^2}{L_1} \right) \cos \beta + \left(\frac{2}{3} \frac{H^3}{L_1} + 2 \frac{Hu^2}{L_1} \right) \cos^2 \beta \right] \dot{\theta} \vec{e}_x \right\} \quad , \\
 &\quad (2.58)
 \end{aligned}$$

$$D_{Ax} = m_f (\bar{\kappa}_3 H^2 + \bar{\kappa}_1 u^2) \dot{\theta}, \quad (2.59)$$

with the following two geometry coefficients

$$\bar{\kappa}_3 = \bar{\kappa}_{T3} \left[\left(\frac{B}{2H} \right)^2 + \frac{A_B}{3A_H} \left(\frac{B}{2H} \right)^3 + \frac{B}{2H} \cos \beta + \frac{1}{3} \cos^2 \beta \right], \quad \bar{\kappa}_1 = \kappa_1 \frac{L_{eff}}{L_1}, \quad \bar{\kappa}_{T3} = \frac{2H}{L_1},$$

$$\frac{dD_{Ax}}{dt} = m_f \left[\bar{\kappa}_3 H^2 \ddot{\theta} + \bar{\kappa}_1 (u^2 \ddot{\theta} + 2ui\dot{\theta}) \right]. \quad (2.60)$$

where κ_1 is defined in Eq. (2.34a).

Substituting Eqs. (2.43) and (2.46) into Eq. (2.53), yields,

$$\begin{aligned}
 m_f (\vec{r}'_f + x_f \vec{e}_x) \times \vec{a}_A &= m_f \left\{ -\bar{\kappa}_2 \frac{1}{2H} (H^2 + u^2) \left[-a_y \sin(\gamma + \theta) + a_z \cos(\gamma + \theta) \right] \vec{e}'_A \right. \\
 &\left. + \bar{\kappa}_2 \frac{1}{2H} (H^2 + u^2) \left[a_y \cos(\gamma + \theta) + a_z \sin(\gamma + \theta) \right] \hat{e}'_A + \bar{\kappa} u \left[-a_y \sin(\gamma + \theta) + a_z \cos(\gamma + \theta) \right] \vec{e}_x \right\} \\
 &\quad (2.61)
 \end{aligned}$$

The undesired additional moment \vec{M}_p from gravity force with respect to the reference point A is

$$\vec{M}_p = -m_f g (\vec{r}'_f + x_f \vec{e}_x) \times \vec{e}_x = m_f g \bar{\kappa} u \hat{e}'_A. \quad (2.62)$$

The undesired axial moment M_A about \hat{e}'_A direction is the sum of the TLCGD-floor interaction, Eq. (2.58) and a second contribution resulting from gravity force acting at the (displaced) center of fluid-mass $m_f g \bar{\kappa} u$, Eq. (2.62). The latter is similar to that of a TMD.

The axial moments M_A about \hat{e}'_A and \bar{e}'_A directions are generally both found negligible in their action on the structure. The nonlinear resultant control moment M_{Ax} (acting on the piping system) becomes finally, adding Eq. (2.60) and the proper component of Eq. (2.61), see again Fig. 2.9,

$$M_{Ax} = m_f \left\{ \bar{\kappa} u \left[-a_y \sin(\gamma + \theta) + a_z \cos(\gamma + \theta) \right] + \bar{\kappa}_3 H^2 \ddot{\theta} + \bar{\kappa}_1 \left(u^2 \ddot{\theta} + 2u\dot{u}\dot{\theta} \right) \right\}. \quad (2.63)$$

Equation (2.63) is simplified under the condition $|\theta| \ll 1$ and, when properly linearized, becomes

$$M_{Ax} = m_f \bar{\kappa}_3 H^2 \ddot{\theta}. \quad (2.64)$$

2.7 Control of SDOF main structure by a single TLCGD when compared to an equivalent TMD

The modal tuning of liquid column damper can be presented from the purely geometric analogy between the classical tuned mechanical damper and the tuned liquid column damper, Hochrainer¹, page 98. In this Section the representative model under both base and force (wind) excitation in purely horizontal translation is investigated, thus repeating the derivation of Hochrainer¹.

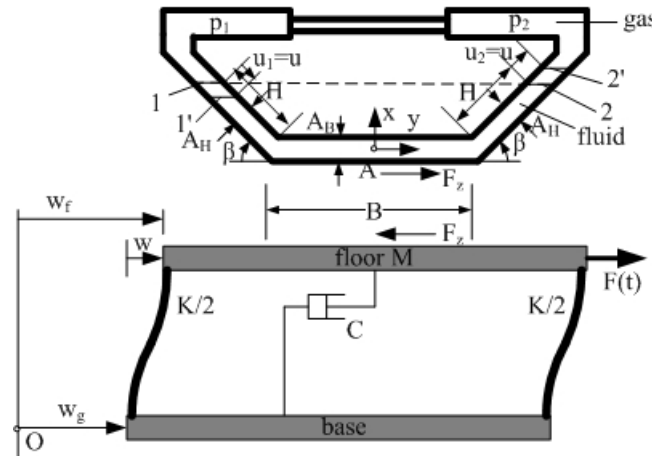


Fig. 2.12: U-shaped TLCGD rigidly attached to the floor of a horizontally displaced SDOF-main system, ground acceleration \ddot{w}_g and wind force $F(t)$. Total floor displacement $w_f = w_g + w$. Action of the control force F_z shown.

A TLCGD installed on the floor is illustrated in Fig. (2.18). The equations of motion for the TLCGD-main structure interaction, w is the relative horizontal displacement of the floor, become

$$M\ddot{w} + C\dot{w} + Kw = -M\ddot{w}_g + F(t) + F_z, \text{ control force: } F_z = -m_f \left(\ddot{w}_g + \ddot{w} + \bar{\kappa}\ddot{u} \right), \quad (2.65)$$

see Hochrainer¹, page 97, and the properly simplified Eq. (2.36) with $\gamma = \pi/2$,

$$\ddot{u} + 2\zeta_A \omega_A \dot{u} + \omega_A^2 u = -\kappa \left(\ddot{w}_g + \ddot{w} \right). \quad (2.66)$$

Combining Eqs. (2.65) and (2.66), the matrix form of the coupled system of linearized equations results

$$\begin{bmatrix} 1 + \mu & \bar{\kappa}\mu \\ \kappa & 1 \end{bmatrix} \begin{bmatrix} \ddot{w} \\ \ddot{u} \end{bmatrix} + \begin{bmatrix} 2\zeta_S \omega_S & 0 \\ 0 & 2\zeta_A \omega_A \end{bmatrix} \begin{bmatrix} \dot{w} \\ \dot{u} \end{bmatrix} + \begin{bmatrix} \omega_S^2 & 0 \\ 0 & \omega_A^2 \end{bmatrix} \begin{bmatrix} w \\ u \end{bmatrix} = - \begin{bmatrix} 1 + \mu \\ \kappa \end{bmatrix} \ddot{w}_g + \begin{bmatrix} 1/M \\ 0 \end{bmatrix} F(t),$$

$$\mu = \frac{m_f}{M} < 6\%, \quad \omega_S^2 = \frac{K}{M}, \quad 2\zeta_S\omega_S = \frac{C}{M}, \quad (2.67)$$

where μ, ζ_S, ω_S and ω_A are the mass ratio, the light structural damping ($\zeta_S \ll 1$), the circular natural frequency of the main structure and the TLCGD's circular natural frequency, respectively. Substituting the "equivalent" tuned mechanical damper TMD for the TLCGD changes also the main system, see again Hochrainer¹, page 38, the parameters carry a star,

$$M^* \ddot{w} + C^* \dot{w} + K^* w = -M^* \ddot{w}_g + F(t) + F_z^*, \quad F_z^* = -m_A^* (\ddot{w}_g + \dot{w} + \ddot{u}^*), \quad (2.68)$$

$$\ddot{u}^* + 2\zeta_A^* \omega_A^* \dot{u}^* + \omega_A^{*2} u^* = -(\ddot{w}_g + \dot{w}). \quad (2.69)$$

Combining equations (2.68) and (2.69), the TMD-structure interactive equation takes on its matrix form

$$\begin{bmatrix} 1 + \mu^* & \mu^* \\ 1 & 1 \end{bmatrix} \begin{bmatrix} \dot{w} \\ \dot{u}^* \end{bmatrix} + \begin{bmatrix} 2\zeta_S^* \omega_S^* & 0 \\ 0 & 2\zeta_A^* \omega_A^* \end{bmatrix} \begin{bmatrix} \dot{w} \\ \dot{u}^* \end{bmatrix} + \begin{bmatrix} \omega_S^{*2} & 0 \\ 0 & \omega_A^{*2} \end{bmatrix} \begin{bmatrix} w \\ u^* \end{bmatrix} = - \begin{bmatrix} 1 + \mu^* \\ 1 \end{bmatrix} \ddot{w}_g + \begin{bmatrix} 1/M^* \\ 0 \end{bmatrix} F(t)$$

$$\mu^* = \frac{m_A^*}{M^*}, \quad \omega_S^{*2} = \frac{K^*}{M^*}, \quad 2\zeta_S^* \omega_S^* = \frac{C^*}{M^*}, \quad (2.70)$$

where μ^*, ω_S^* and ω_A^* are the alternative mass ratio, the natural frequency of the main structure and the TMD's natural frequency (indicated by the superscript *), respectively. A strong indication for existence of an analogy is the fact that the TMD behaviour can be derived from the corresponding TLCGD by setting $\kappa = \bar{\kappa} = 1$.

2.7.1 Analogy between TMD and TLCGD when attached to SDOF-main structure

Hochrainer¹, page 98 established such an analogy. We repeat his derivation to form the basis for the more general case of a space-structure. The first step is to define the relationship between u and u^* . If Eqs. (2.66) and (2.69) on the right hand side have the same excitation, u^* turns out proportional to u ,

$$u^* = u/\kappa. \quad (2.71)$$

Substituting this result and comparing the left hand side of the second equation in Eqs. (2.67) and (2.70), yield at once

$$\omega_A^* = \omega_A, \quad \zeta_A^* = \zeta_A. \quad (2.72)$$

In a second step, substituting these results into the first equation in Eqs. (2.67) and (2.70) renders by inspection

$$\frac{\mu \bar{\kappa}}{1 + \mu} = \frac{\mu^*}{\kappa(1 + \mu^*)}, \quad \frac{1}{1 + \mu} \omega_S^2 = \frac{1}{1 + \mu^*} \omega_S^{*2}, \quad \frac{1}{1 + \mu} 2\zeta_S \omega_S = \frac{1}{1 + \mu^*} 2\zeta_S^* \omega_S^*,$$

$$\frac{1}{M(1 + \mu)} = \frac{1}{M^*(1 + \mu^*)},$$

and thus the mass ratio of the equivalent TMD-main system becomes

$$\mu^* = \frac{\mu \kappa \bar{\kappa}}{1 + \mu(1 - \kappa \bar{\kappa})} < \mu, \quad \omega_S^* = \frac{\omega_S}{\sqrt{1 + \mu(1 - \kappa \bar{\kappa})}} < \omega_S, \quad \zeta_S^* = \frac{\zeta_S}{\sqrt{1 + \mu(1 - \kappa \bar{\kappa})}} < \zeta_S, \quad (2.73)$$

and

$$M^* = M(1 + \mu(1 - \kappa \bar{\kappa})) > M, \quad m_A^* = \kappa \bar{\kappa} m_f < m_f. \quad (2.74)$$

The conjugate main structural mass includes the dead fluid mass of the TLCD, $m_f(1 - \kappa \bar{\kappa})$,

i.e. $\kappa\bar{\kappa}$ should be maximal.

2.8 Control of single-storey moderately plan-asymmetric space frame by a single TLCGD when compared to an equivalent TMD

2.8.1 TMD attached to space frame

A model of the single-storey asymmetric structure with the mass matrix \underline{M}^* and the stiffness matrix \underline{K}^* is considered, analogous to Section 2.4. A TMD is set with the general angle γ to y -direction. The position coordinate of TMD is $(y_A, z_A, 0)$.

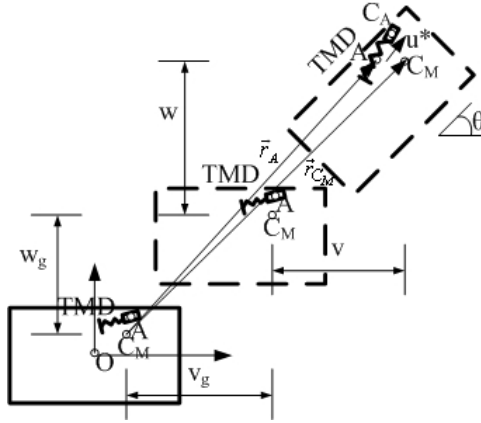


Fig. 2.13: TMD under general in-plane acceleration of the floor: \ddot{v}_t , \ddot{w}_t and $\ddot{\theta}$.

The instant coordinate position of the point mass C_A is $u^* \vec{e}'_A$, for its TLCGD counterpoint C_f . Hence,

$$\vec{r}_{C_A} = \vec{r}_A + u^* \vec{e}'_A, \quad \vec{v}_{C_A} = \vec{v}_A + \dot{u}^* \vec{e}'_A + u^* \dot{\theta} \hat{e}'_A, \quad (2.75)$$

$$\vec{a}_{C_A} = \vec{a}_A + \ddot{u}^* \vec{e}'_A + 2\dot{u}^* \dot{\theta} \hat{e}'_A + u^* \ddot{\theta} \hat{e}'_A - u^* \dot{\theta}^2 \vec{e}'_A = \vec{a}_A + (\ddot{u}^* - u^* \dot{\theta}^2) \vec{e}'_A + (2\dot{u}^* \dot{\theta} + u^* \ddot{\theta}) \hat{e}'_A, \quad (2.76)$$

$$\vec{R} = m_A^* \vec{a}_{C_A} = m_A^* \vec{a}_A + m_A^* (\ddot{u}^* - u^* \dot{\theta}^2) \vec{e}'_A + m_A^* (2\dot{u}^* \dot{\theta} + u^* \ddot{\theta}) \hat{e}'_A. \quad (2.77)$$

Equation (2.77) compares favorably with Eq. (2.45), TMD has not relative displacement in x direction. The equation of motion for the TMD, viscous damping is added subsequently, is derived by considering the A' component and inserting Eq. (2.46) for \vec{a}_A ,

$$m_A^* \vec{a}_{C_A} \cdot \vec{e}'_A + c^* \dot{u}^* + k^* u^* = 0,$$

$$\vec{a}_{C_A} \cdot \vec{e}'_A = a_y \cos(\gamma + \theta) + a_z \sin(\gamma + \theta) + \ddot{u}^* - u^* \dot{\theta}^2,$$

$$m_A^* [a_y \cos(\gamma + \theta) + a_z \sin(\gamma + \theta) + \ddot{u}^* - u^* \dot{\theta}^2] + c^* \dot{u}^* + k^* u^* = 0 \quad (2.78)$$

and takes on its linearized form with parametric forcing neglected, related to Eq. (2.35) of the linearized TLCGD,

$$\ddot{u}^* + 2\zeta_A^* \omega_A^* \dot{u}^* + \omega_A^{*2} u^* = -[\ddot{v}_g + \ddot{v} - (z_A - z_{C_M}) \ddot{\theta}] \cos \gamma - [\ddot{w}_g + \ddot{w} + (y_A - y_{C_M}) \ddot{\theta}] \sin \gamma,$$

$$\omega_A^* = \sqrt{\frac{k^*}{m_A^*}}, \quad 2\zeta_A^* \omega_A^* = \frac{c^*}{m_A^*}. \quad (2.79)$$

The control forces are, see Eqs. (2.47)- (2.50) for the TLCDG

$$F_A^* \vec{e}'_A = m_A^* \left[a_y \cos(\gamma + \theta) + a_z \sin(\gamma + \theta) + \dot{u}^* - u^* \dot{\theta}^2 \right], \quad (2.80)$$

$$F_A^* \hat{\vec{e}}'_A = m_A^* \left[-a_y \sin(\gamma + \theta) + a_z \cos(\gamma + \theta) + 2\dot{u}^* \dot{\theta} + u^* \ddot{\theta} \right], \quad (2.81)$$

and when rotated become

$$F_{Ay}^* = m_A^* \left[a_y + (\dot{u}^* - u^* \dot{\theta}^2) \cos(\gamma + \theta) - (2\dot{u}^* \dot{\theta} + u^* \ddot{\theta}) \sin(\gamma + \theta) \right], \quad (2.82)$$

$$F_{Az}^* = m_A^* \left[a_z + (\dot{u}^* - u^* \dot{\theta}^2) \sin(\gamma + \theta) + (2\dot{u}^* \dot{\theta} + u^* \ddot{\theta}) \cos(\gamma + \theta) \right]. \quad (2.83)$$

Equations (2.82), (2.83) are simplified under the condition $|\theta| \ll 1$ and the essential linear parts are

$$F_{Ay}^* = m_A^* \left[\ddot{v}_g + \ddot{v} - (z_A - z_{C_M}) \ddot{\theta} \right] + m_A^* \dot{u}^* \cos \gamma, \quad (2.84)$$

$$F_{Az}^* = m_A^* \left[\ddot{w}_g + \ddot{w} + (y_A - y_{C_M}) \ddot{\theta} \right] + m_A^* \dot{u}^* \sin \gamma. \quad (2.85)$$

Conservation of angular momentum of the point mass m_A^* requires, compare with Eq. (2.63),

$$\frac{d\vec{D}_A^*}{dt} + m_A^* \dot{u}^* \vec{e}'_A \times \vec{a}_A = \vec{M}_A^*, \quad \frac{d\vec{D}_A^*}{dt} = \frac{d'\vec{D}_A^*}{dt} + \dot{\theta} (\vec{e}_x \times \vec{D}_A^*),$$

$$I_{Ax}^* = m_A^* u^{*2}, \quad D_{Ax}^* = I_{Ax}^* \dot{\theta} = m_A^* u^{*2} \dot{\theta}, \quad \frac{dD_{Ax}^*}{dt} = m_A^* (2u^* \dot{u}^* \dot{\theta} + u^{*2} \ddot{\theta}),$$

$$m_A^* \dot{u}^* \vec{e}'_A \times \vec{a}_A = m_A^* \dot{u}^* \left[-a_y \sin(\gamma + \theta) + a_z \cos(\gamma + \theta) \right] \vec{e}_x,$$

$$M_{Ax}^* = m_A^* \left\{ u^* \left[-a_y \sin(\gamma + \theta) + a_z \cos(\gamma + \theta) \right] + 2u^* \dot{u}^* \dot{\theta} + u^{*2} \ddot{\theta} \right\}. \quad (2.86)$$

Equation (2.86) is simplified under the condition $|\theta| \ll 1$ and when properly linearized, the moment vanishes,

$$M_{Ax}^* = 0, \quad (2.87)$$

in contrast to Eq. (2.64) of the TLCDG.

The equation of motion for the coupled undamped main-system can be given in matrix form,

$$\underline{M}^* \ddot{\vec{x}} + \underline{K}^* \vec{x} = -\underline{M}^* \ddot{\vec{x}}_g + \vec{P}^*,$$

$$\vec{x}^T = [v \quad w \quad u_T], \quad \ddot{\vec{x}}_g^T = [\ddot{v}_g \quad \ddot{w}_g \quad 0], \quad \vec{P}^{*T} = -\left[F_{Ay}^* \quad F_{Az}^* \quad M_x^*/r_S \right], \quad (2.88)$$

where Eqs. (2.84), (2.85) and (2.87) are considered, \vec{P}^* is the linearized control force vector and $M_x^* = M_{Ax}^* - F_{Ay}^* (z_A - z_{C_M}) + F_{Az}^* (y_A - y_{C_M})$ is the moment about C_M .

If the floor displacements \vec{x} are expanded into modal displacements $\vec{x} = \sum_{j=1}^N \vec{\phi}_j q_j$ on the left hand side, Eq. (2.88) decouples on the left hand side for all classically damped systems by pre-multiplication with the transposed $\vec{\phi}_j^T$,

$$\underbrace{\vec{\phi}_j^T \underline{M}^* \vec{\phi}_j}_{m_j^*} \ddot{q}_j + \underbrace{\vec{\phi}_j^T \underline{K}^* \vec{\phi}_j}_{k_j^*} q_j = -\vec{\phi}_j^T \underline{M}^* \ddot{\vec{x}}_g + \vec{\phi}_j^T \vec{P}^*, \quad (2.89)$$

then Eq. (2.89) divided by the modal mass m_j^* becomes

$$\ddot{q}_j + \omega_{Sj}^{*2} q_j = -\frac{\bar{\phi}_j^T \underline{M}^*}{m_j^*} \ddot{x}_g + \frac{\bar{\phi}_j^T}{m_j^*} \bar{P}^*, \quad \omega_{Sj}^{*2} = \frac{\bar{\phi}_j^T \underline{K}^* \bar{\phi}_j}{m_j^*}, \quad j = 1, 2, 3. \quad (2.90)$$

However, $\bar{x} = \bar{\phi}_j q_j$ must approximately hold in the narrow frequency window around ω_j in the case of base excitation, i.e. on the right hand side to decouple the modal equations: $v = q_j \phi_{j1}$, $w = q_j \phi_{j2}$, $u_T = r_S \theta = q_j \phi_{j3}$ are substituted in the control forces and on the right hand side of the TMD equation.

Inserting the linearized coupling forces \bar{P}^* , Eqs. (2.84), (2.85) and (2.86), into Eq. (2.90) renders the approximated equation of the selected mode,

$$\begin{aligned} & (1 + \mu_j^*) \ddot{q}_j + \omega_{Sj}^{*2} q_j + \frac{m_{Aj}^*}{m_j^*} (v_{A,j} \cos \gamma + w_{A,j} \sin \gamma) \ddot{u}^* \\ & = -\frac{1}{m_j^*} (m_S^* \phi_{j1} + m_{Aj}^* v_{A,j}) \ddot{v}_g - \frac{1}{m_j^*} (m_S^* \phi_{j2} + m_{Aj}^* w_{A,j}) \ddot{w}_g \\ & \mu_j^* = \frac{m_{Aj}^*}{m_j^*} V_j^{*2}, \quad V_j^{*2} = v_{A,j}^2 + w_{A,j}^2, \\ & v_{A,j} = \phi_{j1} - \phi_{j3} (z_{Aj} - z_{C_M}) / r_S, \quad w_{A,j} = \phi_{j2} + \phi_{j3} (y_{Aj} - y_{C_M}) / r_S, \end{aligned} \quad (2.91)$$

where $v_{A,j}$ and $w_{A,j}$ denote the modal displacements of reference point A in y - and z -directions, respectively. Further the displacements of the main system in the equation of motion of TMD in Eq. (2.79) are substituted, to approximately render

$$\ddot{u}^* + 2\zeta_{Aj}^* \omega_{Aj}^* \dot{u}^* + \omega_{Aj}^{*2} u^* = - (v_{A,j} \cos \gamma + w_{A,j} \sin \gamma) \ddot{q}_j - \bar{r}_S^T \ddot{x}_g, \quad \bar{r}_S^T = [\cos \gamma \quad \sin \gamma \quad 0]. \quad (2.92)$$

With light structural damping of the main system $\zeta_{S1} \leq \zeta_{S2} \leq \zeta_{S3} < 0.1$ added, the coupled equations of motion of the main system with TMD attached, in matrix notation become

$$\begin{aligned} & \begin{bmatrix} 1 + \mu_j^* & (v_{A,j} \cos \gamma + w_{A,j} \sin \gamma) m_{Aj}^* / m_j^* \\ (v_{A,j} \cos \gamma + w_{A,j} \sin \gamma) & 1 \end{bmatrix} \begin{bmatrix} \ddot{q}_j \\ \ddot{u}^* \end{bmatrix} + \\ & \begin{bmatrix} 2\zeta_{Sj}^* \omega_{Sj}^* & 0 \\ 0 & 2\zeta_{Aj}^* \omega_{Aj}^* \end{bmatrix} \begin{bmatrix} \dot{q}_j \\ \dot{u}^* \end{bmatrix} + \begin{bmatrix} \omega_{Sj}^{*2} & 0 \\ 0 & \omega_{Aj}^{*2} \end{bmatrix} \begin{bmatrix} q_j \\ u^* \end{bmatrix} = - \begin{bmatrix} \bar{L}_j^{*T} / m_j^* \\ \bar{r}_S^T \end{bmatrix} \ddot{x}_g \end{aligned} \quad (2.93)$$

where the generalized participation factors are

$\bar{L}_j^{*T} = [L_{jy}^* \quad L_{jz}^* \quad 0]$, $L_{jy}^* = m_S^* \phi_{j1} + m_{Aj}^* v_{A,j}$, $L_{jz}^* = m_S^* \phi_{j2} + m_{Aj}^* w_{A,j}$. m_S^* is the floor mass of the conjugate structure.

2.8.2 TLCDG attached to space frame

The equation of motion for the coupled system considering the undamped single-storey space frame Eq. (2.2) and the TLCDG, Fig.2.9, Eqs. (2.36), (2.51), (2.52) and (2.64) under the ground excitation can be combined in matrix form

$$\begin{aligned} & \underline{M} \ddot{\bar{x}} + \underline{K} \bar{x} = -\underline{M} \ddot{x}_g + \bar{P}, \\ & \bar{x}^T = [v \quad w \quad u_T], \quad \ddot{x}_g^T = [\ddot{v}_g \quad \ddot{w}_g \quad 0], \quad \bar{P}^T = -[F_{Ay} \quad F_{Az} \quad M_x / r_S], \end{aligned} \quad (2.94)$$

where \vec{P} is the control force vector and $M_x = M_{Ax} - F_{Ay}(z_A - z_{C_M}) + F_{Az}(y_A - y_{C_M})$.

If the floor displacements \vec{x} are expanded into modal displacements $\vec{x} = \sum_{j=1}^N \vec{\phi}_j q_j$ on the left hand side, Eq. (2.94) decouples the left hand side for all classically damped systems by pre-multiplication with the transposed modal vector $\vec{\phi}_j^T$,

$$\underbrace{\vec{\phi}_j^T \underline{M} \vec{\phi}_j}_{m_j} \ddot{q}_j + \underbrace{\vec{\phi}_j^T \underline{K} \vec{\phi}_j}_{k_j} q_j = -\vec{\phi}_j^T \underline{M} \ddot{\vec{x}}_g + \vec{\phi}_j^T \vec{P}. \quad (2.95)$$

Equation (2.95) divided by the modal mass m_j with light modal structural damping added, becomes

$$\ddot{q}_j + 2\zeta_{Sj}\omega_{Sj}\dot{q}_j + \omega_{Sj}^2 q_j = -\frac{\vec{\phi}_j^T \underline{M} \ddot{\vec{x}}_g}{m_j} + \frac{\vec{\phi}_j^T \vec{P}}{m_j}, \quad \omega_{Sj}^2 = \frac{\vec{\phi}_j^T \underline{K} \vec{\phi}_j}{m_j}. \quad (2.96)$$

Modal approximations $v = q_j \phi_{j1}$, $w = q_j \phi_{j2}$, $u_T = r_S \theta = q_j \phi_{j3}$ are substituted in the control forces and on the right hand side of the TLCDG equation. Inserting the linearized coupling forces \vec{P} , Eqs. (2.51), (2.52) and (2.64) modally approximated into Eq. (2.96) renders

$$\begin{aligned} & (1 + \mu_j) \ddot{q}_j + 2\zeta_{Sj}\omega_{Sj}\dot{q}_j + \omega_{Sj}^2 q_j + \frac{m_{ff}}{m_j} \bar{\kappa} (v_{A,j} \cos \gamma + w_{A,j} \sin \gamma) \ddot{u} \\ & = -\frac{1}{m_j} [(m_S + m_1) \phi_{j1} + m_{ff} v_{A,j}] \ddot{v}_g - \frac{1}{m_j} [(m_S + m_1) \phi_{j2} + m_{ff} w_{A,j}] \ddot{w}_g \\ & \mu_j = \frac{m_{ff}}{m_j} V_j^2, \quad V_j^2 = V_j^{*2} + \bar{\kappa}_3 (\phi_{j3} H / r_S)^2. \end{aligned} \quad (2.97)$$

Here, $\bar{\kappa}_3$ and V_j^{*2} are given by Eq. (2.60) and (2.91). Eq. (2.36) renders the approximate equation in the selected mode,

$$\ddot{u} + 2\zeta_{Aj}\omega_{Aj}\dot{u} + \omega_{Aj}^2 u = -\kappa (v_{A,j} \cos \gamma + w_{A,j} \sin \gamma) \ddot{q}_j - \kappa \bar{\Gamma}_S^T \ddot{\vec{x}}_g. \quad (2.98)$$

In matrix form the linearized coupled system of modal equations of the main system with TLCDG attached results by substituting the control force,

$$\begin{aligned} & \begin{bmatrix} 1 + \mu_j & \bar{\kappa} (v_{A,j} \cos \gamma + w_{A,j} \sin \gamma) m_{ff} / m_j \\ \kappa (v_{A,j} \cos \gamma + w_{A,j} \sin \gamma) & 1 \end{bmatrix} \begin{bmatrix} \ddot{q}_j \\ \ddot{u} \end{bmatrix} \\ & + \begin{bmatrix} 2\zeta_{Sj}\omega_{Sj} & 0 \\ 0 & 2\zeta_{Aj}\omega_{Aj} \end{bmatrix} \begin{bmatrix} \dot{q}_j \\ \dot{u} \end{bmatrix} + \begin{bmatrix} \omega_{Sj}^2 & 0 \\ 0 & \omega_{Aj}^2 \end{bmatrix} \begin{bmatrix} q_j \\ u \end{bmatrix} = - \begin{bmatrix} \bar{L}_j^T / m_j \\ \kappa \bar{\Gamma}_S^T \end{bmatrix} \ddot{\vec{x}}_g \end{aligned} \quad (2.99)$$

where the generalized participation factors are, cf. Eq.(2.93),

$$\bar{L}_j^T = [L_{jy} \quad L_{jz} \quad 0], \quad L_{jy} = (m_S + m_1) \phi_{j1} + m_{ff} v_{A,j}, \quad L_{jz} = (m_S + m_1) \phi_{j2} + m_{ff} w_{A,j},$$

and $v_{A,j}$ and $w_{A,j}$ are same as defined in Eqs. (2.91).

2.8.3 Analogy between TMD and TLCGD when attached to 3DOF-main system

We follow closely the procedure developed by Hochrainer¹ for the simplest case, Section 2.6.1. If Eqs. (2.92) and (2.98) on the right hand side have the same excitation, u^* turns out proportional to u , same as in the case of Eq. (2.71),

$$u^* = u/\kappa. \quad (2.100)$$

Using this result and comparing the left hand side of the second equation in Eqs. (2.93) and (2.99), yield at once

$$\omega_{Aj}^* = \omega_{Aj}, \quad \zeta_{Aj}^* = \zeta_{Aj}. \quad (2.101)$$

The results are the same as in the case of Eq. (2.72). In a second step, substituting these results into the first equation in Eqs. (2.93) and (2.99) renders by inspection

$$\frac{\mu_j \bar{\kappa}}{(1 + \mu_j) V_j^2} = \frac{\mu_j^*}{\kappa (1 + \mu_j^*) V_j^{*2}}, \quad \frac{1}{1 + \mu_j} \omega_{Sj}^2 = \frac{1}{1 + \mu_j^*} \omega_{Sj}^{*2},$$

$$\frac{1}{1 + \mu_j} 2\zeta_{Sj} \omega_{Sj} = \frac{1}{1 + \mu_j^*} 2\zeta_{Sj}^* \omega_{Sj}^*,$$

and thus the mass ratio of the equivalent TMD-modal system is defined by

$$\mu_j^* = \mu_j \frac{\kappa \bar{\kappa} (V_j^*/V_j)^2}{1 + \mu_j [1 - \kappa \bar{\kappa} (V_j^*/V_j)^2]} < \mu_j, \quad (2.102)$$

and

$$\omega_{Sj}^* = \frac{\omega_{Sj}}{\sqrt{1 + \mu_j [1 - \kappa \bar{\kappa} (V_j^*/V_j)^2]}} < \omega_{Sj}, \quad \zeta_{Sj}^* = \frac{\zeta_{Sj}}{\sqrt{1 + \mu_j [1 - \kappa \bar{\kappa} (V_j^*/V_j)^2]}} < \zeta_{Sj}. \quad (2.103)$$

The TMD frequency ratio $\delta_{jopt}^* = \frac{\omega_{Aj,opt}^*}{\omega_{Sj}^*}$ and the TLCGD frequency ratio $\delta_{jopt} = \frac{\omega_{Aj,opt}}{\omega_{Sj}}$

are thus related by the more general transformation

$$\delta_{jopt} = \frac{\delta_{jopt}^*}{\sqrt{1 + \mu_j [1 - \kappa \bar{\kappa} (V_j^*/V_j)^2]}} < \delta_{jopt}^*. \quad (2.104)$$

The optimal frequency ratio δ_{jopt} of the TLCGD turns out slightly lowered. The remaining impulsive fluid-mass must be regard as dead load of the main structure, thereby slightly lowering its natural frequency.

2.9 Dynamic magnification factor

In this Section, assuming a time harmonic horizontal ground excitation under various oblique angles of attack α ($0 \leq \alpha \leq \pi$ with respect to the y -direction), thus $\ddot{v}_g(t) = (a_0 \cos \alpha) e^{i\omega t}$, $\ddot{w}_g(t) = (a_0 \sin \alpha) e^{i\omega t}$, a_0 and ω are the ground acceleration that is commonly assigned as a fraction of $g = 9.81 m/s^2$ and the circular forcing frequency, respectively. The relationship between the amplitude of the modal displacement q_j of the main structure and the amplitude u of the relative liquid motion under a given forcing

frequency is consequently determined in the steady-state: $q_j = q_{j0} e^{i\omega t}$, $u = u_0 e^{i\omega t}$, q_{j0} and u_0 are complex valued. The dynamic magnification factor (DMF), i.e., the ratio of dynamic response to static response can be determined as $DMF = \frac{|q_{j0}|}{q_{jstat}}$, $q_{jstat} = \frac{L_j(\alpha)}{m_j \omega_{Sj}^2} a_0$.

2.9.1 Steady state vibration of the lightly damped main structure without TLCGD

Equation (2.2) with light structural damping added is

$$\bar{\phi}_j^T \bar{M} \bar{\phi}_j \ddot{q}_j + \bar{\phi}_j^T \bar{C} \bar{\phi}_j \dot{q}_j + \underbrace{\bar{\phi}_j^T \bar{K} \bar{\phi}_j}_{L_j(\alpha)} q_j = -\underbrace{\bar{\phi}_j^T \bar{M} \bar{e}_S}_{L_j(\alpha)} a_0 e^{i\omega t}, \quad \bar{e}_S^T = [\cos \alpha \quad \sin \alpha \quad 0],$$

$$\ddot{q}_j + 2\zeta_{Sj} \omega_{Sj} \dot{q}_j + \omega_{Sj}^2 q_j = -\frac{L_j(\alpha)}{m_j} a_0 e^{i\omega t}, \quad L_j(\alpha) = (m_S + m_1)(\phi_{j1} \cos \alpha + \phi_{j2} \sin \alpha), \quad (2.105)$$

where the modal damping ratio $\zeta_{Sj} \ll 1$, for convenience might be assumed constant for $j=1,2,3$ and $L_j(\alpha)$ denotes the classical modal participation factor.

$$DMF = \frac{|q_{j0}|}{q_{jstat}} = \frac{1}{\sqrt{[1 - \beta_{Sj}^2]^2 + (2\zeta_{Sj} \beta_{Sj})^2}}, \quad (2.106)$$

where $\beta_{Sj} = \omega / \omega_{Sj}$ is the ratio of the forcing frequency to the natural frequency of the main structure vibrating in its j mode. Sufficiently separated modes are understood.

2.9.2 Steady state vibration of the main structure with TLCGD attached parallel to y-direction

Inserting $q_j = q_{j0} e^{i\omega t}$, $u = u_0 e^{i\omega t}$ into Eq. (2.99), the time-reduced linearized equation for TLCGD-main structure becomes

$$\left\{ \begin{array}{cc} 1 + \mu_j & \bar{\kappa} (v_{A,j} \cos \gamma + w_{A,j} \sin \gamma) m_{fj} / m_j \\ \kappa (v_{A,j} \cos \gamma + w_{A,j} \sin \gamma) & 1 \end{array} \right\} \begin{bmatrix} q_{j0} \\ u_0 \end{bmatrix} = - \begin{bmatrix} \bar{L}_j^T / m_j \\ \kappa \bar{\Gamma}_S^T \end{bmatrix} \bar{e}_S a_0$$

$$+ (i\omega) \begin{bmatrix} 2\zeta_{Sj} \omega_{Sj} & 0 \\ 0 & 2\zeta_{Aj} \omega_{Aj} \end{bmatrix} + \begin{bmatrix} \omega_{Sj}^2 & 0 \\ 0 & \omega_{Aj}^2 \end{bmatrix} \begin{bmatrix} q_{j0} \\ u_0 \end{bmatrix} = - \begin{bmatrix} \bar{L}_j^T / m_j \\ \kappa \bar{\Gamma}_S^T \end{bmatrix} \bar{e}_S a_0 \quad (2.107)$$

$$j = 1, 2, 3, \quad \bar{e}_S^T = [\cos \alpha \quad \sin \alpha \quad 0]$$

Thus, the linear system of equations results,

$$\begin{bmatrix} \omega_{Sj}^2 - (1 + \mu_j) \omega^2 + 2\zeta_{Sj} \omega_{Sj} i\omega & -\bar{\kappa} (v_{A,j} \cos \gamma + w_{A,j} \sin \gamma) \omega^2 m_{fj} / m_j \\ -\kappa (v_{A,j} \cos \gamma + w_{A,j} \sin \gamma) \omega^2 & \omega_{Aj}^2 - \omega^2 + 2\zeta_{Aj} \omega_{Aj} i\omega \end{bmatrix} \begin{bmatrix} q_{j0} \\ u_0 \end{bmatrix} = - \begin{bmatrix} \bar{L}_j^T / m_j \\ \kappa \bar{\Gamma}_S^T \end{bmatrix} \bar{e}_S a_0 \quad (2.108)$$

The relative fluid motion has the complex displacement

$$u_0 = \frac{-\kappa \bar{\mathbf{r}}_S^T \bar{\mathbf{e}}_S a_0 + \kappa (v_{A,j} \cos \gamma + w_{A,j} \sin \gamma) \omega^2 q_{j0}}{(\omega_{Aj}^2 - \omega^2)^2 + 4\zeta_{Aj}^2 \omega_{Aj}^2} (\omega_{Aj}^2 - \omega^2 - 2i\zeta_{Aj} \omega_{Aj} \omega). \quad (2.109)$$

The dynamic magnification factor and the amplitude of the fluid motion are

$$DMF = \frac{|q_{j0}|}{q_{jstat}} = \frac{\sqrt{[a_1 + a_2 \beta_{Sj}^2]^2 + (a_3 \beta_{Sj})^2}}{q_{jstat} \omega_{Sj}^2 \sqrt{[b_1 + b_2 \beta_{Sj}^2 + b_3 \beta_{Sj}^4]^2 + [b_4 \beta_{Sj} + b_5 \beta_{Sj}^3]^2}}, \quad (2.110)$$

$$|u_0| = \frac{|\kappa \bar{\mathbf{r}}_S^T \bar{\mathbf{e}}_S a_0 + \kappa (v_{A,j} \cos \gamma + w_{A,j} \sin \gamma) \omega^2 q_{j0}|}{(\omega_{Aj}^2 - \omega^2)^2 + 4\zeta_{Aj}^2 \omega_{Aj}^2}, \quad (2.111)$$

where

$$\begin{aligned} b_1 &= \delta_j^2, \quad b_2 = -1 - (1 + \mu_j) \delta_j^2 - 4\zeta_{Sj} \zeta_{Aj} \delta_j, \\ b_3 &= 1 + \mu_j - \bar{\kappa} \kappa (v_{A,j} \cos \gamma + w_{A,j} \sin \gamma)^2 m_{ff} / m_j, \quad b_4 = 2\zeta_{Sj} \delta_j^2 + 2\zeta_{Aj} \delta_j, \\ b_5 &= -2\zeta_{Sj} - 2\zeta_{Aj} \delta_j (1 + \mu_j), \quad a_1 = -\bar{\mathbf{L}}_j^T \bar{\mathbf{e}}_S \delta_j^2 a_0 / m_j, \\ a_2 &= \bar{\mathbf{L}}_j^T \bar{\mathbf{e}}_S a_0 / m_j - \bar{\kappa} \kappa \bar{\mathbf{r}}_S^T \bar{\mathbf{e}}_S a_0 (v_{A,j} \cos \gamma + w_{A,j} \sin \gamma) m_{ff} / m_j, \\ a_3 &= -2\bar{\mathbf{L}}_j^T \bar{\mathbf{e}}_S \zeta_{Aj} \delta_j a_0 / m_j. \end{aligned}$$

2.10 Numerical example

In order to illustrate the control effectiveness and ability of U-shaped TLCD to reduce lateral and torsional motions of the moderately asymmetric main structure, a numerical simulation is carried out in this section. The performance of TLCD is discussed with respect to the mode shapes of buildings. The optimal frequency and damping ratio of TMD are either given by Den Hartog' method, see Den Hartog¹² and the TMD-TLCD analogy, Eqs. (2.102)- (2.104) or subsequently even subjected to fine-tuning in state space. Two different types of earthquakes are applied to the structure under various oblique angles of attack.

The single-storey mass-asymmetric structure is considered, Section 2.2. The uniformly distributed mass of the rectangular rigid floor $a \times b = 4 \times 8 \text{ m}$ is $m_S = 16 \times 10^3 \text{ kg}$ in Fig. 2.1. The additional point mass $m_1 = 6 \times 10^3 \text{ kg}$ is considered placed in the upper right corner A_1 in Fig. 2.6. The common anisotropic stiffness of columns in y - and z -directions are calculated by Eq. (2.10) $k_y = 981.2 \text{ kN/m}$ and $k_z = 350 \text{ kN/m}$ and the length of each column is 4 m , proper static dimensioning of the elastic columns is performed. The mass moment of inertia about the vertical x -axis is $I_x = (m_S + m_1) r_S^2 = 193.94 \times 10^3 \text{ kg} \cdot \text{m}^2$, $r_S = 2.97 \text{ m}$.

2.10.1 Static dimensioning and a static safety criterion of the columns

The buckling lengths of the cc-columns is $l_c = l = 4 \text{ m}$, see e.g. Ziegler³, page 560. The critical load of a steel profile HEB-160⁵, with respect to the weak axis of buckling, becomes

$$F_c = -\pi^2 EI_y / l_c^2 = -\frac{\pi^2 \times 2.1 \times 10^{11} \times 889 \times 10^{-8}}{4^2} = -1150.43 \text{ kN}, \text{ where } E \text{ denotes the modulus}$$

of elasticity of steel $E = 210 \text{ kN/mm}^2$ and I_y is the principal moment of inertia about the y axis.

The mass of HEB-160 per meter is 42.6 kg/m , the effective mass of a column is calculated by Eq. (2.8) $\bar{m}_1 = 63.3 \text{ kg}$ and total mass of four columns is 253 kg . It is very smaller than the floor mass and the additional point mass, and can be neglected.

Live load for static analysis: $q_k = 4 \text{ kN/m}^2$, $Q_k = 4 \times 8 \times 4 = 128 \text{ kN}$.

Dead load (self weight): $G_1 = m_s g = 16 \times 10^3 \times 9.81 = 156.96 \text{ kN}$,

$$G_2 = m_1 g = 6 \times 10^3 \times 9.81 = 58.86 \text{ kN}.$$

Thus, the combined loads result,

$$N_{sd1} = -1.35 \times G_1 - 1.5 \times Q_k = -403.896 \text{ kN}, \quad N_{sd2} = -1.35 \times G_2 = -79.461 \text{ kN}.$$

The combined load without TLCGD at point A_1 : $F_1 = \frac{N_{sd1}}{4} + N_{sd2} = -180.435 \text{ kN}$. The

combined load without TLCGD at points A_2, A_3, A_4 : $F_2 = \frac{N_{sd1}}{4} = -100.974 \text{ kN}$.

Thus $\frac{F_1}{F_c} = \frac{-180.435}{-1150.43} = 0.16 < 0.33$ and the geometric flexural stiffness correction can be

applied. At point A_1 with weight of the point mass considered,

$$k_{G_1} = \frac{6F_1}{5l} = \frac{6}{5} \times \frac{-180.435}{4} = -54.13 \text{ kN/m}. \quad \text{At points } A_2, A_3, A_4,$$

$$k_{G_2} = \frac{6F_2}{5l} = \frac{6}{5} \times \frac{-100.974}{4} = -30.3 \text{ kN/m}. \quad \text{The corrected stiffness of column at point } A_1 \text{ in } y-$$

and z -direction become 927.07 kN/m and 295.87 kN/m . The corrected stiffness of columns at points A_2, A_3, A_4 in y - and z -direction become 950.9 kN/m and 319.7 kN/m .

2.10.2 Natural modes of the main structure

Natural frequencies are calculated by solving the characteristic Eq. (2.14) by means of Matlab⁷. The result is, columns are assumed to be massless.

$$\tilde{f} = \begin{bmatrix} 1.16 & 0 & 0 \\ 0 & 1.96 & 0 \\ 0 & 0 & 2.37 \end{bmatrix} [\text{Hz}].$$

The orthonormalized modal matrix of the undamped main system is the output of Matlab⁷, displacements of the center of mass are used,

$$\tilde{\phi} = 10^{-2} \begin{bmatrix} -0.030237 & -0.563450 & 0.368990 \\ 0.664320 & -0.085801 & -0.076579 \\ 0.110960 & 0.360150 & 0.559040 \end{bmatrix}.$$

Correction of this output of orthonormalized eigenvectors might become necessary with respect to orthogonality,

$$\tilde{\phi}_j^T \tilde{M} \tilde{\phi}_i = \delta_{ij} = \begin{cases} 0, & i \neq j \\ 1, & i = j \end{cases}, \quad \tilde{\phi}_j^T \tilde{K} \tilde{\phi}_i = \delta_{ij} = \begin{cases} 0, & i \neq j \\ \omega_i^2, & i = j \end{cases}.$$

Test calculations render sufficient accuracy, δ_{ij} is the Kronecker symbol.

$$\tilde{\phi}_1^T \tilde{M} \tilde{\phi}_1 = \delta_{11} = 1, \quad \tilde{\phi}_2^T \tilde{M} \tilde{\phi}_2 = \delta_{22} = 1, \quad \tilde{\phi}_3^T \tilde{M} \tilde{\phi}_3 = \delta_{33} = 1,$$

$$\begin{aligned} \bar{\phi}_2^T \underline{M} \bar{\phi}_1 &= \delta_{12} = \delta_{21} = 2.78 \times 10^{-17}, & \bar{\phi}_3^T \underline{M} \bar{\phi}_1 &= \delta_{13} = \delta_{31} = 5.55 \times 10^{-17}, \\ \bar{\phi}_3^T \underline{M} \bar{\phi}_2 &= \delta_{23} = 2.22 \times 10^{-16}, & \bar{\phi}_2^T \underline{M} \bar{\phi}_3 &= \delta_{32} = 1.11 \times 10^{-16}. \end{aligned}$$

The mode shapes are exaggerated and plotted in Figs. 2.14-2.16. The motion of the structure in each mode consists of coupled translation and torsion.

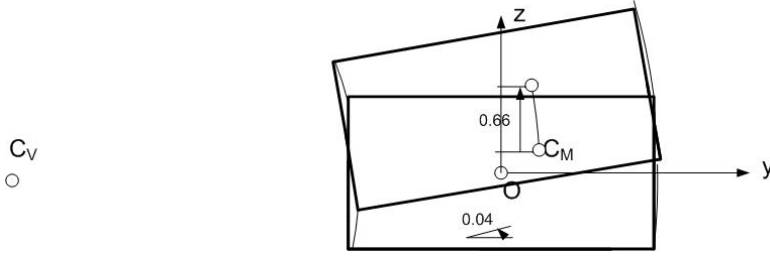


Fig. 2.14: First mode $f_1 = 1.16\text{Hz}$.

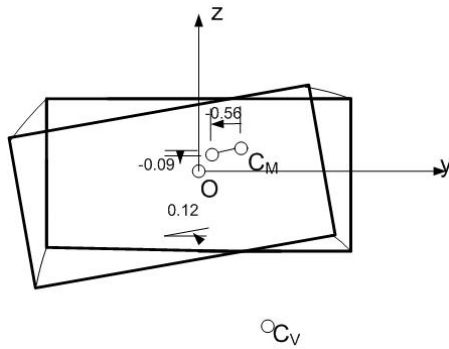


Fig. 2.15: Second mode $f_2 = 1.96\text{Hz}$.

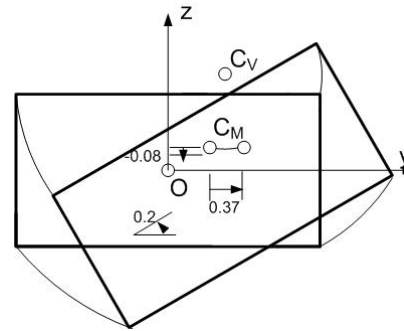


Fig. 2.16: Third mode $f_3 = 2.37\text{Hz}$.

2.10.3 Position of the center of velocity C_V for the modes numbered $j=1,2,3$

The coordinates of the modal centers of velocity C_V are defined by Eq. (2.18) and illustrated in Figs. 2.14-2.16. All centers of velocity are outside of the floor plan thus defining a moderately asymmetric structure.

$$\vec{r}_{C_{V1}} = \begin{bmatrix} -16.685 \\ -0.264 \end{bmatrix} m, \quad \vec{r}_{C_{V2}} = \begin{bmatrix} 1.798 \\ -4.10 \end{bmatrix} m, \quad \vec{r}_{C_{V3}} = \begin{bmatrix} 1.498 \\ 2.505 \end{bmatrix} m.$$

(i) Installation of the TLCGDs

A single tuned liquid column damper for each mode is placed on the floor, as illustrated in Figure 2.17. Rendering the normal distance of its trace to C_V as large as possible within the plan, the TLCGD are installed as follows. Suppressing the first mode TLCGD1 is installed in the middle with respect to the dominant horizontal displacement in z -direction. TLCGD2 can be installed along the long side or alternatively on the short side, tuned to effectively damp the second mode. We choose it parallel to the y -direction. In addition, TLCGD3 can be installed on the opposite side of TLCGD2, thus parallel to the y -direction, or alternatively, on the short side parallel to the z -direction, to be considered subsequently in Section 2.10.8. We will investigate both installations of TLCGD3 to compare both locations with respect to the effectiveness for structural control.

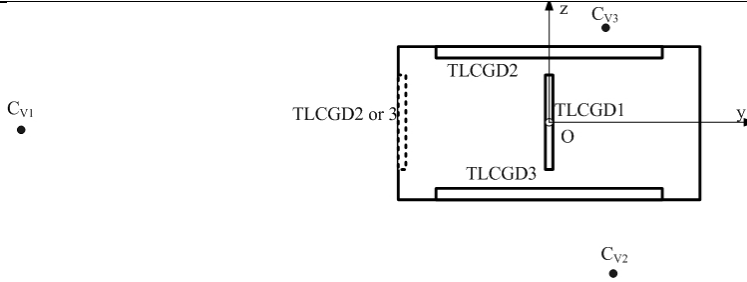


Fig. 2.17: Positioning of 3 TLCGDs, an alternative shown. Here, • indicates the modal centers velocity.

2.10.4 The linearized equation of motion for TLCGD

In Equation (2.36), putting $y_A = 0$, $z_A = 0$, $u_T = \theta r_S$, $\gamma = \pi/2$ renders the equation of motion for the TLCGD1 (z-parallel)

$$\ddot{u}_1 + 2\zeta_{A1}\omega_{A1}\dot{u}_1 + \omega_{A1}^2 u_1 = -\kappa_{(1)}(\ddot{w}_g + \ddot{w} - y_{C_M}\ddot{u}_T/r_S).$$

In Equation (2.36), putting $y_{A2} = 0$, $y_{A3} = 0$, $u_T = \theta r_S$, $\gamma = 0$ yields the equation of motion for both TLCGD2 and TLCGD3 (y-parallel)

$$\ddot{u}_2 + 2\zeta_{A2}\omega_{A2}\dot{u}_2 + \omega_{A2}^2 u_2 = -\kappa_{(2)}[\ddot{v}_g + \ddot{v} - (z_{A2} - z_{C_M})\ddot{u}_T/r_S],$$

$$\ddot{u}_3 + 2\zeta_{A3}\omega_{A3}\dot{u}_3 + \omega_{A3}^2 u_3 = -\kappa_{(3)}[\ddot{v}_g + \ddot{v} - (z_{A3} - z_{C_M})\ddot{u}_T/r_S].$$

2.10.5 The linearized control forces for TLCGD acting on the floor applying the substructure synthesis

In Equations (2.51) and (2.52), putting $y_A = 0$, $z_A = 0$, $u_T = \theta r_S$, $\gamma = \pi/2$ and considering Eq. (2.64) render the linearized control forces exerted by TLCGD1 on the space frame

$$F_{Ay1} = -m_{f1}(\ddot{v}_g + \ddot{v} + z_{C_M}\ddot{u}_T/r_S), \quad F_{Az1} = -m_{f1}(\ddot{w}_g + \ddot{w} - y_{C_M}\ddot{u}_T/r_S + \bar{\kappa}_{(1)}\ddot{u}_1),$$

$$M_{Ax1} = -m_{f1}\bar{\kappa}_{3(1)}H_1^2\ddot{u}_T/r_S.$$

The linearized control forces exerted by TLCGD 2 and TLCGD 3 become, Eqs. (2.51), (2.52) and (2.64) are properly considered

$$F_{Ay2} = -m_{f2}[\ddot{v}_g + \ddot{v} - (z_{A2} - z_{C_M})\ddot{u}_T/r_S + \bar{\kappa}_{(2)}\ddot{u}_2], \quad F_{Az2} = -m_{f2}(\ddot{w}_g + \ddot{w} - y_{C_M}\ddot{u}_T/r_S),$$

$$M_{Ax2} = -m_{f2}\bar{\kappa}_{3(2)}H_2^2\ddot{u}_T/r_S,$$

$$F_{Ay3} = -m_{f3}[\ddot{v}_g + \ddot{v} - (z_{A3} - z_{C_M})\ddot{u}_T/r_S + \bar{\kappa}_{(3)}\ddot{u}_3], \quad F_{Az3} = -m_{f3}(\ddot{w}_g + \ddot{w} - y_{C_M}\ddot{u}_T/r_S),$$

$$M_{Ax3} = -m_{f3}\bar{\kappa}_{3(3)}H_3^2\ddot{u}_T/r_S.$$

Fig. 2.18 indicates their action.

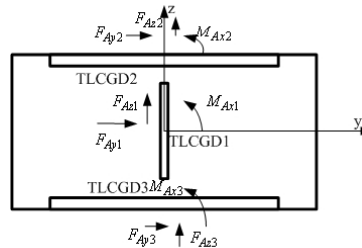


Fig. 2.18: Reaction forces and moments for TLCGD1, 2, and 3.

2.10.6 TLCGD design, Den Hartog' optimization

Since the modes of the main structure seem to be sufficiently separated, modal tuning of TLCGD is performed in a first step by a transformation of the classical Den Hartog formulas by means of the analogy between TMD and TLCGD. Optimal TMD design parameters, frequency ratio and damping ratio, are determined subjected to the harmonic excitation. The optimum tuning frequency ratio between the equivalent mechanical absorber and the main structure for minimum total acceleration is, see Den Hartog¹², page 97 and 101

$$\delta_{opt}^* = \frac{1}{1 + \mu^*}, \quad (2.112)$$

and the corresponding optimum linear viscous damping coefficient is given by

$$\zeta_{opt}^* = \sqrt{\frac{3\mu^*}{8(1 + \mu^*)}}. \quad (2.113)$$

The same parameters apply also in case of time harmonic forcing and minimizing the dynamic displacement magnification factor of the main system.

The fluid mass is chosen as $m_{f1} = 770kg$, $m_{f2} = 320kg$ and $m_{f3} = 180kg$ of water. Dimensions of the three TLCGDs tuned first by means of the TMD analogy Eqs. (2.102)-(2.104) applying Den Hartog's formulas are summarized in Table 2.1.

	TLCGD1	TLCGD2	TLCGD3
	z-parallel	y-parallel	y-parallel
Horizontal length of the liquid column B [m]	3.00	2.50	3.00
Inclined length of the liquid column H [m]	1.40	0.86	0.60
Cross-sectional area of the pipe [m ²] $A_H=A_B$	0.1330	0.0760	0.0430
Effective length $L_{eff} = L_1 = 2H + B$ [m], Eq. (2.34a)	5.80	4.22	4.20
Angle of the inclined pipe section β [rad]	$\pi/4$	$\pi/4$	$\pi/4$
Equivalent mathematical pendulum length L_0 [m], Eq. (2.37)	0.19	0.07	0.05
Geometry factor $\kappa = \bar{\kappa}$, Eqs. (2.34a), (2.44)	0.86	0.88	0.92
Geometry factor $\bar{\kappa}_3$, Eq. (2.59)	1.20	1.77	3.83
Equilibrium pressure head h_0 [m], $n=1.2$, Eq. (2.34a)	36.70	45.26	46.50
Gas volume $V_0 = A_H H_a$ [m ³], Eq. (2.38)	0.340000	0.110000	0.044000
The mass ratio of the TLCGD-main system μ , Eq. (2.97)	3.02%	2%	1.53%
The mass ratio of the equivalent TMD-main system μ^* , Eq. (2.102)	2.19%	1.47%	1.20%
Natural frequency $f_{A,opt}$ [Hz] Eq. (2.104), (2.112)	1.13	1.92	2.33
Optimal linear damping %, Eq. (2.113)	8.96	7.37	6.68

Table 2.1: Layout of the modally tuned TLCGDs, gas volume and gas equilibrium pressure assigned, cf. Fig. (2.17).

Fig.2.19 illustrates the scaled scheme of TLCGDs. The modal dynamic magnification factor (DMF) calculated with Matlab 7.0⁷, equivalently linearized damping of the TLCGD considered, is illustrated in Figure 2. 20.

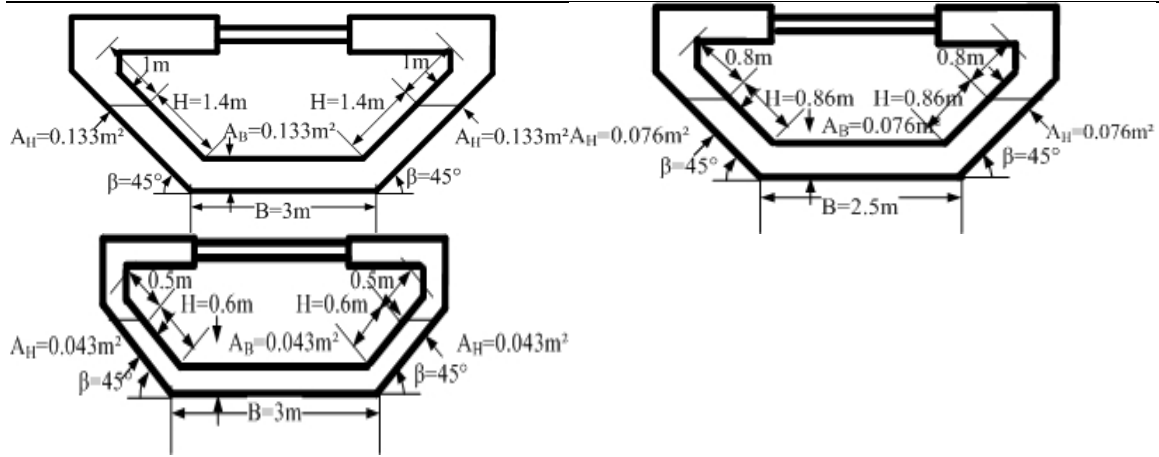


Fig. 2.19: Scaled sketches of TLCGDs.

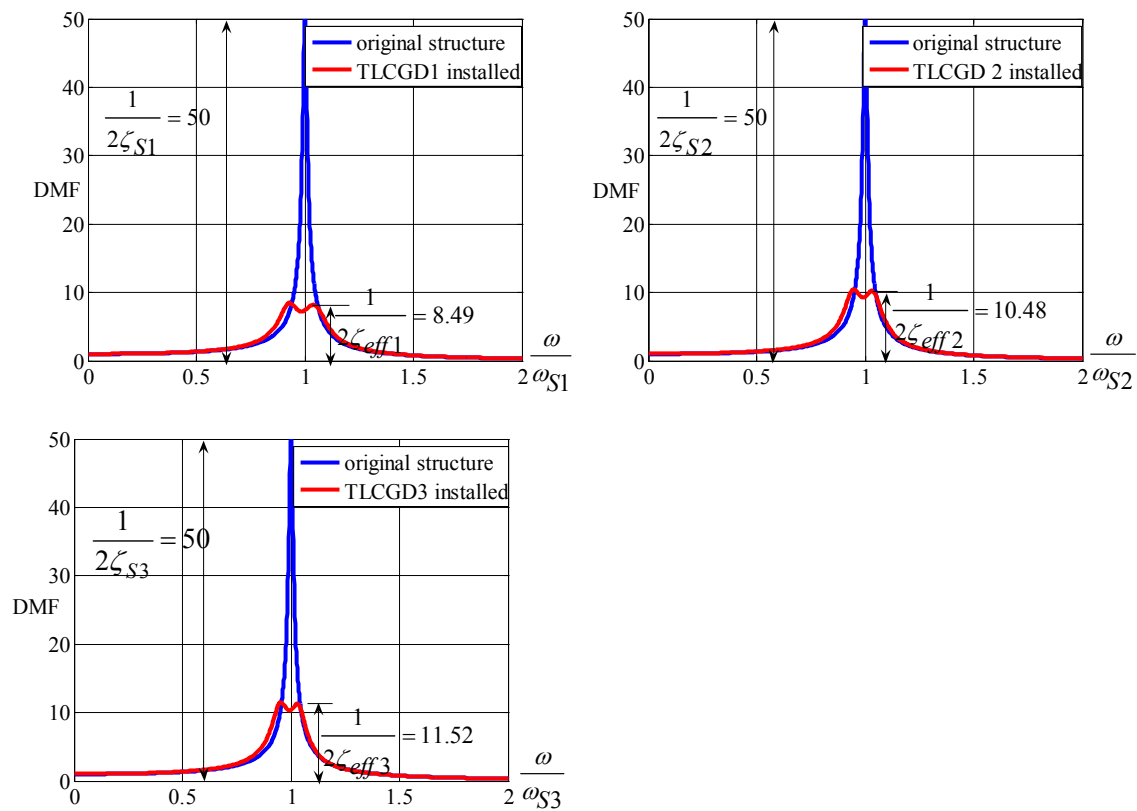


Fig. 2.20: Modal frequency response curves without and with linearized TLCGDs attached, Eqs. (2.106) and (2.110), TLCGDs with Den Hartog's optimal parameters.

The TLCGD in its passive mode considerably reduces steady state vibrations of lightly damped structures similarly to an increase of the effective structural damping. The effective modal damping coefficients of the system in each mode are increased from $\zeta_{Sj} = 1\%$ to $\zeta_{eff1} = 5.9\%$, $\zeta_{eff2} = 4.77\%$ and $\zeta_{eff3} = 4.34\%$.

From Table 2.2a-c it follows that all of the maximum fluid displacements for varying angles of attack of the time harmonic excitation, are within the acceptable limits, $u_0 < H_a/3$ (of linearized gas compression) and $u_0 < H/2$. The maximum fluid velocities of three TLCGDs are calculated by Eq. (2.35) 4.81, 4.32 and 3.43m/s and are within the acceptable speed limit.

Single-storey Moderately Plan-asymmetric Space Frame with TLCDs

Forcing direction	structure			TLCGD1	
		v[mm]	w[mm]	$u_T = r_S \theta$ [mm]	u_0 [mm]
$\alpha = 0$	C _M	0	7	1	27
	A	0	6		
$\alpha = \pi/6$	C _M	-3	76	13	315
	A	-1	71		
$\alpha = \pi/4$	C _M	-5	111	19	460
	A	-2	104		
$\alpha = \pi/3$	C _M	-6	138	23	573
	A	-2	130		
$\alpha = \pi/2$	C _M	-7	164	27	678
	A	-2	154		
$\alpha = 2\pi/3$	C _M	-7	145	24	600
	A	-2	136		
$\alpha = 3\pi/4$	C _M	-5	121	20	498
	A	-2	113		
$\alpha = 5\pi/6$	C _M	-4	88	15	362
	A	-1	82		

Table 2.2a: Maximum displacements in the first mode from time-harmonic excitation in α -directions, $a_0=0.1g$, $r_S = 2.97m$.

Forcing direction	structure			TLCGD2	
		v[mm]	w[mm]	$u_T = r_S \theta$ [mm]	u_0 [mm]
$\alpha = 0$	C _M	-49.	-7	31	358
	A	-64	-19		
$\alpha = \pi/6$	C _M	-46	-7	29	355
	A	-61	-18		
$\alpha = \pi/4$	C _M	-40	-6	25	289
	A	-52	-15		
$\alpha = \pi/3$	C _M	-31	-5	20	223
	A	-40	-12		
$\alpha = \pi/2$	C _M	-7	-1	5	52
	A	-10	-3		
$\alpha = 2\pi/3$	C _M	-18	-3	12	134
	A	-24	-7		
$\alpha = 3\pi/4$	C _M	-30	-5	19	217
	A	-39	-11		
$\alpha = 5\pi/6$	C _M	-39	-6	25	284
	A	-51	-15		

Table 2.2b: Maximum displacements in the second mode from time-harmonic excitation in α -directions, $a_0=0.1g$, $r_S = 2.97m$.

Forcing direction	structure			TLCGD3	
		v[mm]	w[mm]	$u_T = r_S \theta$ [mm]	u_0 [mm]
$\alpha = 0$	C_M	16	-3	24	234
	A	36	-12		
$\alpha = \pi/6$	C_M	12	-3	18	181
	A	28	-9		
$\alpha = \pi/4$	C_M	9	-2	14	134
	A	21	-7		
$\alpha = \pi/3$	C_M	5	-1	8	78
	A	12	-4		
$\alpha = \pi/2$	C_M	3	-1	5	45
	A	7	-2		
$\alpha = 2\pi/3$	C_M	11	-2	16	156
	A	25	-8		
$\alpha = 3\pi/4$	C_M	13	-3	20	198
	A	31	-10		
$\alpha = 5\pi/6$	C_M	15	-3	23	225
	A	35	-12		

Table 2.2c: Maximum displacements in the third mode from time-harmonic excitation in α -directions, $a_0=0.1g$, $r_S = 2.97m$.

2.10.7 Optimization of single-storey space frame with 3 TLCGDs in the state space domain

The equation of motion for the combined multiple degree of freedom structure (primary system) and several TLCGDs (secondary system) can be derived as follows

$$\underline{M}\ddot{\bar{x}} + \underline{C}\dot{\bar{x}} + \underline{K}\bar{x} = -\underline{M}\ddot{\bar{x}}_g + \underline{L}\bar{P}, \quad \bar{x}^T = [v \quad w \quad u_T], \quad \ddot{\bar{x}}_g^T = [\ddot{v}_g \quad \ddot{w}_g \quad 0],$$

$$\bar{P}^T = [\bar{P}_1^T \quad \bar{P}_2^T \quad \bar{P}_3^T], \quad \bar{P}_j^T = [F_{A_{yj}} \quad F_{A_{zj}} \quad M_{xj}/r_S] \quad (2.114)$$

where $\underline{M} = M_S \text{diag}[1 \ 1 \ 1]$ is the mass matrix of the main structure, $M_S = m_S + m_1 + m'_1 + m'_2 + m'_3$, where m'_1 , m'_2 and m'_3 denote the mass of the rigid piping systems; \bar{x} is the displacement vector of the structure; \underline{C} is such a damping matrix of the structure that keeps the modal vectors orthogonal, light modal damping coefficients are all assumed to be 1%. \underline{K} is the stiffness matrix of the structure; $\ddot{\bar{x}}_g$ denotes the seismic ground acceleration vector. \bar{P}^T is the control force vector and $\underline{L} = [\underline{L}_1 \quad \underline{L}_2 \quad \underline{L}_3]$; $\underline{L}_j = \text{diag}[1 \ 1 \ 1]$ is the position matrix of the TLCGDs.

The linearized control force produced by several TLCGDs takes on the hyper matrix form, for a single TLCGD see e.g. Eq. (2.57), $\bar{P} = -\underline{M}_f (\underline{T}\ddot{\bar{x}} + \underline{i}\ddot{\bar{x}}_g + \underline{\bar{\kappa}}\ddot{u})$, see section 2.9.5. Here, for TLCGD1 (z-parallel), TLCGD2 and TLCGD3 (both y-parallel)

$$\underline{T}^T = [\underline{T}_{1z} \quad \underline{T}_{2y} \quad \underline{T}_{3y}], \quad \underline{T}_z = \begin{bmatrix} 1 & 0 & z_{C_M}/r_S \\ 0 & 1 & (y_A - y_{C_M})/r_S \\ z_{C_M}/r_S & (y_A - y_{C_M})/r_S & [(y_A - y_{C_M})^2 + z_{C_M}^2 + \bar{\kappa}_3 H^2]/r_S^2 \end{bmatrix}$$

$$\begin{aligned}
 \underline{\mathbf{T}}_y &= \begin{bmatrix} 1 & 0 & -(z_A - z_{C_M})/r_S \\ 0 & 1 & -y_{C_M}/r_S \\ -(z_A - z_{C_M})/r_S & -y_{C_M}/r_S & [(z_A - z_{C_M}^2)^2 + y_{C_M}^2 + \bar{\kappa}_3 H^2]/r_S^2 \end{bmatrix}, \\
 \underline{\dot{\mathbf{i}}}^T &= [\underline{\dot{i}}_{1z} \quad \underline{\dot{i}}_{2y} \quad \underline{\dot{i}}_{3y}], \quad \underline{\dot{\mathbf{z}}} = \begin{bmatrix} 1 & 0 & 0 \\ 0 & 1 & 0 \\ z_{C_M}/r_S & (y_A - y_{C_M})/r_S & 0 \end{bmatrix}, \\
 \underline{\dot{\mathbf{i}}}_y &= \begin{bmatrix} 1 & 0 & 0 \\ 0 & 1 & 0 \\ -(z_A - z_{C_M})/r_S & -y_{C_M}/r_S & 0 \end{bmatrix}, \\
 \underline{\bar{\mathbf{K}}}^T &= [\underline{\bar{\mathbf{K}}}_{1z} \quad \underline{\bar{\mathbf{K}}}_{2y} \quad \underline{\bar{\mathbf{K}}}_{3y}], \quad \underline{\bar{\mathbf{K}}}_{1z} = \begin{bmatrix} 0 & 0 & 0 \\ \bar{\kappa}_1 & 0 & 0 \\ (y_{A1} - y_{C_M})\bar{\kappa}_1/r_S & 0 & 0 \end{bmatrix}, \\
 \underline{\bar{\mathbf{K}}}_{2y} &= \begin{bmatrix} 0 & \bar{\kappa}_2 & 0 \\ 0 & 0 & 0 \\ 0 & -(z_{A2} - z_{C_M})\bar{\kappa}_2/r_S & 0 \end{bmatrix}, \quad \underline{\bar{\mathbf{K}}}_{3y} = \begin{bmatrix} 0 & 0 & \bar{\kappa}_3 \\ 0 & 0 & 0 \\ 0 & 0 & -(z_{A3} - z_{C_M})\bar{\kappa}_3/r_S \end{bmatrix}, \\
 \underline{\mathbf{M}}_f &= \text{diag}(m_{f1}, m_{f1}, m_{f1}, m_{f2}, m_{f2}, m_{f2}, m_{f3}, m_{f3}, m_{f3}). \tag{2.115}
 \end{aligned}$$

$\underline{\mathbf{u}}^T = [u_1 \quad u_2 \quad u_3]$ samples the relative fluid displacements.

The equations of motion for TLCGD-main structure system by substituting the control force and rearranging terms, can be given as

$$\begin{bmatrix} \underline{\mathbf{M}} + \underline{\mathbf{L}}\underline{\mathbf{M}}_f\underline{\mathbf{T}} & \underline{\mathbf{L}}\underline{\mathbf{M}}_f\underline{\bar{\mathbf{K}}} \\ \underline{\kappa}\underline{\mathbf{T}}' & \underline{\mathbf{I}} \end{bmatrix} \begin{Bmatrix} \underline{\ddot{\mathbf{x}}} \\ \underline{\ddot{\mathbf{u}}} \end{Bmatrix} + \begin{bmatrix} \underline{\mathbf{C}} & \underline{\mathbf{0}} \\ \underline{\mathbf{0}} & \underline{\mathbf{C}}_f \end{bmatrix} \begin{Bmatrix} \underline{\dot{\mathbf{x}}} \\ \underline{\dot{\mathbf{u}}} \end{Bmatrix} + \begin{bmatrix} \underline{\mathbf{K}} & \underline{\mathbf{0}} \\ \underline{\mathbf{0}} & \underline{\mathbf{K}}_f \end{bmatrix} \begin{Bmatrix} \underline{\mathbf{x}} \\ \underline{\mathbf{u}} \end{Bmatrix} = - \begin{bmatrix} \underline{\mathbf{M}} + \underline{\mathbf{L}}\underline{\mathbf{M}}_f\underline{\dot{\mathbf{i}}} \\ \underline{\kappa}\underline{\dot{\mathbf{i}}}' \end{bmatrix} \{\underline{\ddot{\mathbf{x}}}_g\}, \tag{2.116}$$

$$\text{where } \underline{\mathbf{T}}' = \begin{bmatrix} 0 & 1 & (y_{A1} - y_{C_M})/r_S \\ 1 & 0 & -(z_{A2} - z_{C_M})/r_S \\ 1 & 0 & -(z_{A3} - z_{C_M})/r_S \end{bmatrix}, \quad \underline{\dot{\mathbf{i}}}' = \begin{bmatrix} 0 & 1 & 0 \\ 1 & 0 & 0 \\ 1 & 0 & 0 \end{bmatrix}, \quad \underline{\kappa} = \text{diag}(\kappa_1, \kappa_2, \kappa_3),$$

$\underline{\mathbf{C}}_f = \text{diag}[2\zeta_{A1}\omega_{A1}, 2\zeta_{A2}\omega_{A2}, 2\zeta_{A3}\omega_{A3}]$ denotes the linearized damping matrix of TLCGDs;

$\underline{\mathbf{K}}_f = \text{diag}[\omega_{A1}^2, \omega_{A2}^2, \omega_{A3}^2]$ denotes the ‘‘stiffness’’ matrix of TLCGDs.

$$\underline{\mathbf{M}}' = \begin{bmatrix} \underline{\mathbf{M}} + \underline{\mathbf{L}}\underline{\mathbf{M}}_f\underline{\mathbf{T}} & \underline{\mathbf{L}}\underline{\mathbf{M}}_f\underline{\bar{\mathbf{K}}} \\ \underline{\kappa}\underline{\mathbf{T}}' & \underline{\mathbf{I}} \end{bmatrix}, \tag{2.117}$$

$$\begin{Bmatrix} \underline{\ddot{\mathbf{x}}} \\ \underline{\ddot{\mathbf{u}}} \end{Bmatrix} = -\underline{\mathbf{M}}'^{-1} \begin{bmatrix} \underline{\mathbf{C}} & \underline{\mathbf{0}} \\ \underline{\mathbf{0}} & \underline{\mathbf{C}}_f \end{bmatrix} \begin{Bmatrix} \underline{\dot{\mathbf{x}}} \\ \underline{\dot{\mathbf{u}}} \end{Bmatrix} - \underline{\mathbf{M}}'^{-1} \begin{bmatrix} \underline{\mathbf{K}} & \underline{\mathbf{0}} \\ \underline{\mathbf{0}} & \underline{\mathbf{K}}_f \end{bmatrix} \begin{Bmatrix} \underline{\mathbf{x}} \\ \underline{\mathbf{u}} \end{Bmatrix} - \underline{\mathbf{M}}'^{-1} \begin{bmatrix} \underline{\mathbf{M}} + \underline{\mathbf{L}}\underline{\mathbf{M}}_f\underline{\dot{\mathbf{i}}} \\ \underline{\kappa}\underline{\dot{\mathbf{i}}}' \end{bmatrix} \{\underline{\ddot{\mathbf{x}}}_g\}. \tag{2.118}$$

This system of second order differential equations can be lastly converted to a first order state space representation by introducing the state hyper vector $2(N+n)$, $\underline{\mathbf{z}} = [\underline{\mathbf{x}}^T \quad \underline{\mathbf{u}}^T \quad \underline{\dot{\mathbf{x}}}^T \quad \underline{\dot{\mathbf{u}}}^T]^T$

and its time derivative, see e.g. Ziegler³, page 438

$$\dot{\bar{z}} = (\underline{\mathbf{A}} + \underline{\mathbf{B}}\underline{\mathbf{R}})\bar{z} + \underline{e}_g \ddot{x}_g(t), \quad (2.119)$$

where, in a hypermatrix notation, the system matrix remains separated,

$$\underline{\mathbf{A}} = \begin{bmatrix} \underline{\mathbf{0}} & \underline{\mathbf{0}} & \underline{\mathbf{I}} & \underline{\mathbf{0}} \\ \underline{\mathbf{0}} & \underline{\mathbf{0}} & \underline{\mathbf{0}} & \underline{\mathbf{I}} \\ -\underline{\mathbf{M}}^{-1} \begin{bmatrix} \underline{\mathbf{K}} & \underline{\mathbf{0}} \\ \underline{\mathbf{0}} & \underline{\mathbf{0}} \end{bmatrix} & -\underline{\mathbf{M}}^{-1} \begin{bmatrix} \underline{\mathbf{C}} & \underline{\mathbf{0}} \\ \underline{\mathbf{0}} & \underline{\mathbf{0}} \end{bmatrix} & & \end{bmatrix}, \quad \underline{\mathbf{B}} = \begin{bmatrix} \underline{\mathbf{0}} & \underline{\mathbf{0}} & \underline{\mathbf{0}} & \underline{\mathbf{0}} \\ \underline{\mathbf{0}} & \underline{\mathbf{0}} & \underline{\mathbf{0}} & \underline{\mathbf{0}} \\ -\underline{\mathbf{M}}^{-1} \begin{bmatrix} \underline{\mathbf{I}} & \underline{\mathbf{0}} \\ \underline{\mathbf{0}} & \underline{\mathbf{I}} \end{bmatrix} & -\underline{\mathbf{M}}^{-1} \begin{bmatrix} \underline{\mathbf{I}} & \underline{\mathbf{0}} \\ \underline{\mathbf{0}} & \underline{\mathbf{I}} \end{bmatrix} & & \end{bmatrix},$$

$$\underline{\mathbf{R}} = \begin{bmatrix} \underline{\mathbf{0}} & \underline{\mathbf{0}} & \underline{\mathbf{0}} & \underline{\mathbf{0}} \\ \underline{\mathbf{0}} & \underline{\mathbf{K}}_f & \underline{\mathbf{0}} & \underline{\mathbf{0}} \\ \underline{\mathbf{0}} & \underline{\mathbf{0}} & \underline{\mathbf{0}} & \underline{\mathbf{0}} \\ \underline{\mathbf{0}} & \underline{\mathbf{0}} & \underline{\mathbf{0}} & \underline{\mathbf{C}}_f \end{bmatrix}, \quad \underline{e}_g = \begin{bmatrix} \underline{\mathbf{0}} \\ \underline{\mathbf{0}} \\ -\underline{\mathbf{M}}^{-1} \begin{bmatrix} \underline{\mathbf{M}} + \underline{\mathbf{L}}\underline{\mathbf{M}}_f \underline{\mathbf{I}} \\ \underline{\kappa} \underline{\mathbf{I}}' \end{bmatrix} \end{bmatrix}. \quad (2.120)$$

The time-harmonic solution $\bar{z}(t) = \bar{z}e^{i\omega t}$, assuming the ground excitation to be time-harmonic

$$\ddot{x}_g(t) = \begin{Bmatrix} \ddot{v}_g(t) \\ \ddot{w}_g(t) \\ 0 \end{Bmatrix} = a_0 \bar{e}_S e^{i\omega t}, \quad \bar{e}_S^T = [\cos \alpha \quad \sin \alpha \quad 0], \quad (2.121)$$

simply becomes

$$\bar{z}(\alpha, \omega) = [i\omega \underline{\mathbf{I}} - (\underline{\mathbf{A}} + \underline{\mathbf{B}}\underline{\mathbf{R}})]^{-1} \underline{e}_g \bar{e}_S a_0. \quad (2.122)$$

The optimal natural frequency and the damping ratios of the TLCD are calculated by minimizing the following performance index, corresponding to the minimum of the area under the resonance curve,

$$J = \int_{-\infty}^{\infty} \bar{z}_S^T(\omega) \underline{\mathbf{S}} \bar{z}_S(\omega) d\omega = 2\pi \bar{b}^T \underline{\mathbf{P}} \bar{b} \rightarrow \text{Minimum}, \quad u_T = r_S \theta, \quad (2.123)$$

where $\bar{z}_S = [v, w, u_T, \dot{v}, \dot{w}, \dot{u}_T]^T$ represents the main structure's state vector 2N. The positive semidefinite weighing matrix $\underline{\mathbf{S}} = \text{diag}(10, 10, 10, 1, 1, 1)$ is chosen e.g. to pronounce displacements. $\bar{b} = \underline{e}_g \bar{e}_S a_0$ is the excitation vector. $\underline{\mathbf{P}}$ is consequently the solution of the

algebraic Lyapunov matrix equation, $(\underline{\mathbf{A}} + \underline{\mathbf{B}}\underline{\mathbf{R}})^T \underline{\mathbf{P}} + \underline{\mathbf{P}}(\underline{\mathbf{A}} + \underline{\mathbf{B}}\underline{\mathbf{R}}) = -\underline{\mathbf{S}}$. The latter is numerically evaluated by means of the software Matlab⁷. The minimization of J is performed numerically by calling the function *fminsearch* of the Matlab Optimization Toolbox. *fminsearch* finds the minimum of the scalar function J of several variables quickly, when substituting Den Hartog's modal tuning parameters $x_0 = [\omega_{A1}, \omega_{A2}, \omega_{A3}; \zeta_{A1}, \zeta_{A2}, \zeta_{A3}]$, for the initial estimate, e.g. $x_0 = [7.12, 12.09, 14.66; 8.96\%, 7.37\%, 6.68\%]$. The optimal natural frequencies and damping ratios determined by this fine tuning process turn out $f_{A1} = 1.13\text{Hz}$, $f_{A2} = 1.90\text{Hz}$, $f_{A3} = 2.33\text{Hz}$, $\zeta_{A1} = 7.51\%$, $\zeta_{A2} = 5.72\%$, $\zeta_{A3} = 4.91\%$, i.e. frequencies are slightly lowered and the damping coefficients of the fluid flow are commonly "dramatically" lowered. The equilibrium pressure head h_0 of the three TLCDs are properly adjusted 34.47, 42.79 and 45.15m, see Table 2.1 for the former slightly higher values. Figs. 2.21-2.28 show the

frequency response of the weighed sum $\sum_{i=1}^6 s_i |z_{S_i}(v)|$ of the building states for the original and the optimized system under ground acceleration with various angles of attack, in the logarithmic decibel scale $x[\text{dB}] = 20 \log x$ within the frequency window $0 \leq f \leq 3\text{Hz}$. The

results with fine-tuning optimal parameters are somewhat better, since the curves have broader resonance peaks.

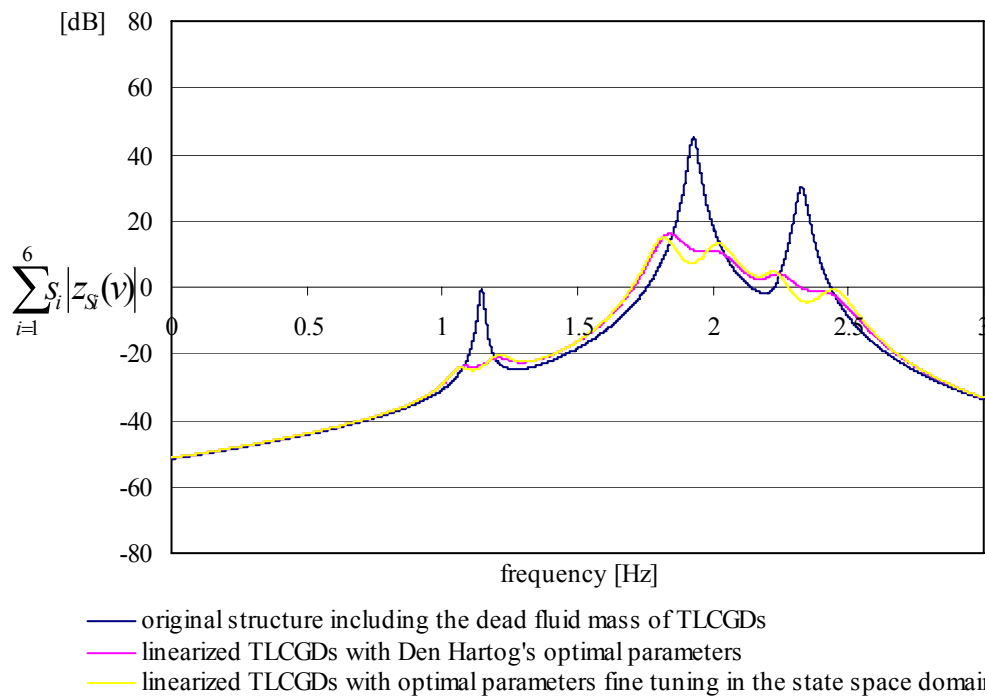


Fig. 2.21: Weighed sum of amplitude response functions for the 3-DOF linearized, single-storey, moderately asymmetric space frame, with three linearized TLCGDs attached (TLCGD3 y -parallel) and without the TLCGDs (angle of attack of the time-harmonic base acceleration $\alpha = 0$), maximum gain 29.98dB.

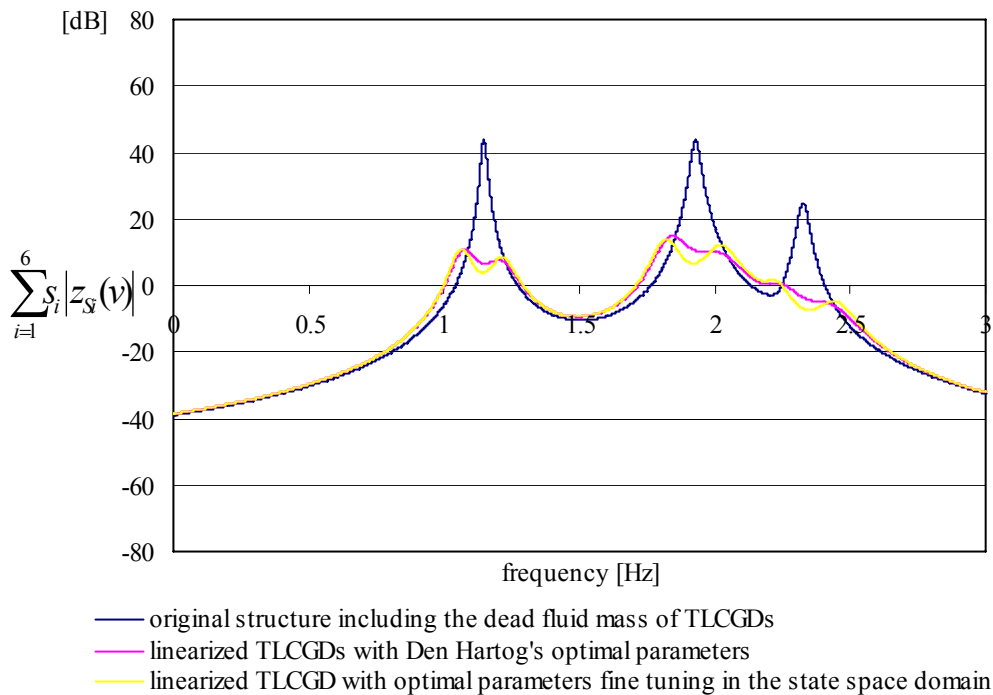


Fig. 2.22: Weighed sum of amplitude response functions for the 3-DOF linearized, single-storey, moderately asymmetric space frame, with three linearized TLCGDs attached (TLCGD3 y -parallel) and without the TLCGDs (angle of attack of the time-harmonic base acceleration $\alpha = \pi/6$), maximum gain 30.15dB.

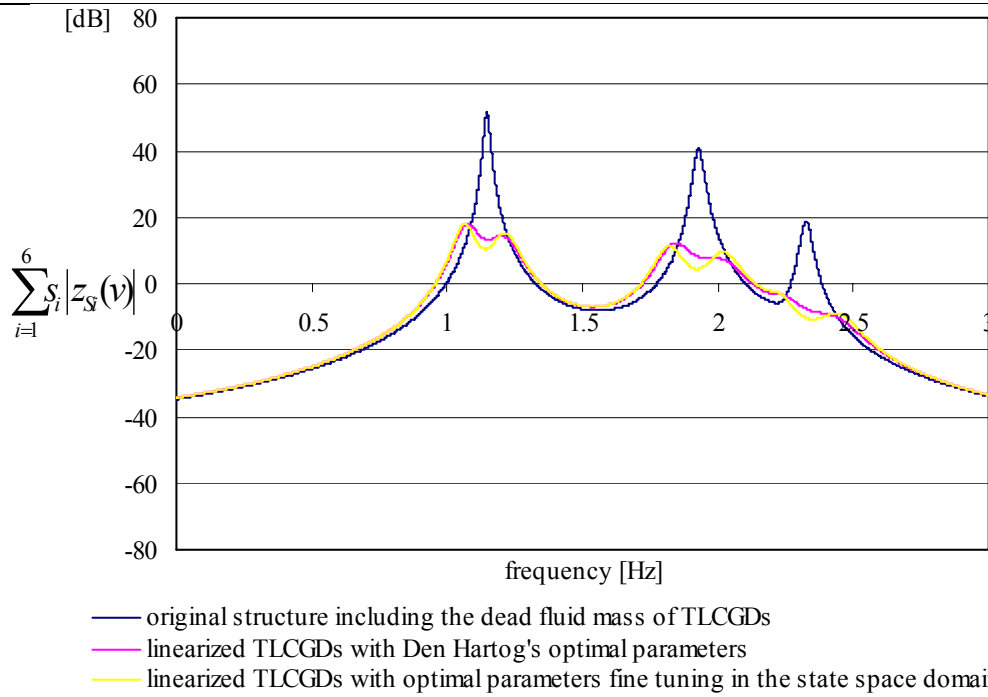


Fig. 2.23: Weighed sum of amplitude response functions for the 3-DOF linearized, single-storey, moderately asymmetric space frame, with three linearized TLCGDs attached (TLCGD3 y -parallel) and without the TLCGDs (angle of attack of the time-harmonic base acceleration $\alpha = \pi/4$), maximum gain 33.58dB.

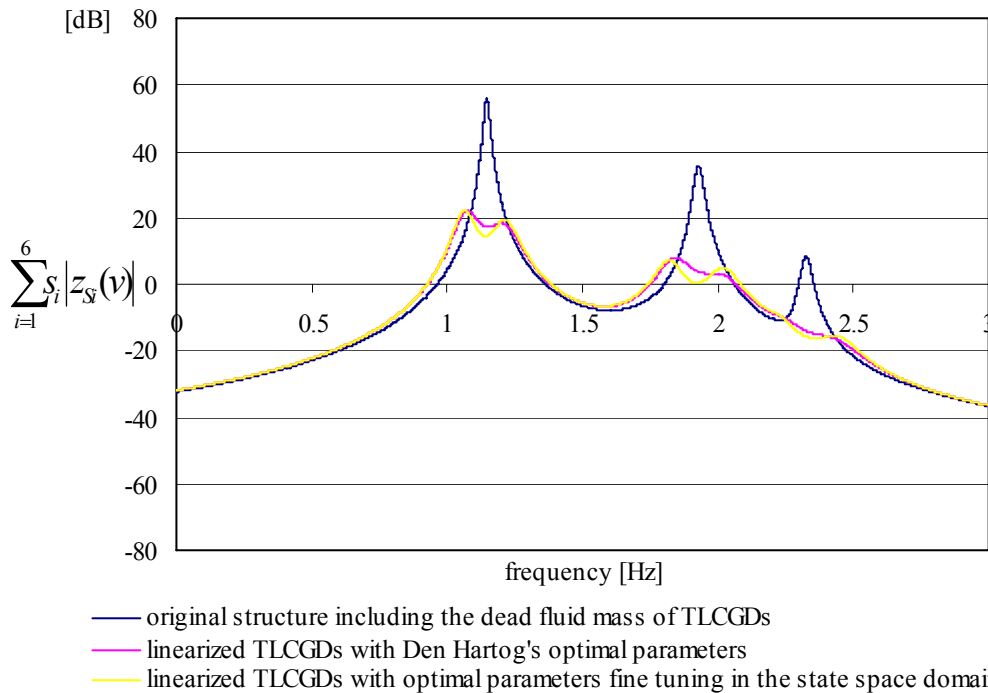


Fig. 2.24: Weighed sum of amplitude response functions for the 3-DOF linearized, single-storey, moderately asymmetric space frame, with three linearized TLCGDs attached (TLCGD3 y -parallel) and without the TLCGDs (angle of attack of the time-harmonic base acceleration $\alpha = \pi/3$), maximum gain 33.8dB.

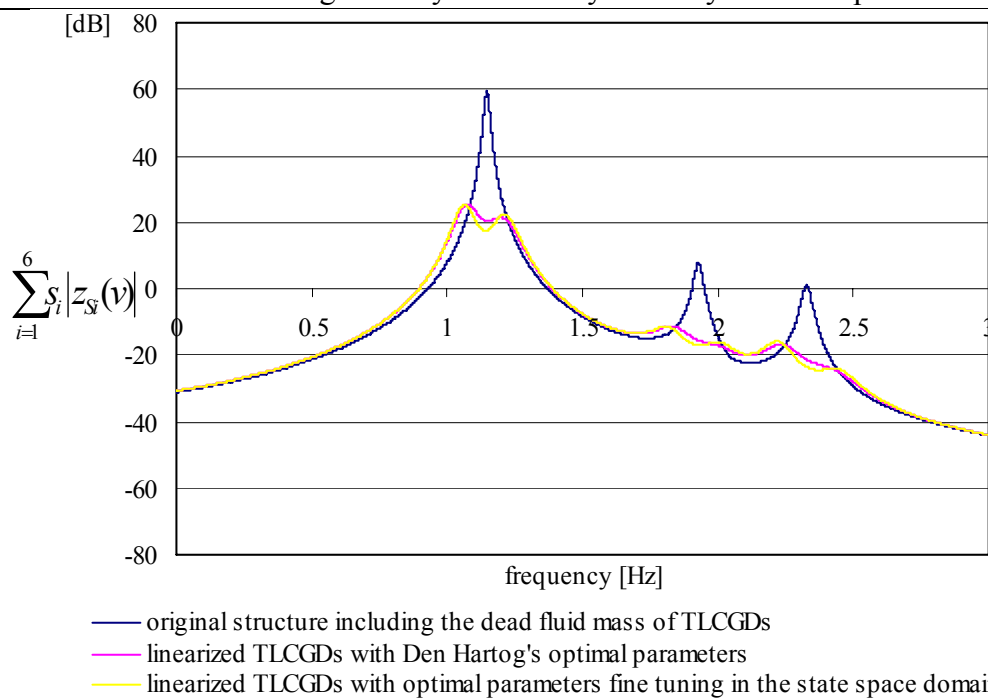


Fig. 2.25: Weighed sum of amplitude response functions for the 3-DOF linearized, single-storey, moderately asymmetric space frame, with three linearized TLCGDs attached (TLCGD3 y -parallel) and without the TLCGDs (angle of attack of the time-harmonic base acceleration $\alpha = \pi/2$), maximum gain 33.78dB.

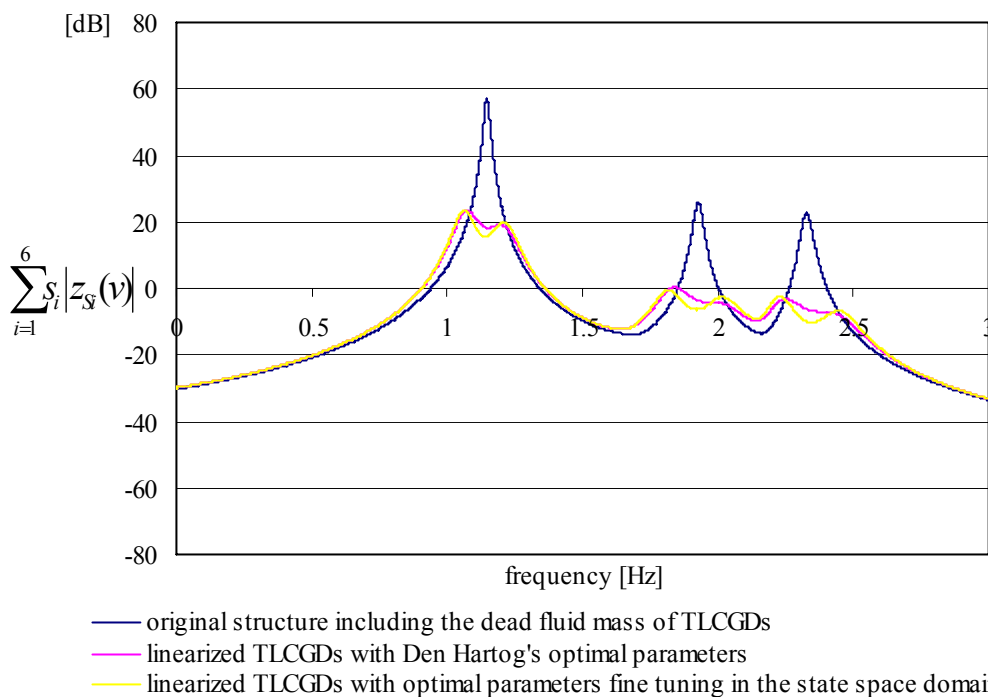


Fig. 2.26: Weighed sum of amplitude response functions for the 3-DOF linearized, single-storey, moderately asymmetric space frame, with three linearized TLCGDs attached (TLCGD3 y -parallel) and without the TLCGDs (angle of attack of the time-harmonic base acceleration $\alpha = 2\pi/3$), maximum gain 33.5dB.

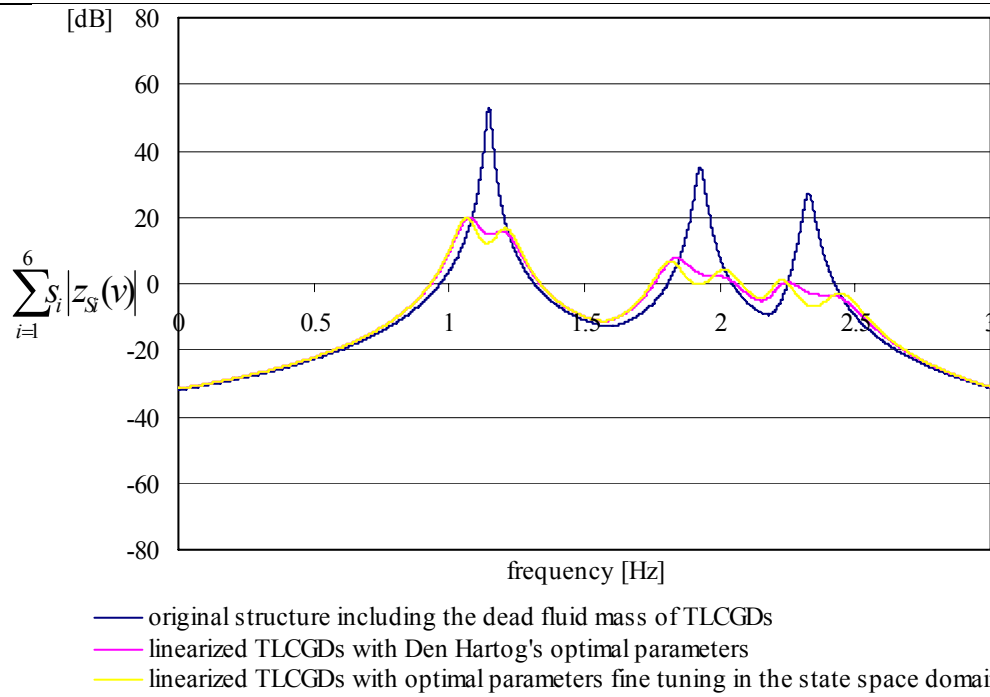


Fig. 2.27: Weighed sum of amplitude response functions for the 3-DOF linearized, single-storey, moderately asymmetric space frame, with three linearized TLCGDs attached (TLCGD3 y -parallel) and without the TLCGDs (angle of attack of the time-harmonic base acceleration $\alpha = 3\pi/4$), maximum gain 33.25dB.

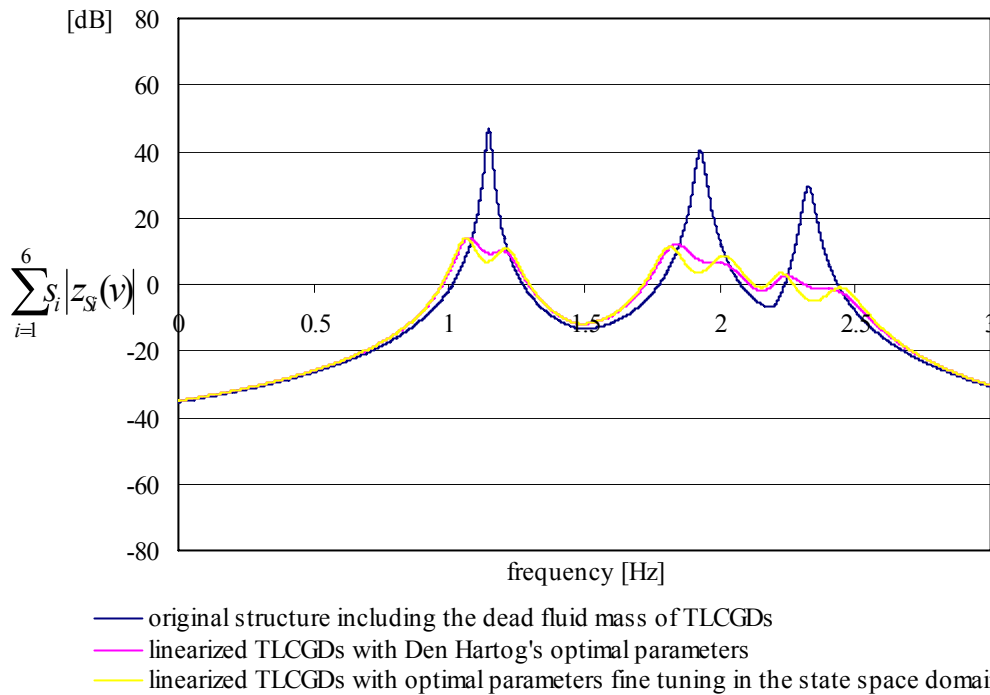


Fig. 2.28: Weighed sum of amplitude response functions for the 3-DOF linearized, single-storey, moderately asymmetric space frame, with three linearized TLCGDs attached (TLCGD3 y -parallel) and without the TLCGDs (angle of attack of the time-harmonic base acceleration $\alpha = 5\pi/6$), maximum gain 32.84dB.

Figures 2.29-2.36 show the comparison of the response of three TLCGDs, alternatively with Den Hartog's optimal parameters and, after fine-tuning in state space, under various angles of attack of the base excitation. From inspection of these figures it is apparent that the maximum relative fluid displacements for all cases are well within the acceptable limits. The

maximum fluid velocities of three TLCGDs are calculated by Eq. (2.35) 5.68, 5.37 and 3.66m/s and are also within the acceptable speed limit.

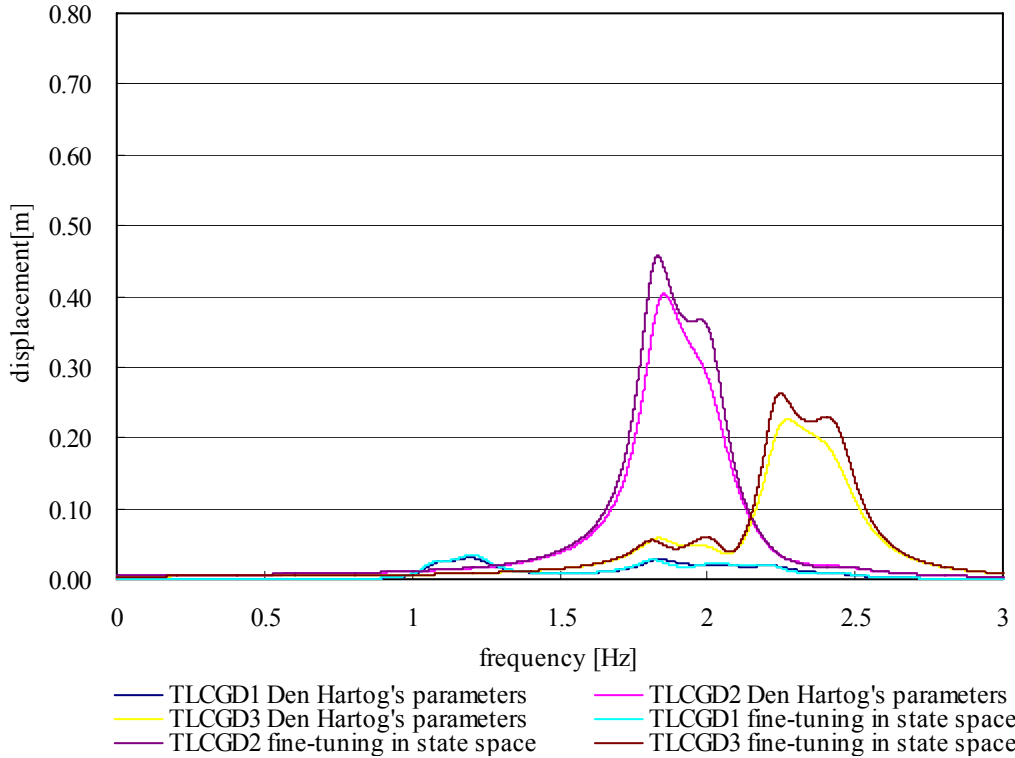


Fig. 2.29: Amplitude response curves of fluid displacement $|u|$ of three linearized TLCGDs attached to the 3-DOF space frame (TLCGD3 y -parallel). TLCGDs either with Den Hartog's optimal parameters or those resulting from fine-tuning in state space ($\alpha = 0$).

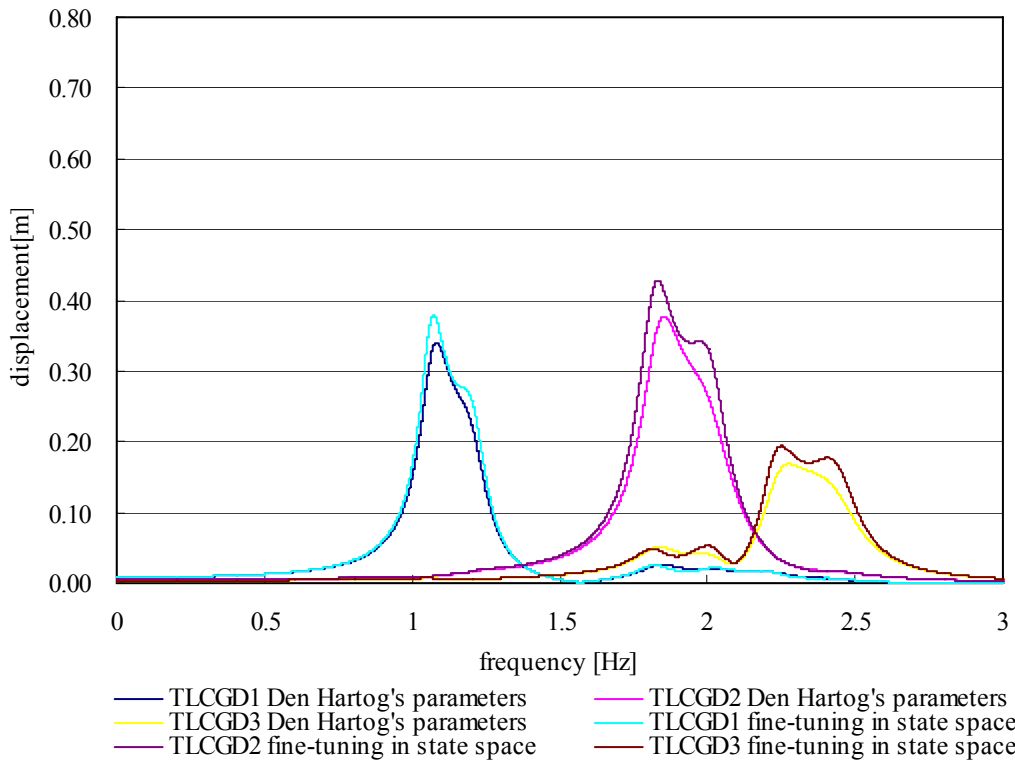


Fig. 2.30: Amplitude response curves of fluid displacement $|u|$ of three linearized TLCGDs attached to the 3-DOF space frame (TLCGD3 y -parallel). TLCGDs either with Den Hartog's optimal parameters or those resulting from fine-tuning in state space ($\alpha = \pi/6$).

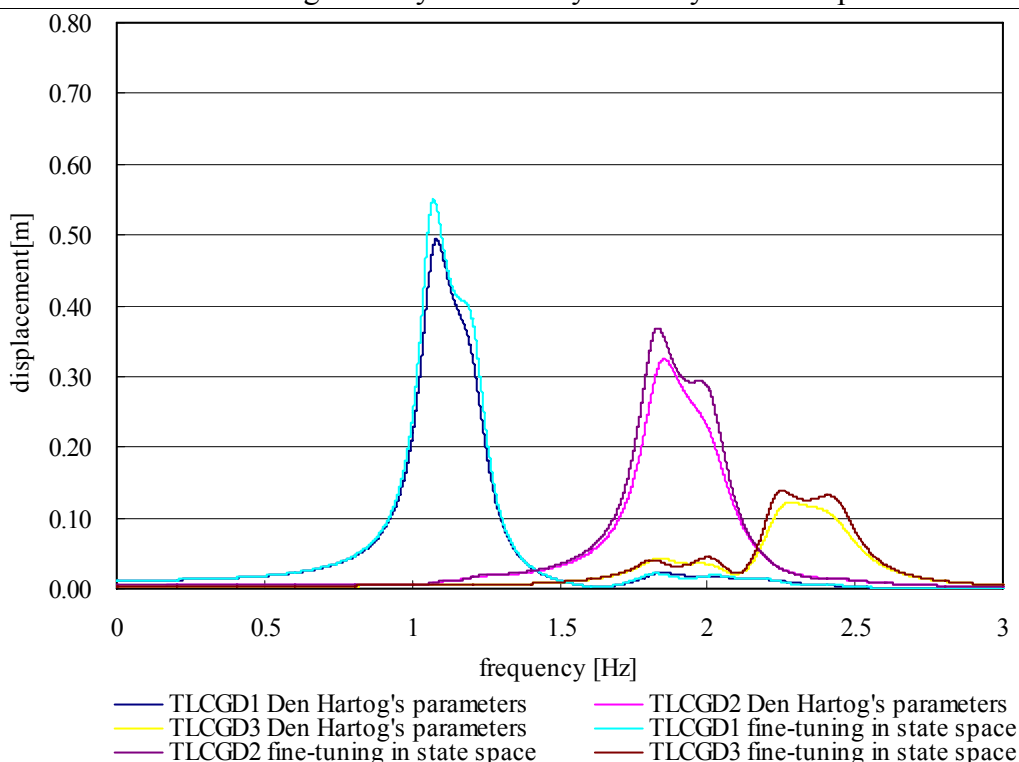


Fig. 2.31: Amplitude response curves of fluid displacement $|u|$ of three linearized TLCGDs attached to the 3-DOF space frame (TLCGD3 y -parallel). TLCGDs either with Den Hartog's optimal parameters or those resulting from fine-tuning in state space ($\alpha = \pi/4$).

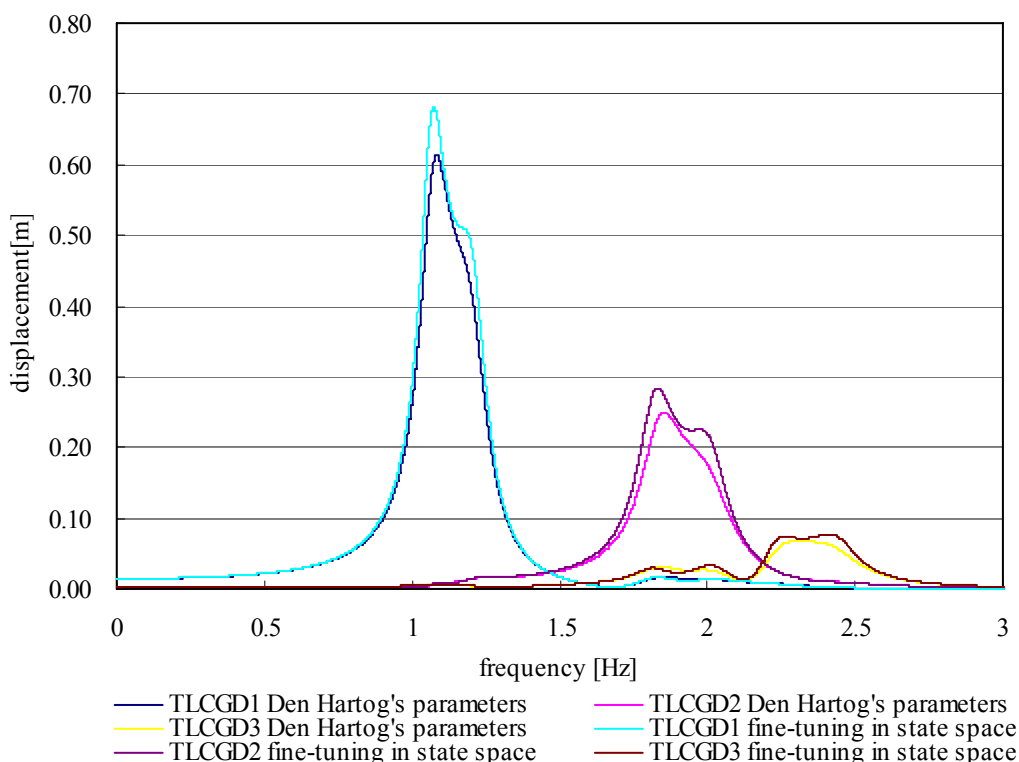


Fig. 2.32: Amplitude response curves of fluid displacement $|u|$ of three linearized TLCGDs attached to the 3-DOF space frame (TLCGD3 y -parallel). TLCGDs either with Den Hartog's optimal parameters or those resulting from fine-tuning in state space ($\alpha = \pi/3$).

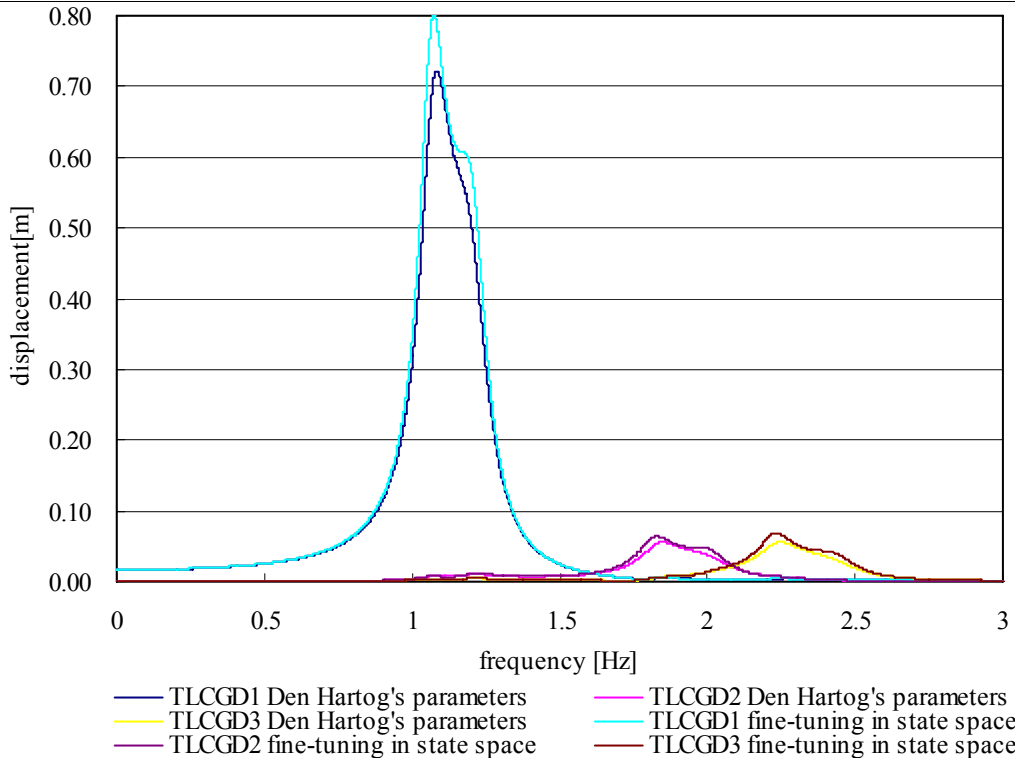


Fig. 2.33: Amplitude response curves of fluid displacement $|u|$ of three linearized TLCGDs attached to the 3-DOF space frame (TLCGD3 y -parallel). TLCGDs either with Den Hartog's optimal parameters or those resulting from fine-tuning in state space ($\alpha = \pi/2$).

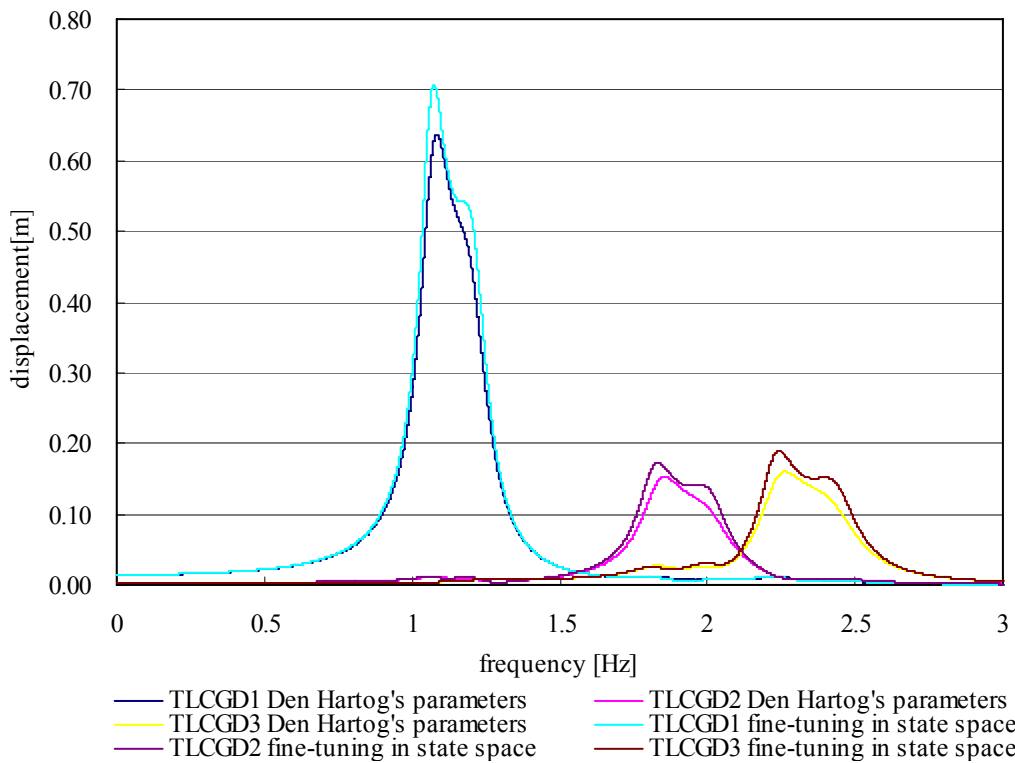


Fig. 2.34: Amplitude response curves of fluid displacement $|u|$ of three linearized TLCGDs attached to the 3-DOF space frame (TLCGD3 y -parallel). TLCGDs either with Den Hartog's optimal parameters or those resulting from fine-tuning in state space ($\alpha = 2\pi/3$).

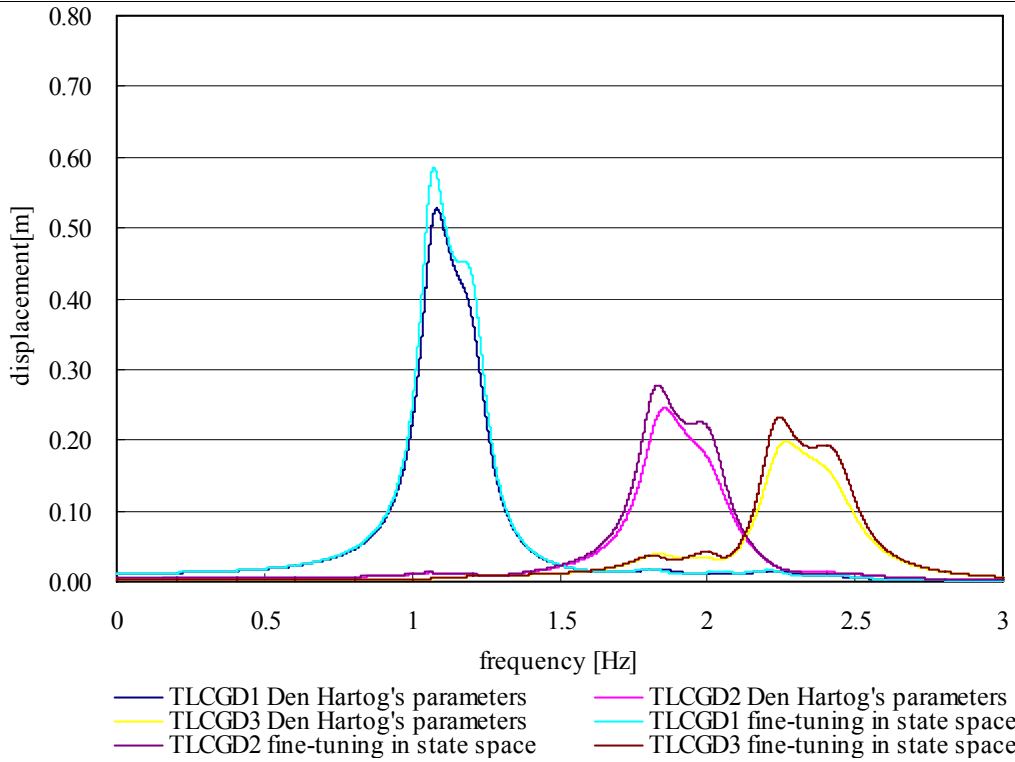


Fig. 2.35: Amplitude response curves of fluid displacement $|u|$ of three linearized TLCGDs attached to the 3-DOF space frame (TLCGD3 y -parallel). TLCGDs either with Den Hartog's optimal parameters or those resulting from fine-tuning in state space ($\alpha = 3\pi/4$).

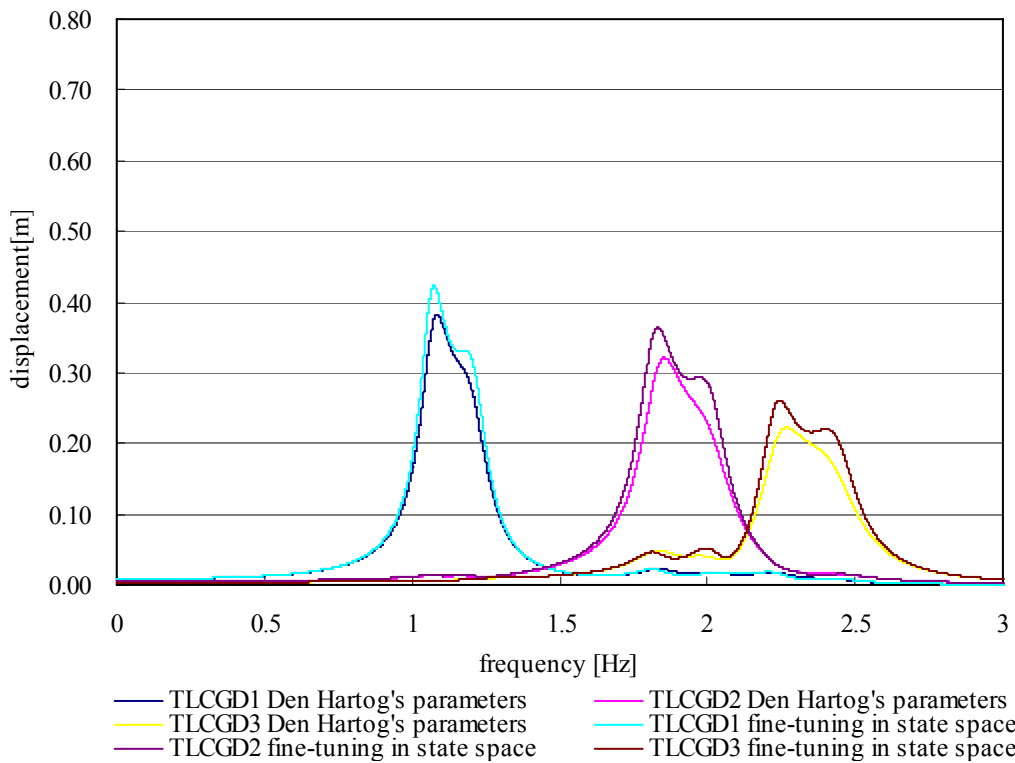


Fig. 2.36: Amplitude response curves of fluid displacement $|u|$ of three linearized TLCGDs attached to the 3-DOF space frame (TLCGD3 y -parallel). TLCGDs either with Den Hartog's optimal parameters or those resulting from fine-tuning in state space ($\alpha = 5\pi/6$).

2.10.8 TLCGD3 alternatively installed on the short side of the floor and oriented parallel to the z -direction

To compare the vibration control effectiveness using TLCGD3 parallel to the y -direction and alternatively parallel to the z -direction, the same fluid mass is used for both cases. Likewise to section 2.10.6, the design of TLCGD3 has the same parameters: A_{H3} , B_3 , H_3 , κ_3 , $\bar{\kappa}_{3(3)}$ and $h_{0(3)}$. However, $\mu_3 = 2.42\%$, Equation (2.102) renders $\mu_3^* = 1.95\%$, the optimal parameters of TLCGD3 are $\delta_{A3,opt} = 0.979$, $\zeta_{A3,opt} = \zeta_{opt3}^* = 8.46\%$. It shows that the mass ratio increases and $\zeta_{A3,opt}$ also increases. Hence, its optimal linear frequency is $f_{A3,opt} = f_{S3}\delta_{A3,opt} = 2.32\text{Hz}$.

The effective modal damping coefficient of the system in third mode is increased to $\zeta_{eff3} = 5.27\%$ in Fig. 2.37, the gain is higher when compared to TLCGD3 oriented parallel to the y -direction because the normal distance to the modal center of velocity is somewhat larger.

Forcing direction	structure			$u_T = r_S\theta$ [mm]	TLCGD3 u_0 [mm]
	v [mm]	w [mm]			
$\alpha = 0$	C_M	13	-3	19	181
	A	16	-36		
$\alpha = \pi/6$	C_M	10	-2	15	141
	A	13	-28		
$\alpha = \pi/4$	C_M	7	-2	11	107
	A	9	-21		
$\alpha = \pi/3$	C_M	5	-1	7	67
	A	6	-13		
$\alpha = \pi/2$	C_M	4	-1	5	59
	A	5	-10		
$\alpha = 2\pi/3$	C_M	9	-2	14	139
	A	12	-26		
$\alpha = 3\pi/4$	C_M	11	-2	17	167
	A	15	-32		
$\alpha = 5\pi/6$	C_M	13	-3	19	184
	A	16	-36		

Table 2.3: Maximum displacements in the third mode from time-harmonic excitation in α -directions, $a_0=0.1g$, $r_S = 2.97m$.

The data in Table 2.3 show that the maximum fluid displacement of $u_0 = 0.18m$, at angle of attack $\alpha = 5\pi/6$, is within the acceptable limits, $u_0 < H_a/3 = 0.32m$ (of linearized gas compression), $u_0 < H/2 = 0.3m$ and $\max|\dot{u}| = 2.68 < 10m/s$. When compared with Table 2.2c, it is noted that the maximum fluid displacement and velocity are lowered.

The optimal natural frequencies and damping ratios are determined by fine tuning, Eq. (2.117) $f_{A1} = 1.13\text{Hz}$, $f_{A2} = 1.86\text{Hz}$, $f_{A3} = 2.17\text{Hz}$, $\zeta_{A1} = 7.46\%$, $\zeta_{A2} = 5.56\%$, $\zeta_{A3} = 7.45\%$. The equilibrium pressure head h_0 of three TLCGDs is properly changed to 34.51, 40.87 and 39.02m. The Figs. 2.38-2.45 contain the frequency response functions of the weighed sum $\sum_{i=1}^6 s_i |z_{Si}(v)|$ of the building states for the original and the optimized system at various angles of attack, in the logarithmic decibel scale within the frequency window $0 \leq f \leq 3\text{Hz}$. The resonance curve with fine-tuning optimal parameters have broader

resonance peak. From inspection of figures 2.46-2.53 the maximum relative fluid displacements and velocities for all cases are well within the acceptable limits.

In conclusion, from the previous analyses, the TLCGD3 parallel to z -direction and alternatively parallel to y -direction can be applied in practice but TLCGD3 parallel to z -direction is slightly preferable.

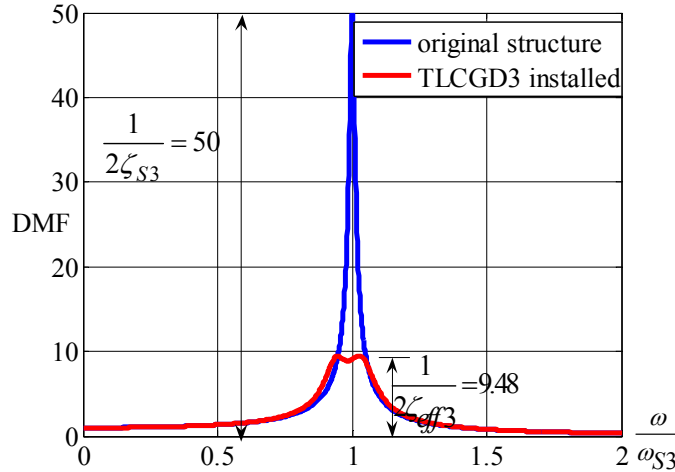


Fig.2.37: Frequency response curves of the isolated third mode without and with linearized TLCGD3 attached, TLCGD3 parallel to z -direction with Den Hartog’s optimal parameter.

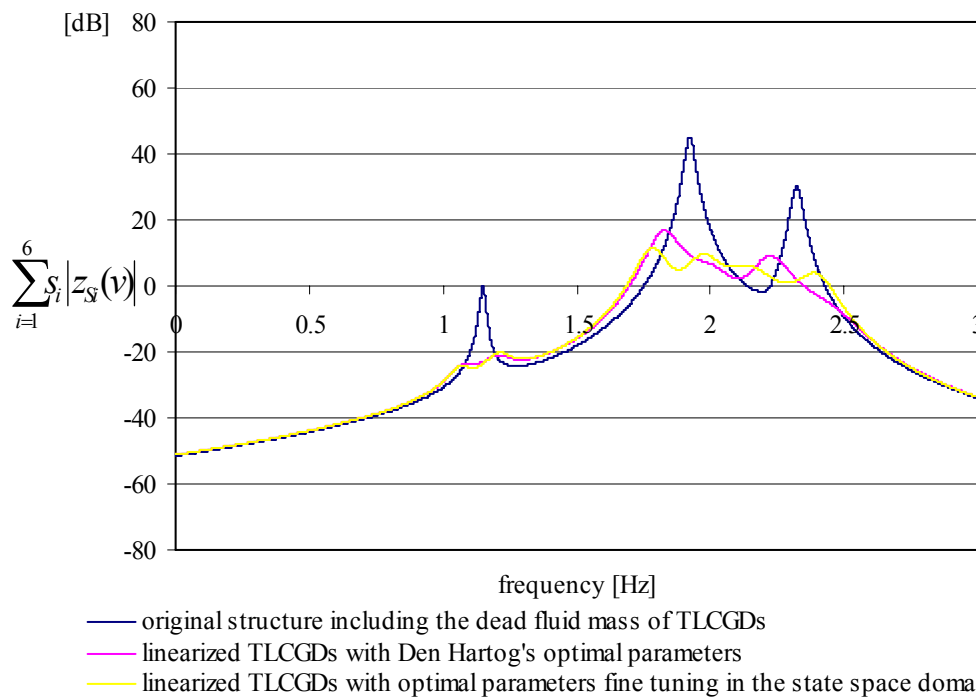


Fig. 2.38: Weighed sum of amplitude response functions for the 3-DOF linearized, single-storey, moderately asymmetric space frame, with three linearized TLCGDs attached (TLCGD3 z -parallel) and without the TLCGDs (angle of attack of the time-harmonic base acceleration $\alpha = 0$), maximum gain 33.6dB.

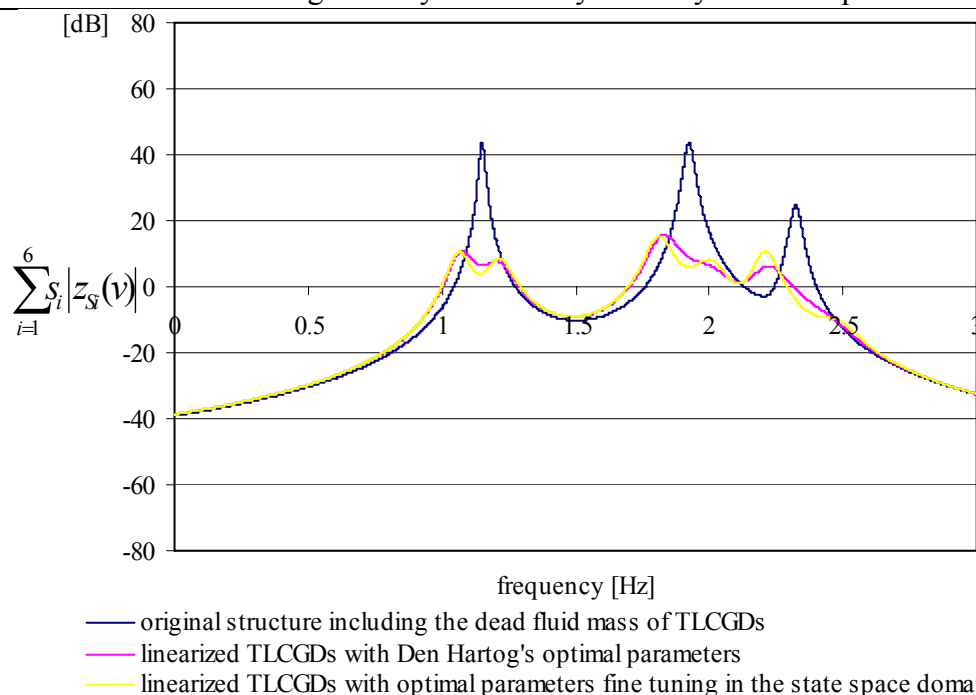


Fig. 2.39: Weighed sum of amplitude response functions for the 3-DOF linearized, single-storey, moderately asymmetric space frame, with three linearized TLCGDs attached (TLCGD3 z -parallel) and without the TLCGDs (angle of attack of the time-harmonic base acceleration $\alpha = \pi/6$), maximum gain 32.97dB.

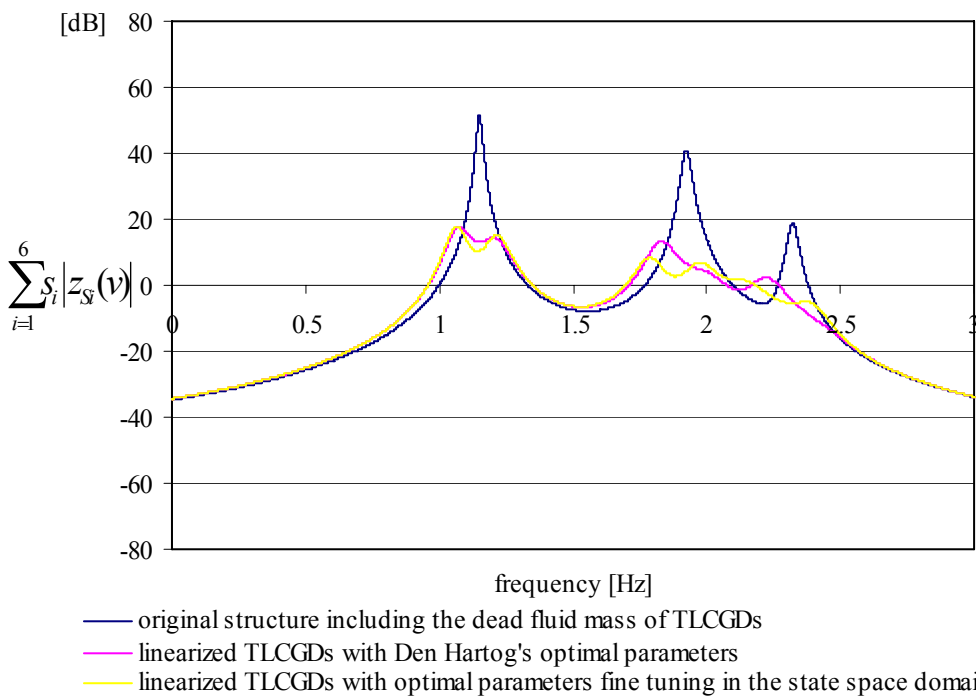


Fig. 2.40: Weighed sum of amplitude response functions for the 3-DOF linearized, single-storey, moderately asymmetric space frame, with three linearized TLCGDs attached (TLCGD3 z -parallel) and without the TLCGDs (angle of attack of the time-harmonic base acceleration $\alpha = \pi/4$), maximum gain 33.67 dB.

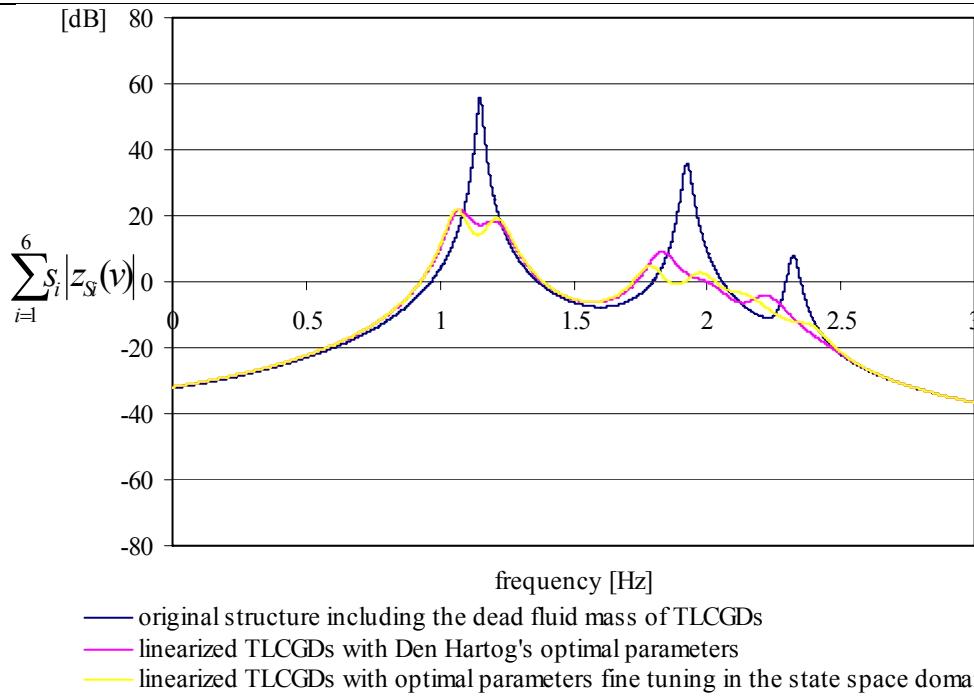


Fig. 2.41: Weighed sum of amplitude response functions for the 3-DOF linearized, single-storey, moderately asymmetric space frame, with three linearized TLCGDs attached (TLCGD3 z -parallel) and without the TLCGDs (angle of attack of the time-harmonic base acceleration $\alpha = \pi/3$), maximum gain 33.9 dB.

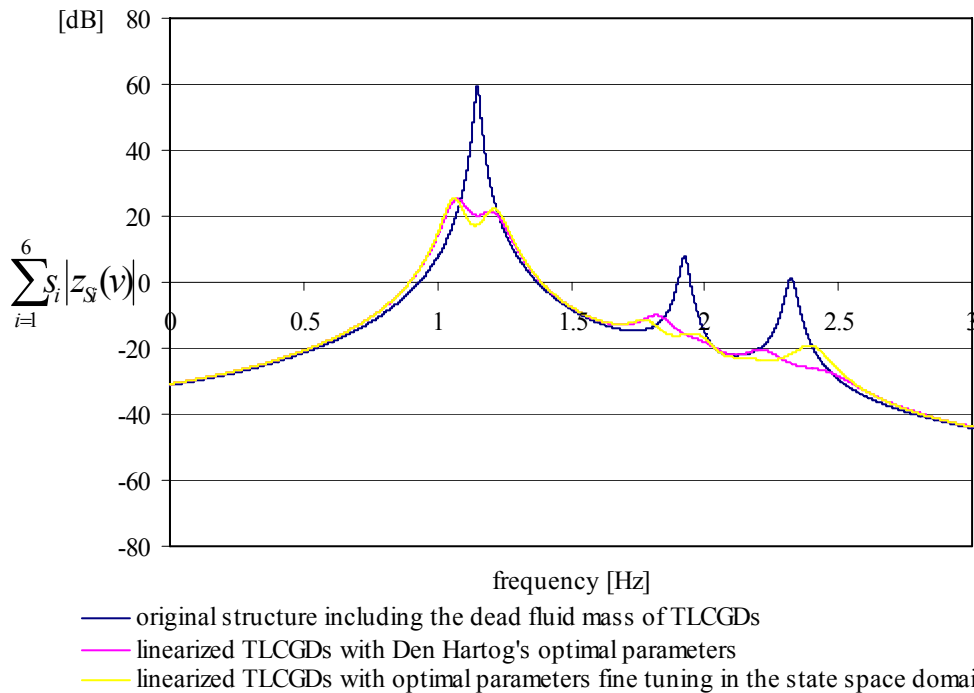


Fig. 2.42: Weighed sum of amplitude response functions for the 3-DOF linearized, single-storey, moderately asymmetric space frame, with three linearized TLCGDs attached (TLCGD3 z -parallel) and without the TLCGDs (angle of attack of the time-harmonic base acceleration $\alpha = \pi/2$), maximum gain 33.9 dB.

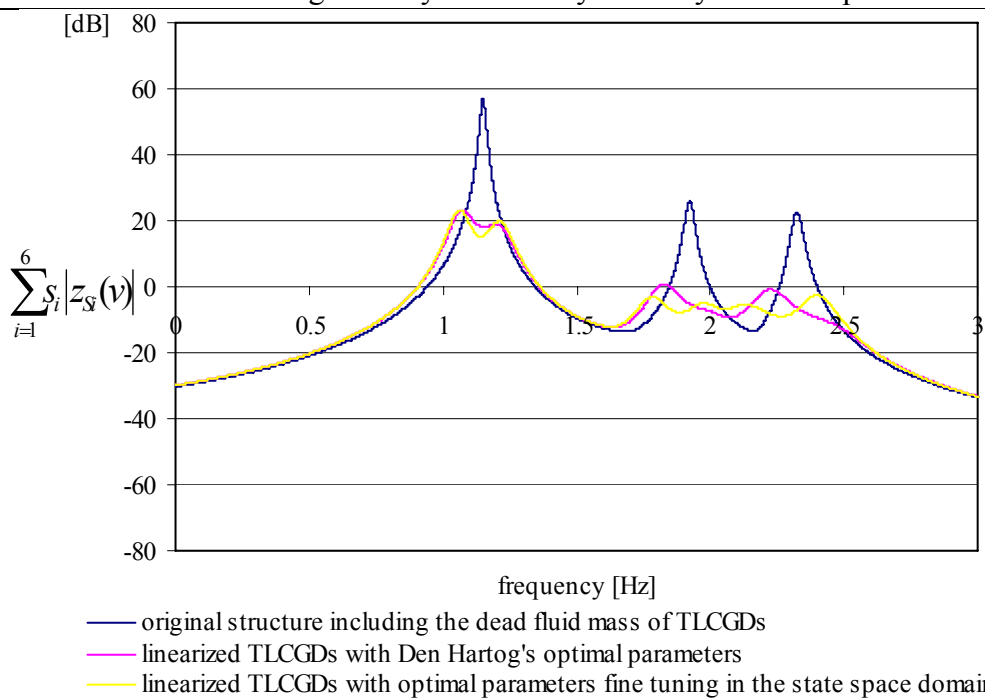


Fig. 2.43: Weighed sum of amplitude response functions for the 3-DOF linearized, single-storey, moderately asymmetric space frame, with three linearized TLCGDs attached (TLCGD3 z-parallel) and without the TLCGDs (angle of attack of the time-harmonic base acceleration $\alpha = 2\pi/3$), maximum gain 33.6 dB.

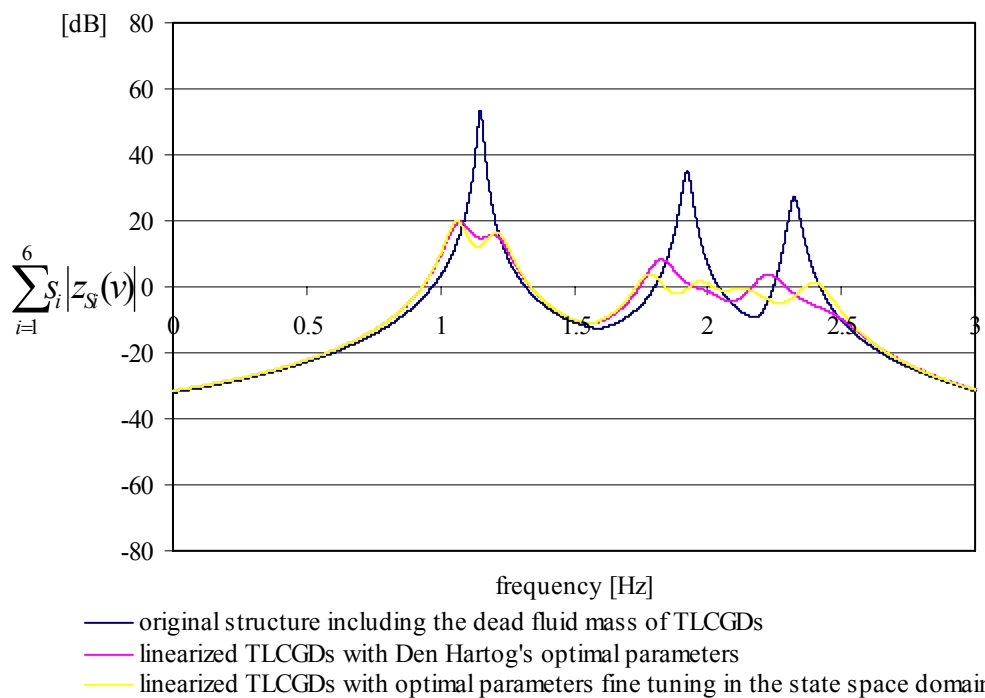


Fig. 2.44: Weighed sum of amplitude response functions for the 3-DOF linearized, single-storey, moderately asymmetric space frame, with three linearized TLCGDs attached (TLCGD3 z-parallel) and without the TLCGDs (angle of attack of the time-harmonic base acceleration $\alpha = 3\pi/4$), maximum gain 33.33dB.

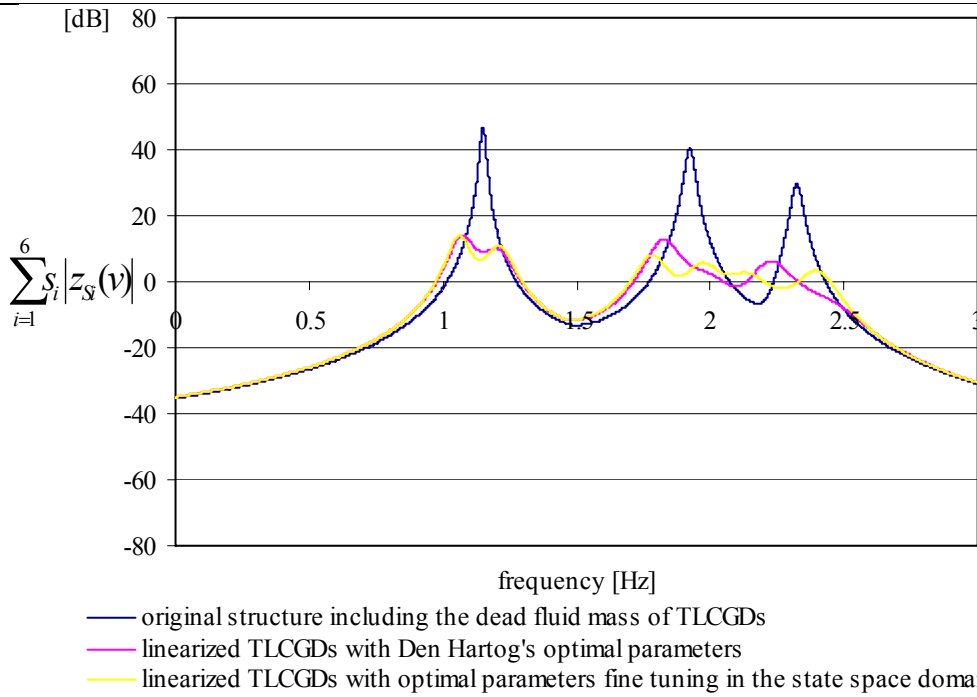


Fig. 2.45: Weighed sum of amplitude response functions for the 3-DOF linearized, single-storey, moderately asymmetric space frame, with three linearized TLCGDs attached (TLCGD3 z -parallel) and without the TLCGDs (angle of attack of the time-harmonic base acceleration $\alpha = 5\pi/6$), maximum gain 32.9 dB.

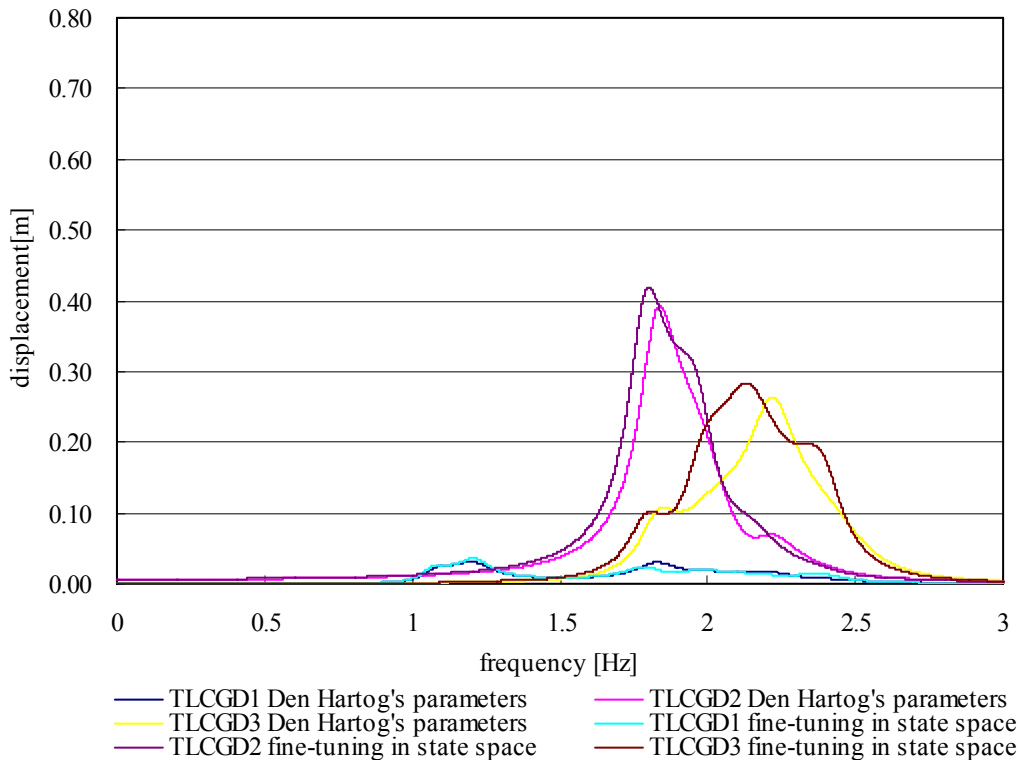


Fig. 2.46: Amplitude response curves of fluid displacement $|u|$ of three linearized TLCGDs attached to the 3-DOF space frame (TLCGD3 z -parallel). TLCGDs either with Den Hartog's optimal parameters or those resulting from fine-tuning in state space ($\alpha = 0$).

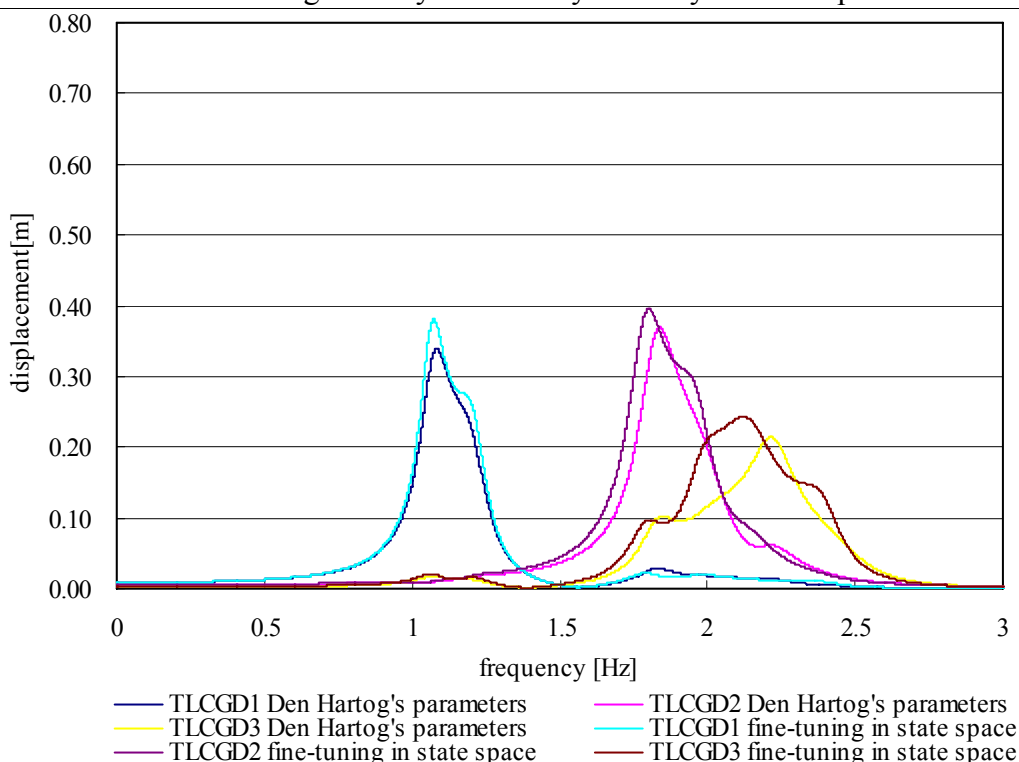


Fig. 2.47: Amplitude response curves of fluid displacement $|u|$ of three linearized TLCGDs attached to the 3-DOF space frame (TLCGD3 z-parallel). TLCGDs either with Den Hartog's optimal parameters or those resulting from fine-tuning in state space ($\alpha = \pi/6$).

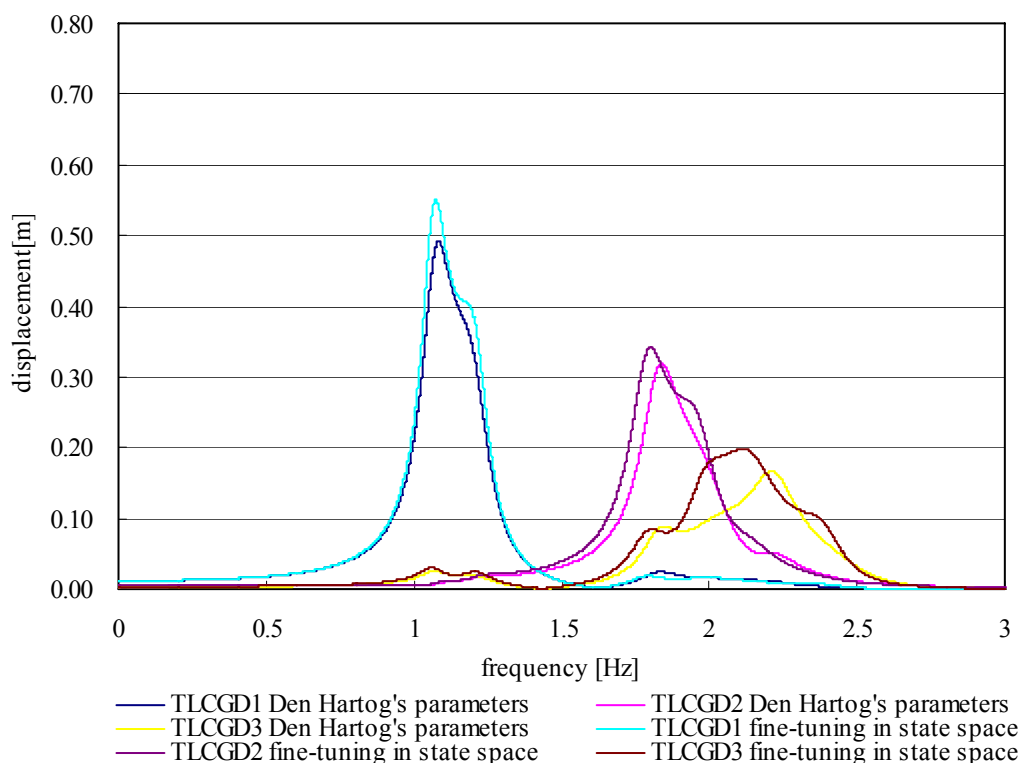


Fig. 2.48: Amplitude response curves of fluid displacement $|u|$ of three linearized TLCGDs attached to the 3-DOF space frame (TLCGD3 z-parallel). TLCGDs either with Den Hartog's optimal parameters or those resulting from fine-tuning in state space ($\alpha = \pi/4$).

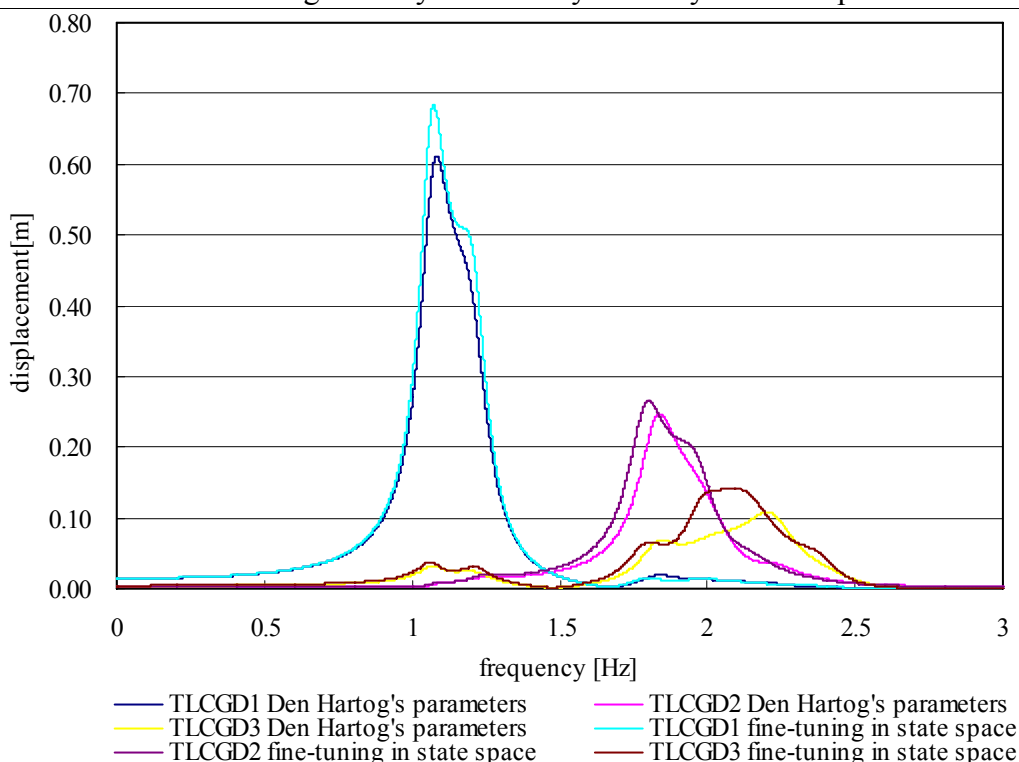


Fig. 2.49: Amplitude response curves of fluid displacement $|u|$ of three linearized TLCGDs attached to the 3-DOF space frame (TLCGD3 z-parallel). TLCGDs either with Den Hartog's optimal parameters or those resulting from fine-tuning in state space ($\alpha = \pi/3$).

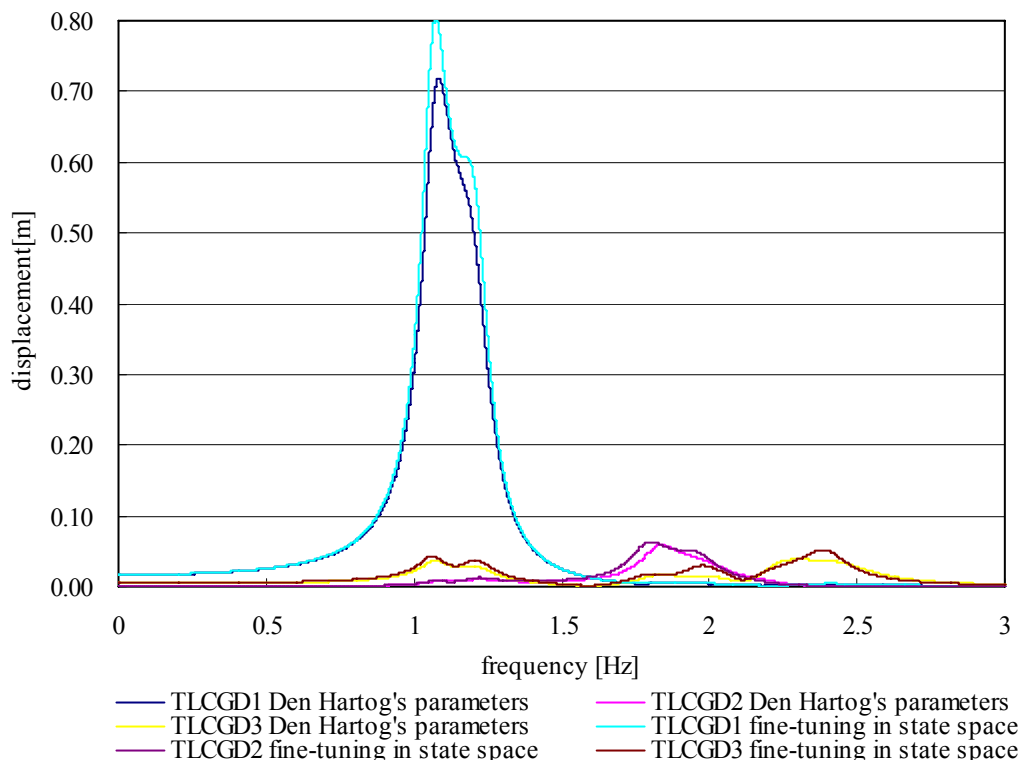


Fig. 2.50: Amplitude response curves of fluid displacement $|u|$ of three linearized TLCGDs attached to the 3-DOF space frame (TLCGD3 z-parallel). TLCGDs either with Den Hartog's optimal parameters or those resulting from fine-tuning in state space ($\alpha = \pi/2$).

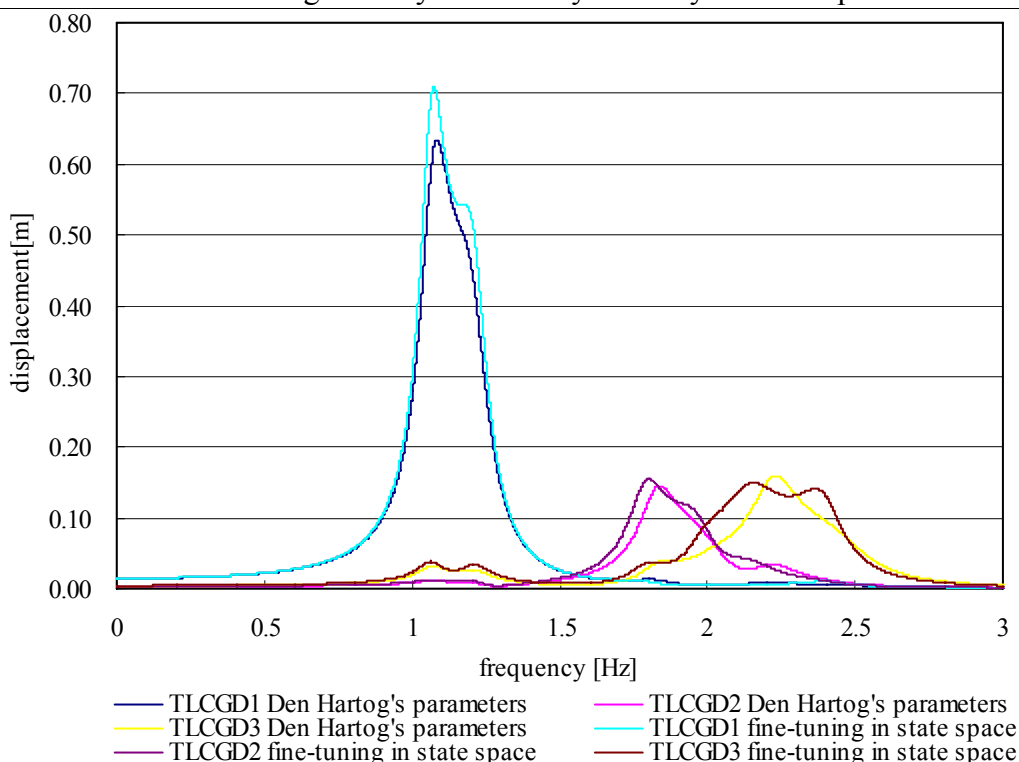


Fig. 2.51: Amplitude response curves of fluid displacement $|u|$ of three linearized TLCGDs attached to the 3-DOF space frame (TLCGD3 z -parallel). TLCGDs either with Den Hartog's optimal parameters or those resulting from fine-tuning in state space ($\alpha = 2\pi/3$).

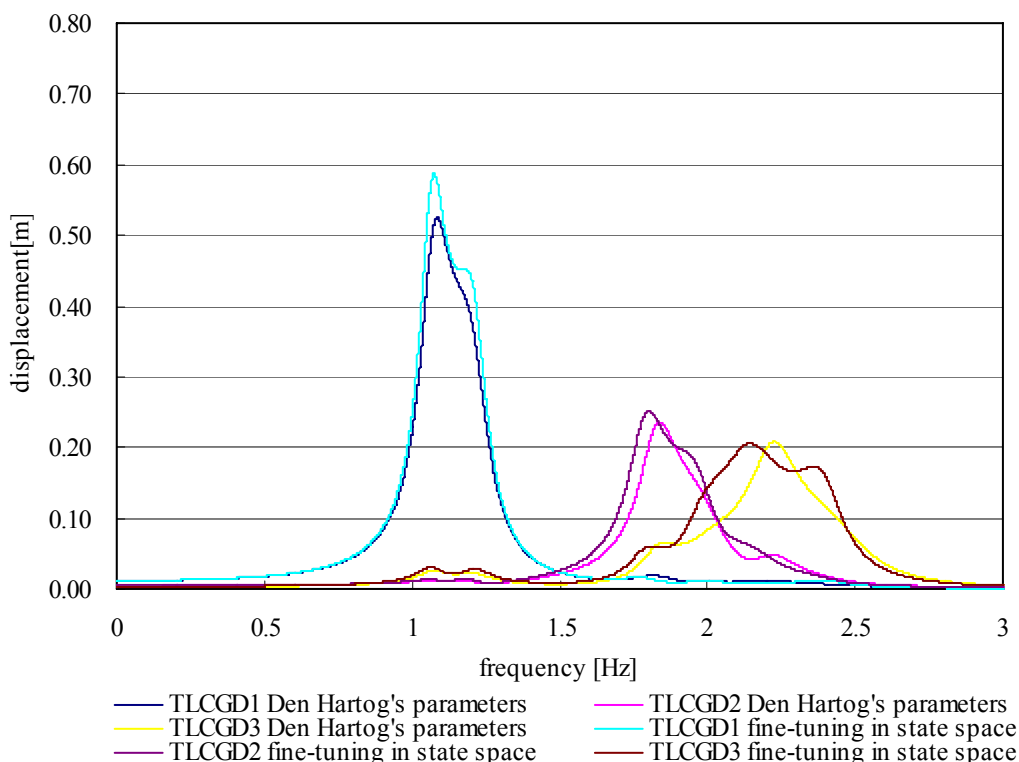


Fig. 2.52: Amplitude response curves of fluid displacement $|u|$ of three linearized TLCGDs attached to the 3-DOF space frame (TLCGD3 z -parallel). TLCGDs either with Den Hartog's optimal parameters or those resulting from fine-tuning in state space ($\alpha = 3\pi/4$).

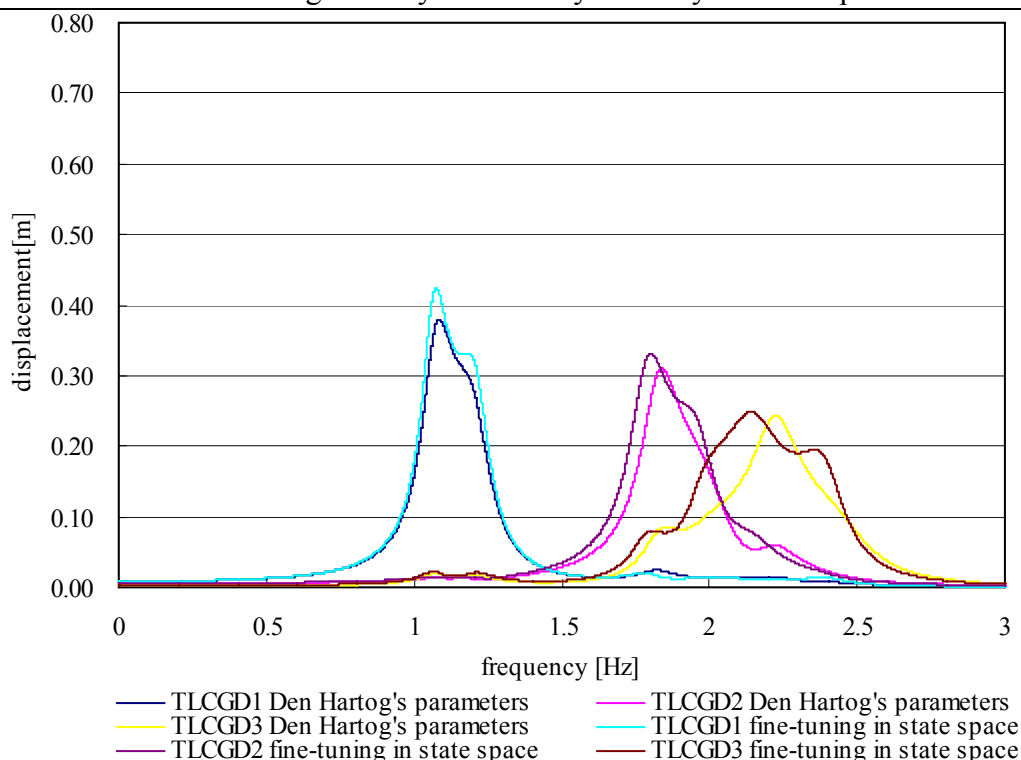


Fig. 2.53: Amplitude response curves of fluid displacement $|u|$ of three linearized TLCGDs attached to the 3-DOF space frame (TLCGD3 z -parallel). TLCGDs either with Den Hartog's optimal parameters or those resulting from fine-tuning in state space ($\alpha = 5\pi/6$).

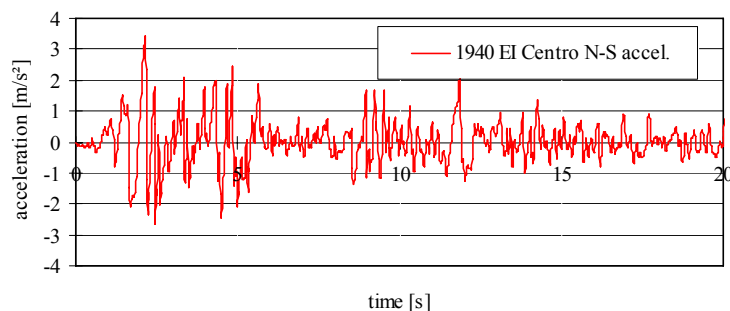


Fig. 2.54: 1940 El Centro N-S ground acceleration record in time domain, sampling time $\Delta t=0.02s$, <http://www.eerc.berkeley.edu/>.

2.10.9 Original structure with the dead fluid-mass of TLCGD included

Table 2.4 shows the natural frequencies and the positions of the center of velocity considering the dead fluid mass of the three TLCGDs when attached according to Fig.2.16. The dead fluid mass of the three TLCGDs is $\tilde{L}\tilde{M}_f\tilde{T} - \tilde{L}\tilde{M}_f\tilde{\kappa}\tilde{\kappa}'\tilde{T}'$. The natural frequencies turn out to be slightly lowered. Consequently, Den Hartog's modal tuning parameters are also slightly changed as listed in Table 2.5.

The changing parameters are the equilibrium pressure head h_0 , the proportional damping ζ_{opt} and the optimal frequency f_{opt} . For in situ testing the non permanently attached TLCGD consists of a portable piping system whose parts are assembled directly at the desired floors. In situ tuning of frequency is done by adjusting the equilibrium pressure p_0 .

	original structure	TLCGD3 parallel to y -direction	TLCGD3 parallel to z -direction
f_{S1}	1.16	1.15	1.15
f_{S2}	1.96	1.93	1.92
f_{S3}	2.37	2.33	2.32
C_{V1}	(-16.685, -0.264)	(-17.25, -0.26)	(-17.16, -0.26)
C_{V2}	(1.798, -4.100)	(1.74, -4.3)	(1.76, -4.36)
C_{V3}	(1.498, 2.505)	(1.45, 2.38)	(1.46, 2.35)

Table 2.4: Natural frequencies and the positions of the velocity center considering the dead fluid mass of three TLCGDs (mass of the piping system is still neglected).

		original structure	TLCGD3 parallel to y -direction	TLCGD3 parallel to z -direction
TLCGD1	h_0 [m]	36.70	35.66	35.89
	$\zeta_{A1,opt}$ [%]	8.96	8.87	8.89
	$f_{A1,opt}$ [Hz]	1.13	1.12	1.12
TLCGD2	h_0 [m]	45.26	43.90	43.69
	$\zeta_{A2,opt}$ [%]	7.37	7.25	7.24
	$f_{A2,opt}$ [Hz]	1.92	1.90	1.89
TLCGD3 parallel to y -direction	h_0 [m]	46.50	44.98	
	$\zeta_{A3,opt}$ [%]	6.68	6.52	
	$f_{A3,opt}$ [Hz]	2.33	2.30	
TLCGD3 parallel to z -direction	h_0 [m]	46.50		44.83
	$\zeta_{A3,opt}$ [%]	8.46		8.39
	$f_{A3,opt}$ [Hz]	2.32		2.27

Table 2.5: Parameters of TLCGD1, 2 and 3 optimized by Den Hartog's method when considering the dead fluid mass of three TLCGDs.

2.10.10 Dimensioning of the pipe

For simplicity, let us consider a straight circular cylindrical pipe with radius r and wall thickness $t \ll r$ subjected to the internal gauge pressure $p_{(D)}$. We determine the hoop stress σ_h (membrane stress according to the ‘‘pressure-vessel formula’’), see Ziegler³, page 91.

$$\sigma_h = \frac{p_{(D)}r}{t}, \quad (2.124)$$

where the maximum gauge pressure is considered,

$$p_{(D)} = \rho g (h_0 - 10 + H \sin \beta) + p', \quad \rho = 1000 \text{ kg/m}^3. \quad (2.125)$$

If the pipe is made of steel, p' should be non-linearly calculated for the larger stroke $\max u \doteq 2/3 H_a$, to account for the self-controlling property of the TLCGD under overload and to safely keep the pipe in the linear elastic range of deformation. Thus, the maximum dynamic pressure p' in this case may be defined by assuming an adiabatic gas compression

$$p' = p_0 \left(\frac{\rho'}{\rho_0} \right)^n, \quad n = 1.4. \quad (2.126)$$

Since the amount of gas remains constant during compression, $V_0 = A_H H_a$, the mass ratio can be calculated by substituting the large stroke,

$$\rho_0 V_0 = \rho' (V_0 - \max|u| A_H), \quad \rho' = 3\rho_0. \quad (2.127)$$

Substituting Eq. (2.127) into Eq. (2.126) yields the maximum dynamic pressure $p' = 4.66p_0$ for consideration in Eq. (2.125), to render

$$p_{(D)} = \rho g (5.66h_0 - 10 + H \sin \beta). \quad (2.128)$$

For large stroke it becomes necessary to check the gauge pressure under expansion condition, Eq. (2.127) renders in this case $\rho'' = 3/5\rho_0$. Hence, $p'' = 0.49p_0$ with a negative sign this value is substituted for p' in Eq. (2.125), however putting $H=0$,

$$\bar{p}_{(D)} = \rho g (0.51h_0 - 10). \quad (2.129)$$

Negative values of the gauge pressure in Eq. (2.129) cause compressive hoop stresses and require consideration of a buckling criterion. Since $h_0 \geq 10m$, cavitation is not expected to occur under overload conditions. Equation (2.124) provides the wall thickness by substituting the conservative value of the admissible stress for steel, $\sigma_a = 140 \times 10^6 N/m^2$ for the hoop stress σ_h . Thus finally, the dead mass of the piping system is approximately estimated assuming a constant circular cylindrical cross-section over its total length, the density of steel $\rho_p = 7.8 \times 10^3 kg/m^3$ is inserted in Eq. (2.130),

$$m_p = \rho_p 2\pi r t (B + 2H + 2H_a). \quad (2.130)$$

The wall thickness and the estimated dead mass of the piping system are both listed in Table 2.6 resulting for the three TLCGDs, designed according to Table 2.1.

	TLCGD1	TLCGD2	TLCGD3
h_0 [m]	36.70	45.26	46.50
H_a [m]	2.56	1.45	1.02
$10^{-5} p_{(D)}$ [N/m ²] Eq.(2.128)	16.07	20.0	20.5
pipe diameter $2r$ [mm]	411.5	311.1	234.0
t [mm] Eq.(2.124)	2.4	2.2	1.7
m_p [kg] Eq.(2.130)	259.82	120.41	61.48
dead fluid-mass[kg]	200.51	72.2	27.65
$10^{-5} \bar{p}_{(D)}$ [N/m ²] Eq.(2.129)	0.53	0.89	0.94

Table 2.6: Dimensioning of circular steel pipes.

The gauge pressure under expansion conditions turns out to be positive as listed in Table 2.6. The final dimensions of circular steel pipes must be changed according to their commercial availability. By considering the dead mass of the piping system the peaks of resonance curves move to the left. These reductions of the eigenfrequencies are not calculated again in this dissertation but considered in the in situ testing and final fine tuning.

2.10.11 Oblique seismic excitation by the strong motion phase of the El Centro earthquake (1940)

El Centro north-south seismogram in medium soil site from American Imperial Valley earthquake on May 18, 1940 is the input to the base of the structure, and maximum acceleration is set as $3.417m/s^2 \doteq 0.35g$. These data plotted in Fig. 2.54 can be downloaded from the webpage, <http://www.eerc.berkeley.edu/>. This acceleration record is applied

with the angles of attack varied stepwise within $0 \leq \alpha \leq \pi$, $\alpha = 0, \pi/6, \pi/4, \pi/3, \pi/2, 2\pi/3, 3\pi/4, 5\pi/6$ to the y -direction.

The simulated response output of Matlab 7.0¹³ is displayed from Fig. 2.55 to Fig. 2.78, where the relative floor displacements with respect to the base, the relative displacements of the fluid in three TLCDs, TLCD3 parallel to the z -direction and the relative floor accelerations are displayed. From the numerical results, some conclusions can be drawn that three TLCDs installed and tuned to the structural frequencies can effectively reduce the translational and torsional response of structures excited by uni-directional earthquakes.

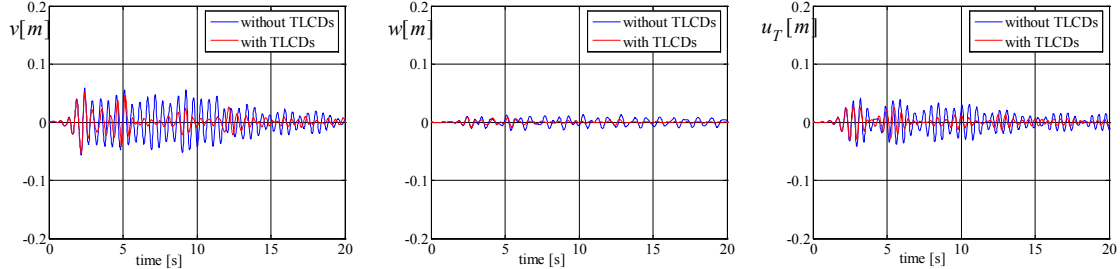


Fig. 2.55: Relative floor displacements of center of mass, v , w and rotation $u_T=r_S\theta$ without and with three TLCDs attached under 1940 El Centro earthquake, angle of attack: $\alpha = 0$, $r_S = 2.97m$, strong motion phase 20s.

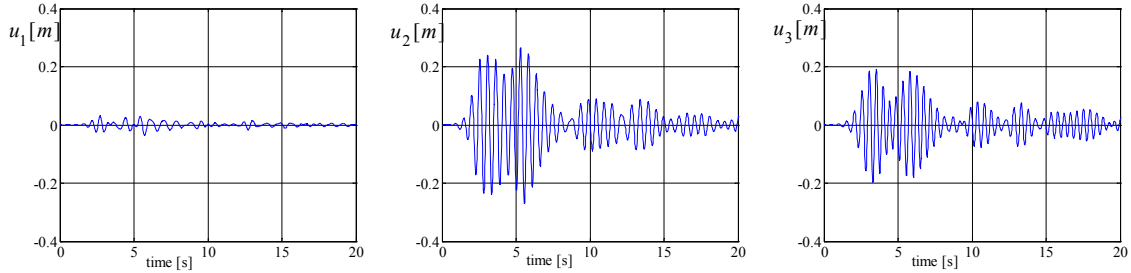


Fig. 2.56: Relative displacement of the fluid in three TLCDs under 1940 El Centro earthquake, angle of attack: $\alpha = 0$, strong motion phase 20s.

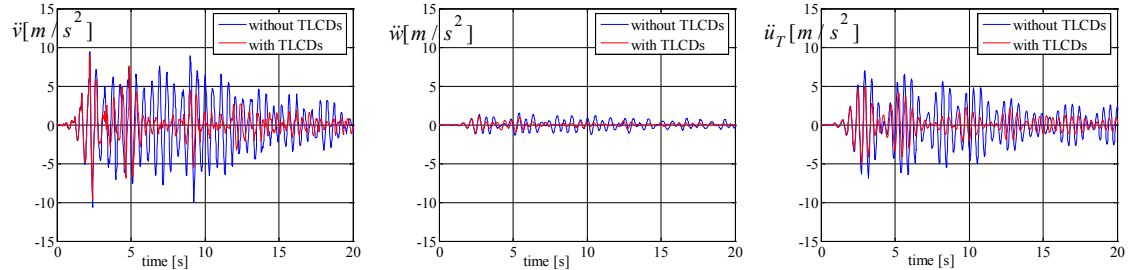


Fig. 2.57: Relative acceleration of single-storey space structure, \ddot{v} , \ddot{w} and $\ddot{u}_T = r_S\ddot{\theta}$ under 1940 El Centro earthquake, angle of attack: $\alpha = 0$, $r_S = 2.97m$, strong motion phase 20s.

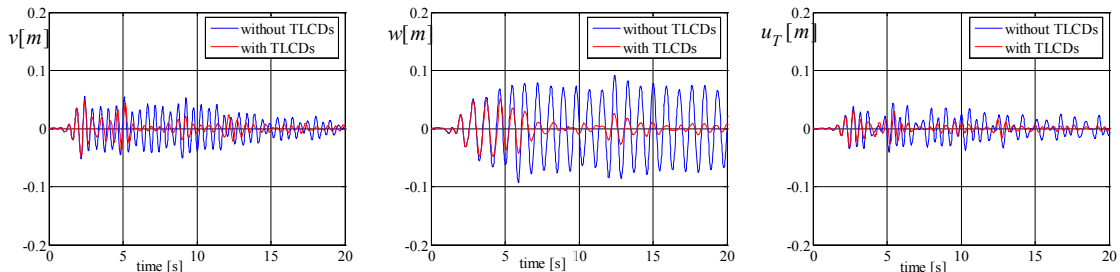


Fig. 2.58: Relative floor displacements of center of mass, v , w and rotation $u_T=r_S\theta$ without and with three TLCDs attached under 1940 El Centro earthquake, angle of attack: $\alpha = \pi/6$, $r_S = 2.97m$, strong motion phase 20s.

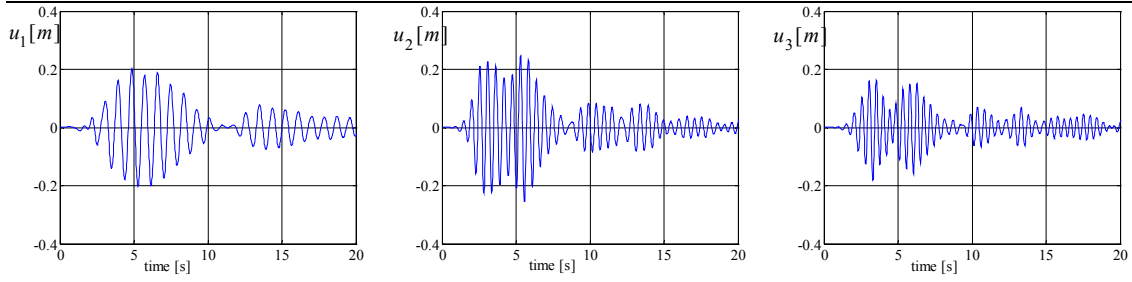


Fig. 2.59: Relative displacement of the fluid in three TLCDs under 1940 El Centro earthquake, angle of attack: $\alpha = \pi/6$, strong motion phase 20s.

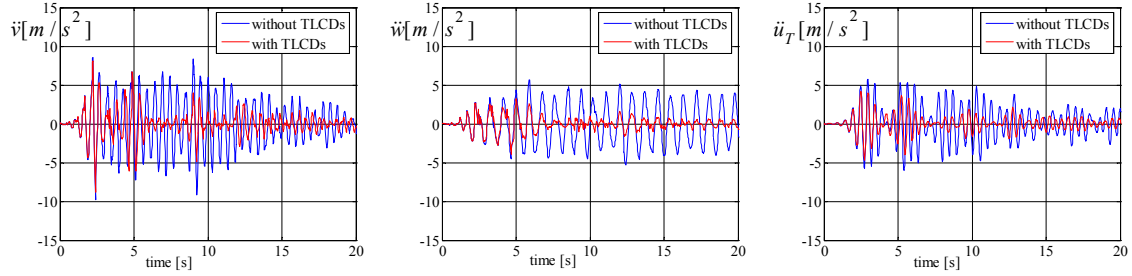


Fig. 2.60: Relative acceleration of single-storey space structure, \ddot{v} , \ddot{w} and $\ddot{u}_T = r_S \ddot{\theta}$ under 1940 El Centro earthquake, angle of attack: $\alpha = \pi/6$, $r_S = 2.97m$, strong motion phase 20s.

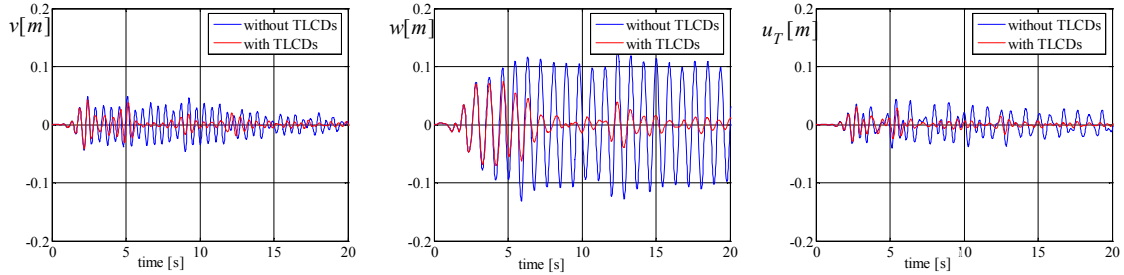


Fig. 2.61: Relative floor displacements of center of mass, v , w and rotation $u_T = r_S \theta$ without and with three TLCDs attached under 1940 El Centro earthquake, angle of attack: $\alpha = \pi/4$, $r_S = 2.97m$, strong motion phase 20s.

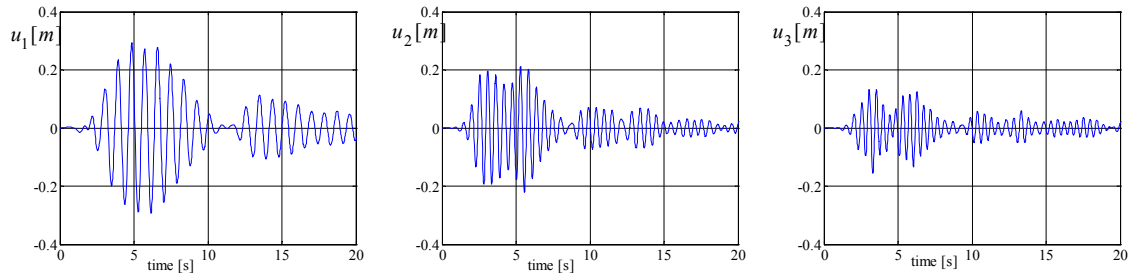


Fig. 2.62: Relative displacement of the fluid in three TLCDs under 1940 El Centro earthquake, angle of attack: $\alpha = \pi/4$, strong motion phase 20s.

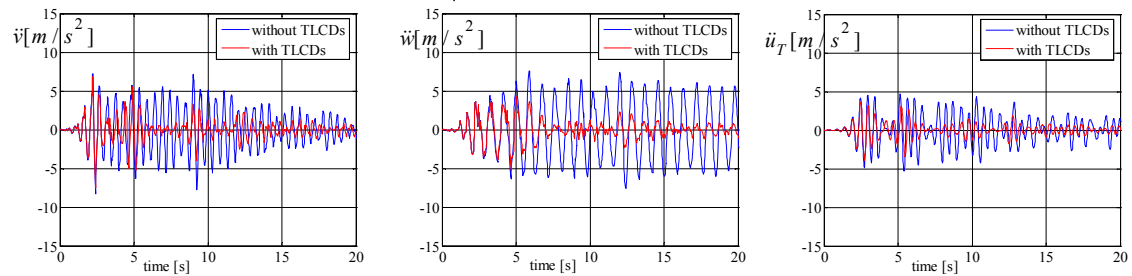


Fig. 2.63: Relative acceleration of single-storey space structure, \ddot{v} , \ddot{w} and $\ddot{u}_T = r_S \ddot{\theta}$ under 1940 El Centro earthquake, angle of attack: $\alpha = \pi/4$, $r_S = 2.97m$, strong motion phase 20s.

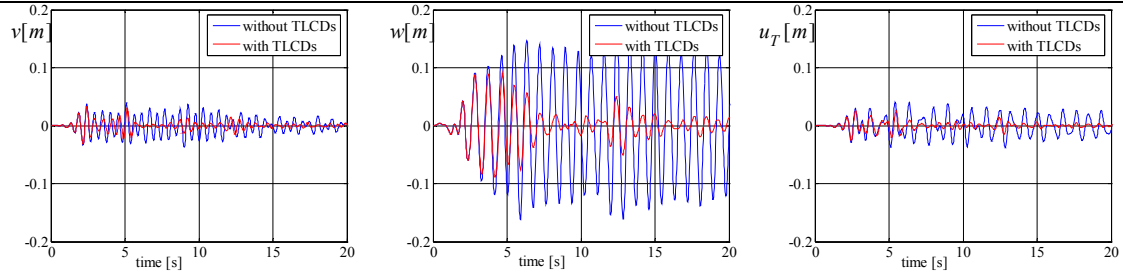


Fig. 2.64: Relative floor displacements of center of mass, v , w and rotation $u_T=r_S\theta$ without and with three TLCDs attached under 1940 El Centro earthquake, angle of attack: $\alpha = \pi/3$, $r_S = 2.97m$, strong motion phase 20s.

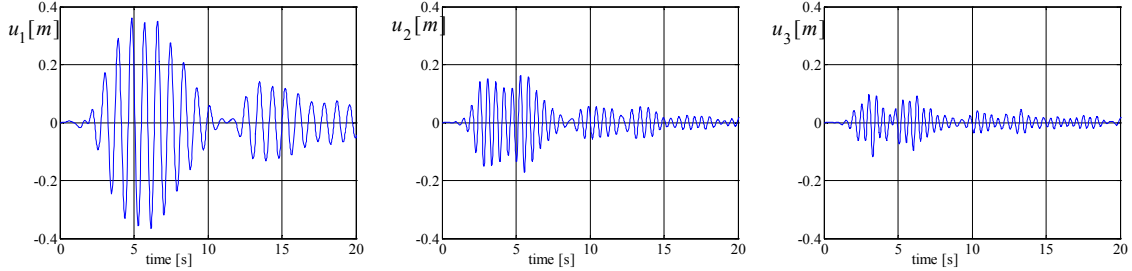


Fig. 2.65: Relative displacement of the fluid in three TLCDs under 1940 El Centro earthquake, angle of attack: $\alpha = \pi/3$, strong motion phase 20s.

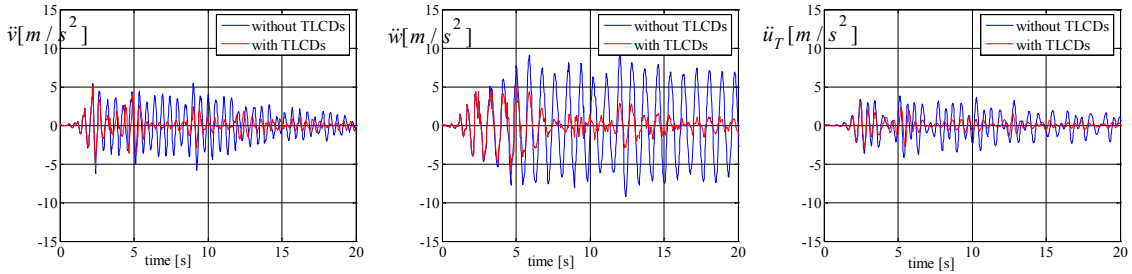


Fig. 2.66: Relative acceleration of single-storey space structure, \ddot{v} , \ddot{w} and $\ddot{u}_T = r_S\ddot{\theta}$ under 1940 El Centro earthquake, angle of attack: $\alpha = \pi/3$, $r_S = 2.97m$, strong motion phase 20s.

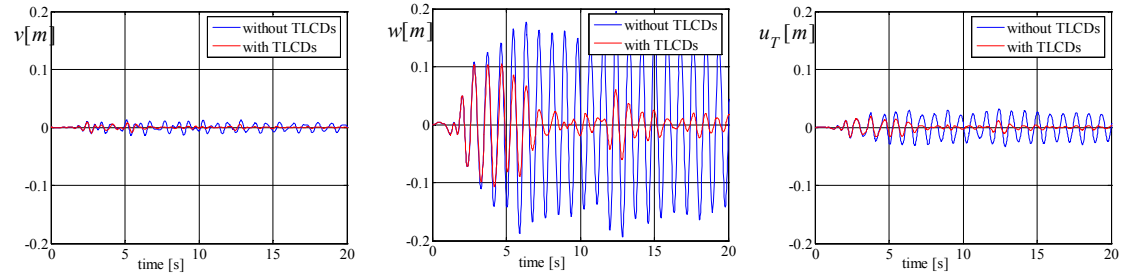


Fig. 2.67: Relative floor displacements of center of mass, v , w and rotation $u_T=r_S\theta$ without and with three TLCDs attached under 1940 El Centro earthquake, angle of attack: $\alpha = \pi/2$, $r_S = 2.97m$, strong motion phase 20s.

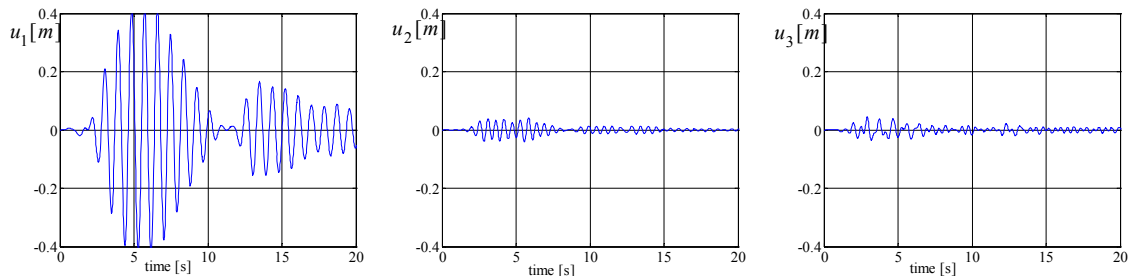


Fig. 2.68: Relative displacement of the fluid in three TLCDs under 1940 El Centro earthquake, angle of attack: $\alpha = \pi/2$, strong motion phase 20s.

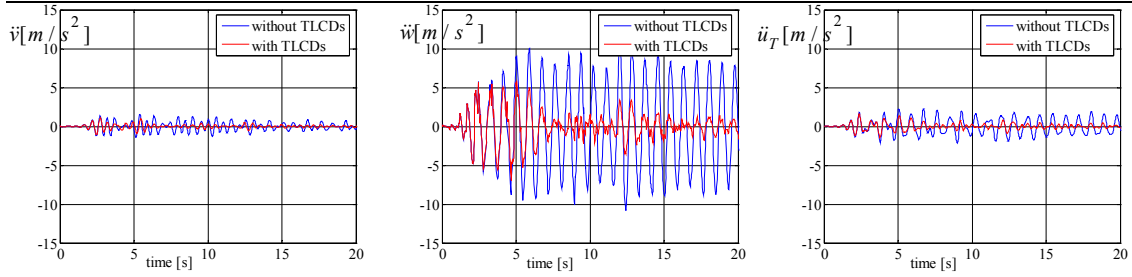


Fig. 2.69: Relative acceleration of single-storey space structure, \ddot{v} , \ddot{w} and $\ddot{u}_T = r_S \ddot{\theta}$ under 1940 El Centro earthquake, angle of attack: $\alpha = \pi/2$, $r_S = 2.97m$, strong motion phase 20s.

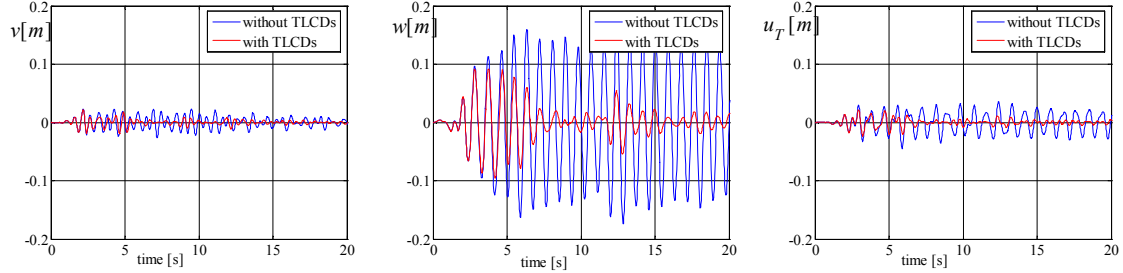


Fig. 2.70: Relative floor displacements of center of mass, v , w and rotation $u_T = r_S \theta$ without and with three TLCDs attached under 1940 El Centro earthquake, angle of attack: $\alpha = 2\pi/3$, $r_S = 2.97m$, strong motion phase 20s.

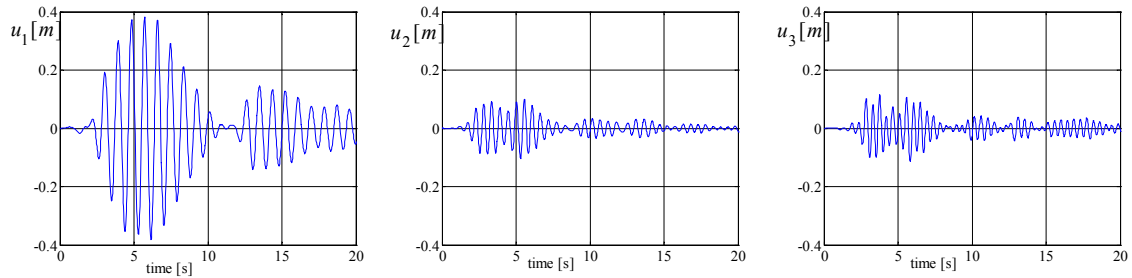


Fig. 2.71: Relative displacement of the fluid in three TLCDs under 1940 El Centro earthquake, angle of attack: $\alpha = 2\pi/3$, strong motion phase 20s.

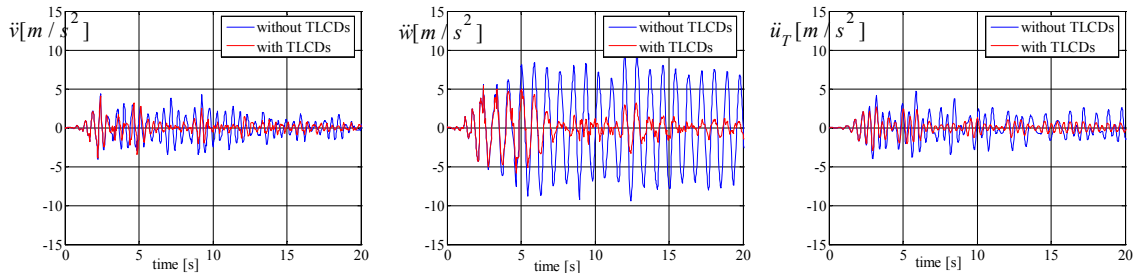


Fig. 2.72: Relative acceleration of single-storey space structure, \ddot{v} , \ddot{w} and $\ddot{u}_T = r_S \ddot{\theta}$ under 1940 El Centro earthquake, angle of attack: $\alpha = 2\pi/3$, $r_S = 2.97m$, strong motion phase 20s.

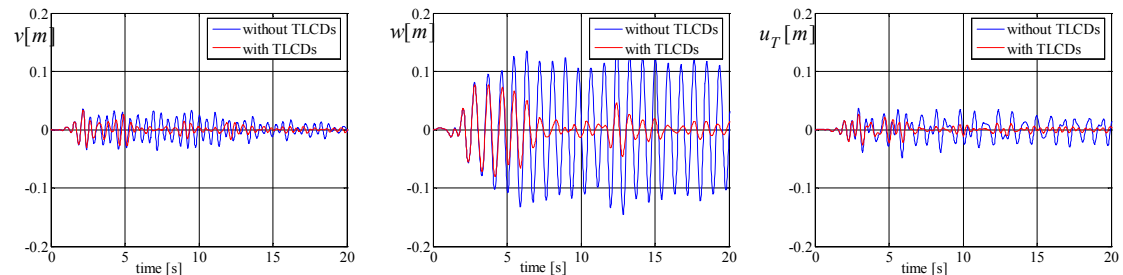


Fig. 2.73: Relative floor displacements of center of mass, v , w and rotation $u_T = r_S \theta$ without and with three TLCDs attached under 1940 El Centro earthquake, angle of attack: $\alpha = 3\pi/4$, $r_S = 2.97m$, strong motion phase 20s.

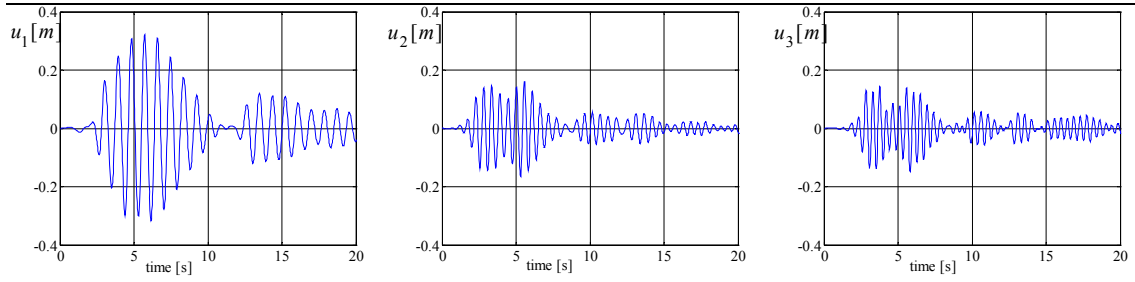


Fig. 2.74: Relative displacement of the fluid in three TLCDs under 1940 El Centro earthquake, angle of attack: $\alpha = 3\pi/4$, strong motion phase 20s.

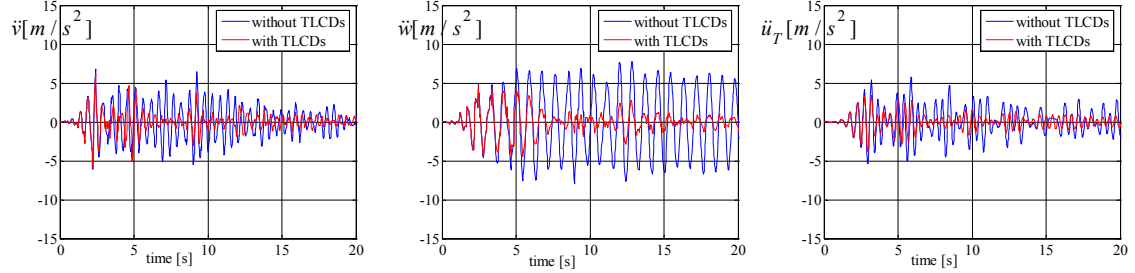


Fig. 2.75: Relative acceleration of single-storey space structure, \dot{v} , \dot{w} and $\dot{u}_T = r_S \ddot{\theta}$ under 1940 El Centro earthquake, angle of attack: $\alpha = 3\pi/4$, $r_S = 2.97m$, strong motion phase 20s.

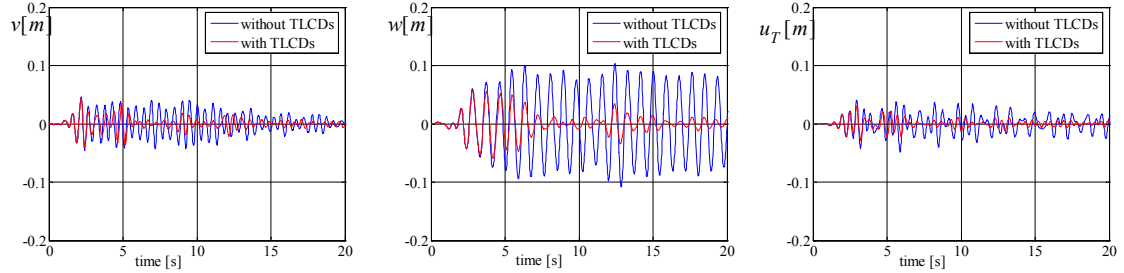


Fig. 2.76: Relative floor displacements of center of mass, v , w and rotation $u_T = r_S \theta$ without and with three TLCDs attached under 1940 El Centro earthquake, angle of attack: $\alpha = 5\pi/6$, $r_S = 2.97m$, strong motion phase 20s.

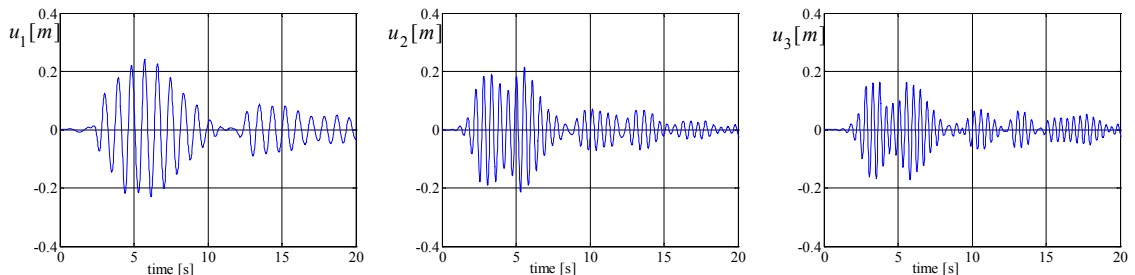


Fig. 2.77: Relative displacement of the fluid in three TLCDs under 1940 El Centro earthquake, angle of attack: $\alpha = 5\pi/6$, strong motion phase 20s.

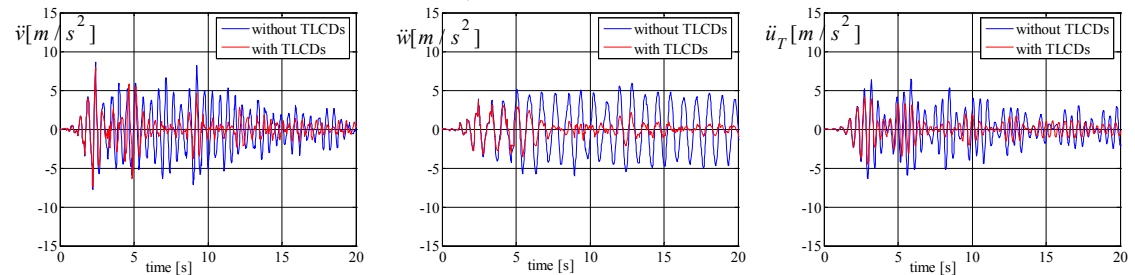


Fig. 2.78: Relative acceleration of single-storey space structure, \dot{v} , \dot{w} and $\dot{u}_T = r_S \ddot{\theta}$ under 1940 El Centro earthquake, angle of attack: $\alpha = 5\pi/6$, $r_S = 2.97m$, strong motion phase 20s.

The numerical values of the maximum response observed in Figs.2.55 to 2.78 are

sampled in Table 2.7a and 2.7b. It is observed that two TLCGDs installed parallel to z-direction provides better displacement and acceleration reduction. The maximum fluid displacements of $u_1 = 0.42m$, $u_2 = 0.27m$, $u_3 = 0.19m$ and velocities of $\dot{u}_1 = 2.98m/s$, $\dot{u}_2 = 3.16m/s$, $\dot{u}_3 = 2.59m/s$ are within the acceptable limits. Peaks within the early period of the strong motion phase are hardly affected by passive damping.

max	original structure			structure with 3 TLCGDs			fluid displacement		
	v [mm]	w [mm]	u_T [mm]	v [mm]	w [mm]	u_T [mm]	u_1 [mm]	u_2 [mm]	u_3 [mm]
$\alpha = 0$	59	13	41	52	9	30	31	266	191
$\alpha = \pi/6$	56	92	44	49	53	32	204	248	163
$\alpha = \pi/4$	49	134	43	43	74	31	293	212	132
$\alpha = \pi/3$	39	166	40	33	91	27	362	163	96
$\alpha = \pi/2$	13	196	33	9	104	19	423	42	45
$\alpha = 2\pi/3$	23	173	36	22	92	22	382	99	115
$\alpha = 3\pi/4$	36	143	36	34	77	26	323	161	144
$\alpha = 5\pi/6$	46	104	41	43	57	29	241	213	163

Table 2.7a: Maximum displacements due to 1940 El Centro earthquake, maximum ground acceleration $a_0/g = 0.348$ with varying angle of attack α . Maximum values indicated in bold, $u_T = r_S\theta$, $r_S = 2.97m$.

max	original structure			structure with 3 TLCGDs		
	\ddot{v}/g	\ddot{w}/g	\ddot{u}_T/g	\ddot{v}/g	\ddot{w}/g	\ddot{u}_T/g
$\alpha = 0$	0.96	0.15	0.71	0.92	0.11	0.50
$\alpha = \pi/6$	0.87	0.57	0.58	0.83	0.32	0.43
$\alpha = \pi/4$	0.74	0.77	0.48	0.70	0.44	0.37
$\alpha = \pi/3$	0.56	0.93	0.39	0.52	0.52	0.29
$\alpha = \pi/2$	0.16	1.08	0.23	0.11	0.58	0.16
$\alpha = 2\pi/3$	0.45	0.95	0.47	0.41	0.55	0.27
$\alpha = 3\pi/4$	0.69	0.80	0.58	0.63	0.48	0.35
$\alpha = 5\pi/6$	0.88	0.60	0.65	0.81	0.38	0.43

Table 2.7b: Maximum accelerations due to 1940 El Centro earthquake, maximum ground acceleration $a_0/g = 0.348$ with varying angle of attack α . Maximum values indicated in bold, $u_T = r_S\theta$, $r_S = 2.97m$.

2.10.12 Kanai-Tajimi model of the ground acceleration: soil amplification

The TLCGD-main structure system is subjected to a filtered white noise process of the Kanai-Tajimi power spectrum accounting for the soil-layer filter. The Kanai-Tajimi spectrum

can be expressed by $S_{\ddot{x}_g(\omega)} = S_0 \frac{1 + 4\zeta_{\psi}^2 (\frac{\omega}{\omega_{\psi}})^2}{(1 - \frac{\omega^2}{\omega_{\psi}^2})^2 + 4\zeta_{\psi}^2 (\frac{\omega}{\omega_{\psi}})^2}$, see e.g. Clough- Penzien⁶, page 613,

where ω_ψ and ζ_ψ represent the characteristic frequency and damping ratio of the soil layer supporting the base of the structure and thus is related to the site soil conditions. S_0 is the spectral intensity of the white noise process model of the earthquake. For the simulation of seismic motions at firm soil conditions, the soil filter parameters take on the values $\omega_\psi = 5\pi \text{ rad/s}$, $\zeta_\psi = 0.6$, see Kanai¹⁴. We assume $S_0 = 72.73 \text{ cm}^2/\text{s}^3$ (firm soil, magnitude 8° and near-field earthquake) corresponding to an RMS value of acceleration 70 cm/s^2 , see Ou¹⁵. The statistical character of the strong motion requires the choice of a modulation function: for two exponential envelopes, see Höllinger^{16, 17}. The following envelope function proposed by Jennings (1964) is preferred and applied here, see Giuseppe¹⁸,

$$\varphi(t) = \begin{cases} \left(\frac{t}{t_1}\right)^2 & t < t_1 \\ 1 & t_1 \leq t \leq t_2 \\ e^{-c(t-t_2)} & t > t_2 \end{cases}$$

Where $t_d = t_2 - t_1$ is the time interval where the excitation is stationary, t_s is the duration time of strong motion and depends on the earthquake magnitude and the epicentral distance. We assume: $t_s = 11.13 \text{ s}$ (firm soil, magnitude 8° and near-field earthquake), $t_1 = 0.5t_s$, $t_2 = 1.2t_s$ and $c = 2.5/t_s$, see again Ou¹⁵. The power spectral density is illustrated in Fig. 2.79 and the corresponding 20 second time segment of the artificially created earthquake is shown in Fig. 2.80. The numerical simulation results are illustrated in Figs. 2.81-2.104.

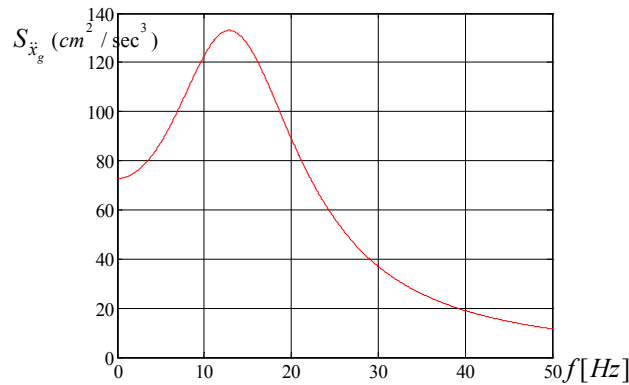


Fig. 2.79: Power spectral density of the ground acceleration in Kanai-Tajimi representation as a function of frequency.

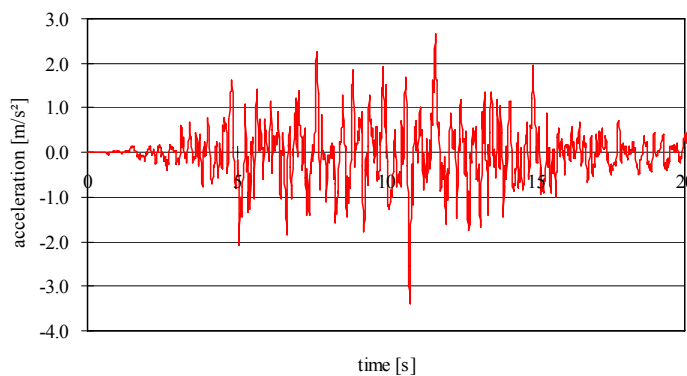


Fig. 2.80: Generated ground acceleration using Kanai-Tajimi model, sampling time $\Delta t = 0.02 \text{ s}$, maximum ground acceleration $a_0/g = 0.34$.

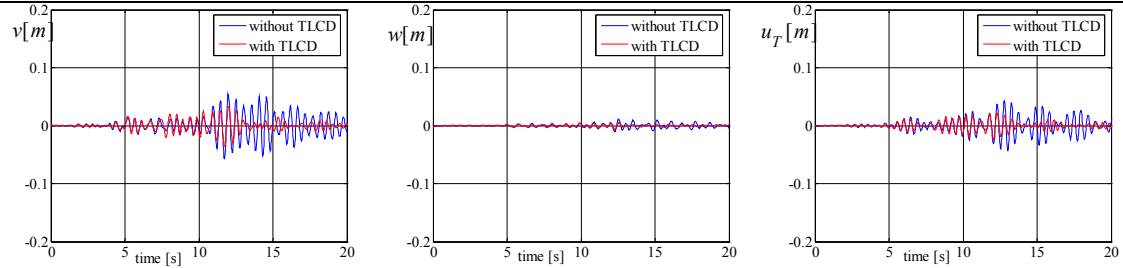


Fig. 2.81: Relative floor displacements of center of mass, v , w and rotation $u_T=r_S\theta$ without and with three TLCDGs attached, angle of attack: $\alpha = 0$ (artificial seismogram) $r_S = 2.97m$, strong motion phase 20s.

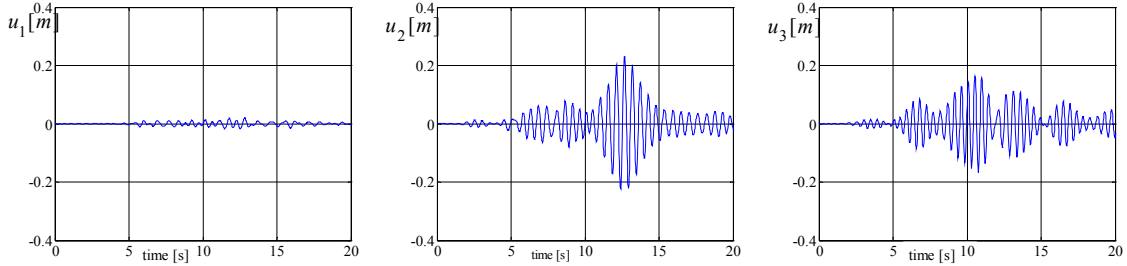


Fig. 2.82: Relative displacement of the fluid in three TLCDGs, angle of attack: $\alpha = 0$ (artificial seismogram), strong motion phase 20s.

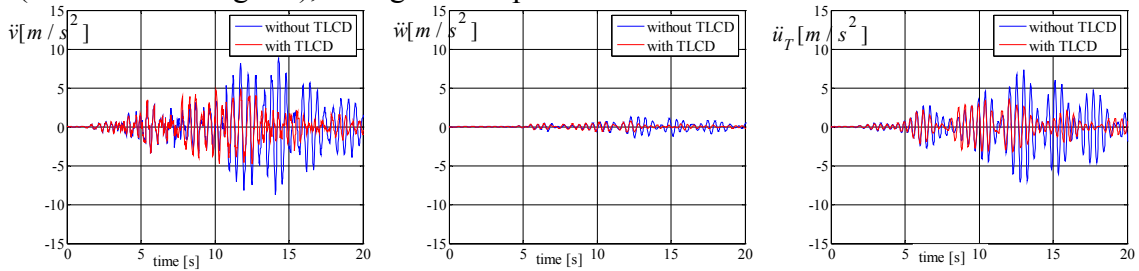


Fig. 2.83: Relative acceleration of single-storey space structure, \ddot{v} , \ddot{w} and $\ddot{u}_T = r_S\ddot{\theta}$, angle of attack: $\alpha = 0$ (artificial seismogram) $r_S = 2.97m$, strong motion phase 20s.

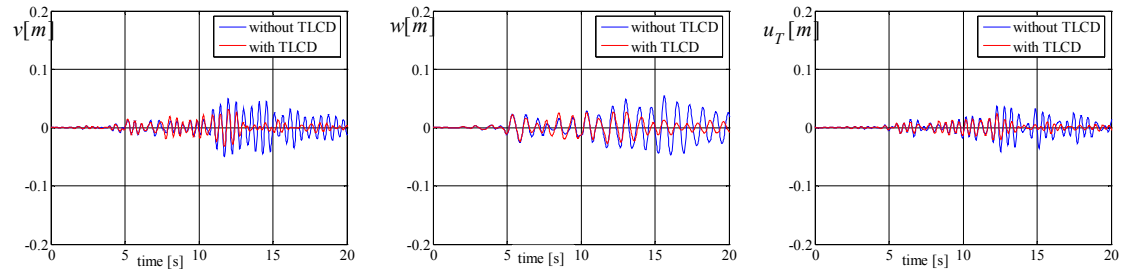


Fig. 2.84: Relative floor displacements of center of mass, v , w and rotation $u_T=r_S\theta$ without and with three TLCDGs attached, angle of attack: $\alpha = \pi/6$ (artificial seismogram) $r_S = 2.97m$, strong motion phase 20s.

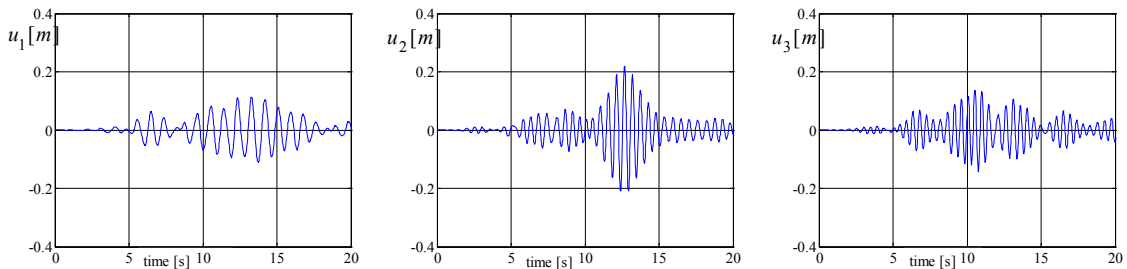


Fig. 2.85: Relative displacement of fluid in three TLCDGs, angle of attack: $\alpha = \pi/6$ (artificial seismogram), strong motion phase 20s.

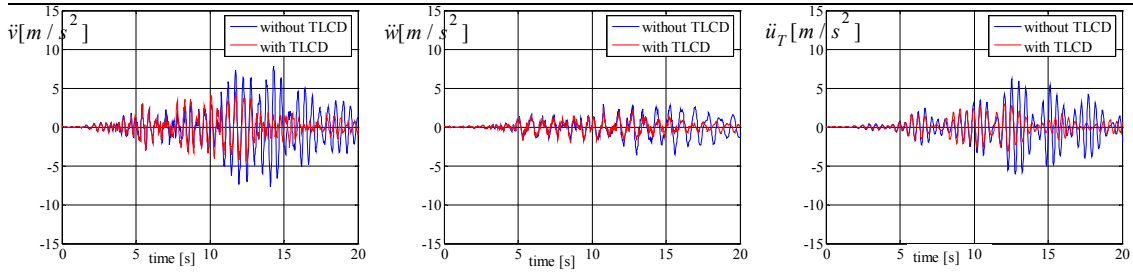


Fig. 2.86: Relative acceleration of single-storey space structure, \ddot{v} , \ddot{w} and $\ddot{u}_T = r_S \ddot{\theta}$, angle of attack: $\alpha = \pi/6$ (artificial seismogram) $r_S = 2.97m$, strong motion phase 20s.

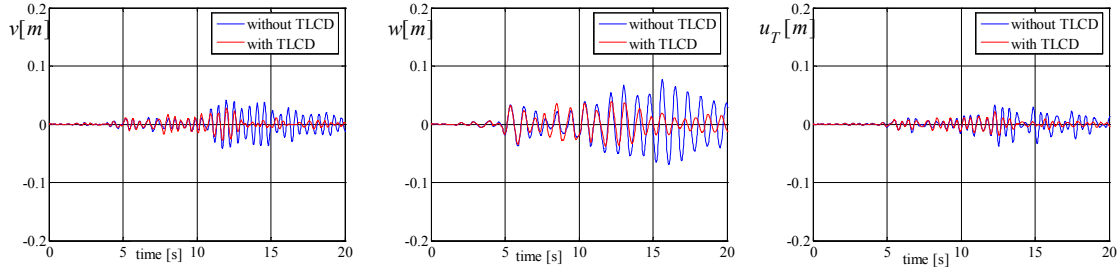


Fig. 2.87: Relative floor displacements of center of mass, v , w and rotation $u_T = r_S \theta$ without and with three TLCDs attached, angle of attack: $\alpha = \pi/4$ (artificial seismogram) $r_S = 2.97m$, strong motion phase 20s.

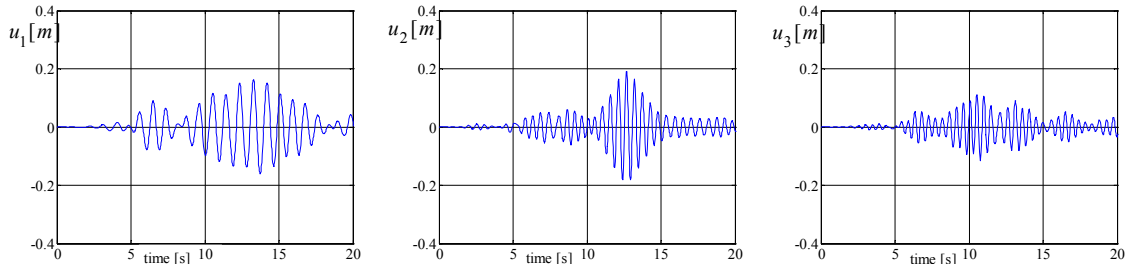


Fig. 2.88: Relative displacement of fluid in three TLCDs, angle of attack: $\alpha = \pi/4$ (artificial seismogram), strong motion phase 20s.

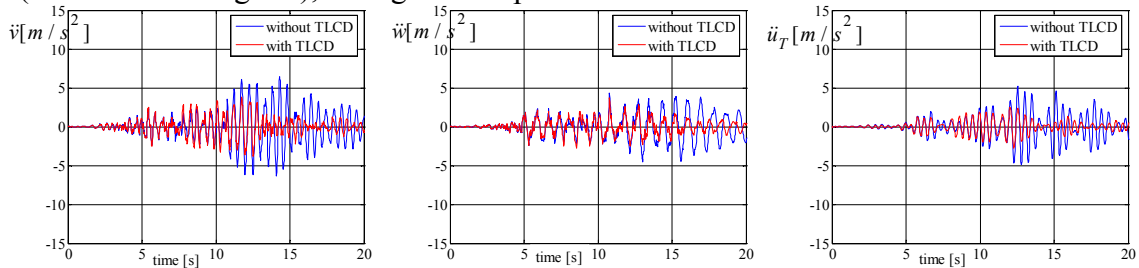


Fig. 2.89: Relative acceleration of single-storey space structure, \ddot{v} , \ddot{w} and $\ddot{u}_T = r_S \ddot{\theta}$, angle of attack: $\alpha = \pi/4$ (artificial seismogram) $r_S = 2.97m$, strong motion phase 20s.

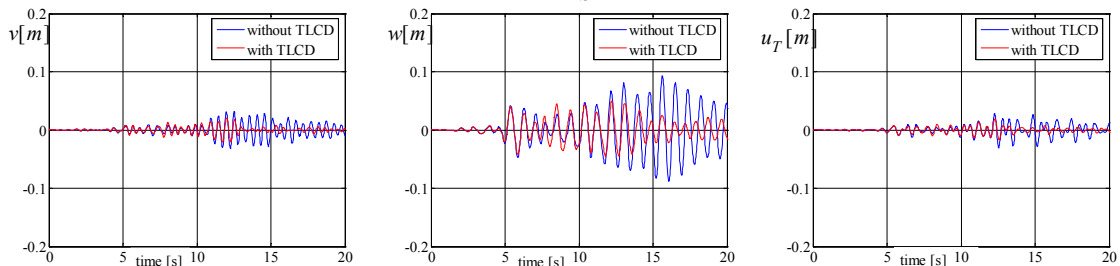


Fig. 2.90: Relative floor displacements of center of mass, v , w and rotation $u_T = r_S \theta$ without and with three TLCDs attached, angle of attack: $\alpha = \pi/3$ (artificial seismogram) $r_S = 2.97m$, strong motion phase 20s.

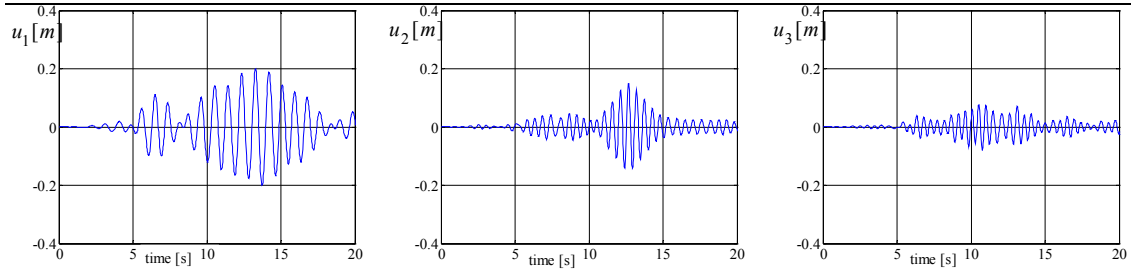


Fig. 2.91: Relative displacement of fluid in three TLCDs, angle of attack: $\alpha = \pi/3$ (artificial seismogram), strong motion phase 20s.

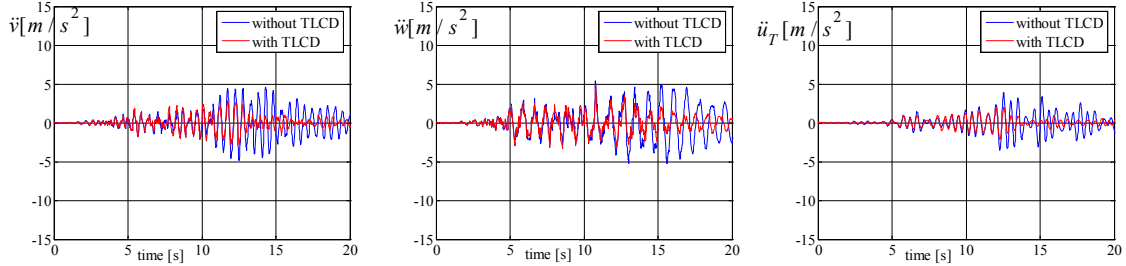


Fig. 2.92: Relative acceleration of single-storey space structure, \ddot{v} , \ddot{w} and $\ddot{u}_T = r_S \ddot{\theta}$, angle of attack: $\alpha = \pi/3$ (artificial seismogram) $r_S = 2.97m$, strong motion phase 20s.

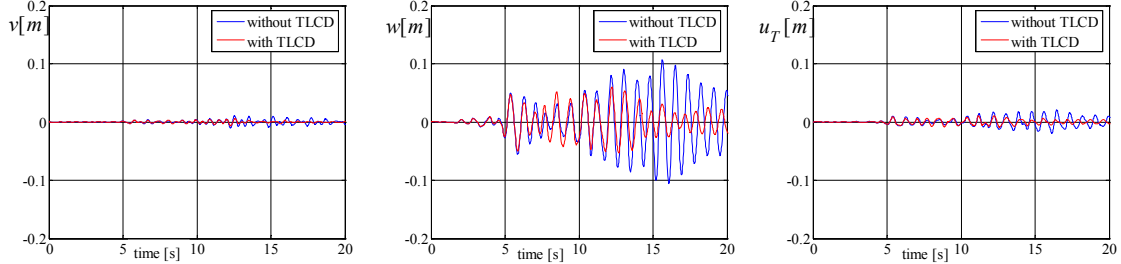


Fig. 2.93: Relative floor displacements of center of mass, v , w and rotation $u_T = r_S \theta$ without and with three TLCDs attached, angle of attack: $\alpha = \pi/2$ (artificial seismogram) $r_S = 2.97m$, strong motion phase 20s.

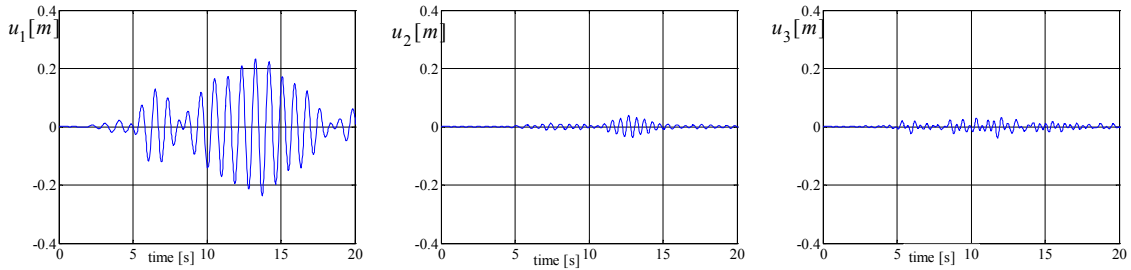


Fig. 2.94: Relative displacement of fluid in three TLCDs, angle of attack: $\alpha = \pi/2$ (artificial seismogram), strong motion phase 20s.

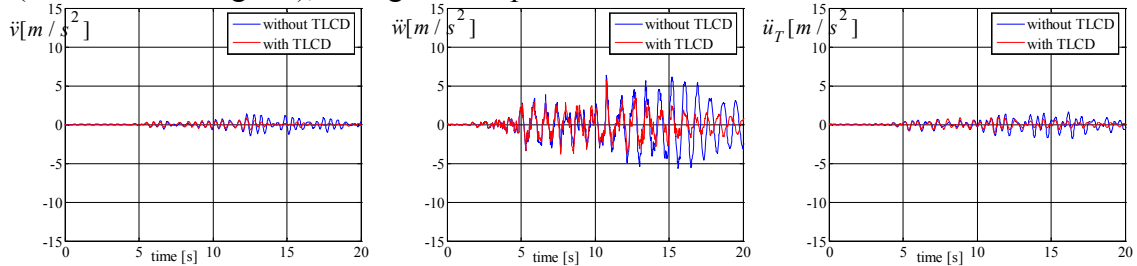


Fig. 2.95: Relative acceleration of single-storey space structure, \ddot{v} , \ddot{w} and $\ddot{u}_T = r_S \ddot{\theta}$, angle of attack: $\alpha = \pi/2$ (artificial seismogram) $r_S = 2.97m$, strong motion phase 20s.

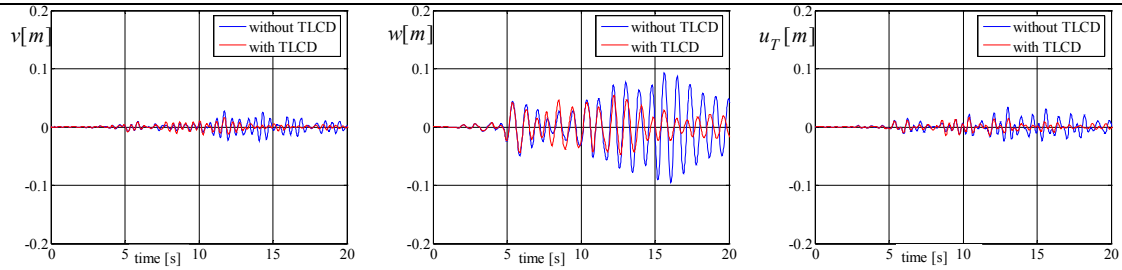


Fig. 2.96: Relative floor displacements of center of mass, v , w and rotation $u_T=r_S\theta$ without and with three TLCDGs attached, angle of attack: $\alpha = 2\pi/3$ (artificial seismogram) $r_S = 2.97m$, strong motion phase 20s.

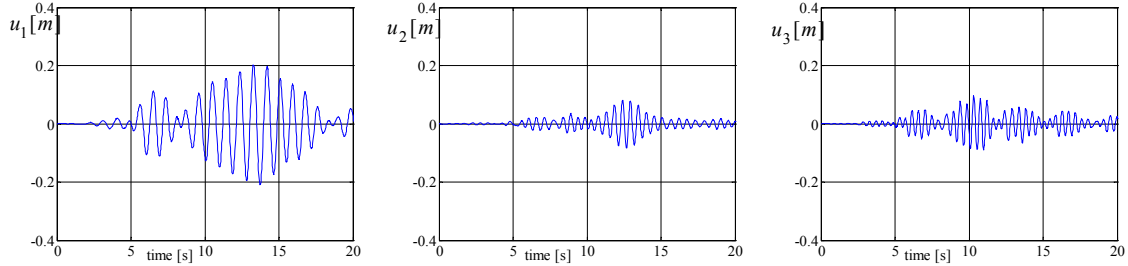


Fig. 2.97: Relative displacement of fluid in three TLCDGs, angle of attack: $\alpha = 2\pi/3$ (artificial seismogram), strong motion phase 20s.

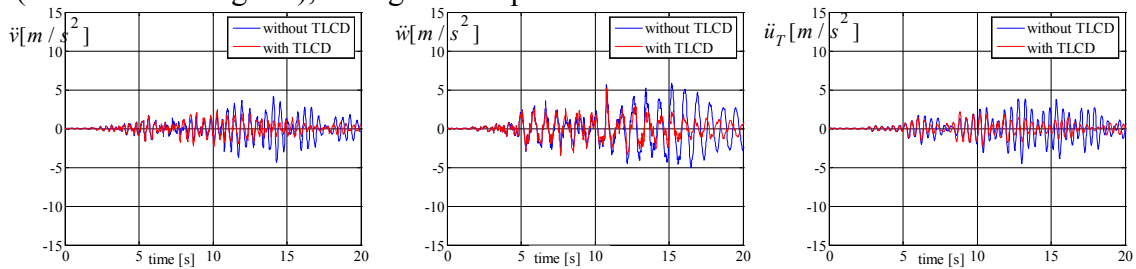


Fig. 2.98: Relative acceleration of single-storey space structure, \ddot{v} , \ddot{w} and $\ddot{u}_T = r_S\ddot{\theta}$, angle of attack: $\alpha = 2\pi/3$ (artificial seismogram) $r_S = 2.97m$, strong motion phase 20s.

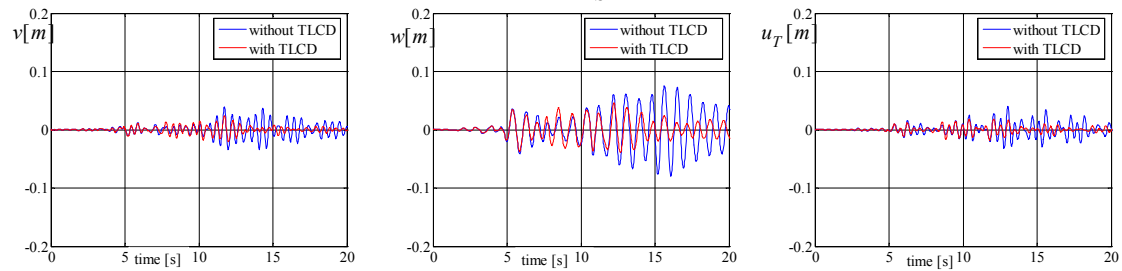


Fig. 2.99: Relative floor displacements of center of mass, v , w and rotation $u_T=r_S\theta$ without and with three TLCDGs attached, angle of attack: $\alpha = 3\pi/4$ (artificial seismogram) $r_S = 2.97m$, strong motion phase 20s.

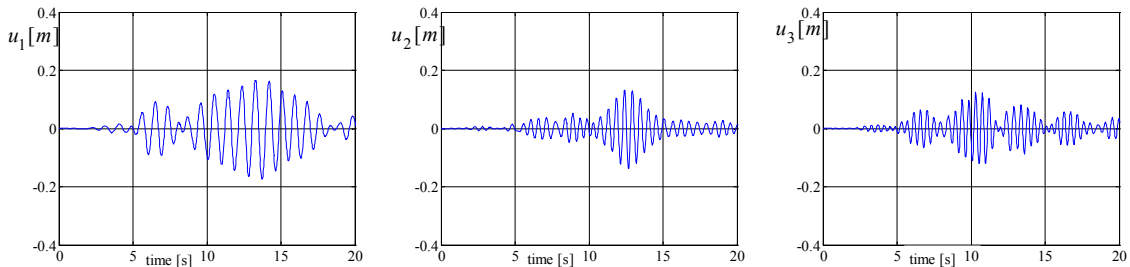


Fig. 2.100: Relative displacement of fluid in three TLCDGs, angle of attack: $\alpha = 3\pi/4$ (artificial seismogram), strong motion phase 20s.

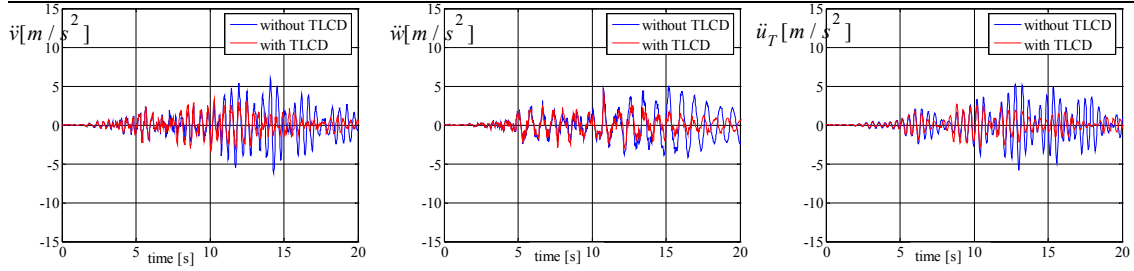


Fig. 2.101: Relative acceleration of single-storey space structure, \ddot{v} , \ddot{w} and $\ddot{u}_T = r_S \ddot{\theta}$, angle of attack: $\alpha = 3\pi/4$ (artificial seismogram) $r_S = 2.97m$, strong motion phase 20s.

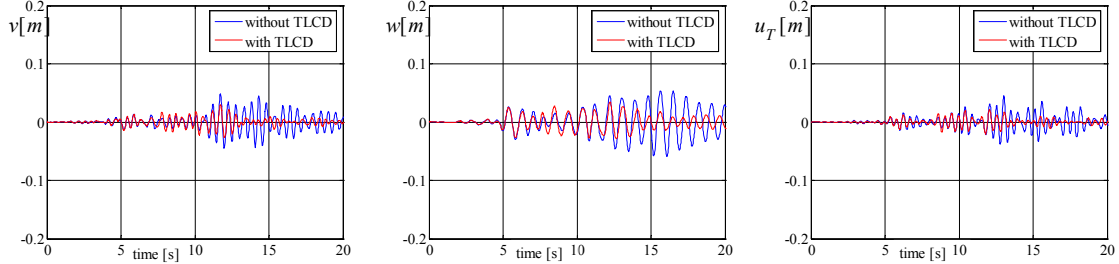


Fig. 2.102: Relative floor displacements of center of mass, v , w and rotation $u_T = r_S \theta$ without and with three TLCDGs attached, angle of attack: $\alpha = 5\pi/6$ (artificial seismogram) $r_S = 2.97m$, strong motion phase 20s.

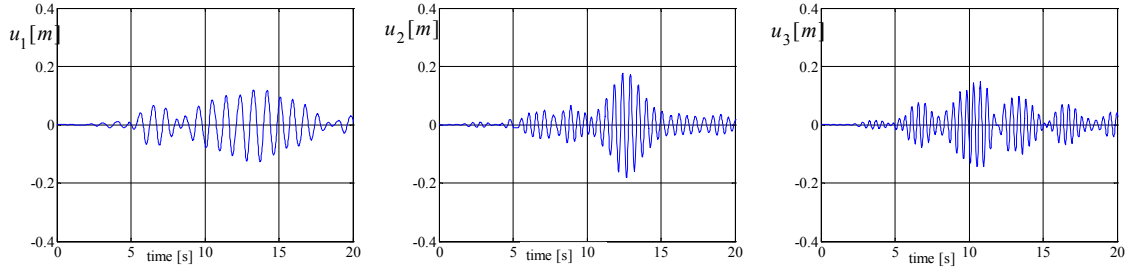


Fig. 2.103: Relative displacement of fluid in three TLCDGs, angle of attack: $\alpha = 5\pi/6$ (artificial seismogram), strong motion phase 20s.

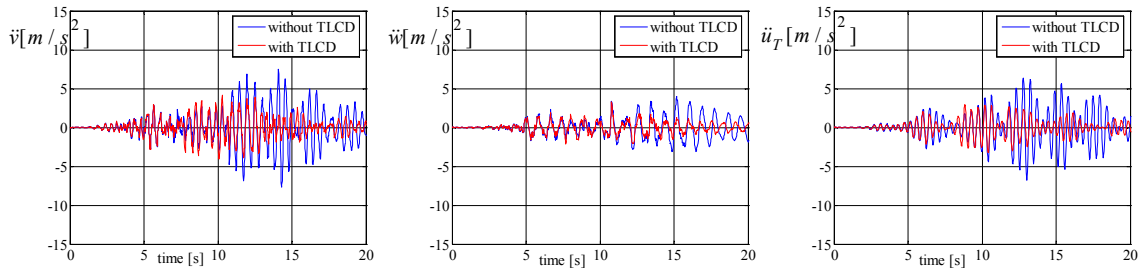


Fig. 2.104: Relative acceleration of single-storey space structure, \ddot{v} , \ddot{w} and $\ddot{u}_T = r_S \ddot{\theta}$, angle of attack: $\alpha = 5\pi/6$ (artificial seismogram) $r_S = 2.97m$, strong motion phase 20s.

The numerical values of the maximum response are sampled in Table 2.8a and 2.8b. The maximum fluid displacements of $u_1 = 0.23m$, $u_2 = 0.23m$, $u_3 = 0.16m$ and velocities of $\dot{u}_1 = 1.63m/s$, $\dot{u}_2 = 2.69m/s$, $\dot{u}_3 = 2.18m/s$ are within the acceptable limits. The results confirm the robust performance of the TLCDGs in reducing the torsionally coupled response of a structure with changing damping.

Single-storey Moderately Plan-asymmetric Space Frame with TLCGDs

max	original structure			structure with 3 TLCGDs			fluid displacement		
	v [mm]	w [mm]	u_T [mm]	v [mm]	w [mm]	u_T [mm]	u_1 [mm]	u_2 [mm]	u_3 [mm]
$\alpha = 0$	54	11	43	34	6	22	20	231	162
$\alpha = \pi/6$	49	54	37	31	26	24	114	219	137
$\alpha = \pi/4$	42	76	34	27	39	22	162	190	110
$\alpha = \pi/3$	32	93	28	21	49	19	200	149	76
$\alpha = \pi/2$	11	108	21	6	60	11	232	38	32
$\alpha = 2\pi/3$	27	93	34	16	54	16	202	82	98
$\alpha = 3\pi/4$	39	76	41	24	46	19	166	133	125
$\alpha = 5\pi/6$	48	54	45	30	34	21	119	176	148

Table 2.8a: Maximum displacements, artificial seismogram using Kanai-Tajimi model, maximum ground acceleration $a_0/g = 0.34$. Varying angle of attack α . Extreme values indicated in bold, $u_T = r_S \theta$, $r_S = 2.97m$.

max	original structure			structure with 3 TLCGDs		
	\ddot{v}/g	\ddot{w}/g	\ddot{u}_T/g	\ddot{v}/g	\ddot{w}/g	\ddot{u}_T/g
$\alpha = 0$	0.91	0.13	0.75	0.49	0.08	0.36
$\alpha = \pi/6$	0.80	0.30	0.63	0.45	0.25	0.31
$\alpha = \pi/4$	0.65	0.44	0.53	0.38	0.38	0.26
$\alpha = \pi/3$	0.47	0.55	0.40	0.29	0.49	0.20
$\alpha = \pi/2$	0.13	0.65	0.17	0.08	0.56	0.09
$\alpha = 2\pi/3$	0.43	0.60	0.39	0.25	0.53	0.22
$\alpha = 3\pi/4$	0.62	0.52	0.54	0.35	0.45	0.27
$\alpha = 5\pi/6$	0.76	0.40	0.65	0.42	0.34	0.30

Table 2.8b: Maximum accelerations, artificial seismogram using Kanai-Tajimi model, maximum ground acceleration $a_0/g = 0.34$. Varying angle of attack α . Extreme values indicated in bold, $u_T = r_S \theta$, $r_S = 2.97m$.

References

[1] Hochrainer M.J., Control of vibrations of civil engineering structures with special emphasis on tall buildings. Dissertation (in English), TU-Wien, A-1040 Vienna, Austria, 2001.

[2] Hochrainer M.J., Ziegler F., Control of tall building vibrations by sealed tuned liquid column dampers, Structural Control and Health Monitoring. 2006; 6, 13, 980-1002.

[3] Ziegler F., Mechanics of Solids and Fluids, correct reprint of second edition, Springer, New York 1998.

[4] Chopra A.K., Dynamics of Structures, Prentice-Hall, New Jersey, 1995.

[5] Robert K., Bautabellen, Wien, Verl.Jugend&Volk, 2002.

[6] Clough R.W., Penzien J., Dynamics of Structures, 2nd edition, McGraw-Hill, 1993.

[7] MATLAB, User Guide, Control Toolbox. MathWorks Inc., Version 6.5.1, 2002.

[8] Reiterer M., Damping of vibration-prone civil engineering structures with emphasis on bridges. Dissertation (in German), TU-Wien, A-1040 Vienna, Austria, 2004.

[9] Reiterer M., Ziegler F., Control of pedestrian-induced vibrations of long-span bridges, Structural Control and Health Monitoring. 2006; 13, 6, 1003-1027.

[10] Ziegler F., Special design of tuned liquid column-gas dampers for the control of spatial structural vibrations, Acta Mechanica. 2008, ISSN 0001-5970.

[11] Lindner-Silvester T., Schneider W., The moving contact line with weak viscosity effects-an application and evaluation of Shikhmurzaev's model, Acta Mechanica. 2005, 176, 3, 245-258.

[12] DenHartog J.P., Mechanical vibrations. 4th edn, McGraw-Hill, New York, 1956.

- [13] Matlab, Simulink Version 3.0.1, The MathWorks Inc., 1984-2001, campus licence TU-Wien.
- [14] Kanai K., Semi-empirical formula for the seismic characteristics of the ground, Bulletin of the earthquake research institute. University of Tokyo. 1957; 35, 2, 309-325.
- [15] Ou J.P., Random earthquake ground motion model and its parameter determination used in seismic design, Earthquake engineering and engineering vibration. 1991; 11, 3, 45-54.
- [16] Höllinger F., Bebeneregte Schwingungen elastischer Sperrenkonstruktionen. Dissertation (in German), TU-Wien, A-1040 Vienna, Austria, 1982.
- [17] Höllinger F., Ziegler F., Instationäre Zufallsschwingungen einer elastischen Gewichtsmauer bei beliebig geformtem Becken, ZAMM. 1983; 63, 1, 49-54.
- [18] Giuseppe C.M., Probabilistic seismic response and reliability assessment of isolated bridges, Earthquake engineering and engineering vibration. 2005; 4, 1, 95-106.
- [19] Zhang Z.Y., Sun B.T. and Song T. S., Study on the parameters of seismic power spectrum model based on the new seismic code, World information on earthquake engineering. 2000; 16, 3, 33-38.
- [20] Ziegler F., The tuned liquid column damper as the cost-effective alternative of the mechanical damper in civil engineering structures, International Journal of Acoustics and Vibration. 2007; 12, 1, 25-39.
- [21] Xue S.D., Torsional vibration control of suspension bridge decks using tuned liquid column damper. Dissertation (in English), the Hong Kong Polytechnic University, 1999.
- [22] Ziegler F., Structural dynamics, lecture notes, TU-Wien, 1979.
- [23] Matlab, Signal Processing Toolbox, The MathWorks Inc., 1984-2001, campus licence TU-Wien.
- [24] Lin C.C., Ueng J.M., Huang T.C., Seismic response reduction of irregular building using passive tuned mass dampers, Engineering Structures. 2000; 22, 5, 513-524.
- [25] Fujina Y., Sun L.M., Vibration control by multiple tuned liquid dampers (MTLDs), ASCE J. of Structural Engineering. 1993; 119, 12, 3482-3502.
- [26] Chang.C.C., Mass dampers and their optimal designs for building vibration control, Engineering Structures. 1999; 21, 5, 454-463.
- [27] Alexandros A., Optimal design and performance of liquid column mass dampers for rotational vibration control of structures under white noise excitation, Engineering Structures. 2005; 27, 4, 524-534.
- [28] Adrian Y.J.W., Performance assessment of tuned liquid column damper under random seismic loading, J. Non-linear Mechanics. 1997; 32, 4, 745-758.

3. Single-storey Strongly Plan-asymmetric Space Frame with TTLCGDs and TLCGDs

3.1 Introduction

Torsional tuned liquid column gas damper (TTLCGD) is a novel type of damper that can control the torsional response of structures about the vertical axis. The results of free vibration and forced vibration simulations show that it is effective to control structural torsional response in Hochrainer¹, Hochrainer and Adam² and Liang³, but the determination of the optimal parameters of TTLCGD for effective reduction of torsionally coupled vibration needs to be investigated.

In this chapter we propose TTLCGD to reduce the coupled lateral and torsional motions in single-storey stiffness-asymmetric space frames subjected to uni-directional horizontal seismic excitation. For a strongly asymmetric building, the velocity centers of several modes fall inside the floor plan. In that case the TTLCGD is more effective to mitigate torsional motion when compared to the U-shaped TLCGD. The special design of TTLCGD with emphasis on the analogy in the tuning process to the equivalent torsional tuned mechanical damper (TTMD) is originally developed subsequently. Plan-symmetric buildings have isolated pure torsional modes. In those cases if their excitation is expected, the application of the TTLCGD is recommended too.

3.2 Equation of motion for single-storey strongly asymmetric space frame

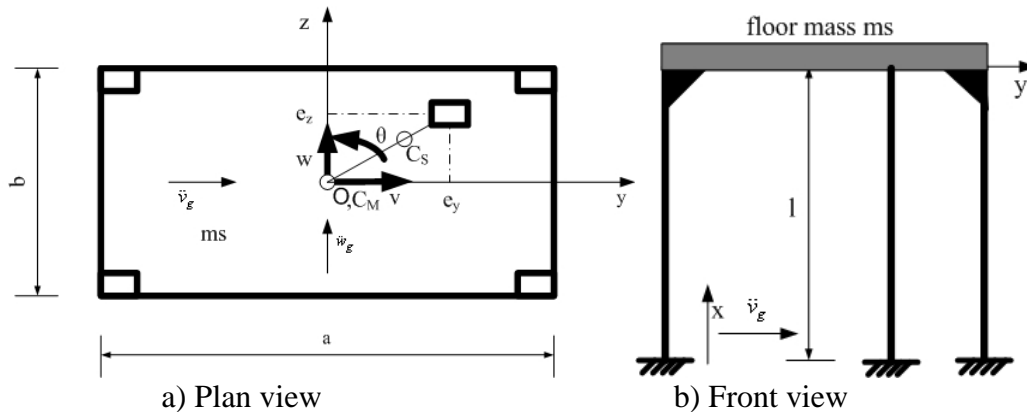


Fig. 3.1: Asymmetric space frame due to unsymmetric stiffness distribution.

For simplicity, a single-storey model is reconsidered with uniformly distributed floor mass. The motion of its center of mass C_M is defined by two horizontal displacements v and w in the y - and z -directions, and rotation angle θ about a vertical x -axis (Figure 3.1a). The origin of the coordinate system is at C_M . The column at each corner has the same anisotropic stiffness k_y and k_z in y - and z -directions. However, an extra column of much stronger stiffness k'_y and k'_z , referring e.g. to the elevator tube, has the eccentricity e_y , e_z . The center of stiffness and center of mass are well separated, see the center of stiffness C_S in Fig. 3.1a.

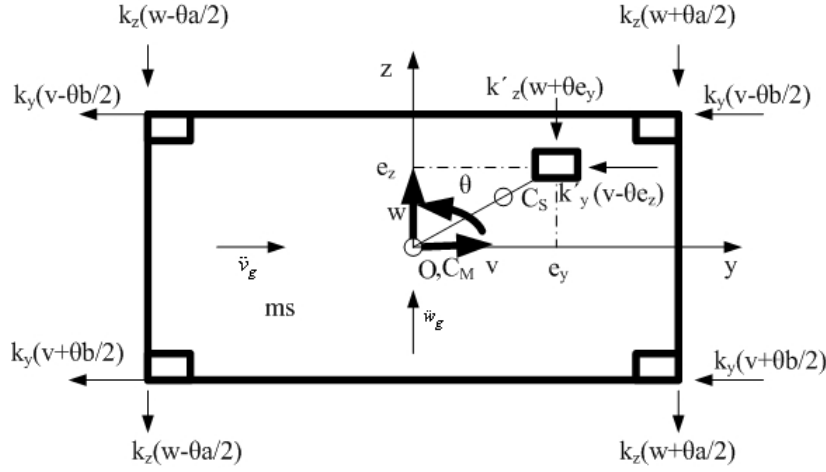


Fig. 3.2: Free-body-diagram of the floor of the strongly asymmetric space-frame, stiff elevator tube shown; derivation of the stiffness matrix.

The free-body-diagram of single-storey structure under ground excitation as indicated in Fig.3.2 is subjected to the basic laws of conservation of momentum and conservation of angular momentum.

(i) Conservation of momentum in the y - z plane

$$\begin{aligned} m_S \vec{a}_{C_M} &= \vec{R}, \quad \vec{a}_{C_M} = \ddot{v}_t \vec{e}_y + \ddot{w}_t \vec{e}_z \\ \ddot{v}_t &= \ddot{v}_g + \ddot{v}, \quad \ddot{w}_t = \ddot{w}_g + \ddot{w}, \end{aligned} \quad (3.1)$$

where \ddot{v}_t and \ddot{w}_t are the absolute accelerations in y - and z -directions, respectively and \vec{R} is the resultant of the external forces,

$$\vec{R} = -\left[(4k_y + k'_y)v - k'_y e_z \theta \right] \vec{e}_y - \left[(4k_z + k'_z)w + k'_z e_y \theta \right] \vec{e}_z.$$

Thus, neglecting structural damping, in y - and z -directions we have respectively,

$$m_S \ddot{v} + (4k_y + k'_y)v - k'_y e_z \theta = -m_S \ddot{v}_g, \quad (3.2a)$$

$$m_S \ddot{w} + (4k_z + k'_z)w + k'_z e_y \theta = -m_S \ddot{w}_g. \quad (3.2b)$$

(ii) Conservation of angular momentum with respect to the center of mass C_M

$$\frac{d\vec{D}_{C_M}}{dt} = \vec{M}_{C_M}, \quad \vec{D}_{C_M} = D_{C_M} \dot{\theta} \vec{e}_x, \quad \vec{M}_{C_M} = M_{C_M} \ddot{\theta} \vec{e}_x, \quad D_{C_M} = I_x \dot{\theta}.$$

According to the free-body diagram in Fig. 3.2, the axial moment of the external forces becomes

$$\begin{aligned} M_{C_M} &= k'_y v e_z - k'_z w e_y - (k_y b^2 + k'_y e_z^2 + k_z a^2 + k'_z e_y^2) \theta, \\ I_x \ddot{\theta} + (k_y b^2 + k'_y e_z^2 + k_z a^2 + k'_z e_y^2) \theta - k'_y v e_z + k'_z w e_y &= 0, \end{aligned} \quad (3.2c)$$

where the mass moment of inertia about the vertical x -axis of the rectangular floor is, Fig. 3.2,

$$I_x = m_S (a^2 + b^2) / 12 = m_S r_S^2,$$

where r_S denotes the radius of inertia with respect to the center of mass C_M .

The three coupled equations of undamped motion, Eqs. (3.2a)- (3.2c) are put in their matrix form.

$$\underline{M} \ddot{\vec{x}} + \underline{K} \vec{x} = -\underline{M} \ddot{\vec{x}}_g, \quad \vec{x}^T = [v \quad w \quad u_T], \quad \ddot{\vec{x}}_g^T = [\ddot{v}_g \quad \ddot{w}_g \quad 0], \quad u_T = \theta r_S. \quad (3.3)$$

The diagonal mass- and the symmetric stiffness matrix of the 3-DOF structure are deduced

from Eqs. (3.2a)- (3.2c) by inspection

$$\underline{\underline{M}} = m_S \begin{bmatrix} 1 & 0 & 0 \\ 0 & 1 & 0 \\ 0 & 0 & 1 \end{bmatrix}, \quad (3.4)$$

$$\underline{\underline{K}} = \begin{bmatrix} 4k_y + k'_y & 0 & -k'_y e_z / r_S \\ 0 & 4k_z + k'_z & k'_z e_y / r_S \\ -k'_y e_z / r_S & k'_z e_y / r_S & (k_y b^2 + k_z a^2 + k'_y e_z^2 + k'_z e_y^2) / r_S^2 \end{bmatrix}. \quad (3.5)$$

3.3 Torsional Tuned Liquid Column Damper, TTLCGD

The control performance of TTLCGD is effective for dominating torsional vibration, i.e., if the modal center of velocity falls within the floor plan. The configuration of TTLCGD is shown in Figure 3.3 and it consists of a liquid filled piping system which encloses in its horizontal section the “arbitrarily” shaped area A_p , thus within the floor, ending with sealed (vertical or if suitable X-braced) columns in close neighborhood to each other.

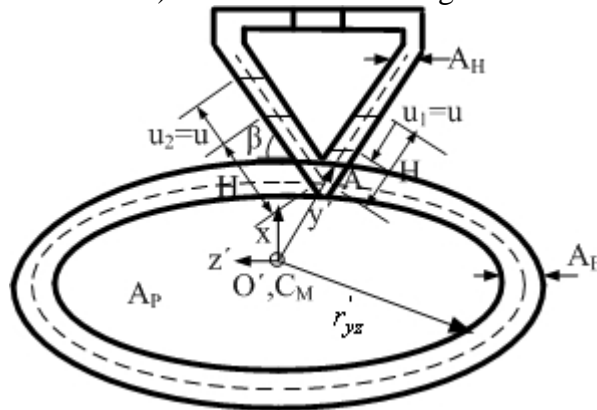


Fig. 3.3: Schematic representation of torsional TLCGD=TTLCGD, encircling the modal center of velocity of the floor. The pipe section within the floor plan encloses the area A_p .

A TTLCGD is fixed to the supporting floor of a single-storey building. When the center of velocity is in the floor as shown in Fig.3.4a, a TTLCGD moves with the structure, the ring-shaped pipe section on the floor enclosing the center of velocity, a relative motion of the viscous liquid inside the pipe is induced which can be used to reduce the torsional structural vibration. Two TTLCGDs with vertical pipe sections on opposite side in parallel action could be installed on the floor in order to somewhat balance the unwanted moments of vertical force components acting on the structure. When the modal center of velocity is outside of the floor, as shown in Fig.3.4b, a relative motion of the liquid is induced by a much smaller amount. As a result, a TTLCGD in the second case is less suitable to mitigate torsional motion and a plane U-shaped TLCGD is substituted to be set on the floor eccentrically, see section 2.9.

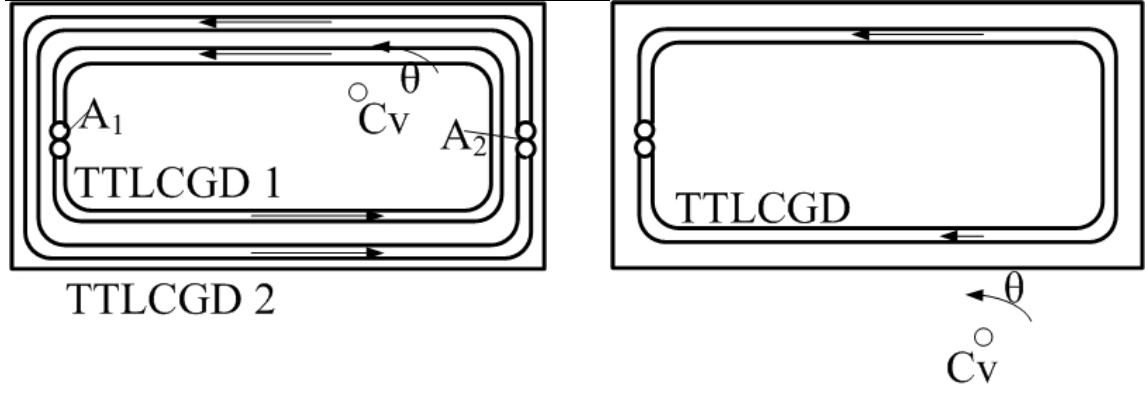


Fig. 3.4a: Center of velocity is in the floor area: apply the TTLCGD. **Fig. 3.4b:** Center of velocity is outside of the floor area: use plane TLCGD, not a TTLCGD.

3.4 Equation of motion of TTLCGD

3.4.1 Equation of motion of TTLCGD (the vertical segment, \mathbf{A} ($y_A, z_A, \mathbf{0}$), $\beta = \pi/2$)

TTLCGD's dynamics can be derived using the generalized instationary Bernoulli equation for moving reference frame. The generalized Bernoulli equation for such a relative streamline of an ideal (inviscid) fluid takes on the form, cf. Eq. (2.19)

$$\int_{1'}^{2'} \frac{\partial \dot{u}}{\partial t} ds' = -g(x_2 - x_1) - \frac{1}{\rho}(p_2 - p_1) - \int_{1'}^{2'} \vec{a}_g \cdot \vec{e}'_t ds', \quad (3.6)$$

where $d\vec{s}' = [dy' \ dz' \ dx']^T$. The guiding acceleration of the moving frame is in the floor plane $\vec{a}_g = \vec{a}_{C_M} + \dot{\theta} \hat{r}'_{y'z'} - \dot{\theta}^2 \vec{r}'_{y'z'}$, $\vec{r}'_{y'z'} = [y' \ z' \ 0]^T$, $\hat{r}'_{y'z'} = [-z' \ y' \ 0]^T$, see also Section 2.4.1. The absolute acceleration of the reference point C_M is given in Eq. (2.1).

The integral term comes separately over the horizontal part of the relative streamline (approximately a loop integral) and over its vertical parts

$$\int_{1'}^{2'} \vec{a}_g \cdot \vec{e}'_t ds' = \int_0^{H-u_1} \vec{a}_g \cdot \vec{e}'_t ds' + \oint_B \vec{a}_g \cdot \vec{e}'_t ds' + \int_0^{H+u_2} \vec{a}_g \cdot \vec{e}'_t ds'.$$

For the vertical segments: $u_1 = u_2 = u(t)$

$$0 \leq s' \leq H - u_1: \vec{e}'_t = -\vec{e}_x, \quad 0 \leq s' \leq H + u_2: \vec{e}'_t = \vec{e}_x,$$

$$\int_0^{H-u_1} \vec{a}_{C_M} \cdot \vec{e}'_t ds' + \int_0^{H+u_2} \vec{a}_{C_M} \cdot \vec{e}'_t ds' = 0. \quad (3.7)$$

For the horizontal curved segment: $0 \leq s' \leq B$: where B denotes the length of the nearly closed horizontal pipe section,

$$\oint_B \vec{a}_{C_M} \cdot \vec{e}'_t ds' = a_{C_M, y'} \oint_{s'} dy' + a_{C_M, z'} \oint_{s'} dz' = 0. \quad (3.8)$$

The integral term $\dot{\theta}^2 \int_{1'}^{2'} \vec{r}'_{y'z'} \cdot \vec{e}'_t ds'$ renders for the vertical segments: $u_1 = u_2 = u(t)$

$$0 \leq s' \leq H - u_1: \vec{r}'_{y'z'} = y_A \vec{e}_{y'} + z_A \vec{e}_{z'}, \quad \vec{r}'_{y'z'} \cdot \vec{e}'_t = 0,$$

$$0 \leq s' \leq H + u_2: \vec{r}'_{y'z'} = y_A \vec{e}_{y'} + z_A \vec{e}_{z'}, \quad \vec{r}'_{y'z'} \cdot \vec{e}'_t = 0,$$

$$\dot{\theta}^2 \left(\int_0^{H-u_1} \vec{r}'_{y'z'} \cdot \vec{e}'_t ds' + \int_0^{H+u_2} \vec{r}'_{y'z'} \cdot \vec{e}'_t ds' \right) = 0. \quad (3.9)$$

For the horizontal segment: $0 \leq s' \leq B$: (nearly a closed curve)

$$\dot{\theta}^2 \oint_B \vec{r}'_{y'z'} \cdot \vec{e}'_t ds' = \dot{\theta}^2 \left(\oint_{s'} y' dy' + \oint_{s'} z' dz' \right) = 0. \quad (3.10)$$

The path integration $\ddot{\theta} \int_1^{2'} \hat{\vec{r}}'_{y'z'} \cdot \vec{e}'_t ds'$ is performed similarly to the aforementioned.

For the vertical segment:

$$0 \leq s' \leq H - u_1: \hat{\vec{r}}'_{y'z'} = -z_A \vec{e}_{y'} + y_A \vec{e}_{z'}, \quad \hat{\vec{r}}'_{y'z'} \cdot \vec{e}'_t = 0,$$

$$0 \leq s' \leq H + u_2: \hat{\vec{r}}'_{y'z'} = -z_A \vec{e}_{y'} + y_A \vec{e}_{z'}, \quad \hat{\vec{r}}'_{y'z'} \cdot \vec{e}'_t = 0,$$

$$\ddot{\theta} \left(\int_0^{H-u_1} \hat{\vec{r}}'_{y'z'} \cdot \vec{e}'_t ds' + \int_0^{H+u_2} \hat{\vec{r}}'_{y'z'} \cdot \vec{e}'_t ds' \right) = 0. \quad (3.11)$$

For the horizontal segment: $0 \leq s' \leq B$: (nearly a closed curve)

$$\ddot{\theta} \oint_B \hat{\vec{r}}'_{y'z'} \cdot \vec{e}'_t ds = 2A_p \ddot{\theta}, \quad (3.12)$$

where A_p is the enclosed area in the floor plan, see Fig.3.3.

Finally, substitution of Eqs. (3.7)- (3.12) into Eq. (3.6), the generalized Bernoulli equation becomes,

$$\ddot{u} \left(2H + \frac{A_H}{A_B} B \right) = -2gu - \frac{1}{\rho} (p_2 - p_1) - 2A_p \ddot{\theta}, \quad (3.13)$$

adding the equivalently linearized damping, see Eq. (2.36) and considering the linearized gas compression, yield the equation of motion of the relative fluid motion in the TTLCGD for $\beta = \pi/2$,

$$\ddot{u} + 2\zeta_A \omega_A \dot{u} + \omega_A^2 u = -\kappa_{T0} \ddot{u}_{TT}, \quad (3.14)$$

$$\kappa_{T0} = \frac{2A_p}{r_f L_{eff}}, \quad L_{eff} = 2H + \frac{A_H}{A_B} B, \quad \ddot{u}_{TT} = r_f \ddot{\theta}, \quad I_{fx} = m_f r_f^2, \quad (3.14a)$$

where I_{fx} , r_f denote the axial moment of inertia of the fluid mass and the radius of inertia for the fluid mass with respect to reference point C_M .

3.4.2 Equation of motion of TTLCGD (the inclined segment parallel to z-axis, $\mathbf{A} (y_A, 0, 0)$, $\pi/4 \leq \beta < \pi/2$)

\vec{e}'_t is changed for the X-braced inclined segments, cf. Eq. (3.7),

$$0 \leq s' \leq H - u_1: \vec{e}'_t = \cos \beta \vec{e}_{z'} - \sin \beta \vec{e}_x, \quad 0 \leq s' \leq H + u_2: \vec{e}'_t = \cos \beta \vec{e}_{z'} + \sin \beta \vec{e}_x,$$

$$\int_0^{H-u_1} \vec{a}_{C_M} \cdot \vec{e}'_t ds' + \int_0^{H+u_2} \vec{a}_{C_M} \cdot \vec{e}'_t ds' = 2H a_{C_M, z'} \cos \beta. \quad (3.15)$$

For the horizontal curved segment $\oint_B \vec{a}_{C_M} \cdot \vec{e}'_t ds' = 0$.

The integral term $\ddot{\theta}^2 \int_1^{2'} \vec{r}'_{y'z'} \cdot \vec{e}'_t ds'$ renders for the horizontal segment $\dot{\theta}^2 \oint_B \vec{r}'_{y'z'} \cdot \vec{e}'_t ds = 0$.

For the X-braced inclined segments: cf. Eq. (3.9),

$$0 \leq s' \leq H - u_1: \vec{r}'_{y'z'} \cdot \vec{e}'_t = y_A \vec{e}_{y'} - [(H - u_1) \cos \beta - s' \cos \beta] \vec{e}_{z'},$$

$$\vec{r}'_{y'z'} \cdot \vec{e}'_t = -[(H - u_1) \cos \beta - s' \cos \beta] \cos \beta,$$

$$0 \leq s' \leq H + u_2: \vec{r}'_{y'z'} = y_A \vec{e}_{y'} + s' \cos \beta \vec{e}_{z'}, \quad \vec{r}'_{y'z'} \cdot \vec{e}'_t = s' \cos^2 \beta,$$

$$\dot{\theta}^2 \left(\int_0^{H-u_1} \vec{r}'_{y'z'} \cdot \vec{e}'_t ds' + \int_0^{H+u_2} \vec{r}'_{y'z'} \cdot \vec{e}'_t ds' \right) = 2H\dot{\theta}^2 u \cos^2 \beta. \quad (3.16)$$

The path integration $\ddot{\theta} \int_1^{2'} \hat{r}'_{y'z'} \cdot \vec{e}'_t ds'$ is performed similarly to the aforementioned, for the

$$\text{horizontal segment } \ddot{\theta} \oint_B \hat{r}'_{y'z'} \cdot \vec{e}'_t ds = 2A_p \ddot{\theta}.$$

For the X-braced inclined segment: cf. Eq. (3.11),

$$0 \leq s' \leq H - u_1: \hat{r}'_{y'z'} = [(H - u_1) \cos \beta - s' \cos \beta] \vec{e}_{y'} + y_A \vec{e}_{z'}, \quad \hat{r}'_{y'z'} \cdot \vec{e}'_t = y_A \cos \beta,$$

$$0 \leq s' \leq H + u_2: \hat{r}'_{y'z'} = -s' \cos \beta \vec{e}_{y'} + y_A \vec{e}_{z'}, \quad \hat{r}'_{y'z'} \cdot \vec{e}'_t = y_A \cos \beta,$$

$$\ddot{\theta} \left(\int_0^{H-u_1} \hat{r}'_{y'z'} \cdot \vec{e}'_t ds' + \int_0^{H+u_2} \hat{r}'_{y'z'} \cdot \vec{e}'_t ds' \right) = 2Hy_A \ddot{\theta} \cos \beta. \quad (3.17)$$

Finally, substitution of Eqs. (3.16), (3.17), (3.10) and (3.12) into Eq. (3.6), the Bernoulli type equation results, cf. Eq. (3.13),

$$\ddot{u} \left(2H + \frac{A_H}{A_B} B \right) = -2gu \sin \beta - \frac{1}{\rho} (p_2 - p_1) - 2Ha_{C_M, z'} \cos \beta - \left(2A_p + 2Hy_A \cos \beta \right) \ddot{\theta} + 2H\dot{\theta}^2 u \cos^2 \beta. \quad (3.18)$$

Adding the equivalently linearized damping and considering the linearized gas compression, yield the parametrically forced equation of motion of the relative fluid motion in the TTLCGD, note the additional forcing term when compared to Eq. (3.14),

$$\ddot{u} + 2\zeta_A \omega_A \dot{u} + \omega_A^2 \left(1 - \kappa_{T1} \frac{\dot{\theta}^2}{\omega_A^2} \right) u = -\kappa_{Tz} \ddot{u}_{TT} - \kappa_T a_{C_M, z'}, \quad (3.19)$$

$$\kappa_T = \frac{2H \cos \beta}{L_{eff}}, \quad \kappa_{T1} = \kappa_T \cos \beta, \quad \kappa_{Tz} = \kappa_{T0} + \kappa_T y_A / r_f,$$

$$L_{eff} = 2H + \frac{A_H}{A_B} B, \quad \ddot{u}_{TT} = r_f \ddot{\theta}, \quad I_{fx} = m_f r_f^2. \quad (3.19a)$$

Substituting $a_{C_M, z'}$, Eq.(3.1), into Eq. (3.19), and further linearizing the forcing term, yield the simplified and linearized equation of motion for the relative fluid flow in the TTLCGD, parametric forcing is negligible with sufficient damping understood, see also Eq. (2.36),

$$\ddot{u} + 2\zeta_A \omega_A \dot{u} + \omega_A^2 u = -\kappa_{Tz} \ddot{u}_{TT} - \kappa_T (\ddot{w}_g + \ddot{w}). \quad (3.20)$$

3.4.3 Equation of motion of TTLCGD (the inclined segment parallel to y-axis, $\mathbf{A}(\mathbf{0}, \mathbf{z}_A, \mathbf{0})$, $\pi/4 \leq \beta < \pi/2$)

A TTLCGD is installed on the floor and the inclined part of TTLCGD is oriented parallel to y axis. Equation (3.18) with κ_{Ty} substituted for κ_{Tz} still holds, when the y-component of acceleration $a_{C_M, y'}$ is substituted for $a_{C_M, z'}$,

$$\ddot{u} + 2\zeta_A \omega_A \dot{u} + \omega_A^2 \left(1 - \kappa_{T1} \frac{\dot{\theta}^2}{\omega_A^2} \right) u = -\kappa_{Ty} \ddot{u}_{TT} + \kappa_T a_{C_M, y'} \quad (3.21)$$

Substituting $a_{C_M, y'}$, Eq. (3.1), into Eq. (3.21) and considering its linearized form with parametric excitation neglected, compare with Eq. (3.20),

$$\ddot{u} + 2\zeta_A \omega_A \dot{u} + \omega_A^2 u = -\kappa_{Ty} \ddot{u}_{TT} + \kappa_T (\ddot{v}_g + \ddot{v}), \quad \kappa_{Ty} = \kappa_{T0} + \kappa_T z_A / r_f \quad (3.22)$$

3.5 Forces and Moments of TTLCGD

3.5.1 Forces and Moments (the vertical segment, \mathbf{A} ($\mathbf{y}_A, \mathbf{z}_A, \mathbf{0}$), $\beta = \pi/2$)

(i) The interaction forces $F_{C_M y}$, $F_{C_M z}$, conservation of momentum $\vec{R} = m_f \vec{a}_f$.

The instant position of center of fluid mass C_f with respect to reference point C_M is given by $\vec{r}'_f + x_f \vec{e}_x$, where the in-plane component is $\vec{r}'_f = y'_f \vec{e}_y + z'_f \vec{e}_z$. Hence,

$$\vec{r}_f = \vec{r}_{C_M} + \vec{r}'_f + x_f \vec{e}_x,$$

$$\frac{d\vec{r}'_f}{dt} = \dot{y}'_f \vec{e}_y + \dot{z}'_f \vec{e}_z + \dot{\theta} \hat{r}'_f,$$

$$\vec{v}_f = \dot{\vec{r}}_f = \vec{v}_{C_M} + (\dot{y}'_f - z'_f \dot{\theta}) \vec{e}_y + (\dot{z}'_f + y'_f \dot{\theta}) \vec{e}_z + \dot{x}_f \vec{e}_x, \quad (3.23)$$

$$\vec{a}_f = \dot{\vec{v}}_f = \vec{a}_{C_M} + (\ddot{y}'_f - z'_f \ddot{\theta} - y'_f \dot{\theta}^2 - 2\dot{z}'_f \dot{\theta}) \vec{e}_y + (\ddot{z}'_f + y'_f \ddot{\theta} - z'_f \dot{\theta}^2 + 2\dot{y}'_f \dot{\theta}) \vec{e}_z + \ddot{x}_f \vec{e}_x, \quad (3.24)$$

where \vec{v}_f , \vec{a}_f are absolute velocity and absolute acceleration of the center of fluid mass C_f .

Considering the static mass-moments:

$$m_f y'_f = \rho A_H (H + u) y_A + \rho A_H (H - u) y_A = 2\rho A_H H y_A, \quad (3.25)$$

$$m_f z'_f = \rho A_H (H + u) z_A + \rho A_H (H - u) z_A = 2\rho A_H H z_A, \quad (3.26)$$

$$m_f x_f = \rho A_H (H + u) \frac{H + u}{2} + \rho A_H (H - u) \frac{H - u}{2} = \rho A_H (H^2 + u^2), \quad (3.27)$$

we determine

$$z'_f = \frac{2Hz_A}{L_1} = \bar{\kappa}_{T3} z_A, \quad \dot{z}'_f = 0, \quad \ddot{z}'_f = 0, \quad L_1 = 2H + \frac{A_B}{A_H} B, \quad (3.28)$$

$$y'_f = \frac{2Hy_A}{L_1} = \bar{\kappa}_{T3} y_A, \quad \dot{y}'_f = 0, \quad \ddot{y}'_f = 0, \quad (3.29)$$

$$x_f = \frac{(H^2 + u^2)}{L_1} = \bar{\kappa}_{T3} \frac{1}{2H} (H^2 + u^2), \quad \dot{x}_f = \bar{\kappa}_{T3} \frac{1}{H} u \dot{u}, \quad \ddot{x}_f = \bar{\kappa}_{T3} \frac{1}{H} (\dot{u}^2 + u \ddot{u}). \quad (3.30)$$

with the following geometry coefficient $\bar{\kappa}_{T3} = 2H/L_1$. Substituting Eqs. (3.28)-(3.30) into Eq. (3.24) confirms, after multiplication with m_f the resultant,

$$\vec{R} = m_f \vec{a}_{C_M} + m_f \bar{\kappa}_{T3} \left[- (z_A \ddot{\theta} + y_A \dot{\theta}^2) \vec{e}_y + (y_A \ddot{\theta} - z_A \dot{\theta}^2) \vec{e}_z + \frac{1}{H} (\dot{u}^2 + u \ddot{u}) \vec{e}_x \right]. \quad (3.31)$$

Equation (3.31) renders the horizontal components of the control force acting on the piping system,

$$F_{C_M y'} = m_f (a_y \cos \theta + a_z \sin \theta - \bar{\kappa}_{T3} z_A \ddot{\theta} - \bar{\kappa}_{T3} y_A \dot{\theta}^2), \quad (3.32)$$

$$F_{C_M z'} = m_f \left(-a_y \sin \theta + a_z \cos \theta + \bar{\kappa}_{T3} y_A \ddot{\theta} - \bar{\kappa}_{T3} z_A \dot{\theta}^2 \right), \quad (3.33)$$

and, when rotated

$$F_{C_M y} = m_f \left[a_y - \left(z_A \ddot{\theta} + y_A \dot{\theta}^2 \right) \bar{\kappa}_{T3} \cos \theta - \left(y_A \ddot{\theta} - z_A \dot{\theta}^2 \right) \bar{\kappa}_{T3} \sin \theta \right], \quad (3.34)$$

$$F_{C_M z} = m_f \left[a_z - \left(z_A \ddot{\theta} + y_A \dot{\theta}^2 \right) \bar{\kappa}_{T3} \sin \theta + \left(y_A \ddot{\theta} - z_A \dot{\theta}^2 \right) \bar{\kappa}_{T3} \cos \theta \right]. \quad (3.35)$$

Equations (3.34) and (3.35) are simplified under the condition $|\theta| \ll 1$ and the essential linear parts become

$$F_{C_M y} = m_f \left(\ddot{v}_g + \ddot{v} - \bar{\kappa}_{T3} \ddot{u}_{TT} z_A / r_f \right), \quad (3.36)$$

$$F_{C_M z} = m_f \left(\ddot{w}_g + \ddot{w} + \bar{\kappa}_{T3} \ddot{u}_{TT} y_A / r_f \right), \quad (3.37)$$

(ii) Conservation of the angular momentum of the fluid body with respect to the accelerated point of reference C_M , see Ziegler⁴, page 405

$$\bar{D}_{C_M} = \int_{m_f} (\bar{\mathbf{r}}' \times \bar{\mathbf{v}}') dm_f = \int_{m_f} \left[\bar{\mathbf{r}}' \times \left(\dot{\theta} \hat{\mathbf{r}}'_{y'z'} + \dot{\mathbf{u}} \right) \right] dm_f \quad (3.38)$$

$$\begin{aligned} &= \rho \left[\dot{\theta} \int_1^{2'} A(s') (\bar{\mathbf{r}}' \times \hat{\mathbf{r}}'_{y'z'}) ds' + \int_1^{2'} A(s') \dot{\mathbf{u}}(s', t) (\bar{\mathbf{r}}' \times \bar{\mathbf{e}}'_i(s')) ds' \right] \\ &\rho \int_1^{2'} A(s') \dot{\mathbf{u}}(s', t) (\bar{\mathbf{r}}' \times \bar{\mathbf{e}}'_i(s')) ds' = \rho A_H \dot{\mathbf{u}} \int_0^{H-u_1} (y_A \bar{\mathbf{e}}_{z'} - z_A \bar{\mathbf{e}}_{y'}) ds' + \rho A_H \dot{\mathbf{u}} \int_0^{H+u_2} (-y_A \bar{\mathbf{e}}_{z'} + z_A \bar{\mathbf{e}}_{y'}) ds' \\ &+ \rho A_B \oint_B \frac{A_H}{A_B} \dot{\mathbf{u}} dA_p \bar{\mathbf{e}}_x = 2\rho A_H \dot{\mathbf{u}} (-y_A u \bar{\mathbf{e}}_{z'} + z_A u \bar{\mathbf{e}}_{y'} + A_p \bar{\mathbf{e}}_x) \end{aligned} \quad (3.39)$$

$$\begin{aligned} &\rho \dot{\theta} \int_1^{2'} A(s') (\bar{\mathbf{r}}' \times \hat{\mathbf{r}}'_{y'z'}) ds' = \rho \dot{\theta} A_H \left[-(H^2 + u^2) y_A \bar{\mathbf{e}}_{y'} - (H^2 + u^2) z_A \bar{\mathbf{e}}_{z'} \right] \\ &+ \rho \dot{\theta} A_H \left[2(y_A^2 + z_A^2) H + \frac{A_B}{A_H} \oint_B |\bar{\mathbf{r}}'_{y'z'}|^2 ds' \right] \bar{\mathbf{e}}_x \end{aligned} \quad (3.40)$$

$$\begin{aligned} \bar{D}_{C_M} &= m_f \left\{ \left(\frac{-(H^2 + u^2) y_A}{L_1} \dot{\theta} + 2 \frac{z_A}{L_1} u \dot{\mathbf{u}} \right) \bar{\mathbf{e}}_{y'} + \left(\frac{-(H^2 + u^2) z_A}{L_1} \dot{\theta} - 2 \frac{y_A}{L_1} u \dot{\mathbf{u}} \right) \bar{\mathbf{e}}_{z'} \right. \\ &\left. + \left[\left(\frac{2(y_A^2 + z_A^2) H}{L_1} + \frac{A_B}{A_H} \frac{\oint_B |\bar{\mathbf{r}}'_{y'z'}|^2 ds'}{L_1} \right) \dot{\theta} + \frac{2A_p}{L_1} \dot{\mathbf{u}} \right] \bar{\mathbf{e}}_x \right\} \end{aligned} \quad (3.41)$$

Differentiating $D_{C_M x}$ renders

$$\frac{dD_{C_M x}}{dt} = m_f \left[\frac{2A_p}{L_1} \ddot{\mathbf{u}} + \left(\frac{2(y_A^2 + z_A^2)}{L_1} H + \frac{A_B}{A_H} \frac{\oint_B |\bar{\mathbf{r}}'_{y'z'}|^2 ds'}{L_1} \right) \ddot{\theta} \right], \quad (3.42)$$

$$\begin{aligned}
 m_f (\vec{r}'_f + x_f \vec{e}_x) \times \vec{a}_{C_M} &= m_f \bar{\kappa}_{T3} \left\{ \left[-\frac{1}{2H} (H^2 + u^2) (-a_y \sin \theta + a_z \cos \theta) \right] \vec{e}_{y'} \right. \\
 &+ \left[\frac{1}{2H} (H^2 + u^2) (a_y \cos \theta + a_z \sin \theta) \right] \vec{e}_{z'} \\
 &\left. + \left[y_A (-a_y \sin \theta + a_z \cos \theta) - z_A (a_y \cos \theta + a_z \sin \theta) \right] \vec{e}_x \right\}
 \end{aligned} \quad (3.43)$$

The parametric forcing $-\bar{\kappa}_{T3} (y_A a_y - z_A a_z) \theta$ in Eq. (3.43) is negligible with sufficient damping understood. The linear resultant control moment $M_{C_M x}$ (acting on the piping system) becomes finally

$$M_{C_M x} = m_f r_f \left(\ddot{u}_{TT} + \frac{\bar{\kappa}_{T3} y_A}{r_f} a_z - \frac{\bar{\kappa}_{T3} z_A}{r_f} a_y \right) + m_f r_f \bar{\kappa}_{T0} \ddot{u}, \quad (3.44)$$

$$\bar{I}_{f\dot{x}} = \rho A_B \oint_B |\vec{r}'_{y'z'}|^2 ds', \quad I_{f\dot{x}} = 2\rho A_H H (y_A^2 + z_A^2) + \bar{I}_{f\dot{x}}, \quad \bar{\kappa}_{T0} = \kappa_{T0} L_{eff} / L_1,$$

where κ_{T0} is defined in Eq.(3.14a).

3.5.2 Forces and Moments (the inclined segment parallel to z -axis, $\mathbf{A} (y_A, \mathbf{0}, \mathbf{0})$, $\pi/4 \leq \beta < \pi/2$)

The interaction forces $F_{C_M y}$, $F_{C_M z}$ are derived by conversation of momentum $\vec{R} = m_f \vec{a}_f$. We take into account the geometrically changed configuration and proceed analogously to section 3.5.1. The linear interaction forces are

$$F_{C_M y} = m_f (\ddot{v}_g + \ddot{v}), \quad (3.45)$$

$$F_{C_M z} = m_f (\ddot{w}_g + \ddot{w} + \bar{\kappa}_{T3} \ddot{u}_{TT} y_A / r_f + \bar{\kappa}_T \ddot{u}). \quad (3.46)$$

The control moment is derived by conservation of the angular momentum of the fluid body with respect to the accelerated point C_M . The linear resultant control moment $M_{C_M x}$ (acting on the piping system) becomes finally

$$M_{C_M x} = m_f r_f \left(\ddot{u}_{TT} + \frac{\bar{\kappa}_{T3} y_A}{r_f} a_z \right) + m_f r_f \bar{\kappa}_{Tz} \ddot{u}, \quad (3.47)$$

$$\bar{I}_{f\dot{x}} = \rho A_B \oint_B |\vec{r}'_{y'z'}|^2 ds', \quad I_{f\dot{x}} = 2\rho A_H \left(y_A^2 H + \frac{H^3 \cos^2 \beta}{3} \right) + \bar{I}_{f\dot{x}}, \quad \bar{\kappa}_{Tz} = \kappa_{Tz} L_{eff} / L_1,$$

where κ_{Tz} is defined in Eq.(3.19a), cf. Eq. (3.44) with $z_A = 0$.

3.5.3 Forces and Moments (the inclined segment parallel to y -axis, $\mathbf{A} (\mathbf{0}, z_A, \mathbf{0})$, $\pi/4 \leq \beta < \pi/2$)

A TTLCD is set on the floor and the inclined segment is parallel to y axis. The interface forces can be obtained, cf. Eqs. (3.45) and (3.46)

$$F_{C_M y} = m_f (\ddot{v}_g + \ddot{v} - \bar{\kappa}_{T3} \ddot{u}_{TT} z_A / r_f + \bar{\kappa}_T \ddot{u}), \quad (3.48)$$

$$F_{C_M z} = m_f (\ddot{w}_g + \ddot{w}). \quad (3.49)$$

The linear resultant control moment $M_{C_M x}$ (acting on the piping system) becomes, cf.

Eqs.(3.47)

$$M_{C_Mx} = m_f r_f \left(\ddot{u}_{TT} - \frac{\bar{\kappa}_{T3zA}}{r_f} a_y \right) + m_f r_f \bar{\kappa}_{Ty} \ddot{u}, \quad \bar{\kappa}_{Ty} = \kappa_{Ty} L_{eff} / L_1. \quad (3.50)$$

3.6 Control of single-storey strongly plan-asymmetric space frame by a single TTLCGD ($\beta = \pi/2$) when compared to an equivalent TTMD

3.6.1 Torsional Tuned Mechanical Damper, TTMD

An equivalent TTMD with a symmetrically distributed mass m_A^* is set on the single-storey asymmetric structure, shown in Fig.3.5. $\bar{I}_{C_Mx}^*$ and r_A^* are the axial moment of inertia and radius of inertia with respect to the absorber's (floor's) center of mass. That radius solely depends on the geometrical, doubly symmetric shape of TTMD. $\frac{u^*}{r_A^*}$ is the rotational angle of TTMD.

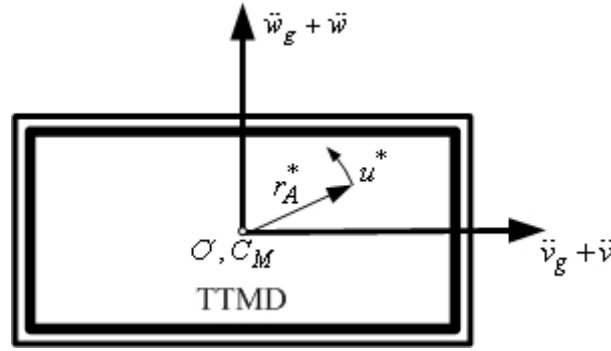


Fig. 3.5: Single-storey asymmetric structure with TTMD: extended mass with rotational spring support.

Conservation of angular momentum with respect to its center of mass $C_M = O$ is applied:

$$D_{C_Mx}^* = \bar{I}_{C_Mx}^* (\dot{u}_{TT}^* + \dot{u}^*) / r_A^*, \quad \bar{I}_{C_Mx}^* = m_A^* r_A^{*2}, \quad M_{C_Mx}^* = -k^* \frac{u^*}{r_A^*}, \quad \dot{u}_{TT}^* = r_A^* \ddot{\theta}, \quad (3.51)$$

$$\bar{I}_{C_Mx}^* (\ddot{u}_{TT}^* + \ddot{u}^*) = -k^* u^*. \quad (3.52)$$

The equation of motion for the TTMD, viscous damping is added to Eq. (3.52), becomes,

$$\ddot{u}_T^* + 2\zeta_A^* \omega_A^* \dot{u}_T^* + \omega_A^{*2} u_T^* = -\ddot{u}_{TT}^*, \quad \omega_A^* = \sqrt{\frac{k^*}{\bar{I}_{C_Mx}^*}}, \quad 2\zeta_A^* \omega_A^* = \frac{c^*}{\bar{I}_{C_Mx}^*}. \quad (3.53)$$

The resulting forces are,

$$F_{C_My}^* = m_A^* (\ddot{v}_g + \ddot{v}), \quad (3.54)$$

$$F_{C_Mz}^* = m_A^* (\ddot{w}_g + \ddot{w}). \quad (3.55)$$

The control moment is,

$$M_{C_Mx}^* = \bar{I}_{C_Mx}^* (\ddot{u}_{TT}^* + \ddot{u}^*) / r_A^*. \quad (3.56)$$

The equations of a single storey space frame with a single TTMD attached are approximated by the selected mode number j

$$\begin{aligned}
 (1 + \mu_j^*) \ddot{q}_j + \omega_{Sj}^{*2} q_j + \frac{m_{Aj}^*}{m_j} \lambda_j^* \ddot{u}^* &= -\frac{1}{m_j^*} (m_S^* + m_{Aj}^*) \phi_{j1} \ddot{v}_g - \frac{1}{m_j^*} (m_S^* + m_{Aj}^*) \phi_{j2} \ddot{w}_g, \\
 \mu_j^* &= \frac{m_{Aj}^*}{m_j^*} v_{Tj}^{*2}, \quad v_{Tj}^{*2} = \phi_{j1}^2 + \phi_{j2}^2 + (\phi_{j3} r_{Aj}^* / r_S)^2, \quad \lambda_j^* = \frac{r_{Aj}^*}{r_S} \phi_{j3}.
 \end{aligned} \tag{3.57}$$

The approximated equation of motion of TTMD (Eq. (3.53)) renders

$$\ddot{u}_T^* + 2\zeta_{Aj}^* \omega_{Aj}^* \dot{u}^* + \omega_{Aj}^{*2} u^* = -\lambda_j^* \ddot{q}_j. \tag{3.58}$$

The right-hand side of the resulting system of modal equations decouples approximately only under the severe assumption of well-separated natural frequencies. With light modal damping of the main system added, the coupled equations of motion of main system with TTMD attached in matrix notation become,

$$\begin{bmatrix} 1 + \mu_j^* & \lambda_j^* m_{Aj}^* / m_j^* \\ \lambda_j^* & 1 \end{bmatrix} \begin{bmatrix} \ddot{q}_j \\ \ddot{u}^* \end{bmatrix} + \begin{bmatrix} 2\zeta_{Sj}^* \omega_{Sj}^* & 0 \\ 0 & 2\zeta_{Aj}^* \omega_{Aj}^* \end{bmatrix} \begin{bmatrix} \dot{q}_j \\ \dot{u}^* \end{bmatrix} + \begin{bmatrix} \omega_{Sj}^{*2} & 0 \\ 0 & \omega_{Aj}^{*2} \end{bmatrix} \begin{bmatrix} q_j \\ u^* \end{bmatrix} = - \begin{bmatrix} \bar{L}_{Tj}^* / m_j^* \\ \bar{0}^T \end{bmatrix} \ddot{x}_g, \tag{3.59}$$

where the generalized participation factors are

$$\bar{L}_{Tj}^* = \begin{bmatrix} L_{Tjy}^* & L_{Tjz}^* & 0 \end{bmatrix}, \quad L_{Tjy}^* = (m_S^* + m_{Aj}^*) \phi_{j1}, \quad L_{Tjz}^* = (m_S^* + m_{Aj}^*) \phi_{j2}.$$

The second of the coupled equations turns out to be homogenous.

3.6.2 TTLCGD attached to space frame (the vertical segment, \mathbf{A} ($\mathbf{y}_A, \mathbf{z}_A, \mathbf{0}$), $\beta = \pi/2$)

Inserting the linearized coupling forces \bar{P} , Eqs. (3.36), (3.37) and (3.44), the equation of a single storey space frame with a single TTLCGD attached becomes

$$\begin{aligned}
 (1 + \mu_j) \ddot{q}_j + \omega_{Sj}^2 q_j + \frac{m_{fj}}{m_j} \bar{\lambda}_j \ddot{u} &= -\frac{1}{m_j} \left[m_S \phi_{j1} + m_{fj} (\phi_{j1} - \bar{\kappa}_{T3} \phi_{j3} z_{Aj} / r_S) \right] \ddot{v}_g \\
 &\quad - \frac{1}{m_j} \left[m_S \phi_{j2} + m_{fj} (\phi_{j2} + \bar{\kappa}_{T3} \phi_{j3} y_{Aj} / r_S) \right] \ddot{w}_g \\
 \mu_j &= \frac{m_{fj}}{m_j} V_{Tj}^2, \quad V_{Tj}^2 = v_{Tj}^2 + 2\phi_{j3} \bar{\kappa}_{T3} (y_{Aj} \phi_{j2} - z_{Aj} \phi_{j1}) / r_S \rightarrow \max \left|_{A_j(y_{Aj} \quad z_{Aj} \quad 0)} \right., \\
 v_{Tj}^2 &= \phi_{j1}^2 + \phi_{j2}^2 + (\phi_{j3} r_{fj} / r_S)^2, \quad \lambda_j = \kappa_{T0} \phi_{j3} r_{fj} / r_S, \quad \bar{\lambda}_j = \lambda_j L_{eff} / L_1.
 \end{aligned} \tag{3.60}$$

Light structural modal damping of the main system is added and Eq. (3.14) is approximated by the selected mode

$$\ddot{u} + 2\zeta_{Aj} \omega_{Aj} \dot{u} + \omega_{Aj}^2 u = -\lambda_j \ddot{q}_j. \tag{3.61}$$

The linearized coupled system of modal equations of the main system with TTLCGD attached takes on the matrix form

$$\begin{bmatrix} 1 + \mu_j & \bar{\lambda}_j m_{ff} / m_j \\ \lambda_j & 1 \end{bmatrix} \begin{bmatrix} \ddot{q}_j \\ \ddot{u} \end{bmatrix} + \begin{bmatrix} 2\zeta_{Sj}\omega_{Sj} & 0 \\ 0 & 2\zeta_{Aj}\omega_{Aj} \end{bmatrix} \begin{bmatrix} \dot{q}_j \\ \dot{u} \end{bmatrix} + \begin{bmatrix} \omega_{Sj}^2 & 0 \\ 0 & \omega_{Aj}^2 \end{bmatrix} \begin{bmatrix} q_j \\ u \end{bmatrix} = - \begin{bmatrix} \bar{L}_{Tj}^T / m_j \\ \bar{0}^T \end{bmatrix} \ddot{x}_g, \quad (3.62)$$

the participation factors are formally still given by Eq. (2.92), however, before their substitution, the modal displacements of Eq. (2.84) have to be altered by the substitutions, $v_{A,j} \rightarrow \phi_{j1} - \bar{\kappa}_{T3} \phi_{j3} z_{Aj} / r_S$, $w_{A,j} \rightarrow \phi_{j2} + \bar{\kappa}_{T3} \phi_{j3} y_{Aj} / r_S$.

Ideally the TTLCGD should be placed in the floor with the largest modal displacement, because this will maximize the modal mass ratio and thus yield the best absorbing behaviour. The sign of $(y_{Aj}\phi_{j2} - z_{Aj}\phi_{j1})$ should be chosen design-compatible to maximize the modal ratio, render the best location of point A ($y_A, z_A, 0$).

3.6.3 Analogy between TTMD and TTLCGD ($\beta = \pi/2$) when attached to 3DOF-main system

To keep the forcing by the angular acceleration $\ddot{\theta}$, apparent on the right hand side of Eq. (3.14) and (3.53), we require $\ddot{u}_{TT} = r_f \ddot{\theta} = \dot{u}_{TT}^* = r_A^* \ddot{\theta}$. Consequently, the first result within the analogy is $r_{Aj}^* = r_{ff}$. Eqs. (3.58) and (3.61) on the right hand side have the same excitation, u^* turns out proportional to u ,

$$u^* = u / \kappa_{T0} \quad \text{since} \quad \lambda_j^* = \lambda_j / \kappa_{T0}. \quad (3.63)$$

Using this result and comparing the left hand side of the second equation in Eqs. (3.59) and (3.62), yield at once

$$\omega_{Aj}^* = \omega_{Aj}, \quad \zeta_{Aj}^* = \zeta_{Aj}. \quad (3.64)$$

In a second step, substituting these results into the first equation in Eqs. (3.59) and (3.62) renders by inspection

$$\begin{aligned} \frac{\mu_j \kappa_{T0}}{(1 + \mu_j) V_{Tj}^2} &= \frac{\mu_j^*}{\bar{\kappa}_{T0} (1 + \mu_j^*) v_{Tj}^{*2}}, \quad \frac{1}{1 + \mu_j} \omega_{Sj}^2 = \frac{1}{1 + \mu_j^*} \omega_{Sj}^{*2}, \\ \frac{1}{1 + \mu_j} 2\zeta_{Sj} \omega_{Sj} &= \frac{1}{1 + \mu_j^*} 2\zeta_{Sj}^* \omega_{Sj}^*, \end{aligned} \quad (3.65)$$

and thus the mass ratio of the equivalent TTMD becomes

$$\mu_j^* = \mu_j \frac{\kappa_{T0} \bar{\kappa}_{T0} (v_{Tj}^* / V_{Tj})^2}{1 + \mu_j [1 - \kappa_{T0} \bar{\kappa}_{T0} (v_{Tj}^* / V_{Tj})^2]} < \mu_j, \quad (3.66)$$

and further,

$$\omega_{Sj}^* = \frac{\omega_{Sj}}{\sqrt{1 + \mu_j [1 - \kappa_{T0} \bar{\kappa}_{T0} (v_{Tj}^* / V_{Tj})^2]}}, \quad \zeta_{Sj}^* = \frac{\zeta_{Sj}}{\sqrt{1 + \mu_j [1 - \kappa_{T0} \bar{\kappa}_{T0} (v_{Tj}^* / V_{Tj})^2]}}, \quad (3.67)$$

The TTLCGD-TMD transformation of optimal parameters is thus established

$$\delta_{jopt}^* = \frac{\omega_{Aj,opt}}{\omega_{Sj}} = \frac{\delta_{jopt}^*}{\sqrt{1 + \mu_j [1 - \kappa_{T0} \bar{\kappa}_{T0} (v_{Tj}^* / V_{Tj})^2]}}, \quad \zeta_{Aj}^* = \zeta_{Aj}. \quad (3.68)$$

3.7 Control of single-storey strongly plan-asymmetric space frame by a single TTLCGD ($\pi/4 \leq \beta < \pi/2$) when compared to an equivalent TTMD

3.7.1 TTMD attached to space frame, a point mass in y-axis

A TTMD is set on the single-storey asymmetric structure, y_1 is the position coordinate of an additional point mass m_1^* at A ($y_1, 0, 0$).

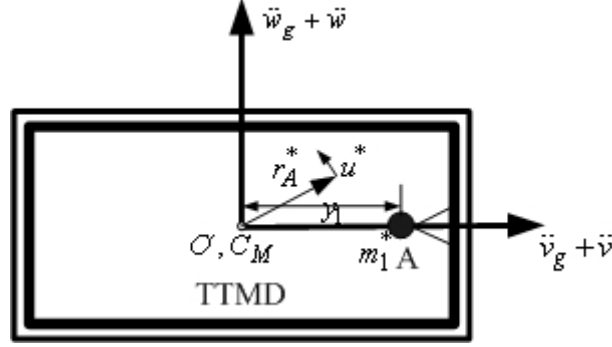


Fig. 3.6: Single-storey asymmetric structure with TTMD with an additional point mass m_1^* .

Conservation of angular momentum with respect to the accelerated point $O=C_M$.

$$\bar{I}_{C_M^x}^* (\ddot{u}_{TT}^* + \ddot{u}^*) / r_A^* = -k^* \frac{u^*}{r_A^*} - m_1^* \left[\ddot{w}_g + \ddot{w} + (\ddot{u}_{TT}^* + \ddot{u}^*) y_1 / r_A^* \right] y_1, \quad (3.69)$$

$I_{C_M^x}^* = \bar{I}_{C_M^x}^* + m_1^* y_1^2$ is the axial moment of inertia of the total mass $m_A^* + m_1^*$.

The resulting forces are, cf. Eqs. (3.54) and (3.55) for TTMD without additional mass,

$$F_{C_M^y}^* = m_A^* (\ddot{v}_g + \ddot{v}) + m_1^* \left[\ddot{v}_g + \ddot{v} - (\ddot{u}_{TT}^* + \ddot{u}^*)^2 y_1 / r_A^{*2} \right], \quad (3.70)$$

$$F_{C_M^z}^* = m_A^* (\ddot{w}_g + \ddot{w}) + m_1^* \left[\ddot{w}_g + \ddot{w} + (\ddot{u}_{TT}^* + \ddot{u}^*) y_1 / r_A^* \right]. \quad (3.71)$$

The control moment is, cf. Eq. (3.56) for TTMD without additional mass,

$$M_{C_M^x}^* = \left[I_{C_M^x}^* \ddot{u}_{TT}^* / r_A^* + m_1^* (\ddot{w}_g + \ddot{w}) y_1 \right] + I_{C_M^x}^* \ddot{u}^* / r_A^*. \quad (3.72)$$

The equation of motion for the TTMD, viscous damping is added to Eq. (3.69), becomes, cf. Eq. (3.53)

$$\ddot{u}_T^* + 2\zeta_{Aj}^* \omega_{Aj}^* \dot{u}_T^* + \omega_{Aj}^{*2} u^* = -\ddot{u}_{TT}^* - \frac{m_1^* r_A^* y_1}{I_{C_M^x}^*} (\ddot{w}_g + \ddot{w}), \quad \omega_A^* = \sqrt{\frac{k^*}{I_{C_M^x}^*}}, \quad 2\zeta_A^* \omega_A^* = \frac{c^*}{I_{C_M^x}^*}. \quad (3.73)$$

Assuming $y_1 = r_A^*$, substituted in Eqs. (3.70)-(3.73). The equation of a single storey space frame with a single TTMD when approximated by the selected mode is

$$\begin{aligned} (1 + \mu_j^*) \ddot{q}_j + \omega_{Sj}^{*2} q_j + \frac{m_{Aj}^* + m_{1j}^*}{m_j^*} \lambda_j^* \dot{u}^* = & -\frac{1}{m_j^*} (m_S^* + m_{Aj}^* + m_{1j}^*) \phi_{j1} \ddot{v}_g \\ & - \frac{1}{m_j^*} \left[m_S^* \phi_{j2} + (m_{Aj}^* + m_{1j}^*) \left(\phi_{j2} + \eta \frac{r_{Aj}^*}{r_S} \phi_{j3} \right) \right] \ddot{w}_g, \end{aligned}$$

$$\mu_j^* = \frac{m_{Aj}^* + m_{1j}^*}{m_j^*} V_{Tj}^{*2}, \quad \eta = \frac{m_{1j}^*}{m_{Aj}^* + m_{1j}^*}, \quad V_{Tj}^{*2} = v_{Tj}^{*2} + 2\eta \frac{r_{Aj}^*}{r_s} \phi_{j2} \phi_{j3}, \quad \lambda_j^* = \eta \phi_{j2} + \frac{r_{Aj}^*}{r_s} \phi_{j3}. \quad (3.74)$$

The approximated equation of motion of TTMD in mode j (Eq. (3.58)) renders

$$\ddot{u}_T^* + 2\zeta_{Aj}^* \omega_{Aj}^* \dot{u}_T^* + \omega_{Aj}^{*2} u^* = -\lambda_j^* \ddot{q}_j - \eta \bar{\mathbf{r}}_{S,z}^T \ddot{\mathbf{x}}_g, \quad \bar{\mathbf{r}}_{S,z}^T = [0 \quad 1 \quad 0]. \quad (3.75)$$

With light modal damping of the main system added, the coupled equations of motion of main system with TTMD attached in matrix notation become, cf. (3.59), $m_{1j}^* = 0$,

$$\begin{bmatrix} 1 + \mu_j^* & \frac{m_{Aj}^* + m_{1j}^*}{m_j^*} \lambda_j^* \\ \lambda_j^* & 1 \end{bmatrix} \begin{bmatrix} \ddot{q}_j \\ \ddot{u}^* \end{bmatrix} + \begin{bmatrix} 2\zeta_{Sj}^* \omega_{Sj}^* & 0 \\ 0 & 2\zeta_{Aj}^* \omega_{Aj}^* \end{bmatrix} \begin{bmatrix} \dot{q}_j \\ \dot{u}^* \end{bmatrix} + \begin{bmatrix} \omega_{Sj}^{*2} & 0 \\ 0 & \omega_{Aj}^{*2} \end{bmatrix} \begin{bmatrix} q_j \\ u^* \end{bmatrix} = - \begin{bmatrix} \bar{L}_{Tj}^{*T} / m_j^* \\ \eta \bar{\mathbf{r}}_{S,z}^T \end{bmatrix} \ddot{\mathbf{x}}_g, \quad (3.76)$$

where the generalized participation factors are

$$L_{Tjy}^* = (m_S^* + m_{Aj}^* + m_{1j}^*) \phi_{j1}, \quad L_{Tjz}^* = m_S^* \phi_{j2} + (m_{Aj}^* + m_{1j}^*) \left(\phi_{j2} + \eta \frac{r_{Aj}^*}{r_s} \phi_{j3} \right),$$

here, \bar{L}_{Tj}^{*T} is given by Eq. (3.59).

3.7.2 TTLCGD attached to space frame (the inclined segment parallel to z -axis, $\mathbf{A} (y_A, 0, 0)$, $\pi/4 \leq \beta < \pi/2$)

Inserting the linearized coupling forces \bar{P} , Eqs.(3.45), (3.46) and (3.47), the equation of a single storey space frame with a single TTLCGD renders

$$(1 + \mu_j) \ddot{q}_j + \omega_{Sj}^2 q_j + \frac{m_{ff}}{m_j} \bar{\lambda}_j \ddot{u} = -\frac{1}{m_j} (m_S + m_{ff}) \phi_{j1} \ddot{v}_g - \frac{1}{m_j} \left[m_S \phi_{j2} + m_{ff} \left(\phi_{j2} + \bar{\kappa}_{T3} \phi_{j3} y_{Aj} / r_s \right) \right] \ddot{w}_g$$

$$\mu_j = \frac{m_{ff}}{m_j} V_{Tj}^2, \quad \lambda_j = \kappa_T \phi_{j2} + \phi_{j3} \kappa_{Tz} r_{ff} / r_s, \quad \bar{\lambda}_j = \lambda_j L_{eff} / L_1. \quad (3.77)$$

here, V_{Tj}^2 , v_{Tj}^2 are given by Eq. (3.60) with $z_{Aj} = 0$.

Light structural modal damping of the main system is added and Eq. (3.19) are approximated by the selected mode

$$\ddot{u} + 2\zeta_{Aj} \omega_{Aj} \dot{u} + \omega_{Aj}^2 u = -\lambda_j \ddot{q}_j - \kappa_T \bar{\mathbf{r}}_{S,z}^T \ddot{\mathbf{x}}_g. \quad (3.78)$$

In matrix form the linearized coupled system of equations of the main system with TTLCD attached becomes

$$\begin{bmatrix} 1 + \mu_j & \bar{\lambda}_j m_{ff} / m_j \\ \lambda_j & 1 \end{bmatrix} \begin{bmatrix} \ddot{q}_j \\ \ddot{u} \end{bmatrix} + \begin{bmatrix} 2\zeta_{Sj} \omega_{Sj} & 0 \\ 0 & 2\zeta_{Aj} \omega_{Aj} \end{bmatrix} \begin{bmatrix} \dot{q}_j \\ \dot{u} \end{bmatrix} + \begin{bmatrix} \omega_{Sj}^2 & 0 \\ 0 & \omega_{Aj}^2 \end{bmatrix} \begin{bmatrix} q_j \\ u \end{bmatrix} = - \begin{bmatrix} \bar{L}_{Tj}^T / m_j \\ \kappa_T \bar{\mathbf{r}}_{S,z}^T \end{bmatrix} \ddot{\mathbf{x}}_g, \quad (3.79)$$

here, \bar{L}_{Tj}^T is given by Eq. (3.62) with $z_{Aj} = 0$.

3.7.3 Analogy between TTMD and TTLCGD ($\pi/4 \leq \beta < \pi/2$) when attached to 3DOF-main system

If Eqs. (3.75) and (3.78) on the right hand side have the same excitation, u_T^* turns out proportional to u ,

$$u^* = \lambda_j^* u / \lambda_j. \quad (3.80)$$

Using this result and comparing the left hand side of the second equation in Eqs. (3.76) and (3.79), yield at once

$$\omega_{Aj}^* = \omega_{Aj}, \quad \zeta_{Aj}^* = \zeta_{Aj}, \quad m_{1j}^* = \frac{\kappa_T m_{Aj}^*}{\kappa_{Tz} r_{fj}^* / r_{Aj}^* - \kappa_T}. \quad (3.81)$$

In a second step, substituting these results into the first equation in Eqs. (3.76) and (3.79) renders by inspection

$$\frac{\mu_j \lambda_j}{(1 + \mu_j) V_{Tj}^2} = \frac{\mu_j^* \lambda_j^{*2}}{(1 + \mu_j^*) V_{Tj}^{*2} \bar{\lambda}_j}, \quad \frac{1}{1 + \mu_j} \omega_{Sj}^2 = \frac{1}{1 + \mu_j^*} \omega_{Sj}^{*2},$$

$$\frac{1}{1 + \mu_j} 2\zeta_{Sj} \omega_{Sj} = \frac{1}{1 + \mu_j^*} 2\zeta_{Sj}^* \omega_{Sj}^*,$$

and thus the mass ratio of the equivalent TTMD becomes

$$\mu_j^* = \mu_j \frac{\lambda_j \bar{\lambda}_j V_{Tj}^{*2} / \lambda_j^{*2} V_{Tj}^2}{1 + \mu_j (1 - \lambda_j \bar{\lambda}_j V_{Tj}^{*2} / \lambda_j^{*2} V_{Tj}^2)} < \mu_j, \quad (3.82)$$

and further,

$$\omega_{Sj}^* = \frac{\omega_{Sj}}{\sqrt{1 + \mu_j (1 - \lambda_j \bar{\lambda}_j V_{Tj}^{*2} / \lambda_j^{*2} V_{Tj}^2)}} < \omega_{Sj}, \quad (3.83)$$

$$\zeta_{Sj}^* = \frac{\zeta_{Sj}}{\sqrt{1 + \mu_j (1 - \lambda_j \bar{\lambda}_j V_{Tj}^{*2} / \lambda_j^{*2} V_{Tj}^2)}} < \zeta_{Sj}, \quad (3.84)$$

The TTLCGD-TMD transformation of optimal parameters is established

$$\delta_{jopt} = \frac{\omega_{Aj,opt}}{\omega_{Sj}} = \frac{\delta_{jopt}^*}{\sqrt{1 + \mu_j (1 - \lambda_j \bar{\lambda}_j V_{Tj}^{*2} / \lambda_j^{*2} V_{Tj}^2)}} < \delta_{jopt}^*, \quad \zeta_{Aj}^* = \zeta_{Aj}. \quad (3.85)$$

For TTLCGD attached to space frame, the inclined segment parallel to the y -direction, A (0, z_A , 0), $V_{Tj}^2 = v_{Tj}^2 - 2\phi_{j1}\phi_{j3}\bar{\kappa}_{T3z_{Aj}}/r_S$ is to be substituted with $y_{Aj} = 0$ above.

3.8 Numerical example

The single-storey stiffness-asymmetric structure is considered. The size of the rectangular floor in Fig. 3.1 is unchanged and given by 4m×8m, its mass is $m_S=16 \times 10^3$ kg. The common anisotropic stiffness of column in each corner in y - and z -directions are calculated by Eq. (2.10) $k_y=340.20$ kN/m and $k_z=125.21$ kN/m. The anisotropic stiffness of the extra column in y - and z -directions are $k'_y=3402$ kN/m and $k'_z=1252.1$ kN/m, the eccentricity of the column with respect to $C_M=O$ is given by $e_y=e_z=1$ m. The length of each column is 4m, proper static dimensioning of the elastic columns is also performed. The mass moment of inertia of the floor about the vertical x -axis is $I_x=106.67 \times 10^3$ kg·m², $r_S = 2.58$ m.

3.8.1 Static dimensioning and a static safety criterion of the columns

The buckling length of the cc-columns is $4m$. The critical load of a steel profile HEB-120 with respect to the weak axis of buckling becomes $F_c = -411.5kN$. If the live load of square meter is assumed to be $q_k = 4kN/m^2$, the live load of floor to be considered in the static analysis is $Q_k = 128kN$. The dead weight of the floor is $m_s g = 156.96kN$. The combined load of the floor is $N_{sd} = -403.896kN$. The combined load, without TLCGD, in the column is $F = \frac{N_{sd}}{4} = -100.974kN$. Thus $\frac{F}{F_c} = \frac{-100.974}{-411.5} = 0.245 < 0.33$, the geometric

flexural stiffness correction can be applied, $k_G = \frac{6F}{5l} = \frac{6}{5} \times \frac{-100.974}{4} = -30.3kN/m$.

The mass of HEB-120 per meter is $26.7 kg/m$, the effective mass of a column is calculated from Eq. (2.8) $\bar{m}_1 = 39.7kg$ and the mass of extra column is decuple of \bar{m}_1 . Thus, the total mass of columns is $555.7kg$. It is very smaller than the floor mass and can be neglected. In the following chapters the mass of column is also neglected.

The corrected stiffness of column in y direction becomes:

$$\bar{k}_y = k_y + k_G = 340.2 - 30.3 = 309.9kN/m.$$

The corrected stiffness of column in z direction becomes:

$$\bar{k}_z = k_z + k_G = 125.21 - 30.3 = 94.91kN/m.$$

3.8.2 Natural modes of the main structure

The natural computed frequencies by means of Matlab 7.0⁵ are derived as follow 1.40, 1.84 and 2.89 Hz, prestress of the column considered and extra column comes no weight of the floors. The orthonormalized modal matrix of the undamped main system is the output of Matlab.

$$\underline{\phi} = 10^{-2} \begin{bmatrix} 0.18677 & 0.27878 & -0.71582 \\ -0.59811 & 0.51506 & 0.04453 \\ 0.48206 & 0.53103 & 0.33259 \end{bmatrix}.$$

Correction of this output of orthonormalized eigenvectors might become necessary with respect to orthogonality, see section 2.9.2. Test calculations render sufficient accuracy,

$$\delta_{11} = 1, \quad \delta_{22} = 1, \quad \delta_{33} = 1, \quad \delta_{12} = 5.55 \times 10^{-16}, \quad \delta_{13} = \delta_{31} = 2.22 \times 10^{-16}, \quad \delta_{32} = 0, \\ \delta_{21} = 4.44 \times 10^{-16}, \quad \delta_{23} = -5.55 \times 10^{-17}.$$

The three mode shapes are amplified and plotted in Figs. 3.7-3.9. The motion of the structure in each mode consists of coupled translation and torsion.

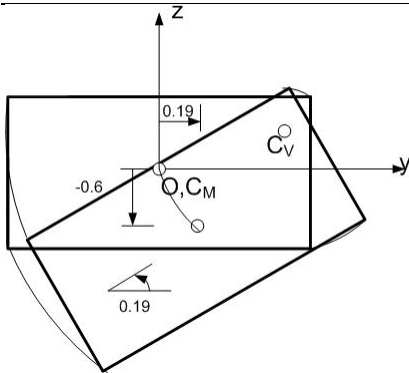


Fig. 3.7: Basic mode $f_1 = 1.40\text{Hz}$.

C_V within floor-plan

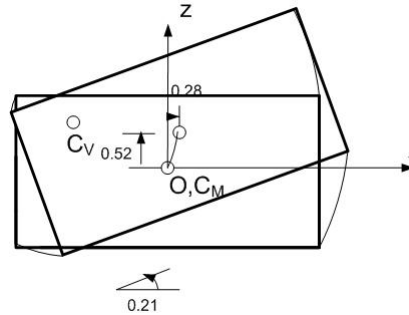


Fig. 3.8: Second mode $f_2 = 1.84\text{Hz}$.

C_V within floor-plan

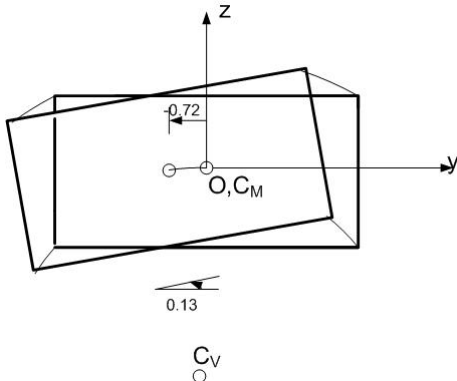


Fig. 3.9: Third mode $f_3 = 2.89\text{Hz}$, C_V outside floor-plan.

3.8.3 Position of the modal centers of velocity C_V

The coordinates of the centers of velocity C_V for each mode is defined by Eq. (2.18), two of the three modal centers of velocity lie within the floor plan.

$$\vec{r}_{C_{V1}} = \begin{bmatrix} 3.2 \\ 1 \end{bmatrix} m, \quad \vec{r}_{C_{V2}} = \begin{bmatrix} -2.5 \\ 1.36 \end{bmatrix} m, \quad \vec{r}_{C_{V3}} = \begin{bmatrix} -0.35 \\ -5.56 \end{bmatrix} m.$$

(i) Selection of the absorbers and positioning

The building is equipped with two TTLCGDs to suppress the first two modes (C_{V1} and C_{V2} lie in the floor, planstrong asymmetry) and one plane TLCGD parallel to y -direction for third mode (C_{V3} is outside floor plan), as shown in Fig. 3.10.

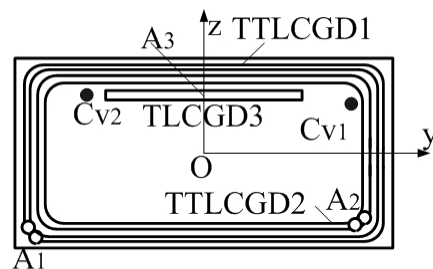


Fig. 3.10: Installation of absorbers, • indicates the centers of velocity C_{Vj} .

3.8.4 TTLCGD and TLCGD design, Den Hartog' optimization

The fluid mass $m_{f1} = 500kg$, $m_{f2} = 500kg$ and $m_{f3} = 200kg$ of water is chosen. Dimensions of three absorbers tuned first by means of the mechanical damper analogies applying Den Hartog's formulas, Eqs. (3.66)- (3.68) for TTLCGD and Eqs. (2.102)-(2.104) for TLCGD are summarized in Table 3.1.

	TTLCGD1	TTLCGD2	TLCGD3
Horizontal length of the liquid column B [m]	24.00	24.00	2.50
Length of the upright liquid column H [m]	1.40	0.90	0.80
Cross-sectional area of the pipe [m^2] $A_H=A_B$	0.0187	0.0194	0.0410
Effective length $L_{eff} = L_1 = 2H + B$ [m], Eq. (2.34a)	26.80	25.80	4.10
Angle of the inclined pipe section β [rad]	$\pi/2$	$\pi/2$	$\pi/4$
Equivalent mathematical pendulum length L_0 [m] Eq. (2.37)	0.13	0.08	0.03
Geometry factor $\kappa = \bar{\kappa}$ or $\kappa_{T0} = \bar{\kappa}_{T0}$, Eqs. (2.34a), (2.44),(3.14a),(3.44)	0.67	0.70	0.89
Equilibrium pressure head h_0 [m], $n=1.2$, Eq. (2.34a)	220.00	208.00	85.63
Gas volume $V_0 = A_H H_a$ [m^3], Eq. (2.38)	0.041000	0.025000	0.053000
The mass ratio of the TLCGD-main system μ , Eqs. (2.97), (3.60)	4.74%	4.75%	1.94%
The mass ratio of the equivalent TMD-main system μ^* , Eqs. (2.102), (3.66)	1.81%	2.09%	1.48%
Natural frequency $f_{A,opt}$ [Hz] Eq. (2.104), (2.112)	1.36	1.78	2.84
Optimal linear damping %, Eq. (2.113)	8.17	8.76	7.40

Table 3.1: Layout of the modally tuned absorbers, gas volume and gas equilibrium pressure assigned. Note the relatively high gas pressure in TTLCGD.

Due to its long effective horizontal length, the equilibrium gas-pressure in TTLCGD becomes rather high, as shown in Table 3.1. Fig.3.11 illustrates the scaled scheme of TTLCGD1. The dynamic magnification factor (DMF) calculated with Matlab 7.0⁵, linearized damping of the absorbers considered, is illustrated in Figure 3. 12.

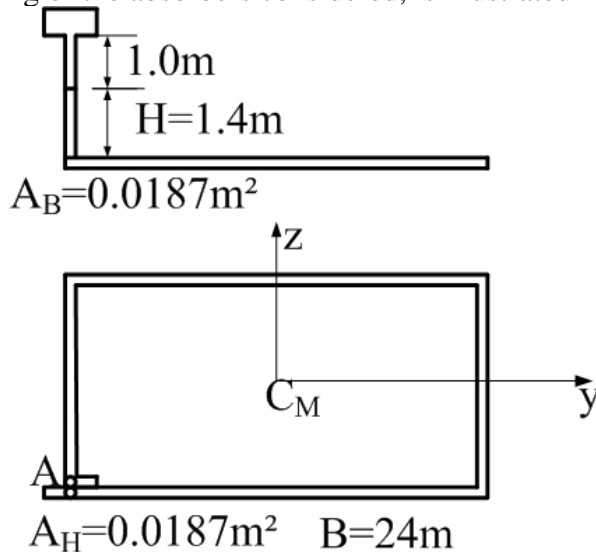


Fig.3.11: Scaled sketch of TTLCGD1.

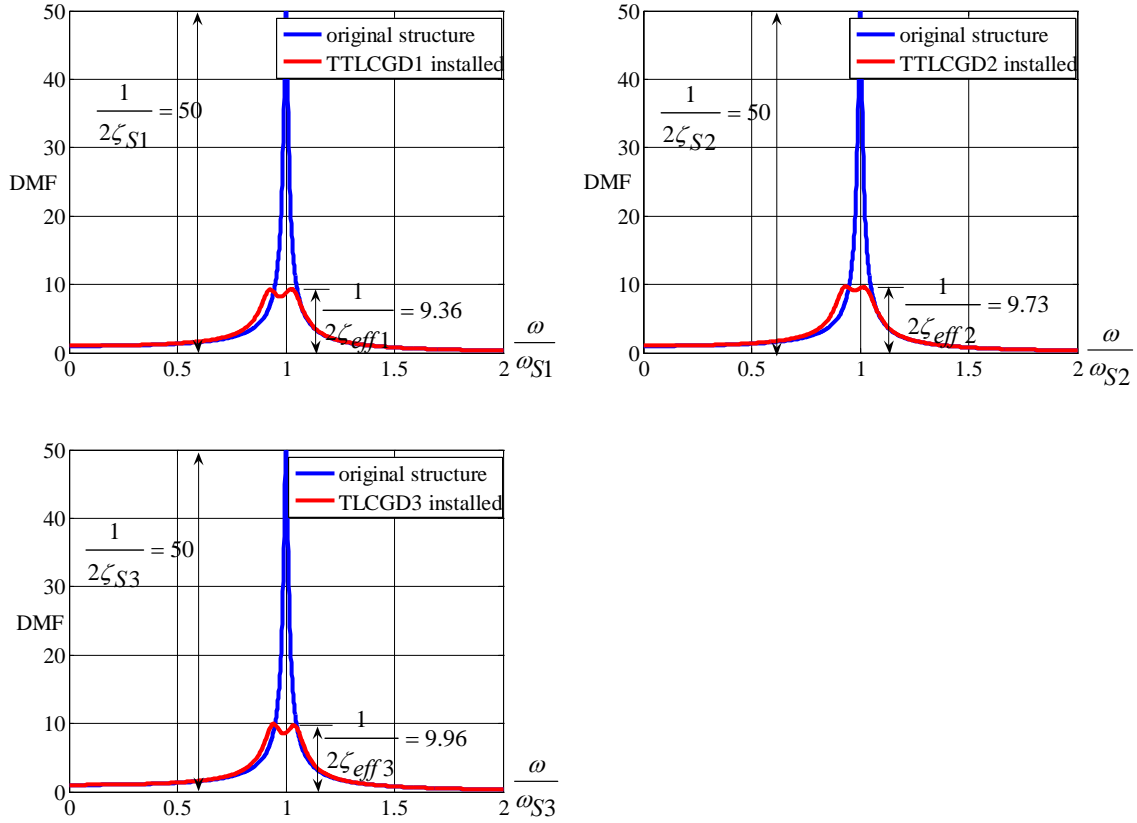


Fig. 3.12: Modal frequency response curves without and with linearized absorbers attached, Den Hartog's optimal parameters.

The effective modal damping coefficients of the system are increased from 1% to $\zeta_{eff1} = 5.34\%$, $\zeta_{eff2} = 5.14\%$, $\zeta_{eff3} = 5.02\%$. From Table 3.2a-c it follows that all the maximum fluid displacements resulting by varying the angles of attack, are within the acceptable limits, $u_0 < H_a/3$ (of linearized gas compression) and $u_0 < H/2$. The maximum fluid velocities of three absorbers are calculated by Eq. (2.35) 3.86, 2.57 and 3.35m/s and are within the acceptable speed limit.

Forcing direction	structure			TTLCGD1	
	C_M	v[mm]	w[mm]	u_0 [mm]	
$\alpha = 0$	C_M	9	-30	24	138
$\alpha = \pi/6$	C_M	7	-22	18	101
$\alpha = \pi/4$	C_M	15	-47	38	215
$\alpha = \pi/3$	C_M	21	-69	55	313
$\alpha = \pi/2$	C_M	30	-97	78	442
$\alpha = 2\pi/3$	C_M	31	-99	80	452
$\alpha = 3\pi/4$	C_M	28	-90	73	410
$\alpha = 5\pi/6$	C_M	23	-75	60	341

Table 3.2a: Maximum displacements in the first mode from time-harmonic excitation in α -directions, $a_0=0.1g$, $r_S = 2.58m$.

Single-storey Strongly Plan-asymmetric Space Frame with TTLCGDs and TLCGDs

Forcing direction	structure			TTLCGD2	
	v[mm]	w[mm]	$u_T = r_S \theta$ [mm]	u_0 [mm]	
$\alpha = 0$	C _M	11	20	20	110
$\alpha = \pi/6$	C _M	19	35	36	196
$\alpha = \pi/4$	C _M	21	39	41	221
$\alpha = \pi/3$	C _M	22	41	42	230
$\alpha = \pi/2$	C _M	20	36	37	203
$\alpha = 2\pi/3$	C _M	12	21	22	121
$\alpha = 3\pi/4$	C _M	6	12	12	66
$\alpha = 5\pi/6$	C _M	1	1	1	6

Table 3.2b: Maximum displacements in the second mode from time-harmonic excitation in α -directions, $a_0=0.1g$, $r_S = 2.58m$.

Forcing direction	structure			TLCGD3	
	v[mm]	w[mm]	$u_T = r_S \theta$ [mm]	u_0 [mm]	
$\alpha = 0$	C _M	-26	2	12	188
	A	-35	2		
$\alpha = \pi/6$	C _M	-21	1	10	157
	A	-29	1		
$\alpha = \pi/4$	C _M	-17	1	8	125
	A	-23	1		
$\alpha = \pi/3$	C _M	-11	1	5	85
	A	-16	1		
$\alpha = \pi/2$	C _M	-2	0	1	11
	A	-2	0		
$\alpha = 2\pi/3$	C _M	-14	1	7	103
	A	-19	1		
$\alpha = 3\pi/4$	C _M	-19	1	9	141
	A	-26	1		
$\alpha = 5\pi/6$	C _M	-23	1	11	168
	A	-31	1		

Table 3.2c: Maximum displacements in the third mode from time-harmonic excitation in α -directions, $a_0=0.1g$, $r_S = 2.58m$.

3.8.5 Optimization of the TTLCGD-, TLCGD-main structure system in the state space domain

Again the numerical optimization was performed with the very robust *fminsearch* procedure available in Matlab Optimization Toolbox, see explanations in Section 2.9.7. Calling *fminsearch* with the initial DenHartog parameter $x_0 = [8.52, 11.16, 17.82; 8.17\%, 8.76\%, 7.40\%]$ given, immediately renders the fine tuned optimal natural frequencies and damping ratios $f_{A1} = 1.35Hz$, $f_{A2} = 1.73Hz$, $f_{A3} = 2.76Hz$, $\zeta_{A1} = 5.65\%$, $\zeta_{A2} = 6.61\%$, $\zeta_{A3} = 5.89\%$, i.e. frequencies are slightly lowered and the damping coefficients of the fluid flow turn out commonly “dramatically” lowered. Frequency fine tuning is simply achieved by adjusting the equilibrium gas pressure head h_0 in absorbers, 203.41, 184.39 and 78.38m. Figs. 3.13-3.20

show the frequency response of the weighed sum $\sum_{i=1}^6 s_i |z_{S_i}(v)|$ of the building states for the original and the optimized system under various angles of attack, in the logarithmic decibel

scale $x[dB] = 20 \log x$ within the relevant frequency window $0 \leq f \leq 3Hz$. The resonance curves with fine-tuning optimal parameters have broader peaks rendering a more robust control.

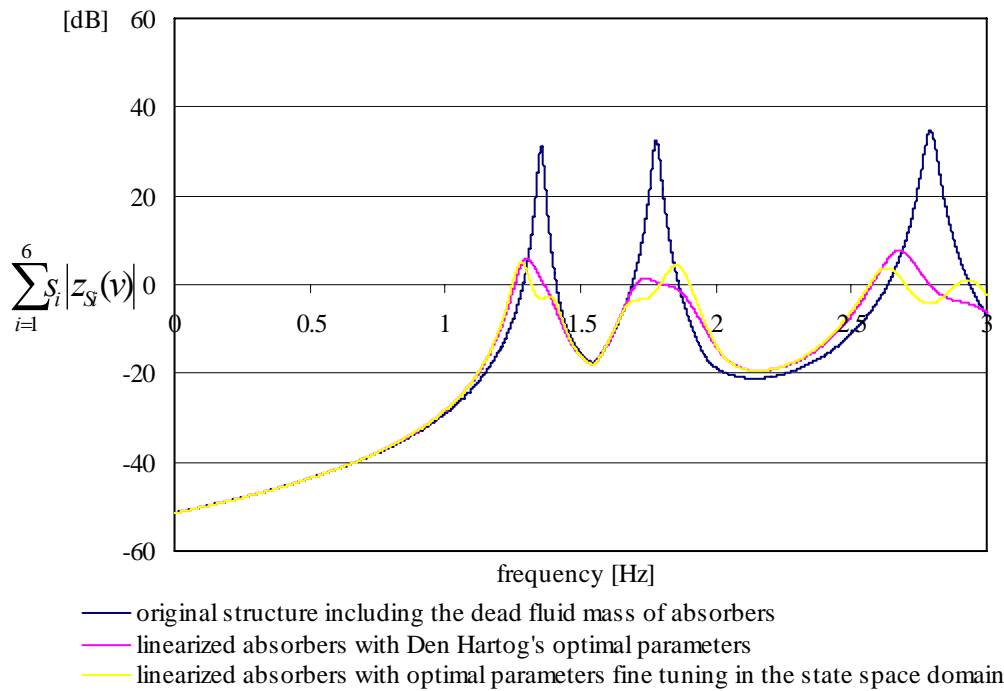


Fig. 3.13: Weighed sum of amplitude response functions for the 3-DOF linearized, single-storey, strongly asymmetric space frame, with three linearized absorbers attached and without the absorbers (angle of attack of the time-harmonic base acceleration $\alpha = 0$), maximum gain 29.56 dB.

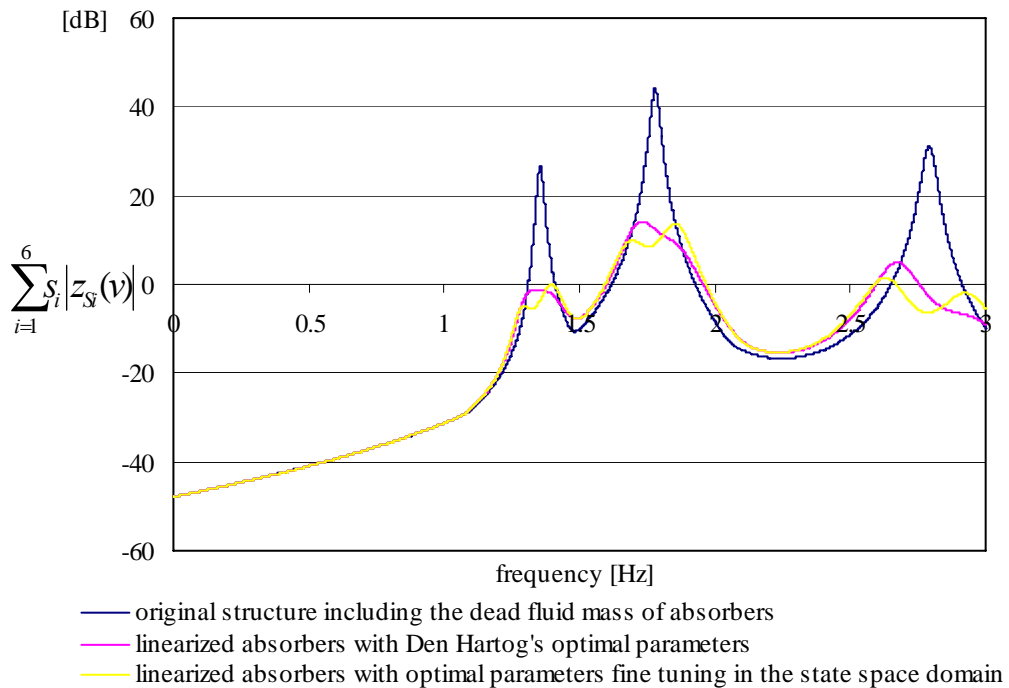


Fig. 3.14: Weighed sum of amplitude response functions for the 3-DOF linearized, single-storey, strongly asymmetric space frame, with three linearized absorbers attached and without the absorbers (angle of attack of the time-harmonic base acceleration $\alpha = \pi/6$), maximum gain 30.35dB.

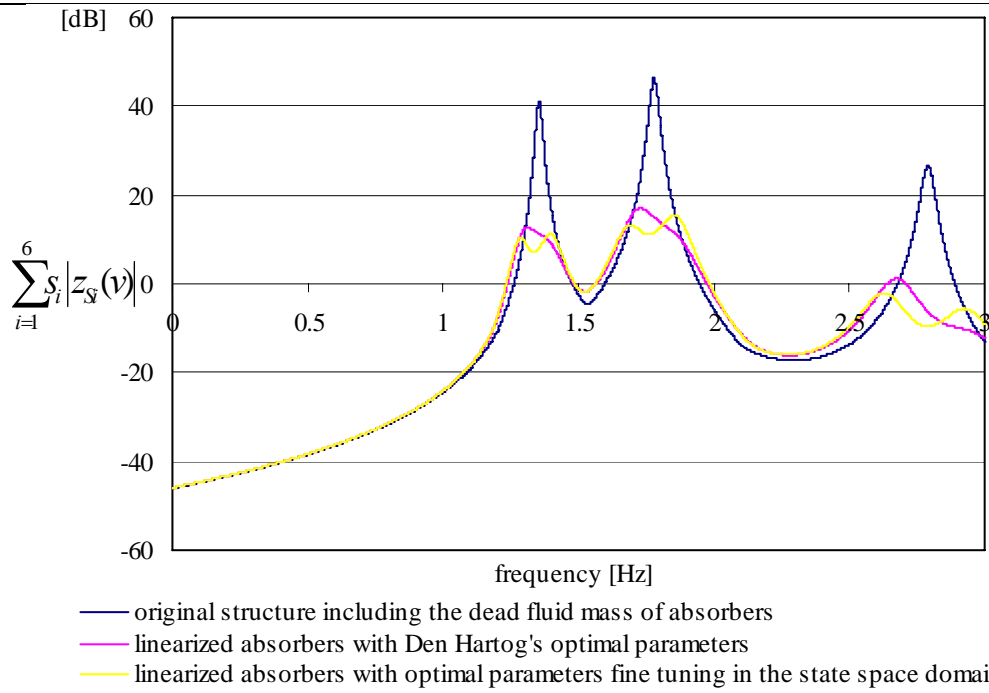


Fig. 3.15: Weighed sum of amplitude response functions for the 3-DOF linearized, single-storey, strongly asymmetric space frame, with three linearized absorbers attached and without the absorbers (angle of attack of the time-harmonic base acceleration $\alpha = \pi/4$), maximum gain 30.83 dB.

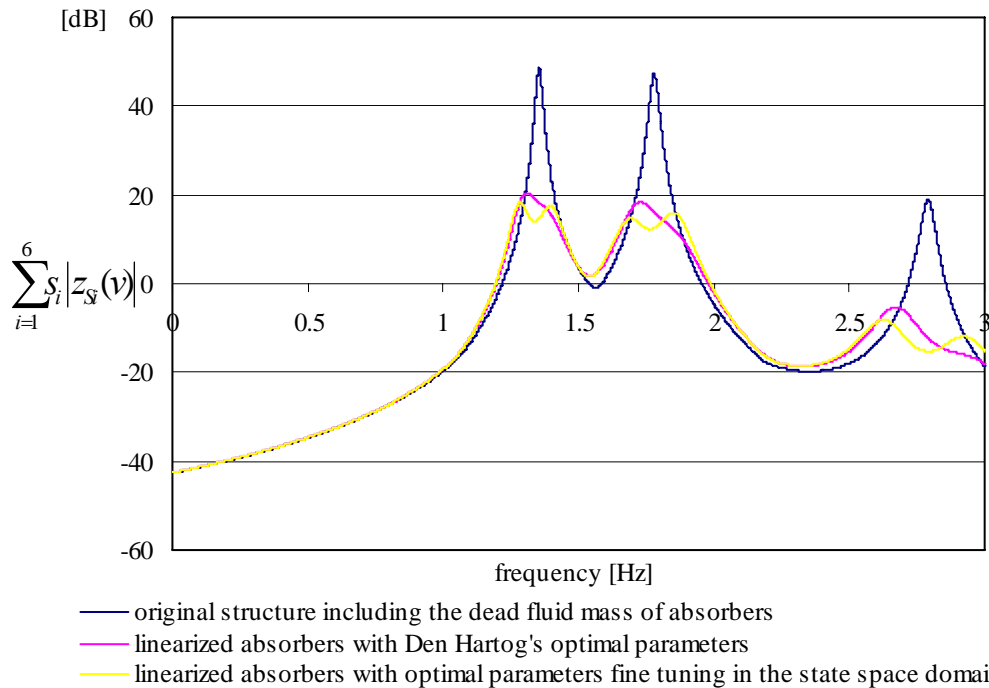


Fig. 3.16: Weighed sum of amplitude response functions for the 3-DOF linearized, single-storey, strongly asymmetric space frame, with three linearized absorbers attached and without the absorbers (angle of attack of the time-harmonic base acceleration $\alpha = \pi/3$), maximum gain 30.33 dB.

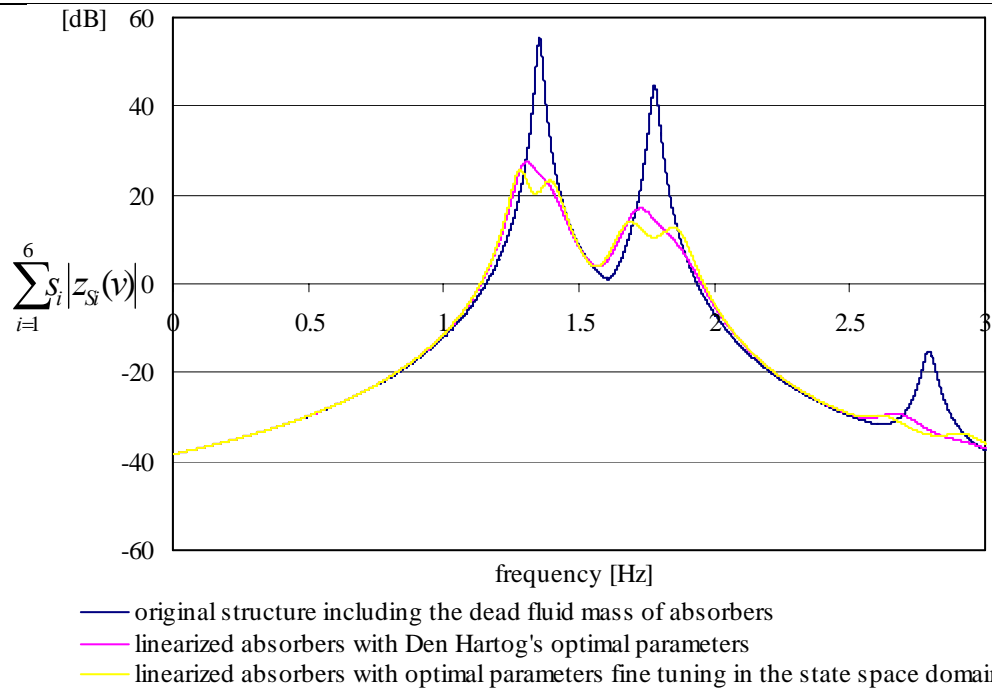


Fig. 3.17: Weighed sum of amplitude response functions for the 3-DOF linearized, single-storey, strongly asymmetric space frame, with three linearized absorbers attached and without the absorbers (angle of attack of the time-harmonic base acceleration $\alpha = \pi/2$), maximum gain 29.70 dB.

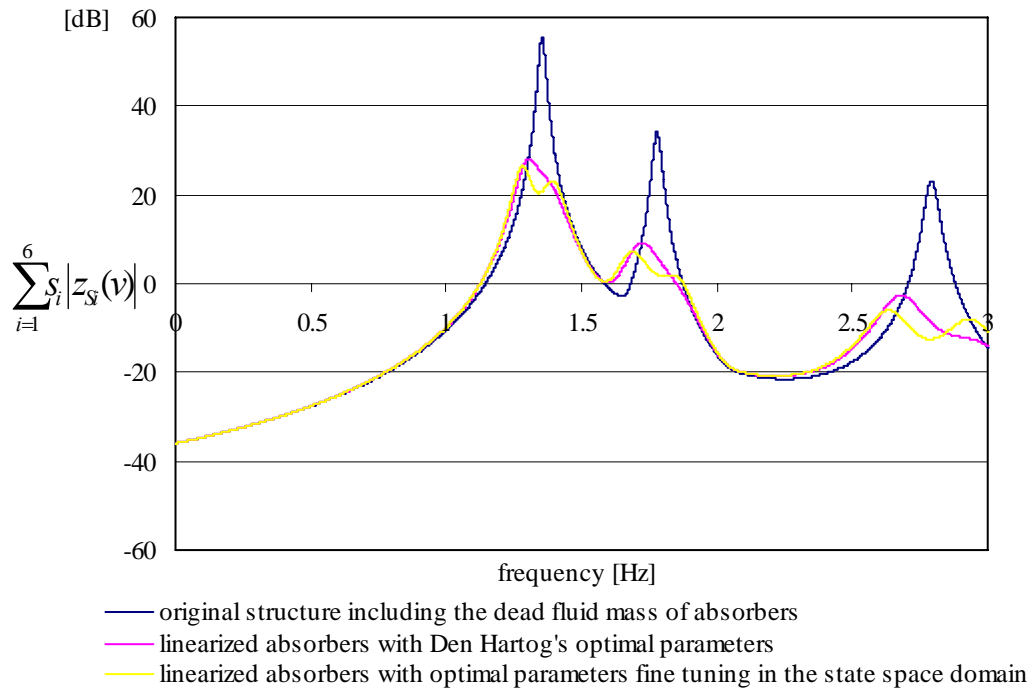


Fig. 3.18: Weighed sum of amplitude response functions for the 3-DOF linearized, single-storey, strongly asymmetric space frame, with three linearized absorbers attached and without the absorbers (angle of attack of the time-harmonic base acceleration $\alpha = 2\pi/3$), maximum gain 29.21 dB.

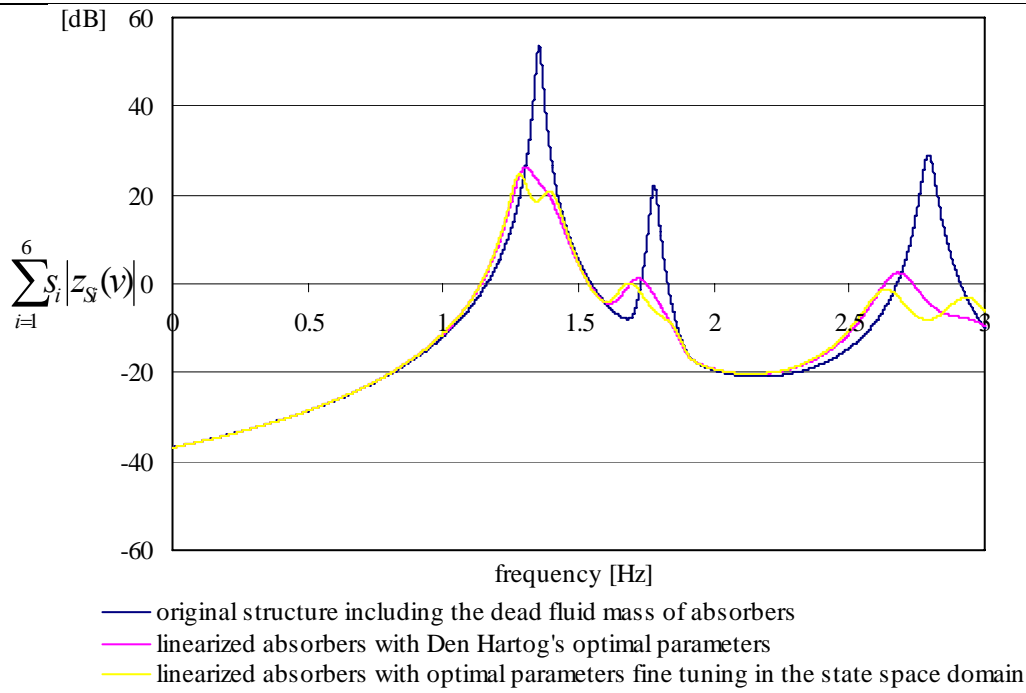


Fig. 3.19: Weighed sum of amplitude response functions for the 3-DOF linearized, single-storey, strongly asymmetric space frame, with three linearized absorbers attached and without the absorbers (angle of attack of the time-harmonic base acceleration $\alpha = 3\pi/4$), maximum gain 28.93 dB.

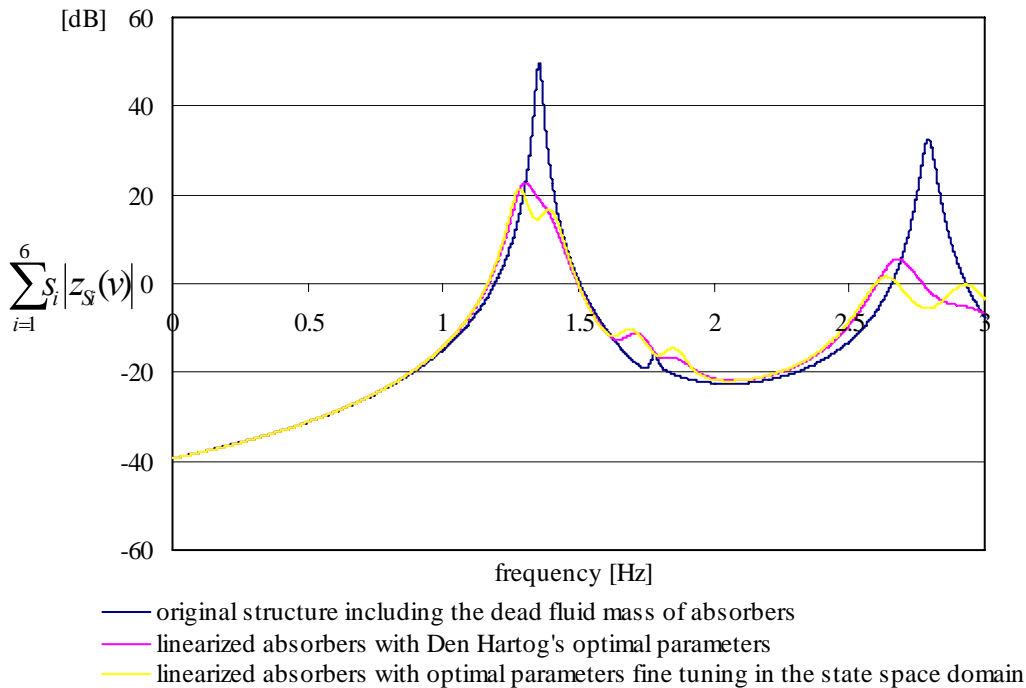


Fig. 3.20: Weighed sum of amplitude response functions for the 3-DOF linearized, single-storey, strongly asymmetric space frame, with three linearized absorbers attached and without the absorbers (angle of attack of the time-harmonic base acceleration $\alpha = 5\pi/6$), maximum gain 28.55 dB.

Figures 3.21-3.28 show the comparison of the response of three absorbers, alternatively with Den Hartog's optimal parameter and after fine-tuning in state space, under various angles of attack. The maximum fluid displacement amplitudes of three absorbers are well within the acceptable limits. The maximum fluid velocities of three absorbers are calculated

by Eq. (2.35) 4.33, 2.93 and 3.99m/s and are also within the acceptable speed limit.

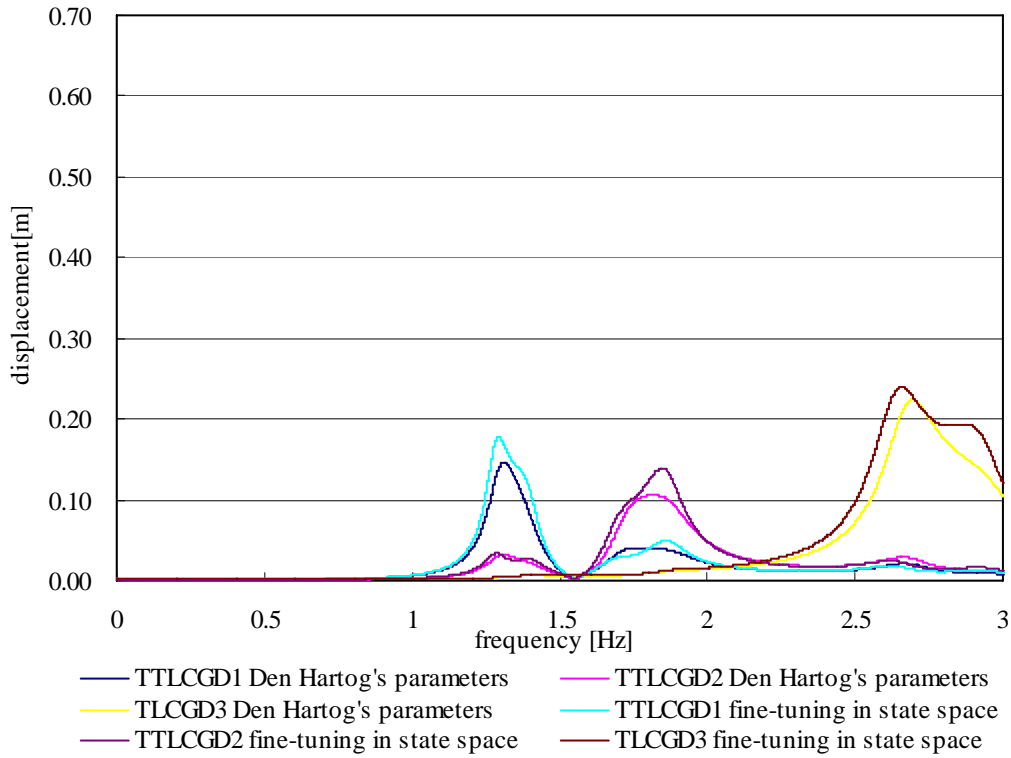


Fig. 3.21: Amplitude response curves of fluid displacement $|u|$ of three linearized absorbers attached to the 3-DOF space frame. Absorbers either with Den Hartog's optimal parameters or those resulting from fine-tuning in state space ($\alpha = 0$).

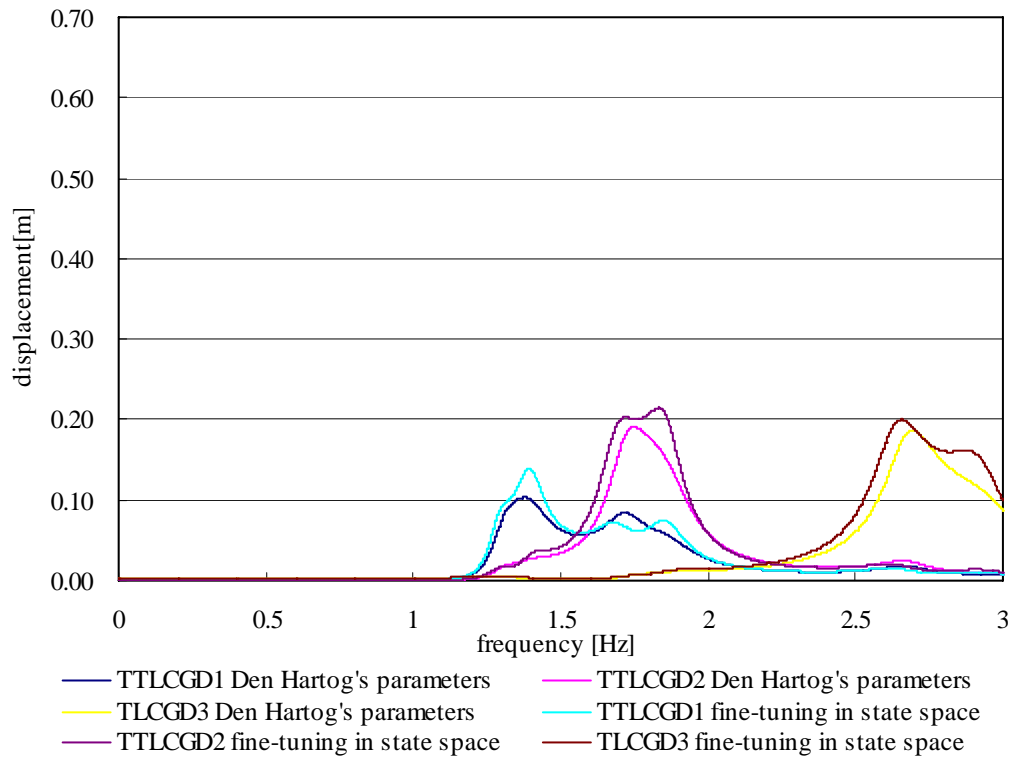


Fig. 3.22: Amplitude response curves of fluid displacement $|u|$ of three linearized absorbers attached to the 3-DOF space frame. Absorbers either with Den Hartog's optimal parameters or those resulting from fine-tuning in state space ($\alpha = \pi/6$).

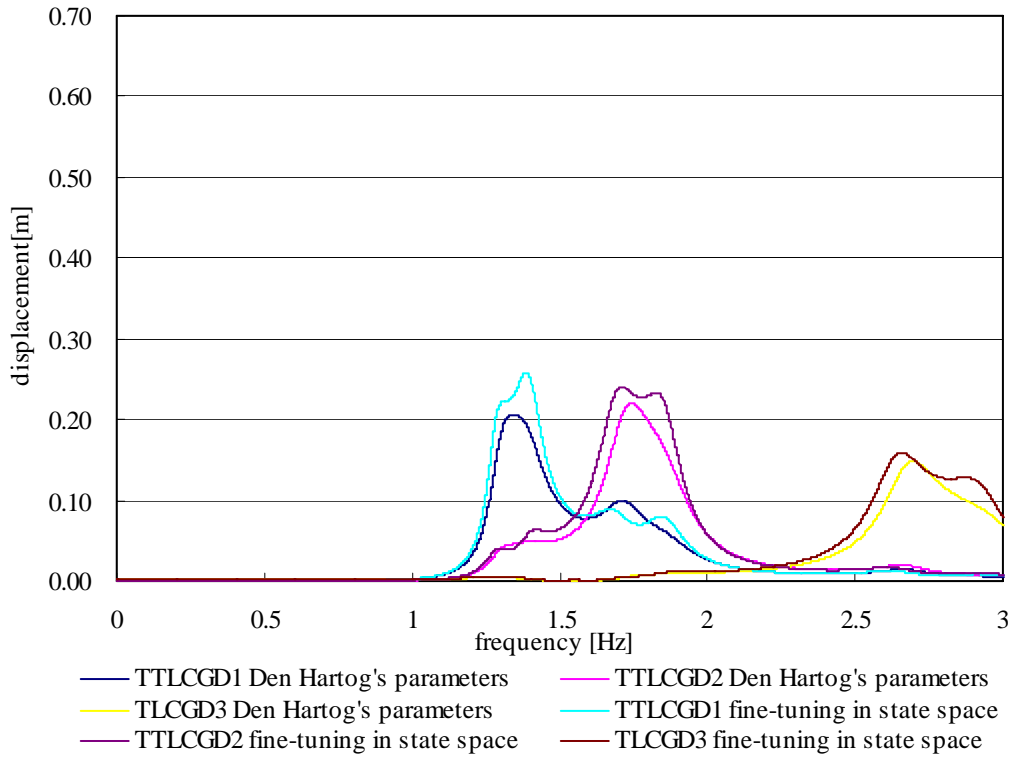


Fig. 3.23: Amplitude response curves of fluid displacement $|u|$ of three linearized absorbers attached to the 3-DOF space frame. Absorbers either with Den Hartog's optimal parameters or those resulting from fine-tuning in state space ($\alpha = \pi/4$).

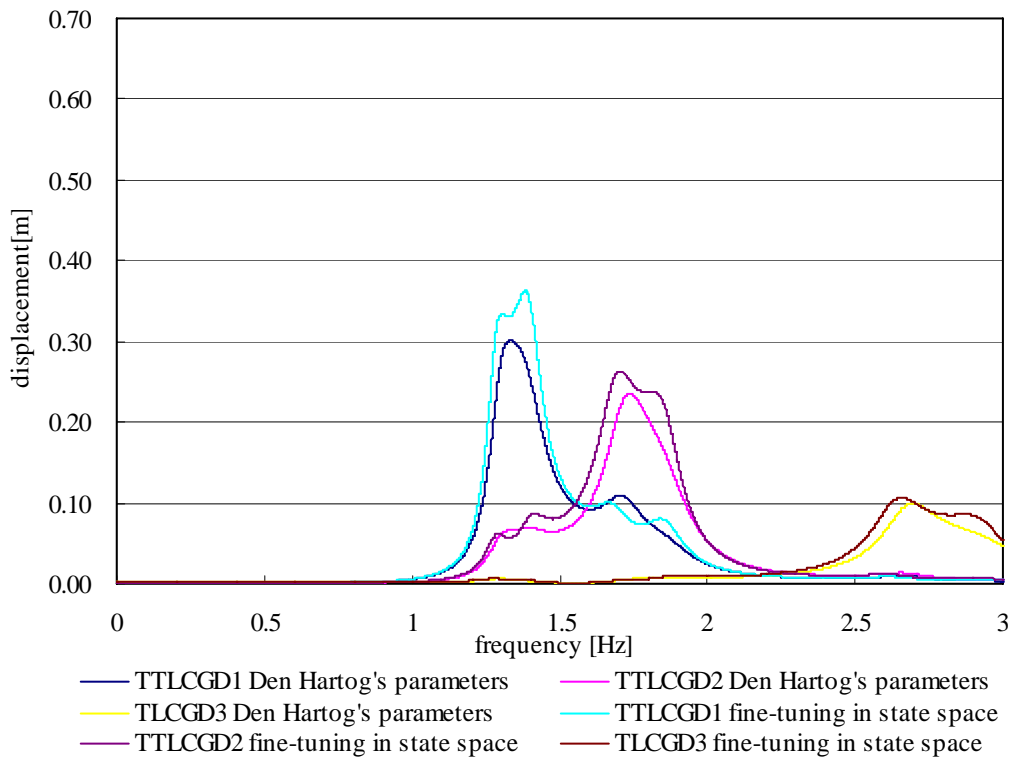


Fig. 3.24: Amplitude response curves of fluid displacement $|u|$ of three linearized absorbers attached to the 3-DOF space frame. Absorbers either with Den Hartog's optimal parameters or those resulting from fine-tuning in state space ($\alpha = \pi/3$).

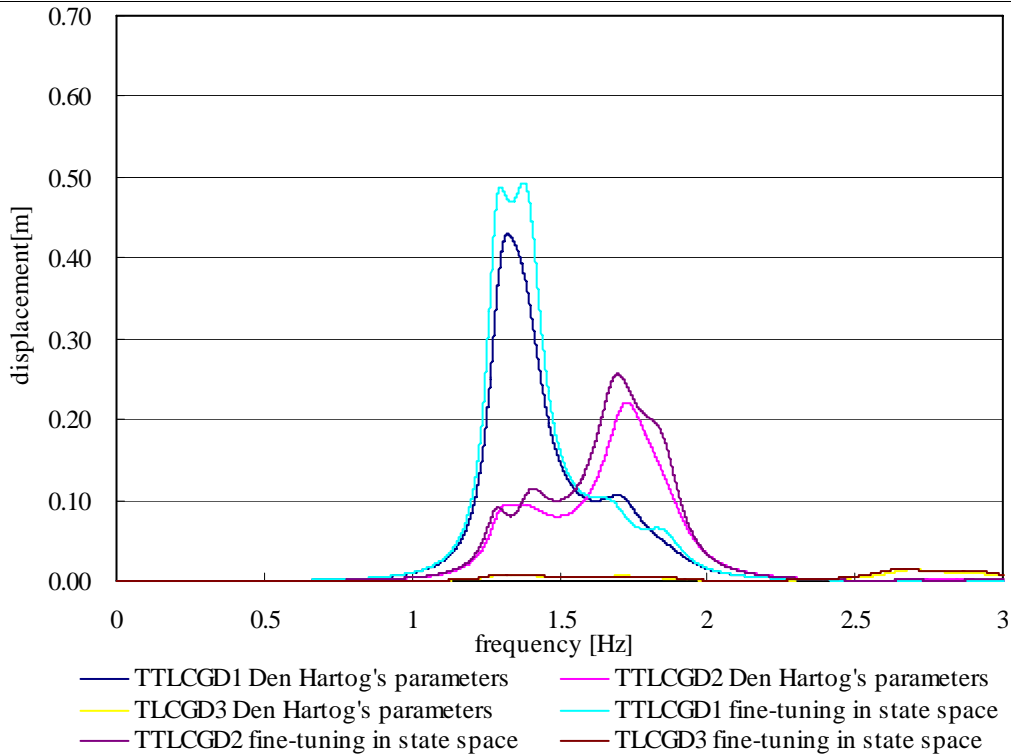


Fig. 3.25: Amplitude response curves of fluid displacement $|u|$ of three linearized absorbers attached to the 3-DOF space frame. Absorbers either with Den Hartog's optimal parameters or those resulting from fine-tuning in state space ($\alpha = \pi/2$).

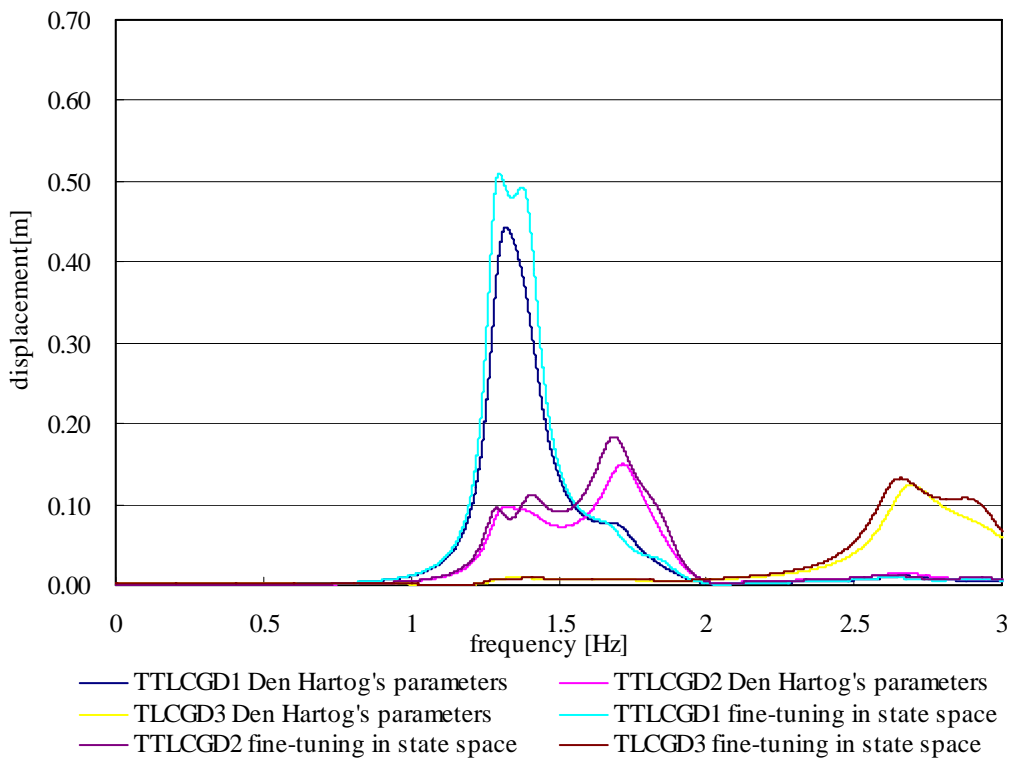


Fig. 3.26: Amplitude response curves of fluid displacement $|u|$ of three linearized absorbers attached to the 3-DOF space frame. Absorbers either with Den Hartog's optimal parameters or those resulting from fine-tuning in state space ($\alpha = 2\pi/3$).

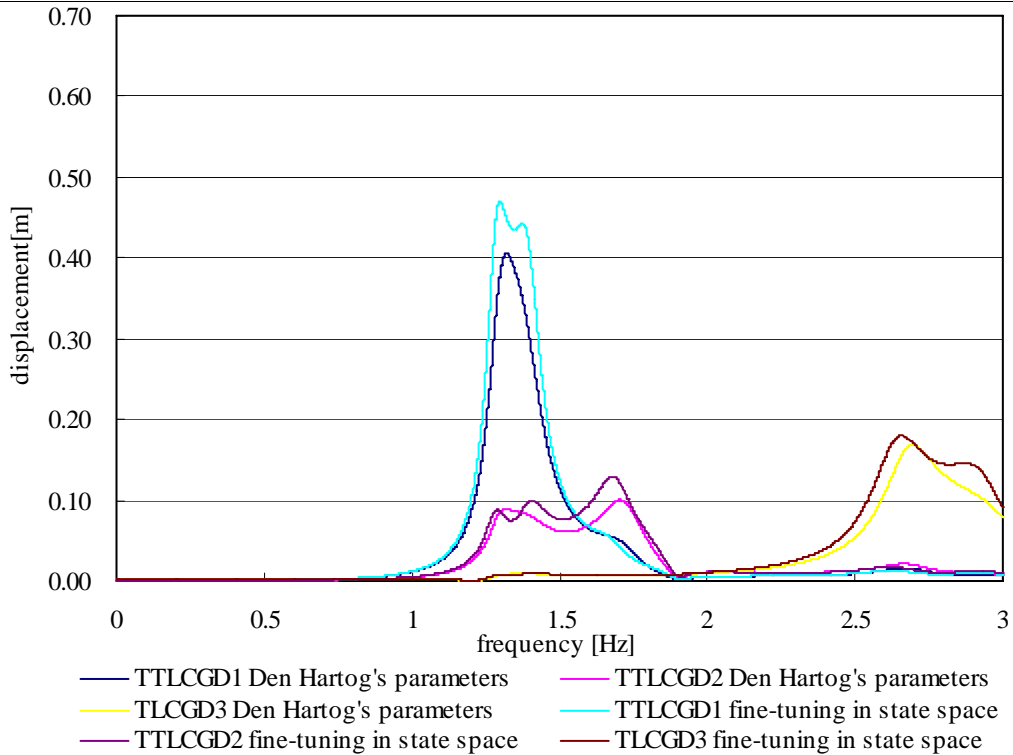


Fig. 3.27: Amplitude response curves of fluid displacement $|u|$ of three linearized absorbers attached to the 3-DOF space frame. Absorbers either with Den Hartog's optimal parameters or those resulting from fine-tuning in state space ($\alpha = 3\pi/4$).

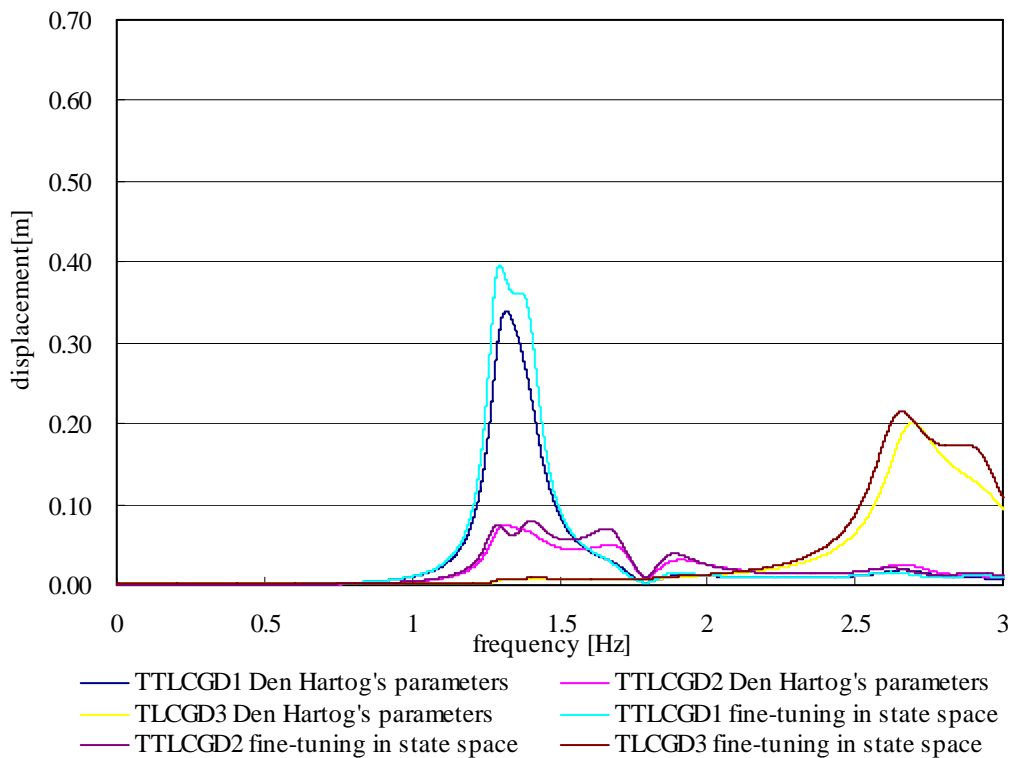


Fig. 3.28: Amplitude response curves of fluid displacement $|u|$ of three linearized absorbers attached to the 3-DOF space frame. Absorbers either with Den Hartog's optimal parameters or those resulting from fine-tuning in state space ($\alpha = 5\pi/6$).

The wall thickness and the estimated dead mass of the piping system are listed in Table 3.3 for the three absorbers, designed according to Table 3.1.

	TTLCGD1	TTLCGD2	TLCGD3
h_0 [m]	220	208	85.63
H_a [m]	2.19	1.29	1.29
$10^{-5} p_{(D)}$ [N/m ²] Eq.(2.128)	100.81	95.23	38.65
pipe diameter $2r$ [mm]	154.3	157.2	228.5
t [mm] Eq.(2.124)	5.6	5.3	3.2
m_p [kg] Eq.(2.130)	655.08	584.17	118.03
dead fluid-mass[kg]	275.55	255	41.58
$10^{-5} \bar{p}_{(D)}$ [N/m ²] Eq.(2.129)	8.19	7.69	2.58

Table 3.3: Dimensioning of circular steel pipes.

The gauge pressure under expansion conditions turns out to be positive as listed in Table 3.3. The final dimensions of circular steel pipes must be changed according to their commercial availability.

3.8.6 Oblique seismic excitation by the strong motion phase of the El Centro earthquake (1940)

The N-S El Centro earthquake acceleration record with a peak ground acceleration of 0.35g, see Section 2.9.10, is again applied to the strongly asymmetric structure under different angles of attack. The 3 absorbers with fine-tuned parameters are considered in their linearized modal damping assigned.

The numerical values of the maximum response observed in Figs.3.29 to 3.52 are sampled in Table 3.4a and 3.4b. The maximum fluid displacements of $u_1 = 0.19m$, $u_2 = 0.18m$, $u_3 = 0.10m$ and velocities of $\dot{u}_1 = 1.61m/s$, $\dot{u}_2 = 1.96m/s$, $\dot{u}_3 = 1.73m/s$ are within the acceptable limits.

Max	original structure			structure with 3 absorbers			fluid displacement		
	v [mm]	w [mm]	u_T [mm]	v [mm]	w [mm]	u_T [mm]	u_1 [mm]	u_2 [mm]	u_3 [mm]
$\alpha = 0$	29	29	35	21	21	25	64	91	104
$\alpha = \pi/6$	37	44	49	25	33	37	84	140	88
$\alpha = \pi/4$	37	50	55	27	41	42	120	163	71
$\alpha = \pi/3$	36	56	60	27	48	46	153	177	48
$\alpha = \pi/2$	30	60	69	22	55	53	186	179	10
$\alpha = 2\pi/3$	26	50	62	18	53	50	171	133	57
$\alpha = 3\pi/4$	25	48	52	19	48	43	145	96	76
$\alpha = 5\pi/6$	22	44	38	21	42	33	120	69	89

Table 3.4a: Maximum displacements due to 1940 El Centro earthquake, maximum ground acceleration $a_0/g = 0.35$ with varying angle of attack α . Maximum values indicated in bold, $u_T = r_S \theta$, $r_S = 2.58m$.

Single-storey Strongly Plan-asymmetric Space Frame with TTLCGDs and TLCGDs

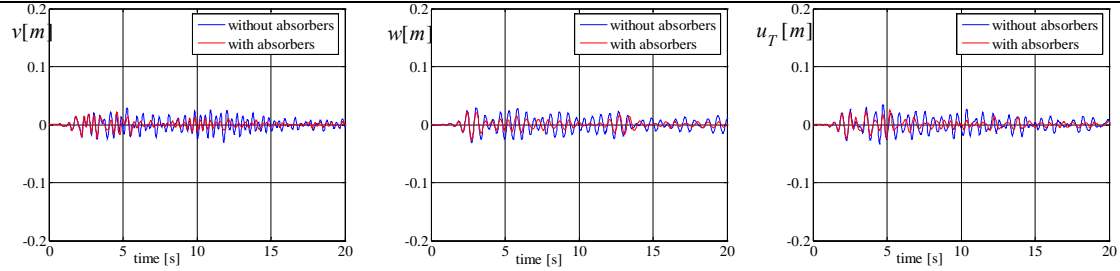


Fig. 3.29: Relative floor displacements of center of mass, v , w and rotation $u_T=r_S\theta$ without and with three absorbers attached under 1940 El Centro earthquake $a_0/g = 0.35$, angle of attack: $\alpha = 0$, $r_S = 2.58m$.

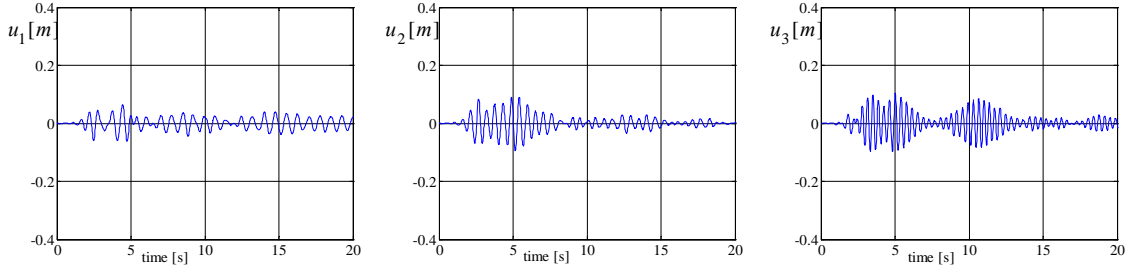


Fig. 3.30: Relative displacement of the fluid in three absorbers under 1940 El Centro earthquake $a_0/g = 0.35$, angle of attack: $\alpha = 0$, $r_S = 2.58m$.

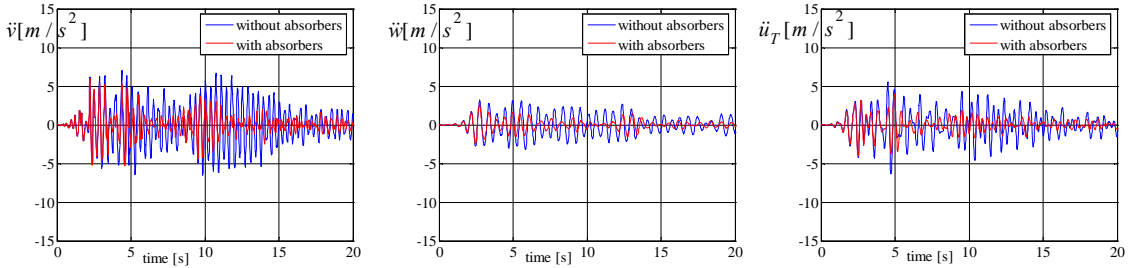


Fig. 3.31: Relative acceleration of single-storey space structure, \ddot{v} , \ddot{w} and $\ddot{u}_T = r_S\ddot{\theta}$ under 1940 El Centro earthquake $a_0/g = 0.35$, angle of attack: $\alpha = 0$, $r_S = 2.58m$.

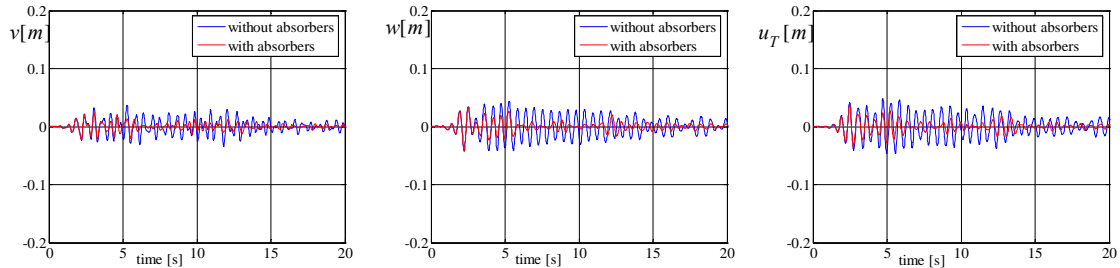


Fig. 3.32: Relative floor displacements of center of mass, v , w and rotation $u_T=r_S\theta$ without and with three absorbers attached under 1940 El Centro earthquake $a_0/g = 0.35$, angle of attack: $\alpha = \pi/6$, $r_S = 2.58m$.

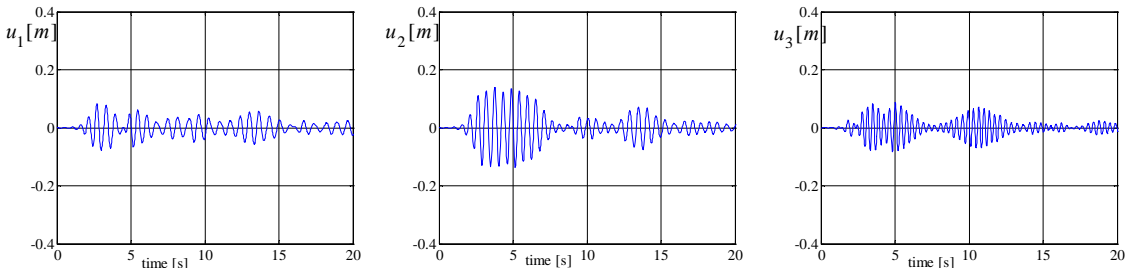


Fig. 3.33: Relative displacement of the fluid in three absorbers under 1940 El Centro earthquake $a_0/g = 0.35$, angle of attack: $\alpha = \pi/6$, $r_S = 2.58m$.

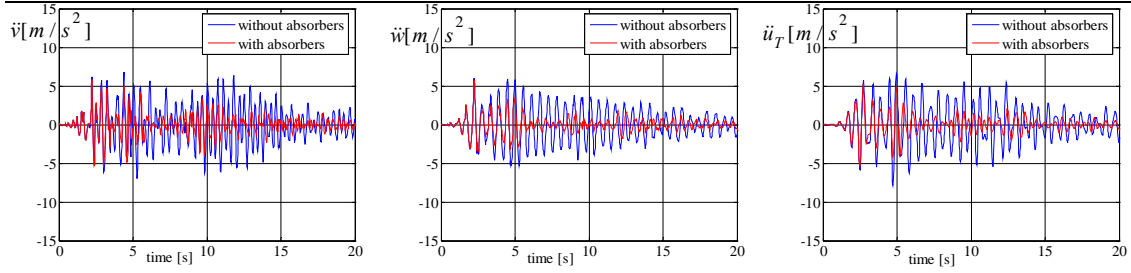


Fig. 3.34: Relative acceleration of single-storey space structure, \ddot{v} , \ddot{w} and $\ddot{u}_T = r_S \ddot{\theta}$ under 1940 El Centro earthquake $a_0/g = 0.35$, angle of attack: $\alpha = \pi/6$, $r_S = 2.58m$.

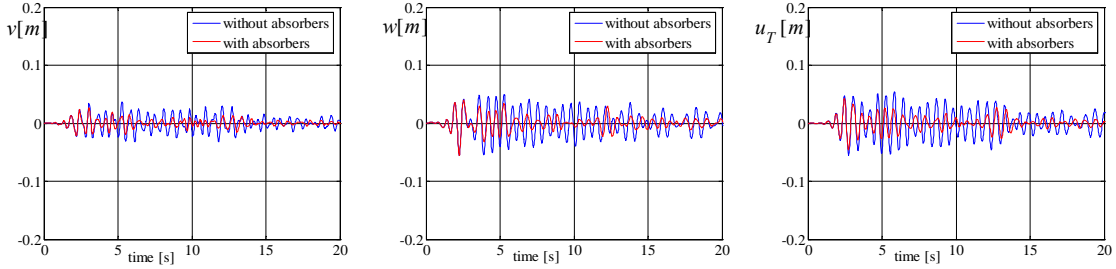


Fig. 3.35: Relative floor displacements of center of mass, v , w and rotation $u_T = r_S \theta$ without and with three absorbers attached under 1940 El Centro earthquake $a_0/g = 0.35$, angle of attack: $\alpha = \pi/4$, $r_S = 2.58m$.

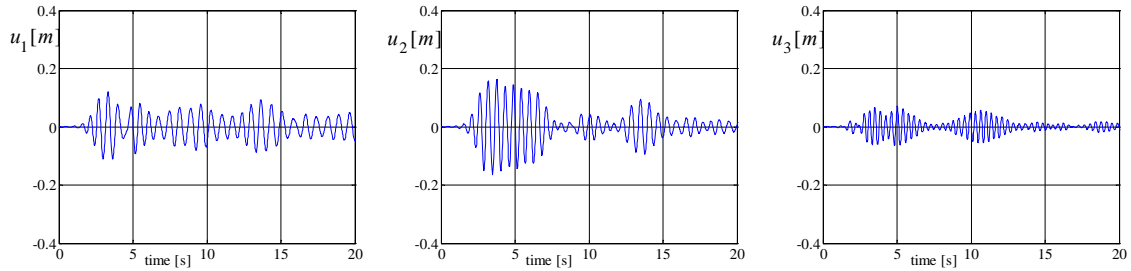


Fig. 3.36: Relative displacement of the fluid in three absorbers under 1940 El Centro earthquake $a_0/g = 0.35$, angle of attack: $\alpha = \pi/4$, $r_S = 2.58m$.

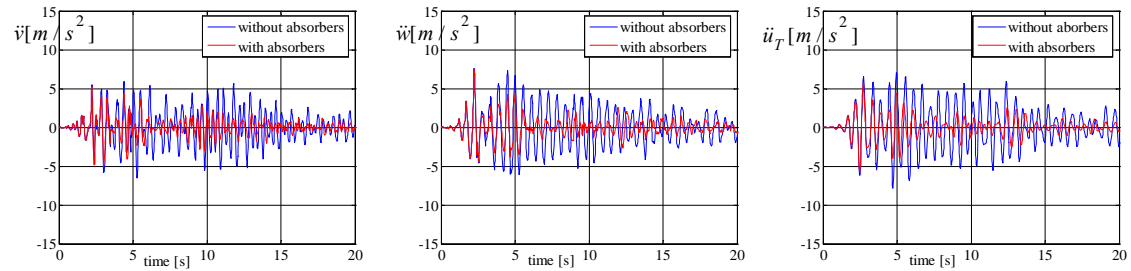


Fig. 3.37: Relative acceleration of single-storey space structure, \ddot{v} , \ddot{w} and $\ddot{u}_T = r_S \ddot{\theta}$ under 1940 El Centro earthquake $a_0/g = 0.35$, angle of attack: $\alpha = \pi/4$, $r_S = 2.58m$.

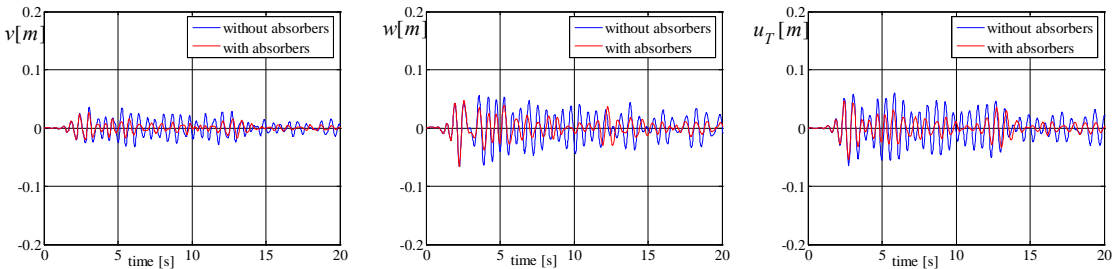


Fig. 3.38: Relative floor displacements of center of mass, v , w and rotation $u_T = r_S \theta$ without and with three absorbers attached under 1940 El Centro earthquake $a_0/g = 0.35$, angle of attack: $\alpha = \pi/3$, $r_S = 2.58m$.

Single-storey Strongly Plan-asymmetric Space Frame with TTLCGDs and TLCGDs

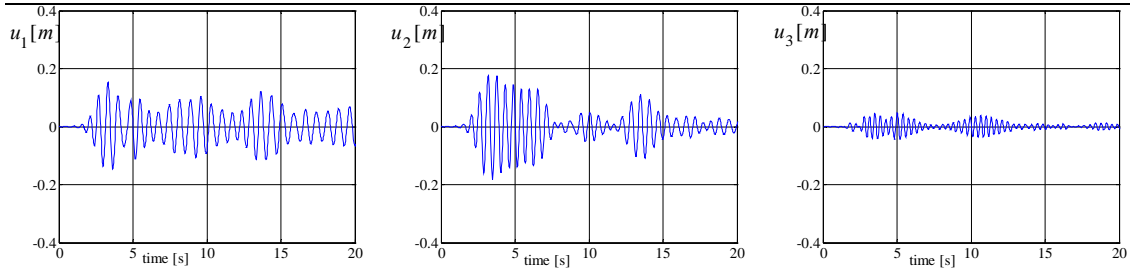


Fig. 3.39: Relative displacement of the fluid in three absorbers under 1940 El Centro earthquake $a_0/g = 0.35$, angle of attack: $\alpha = \pi/3$, $r_S = 2.58m$.

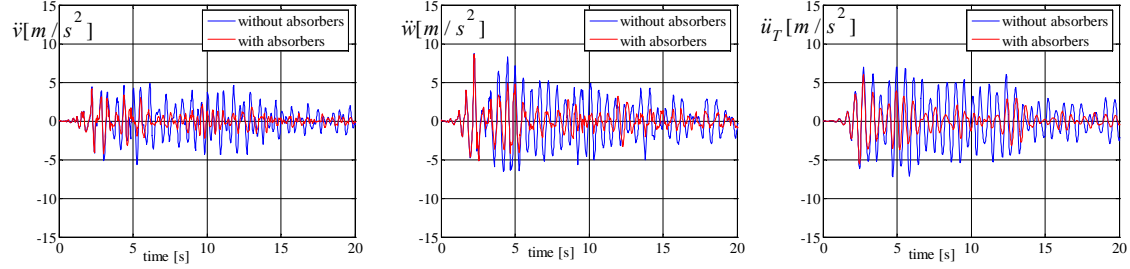


Fig. 3.40: Relative acceleration of single-storey space structure, \ddot{v} , \ddot{w} and $\ddot{u}_T = r_S \ddot{\theta}$ under 1940 El Centro earthquake $a_0/g = 0.35$, angle of attack: $\alpha = \pi/3$, $r_S = 2.58m$.

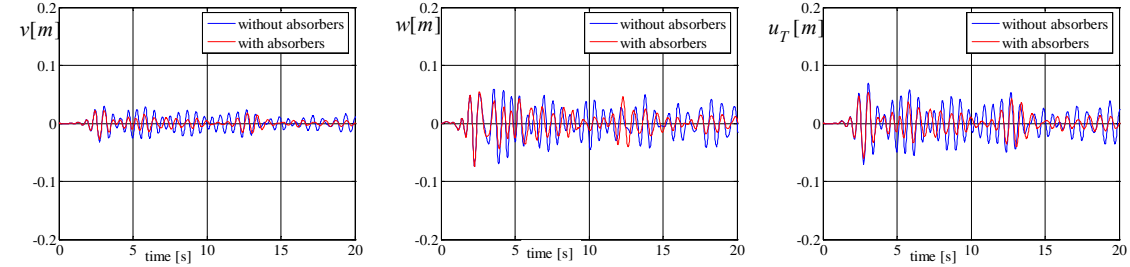


Fig. 3.41: Relative floor displacements of center of mass, v , w and rotation $u_T = r_S \theta$ without and with three absorbers attached under 1940 El Centro earthquake $a_0/g = 0.35$, angle of attack: $\alpha = \pi/2$, $r_S = 2.58m$.

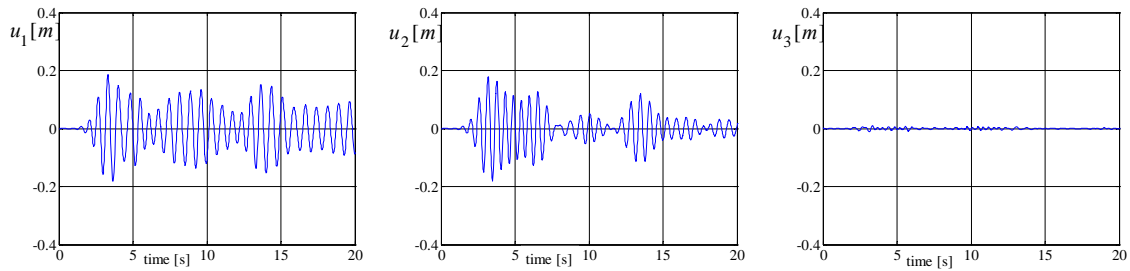


Fig. 3.42: Relative displacement of the fluid in three absorbers under 1940 El Centro earthquake $a_0/g = 0.35$, angle of attack: $\alpha = \pi/2$, $r_S = 2.58m$.

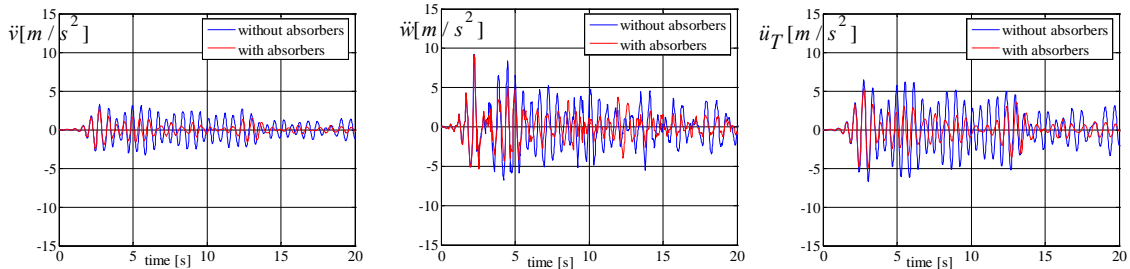


Fig. 3.43: Relative acceleration of single-storey space structure, \ddot{v} , \ddot{w} and $\ddot{u}_T = r_S \ddot{\theta}$ under 1940 El Centro earthquake $a_0/g = 0.35$, angle of attack: $\alpha = \pi/2$, $r_S = 2.58m$.

Single-storey Strongly Plan-asymmetric Space Frame with TTLCGDs and TLCGDs

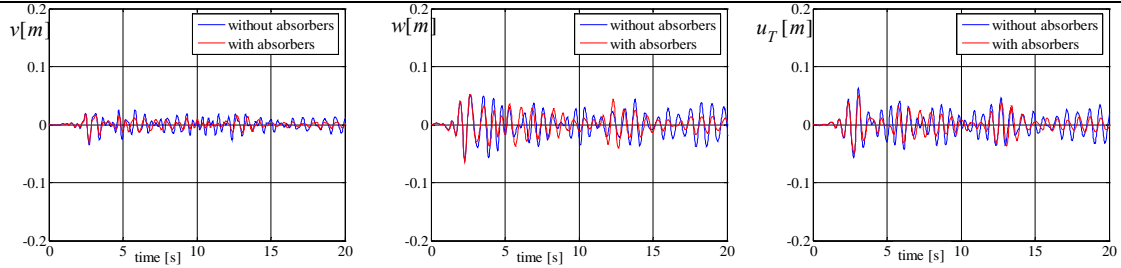


Fig. 3.44: Relative floor displacements of center of mass, v , w and rotation $u_T=r_S\theta$ without and with three absorbers attached under 1940 El Centro earthquake $a_0/g = 0.35$, angle of attack: $\alpha = 2\pi/3$, $r_S = 2.58m$.

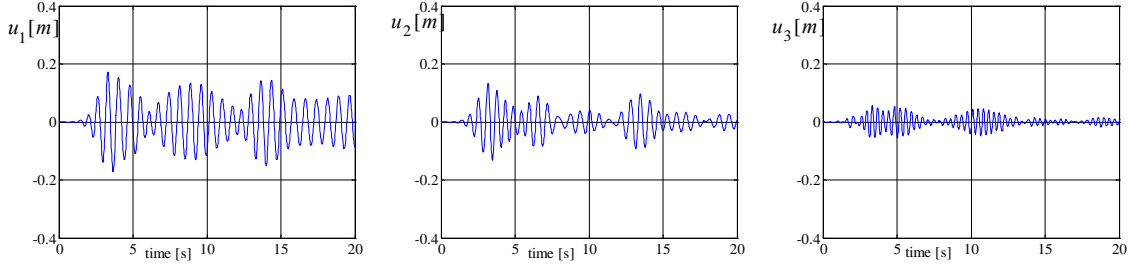


Fig. 3.45: Relative displacement of the fluid in three absorbers under 1940 El Centro earthquake $a_0/g = 0.35$, angle of attack: $\alpha = 2\pi/3$, $r_S = 2.58m$.

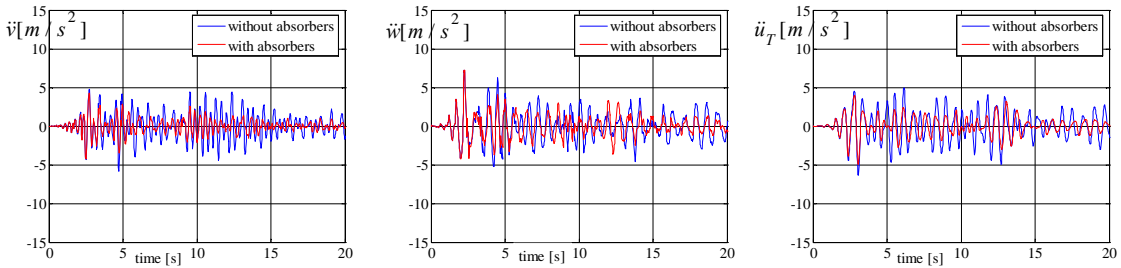


Fig. 3.46: Relative acceleration of single-storey space structure, \ddot{v} , \ddot{w} and $\ddot{u}_T = r_S\ddot{\theta}$ under 1940 El Centro earthquake $a_0/g = 0.35$, angle of attack: $\alpha = 2\pi/3$, $r_S = 2.58m$.

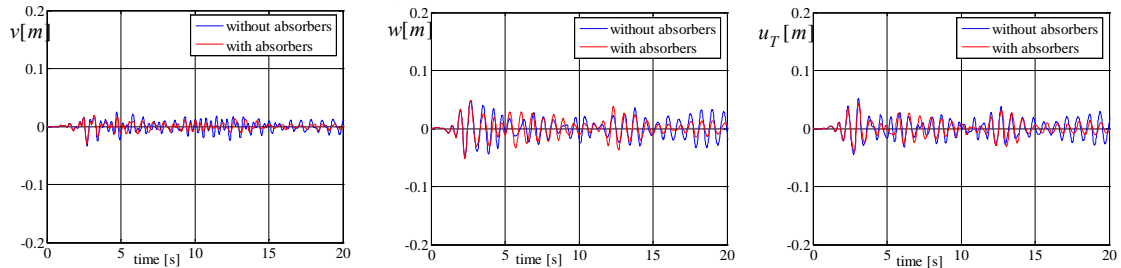


Fig. 3.47: Relative floor displacements of center of mass, v , w and rotation $u_T=r_S\theta$ without and with three absorbers attached under 1940 El Centro earthquake $a_0/g = 0.35$, angle of attack: $\alpha = 3\pi/4$, $r_S = 2.58m$.

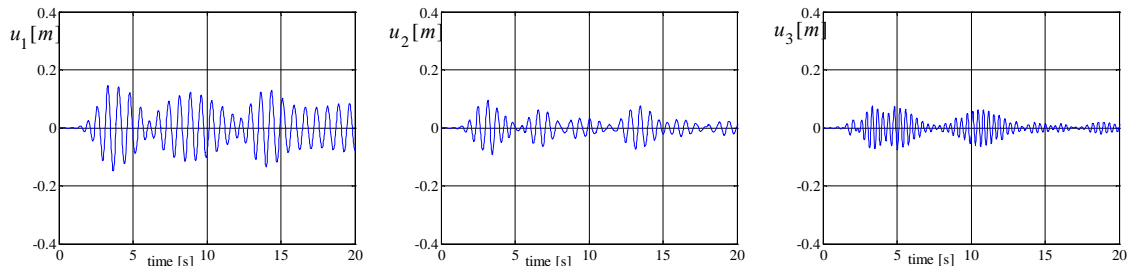


Fig. 3.48: Relative displacement of the fluid in three absorbers under 1940 El Centro earthquake $a_0/g = 0.35$, angle of attack: $\alpha = 3\pi/4$, $r_S = 2.58m$.

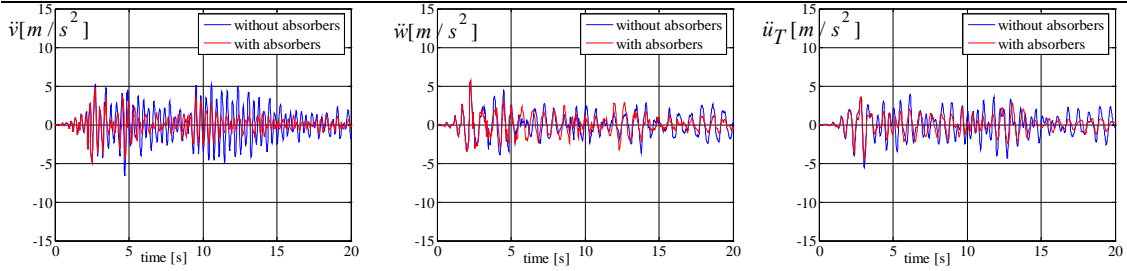


Fig. 3.49: Relative acceleration of single-storey space structure, \ddot{v} , \ddot{w} and $\ddot{u}_T = r_S \ddot{\theta}$ under 1940 El Centro earthquake $a_0/g = 0.35$, angle of attack: $\alpha = 3\pi/4$, $r_S = 2.58m$.

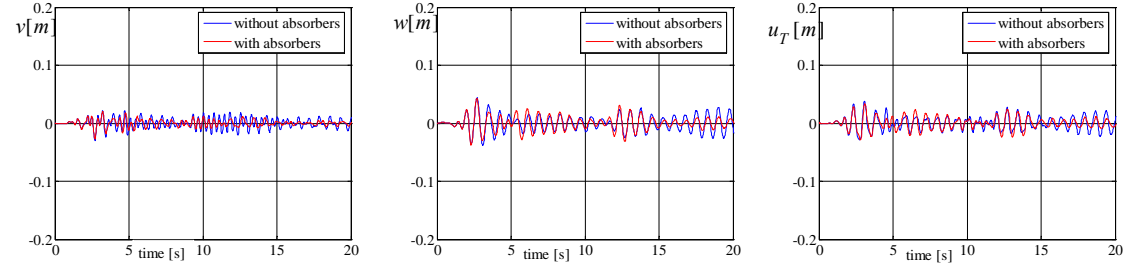


Fig. 3.50: Relative floor displacements of center of mass, v , w and rotation $u_T = r_S \theta$ without and with three absorbers attached under 1940 El Centro earthquake $a_0/g = 0.35$, angle of attack: $\alpha = 5\pi/6$, $r_S = 2.58m$.

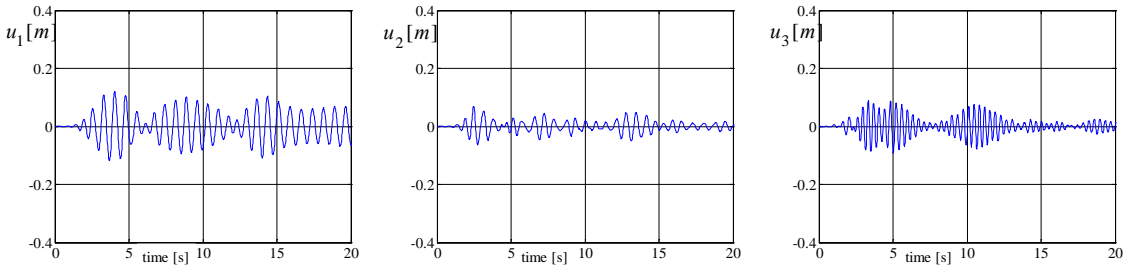


Fig. 3.51: Relative displacement of the fluid in three absorbers under 1940 El Centro earthquake $a_0/g = 0.35$, angle of attack: $\alpha = 5\pi/6$, $r_S = 2.58m$.

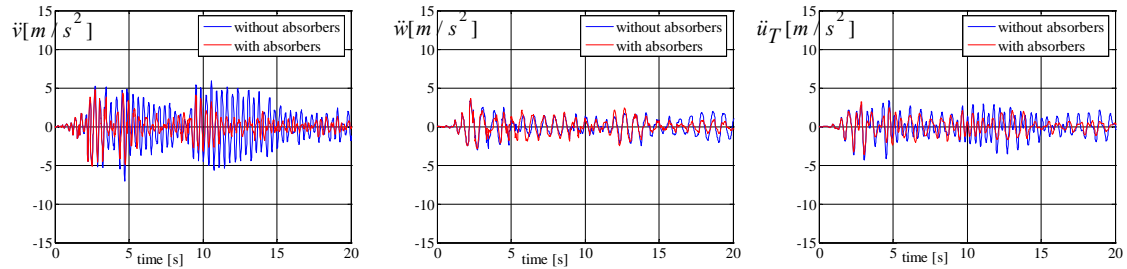


Fig. 3.52: Relative acceleration of single-storey space structure, \ddot{v} , \ddot{w} and $\ddot{u}_T = r_S \ddot{\theta}$ under 1940 El Centro earthquake $a_0/g = 0.35$, angle of attack: $\alpha = 5\pi/6$, $r_S = 2.58m$.

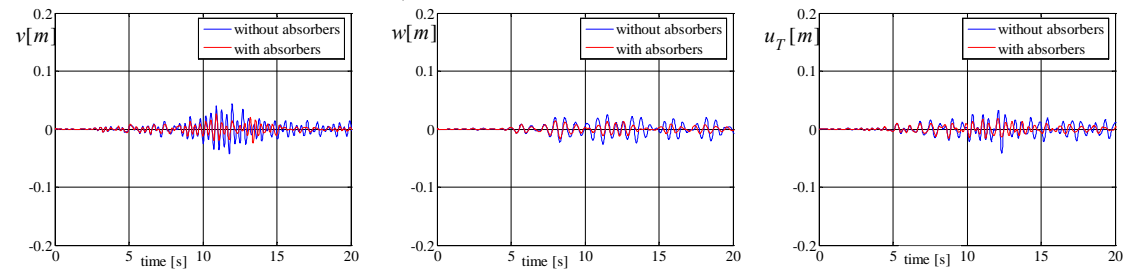


Fig. 3.53: Relative floor displacements of center of mass, v , w and rotation $u_T = r_S \theta$ without and with three absorbers attached, angle of attack: $\alpha = 0$ (artificial seismicogram) $r_S = 2.58m$.

Single-storey Strongly Plan-asymmetric Space Frame with TTLCGDs and TLCGDs

Max	original structure			structure with 3 absorbers		
	\ddot{v}/g	\ddot{w}/g	\ddot{u}_T/g	\ddot{v}/g	\ddot{w}/g	\ddot{u}_T/g
$\alpha = 0$	0.72	0.33	0.57	0.61	0.27	0.41
$\alpha = \pi/6$	0.69	0.61	0.68	0.60	0.59	0.53
$\alpha = \pi/4$	0.60	0.78	0.72	0.53	0.76	0.59
$\alpha = \pi/3$	0.49	0.89	0.71	0.27	0.88	0.61
$\alpha = \pi/2$	0.33	0.94	0.66	0.30	0.94	0.54
$\alpha = 2\pi/3$	0.49	0.73	0.51	0.44	0.74	0.41
$\alpha = 3\pi/4$	0.54	0.56	0.41	0.48	0.57	0.36
$\alpha = 5\pi/6$	0.60	0.35	0.34	0.49	0.37	0.33

Table 3.4b: Maximum accelerations due to 1940 El Centro earthquake, maximum ground acceleration $a_0/g = 0.35$ with varying angle of attack α . Maximum values indicated in bold, $u_T = r_S\theta$, $r_S = 2.58m$.

3.8.7 Kanai-Tajimi model of the ground acceleration: soil amplification

An artificial seismogram is generated from Kanai-Tajimi model for the modeling of hypothetical ground acceleration, the numerical simulation are done analogous to section 2.9.11.

The numerical values of the maximum response observed in Figs.3.53 to 3.76 are sampled in Table 3.5a and 3.5b. The maximum fluid displacements of $u_1 = 0.18m$, $u_2 = 0.15m$, $u_3 = 0.15m$ and velocities of $\dot{u}_1 = 1.53m/s$, $\dot{u}_2 = 1.63m/s$, $\dot{u}_3 = 2.60m/s$ are within the acceptable limits.

Max	original structure			structure with 3 absorbers			fluid displacement		
	v [mm]	w [mm]	u_T [mm]	v [mm]	w [mm]	u_T [mm]	u_1 [mm]	u_2 [mm]	u_3 [mm]
$\alpha = 0$	44	25	32	26	15	18	52	73	153
$\alpha = \pi/6$	44	39	39	26	24	25	67	128	128
$\alpha = \pi/4$	42	50	47	24	29	27	99	144	102
$\alpha = \pi/3$	36	59	53	19	32	30	133	150	69
$\alpha = \pi/2$	26	64	56	15	40	37	183	132	122
$\alpha = 2\pi/3$	34	54	55	15	38	35	183	95	85
$\alpha = 3\pi/4$	37	48	50	19	33	31	165	67	114
$\alpha = 5\pi/6$	37	40	42	23	28	27	135	44	135

Table 3.5a: Maximum displacements, artificial seismogram using Kanai-Tajimi model, maximum ground acceleration $a_0/g = 0.34$. Varying angles of attack α . Extreme values indicated in bold, $u_T = r_S\theta$, $r_S = 2.58m$.

Single-storey Strongly Plan-asymmetric Space Frame with TTLCGDs and TLCGDs

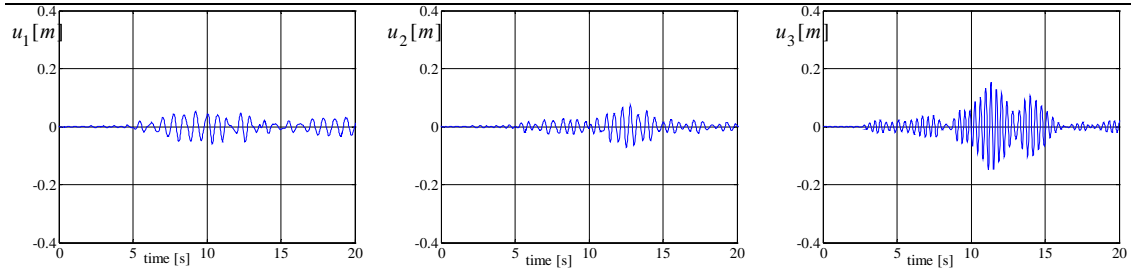


Fig. 3.54: Relative displacement of the fluid in three absorbers, angle of attack: $\alpha = 0$ (artificial seismogram) $r_S = 2.58m$.

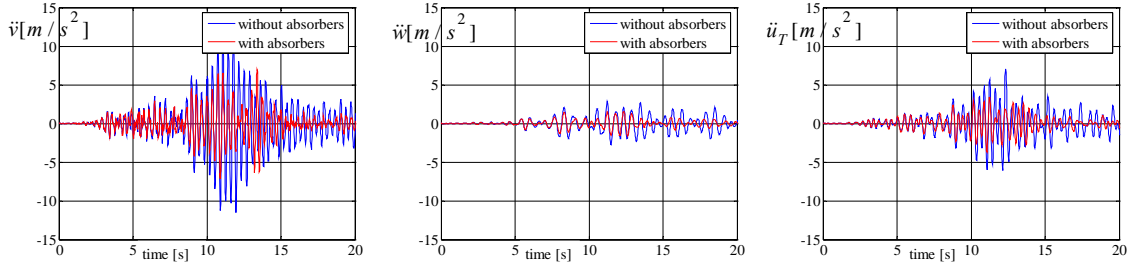


Fig. 3.55: Relative acceleration of single-storey space structure, \ddot{v} , \ddot{w} and $\ddot{u}_T = r_S \ddot{\theta}$, angle of attack: $\alpha = 0$ (artificial seismogram) $r_S = 2.58m$.

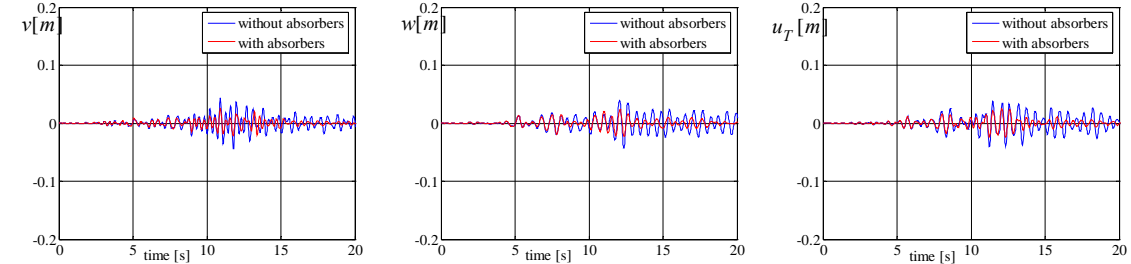


Fig. 3.56: Relative floor displacements of center of mass, v , w and rotation $u_T = r_S \theta$ without and with three absorbers attached, angle of attack: $\alpha = \pi/6$ (artificial seismogram) $r_S = 2.58m$.

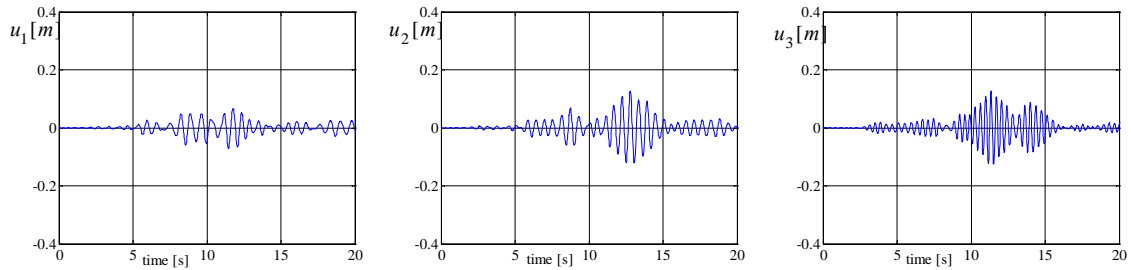


Fig. 3.57: Relative displacement of fluid in three absorbers, angle of attack: $\alpha = \pi/6$ (artificial seismogram) $r_S = 2.58m$.

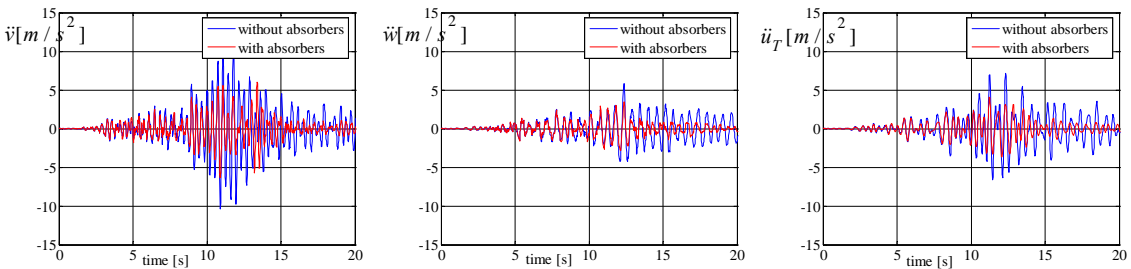


Fig. 3.58: Relative acceleration of single-storey space structure, \ddot{v} , \ddot{w} and $\ddot{u}_T = r_S \ddot{\theta}$, angle of attack: $\alpha = \pi/6$ (artificial seismogram) $r_S = 2.58m$.

Single-storey Strongly Plan-asymmetric Space Frame with TTLCGDs and TLCGDs

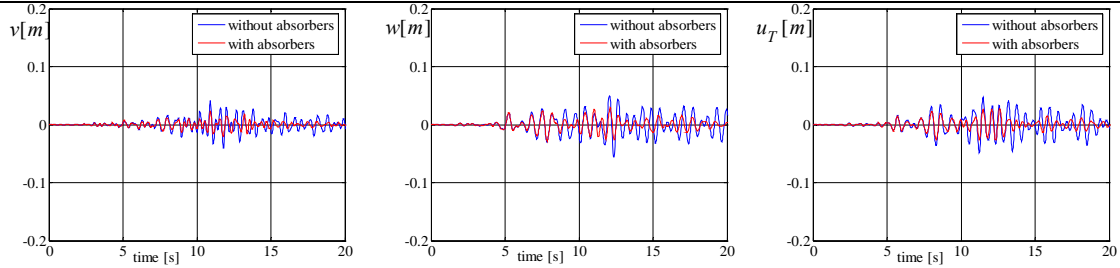


Fig. 3.59: Relative floor displacements of center of mass, v , w and rotation $u_T=r_S\theta$ without and with three absorbers attached, angle of attack: $\alpha = \pi/4$ (artificial seismogram) $r_S = 2.58m$.

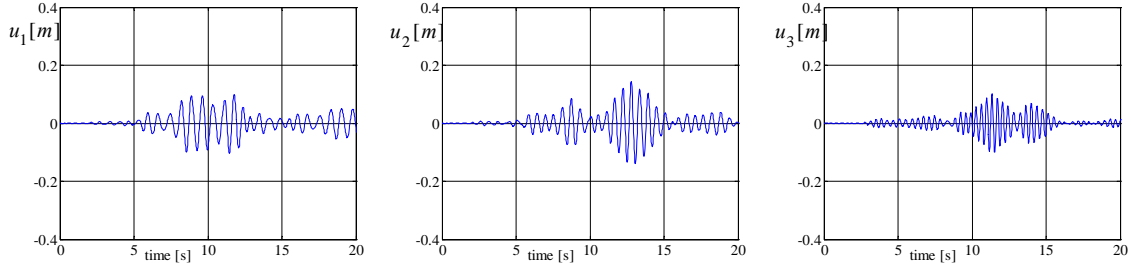


Fig. 3.60: Relative displacement of fluid in three absorbers, angle of attack: $\alpha = \pi/4$ (artificial seismogram) $r_S = 2.58m$.

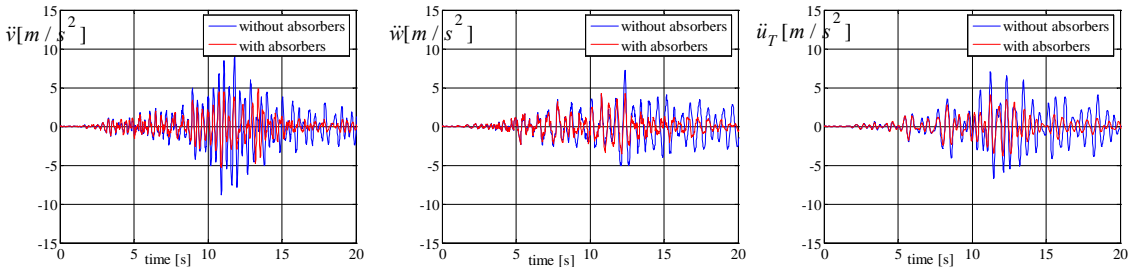


Fig. 3.61: Relative acceleration of single-storey space structure, \ddot{v} , \ddot{w} and $\ddot{u}_T = r_S\ddot{\theta}$, angle of attack: $\alpha = \pi/4$ (artificial seismogram) $r_S = 2.58m$.

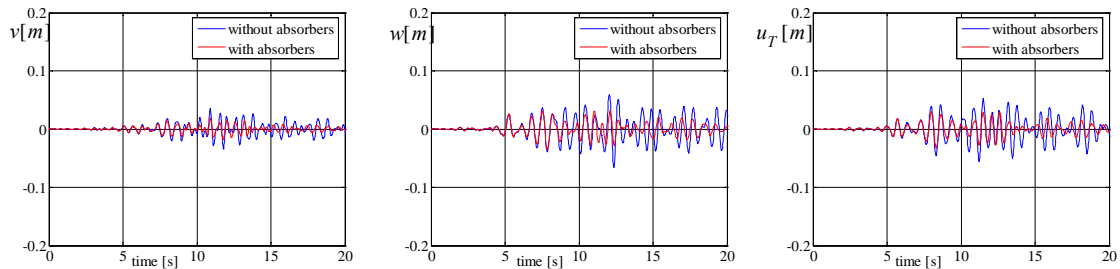


Fig. 3.62: Relative floor displacements of center of mass, v , w and rotation $u_T=r_S\theta$ without and with three absorbers attached, angle of attack: $\alpha = \pi/3$ (artificial seismogram) $r_S = 2.58m$.

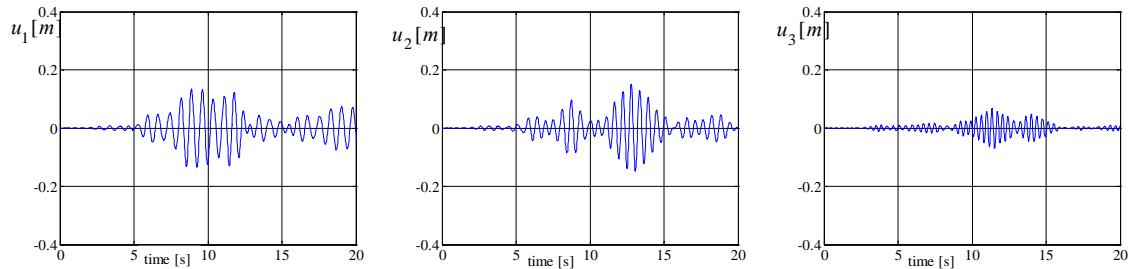


Fig. 3.63: Relative displacement of fluid in three absorbers, angle of attack: $\alpha = \pi/3$ (artificial seismogram) $r_S = 2.58m$.

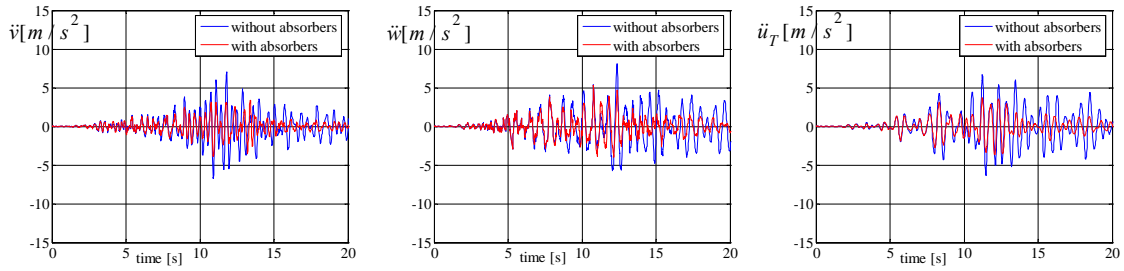


Fig. 3.64: Relative acceleration of single-storey space structure, \ddot{v} , \ddot{w} and $\ddot{u}_T = r_S \ddot{\theta}$, angle of attack: $\alpha = \pi/3$ (artificial seismogram) $r_S = 2.58m$.

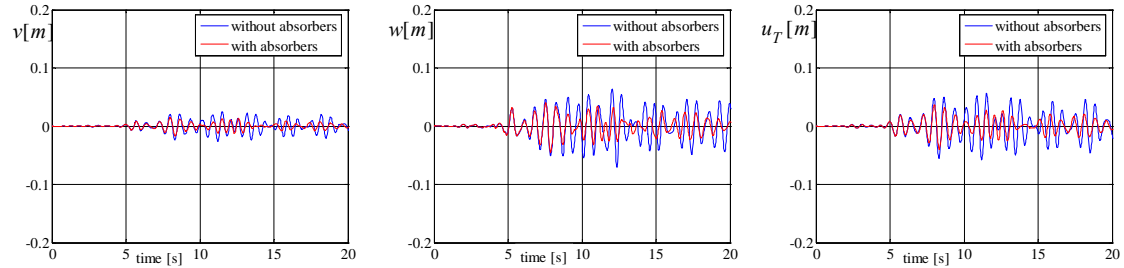


Fig. 3.65: Relative floor displacements of center of mass, v , w and rotation $u_T = r_S \theta$ without and with three absorbers attached, angle of attack: $\alpha = \pi/2$ (artificial seismogram) $r_S = 2.58m$.

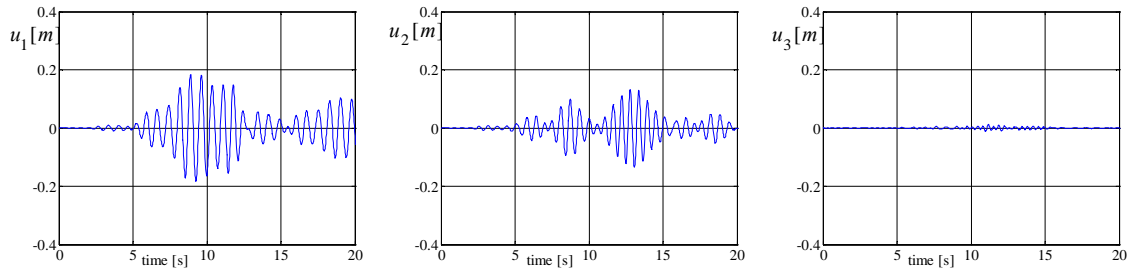


Fig. 3.66: Relative displacement of fluid in three absorbers, angle of attack: $\alpha = \pi/2$ (artificial seismogram) $r_S = 2.58m$.

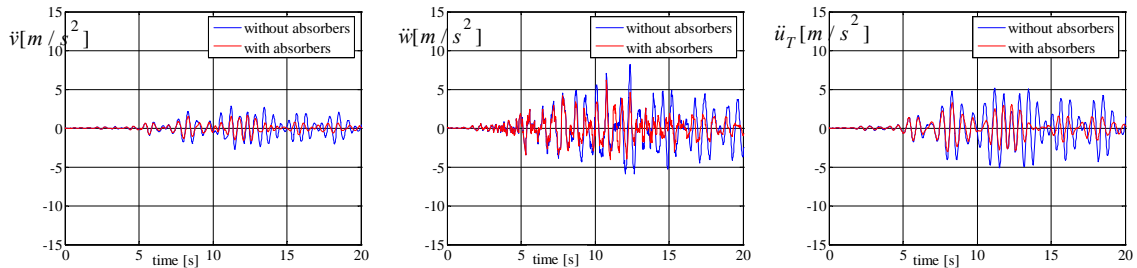


Fig. 3.67: Relative acceleration of single-storey space structure, \ddot{v} , \ddot{w} and $\ddot{u}_T = r_S \ddot{\theta}$, angle of attack: $\alpha = \pi/2$ (artificial seismogram) $r_S = 2.58m$.

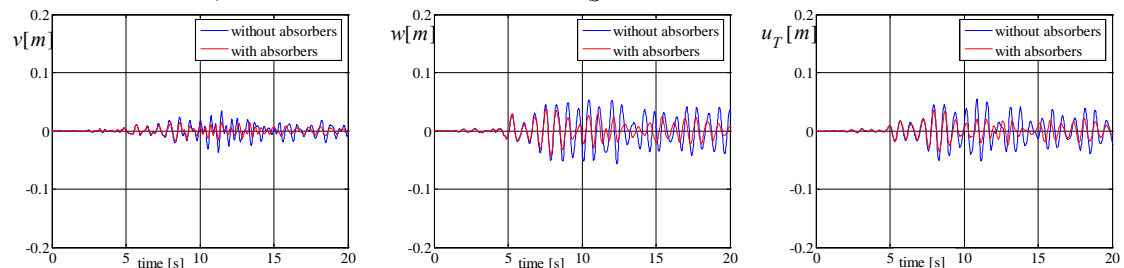


Fig. 3.68: Relative floor displacements of center of mass, v , w and rotation $u_T=r_S\theta$ without and with three absorbers attached, angle of attack: $\alpha = 2\pi/3$ (artificial seismogram) $r_S = 2.58m$.

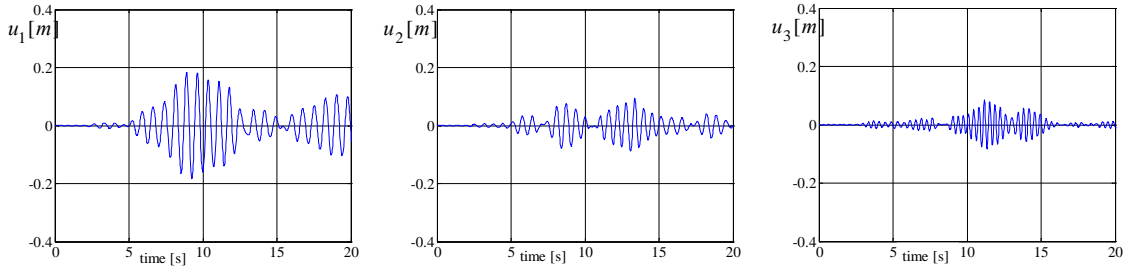


Fig. 3.69: Relative displacement of fluid in three absorbers, angle of attack: $\alpha = 2\pi/3$ (artificial seismogram) $r_S = 2.58m$.

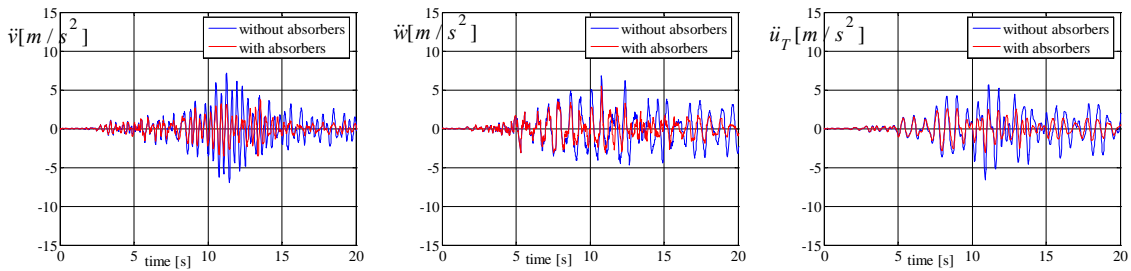


Fig. 3.70: Relative acceleration of single-storey space structure, \ddot{v} , \ddot{w} and $\ddot{u}_T = r_S\ddot{\theta}$, angle of attack: $\alpha = 2\pi/3$ (artificial seismogram) $r_S = 2.58m$.

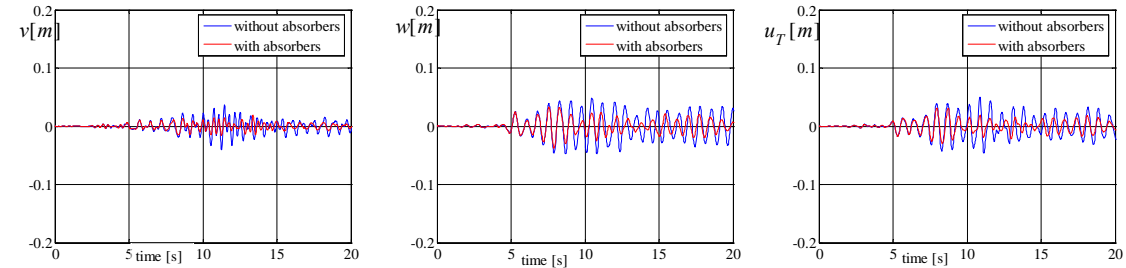


Fig. 3.71: Relative floor displacements of center of mass, v , w and rotation $u_T=r_S\theta$ without and with three absorbers attached, angle of attack: $\alpha = 3\pi/4$ (artificial seismogram) $r_S = 2.58m$.

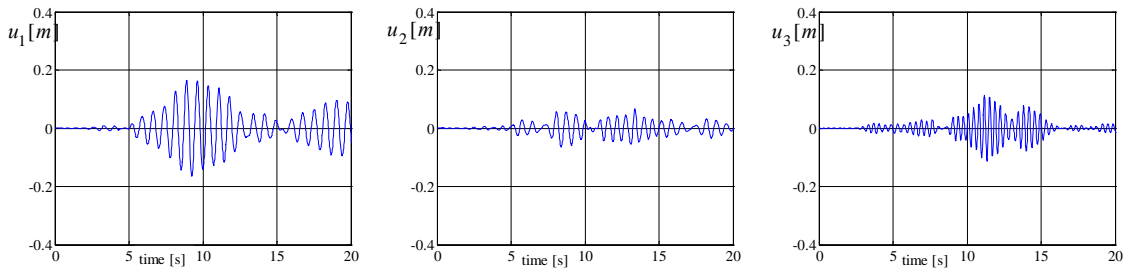


Fig. 3.72: Relative displacement of fluid in three absorbers, angle of attack: $\alpha = 3\pi/4$ (artificial seismogram) $r_S = 2.58m$.

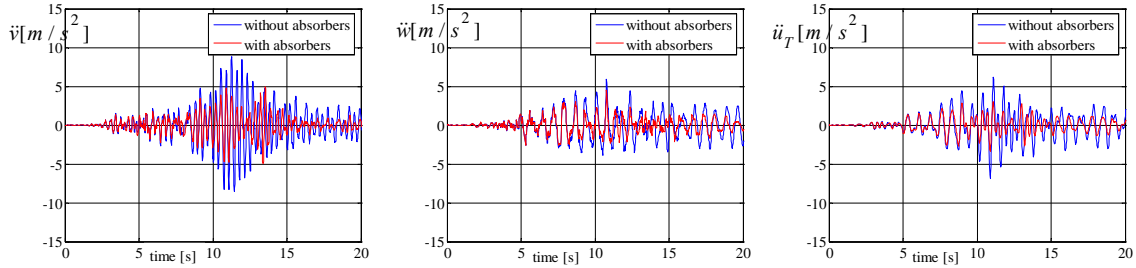


Fig. 3.73: Relative acceleration of single-storey space structure, \ddot{v} , \ddot{w} and $\ddot{u}_T = r_S \ddot{\theta}$, angle of attack: $\alpha = 3\pi/4$ (artificial seismogram) $r_S = 2.58m$.

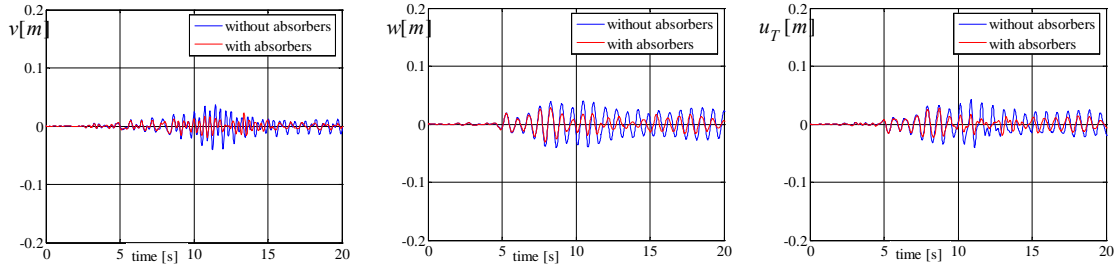


Fig. 3.74: Relative floor displacements of center of mass, v , w and rotation $u_T = r_S \theta$ without and with three absorbers attached, angle of attack: $\alpha = 5\pi/6$ (artificial seismogram) $r_S = 2.58m$.

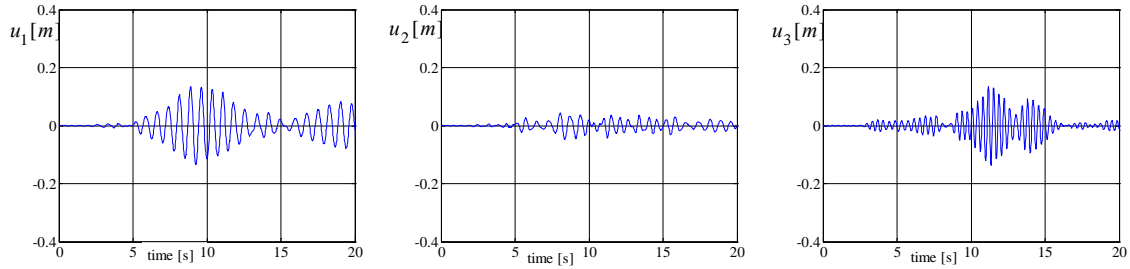


Fig. 3.75: Relative displacement of fluid in three absorbers, angle of attack: $\alpha = 5\pi/6$ (artificial seismogram) $r_S = 2.58m$.

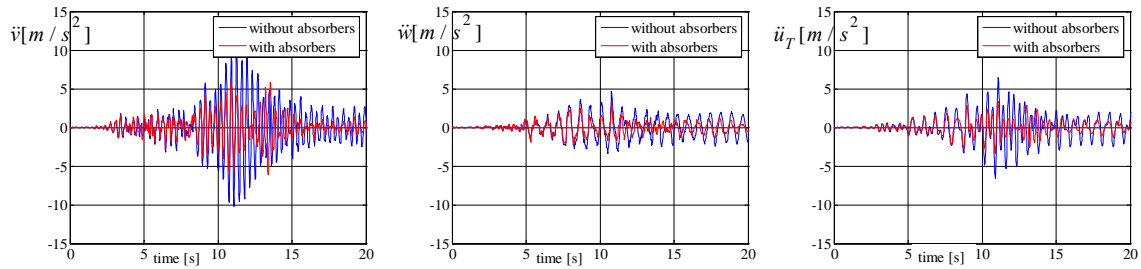


Fig. 3.76: Relative acceleration of single-storey space structure, \ddot{v} , \ddot{w} and $\ddot{u}_T = r_S \ddot{\theta}$, angle of attack: $\alpha = 5\pi/6$ (artificial seismogram) $r_S = 2.58m$.

Max	original structure			structure with 3 absorbers		
	\ddot{v}/g	\ddot{w}/g	\ddot{u}_T/g	\ddot{v}/g	\ddot{w}/g	\ddot{u}_T/g
$\alpha = 0$	1.21	0.29	0.72	0.71	0.16	0.34
$\alpha = \pi/6$	1.09	0.59	0.73	0.61	0.36	0.42
$\alpha = \pi/4$	0.94	0.73	0.72	0.49	0.43	0.41

Single-storey Strongly Plan-asymmetric Space Frame with TTLCGDs and TLCGDs

$\alpha = \pi/3$	0.72	0.83	0.68	0.35	0.54	0.38
$\alpha = \pi/2$	0.29	0.84	0.53	0.16	0.63	0.34
$\alpha = 2\pi/3$	0.73	0.69	0.58	0.38	0.56	0.27
$\alpha = 3\pi/4$	0.90	0.60	0.63	0.50	0.46	0.31
$\alpha = 5\pi/6$	1.04	0.48	0.65	0.61	0.33	0.35

Table 3.5b: Maximum accelerations, artificial seismogram using Kanai-Tajimi model, maximum ground acceleration $a_0/g = 0.34$. Varying angle of attack α . Extreme values indicated in bold, $u_T = r_S\theta$, $r_S = 2.58m$.

3.9 Single-storey symmetric space frame

Consider a special case of a single-storey building with uniformly distributed mass and stiffness in both the y - and z -directions. The symmetric-plan building can be analyzed independently in the two lateral directions and rotation. The center of velocity C_V of the rotational mode coincides with both mass- and stiffness center. When the idealized system is subjected to a biaxial, horizontal earthquake excitation, the participation factor $L_j(\alpha)$ of the rotational mode vanishes, and two TLCGDs are set in orthogonal directions intersecting in the mass- and stiffness center to control the translational responses of the structure. When the system is expected to vibrate in the torsional mode, the TTLCGD is proposed to lessen the purely torsional response.

References

- [1] Hochrainer M.J., Control of vibrations of civil engineering structures with special emphasis on tall buildings. Dissertation (in English), TU-Wien, A-1040 Vienna, Austria, 2001.
- [2] Hochrainer M.J., Adam C, Ziegler F., Application of tuned liquid column dampers for passive structural control. Proceeding of the 7th ICSV, CD ROM paper, Garmisch-Partenkirchen, Germany, 2000.
- [3] Liang S.G., Experiment study of torsionally structure vibration control using circular tuned liquid column dampers [J], Special structures. 1996, 13, 3, 33-35.
- [4] Ziegler F., Mechanics of Solids and Fluids, correct reprint of second edition, Springer, New York 1998.
- [5] MATLAB, User Guide, Control Toolbox. MathWorks Inc., Version 6.5.1, 2002.
- [6] Matlab, Signal Processing Toolbox, The MathWorks Inc., 1984-2001, campus licence TU-Wien.
- [7] Matlab, Simulink Version 3.0.1, The MathWorks Inc., 1984-2001, campus licence TU-Wien.
- [8] Huo, L.S., Li. H.N., Torsion-coupled response control of structure using circular tuned liquid column dampers, Engineering mechanics. 2005; 22, 2, 124-131.
- [9] Shum K.M., Xu Y.L., Multiple tuned liquid column dampers for reducing coupled lateral and torsional vibration of structures, Engineering structures. 2004; 26, 6, 745-758.
- [10] Ying Z.G., Ni Y.Q., Semi-active optimal control of linearized systems with multi-degree of freedom and application, Journal of sound and vibration. 2005; 279, 1-2, 373-388.
- [11] Huo L.S., Li H.N., Torsionally coupled response control of offshore platform structures using circular tuned liquid column dampers, China Ocean Engineering. 2004; 18, 2, 173-183.

4. Multi-storey Moderately Plan-asymmetric Space Frame with TLCGDs

4.1 Introduction

In Chapter 2, the simplest model of U-shaped TLCGD for suppressing coupled lateral and torsional vibrations of a 3-DOF single-storey moderately asymmetric building has been analyzed. The TLCGD-main system coupled equations have been formulated by substructure synthesis. Time-harmonic loading was applied to the system to analyze the dynamic performance of the 3DOF-structure. In this chapter the dynamic problem is extended to moderately asymmetric multi-storey space frames. Two-storey, three-storey and four-storey buildings are consecutively analyzed to demonstrate the design procedure and vibration control effectiveness of the proposed optimal TLCGDs. Modally tuned TLCGDs attached to the top floor of the structure control the movement of the structure during the strong motion phase of an earthquake. For higher order modes, however, a floor at intermediate height might become suitable. The root-mean square (RMS) responses¹ of the relative floor displacement and the floor accelerations under El Centro seismogram for a four-storey building are also illustrated. The RMS value is the square root of the mean-square value in a strong motion phase. These useful conclusions are obtained for guiding the positioning and the practical design of TLCGDs in the lateral and torsional vibration control.

4.2 Equation of motion for multi-storey moderately asymmetric space frame

The equation of motion are developed first for a simple multi-storey building, a two-storey space frame is selected to permit easy visualization of the direct method. Subsequently, a general formulation is presented for multi-storey buildings subjected to earthquake-induced ground motion.

4.2.1 Equation of motion for two-storey moderately asymmetric space frame

A two-storey moderately asymmetric space frame is considered with six DOFs and the positioning and optimal design of TLCGDs to minimize the lateral and torsional vibrations when excited by earthquakes are discussed. At first, we need to develop a model to accurately portray the equations of motion for the building while an earthquake is switched on.

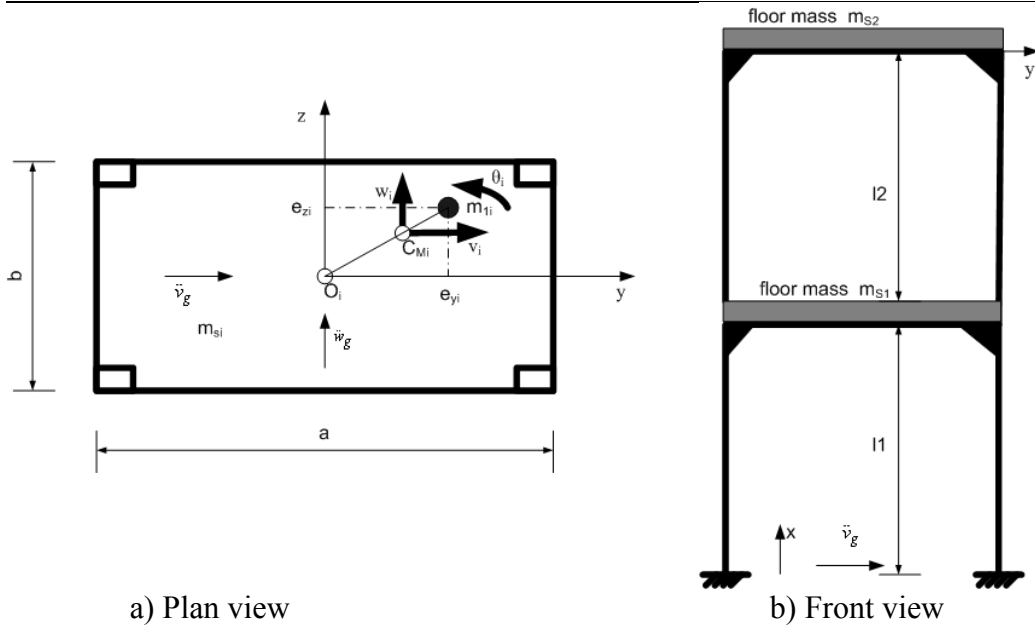


Fig. 4.1: Two-storey moderately asymmetric space frame.

A two-storey building with a rectangular base of the length a and the width b , is shown in Fig. 4.1, see also Fig.2.1. It consists of a homogenous floor of mass m_{S_i} ($i=1, 2$), which is supported by four symmetrically arranged clamped-clamped “massless” and inextensible columns in each corner. The columns have the same anisotropic stiffness k_{y_i} and k_{z_i} in y - and z -directions. Additional point masses m_{1_i} are attached off-center on the rigid floors, e_{y_i} and e_{z_i} denote their eccentricity. The height of the floor is l_i . Let \ddot{v}_g, \ddot{w}_g denote the free-field horizontal components of a seismic ground accelerations in y -, z -directions, while soil-structure interaction remains to be neglected. The origin of the moving frame in each floor is the center of mass C_{M_i} . The lateral displacements of C_{M_i} are denoted v_i and w_i , and θ_i is the rotational angle about the vertical x -axis. The positions of C_{M_i} may vary for the two floors. The coordinates of the center of mass C_{M_i} with respect to C_{S_i} and the geometric center are (Fig.4.1a)

$$y_{C_{M_i}} = \frac{m_{1_i}}{m_{S_i} + m_{1_i}} e_{y_i}, \quad z_{C_{M_i}} = \frac{m_{1_i}}{m_{S_i} + m_{1_i}} e_{z_i}.$$

(i) The stiffness matrix derived by the direct method: see e.g. Chopra¹, page 358

1) $v_1 = 1, w_1 = 0, u_{T1} = \theta_1 r_{S1} = 0$, 2) $v_1 = 0, w_1 = 1, u_{T1} = \theta_1 r_{S1} = 0$, 3) $v_1 = 0, w_1 = 0, u_{T1} = \theta_1 r_{S1} = 1$

First floor:

$$\begin{aligned} k_{y_1 y_1} &= 4(k_{y_1} + k_{y_2}) & k_{y_1 z_1} &= 0 & k_{y_1 \theta_1} &= 4(k_{y_1} + k_{y_2}) z_{C_{M1}} / r_{S1} \\ k_{z_1 y_1} &= 0 & k_{z_1 z_1} &= 4(k_{z_1} + k_{z_2}) & k_{z_1 \theta_1} &= -4(k_{z_1} + k_{z_2}) y_{C_{M1}} / r_{S1} \\ k_{\theta_1 y_1} &= 4(k_{y_1} + k_{y_2}) z_{C_{M1}} / r_{S1} & k_{\theta_1 z_1} &= -4(k_{z_1} + k_{z_2}) y_{C_{M1}} / r_{S1} \\ k_{\theta_1 \theta_1} &= \left[(k_{y_1} + k_{y_2}) b^2 + (k_{z_1} + k_{z_2}) a^2 + 4(k_{y_1} + k_{y_2}) z_{C_{M1}}^2 + 4(k_{z_1} + k_{z_2}) y_{C_{M1}}^2 \right] / r_{S1}^2 \end{aligned} \quad (4.1a)$$

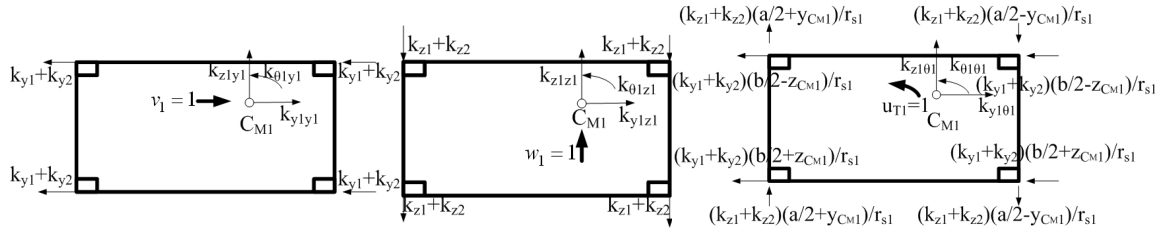


Fig. 4.2a: Evaluation of stiffness matrix of two-storey asymmetric space frame: restoring forces indicated.

Second floor:

$$\begin{aligned}
 k_{y2y1} &= -4k_{y2} & k_{y2z1} &= 0 & k_{y2\theta1} &= -4k_{y2}z_{CM1}/r_{S1} \\
 k_{z2y1} &= 0 & k_{z2z1} &= -4k_{z2} & k_{z2\theta1} &= 4k_{z2}y_{CM1}/r_{S1} \\
 k_{\theta2y1} &= -4k_{y2}z_{CM2}/r_{S2} & k_{\theta2z1} &= 4k_{z2}y_{CM2}/r_{S2} \\
 k_{\theta2\theta1} &= \left(-k_{y2}b^2 - k_{z2}a^2 - 4k_{y2}z_{CM1}z_{CM2} - 4k_{z2}y_{CM1}y_{CM2}\right)/r_{S1}r_{S2}
 \end{aligned} \quad (4.1b)$$

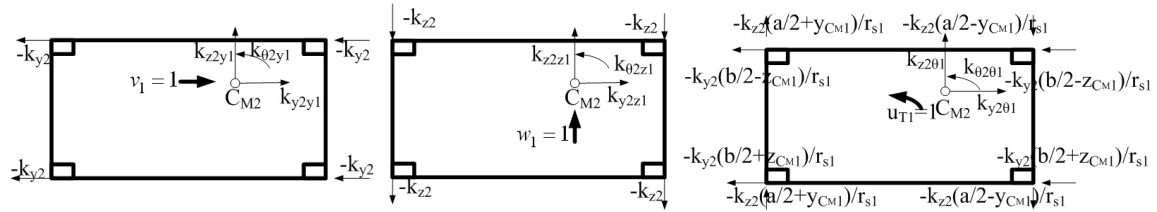


Fig. 4.2b: Evaluation of stiffness matrix of two-storey asymmetric space frame: restoring forces indicated.

4) $v_2 = 1, w_2 = 0, u_{T2} = \theta_2 r_{S2} = 0$, 5) $v_2 = 0, w_2 = 1, u_{T2} = \theta_2 r_{S2} = 0$, 6) $v_2 = 0, w_2 = 0, u_{T2} = \theta_2 r_{S2} = 1$

First floor:

$$\begin{aligned}
 k_{y1y2} &= -4k_{y2} & k_{y1z2} &= 0 & k_{y1\theta2} &= -4k_{y2}z_{CM2}/r_{S2} \\
 k_{z1y2} &= 0 & k_{z1z2} &= -4k_{z2} & k_{z1\theta2} &= 4k_{z2}y_{CM2}/r_{S2} \\
 k_{\theta1y2} &= -4k_{y2}z_{CM1}/r_{S1} & k_{\theta1z2} &= 4k_{z2}y_{CM1}/r_{S1} \\
 k_{\theta1\theta2} &= \left(-k_{y2}b^2 - k_{z2}a^2 - 4k_{y2}z_{CM1}z_{CM2} - 4k_{z2}y_{CM1}y_{CM2}\right)/r_{S1}r_{S2}
 \end{aligned} \quad (4.1c)$$

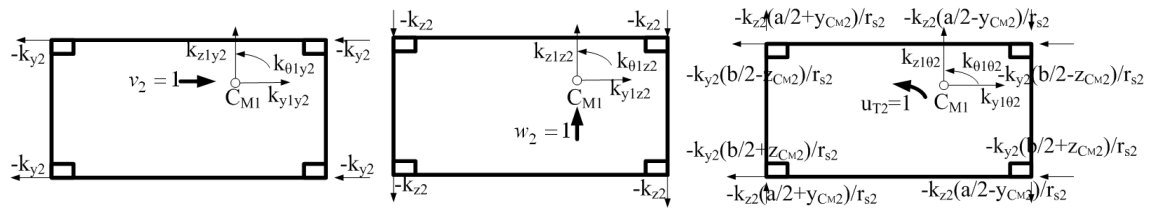


Fig. 4.2c: Evaluation of stiffness matrix of two-storey moderately asymmetric space frame: restoring forces indicated.

Second floor:

$$\begin{aligned}
 k_{y2y2} &= 4k_{y2} & k_{y2z2} &= 0 & k_{y2\theta2} &= 4k_{y2}z_{CM2}/r_{S2} \\
 k_{z2y2} &= 0 & k_{z2z2} &= 4k_{z2} & k_{z2\theta2} &= -4k_{z2}y_{CM2}/r_{S2} \\
 k_{\theta2y2} &= 4k_{y2}z_{CM2}/r_{S2} & k_{\theta2z2} &= -4k_{z2}y_{CM2}/r_{S2} \\
 k_{\theta2\theta2} &= \left(k_{y2}b^2 + k_{z2}a^2 + 4k_{y2}z_{CM2}^2 + 4k_{z2}y_{CM2}^2\right)/r_{S2}^2
 \end{aligned} \quad (4.1d)$$

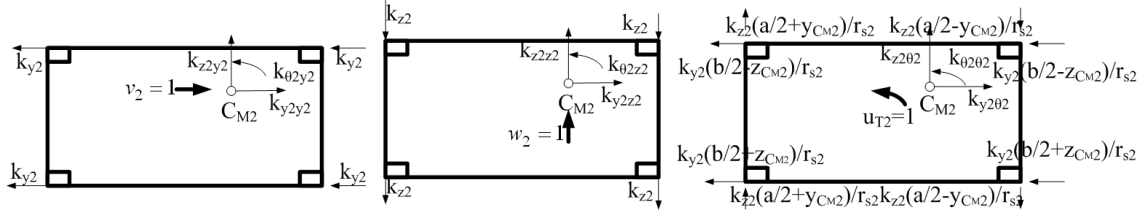


Fig. 4.2d: Evaluation of stiffness matrix of two-storey moderately asymmetric space frame: restoring forces indicated.

Here, the radius of inertia of the second floor $r_{S2} = \sqrt{I_{x2}/(m_{S2} + m_{12})}$, the total mass moment of inertia about the vertical x -axis is

$$I_{x2} = m_{S2}(a^2 + b^2)/12 + m_{S2}(y_{C_{M2}}^2 + z_{C_{M2}}^2) + m_{12} \left[(e_{y2} - y_{C_{M2}})^2 + (e_{z2} - z_{C_{M2}})^2 \right] = (m_{S2} + m_{12})r_{S2}^2$$

(ii) Mass matrix by the direct “stiffness method”:

1) $\dot{v}_1 = 1$, $\dot{w}_1 = 0$, $\dot{u}_{T1} = \dot{\theta}_1 r_{S1} = 0$, 2) $\dot{v}_1 = 0$, $\dot{w}_1 = 1$, $\dot{u}_{T1} = \dot{\theta}_1 r_{S1} = 0$, 3) $\dot{v}_1 = 0$, $\dot{w}_1 = 0$, $\dot{u}_{T1} = \dot{\theta}_1 r_{S1} = 1$

$$m_{y1y1} = m_{S1} + m_{11} \quad m_{z1z1} = m_{S1} + m_{11} \quad m_{\theta1\theta1} = m_{S1} + m_{11} \quad (4.2a)$$

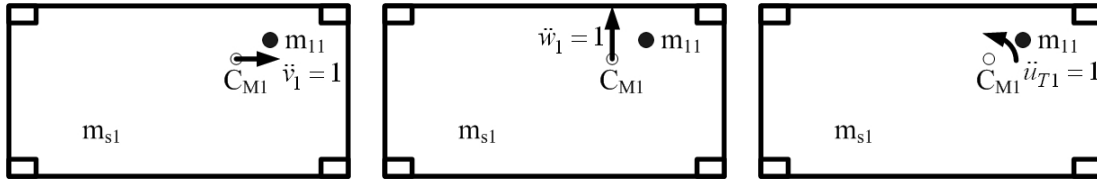


Fig. 4.3a: Evaluation of mass matrix of two-storey moderately asymmetric space frame: inertial forces indicated.

4) $\dot{v}_2 = 1$, $\dot{w}_2 = 0$, $\dot{u}_{T2} = \dot{\theta}_2 r_{S2} = 0$, 5) $\dot{v}_2 = 0$, $\dot{w}_2 = 1$, $\dot{u}_{T2} = \dot{\theta}_2 r_{S2} = 0$, 6) $\dot{v}_2 = 0$, $\dot{w}_2 = 0$, $\dot{u}_{T2} = \dot{\theta}_2 r_{S2} = 1$

$$m_{y2y2} = m_{S2} + m_{12} \quad m_{z2z2} = m_{S2} + m_{12} \quad m_{\theta2\theta2} = m_{S2} + m_{12} \quad (4.2b)$$

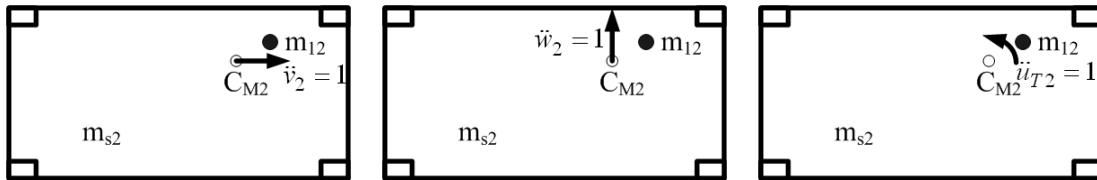


Fig. 4.3b: Evaluation of mass matrix of two-storey moderately asymmetric space frame: inertial forces indicated.

The equation of motion of the undamped two-storey mass asymmetric space frame are given in hypermatrix form, cf. Eq. (2.2),

$$\underline{M}\ddot{\bar{x}} + \underline{K}\bar{x} = -\underline{M}\ddot{\bar{x}}_g, \quad \bar{x}^T = [\bar{x}_1^T \quad \bar{x}_2^T], \quad \bar{x}_i^T = [v_i \quad w_i \quad u_{Ti}],$$

$$\ddot{\bar{x}}_g = \underline{E}_2 \ddot{\bar{x}}_g, \quad \ddot{\bar{x}}_g^T = [\ddot{v}_g \quad \ddot{w}_g \quad 0], \quad u_{Ti} = \theta_i r_{Si},$$

$$\underline{E}_2 = \begin{bmatrix} 1 & 0 & 0 & 1 & 0 & 0 \\ 0 & 1 & 0 & 0 & 1 & 0 \\ 0 & 0 & 0 & 0 & 0 & 0 \end{bmatrix}^T, \quad (4.3)$$

where $\underline{E}_2 = 6 \times 3$ is the influence matrix of the ground excitation for two-storey asymmetric space frame.

The diagonal mass- and the stiffness matrices of the six DOFs (degrees-of-freedom) space frame are deduced from Eqs. (4.1a)-(4.1d) and (4.2a)-(4.2b) by inspection

$$\underline{\mathbf{M}} = \text{diag}[\underline{\mathbf{M}}_1 \quad \underline{\mathbf{M}}_2], \quad (4.4)$$

where

$$\underline{\mathbf{k}}_{11} = 4 \begin{bmatrix} k_{y1} + k_{y2} & 0 & (k_{y1} + k_{y2})z_{C_{M1}}/r_{S1} \\ 0 & k_{z1} + k_{z2} & -(k_{z1} + k_{z2})y_{C_{M1}}/r_{S1} \\ (k_{y1} + k_{y2})z_{C_{M1}}/r_{S1} & -(k_{z1} + k_{z2})y_{C_{M1}}/r_{S1} & k_{\theta 1 \theta 1}/4 \end{bmatrix}, \quad (4.5)$$

$$\underline{\mathbf{k}}_{12} = 4 \begin{bmatrix} -k_{y2} & 0 & -k_{y2}z_{C_{M2}}/r_{S2} \\ 0 & -k_{z2} & k_{z2}y_{C_{M2}}/r_{S2} \\ -k_{y2}z_{C_{M1}}/r_{S1} & k_{z2}y_{C_{M1}}/r_{S1} & k_{\theta 1 \theta 2}/4 \end{bmatrix}, \quad (4.6)$$

$$\underline{\mathbf{k}}_{21} = 4 \begin{bmatrix} -k_{y2} & 0 & -k_{y2}z_{C_{M1}}/r_{S1} \\ 0 & -k_{z2} & k_{z2}y_{C_{M1}}/r_{S1} \\ -k_{y2}z_{C_{M2}}/r_{S2} & k_{z2}y_{C_{M2}}/r_{S2} & k_{\theta 2 \theta 1}/4 \end{bmatrix}, \quad (4.7)$$

$$\underline{\mathbf{k}}_{22} = 4 \begin{bmatrix} k_{y2} & 0 & k_{y2}z_{C_{M2}}/r_{S2} \\ 0 & k_{z2} & -k_{z2}y_{C_{M2}}/r_{S2} \\ k_{y2}z_{C_{M2}}/r_{S2} & -k_{z2}y_{C_{M2}}/r_{S2} & k_{\theta 1 \theta 1}/4 \end{bmatrix}, \quad (4.8)$$

and $\underline{\mathbf{K}} = \begin{bmatrix} \underline{\mathbf{k}}_{11} & \underline{\mathbf{k}}_{12} \\ \underline{\mathbf{k}}_{21} & \underline{\mathbf{k}}_{22} \end{bmatrix}$ is possibly unsymmetric in its stiffness hypermatrix form,

$$\underline{\mathbf{M}}_i = \text{diag}[m_{si} + m_{1i} \quad m_{si} + m_{1i} \quad m_{si} + m_{1i}] = 3 \times 3 \quad \text{mass submatrix, } i=1,2.$$

4.2.2 Equation of motion for N-storey moderately asymmetric space frame

The equation of motion of the undamped N-storey moderately asymmetric space frame are given in hypermatrix form, cf. Eq. (4.3),

$$\underline{\mathbf{M}}\ddot{\bar{\mathbf{x}}} + \underline{\mathbf{K}}\bar{\mathbf{x}} = -\underline{\mathbf{M}}\ddot{\bar{\mathbf{x}}}_{gN}, \quad \bar{\mathbf{x}}^T = [\bar{x}_1^T \cdots \bar{x}_i^T \cdots \bar{x}_N^T], \quad \bar{x}_i^T = [v_i \quad w_i \quad u_{Ti}], \quad u_{Ti} = \theta_i r_{Si},$$

$$\ddot{\bar{\mathbf{x}}}_{gN} = \underline{\mathbf{E}}_N \ddot{\bar{\mathbf{x}}}_g, \quad \ddot{\bar{\mathbf{x}}}_g^T = [\ddot{v}_g \quad \ddot{w}_g \quad 0], \quad \underline{\mathbf{E}}_N = \begin{bmatrix} 1 & 0 & 0 & 1 & 0 & 0 & 1 & \cdots \\ 0 & 1 & 0 & 0 & 1 & 0 & 0 & \cdots \\ 0 & 0 & 0 & 0 & 0 & 0 & 0 & \cdots \end{bmatrix}^T, \quad (4.9)$$

where $\underline{\mathbf{M}}$ is the mass matrix of the structure, $\underline{\mathbf{K}}$ its stiffness matrix, both are positive definite; $\bar{\mathbf{x}}$ is the displacement vector of the floors, $\underline{\mathbf{E}}_N = 3N \times 3$ is the influence matrix of the ground excitation for N-storey structure see Eq. (4.1) and $\ddot{\bar{\mathbf{x}}}_g$ denotes the seismic ground acceleration vector, respectively.

The mass matrix $\underline{\mathbf{M}}$ of the system with dimension of $3N \times 3N$, derived by the direct “stiffness method” referring to 3 DOFs becomes, see e.g. Chopra¹, page 358

$$\underline{\mathbf{M}} = \text{diag}[\underline{\mathbf{M}}_1 \cdots \underline{\mathbf{M}}_i \cdots \underline{\mathbf{M}}_N], \quad (4.10)$$

The stiffness matrix $\underline{\mathbf{K}}$ of the system with dimension of $3N \times 3N$, derived by the direct method becomes with, referring to 3 DOFs

$$\begin{aligned}
 \underline{\underline{M}}^* \ddot{\bar{x}} + \underline{\underline{K}}^* \bar{x} &= -\underline{\underline{M}}^* \ddot{\bar{x}}_{gN} + \bar{P}^*, \quad \underline{\underline{M}}^* = \text{diag} \left[\underline{\underline{M}}_1^* \cdots \underline{\underline{M}}_1^* \cdots \underline{\underline{M}}_N^* \right] = 3N \times 3N, \\
 \bar{x}^T &= \left[\bar{x}_1^T \cdots \bar{x}_i^T \cdots \bar{x}_N^T \right], \quad \bar{x}_i^T = [v_i \quad w_i \quad u_{Ti}], \quad \ddot{\bar{x}}_{gN} = \underline{\underline{E}}_N \ddot{\bar{x}}_g, \quad \ddot{\bar{x}}_g^T = [\ddot{v}_g \quad \ddot{w}_g \quad 0], \\
 \underline{\underline{E}}_N &= \begin{bmatrix} 1 & 0 & 0 & 1 & 0 & 0 & 1 & \cdots \\ 0 & 1 & 0 & 0 & 1 & 0 & 0 & \cdots \\ 0 & 0 & 0 & 0 & 0 & 0 & 0 & \cdots \end{bmatrix}^T, \quad \bar{P}^{*T} = -[0, \cdots, F_{Aiy}^*, F_{Aiz}^*, M_{xi}^*/r_{Si}, \cdots, 0], \\
 F_{Aiy}^* &= m_A^* \left[\ddot{v}_g + \ddot{v}_i - (z_{Aij} - z_{C_Mi}) \ddot{u}_{Ti} / r_{Si} \right] + m_A^* \ddot{u}^* \cos \gamma, \\
 F_{Aiz}^* &= m_A^* \left[\ddot{w}_g + \ddot{w}_i + (y_{Aij} - y_{C_Mi}) \ddot{u}_{Ti} / r_{Si} \right] + m_A^* \ddot{u}^* \sin \gamma, \\
 M_{Aix}^* &= 0, \quad M_{xi}^* = M_{Aix}^* - F_{Aiy}^* (z_{Aij} - z_{C_Mi}) + F_{Aiz}^* (y_{Aij} - y_{C_Mi}). \tag{4.16}
 \end{aligned}$$

If the floor displacements \bar{x} are expanded into modal displacements $\bar{x} = \sum_{j=1}^N \bar{\phi}_j q_j$ on the left hand side, Eq. (4.16) decouples on the left hand side for all classically damped systems by pre-multiplication with the transposed $\bar{\phi}_j^T$ and when divided by m_j^* becomes

$$\ddot{q}_j + \omega_{Sj}^{*2} q_j = -\frac{\bar{\phi}_j^T \underline{\underline{M}}^*}{m_j^*} \ddot{\bar{x}}_{gN} + \frac{\bar{\phi}_j^T}{m_j^*} \bar{P}^*, \quad \omega_{Sj}^{*2} = \frac{\bar{\phi}_j^T \underline{\underline{K}}^* \bar{\phi}_j}{m_j^*}, \quad j = 1, \cdots, N. \tag{4.17}$$

Isolated modal displacement $v_i = q_j \phi_{j(3i-2)}$, $w_i = q_j \phi_{j(3i-1)}$, $u_{Ti} = r_{Si} \theta_i = q_j \phi_{j3i}$ are substituted in the control forces and on the right hand side of the TMD equation. Inserting the coupling forces \bar{P}^* into Eq. (4.17) renders the approximated equation of the selected mode,

$$\begin{aligned}
 \left(1 + \mu_j^*\right) \ddot{q}_j + \omega_{Sj}^{*2} q_j + \frac{m_{Aj}^*}{m_j^*} \left(v_{Ai,j} \cos \gamma + w_{Ai,j} \sin \gamma \right) \ddot{u}^* &= -\frac{1}{m_j^*} \left(\sum_{n=1}^N m_{Sn}^* \phi_{j(3n-2)} + m_{Aj}^* v_{Ai,j} \right) \ddot{v}_g \\
 &\quad - \frac{1}{m_j^*} \left(\sum_{n=1}^N m_{Sn}^* \phi_{j(3n-1)} + m_{Aj}^* w_{Ai,j} \right) \ddot{w}_g, \\
 \mu_j^* &= \frac{m_{Aj}^*}{m_j^*} V_{ij}^{*2}, \quad V_{ij}^{*2} = v_{Ai,j}^2 + w_{Ai,j}^2,
 \end{aligned}$$

$$v_{Ai,j} = \phi_{j(3i-2)} - \phi_{j3i} (z_{Aij} - z_{C_Mi}) / r_{Si}, \quad w_{Ai,j} = \phi_{j(3i-1)} + \phi_{j3i} (y_{Aij} - y_{C_Mi}) / r_{Si}, \tag{4.18}$$

where $v_{Ai,j}$ and $w_{Ai,j}$ denote the modal displacements of reference point A_i in y - and z -directions, respectively. Further the approximated linearized equation of motion of TMD in the i -th storey is, Eq.(2.92) properly generalized,

$$\ddot{u}^* + 2\zeta_{Aj}^* \omega_{Aj}^* \dot{u}^* + \omega_{Aj}^{*2} u^* = -\left(v_{Ai,j} \cos \gamma + w_{Ai,j} \sin \gamma \right) \ddot{q}_j - \bar{r}_S^T \ddot{\bar{x}}_g, \quad \bar{r}_S^T = [\cos \gamma \quad \sin \gamma \quad 0]. \tag{4.19}$$

With light structural damping of the main system added, the coupled modal equations of motion of the main system with TMD attached, in matrix notation in the above mentioned approximation become, natural frequencies must be well separated,

$$\begin{bmatrix} 1 + \mu_j^* & (v_{Ai,j} \cos \gamma + w_{Ai,j} \sin \gamma) m_{Aj}^* / m_j^* \\ (v_{Ai,j} \cos \gamma + w_{Ai,j} \sin \gamma) & 1 \end{bmatrix} \begin{bmatrix} \ddot{q}_j \\ \ddot{u}^* \end{bmatrix} + \begin{bmatrix} 2\zeta_{Sj}^* \omega_{Sj}^* & 0 \\ 0 & 2\zeta_{Aj}^* \omega_{Aj}^* \end{bmatrix} \begin{bmatrix} \dot{q}_j \\ \dot{u}^* \end{bmatrix} + \begin{bmatrix} \omega_{Sj}^{*2} & 0 \\ 0 & \omega_{Aj}^{*2} \end{bmatrix} \begin{bmatrix} q_j \\ u^* \end{bmatrix} = - \begin{bmatrix} \bar{L}_j^{*T} / m_j^* \\ \bar{r}_S^T \end{bmatrix} \ddot{x}_g \quad (4.20)$$

where the generalized participation factors are

$$\bar{L}_j^{*T} = \begin{bmatrix} L_{jy}^* & L_{jz}^* & 0 \end{bmatrix}, \quad L_{jy}^* = \sum_{n=1}^N m_{Sn}^* \phi_{j(3n-2)} + m_{Aj}^* v_{Ai,j}, \quad L_{jz}^* = \sum_{n=1}^N m_{Sn}^* \phi_{j(3n-1)} + m_{Aj}^* w_{Ai,j}.$$

4.3.2 TLCGD attached on the i -th floor

A single TLCGD is installed on the i -th floor of N -storey moderately plan-asymmetric space frame with the general angle γ to y -direction, reference point A ($y_A, z_A, 0$). The equation of motion for the coupled undamped main-system can be given in hypermatrix form, cf. Eq. (2.94),

$$\begin{aligned} \underline{M} \ddot{\bar{x}} + \underline{K} \bar{x} &= -\underline{M} \ddot{x}_{gN} + \bar{P}, \quad \bar{P}^T = -\begin{bmatrix} 0, \dots, F_{Aiy}, F_{Aiz}, M_{xi}/r_{Si}, \dots, 0 \end{bmatrix}, \\ F_{Aiy} &= m_f \left[\ddot{v}_g + \ddot{v}_i - (z_{Aij} - z_{C_M i}) \ddot{u}_{Ti} / r_{Si} \right] + \bar{\kappa} m_f \ddot{u} \cos \gamma, \\ F_{Aiz} &= m_f \left[\ddot{w}_g + \ddot{w}_i - (y_{Aij} - y_{C_M i}) \ddot{u}_{Ti} / r_{Si} \right] + \bar{\kappa} m_f \ddot{u} \sin \gamma, \\ M_{Aix} &= m_f \bar{\kappa}_3 H^2 \ddot{u}_{Ti} / r_{Si}, \quad M_{xi} = M_{Aix} - F_{Aiy} (z_{Aij} - z_{C_M i}) + F_{Aiz} (y_{Aij} - y_{C_M i}). \end{aligned} \quad (4.21)$$

If the floor displacements \bar{x} are expanded into modal displacements $\bar{x} = \sum_{j=1}^N \bar{\phi}_j q_j$ on the left hand side, Eq. (4.21) decouples on the left hand side for all classically damped systems by pre-multiplication with the transposed modal vector $\bar{\phi}_j^T$ and when divided by the modal mass m_j becomes

$$\ddot{q}_j + \omega_{Sj}^2 \bar{q}_j = -\frac{\bar{\phi}_j^T \underline{M}}{m_j} \ddot{x}_{gN} + \frac{\bar{\phi}_j^T \bar{P}}{m_j}, \quad \omega_{Sj}^2 = \frac{\bar{\phi}_j^T \underline{K} \bar{\phi}_j}{m_j}. \quad (4.22)$$

Inserting the linearized coupling forces \bar{P} into Eq. (4.22) renders the approximated equation of the selected mode,

$$\begin{aligned} (1 + \mu_j) \ddot{q}_j + \omega_{Sj}^2 q_j + \frac{m_{ff}}{m_j} \bar{\kappa} (v_{Ai,j} \cos \gamma + w_{Ai,j} \sin \gamma) \ddot{u} &= -\frac{1}{m_j} \left[\sum_{n=1}^N (m_{Sn} + m_{1n}) \phi_{j(3n-2)} + m_{ff} v_{Ai,j} \right] \ddot{v}_g \\ &\quad - \frac{1}{m_j} \left[\sum_{n=1}^N (m_{Sn} + m_{1n}) \phi_{j(3n-2)} + m_{ff} w_{Ai,j} \right] \ddot{w}_g \\ \mu_j &= \frac{m_{ff}}{m_j} V_{ij}^2, \quad V_{ij}^2 = V_{ij}^{*2} + \bar{\kappa}_3 \left(\phi_{j3i} H / r_{Si} \right)^2. \end{aligned} \quad (4.23)$$

Here, V_{ij}^{*2} is given by Eq. (4.18). Light structural modal damping of the main system is added and the approximated linearized equation of motion of TLCGD is considered

$$\ddot{u} + 2\zeta_{Aj} \omega_{Aj} \dot{u} + \omega_{Aj}^2 u = -\kappa (v_{Ai,j} \cos \gamma + w_{Ai,j} \sin \gamma) \ddot{q}_j - \kappa \bar{r}_S^T \ddot{x}_g. \quad (4.24)$$

In matrix form the linearized coupled system of modal equations of the main system with TLCGD attached becomes, within the approximation discussed above

$$\begin{bmatrix} 1 + \mu_j & \bar{\kappa} (v_{Ai,j} \cos \gamma + w_{Ai,j} \sin \gamma) m_{ff} / m_j \\ \kappa (v_{Ai,j} \cos \gamma + w_{Ai,j} \sin \gamma) & 1 \end{bmatrix} \begin{bmatrix} \ddot{q}_j \\ \ddot{u} \end{bmatrix} + \begin{bmatrix} 2\zeta_{Sj} \omega_{Sj} & 0 \\ 0 & 2\zeta_{Aj} \omega_{Aj} \end{bmatrix} \begin{bmatrix} \dot{q}_j \\ \dot{u} \end{bmatrix} + \begin{bmatrix} \omega_{Sj}^2 & 0 \\ 0 & \omega_{Aj}^2 \end{bmatrix} \begin{bmatrix} q_j \\ u \end{bmatrix} = - \begin{bmatrix} \bar{L}_j^T / m_j \\ \kappa \bar{\Gamma}_S^T \end{bmatrix} \ddot{x}_g \quad (4.25)$$

where the generalized participation factors are

$$\bar{L}_j^T = \begin{bmatrix} L_{jy} & L_{jz} & 0 \end{bmatrix}, \quad L_{jy} = \sum_{n=1}^N (m_{Sn} + m_{1n}) \phi_{j(3n-2)} + m_{ff} v_{Ai,j},$$

$$L_{jz} = \sum_{n=1}^N (m_{Sn} + m_{1n}) \phi_{j(3n-1)} + m_{ff} w_{Aj},$$

and $\bar{\Gamma}_S$ is the same as defined in Eq. (4.19).

4.3.3 Analogy between TMD and TLCGD when attached to N-storey space frame

Comparing the approximated modal equations of motion for coupled system consisting of an N-storey structure, see Section 2.8 for single-storey, the result about the relationship μ_j^* and μ_j , the optimal absorber tuning ratio δ_{jopt} and the damping ratio are exactly the same as in the single-storey structure discussed above Eqs. (2.102)- (2.104) are still valid when generalized by adding the storey number, subscript i where appropriate.

4.4 Two-storey moderately asymmetric space frame: numerical example

The two-storey mass asymmetric structure is considered as a numerical example. The mass of each floor is $16 \times 10^3 \text{ kg}$. The additional point mass on the second floor $m_{12} = 8 \times 10^3 \text{ kg}$ is also considered to be placed in the upper right corner A_1 , Fig.4.1. The common stiffness of columns in y - and z -directions of each storey calculated by Eq. (2.10) $k_{yi} = 2242.8 \text{ kN/m}$ and $k_{zi} = 788.68 \text{ kN/m}$. The identical storey heights are 4m, and proper static dimensioning of elastic columns is performed in Subsection 4.4.1. The mass moment of inertia about the vertical x -axis of the second floor is calculated: $I_{x2} = 213.33 \times 10^3 \text{ kg} \cdot \text{m}^2$, $r_{S2} = 2.98 \text{ m}$. The other properties of the building are listed in Section 2.9.

4.4.1 Static dimensioning and a static safety criterion of the columns

The critical load of a steel profile HEB-200 with respect to the weak axis of buckling becomes $F_c = -2592.027 \text{ kN}$. The combined load without TLCGD of the second floor at point A_1 is $F_{12} = -206.922 \text{ kN}$ and that at points A_2, A_3, A_4 $F_{22} = -100.974 \text{ kN}$. The combined load without TLCGD of the first floor at point A_1 is $F_{11} = -387.357 \text{ kN}$ and that at points A_2, A_3, A_4 $F_{21} = -201.948 \text{ kN}$. Thus $\frac{F_{11}}{F_c} = \frac{-387.357}{-2592.027} = 0.15 < \frac{1}{3}$, consequently, a geometric correction of the stiffness is applicable.

The corrected stiffness at point A₁ in *y*-direction becomes:

$$\bar{k}_{y1} = \begin{bmatrix} 2k_y & -k_y \\ -k_y & k_y \end{bmatrix} - \frac{6}{5} \begin{bmatrix} \frac{F_{21}}{l_1} & -\frac{F_{22}}{l_1} \\ -\frac{F_{22}}{l_1} & \frac{F_{22}}{l_1} \end{bmatrix} = \begin{bmatrix} 4369.3929 & -2180.7234 \\ -2180.7234 & 2180.7234 \end{bmatrix} kN/m.$$

The corrected stiffness at point A₁ in *z*-direction becomes:

$$\bar{k}_{z1} = \begin{bmatrix} 2k_z & -k_z \\ -k_z & k_z \end{bmatrix} - \frac{6}{5} \begin{bmatrix} \frac{F_{21}}{l_1} & -\frac{F_{22}}{l_1} \\ -\frac{F_{22}}{l_1} & \frac{F_{22}}{l_1} \end{bmatrix} = \begin{bmatrix} 1461.1529 & -726.6034 \\ -726.6034 & 726.6034 \end{bmatrix} kN/m.$$

The corrected stiffness at points A₂, A₃, and A₄ in *y*-direction becomes:

$$\bar{k}_{y2} = \bar{k}_{y3} = \bar{k}_{y4} = \begin{bmatrix} 2k_y & -k_y \\ -k_y & k_y \end{bmatrix} - \frac{6}{5} \begin{bmatrix} \frac{F_{11}}{l_1} & -\frac{F_{12}}{l_1} \\ -\frac{F_{12}}{l_1} & \frac{F_{12}}{l_1} \end{bmatrix} = \begin{bmatrix} 4425.0156 & -2212.5078 \\ -2212.5078 & 2212.5078 \end{bmatrix} kN/m.$$

The corrected stiffness at points A₂, A₃, and A₄ in *z*-direction becomes:

$$\bar{k}_{z2} = \bar{k}_{z3} = \bar{k}_{z4} = \begin{bmatrix} 2k_z & -k_z \\ -k_z & k_z \end{bmatrix} - \frac{6}{5} \begin{bmatrix} \frac{F_{11}}{l_1} & -\frac{F_{12}}{l_1} \\ -\frac{F_{12}}{l_1} & \frac{F_{12}}{l_1} \end{bmatrix} = \begin{bmatrix} 1516.7756 & -758.3878 \\ -758.3878 & 758.3878 \end{bmatrix} kN/m.$$

4.4.2 Natural modes of the main structure

The natural frequencies computed by means of Matlab 7.0² become 1.07, 1.78, 2.21, 2.88, 4.78 and 5.83 Hz. Columns are assumed to be massless. The orthonormalized modal matrix of the undamped main system with respect to \underline{M} is the output of Matlab 7.0².

$$\tilde{\phi} = 10^{-2} \begin{bmatrix} 0.017391 & 0.279390 & 0.193230 & -0.023691 & 0.491810 & -0.310500 \\ -0.328010 & 0.067991 & -0.083310 & 0.569980 & 0.076364 & 0.068429 \\ -0.061186 & -0.173220 & 0.278960 & 0.125340 & -0.307540 & -0.482380 \\ 0.033474 & 0.473310 & 0.292630 & 0.021224 & -0.273560 & 0.174940 \\ -0.550020 & 0.071957 & -0.047072 & -0.321480 & -0.043216 & -0.039274 \\ -0.103430 & -0.290130 & 0.465720 & -0.012174 & 0.161860 & 0.280270 \end{bmatrix}.$$

Correction of this output of orthonormalized eigenvectors might become necessary with respect to orthogonality, see also Section 2.9.2. However, test calculations render sufficient accuracy,

$$\begin{aligned} \delta_{11} &= 1, & \delta_{12} &= 1.8 \times 10^{-16}, & \delta_{13} &= 1.7 \times 10^{-16}, & \delta_{14} &= 5.4 \times 10^{-17}, & \delta_{15} &= -7.6 \times 10^{-17}, \\ \delta_{16} &= -3.6 \times 10^{-16}, & \delta_{21} &= 1.94 \times 10^{-16}, & \delta_{22} &= 1, & \delta_{23} &= -1.11 \times 10^{-16}, & \delta_{24} &= -1.3 \times 10^{-16}, \\ \delta_{25} &= -5.27 \times 10^{-16}, & \delta_{26} &= 5.55 \times 10^{-17}, & \delta_{31} &= 1.7 \times 10^{-16}, & \delta_{32} &= 0, & \delta_{33} &= 1, & \delta_{34} &= -8.67 \times 10^{-18}, \\ \delta_{35} &= 5.55 \times 10^{-17}, & \delta_{36} &= 0, & \delta_{41} &= -8.7 \times 10^{-19}, & \delta_{42} &= -1.4 \times 10^{-12}, & \delta_{43} &= -5.2 \times 10^{-18}, & \delta_{44} &= 1, \\ \delta_{45} &= -7.5 \times 10^{-17}, & \delta_{46} &= -2.12 \times 10^{-16}, & \delta_{51} &= -9.7 \times 10^{-17}, & \delta_{52} &= -5.3 \times 10^{-16}, & \delta_{53} &= 1.11 \times 10^{-16}, \\ \delta_{54} &= -6.16 \times 10^{-17}, & \delta_{55} &= 1, & \delta_{56} &= -2.22 \times 10^{-16}, & \delta_{61} &= -3.75 \times 10^{-16}, & \delta_{62} &= 5.55 \times 10^{-17}, \\ \delta_{63} &= 0, & \delta_{64} &= -2.12 \times 10^{-16}, & \delta_{65} &= -1.53 \times 10^{-16}, & \delta_{66} &= 1. \end{aligned}$$

The six mode shapes of the two-storey asymmetric space frame are illustrated in the scaled Figure 4.4-4.9, the modal centers of velocity of first floor \odot , that of second floor \ominus . In the first mode the two floors displace in z -direction. In the second and third mode the floors displace obliquely in y - and z -directions and rotate in the same direction. In the fourth mode, the two floors displace in opposite z -directions. The motion in the fifth and sixth mode consists of oblique translational motions in opposite y - and z -directions with opposite torsional motions.

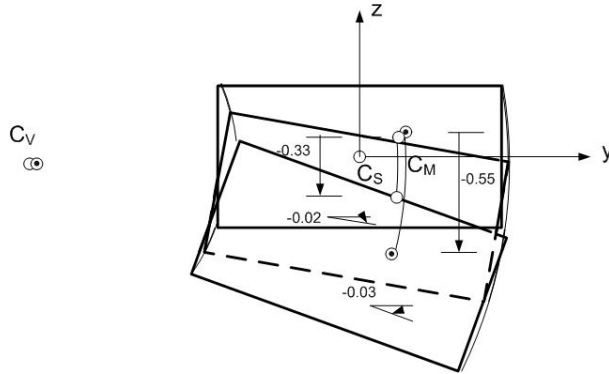


Fig. 4.4: First mode $f_1 = 1.07Hz$.

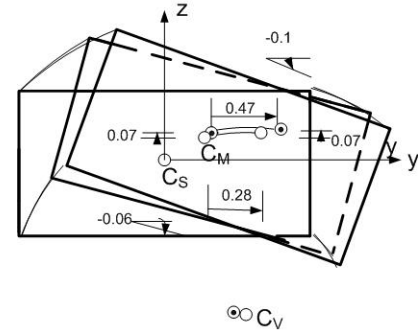


Fig. 4.5: Second mode $f_2 = 1.78Hz$.

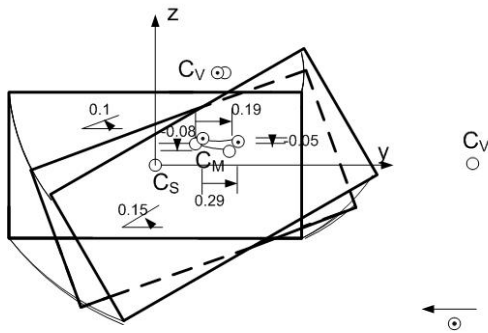


Fig. 4.6: Third mode $f_3 = 2.21Hz$.

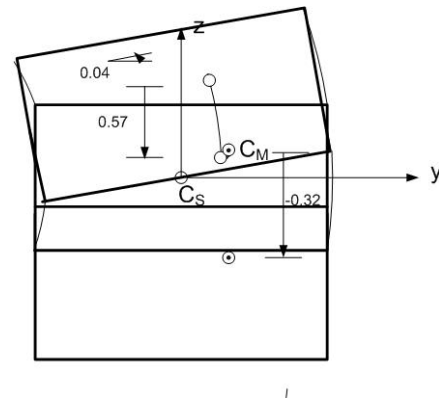


Fig. 4.7: Forth mode $f_4 = 2.88Hz$.

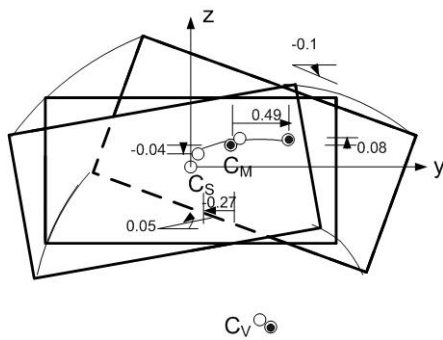


Fig. 4.8: Fifth mode $f_5 = 4.78Hz$.

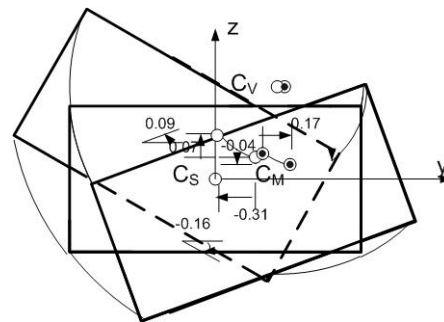


Fig. 4.9: Sixth mode $f_6 = 5.83Hz$.

4.4.3 Position of the modal centers of velocity C_V

The coordinates of the modal centers of velocity C_V with corrected column stiffness taken into account are defined by Eq. (2.18), all fall outside of the floor plan.

mode	1	2	3	4	5	6
Floor 1	(-14.83,-0.30)	(2.26,-4.24)	(1.98,2.60)	(-12.41,-0.02)	(1.83,-4.20)	(1.51,2.46)
Floor 2	(-14.52,-0.30)	(2.07,-4.20)	(1.63,2.54)	(-77.40,-4.53)	(2.13,-4.37)	(1.75,2.53)

Table 4.1: The coordinates of the centers of velocity C_V for six modes.

(i) Installation of the TLCGDs

Three tuned liquid column gas dampers are placed on the top floor to counteract the first three natural modes, since the numerical study shows that higher modes are not remarkably excited by the earthquakes. For the first mode TLCGD1 is installed in the middle. TLCGD2 is installed along the long side suppressing the second mode and TLCGD3 on the short side tuned to the third mode, according to Fig. 4.10 and the positions of the relevant centers of velocity are considered.

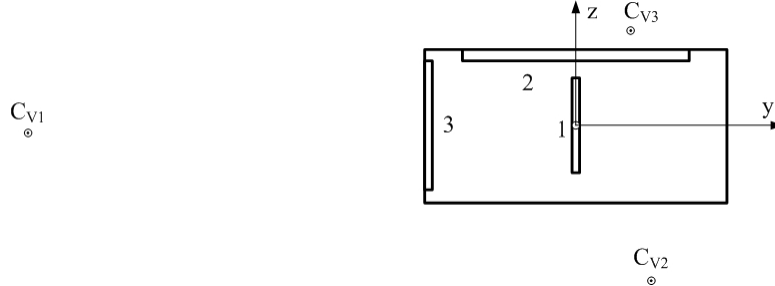


Fig. 4.10: Installation of TLCGD1, 2, 3, ● the modal centers of velocity of top floor.

4.4.4 TLCGD design, Den Hartog' optimization

The fluid mass is chosen as $m_{f1} = 1160\text{kg}$, $m_{f2} = 480\text{kg}$ and $m_{f3} = 160\text{kg}$ of water. Dimensions of the three TLCGDs tuned at first by means of the TMD analogy Eqs. (2.102)-(2.104), applying Den Hartog's formulas are summarized in Table 4.2.

	TLCGD1	TLCGD2	TLCGD3
Horizontal length of the liquid column B [m]	3.00	3.00	3.00
Inclined length of the liquid column H [m]	2.00	1.00	0.80
Cross-sectional area of the pipe [m ²] $A_H=A_B$	0.1660	0.0960	0.0350
Effective length $L_{eff} = L_1 = 2H + B$ [m], Eq. (2.34a)	7.00	5.00	4.60
Angle of the inclined pipe section β [rad]	$\pi/4$	$\pi/4$	$\pi/4$
Equivalent mathematical pendulum length L_0 [m], Eq. (2.37)	0.23	0.08	0.05
Geometry factor $\kappa = \bar{\kappa}$, Eqs. (2.34a), (2.44)	0.833	0.883	0.898
Geometry factor $\bar{\kappa}_3$, Eq. (2.59)	0.80	1.84	2.51
Equilibrium pressure head h_0 [m], $n=1.2$, Eq. (2.34a)	51.37	57.49	67.20
Gas volume $V_0 = A_H H_a$ [m ³], Eq. (2.38)	0.587000	0.183000	0.054000
The mass ratio of the TLCGD-main system μ , Eq. (2.97)	3%	2%	1.55%
The mass ratio of the equivalent TMD-main system μ^* , Eq. (2.102)	2.02%	1.51%	1.20%
Natural frequency $f_{A,opt}$ [Hz] Eq. (2.104), (2.112)	1.04	1.75	2.18
Optimal linear damping %, Eq. (2.113)	8.62	7.46	6.67

Table 4.2: Layout of the modally tuned TLCGDs, gas volume and gas equilibrium pressure assigned, cf. Fig. (4.10).

The modal dynamic magnification factor (DMF) calculated with Matlab 7.0², linearized damping of the TLCGD considered, is illustrated in Figure 4.11.

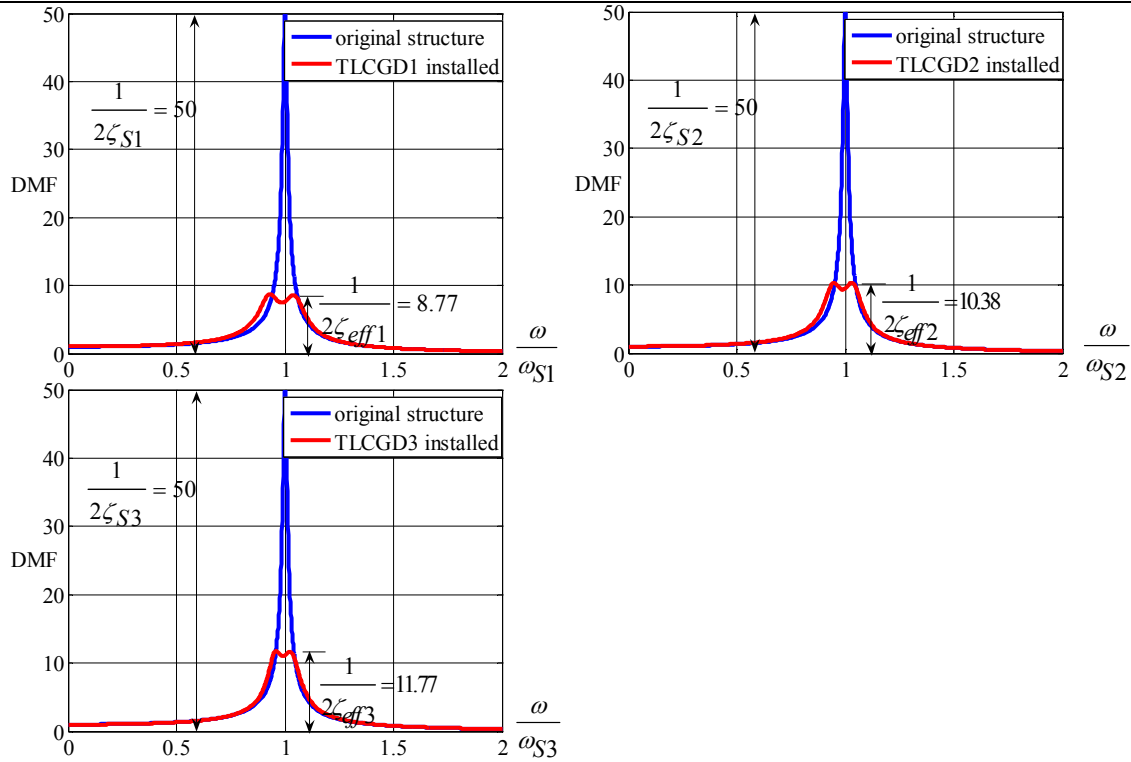


Fig. 4.11: Individual frequency response curves without and with linearized TLCGDs attached, TLCGDs with Den Hartog's optimal parameters.

The effective modal damping coefficients of the system is increased from 1% to $\zeta_{eff1} = 5.7\%$, $\zeta_{eff2} = 4.82\%$ and $\zeta_{eff3} = 4.25\%$. The results of all maximum structural and liquid response with varying angles of attack of the time-harmonic excitation are given in Table 4.3a-c. The maximum fluid displacements are within the acceptable limits, $u_0 < H_a/3$ (of linearized gas compression) and $u_0 < H/2$. The maximum fluid velocities of three TLCGDs are calculated by Eq. (2.35) 6.06, 5.40 and 5.18m/s and are within the acceptable speed limit.

Forcing direction	structure						TLCGD1	
	v_1 [mm]	w_1 [mm]	$u_{T1} = r_{S1}\theta_1$ [mm]	v_2 [mm]	w_2 [mm]	$u_{T2} = r_{S2}\theta_2$ [mm]		
$\alpha = 0$	0	-7	-1	C_{M2}	1	-12	-2	49
				A	0	-11		
$\alpha = \pi/6$	3	-62	-12	C_{M2}	6	-104	-20	422
				A	2	-95		
$\alpha = \pi/4$	5	-91	-17	C_{M2}	9	-153	-29	622
				A	3	-140		
$\alpha = \pi/3$	6	-115	-21	C_{M2}	12	-192	-36	779
				A	4	-176		
$\alpha = \pi/2$	7	-137	-26	C_{M2}	14	-229	-43	928
				A	4	-210		
$\alpha = 2\pi/3$	6	-122	-23	C_{M2}	12	-205	-39	828
				A	4	-188		
$\alpha = 3\pi/4$	5	-102	-19	C_{M2}	10	-171	-32	690
				A	3	-157		
$\alpha = 5\pi/6$	4	-75	-14	C_{M2}	8	-125	-24	506
				A	2	-115		

Table 4.3a: Maximum displacements of two-storey structure in the first mode from time-harmonic excitation in α -directions, $a_0=0.1g$, $r_{S1} = 2.97m$, $r_{S2} = 2.98m$.

Forcing direction	structure						TLCGD2	
	v_1 [mm]	w_1 [mm]	$u_{T1} = r_{S1}\theta_1$ [mm]	v_2 [mm]	w_2 [mm]	$u_{T2} = r_{S2}\theta_2$ [mm]		
$\alpha = 0$	41	10	-26	C_{M2}	70	11	-43	491
				A	89	30		
$\alpha = \pi/6$	39	10	-24	C_{M2}	67	10	-41	468
				A	85	28		
$\alpha = \pi/4$	34	8	-21	C_{M2}	58	9	-36	408
				A	74	25		
$\alpha = \pi/3$	27	7	-17	C_{M2}	46	7	-28	320
				A	58	20		
$\alpha = \pi/2$	7	2	-5	C_{M2}	13	2	-8	87
				A	16	5		
$\alpha = 2\pi/3$	14	3	-9	C_{M2}	24	4	-15	171
				A	31	10		
$\alpha = 3\pi/4$	24	6	-15	C_{M2}	41	6	-25	286
				A	52	17		
$\alpha = 5\pi/6$	32	8	-20	C_{M2}	54	8	-33	382
				A	69	23		

Table 4.3b: Maximum displacements of two-storey structure in the second mode from time-harmonic excitation in α -directions, $a_0=0.1g$, $r_{S1} = 2.97m$, $r_{S2} = 2.98m$.

Forcing direction	structure						TLCGD3	
	v_1 [mm]	w_1 [mm]	$u_{T1} = r_{S1}\theta_1$ [mm]	v_2 [mm]	w_2 [mm]	$u_{T2} = r_{S2}\theta_2$ [mm]		
$\alpha = 0$	13	-6	19	C_{M2}	20	-3	31	369
				A	27	-59		
$\alpha = \pi/6$	10	-4	14	C_{M2}	14	-2	23	274
				A	20	-43		
$\alpha = \pi/4$	7	-3	10	C_{M2}	10	-2	17	199
				A	14	-31		
$\alpha = \pi/3$	4	-2	5	C_{M2}	6	-1	9	112
				A	8	-17		
$\alpha = \pi/2$	4	-2	6	C_{M2}	6	-1	10	123
				A	8	-18		
$\alpha = 2\pi/3$	10	-4	14	C_{M2}	15	-2	24	287
				A	20	-45		
$\alpha = 3\pi/4$	12	-5	17	C_{M2}	18	-3	29	344
				A	24	-54		
$\alpha = 5\pi/6$	13	-6	19	C_{M2}	20	-3	32	378
				A	27	-60		

Table 4.3c: Maximum displacements of the two-storey structure in the third mode from time-harmonic excitation in α -directions, $a_0=0.1g$, $r_{S1} = 2.97m$, $r_{S2} = 2.98m$.

4.4.5 Optimization of the two-storey space frame with 3TLCGDs in the state space domain

The fine tuned optimal natural frequencies and damping ratios by calling the function *fminsearch* of the performance index J , Eq. (2.123), are found to be $f_{A1} = 1.04Hz$, $f_{A2} = 1.71Hz$, $f_{A3} = 2.08Hz$, $\zeta_{A1} = 7.64\%$, $\zeta_{A2} = 5.70\%$, $\zeta_{A3} = 5.95\%$. The equilibrium pressure head h_0 of three TLCGDs are thus changed accordingly to 48.61, 53.21 and 59.84m. Figs. 4.12-4.19 illustrate the weighed sum of the frequency response function $\sum_{i=1}^{12} s_i |z_{Si}(v)|$, $\zeta = \text{diag}(10,10,10,10,10,10,1,1,1,1,1,1)$ of the building states for the original

and the optimized system under various angles of attack, in the logarithmic decibel scale within the relevant frequency window $0 \leq f \leq 3\text{Hz}$. The resonance curves with fine-tuning optimal parameters have broader peaks.

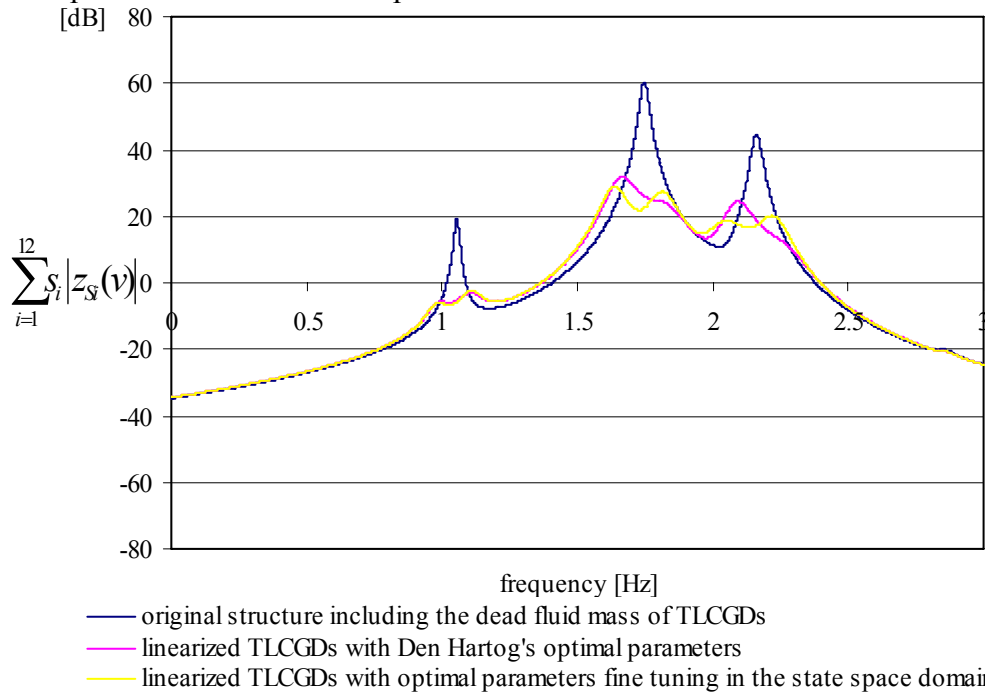


Fig. 4.12: Weighed sum of amplitude response functions for the 6-DOF linearized, two-storey, moderately asymmetric space frame with three linearized TLCGDs attached and without the TLCGDs (angle of attack of the time-harmonic base acceleration $\alpha = 0$), maximum gain 31.6dB.

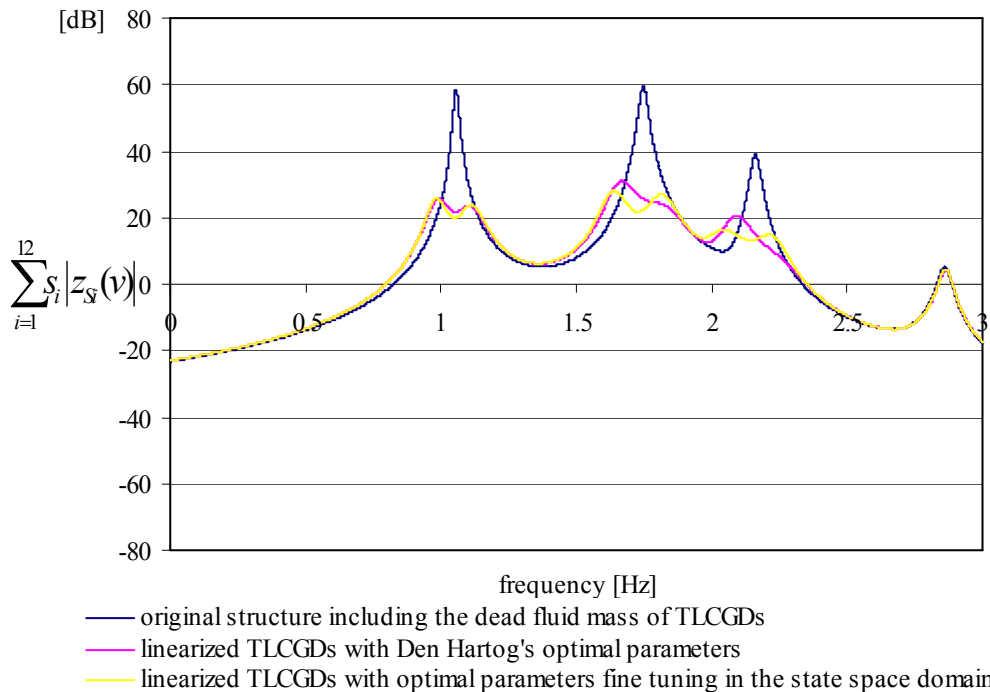


Fig. 4.13: Weighed sum of amplitude response functions for the 6-DOF linearized, two-storey, moderately asymmetric space frame with three linearized TLCGDs attached and without the TLCGDs (angle of attack of the time-harmonic base acceleration $\alpha = \pi/6$), maximum gain 31.4dB.

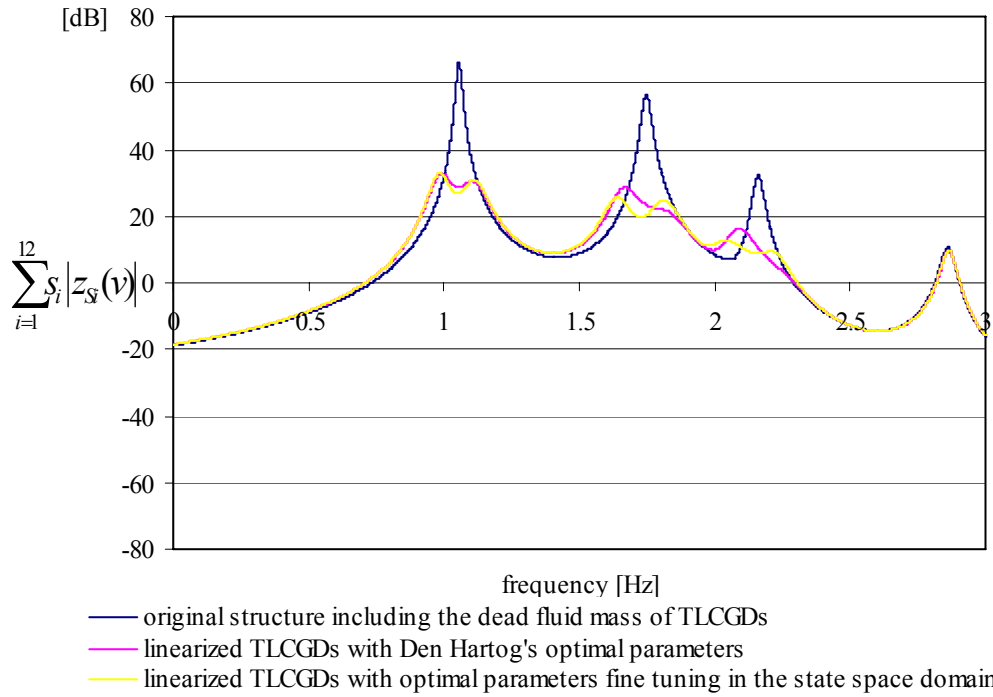


Fig. 4.14: Weighed sum of amplitude response functions for the 6-DOF linearized, two-storey, moderately asymmetric space frame with three linearized TLCGDs attached and without the TLCGDs (angle of attack of the time-harmonic base acceleration $\alpha = \pi/4$), maximum gain 33.5dB.

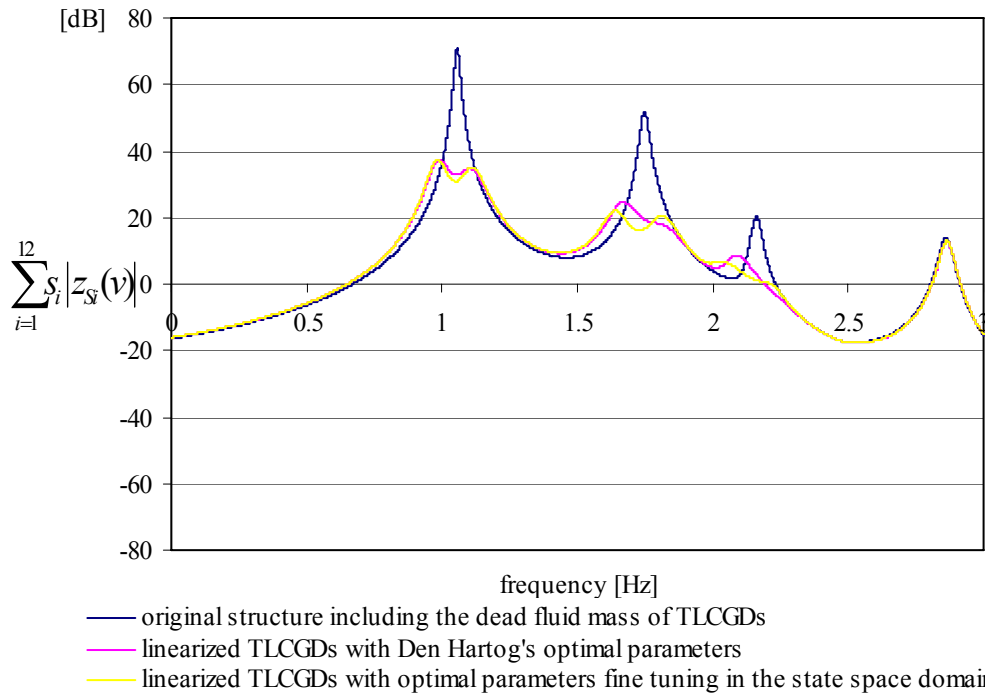


Fig. 4.15: Weighed sum of amplitude response functions for the 6-DOF linearized, two-storey, moderately asymmetric space frame with three linearized TLCGDs attached and without the TLCGDs (angle of attack of the time-harmonic base acceleration $\alpha = \pi/3$), maximum gain 33.7dB.

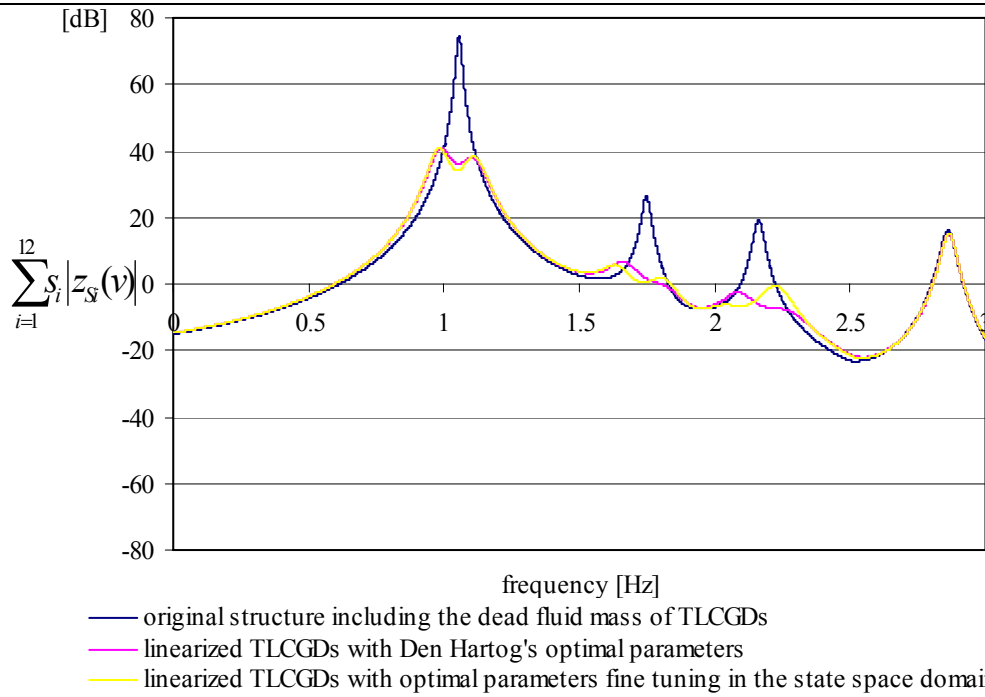


Fig. 4.16: Weighed sum of amplitude response functions for the 6-DOF linearized, two-storey, moderately asymmetric space frame with three linearized TLCGDs attached and without the TLCGDs (angle of attack of the time-harmonic base acceleration $\alpha = \pi/2$), maximum gain 33.6dB.

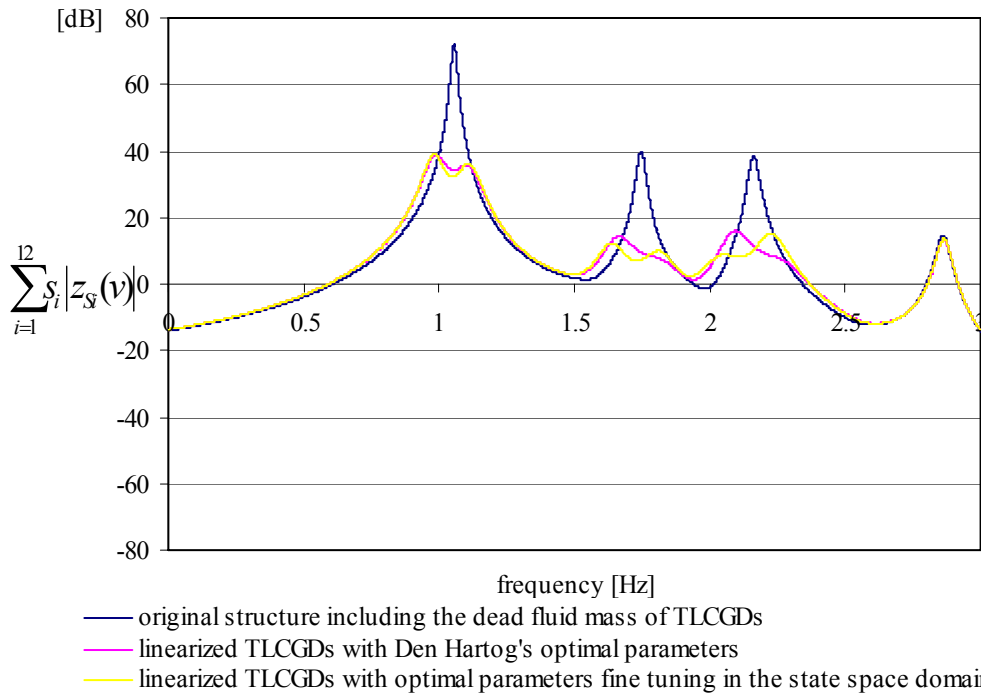


Fig. 4.17: Weighed sum of amplitude response functions for the 6-DOF linearized, two-storey, moderately asymmetric space frame with three linearized TLCGDs attached and without the TLCGDs (angle of attack of the time-harmonic base acceleration $\alpha = 2\pi/3$), maximum gain 33.4dB.

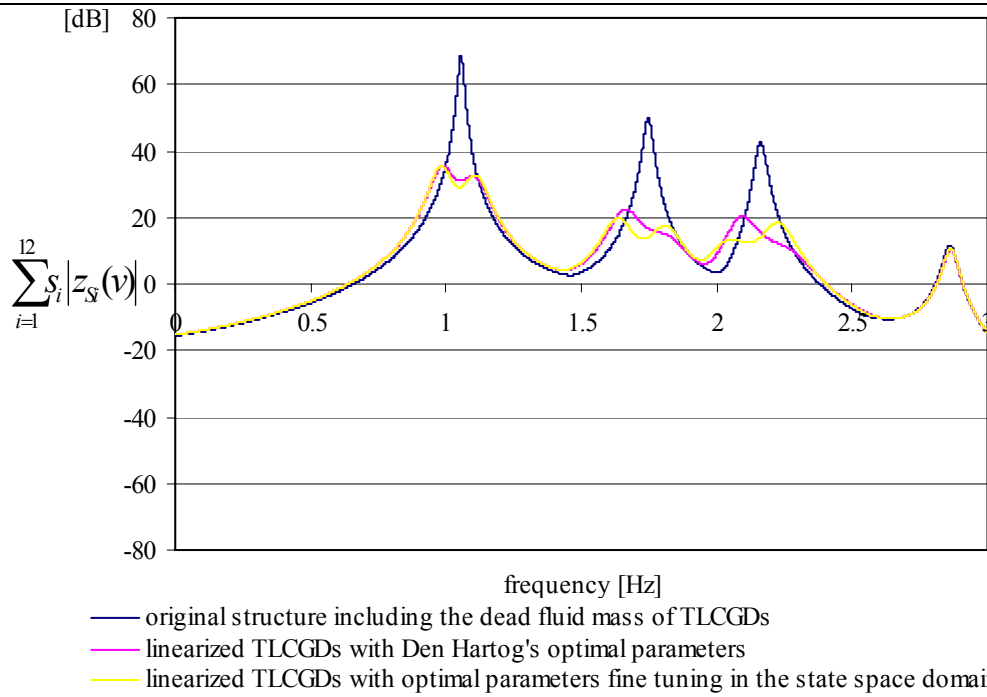


Fig. 4.18: Weighed sum of amplitude response functions for the 6-DOF linearized, two-storey, moderately asymmetric space frame with three linearized TLCGDs attached and without the TLCGDs (angle of attack of the time-harmonic base acceleration $\alpha = 3\pi/4$), maximum gain 33.1dB.

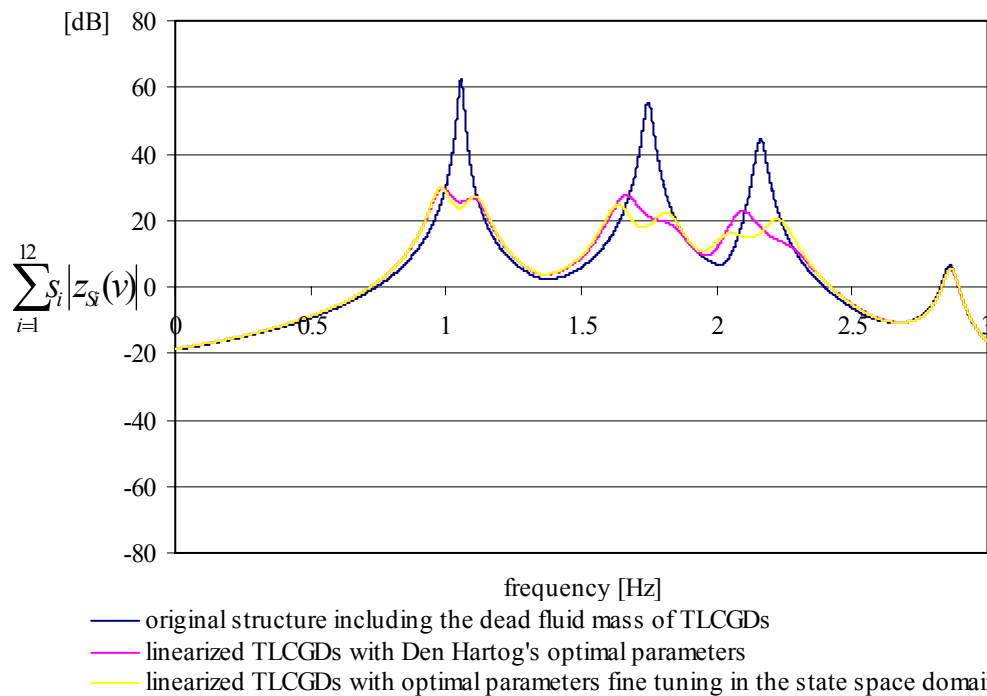


Fig. 4.19: Weighed sum of amplitude response functions for the 6-DOF linearized, two-storey, moderately asymmetric space frame with three linearized TLCGDs attached and without the TLCGDs (angle of attack of the time-harmonic base acceleration $\alpha = 5\pi/6$), maximum gain 32.7dB.

From inspection of figures 4.20-4.27 it is apparent that the maximum relative fluid displacements for all cases are well within the acceptable limits. The maximum fluid velocities of three TLCGDs are calculated by Eq. (2.35) 6.86, 6.45 and 6.53m/s and are also within the acceptable speed limit.

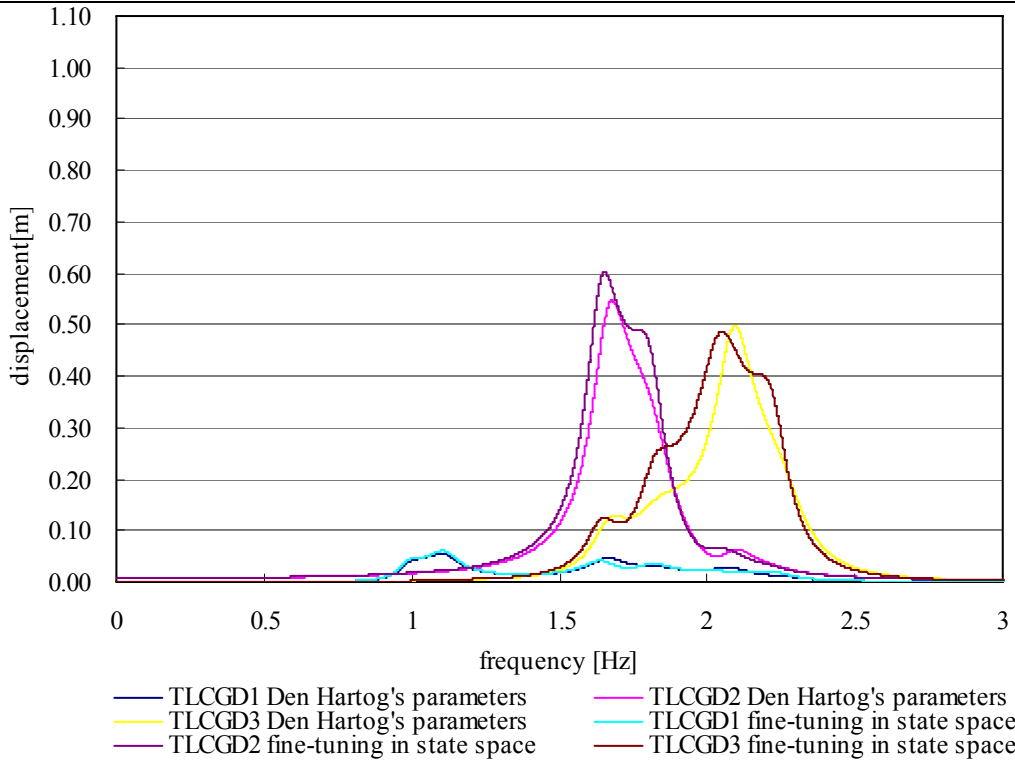


Fig. 4.20: Amplitude response curves of fluid displacement $|u|$ of three linearized TLCGDs attached to the two-storey moderately asymmetric space frame. TLCGDs either with Den Hartog's optimal parameters or those resulting from fine-tuning in state space ($\alpha = 0$).

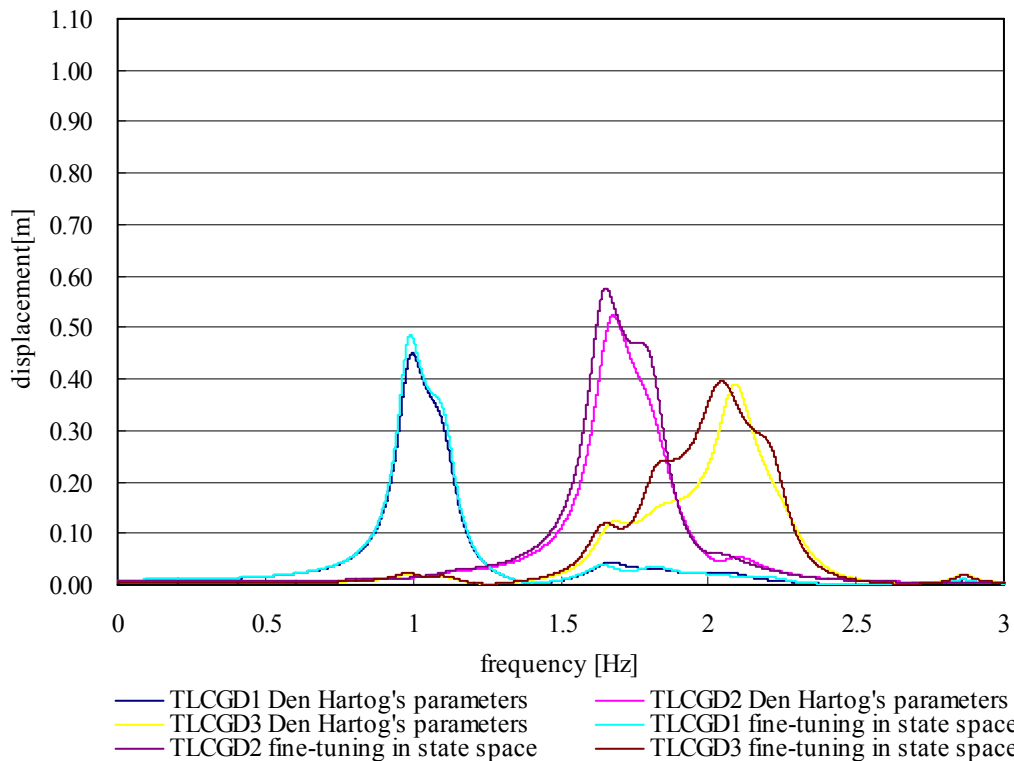


Fig. 4.21: Amplitude response curves of fluid displacement $|u|$ of three linearized TLCGDs attached to the two-storey moderately asymmetric space frame. TLCGDs either with Den Hartog's optimal parameters or those resulting from fine-tuning in state space ($\alpha = \pi/6$).

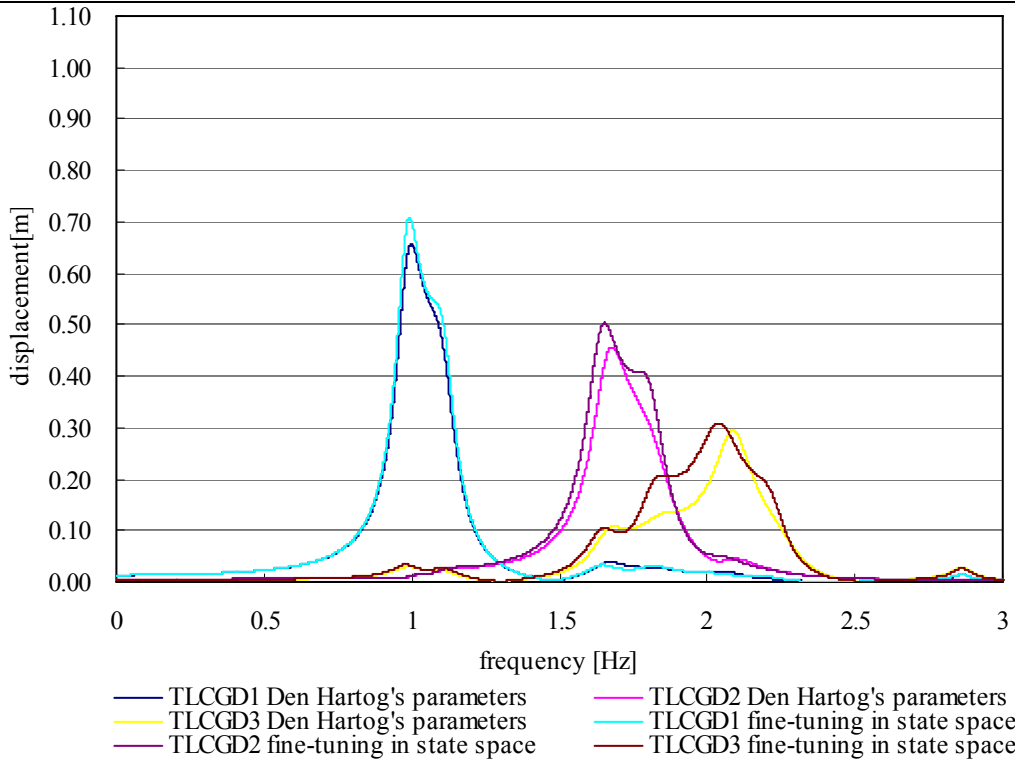


Fig. 4.22: Amplitude response curves of fluid displacement $|u|$ of three linearized TLCGDs attached to the two-storey moderately asymmetric space frame. TLCGDs either with Den Hartog's optimal parameters or those resulting from fine-tuning in state space ($\alpha = \pi/4$).

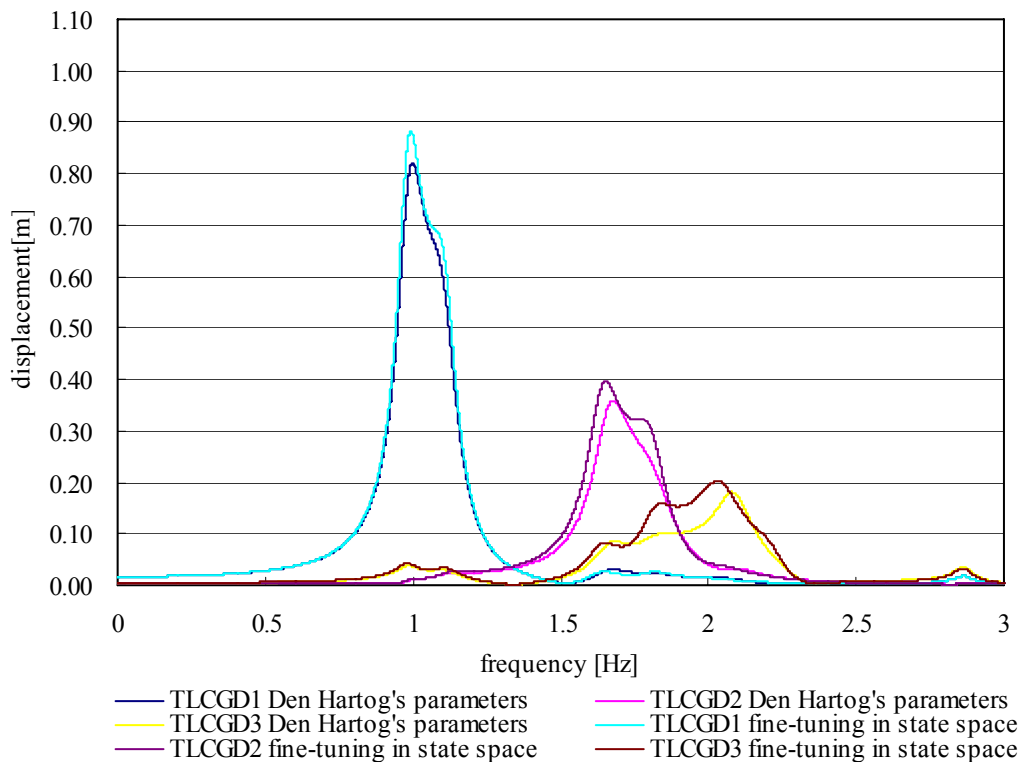


Fig. 4.23: Amplitude response curves of fluid displacement $|u|$ of three linearized TLCGDs attached to the two-storey moderately asymmetric space frame. TLCGDs either with Den Hartog's optimal parameters or those resulting from fine-tuning in state space ($\alpha = \pi/3$).

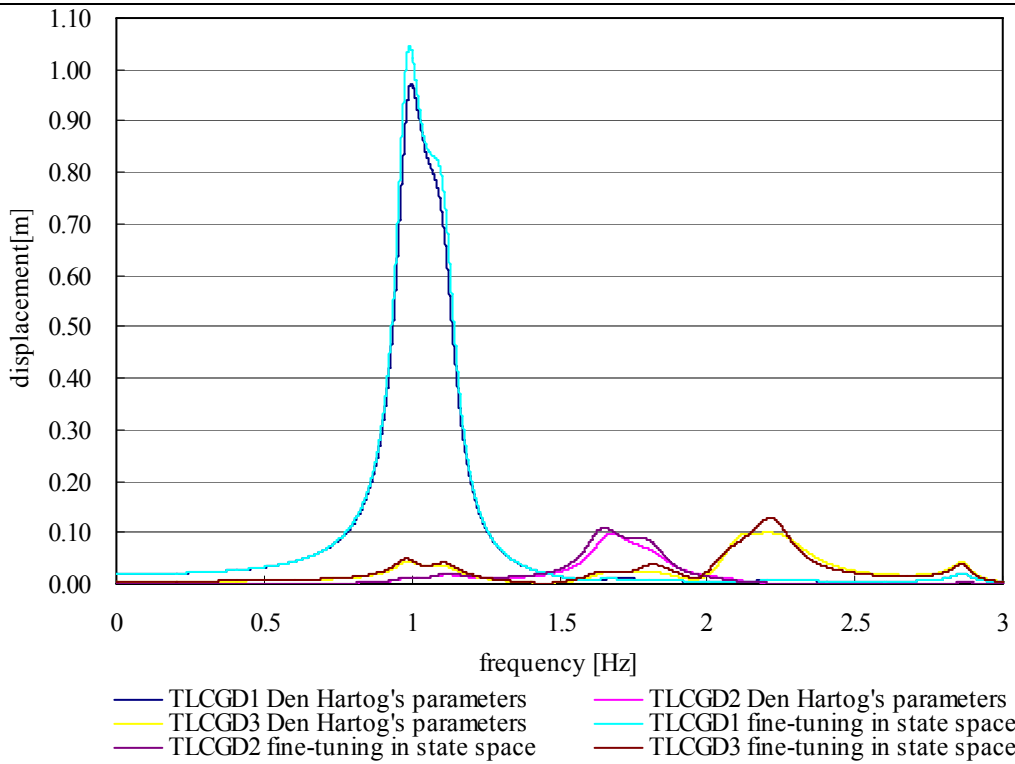


Fig. 4.24: Amplitude response curves of fluid displacement $|u|$ of three linearized TLCGDs attached to the two-storey moderately asymmetric space frame. TLCGDs either with Den Hartog's optimal parameters or those resulting from fine-tuning in state space ($\alpha = \pi/2$).

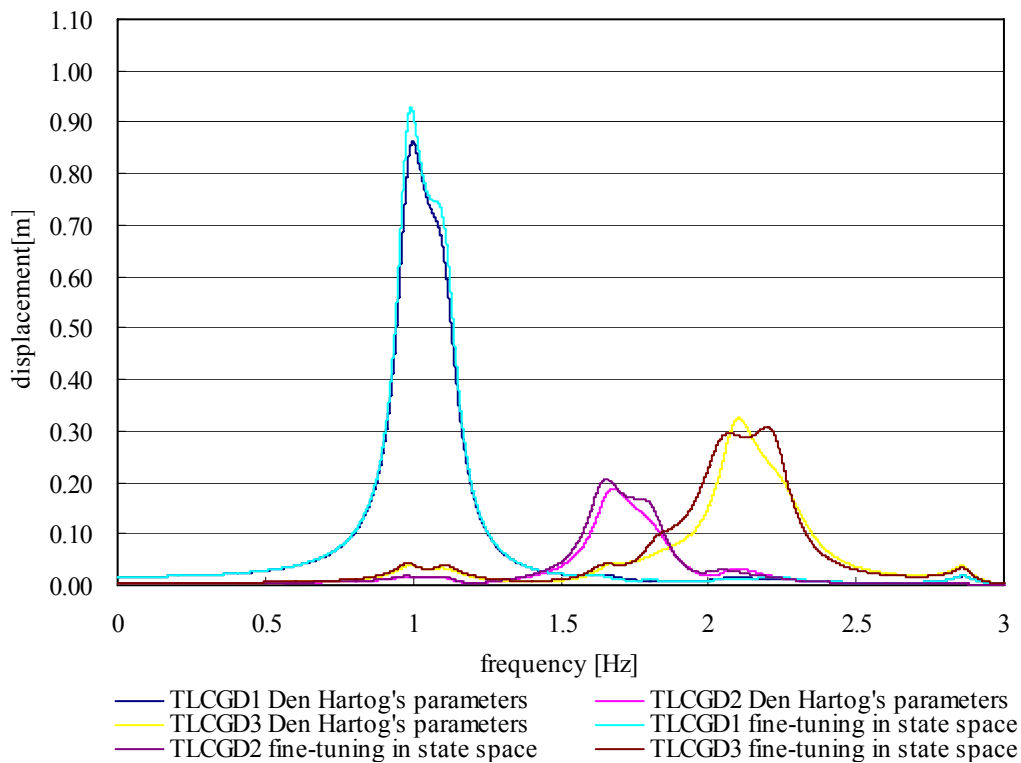


Fig. 4.25: Amplitude response curves of fluid displacement $|u|$ of three linearized TLCGDs attached to the two-storey moderately asymmetric space frame. TLCGDs either with Den Hartog's optimal parameters or those resulting from fine-tuning in state space ($\alpha = 2\pi/3$).

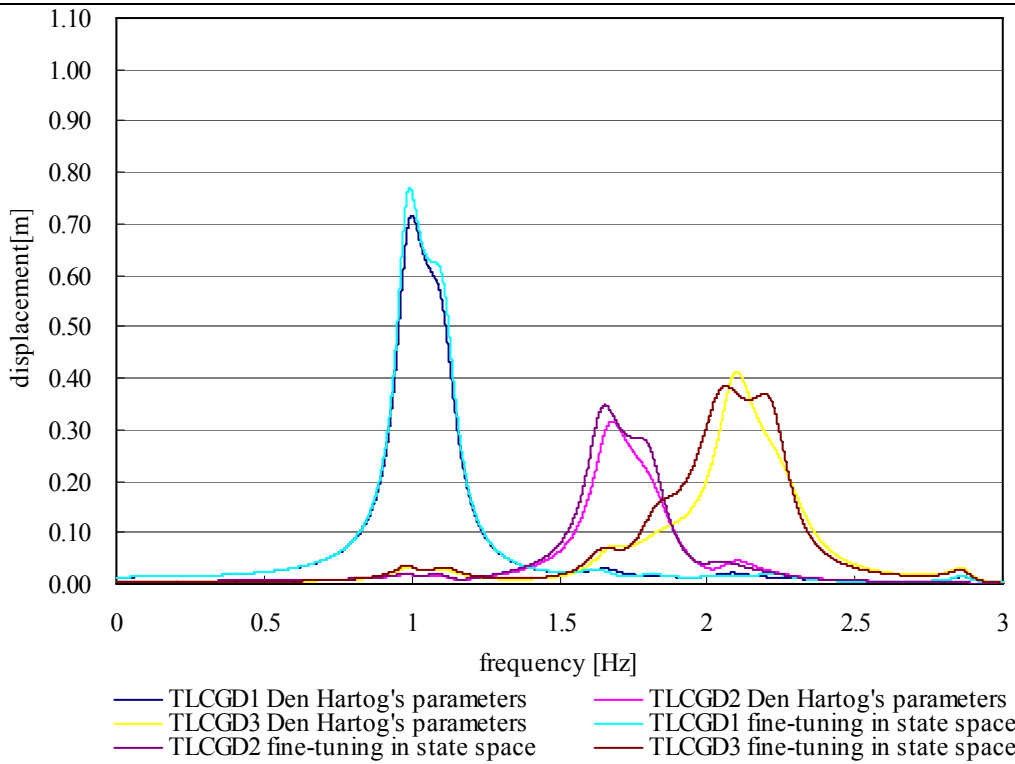


Fig. 4.26: Amplitude response curves of fluid displacement $|u|$ of three linearized TLCGDs attached to the two-storey moderately asymmetric space frame. TLCGDs either with Den Hartog's optimal parameters or those resulting from fine-tuning in state space ($\alpha = 3\pi/4$).

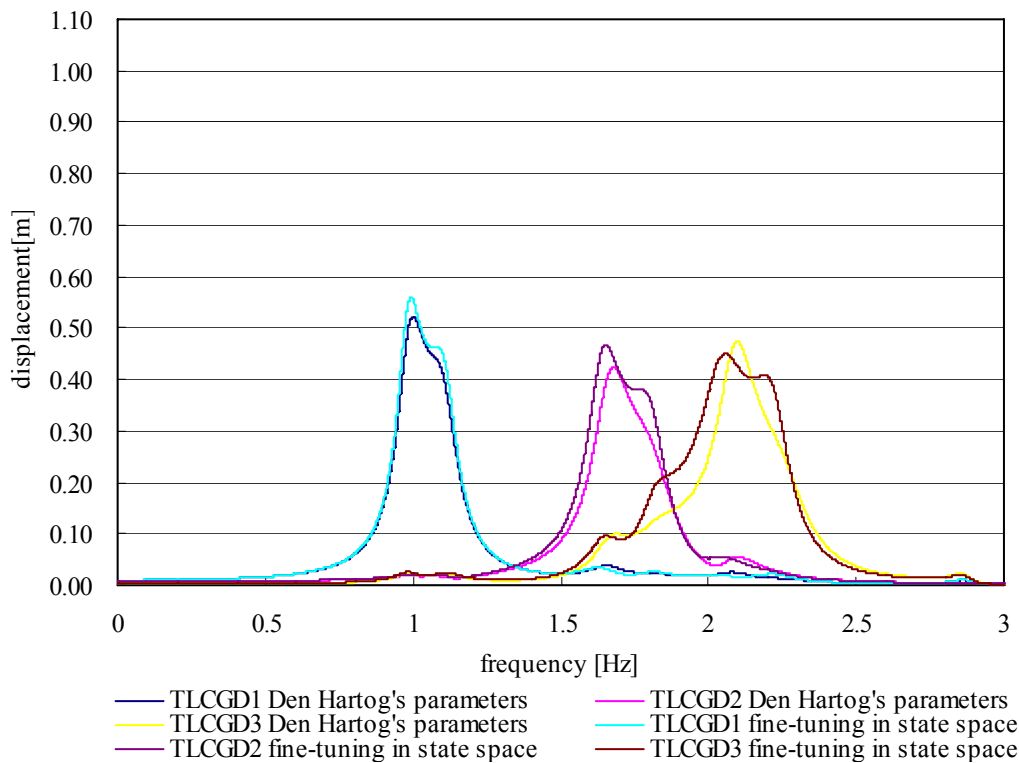


Fig. 4.27: Amplitude response curves of fluid displacement $|u|$ of three linearized TLCGDs attached to the two-storey moderately asymmetric space frame. TLCGDs either with Den Hartog's optimal parameters or those resulting from fine-tuning in state space ($\alpha = 5\pi/6$).

The wall thickness and the estimated dead mass of the piping system are listed in Table

4.4 for the three absorbers, designed according to Table 4.2.

	TLCGD1	TLCGD2	TLCGD3
h_0 [m]	51.37	57.49	67.20
H_a [m]	3.54	1.91	1.54
$10^{-5} p_{(D)}$ [N/m ²] Eq.(2.128)	22.89	25.65	30.13
pipe diameter 2r [mm]	459.7	349.6	211.1
t [mm] Eq.(2.124)	3.8	3.2	2.3
m_p [kg] Eq.(2.130)	595.80	241.79	90.30
dead fluid-mass[kg]	355.09	105.75	30.98
$10^{-5} \bar{p}_{(D)}$ [N/m ²] Eq.(2.129)	1.15	1.40	1.81

Table 4.4: Dimensioning of circular steel pipes.

The gauge pressure under expansion conditions turns out to be positive as listed in Table 4.4. The final dimensions of circular steel pipes must be changed according to their commercial availability.

4.5 Three-storey moderately asymmetric space frame: numerical example

The additional point mass on the third floor is $m_{13}=10 \times 10^3$ kg. The common stiffness of columns in y - and z -directions of each storey are increased to $k_{y1}=4433.23$ kN/m and $k_{z1}=1544.68$ kN/m. The mass moment of inertia about the vertical x -axis of the third floor is calculated: $I_{x3}=229.74 \times 10^3$ kg·m², $r_{S3}=2.97$ m. The other properties of the building are listed in Sections 2.9 and 4.4.

4.5.1 Static dimensioning and a static safety criterion of the columns

The critical load of a steel profile HEB-240 with respect to the weak axis of buckling becomes $F_c = -5076.65$ kN. The combined load without TLCGD of the first floor at point A_1 is $F_{11} = -620.77$ kN and that at points A_2, A_3, A_4 $F_{21} = -302.92$ kN. Thus $\frac{F_{11}}{F_c} = \frac{-620.77}{-5076.65} = 0.12 < \frac{1}{3}$, consequently, a geometric correction of the stiffness is applicable.

The corrected stiffness at point A_1 in y -direction becomes:

$$\bar{k}_{y1} = \begin{bmatrix} 8750.3 & -4371.2 & 0 \\ -4371.2 & 8734.4 & -4363.2 \\ 0 & -4363.2 & 4363.2 \end{bmatrix} \text{ kN/m}.$$

The corrected stiffness at point A_1 in z -direction becomes:

$$\bar{k}_{z1} = \begin{bmatrix} 2973.2 & -1482.6 & 0 \\ -1482.6 & 2957.3 & -1474.7 \\ 0 & -1474.7 & 1474.7 \end{bmatrix} \text{ kN/m}.$$

The corrected stiffness at points $A_2, A_3,$ and A_4 in y -direction becomes:

$$\bar{k}_{y2} = \bar{k}_{y3} = \bar{k}_{y4} = \begin{bmatrix} 8805.9 & -4402.9 & 0 \\ -4402.9 & 8805.9 & -4402.9 \\ 0 & -4402.9 & 4402.9 \end{bmatrix} kN/m.$$

The corrected stiffness at points A₂, A₃, and A₄ in z-direction becomes:

$$\bar{k}_{z2} = \bar{k}_{z3} = \bar{k}_{z4} = \begin{bmatrix} 3028.8 & -1514.4 & 0 \\ -1514.4 & 3028.8 & -1514.4 \\ 0 & -1514.4 & 1514.4 \end{bmatrix} kN/m.$$

4.5.2 Natural modes of the main structure

The natural frequencies are computed 1.05, 1.74, 2.22, 3.04, 4.41, 5.06, 6.29, 7.35 and 9.09 Hz. Columns are assumed to be massless. The orthonormalized modal matrix of the undamped main system with respect to \bar{M} is the output of Matlab 7.0².

$$\bar{\phi}_1 = \begin{bmatrix} \bar{\phi}_{1,1} \\ \bar{\phi}_{1,2} \\ \bar{\phi}_{1,3} \end{bmatrix}, \quad \bar{\phi}_{1,1} = 10^{-2} \begin{bmatrix} 0.011623 \\ -0.1938 \\ -0.039662 \end{bmatrix}, \quad \bar{\phi}_{1,2} = 10^{-2} \begin{bmatrix} 0.024604 \\ -0.36125 \\ -0.074022 \end{bmatrix}, \quad \bar{\phi}_{1,3} = 10^{-2} \begin{bmatrix} 0.034769 \\ -0.46386 \\ -0.094532 \end{bmatrix};$$

$$\bar{\phi}_2 = \begin{bmatrix} \bar{\phi}_{2,1} \\ \bar{\phi}_{2,2} \\ \bar{\phi}_{2,3} \end{bmatrix}, \quad \bar{\phi}_{2,1} = 10^{-2} \begin{bmatrix} -0.16611 \\ -0.051189 \\ 0.10112 \end{bmatrix}, \quad \bar{\phi}_{2,2} = 10^{-2} \begin{bmatrix} -0.31213 \\ -0.070527 \\ 0.18739 \end{bmatrix}, \quad \bar{\phi}_{2,3} = 10^{-2} \begin{bmatrix} -0.40344 \\ -0.06367 \\ 0.238 \end{bmatrix};$$

$$\bar{\phi}_3 = \begin{bmatrix} \bar{\phi}_{3,1} \\ \bar{\phi}_{3,2} \\ \bar{\phi}_{3,3} \end{bmatrix}, \quad \bar{\phi}_{3,1} = 10^{-2} \begin{bmatrix} 0.11966 \\ -0.066607 \\ 0.16837 \end{bmatrix}, \quad \bar{\phi}_{3,2} = 10^{-2} \begin{bmatrix} 0.20277 \\ -0.070966 \\ 0.31078 \end{bmatrix}, \quad \bar{\phi}_{3,3} = 10^{-2} \begin{bmatrix} 0.23856 \\ -0.033281 \\ 0.39368 \end{bmatrix};$$

$$\bar{\phi}_4 = \begin{bmatrix} \bar{\phi}_{4,1} \\ \bar{\phi}_{4,2} \\ \bar{\phi}_{4,3} \end{bmatrix}, \quad \bar{\phi}_{4,1} = 10^{-2} \begin{bmatrix} 0.020778 \\ -0.45006 \\ -0.1013 \end{bmatrix}, \quad \bar{\phi}_{4,2} = 10^{-2} \begin{bmatrix} 0.01415 \\ -0.26369 \\ -0.086885 \end{bmatrix}, \quad \bar{\phi}_{4,3} = 10^{-2} \begin{bmatrix} -0.026801 \\ 0.36252 \\ 0.026479 \end{bmatrix};$$

$$\bar{\phi}_5 = \begin{bmatrix} \bar{\phi}_{5,1} \\ \bar{\phi}_{5,2} \\ \bar{\phi}_{5,3} \end{bmatrix}, \quad \bar{\phi}_{5,1} = 10^{-2} \begin{bmatrix} 0.0028248 \\ 0.44545 \\ 0.044889 \end{bmatrix}, \quad \bar{\phi}_{5,2} = 10^{-2} \begin{bmatrix} 0.041799 \\ -0.43638 \\ -0.099064 \end{bmatrix}, \quad \bar{\phi}_{5,3} = 10^{-2} \begin{bmatrix} -0.031189 \\ 0.15541 \\ 0.058538 \end{bmatrix};$$

$$\bar{\phi}_6 = \begin{bmatrix} \bar{\phi}_{6,1} \\ \bar{\phi}_{6,2} \\ \bar{\phi}_{6,3} \end{bmatrix}, \quad \bar{\phi}_{6,1} = 10^{-2} \begin{bmatrix} -0.39352 \\ -0.027237 \\ 0.24682 \end{bmatrix}, \quad \bar{\phi}_{6,2} = 10^{-2} \begin{bmatrix} -0.2283 \\ -0.07911 \\ 0.13113 \end{bmatrix}, \quad \bar{\phi}_{6,3} = 10^{-2} \begin{bmatrix} 0.31057 \\ 0.068662 \\ -0.17458 \end{bmatrix};$$

$$\bar{\phi}_7 = \begin{bmatrix} \bar{\phi}_{7,1} \\ \bar{\phi}_{7,2} \\ \bar{\phi}_{7,3} \end{bmatrix}, \quad \bar{\phi}_{7,1} = 10^{-2} \begin{bmatrix} -0.26424 \\ 0.045519 \\ -0.40599 \end{bmatrix}, \quad \bar{\phi}_{7,2} = 10^{-2} \begin{bmatrix} -0.11862 \\ 0.046454 \\ -0.19562 \end{bmatrix}, \quad \bar{\phi}_{7,3} = 10^{-2} \begin{bmatrix} 0.18606 \\ -0.052125 \\ 0.31092 \end{bmatrix};$$

$$\bar{\phi}_8 = \begin{bmatrix} \bar{\phi}_{8,1} \\ \bar{\phi}_{8,2} \\ \bar{\phi}_{8,3} \end{bmatrix}, \quad \bar{\phi}_{8,1} = 10^{-2} \begin{bmatrix} -0.37095 \\ -0.060162 \\ 0.23797 \end{bmatrix}, \quad \bar{\phi}_{8,2} = 10^{-2} \begin{bmatrix} 0.38513 \\ 0.065584 \\ -0.22794 \end{bmatrix}, \quad \bar{\phi}_{8,3} = 10^{-2} \begin{bmatrix} -0.14557 \\ -0.025865 \\ 0.080603 \end{bmatrix};$$

$$\bar{\phi}_9 = \begin{bmatrix} \bar{\phi}_{9,1} \\ \bar{\phi}_{9,2} \\ \bar{\phi}_{9,3} \end{bmatrix}, \quad \bar{\phi}_{9,1} = 10^{-2} \begin{bmatrix} -0.22311 \\ 0.05017 \\ -0.34604 \end{bmatrix}, \quad \bar{\phi}_{9,2} = 10^{-2} \begin{bmatrix} 0.24709 \\ -0.058981 \\ 0.39333 \end{bmatrix}, \quad \bar{\phi}_{9,3} = 10^{-2} \begin{bmatrix} -0.09888 \\ 0.024752 \\ -0.1621 \end{bmatrix}.$$

The nine mode shapes are amplified and plotted in Fig. 4.28-4.36, the modal centers of velocity of first floor \circ , that of second floor \odot and of third floor $+$.

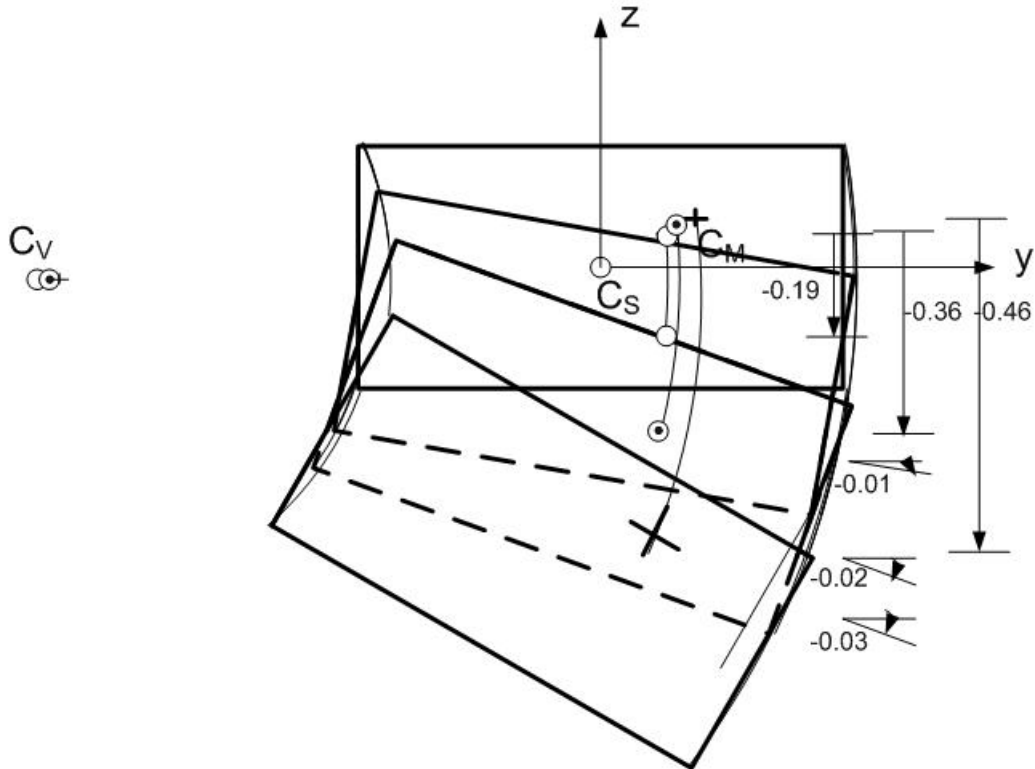


Fig. 4.28: First mode $f_1 = 1.05\text{Hz}$.

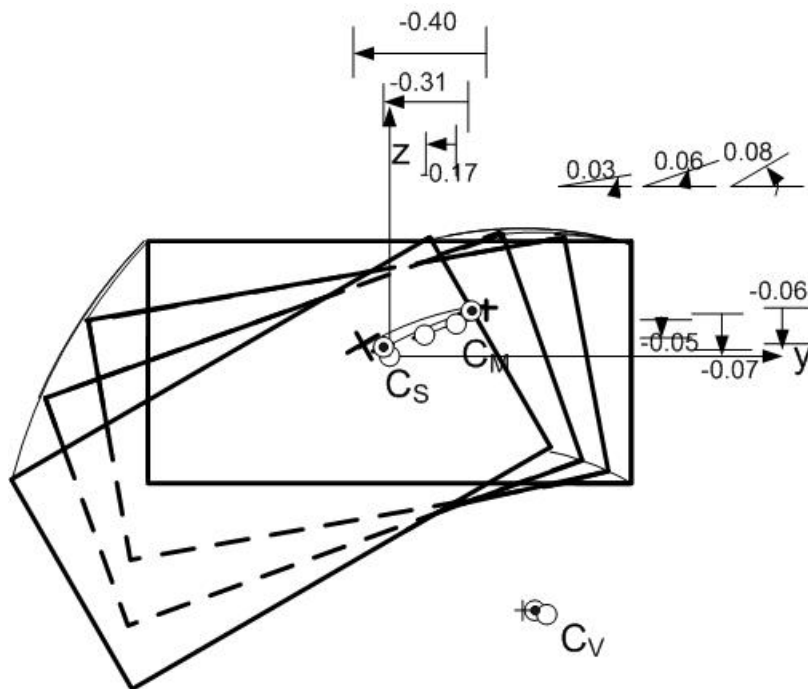


Fig. 4.29: Second mode $f_2 = 1.74\text{Hz}$.

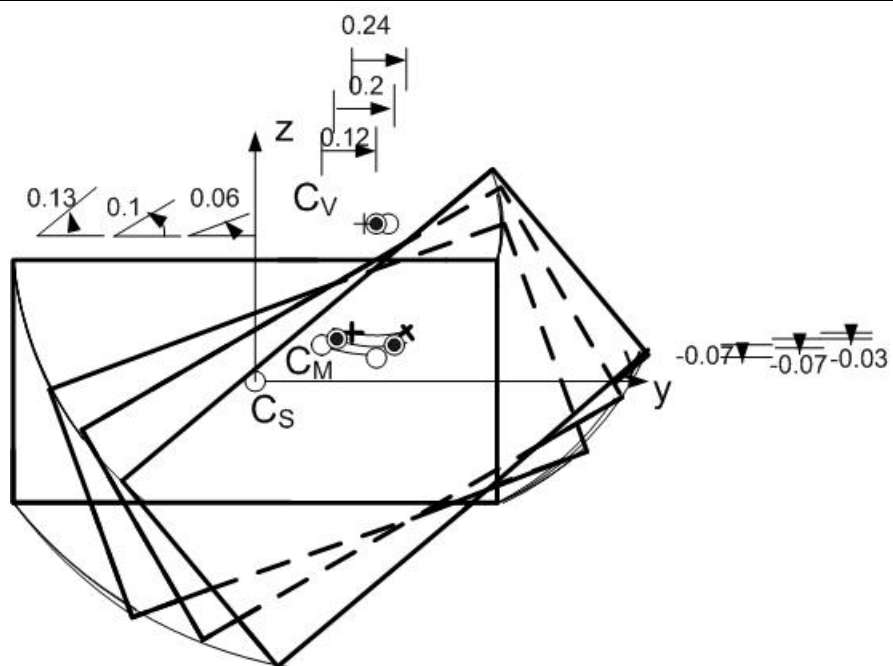


Fig. 4.30: Third mode $f_3 = 2.22Hz$.

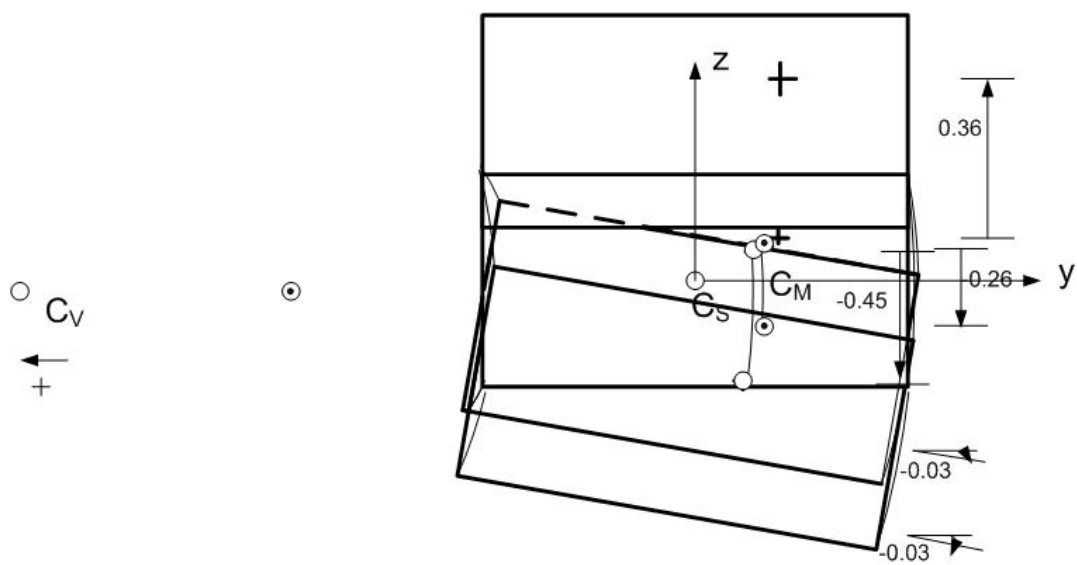


Fig. 4.31: Forth mode $f_4 = 3.04Hz$.

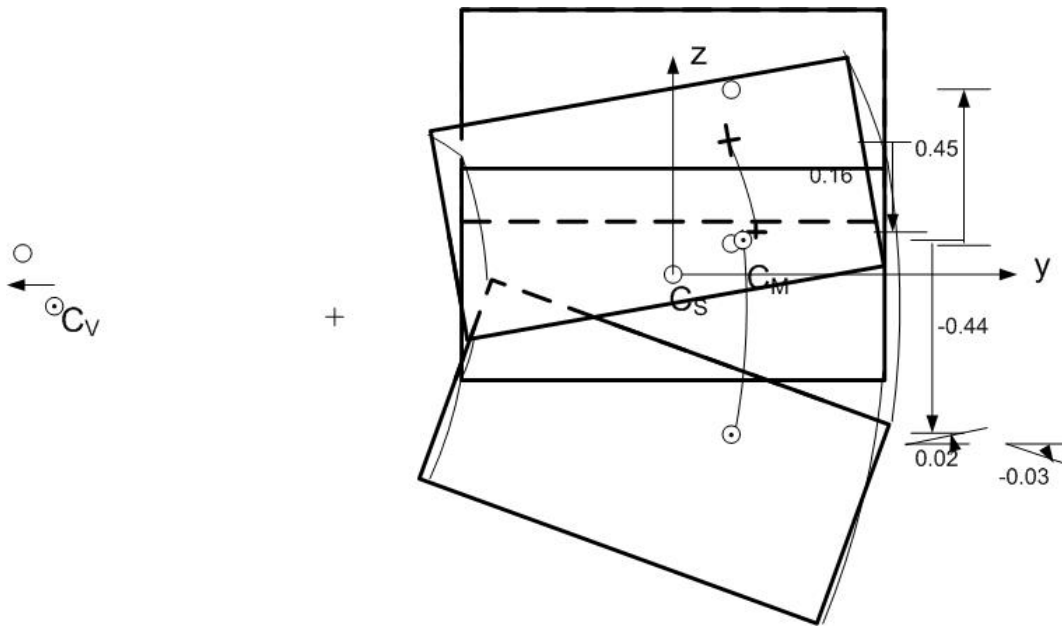


Fig. 4.32: Fifth mode $f_5 = 4.41Hz$.

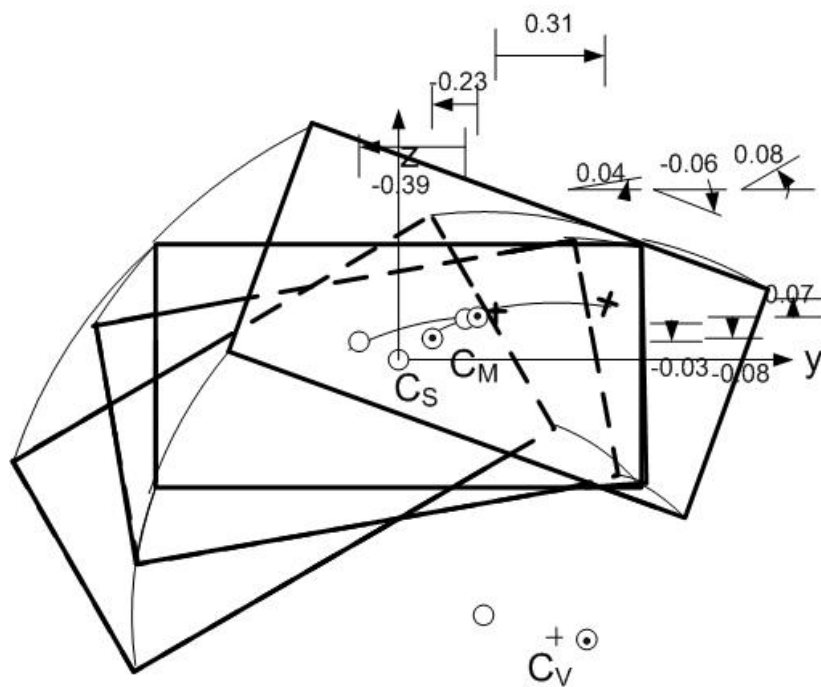


Fig. 4.33: Sixth mode $f_6 = 5.06Hz$.

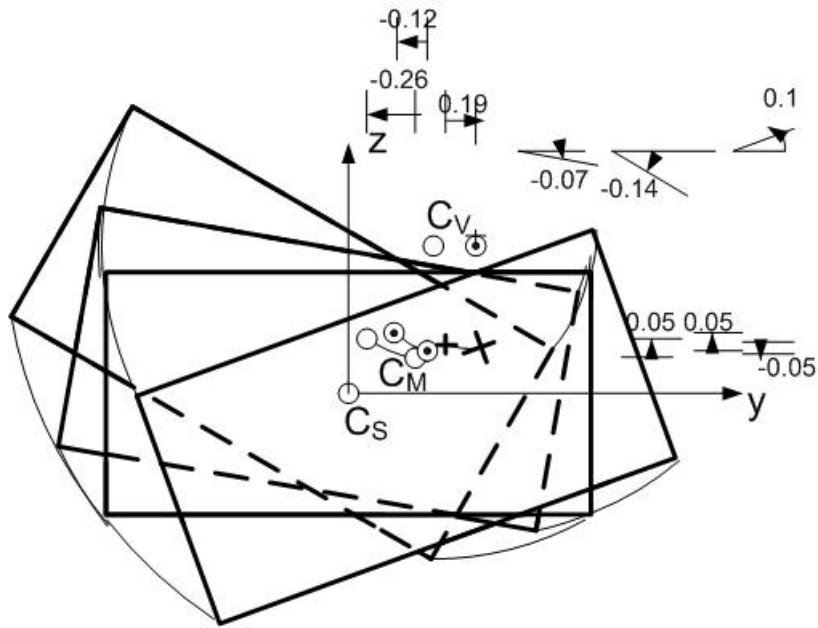


Fig. 4.34: Seventh mode $f_7 = 6.29\text{Hz}$.

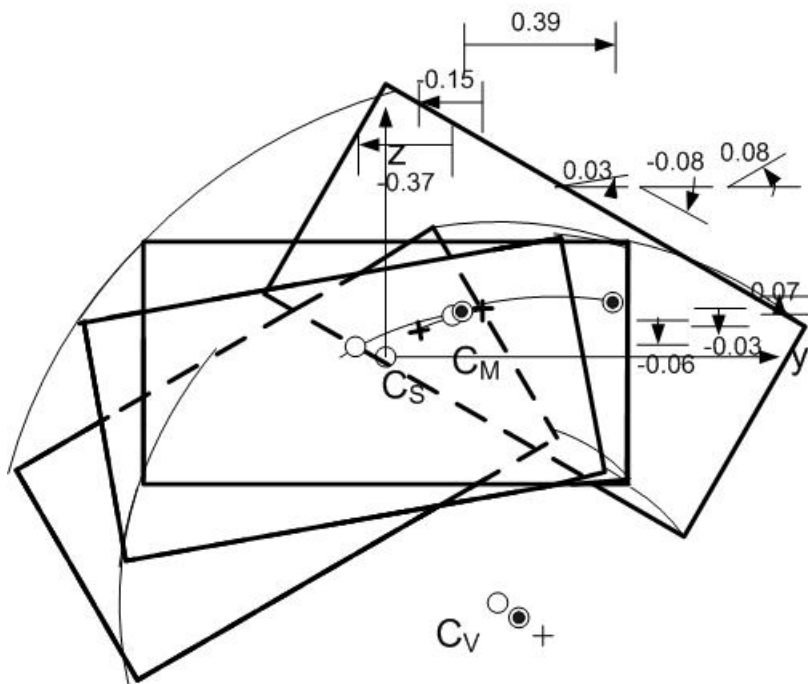


Fig. 4.35: Eighth mode $f_8 = 7.35\text{Hz}$.

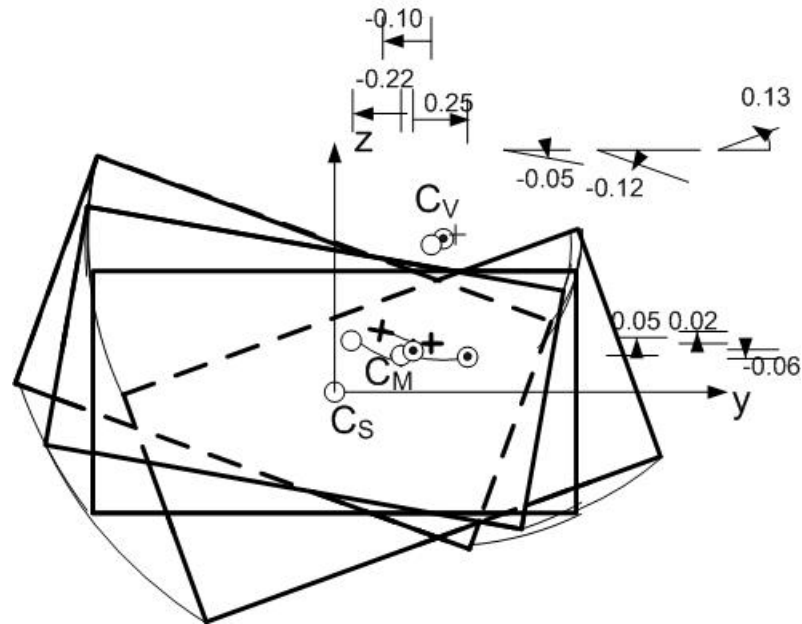


Fig. 4.36: Ninth mode $f_9 = 9.09\text{Hz}$.

4.5.3 Position of the modal centers of velocity C_V

The coordinates of the modal centers of velocity C_V with corrected column stiffness taken into account are defined by Eq. (2.18), all fall outside of the floor plan.

mode	1	2	3	4	5
floor 1	(-13.42,-0.32)	(2.59,-4.33)	(2.27,2.66)	(-12.10,-0.06)	(-28.37,0.73)
floor 2	(-13.22,-0.32)	(2.46,-4.30)	(2.01,2.61)	(-7.71,0.18)	(-11.80,-0.59)
floor 3	(-13.05,-0.32)	(2.33,-4.27)	(1.79,2.57)	(-39.16,-2.14)	(-6.35,-0.81)
mode	6	7	8	9	
floor 1	(1.42,-4.19)	(1.42,2.48)	(1.84,-4.08)	(1.52,2.46)	
floor 2	(3.13,-4.52)	(2.04,2.47)	(2.19,-4.37)	(1.78,2.54)	
floor 3	(2.71,-4.52)	(2.04,2.55)	(2.49,-4.60)	(1.99,2.58)	

Table 4.5: The coordinates of the centers of velocity C_V for 9 modes.

(i) Installation of TLCGDs

For the first mode the center of velocity C_V lies far away, consequently the TLCGD1 might be installed in the middle of the floor. TLCGD2 will be installed along the long side for the second mode and TLCGD3 on the right side for the third mode in order to maximize the normal distance between TLCGD and the corresponding center of velocity C_V .

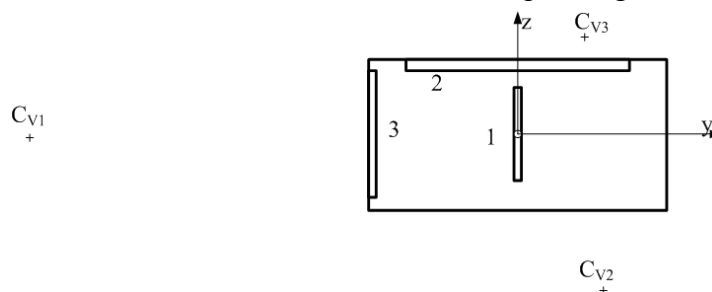


Fig. 4.37: Installation of TLCGD1, 2, 3, + the modal centers of velocity of third floor.

4.5.4 TLCGD design, Den Hartog' optimization

The fluid mass is chosen as $m_{f1} = 1710\text{kg}$, $m_{f2} = 670\text{kg}$ and $m_{f3} = 210\text{kg}$ of water. Dimensions of the three TLCGDs tuned first by means of the TMD analogy Eqs. (2.102)-

(2.104), applying Den Hartog's formulas are summarized in Table 4.6.

	TLCGD1	TLCGD2	TLCGD3
Horizontal length of the liquid column B [m]	3.00	3.00	3.00
Inclined length of the liquid column H [m]	2.0	1.2	0.9
Cross-sectional area of the pipe [m ²] $A_H=A_B$	0.2440	0.1240	0.0440
Effective length $L_{eff} = L_1 = 2H + B$ [m], Eq. (2.34a)	7.00	5.40	4.80
Angle of the inclined pipe section β [rad]	$\pi/4$	$\pi/4$	$\pi/4$
Equivalent mathematical pendulum length L_0 [m], Eq. (2.37)	0.23	0.08	0.05
Geometry factor $\kappa = \bar{\kappa}$, Eqs. (2.34a), (2.44)	0.833	0.87	0.89
Geometry factor $\bar{\kappa}_3$, Eq. (2.59)	0.80	1.45	2.12
Equilibrium pressure head h_0 [m], $n=1.2$, Eq. (2.34a)	48.92	64.80	73.39
Gas volume $V_0 = A_H H_a$ [m ³], Eq. (2.38)	0.800000	0.250000	0.069000
The mass ratio of the TLCGD-main system μ , Eq. (2.97)	3%	2%	1.5%
The mass ratio of the equivalent TMD-main system μ^* , Eq. (2.102)	2.02%	1.45%	1.17%
Natural frequency $f_{A,opt}$ [Hz] Eq. (2.104), (2.112)	1.02	1.71	2.19
Optimal linear damping %, Eq. (2.113)	8.62	7.31	6.58

Table 4.6: Layout of the modally tuned TLCGDs, gas volume and gas equilibrium pressure assigned, cf. Fig. (4.37).

The modal dynamic magnification factor (DMF) calculated with Matlab 7.0², linearized damping of the TLCGD considered, is illustrated in Figure 4.38.

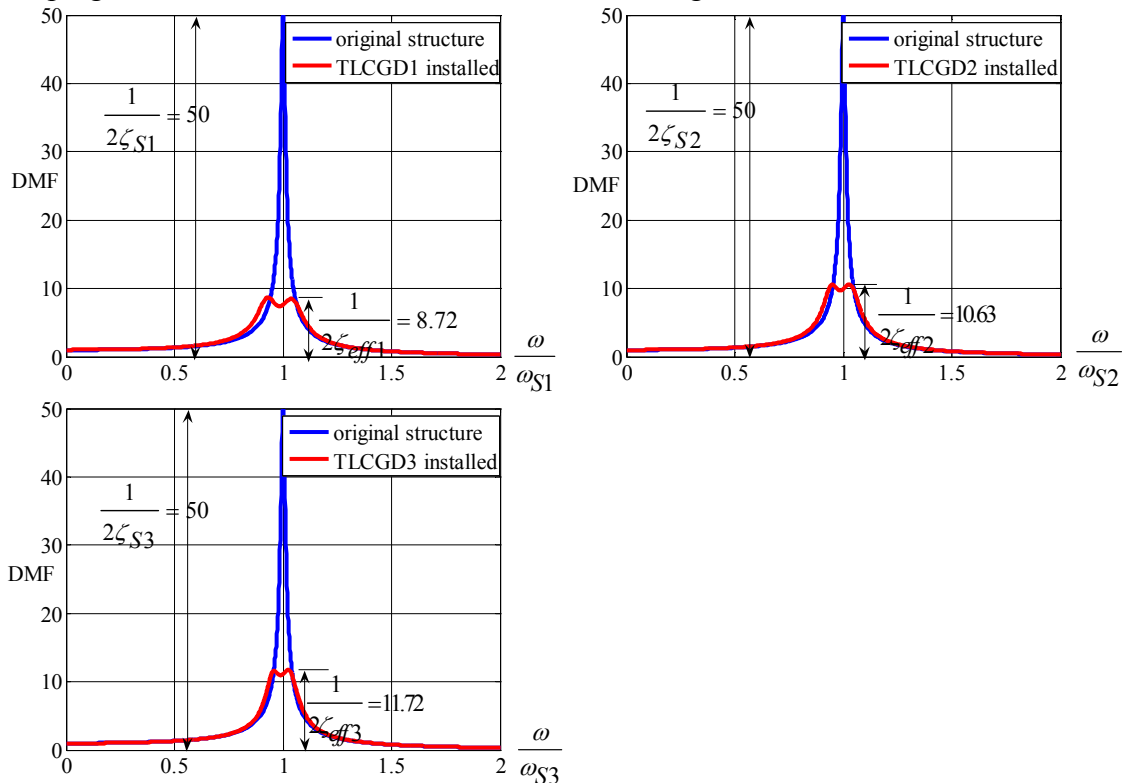


Fig.4.38: Individual frequency response curves without and with linearized TLCGDs attached, TLCGDs with Den Hartog's optimal parameters.

The effective modal damping coefficients of the system are increased from 1% to $\zeta_{eff1} = 5.73\%$, $\zeta_{eff2} = 4.7\%$ and $\zeta_{eff3} = 4.3\%$. The results of all maximum structural and liquid response with varying angles of attack of the time-harmonic excitation are given in Table 4.7a-c. The maximum fluid displacements are within the acceptable limits, $u_0 < H_a/3$ (of linearized gas compression) and $u_0 < H/2$. The maximum fluid velocities of three TLCGDs are calculated by Eq. (2.35) 6.23, 5.82 and 5.89m/s and are within the acceptable speed limit.

Forcing direction	structure			$u_{T3} = r_{S3}\theta_3$ [mm]	TLCGD1 u_0 [mm]
	v_3 [mm]	w_3 [mm]			
$\alpha = 0$	C _{M3}	1	-16	-3	62
	A	0	-14		
$\alpha = \pi/6$	C _{M3}	8	-109	-22	433
	A	2	-98		
$\alpha = \pi/4$	C _{M3}	12	-163	-33	644
	A	4	-145		
$\alpha = \pi/3$	C _{M3}	15	-205	-42	811
	A	5	-183		
$\alpha = \pi/2$	C _{M3}	18	-246	-50	972
	A	5	-220		
$\alpha = 2\pi/3$	C _{M3}	17	-221	-45	872
	A	5	-198		
$\alpha = 3\pi/4$	C _{M3}	14	-185	-38	730
	A	4	-166		
$\alpha = 5\pi/6$	C _{M3}	10	-137	-28	539
	A	3	-123		

Table 4.7a: Maximum displacements of three-storey structure in the first mode from time-harmonic excitation in α -directions, $a_0=0.1g$, $r_{S1} = 2.97m$, $r_{S2} = 2.98m$, $r_{S3} = 2.97m$.

Forcing direction	structure			$u_{T3} = r_{S3}\theta_3$ [mm]	TLCGD2 u_0 [mm]
	v_3 [mm]	w_3 [mm]			
$\alpha = 0$	C _{M3}	-78	-12	46	542
	A	-97	-36		
$\alpha = \pi/6$	C _{M3}	-76	-12	45	523
	A	-94	-35		
$\alpha = \pi/4$	C _{M3}	-67	-11	39	459
	A	-83	-31		
$\alpha = \pi/3$	C _{M3}	-53	-8	31	364
	A	-66	-24		
$\alpha = \pi/2$	C _{M3}	-16	-3	9	108
	A	-20	-7		
$\alpha = 2\pi/3$	C _{M3}	-25	-4	15	178
	A	-32	-12		
$\alpha = 3\pi/4$	C _{M3}	-44	-7	26	307
	A	-55	-20		
$\alpha = 5\pi/6$	C _{M3}	-60	-9	35	415
	A	-74	-28		

Table 4.67: Maximum displacements of three-storey structure in the second mode from time-harmonic excitation in α -directions, $a_0=0.1g$, $r_{S1} = 2.97m$, $r_{S2} = 2.98m$, $r_{S3} = 2.97m$.

Forcing direction	Structure			TLCGD3	
		v_3 [mm]	w_3 [mm]	$u_{T3} = r_{S3}\theta_3$ [mm]	u_0 [mm]
$\alpha = 0$	C_{M3}	15	-4	24	391
	A	21	-50		
$\alpha = \pi/6$	C_{M3}	11	-3	18	284
	A	15	-36		
$\alpha = \pi/4$	C_{M3}	7	-2	12	202
	A	11	-25		
$\alpha = \pi/3$	C_{M3}	4	-1	6	108
	A	6	-13		
$\alpha = \pi/2$	C_{M3}	5	-1	8	140
	A	7	-17		
$\alpha = 2\pi/3$	C_{M3}	12	-3	19	314
	A	17	-39		
$\alpha = 3\pi/4$	C_{M3}	14	-4	23	372
	A	20	-47		
$\alpha = 5\pi/6$	C_{M3}	15	-4	25	406
	A	22	-51		

Table 4.7c: Maximum displacements of three-storey structure in the third mode from time-harmonic excitation in α -directions, $a_0=0.1g$, $r_{S1} = 2.97m$, $r_{S2} = 2.98m$, $r_{S3} = 2.97m$.

4.5.5 Optimization of the three-storey space frame with 3 TLCGDs in the state space domain

The fine tuned optimal natural frequencies and damping ratios by calling the function *fminsearch* of the performance index J , Eq. (2.123), are found to be $f_{A1} = 1.02Hz$, $f_{A2} = 1.68Hz$, $f_{A3} = 2.10Hz$, $\zeta_{A1} = 8.50\%$, $\zeta_{A2} = 5.72\%$, $\zeta_{A3} = 6.2\%$. The equilibrium pressure head h_0 of three TLCGDs are consequently adjusted to 46.39, 60.25 and 65.82m.

The Figures 4.39-4.46 show the weighed sum of the frequency responses $\sum_{i=1}^{18} s_i |z_{Si}(\nu)|$,

$\underline{S} = \text{diag}(10,10,10,10,10,10,10,10,10,10,1,1,1,1,1,1,1,1)$ of the building states for the original and the optimized system, in the logarithmic decibel scale, defined by $x[dB] = 20 \log x$ within the relevant frequency window $0 \leq f \leq 3Hz$. The resonance curves with fine-tuning optimal parameters have broader peaks. From inspection of figures 4.47-4.54 it is apparent that the maximum relative fluid displacements for all cases are well within the acceptable limits. The maximum fluid velocities of three TLCGDs are calculated by Eq. (2.35) 6.54, 6.86 and 6.86m/s and are also within the acceptable speed limit.

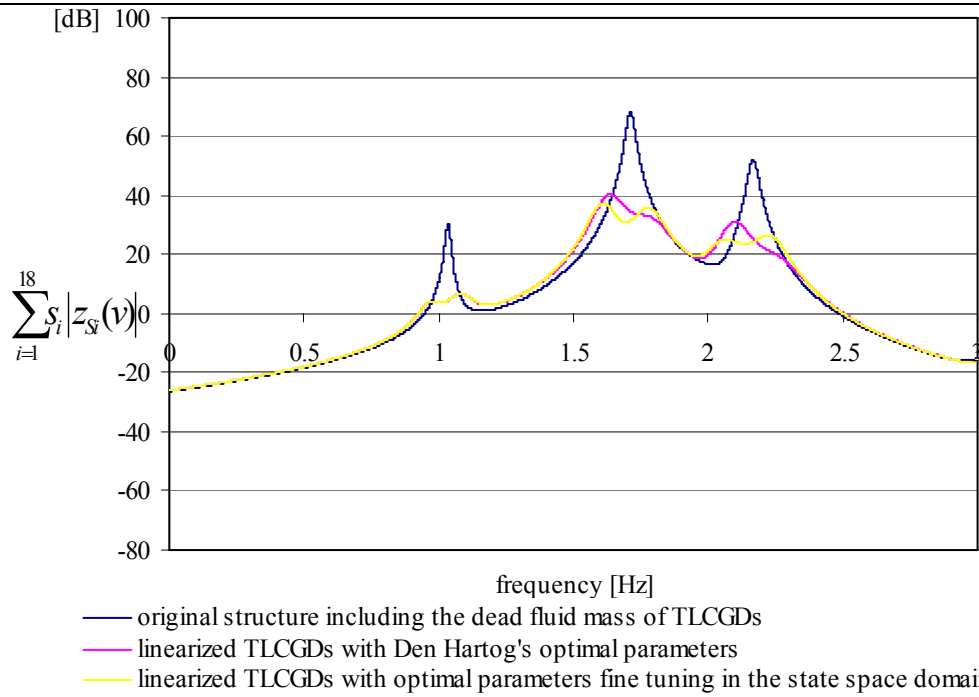


Fig. 4.39: Weighed sum of amplitude response functions for the 9-DOF linearized, three-storey, moderately asymmetric space frame, with three linearized TLCGDs attached and without the TLCGDs (angle of attack of the time-harmonic base acceleration $\alpha = 0$), maximum gain 31dB.

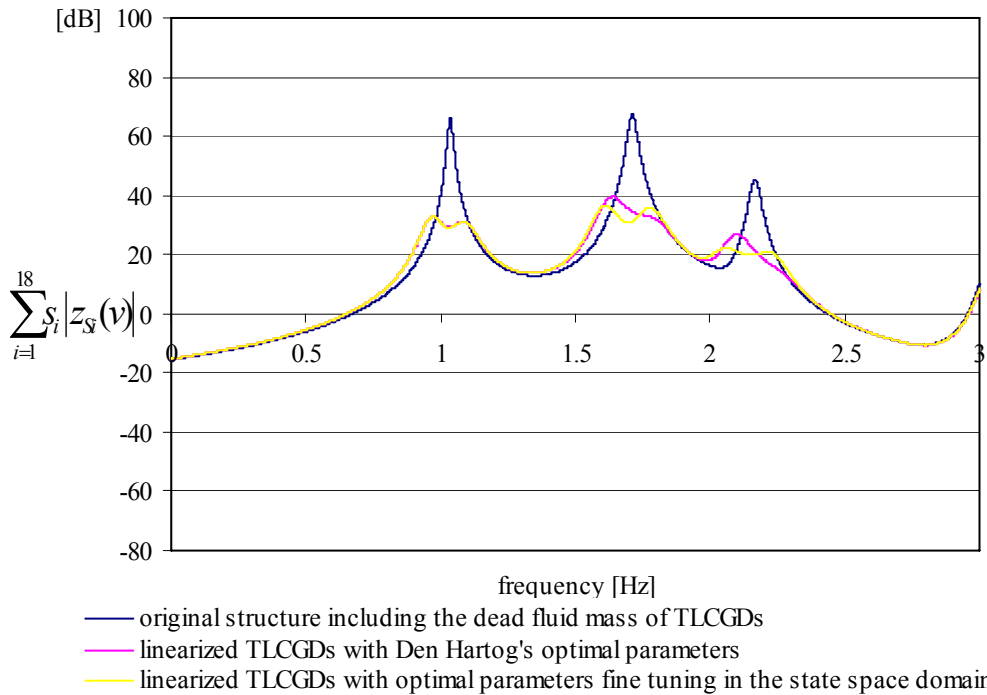


Fig. 4.40: Weighed sum of amplitude response functions for the 9-DOF linearized, three-storey, moderately plan asymmetric space frame, with three linearized TLCGDs attached and without the TLCGDs (angle of attack of the time-harmonic base acceleration $\alpha = \pi/6$), maximum gain 31dB.

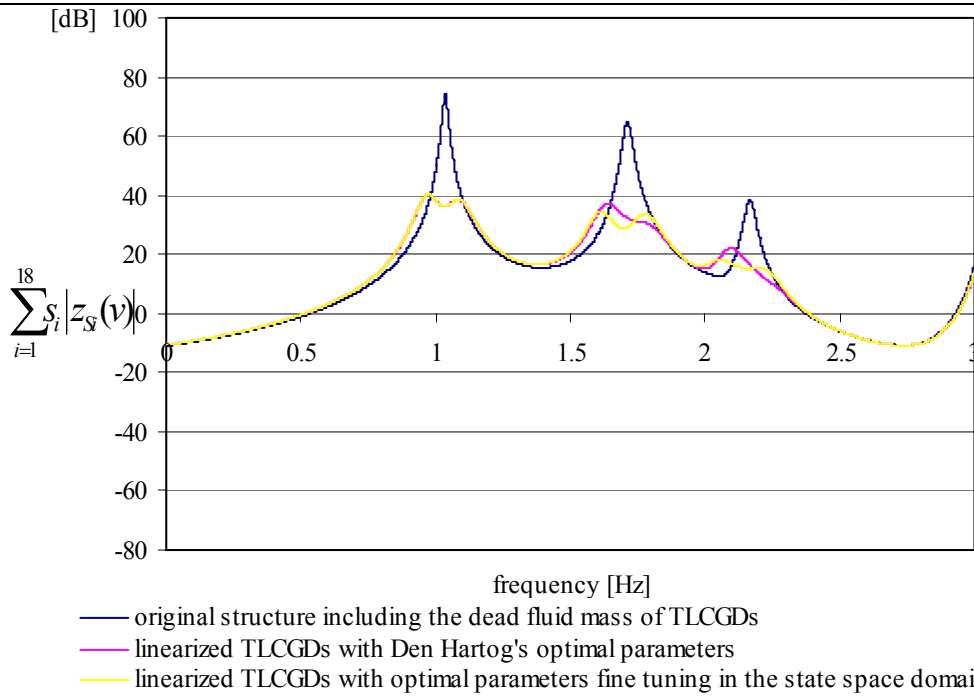


Fig. 4.41: Weighed sum of amplitude response functions for the 9-DOF linearized, three-storey, moderately asymmetric space frame, with three linearized TLCGDs attached and without the TLCGDs (angle of attack of the time-harmonic base acceleration $\alpha = \pi/4$), maximum gain 33.9dB.

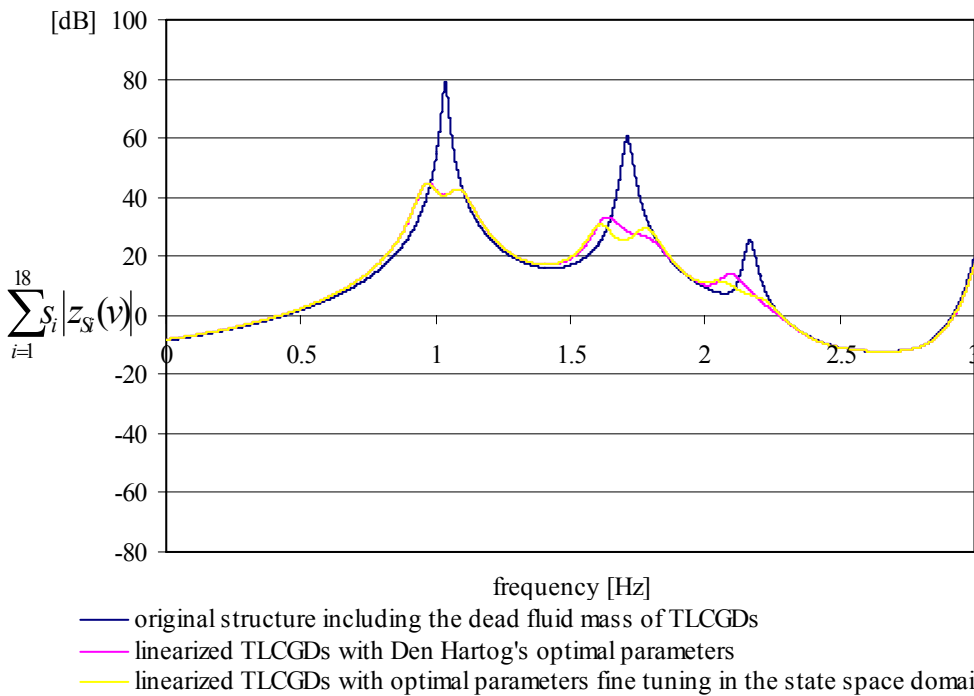


Fig. 4.42: Weighed sum of amplitude response functions for the 9-DOF linearized, three-storey, moderately asymmetric space frame, with three linearized TLCGDs attached and without the TLCGDs (angle of attack of the time-harmonic base acceleration $\alpha = \pi/3$), maximum gain 34.1dB.

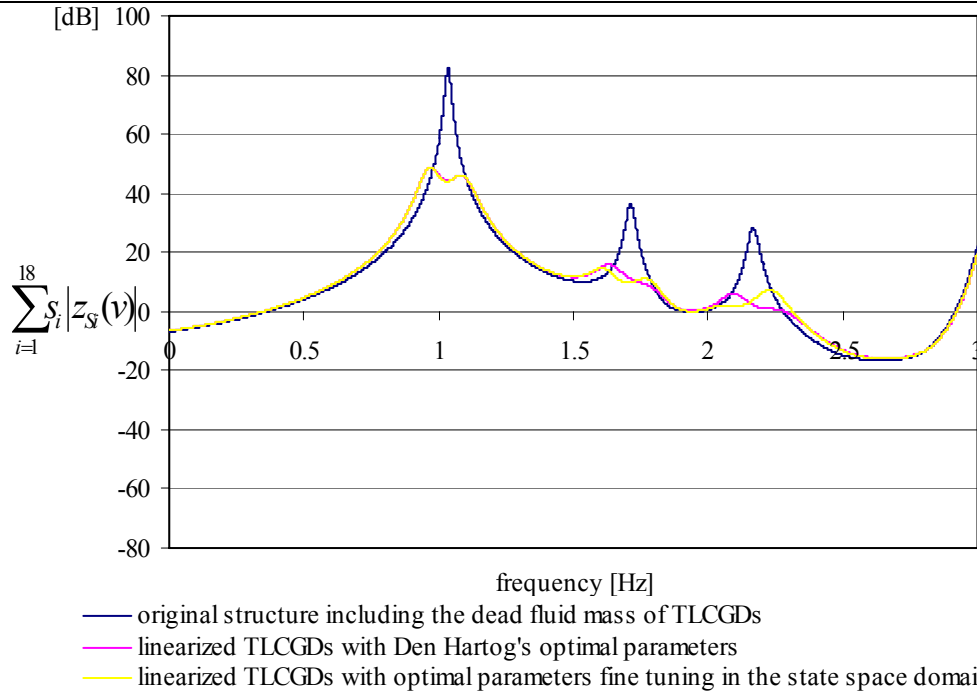


Fig. 4.43: Weighed sum of amplitude response functions for the 9-DOF linearized, three-storey, moderately asymmetric space frame, with three linearized TLCGDs attached and without the TLCGDs (angle of attack of the time-harmonic base acceleration $\alpha = \pi/2$), maximum gain 34dB.

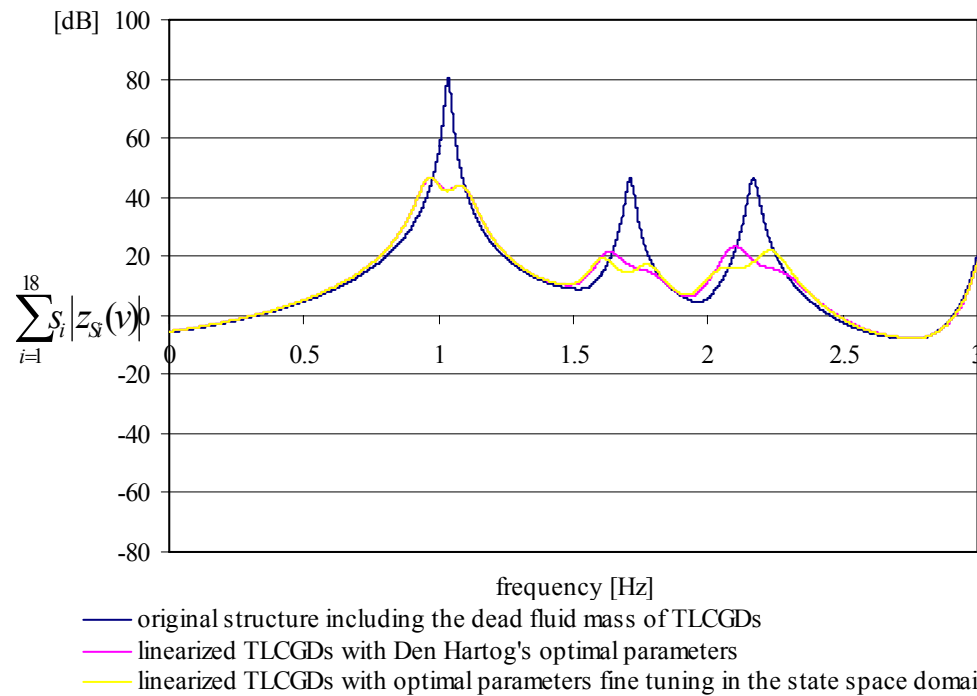


Fig. 4.44: Weighed sum of amplitude response functions for the 9-DOF linearized, three-storey, moderately asymmetric space frame, with three linearized TLCGDs attached and without the TLCGDs (angle of attack of the time-harmonic base acceleration $\alpha = 2\pi/3$), maximum gain 33.8dB.

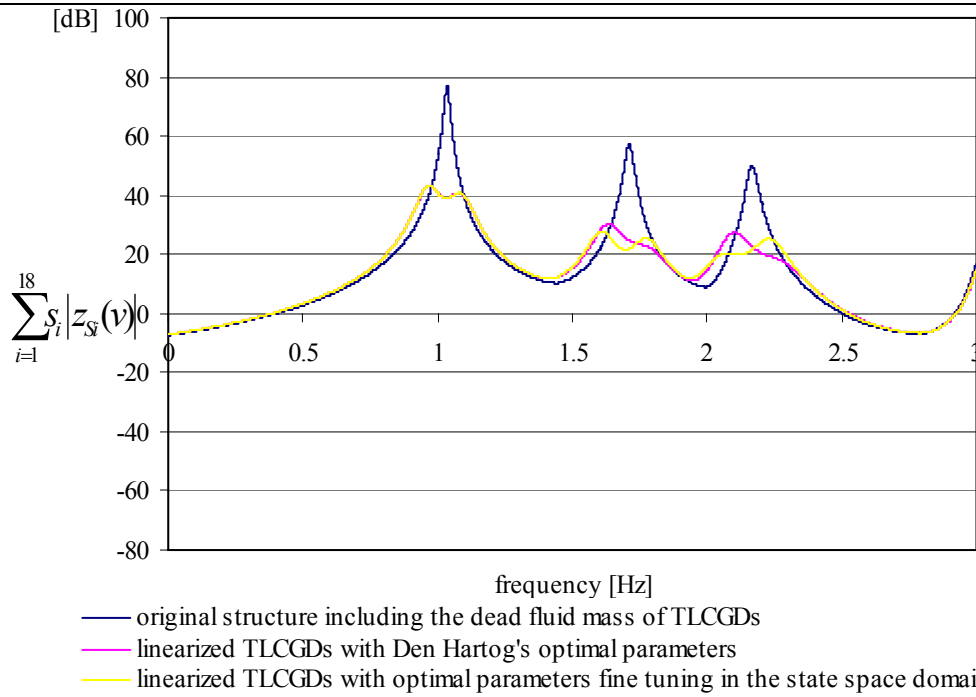


Fig. 4.45: Weighed sum of amplitude response functions for the 9-DOF linearized, three-storey, moderately asymmetric space frame, with three linearized TLCGDs attached and without the TLCGDs (angle of attack of the time-harmonic base acceleration $\alpha = 3\pi/4$), maximum gain 33.5dB.

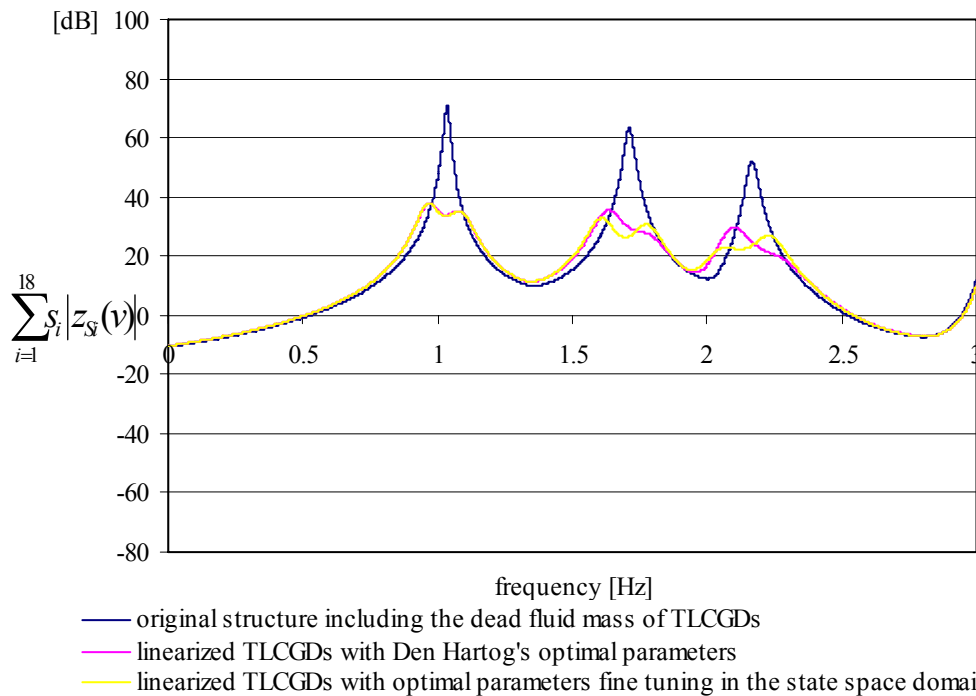


Fig. 4.46: Weighed sum of amplitude response functions for the 9-DOF linearized, two-storey, moderately asymmetric space frame, with three linearized TLCGDs attached and without the TLCGDs (angle of attack of the time-harmonic base acceleration $\alpha = 5\pi/6$), maximum gain 33.2dB.

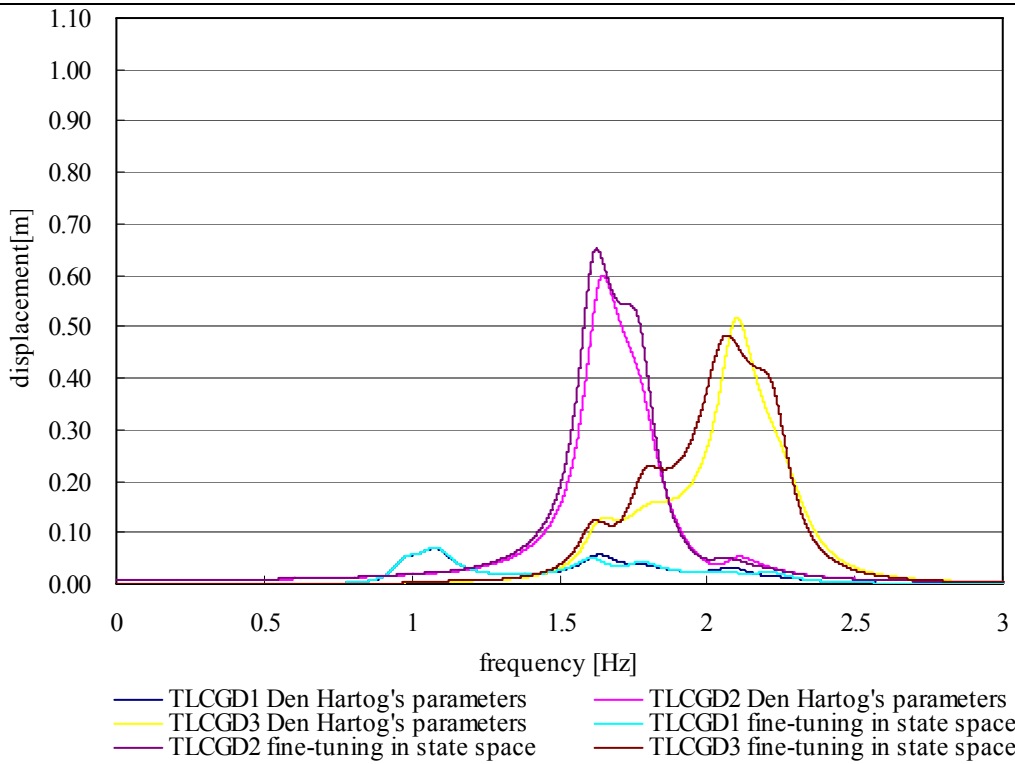


Fig. 4.47: Amplitude response curves of fluid displacement $|u|$ of three linearized TLCGDs attached to the three-storey moderately asymmetric space frame. TLCGDs either with Den Hartog's optimal parameters or those resulting from fine-tuning in state space ($\alpha = 0$).

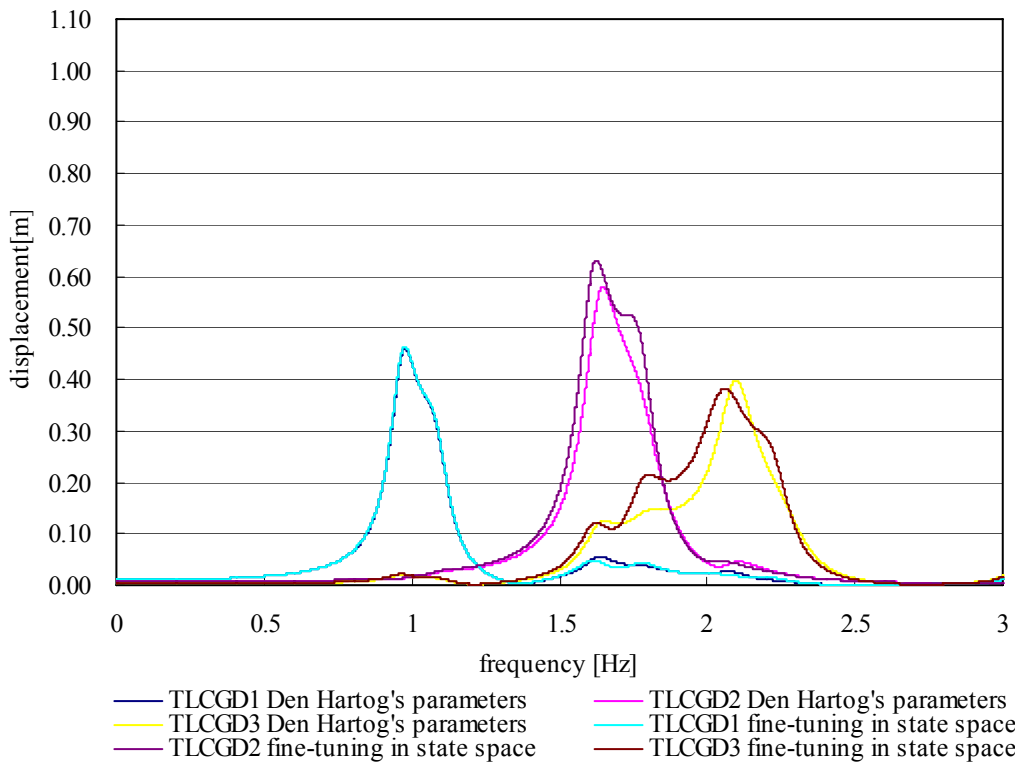


Fig. 4.48: Amplitude response curves of fluid displacement $|u|$ of three linearized TLCGDs attached to the three-storey moderately asymmetric space frame. TLCGDs either with Den Hartog's optimal parameters or those resulting from fine-tuning in state space ($\alpha = \pi/6$).

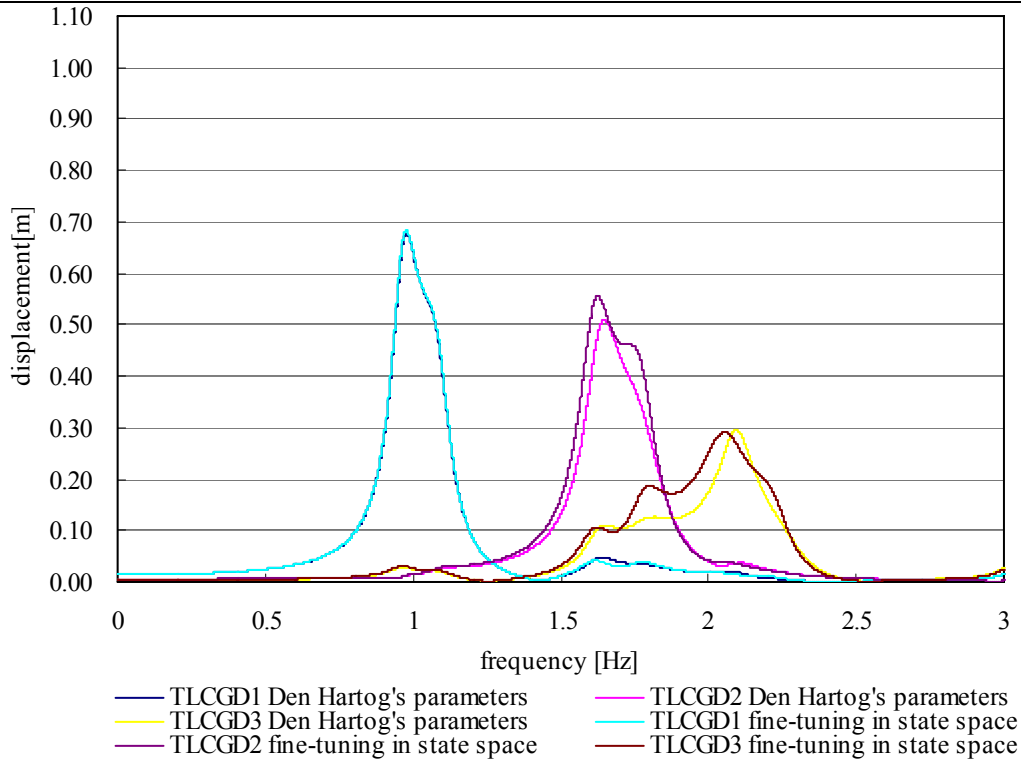


Fig. 4.49: Amplitude response curves of fluid displacement $|u|$ of three linearized TLCGDs attached to the three-storey moderately asymmetric space frame. TLCGDs either with Den Hartog's optimal parameters or those resulting from fine-tuning in state space ($\alpha = \pi/4$).

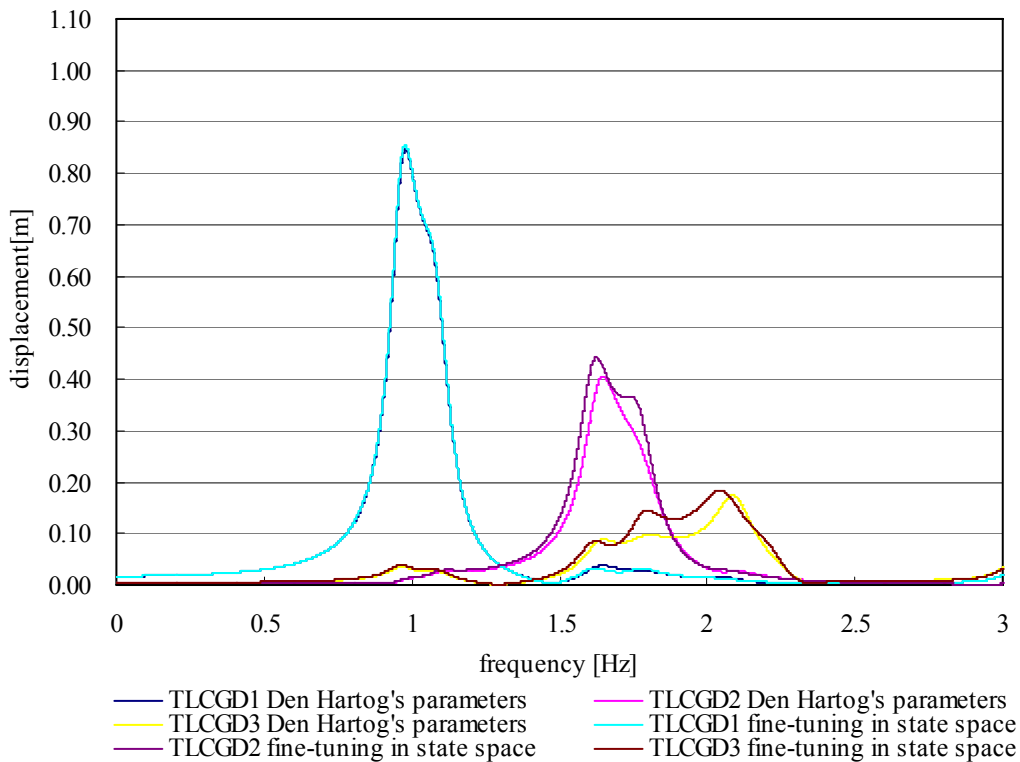


Fig. 4.50: Amplitude response curves of fluid displacement $|u|$ of three linearized TLCGDs attached to the three-storey moderately asymmetric space frame. TLCGDs either with Den Hartog's optimal parameters or those resulting from fine-tuning in state space ($\alpha = \pi/3$).

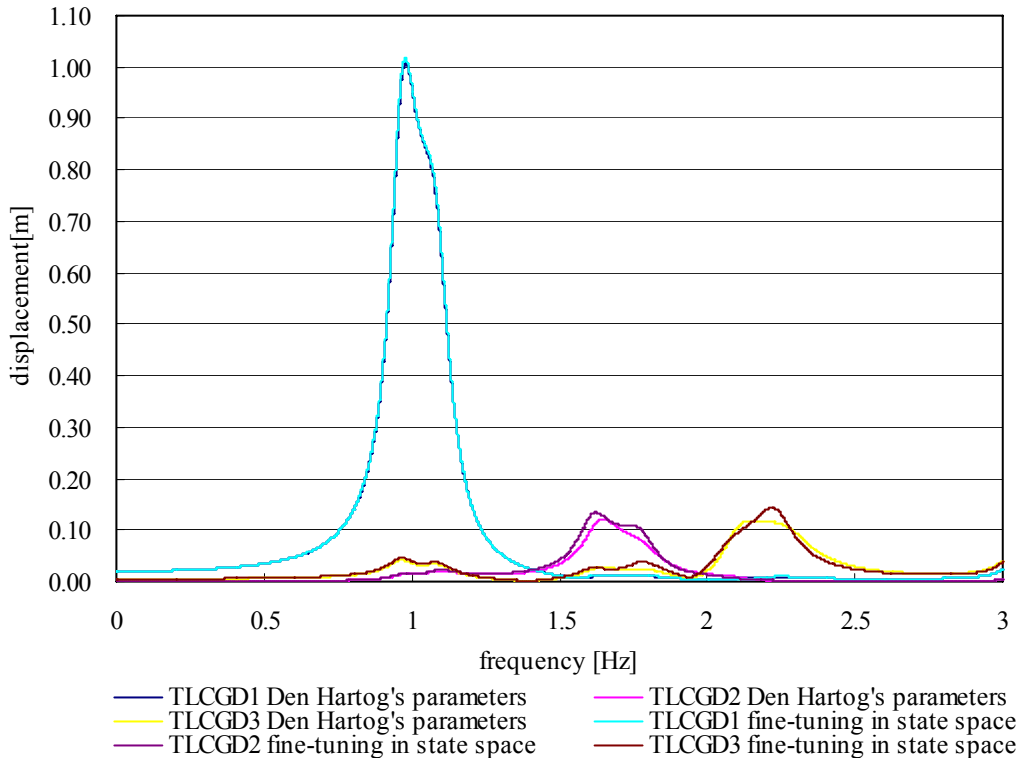


Fig.4.51: Amplitude response curves of fluid displacement $|u|$ of three linearized TLCGDs attached to the three-storey moderately asymmetric space frame. TLCGDs either with Den Hartog’s optimal parameters or those resulting from fine-tuning in state space ($\alpha = \pi/2$).

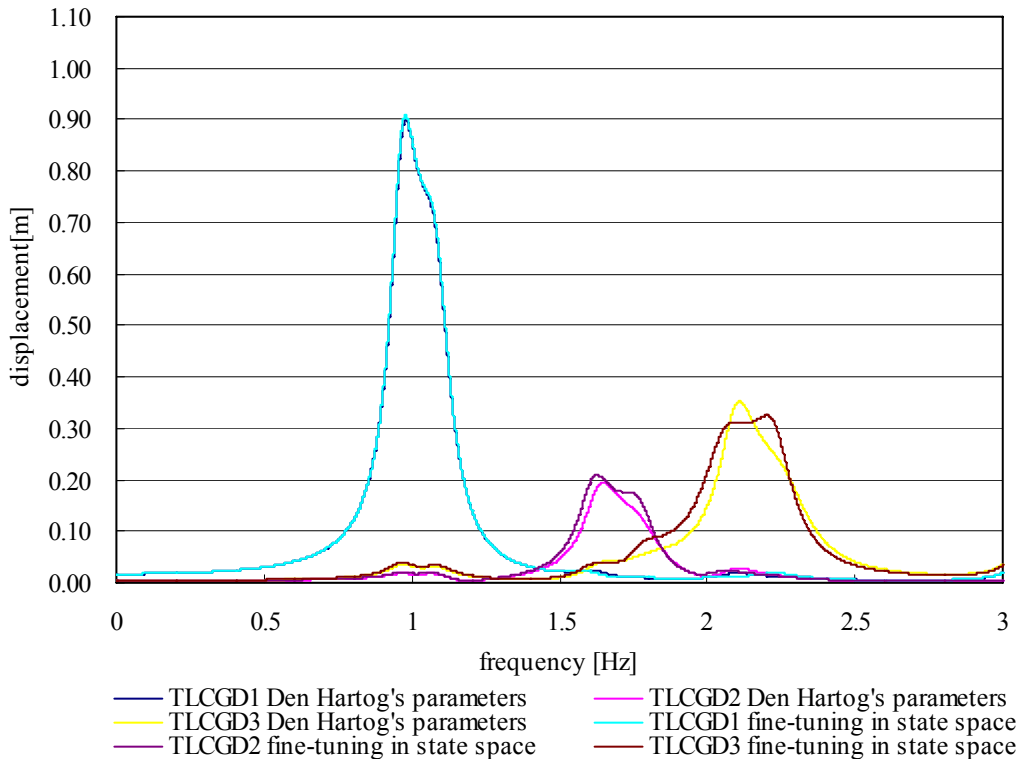


Fig. 4.52: Amplitude response curves of fluid displacement $|u|$ of three linearized TLCGDs attached to the three-storey moderately asymmetric space frame. TLCGDs either with Den Hartog’s optimal parameters or those resulting from fine-tuning in state space ($\alpha = 2\pi/3$).

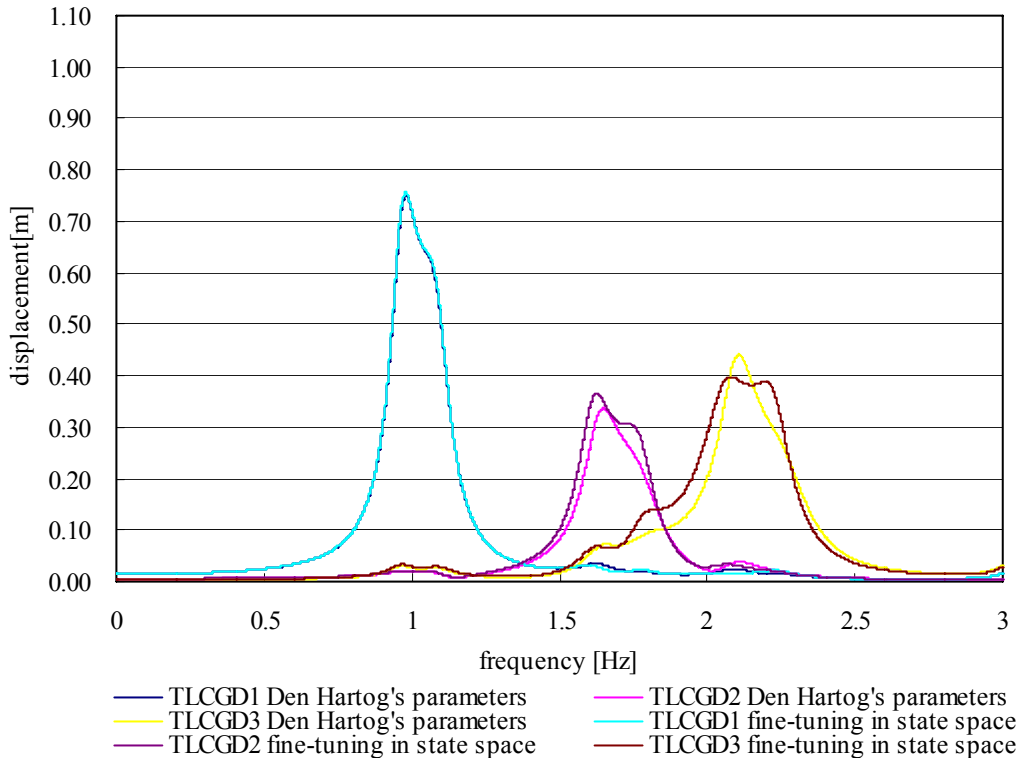


Fig. 4.53: Amplitude response curves of fluid displacement $|u|$ of three linearized TLCGDs attached to the three-storey moderately asymmetric space frame. TLCGDs either with Den Hartog's optimal parameters or those resulting from fine-tuning in state space ($\alpha = 3\pi/4$).

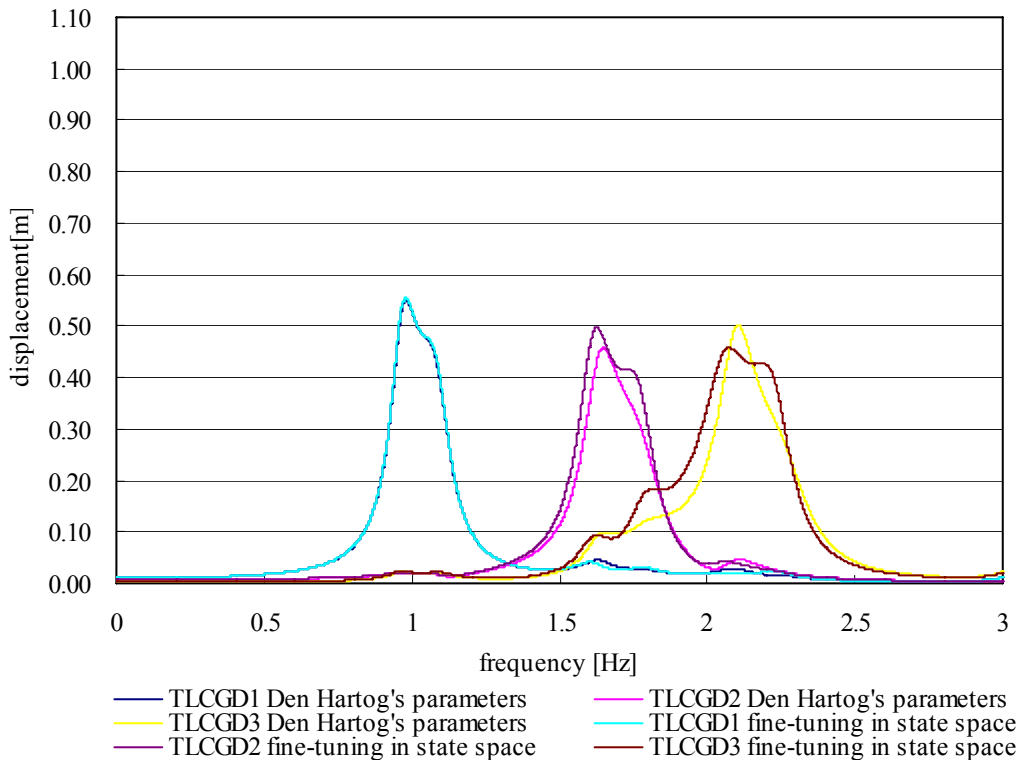


Fig. 4.54: Amplitude response curves of fluid displacement $|u|$ of three linearized TLCGDs attached to the three-storey moderately asymmetric space frame. TLCGDs either with Den Hartog's optimal parameters or those resulting from fine-tuning in state space ($\alpha = 5\pi/6$).

The wall thickness and the estimated dead mass of the piping system are listed in Table 4.8 for the three absorbers, designed according to Table 4.6.

	TLCGD1	TLCGD2	TLCGD3
h_0 [m]	48.92	64.80	73.39
H_a [m]	3.28	2.02	1.57
$10^{-5} p_{(D)}$ [N/m ²] Eq.(2.128)	21.76	29.04	32.99
pipe diameter $2r$ [mm]	557.4	397.3	236.7
t [mm] Eq.(2.124)	4.3	4.1	2.8
m_p [kg] Eq.(2.130)	801.95	378.51	128.38
dead fluid-mass[kg]	523.45	162.88	43.66
$10^{-5} \bar{p}_{(D)}$ [N/m ²] Eq.(2.129)	1.04	1.71	2.07

Table 4.8: Dimensioning of circular steel pipes.

The gauge pressure under expansion conditions turns out to be positive as listed in Table 4.8. The final dimensions of circular steel pipes must be changed according to their commercial availability.

4.6 Four-storey moderately asymmetric space frame: numerical example

The additional point mass on the fourth floor is $m_{14}=6 \times 10^3$ kg. The common stiffness of columns in y - and z -directions of each storey are further increased to $k_{yi}=5874.4$ kN/m and $k_{zi}=2021.9$ kN/m. The mass moment of inertia about the vertical x -axis of the fourth floor is calculated: $I_{x4}=193.94 \times 10^3$ kg \cdot m², $r_{S4}=2.97$ m. The other properties of the building are listed in Sections 2.9, 4.4 and 4.5.

4.6.1 Static dimensioning and a static safety criterion of the columns

The critical load of a steel profile HEB-260 with respect to the weak axis of buckling becomes $F_c = -6645.06$ kN. The combined load without TLCD of the first floor at point A_1 is $F_{11} = -801.2$ kN and that at points A_2, A_3, A_4 $F_{21} = -403.9$ kN. Thus

$$\frac{F_{11}}{F_c} = \frac{-801.201}{-6645.06} = 0.12 < \frac{1}{3}.$$

The corrected stiffness at point A_1 in y -direction becomes:

$$\bar{k}_{y1} = \begin{bmatrix} 11633 & -5812.3 & 0 & 0 \\ -5812.3 & 11617 & -5804.3 & 0 \\ 0 & -5804.3 & 11625 & -5820.2 \\ 0 & 0 & -5820.2 & 5820.2 \end{bmatrix} \text{ kN/m.}$$

The corrected stiffness at point A_1 in z -direction becomes:

$$\bar{k}_{z1} = \begin{bmatrix} 3927.6 & -1959.8 & 0 & 0 \\ -1959.8 & 3911.7 & -1951.9 & 0 \\ 0 & -1951.9 & 3919.7 & -1967.8 \\ 0 & 0 & -1967.8 & 1967.8 \end{bmatrix} \text{ kN/m.}$$

The corrected stiffness at points $A_2, A_3,$ and A_4 in y -direction becomes:

$$\bar{k}_{y2} = \bar{k}_{y3} = \bar{k}_{y4} = \begin{bmatrix} 11688 & -5844.1 & 0 & 0 \\ -5844.1 & 11688 & -5844.1 & 0 \\ 0 & -5844.1 & 11688 & -5844.1 \\ 0 & 0 & -5844.1 & 5844.1 \end{bmatrix} kN/m.$$

The corrected stiffness at points A₂, A₃, and A₄ in z-direction becomes:

$$\bar{k}_{z2} = \bar{k}_{z3} = \bar{k}_{z4} = \begin{bmatrix} 3983.2 & -1991.6 & 0 & 0 \\ -1991.6 & 3983.2 & -1991.6 & 0 \\ 0 & -1991.6 & 3983.2 & -1991.6 \\ 0 & 0 & -1991.6 & 1991.6 \end{bmatrix} kN/m.$$

4.6.2 Natural modes of the main structure

The computed natural frequencies are 0.97, 1.61, 2.01, 2.88, 4.32, 4.78, 5.21, 5.85, 7.18, 8.68, 8.90 and 10.84Hz. Columns are assumed to be massless. The orthonormalized modal matrix of the undamped main system with respect to \bar{M} is the output of Matlab 7.0².

$$\bar{\phi}_i = [\bar{\phi}_{i,1} \quad \bar{\phi}_{i,2} \quad \bar{\phi}_{i,3} \quad \bar{\phi}_{i,4}]^T,$$

$$\bar{\phi}_{1,1} = 10^{-2} [-0.0077267 \quad 0.14299 \quad 0.027177]^T, \quad \bar{\phi}_{1,2} = 10^{-2} [-0.016826 \quad 0.27473 \quad 0.051979]^T,$$

$$\bar{\phi}_{1,3} = 10^{-2} [-0.02516 \quad 0.37555 \quad 0.070057]^T, \quad \bar{\phi}_{1,4} = 10^{-2} [-0.022059 \quad 0.40984 \quad 0.077589]^T;$$

$$\bar{\phi}_{2,1} = 10^{-2} [-0.12157 \quad -0.027548 \quad 0.076558]^T, \quad \bar{\phi}_{2,2} = 10^{-2} [-0.23589 \quad -0.038324 \quad 0.14576]^T;$$

$$\bar{\phi}_{2,3} = 10^{-2} [-0.32495 \quad -0.038032 \quad 0.19606]^T, \quad \bar{\phi}_{2,4} = 10^{-2} [-0.34805 \quad -0.082576 \quad 0.21859]^T;$$

$$\bar{\phi}_{3,1} = 10^{-2} [-0.084013 \quad 0.026433 \quad -0.12277]^T, \quad \bar{\phi}_{3,2} = 10^{-2} [-0.14849 \quad 0.027249 \quad -0.2329]^T,$$

$$\bar{\phi}_{3,3} = 10^{-2} [-0.18938 \quad 0.016374 \quad -0.3128]^T, \quad \bar{\phi}_{3,4} = 10^{-2} [-0.24215 \quad 0.08805 \quad -0.35065]^T;$$

$$\bar{\phi}_{4,1} = 10^{-2} [0.017538 \quad -0.36367 \quad -0.056849]^T, \quad \bar{\phi}_{4,2} = 10^{-2} [0.021729 \quad -0.38289 \quad -0.057978]^T,$$

$$\bar{\phi}_{4,3} = 10^{-2} [-0.0010327 \quad 0.015485 \quad 0.015836]^T, \quad \bar{\phi}_{4,4} = 10^{-2} [-0.01705 \quad 0.38372 \quad 0.080747]^T;$$

$$\bar{\phi}_{5,1} = 10^{-2} [0.018457 \quad -0.39719 \quad -0.079344]^T, \quad \bar{\phi}_{5,2} = 10^{-2} [-0.003049 \quad 0.070442 \quad -0.0094247]^T,$$

$$\bar{\phi}_{5,3} = 10^{-2} [-0.023368 \quad 0.3838 \quad 0.044369]^T, \quad \bar{\phi}_{5,4} = 10^{-2} [0.018004 \quad -0.31364 \quad -0.094244]^T;$$

$$\bar{\phi}_{6,1} = 10^{-2} [-0.30299 \quad -0.092471 \quad 0.18757]^T, \quad \bar{\phi}_{6,2} = 10^{-2} [-0.327 \quad 0.0013993 \quad 0.21046]^T,$$

$$\bar{\phi}_{6,3} = 10^{-2} [0.015775 \quad -0.037525 \quad -0.015627]^T, \quad \bar{\phi}_{6,4} = 10^{-2} [0.32466 \quad 0.070279 \quad -0.20358]^T;$$

$$\bar{\phi}_{7,1} = 10^{-2} [0.075091 \quad -0.3542 \quad -0.046025]^T, \quad \bar{\phi}_{7,2} = 10^{-2} [0.037632 \quad 0.41567 \quad 0.088759]^T,$$

$$\bar{\phi}_{7,3} = 10^{-2} [0.021294 \quad -0.28544 \quad -0.054357]^T, \quad \bar{\phi}_{7,4} = 10^{-2} [-0.075184 \quad 0.12425 \quad 0.036045]^T;$$

$$\bar{\phi}_{8,1} = 10^{-2} [-0.20462 \quad 0.0068593 \quad -0.32101]^T, \quad \bar{\phi}_{8,2} = 10^{-2} [-0.19772 \quad 0.086944 \quad -0.30961]^T,$$

$$\bar{\phi}_{8,3} = 10^{-2} [0.0044371 \quad -0.02826 \quad -0.0013258]^T, \quad \bar{\phi}_{8,4} = 10^{-2} [0.20782 \quad -0.034615 \quad 0.32978]^T;$$

$$\bar{\phi}_{9,1} = 10^{-2} [0.3422 \quad 0.048712 \quad -0.21753]^T, \quad \bar{\phi}_{9,2} = 10^{-2} [-0.060279 \quad 0.00051957 \quad 0.035414]^T,$$

$$\bar{\phi}_{9,3} = 10^{-2} [-0.33046 \quad -0.063644 \quad 0.19184]^T, \quad \bar{\phi}_{9,4} = 10^{-2} [0.27161 \quad 0.048904 \quad -0.17005]^T;$$

$$\bar{\phi}_{10,1} = 10^{-2} [0.30764 \quad 0.047971 \quad -0.1851]^T, \quad \bar{\phi}_{10,2} = 10^{-2} [-0.36363 \quad -0.063506 \quad 0.21683]^T,$$

$$\bar{\phi}_{10,3} = 10^{-2} [0.24919 \quad 0.048667 \quad -0.15678]^T, \quad \bar{\phi}_{10,4} = 10^{-2} [-0.10776 \quad -0.022034 \quad 0.078028]^T;$$

$$\begin{aligned} \bar{\phi}_{1,1} &= 10^{-2} [0.22793 \quad -0.049772 \quad 0.36598]^T, \quad \bar{\phi}_{1,2} = 10^{-2} [-0.055825 \quad 0.010111 \quad -0.10809]^T, \\ \bar{\phi}_{1,3} &= 10^{-2} [-0.19652 \quad 0.047766 \quad -0.30758]^T, \quad \bar{\phi}_{1,4} = 10^{-2} [0.16558 \quad -0.03917 \quad 0.24662]^T; \\ \bar{\phi}_{2,1} &= 10^{-2} [-0.17028 \quad 0.03767 \quad -0.25976]^T, \quad \bar{\phi}_{2,2} = 10^{-2} [0.22757 \quad -0.054171 \quad 0.35643]^T, \\ \bar{\phi}_{2,3} &= 10^{-2} [-0.17708 \quad 0.044044 \quad -0.28638]^T, \quad \bar{\phi}_{2,4} = 10^{-2} [0.081351 \quad -0.02018 \quad 0.12272]^T. \end{aligned}$$

4.6.3 Position of the modal centers of velocity C_V

The coordinates of the centers of velocity C_V with corrected column stiffness taken into account are listed in Table 4.9, all fall outside of the floor plan.

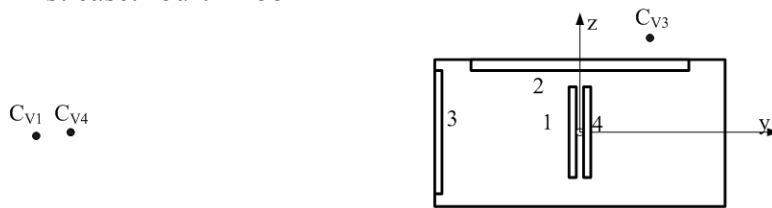
mode	1	2	3	4	5
floor 1	(-14.53,-0.30)	(2.16,-4.17)	(1.73,2.58)	(-17.9,-0.37)	(-13.77,-0.15)
floor 2	(-14.43,-0.30)	(2.12,-4.16)	(1.68,2.57)	(-18.36,0.45)	(23.62,1.63)
floor 3	(-14.40,-0.30)	(2.12,-4.16)	(1.69,2.57)	(-1.37,0.58)	(-24.18,-0.8)
floor 4	(-14.59,-0.30)	(2.21,-4.18)	(1.84,2.60)	(-13.02,-0.08)	(-8.79,-0.02)
mode	6	7	8	9	10
floor 1	(2.55,-4.25)	(-21.76,-4.30)	(1.15,2.44)	(1.76,-4.13)	(1.86,-4.39)
floor 2	(1.31,-3.97)	(-12.63,1.93)	(2.17,2.57)	(1.29,-4.41)	(2.21,-4.33)
floor 3	(-5.60,-2.23)	(-14.07,-0.40)	(-61.82,-9.18)	(2.52,-4.35)	(2.46,-3.95)
floor 4	(2.12,-4.19)	(-9.14,-5.65)	(1.40,2.42)	(1.94,-4.2)	(1.93,-3.56)
mode	11	12			
floor 1	(1.49,2.39)	(1.52,2.49)			
floor 2	(1.61,2.21)	(1.79,2.57)			
floor 3	(2.00,2.67)	(2.00,2.61)			
floor 4	(1.56,2.54)	(1.58,2.51)			

Table 4.9: The coordinates of the centers of velocity C_V for 12 modes.

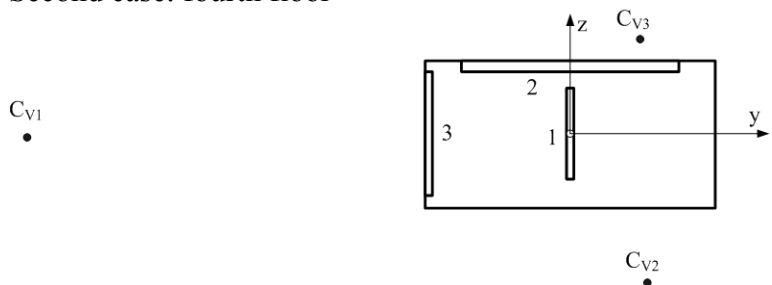
(i) Installation of TLCGDs

Four tuned liquid column gas dampers are installed to counteract the first four natural modes. We investigate the two cases of TLCGD installation and compare the effectiveness of them for structural control. First case: four TLCGDs are placed on the top floor, TLCGD1 and 4 are installed in the middle, respectively tuned to the first and fourth modes. TLCGD2 is installed along the long side suppressing the second mode and TLCGD3 on the short side tuned to the third mode. In second case TLCGD4 is alternatively installed in the middle of the second floor.

First case: fourth floor



Second case: fourth floor



Second floor

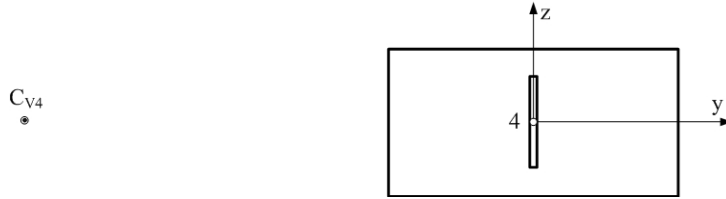


Fig. 4.55: Installation of TLCGD1, 2, 3, 4, ● the modal centers of velocity of second floor, ● the modal centers of velocity of fourth floor.

4.6.4 TLCGD design, Den Hartog' optimization

The fluid mass is chosen as $m_{f1} = 2030kg$, $m_{f2} = 810kg$, $m_{f3} = 250kg$ and $m_{f4} = 400kg$ of water. Dimensions of the three TLCGDs tuned first by means of the TMD analogy Eqs. (2.102)- (2.104), applying Den Hartog's formulas are summarized in Table 4.10. The modal dynamic magnification factor (DMF) calculated with Matlab 7.0², linearized damping of the TLCGD considered, is illustrated in Figure 4.56.

	TLCGD1	TLCGD2	TLCGD3	TLCGD4
Horizontal length of the liquid column B [m]	3.00	3.00	3.00	3.50
Inclined length of the liquid column H [m]	2.4	1.4	1.4	0.5
Cross-sectional area of the pipe [m ²] $A_H=A_B$	0.26	0.14	0.048	0.088
Effective length $L_{eff} = L_1 = 2H + B$ [m], Eq. (2.34a)	7.8	5.8	5.8	4.5
Angle of the inclined pipe section β [rad]	$\pi/4$	$\pi/4$	$\pi/4$	$\pi/4$
Equivalent mathematical pendulum length L_0 [m], Eq. (2.37)	0.27	0.10	0.06	0.03
Geometry factor $\kappa = \bar{\kappa}$, Eqs. (2.34a), (2.44)	0.82	0.859	0.876	0.935
Geometry factor $\bar{\kappa}_3$, Eq. (2.59)	0.665	1.198	1.62	6.485
Equilibrium pressure head h_0 [m], $n=1.2$, Eq. (2.34a)	56.28	69.72	86.88	88.08
Gas volume $V_0 = A_H H_a$ [m ³], Eq. (2.38)	1.040000	0.330000	0.100000	0.110000
The mass ratio of the TLCGD-main system μ , Eq. (2.97)	3%	2%	1.5%	0.51%
The mass ratio of the equivalent TMD-main system μ^* , Eq. (2.102)	1.96%	1.39%	1.09%	0.44%
Natural frequency $f_{A,opt}$ [Hz] Eq. (2.104), (2.112)	0.945	1.585	1.982	2.86
Optimal linear damping %, Eq. (2.113)	8.5	7.16	6.35	4.04

Table 4.10: Layout of the modally tuned TLCGDs, gas volume and gas equilibrium pressure assigned, cf. Fig. (4.55).

The effective modal damping coefficients of the system are increased from 1% to $\zeta_{eff1} = 5.6\%$, $\zeta_{eff2} = 4.67\%$, $\zeta_{eff3} = 4.2\%$ and $\zeta_{eff4} = 3.2\%$. The results of all maximum structural and liquid response with varying angles of attack of the time-harmonic excitation are given in Table 4.11a-d. The maximum fluid displacements are within the acceptable limits, $u_0 < H_a/3$ (of linearized gas compression) and $u_0 < H/2$. The maximum fluid velocities of three TLCGDs are calculated by Eq. (2.35) 7.10, 6.55, 6.40 and 2.73m/s and are within the acceptable speed limit.

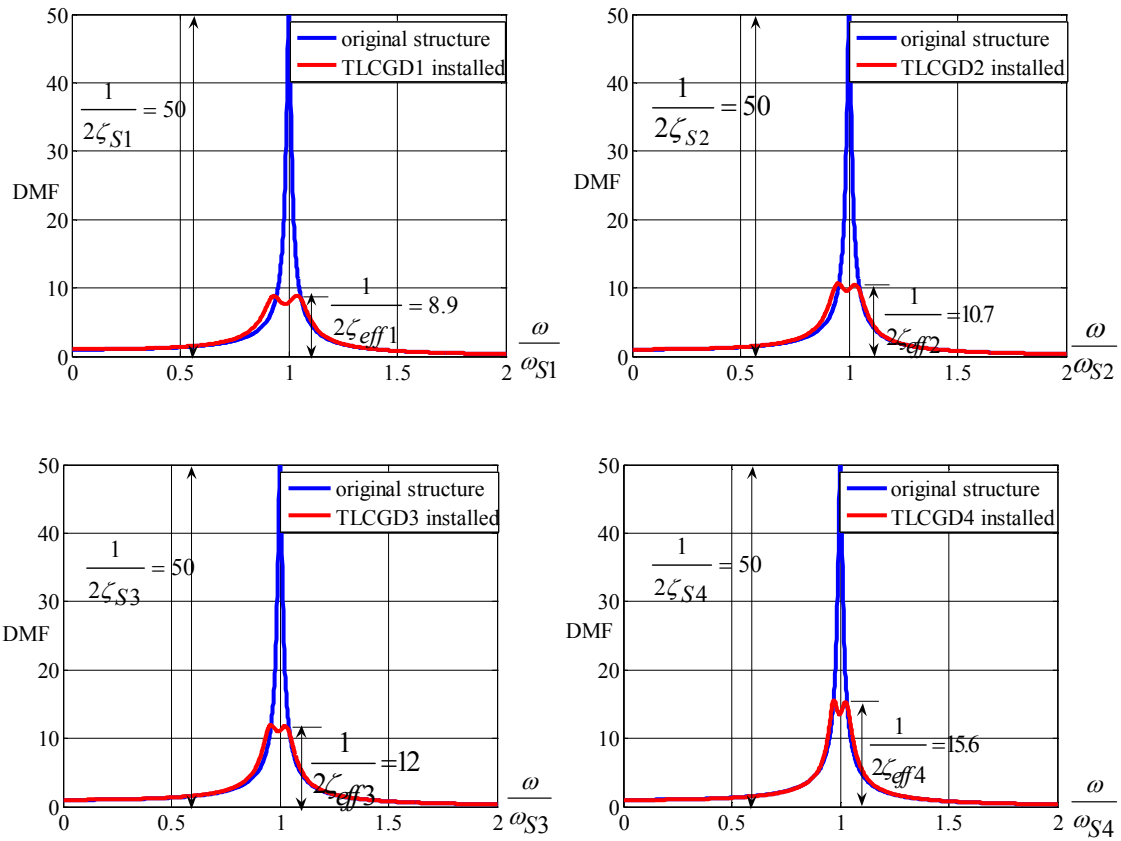


Fig.4.56: Individual frequency response curves without and with linearized TLCGDs attached, TLCGDs with Den Hartog’s optimal parameters.

Forcing direction	structure						TLCGD1
	v_2 [mm]	w_2 [mm]	$u_{T2} = r_{S2}\theta_2$ [mm]	v_4 [mm]	w_4 [mm]	$u_{T4} = r_{S4}\theta_4$ [mm]	
$\alpha = 0$	-1	11	2	C_{M4} -1	17	3	65
				A 0	15		
$\alpha = \pi/6$	-5	88	17	C_{M4} -7	132	25	541
				A -3	123		
$\alpha = \pi/4$	-8	131	25	C_{M4} -10	195	37	799
				A -4	181		
$\alpha = \pi/3$	-10	164	31	C_{M4} -13	245	46	1003
				A -5	228		
$\alpha = \pi/2$	-12	196	37	C_{M4} -16	292	55	1195
				A -6	272		
$\alpha = 2\pi/3$	-11	175	33	C_{M4} -14	261	49	1068
				A -5	243		
$\alpha = 3\pi/4$	-9	146	28	C_{M4} -12	218	41	891
				A -4	203		
$\alpha = 5\pi/6$	-7	107	20	C_{M4} -9	160	30	654
				A -3	149		

Table 4.11a: Maximum displacements of four-storey structure in the first mode from time-harmonic excitation in α -directions, $a_0=0.1g$, $r_{S1} = 2.97m$, $r_{S2} = 2.98m$, $r_{S3} = 2.97m$, $r_{S4} = 2.97m$.

Multi-storey Moderately Plan-asymmetric Space Frame with TLCGDs

Forcing direction	structure						TLCGD2	
	v_2 [mm]	w_2 [mm]	$u_{T2} = r_{S2}\theta_2$ [mm]	v_4 [mm]	w_4 [mm]	$u_{T4} = r_{S4}\theta_4$ [mm]	u_0 [mm]	
$\alpha = 0$	-61	-10	38	C_{M4}	-90	-21	57	658
				A	-118	-42		
$\alpha = \pi/6$	-58	-9	36	C_{M4}	-86	-20	54	626
				A	-112	-40		
$\alpha = \pi/4$	-51	-8	31	C_{M4}	-75	-18	47	544
				A	-98	-35		
$\alpha = \pi/3$	-40	-6	25	C_{M4}	-59	-14	37	426
				A	-77	-27		
$\alpha = \pi/2$	-11	-2	7	C_{M4}	-16	-4	10	113
				A	-21	-7		
$\alpha = 2\pi/3$	-21	-3	13	C_{M4}	-31	-7	20	232
				A	-41	-15		
$\alpha = 3\pi/4$	-36	-6	22	C_{M4}	-53	-12	33	386
				A	-69	-25		
$\alpha = 5\pi/6$	-48	-8	29	C_{M4}	-70	-17	44	514
				A	-92	-33		

Table 4.11b: Maximum displacements of four-storey structure in the second mode from time-harmonic excitation in α -directions, $a_0=0.1g$, $r_{S1} = 2.97m$, $r_{S2} = 2.98m$, $r_{S3} = 2.97m$, $r_{S4} = 2.97m$.

Forcing direction	structure						TLCGD3	
	v_2 [mm]	w_2 [mm]	$u_{T2} = r_{S2}\theta_2$ [mm]	v_4 [mm]	w_4 [mm]	$u_{T4} = r_{S4}\theta_4$ [mm]	u_0 [mm]	
$\alpha = 0$	-17	3	-27	C_{M4}	-28	10	-41	513
				A	-36	80		
$\alpha = \pi/6$	-13	2	-20	C_{M4}	-21	8	-31	388
				A	-27	60		
$\alpha = \pi/4$	-10	2	-15	C_{M4}	-16	6	-22	287
				A	-20	44		
$\alpha = \pi/3$	-5	1	-9	C_{M4}	-9	3	-13	168
				A	-11	25		
$\alpha = \pi/2$	-5	1	-7	C_{M4}	-8	3	-11	150
				A	-10	22		
$\alpha = 2\pi/3$	-13	2	-20	C_{M4}	-21	7	-30	381
				A	-26	58		
$\alpha = 3\pi/4$	-15	3	-24	C_{M4}	-25	9	-36	463
				A	-32	72		
$\alpha = 5\pi/6$	-17	3	-27	C_{M4}	-28	10	-41	514
				A	-36	80		

Table 4.11c: Maximum displacements of four-storey structure in the third mode from time-harmonic excitation in α -directions, $a_0=0.1g$, $r_{S1} = 2.97m$, $r_{S2} = 2.98m$, $r_{S3} = 2.97m$, $r_{S4} = 2.97m$.

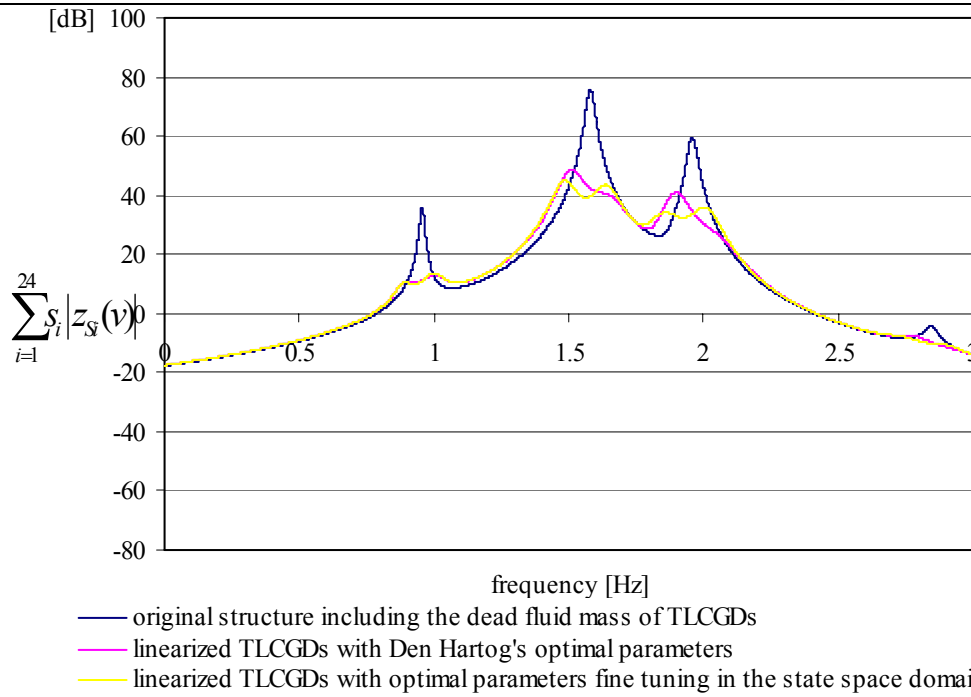


Fig. 4.57: Weighed sum of amplitude response functions for the 12-DOF linearized, four-storey, moderately asymmetric space frame, with four linearized TLCGDs attached (TLCGD4 on the fourth floor) and without the TLCGDs (angle of attack of the time-harmonic base acceleration $\alpha = 0$), maximum gain 30.9dB.

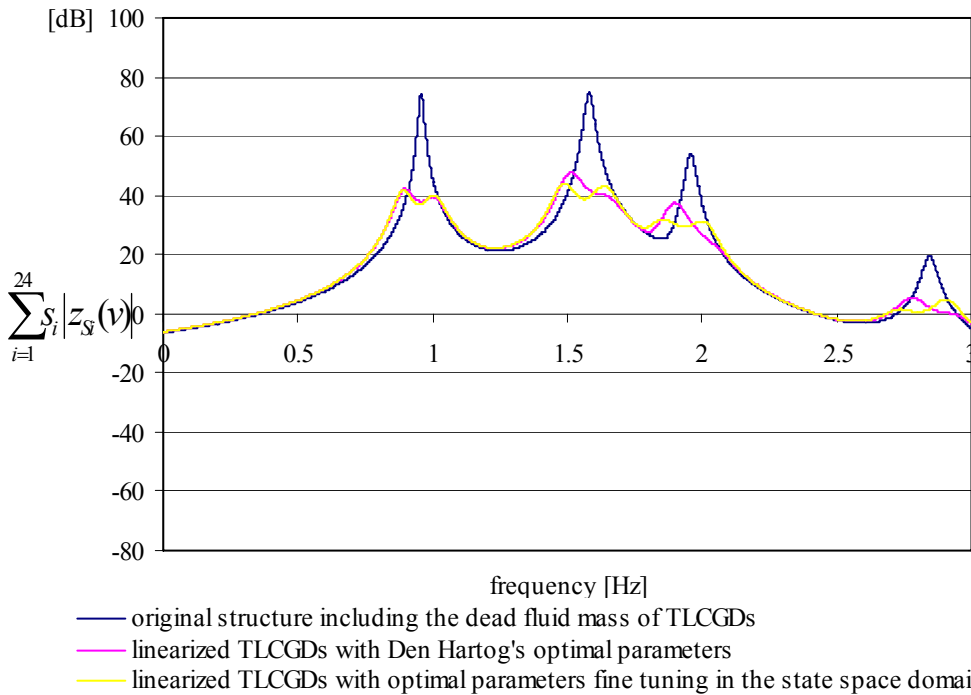


Fig. 4.58: Weighed sum of amplitude response functions for the 12-DOF linearized, four-storey, moderately asymmetric space frame, with four linearized TLCGDs attached (TLCGD4 on the fourth floor) and without the TLCGDs (angle of attack of the time-harmonic base acceleration $\alpha = \pi/6$), maximum gain 30.8dB.

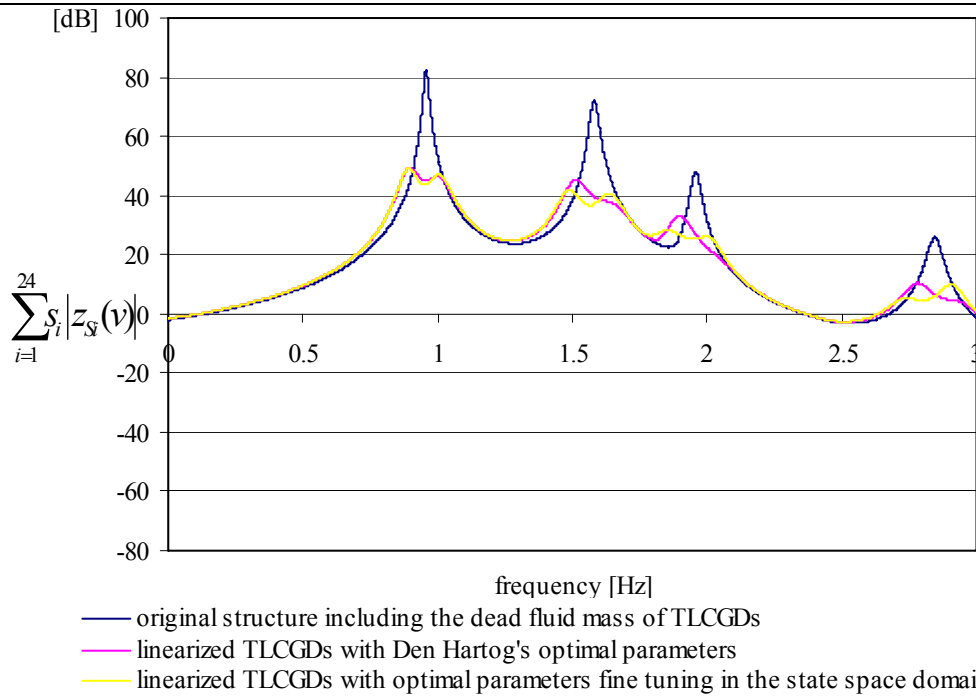


Fig. 4.59: Weighed sum of amplitude response functions for the 12-DOF linearized, four-storey, moderately asymmetric space frame, with four linearized TLCGDs attached (TLCGD4 on the fourth floor) and without the TLCGDs (angle of attack of the time-harmonic base acceleration $\alpha = \pi/4$), maximum gain 33.1dB.

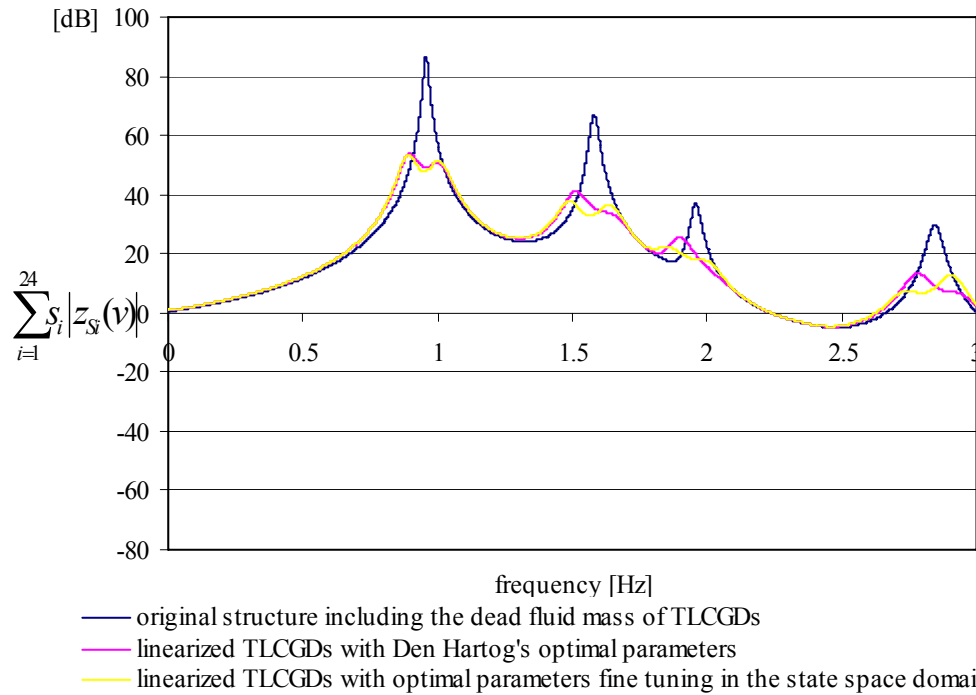


Fig. 4.60: Weighed sum of amplitude response functions for the 12-DOF linearized, four-storey, moderately asymmetric space frame, with four linearized TLCGDs attached (TLCGD4 on the fourth floor) and without the TLCGDs (angle of attack of the time-harmonic base acceleration $\alpha = \pi/3$), maximum gain 33.3dB.

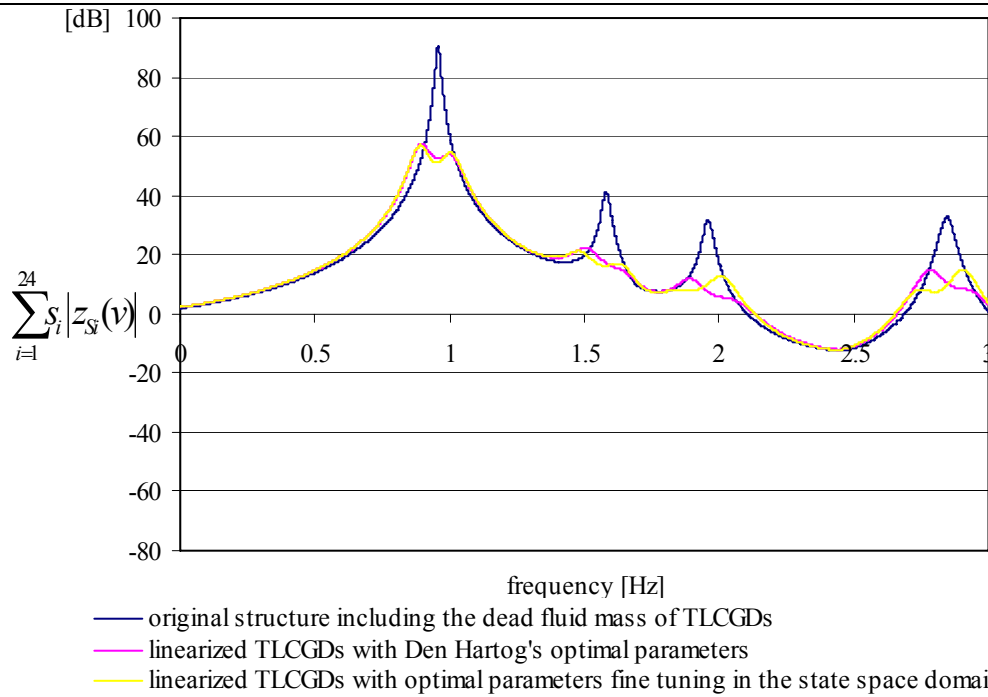


Fig. 4.61: Weighed sum of amplitude response functions for the 12-DOF linearized, four-storey, moderately asymmetric space frame, with four linearized TLCGDs attached (TLCGD4 on the fourth floor) and without the TLCGDs (angle of attack of the time-harmonic base acceleration $\alpha = \pi/2$), maximum gain 33.2dB.

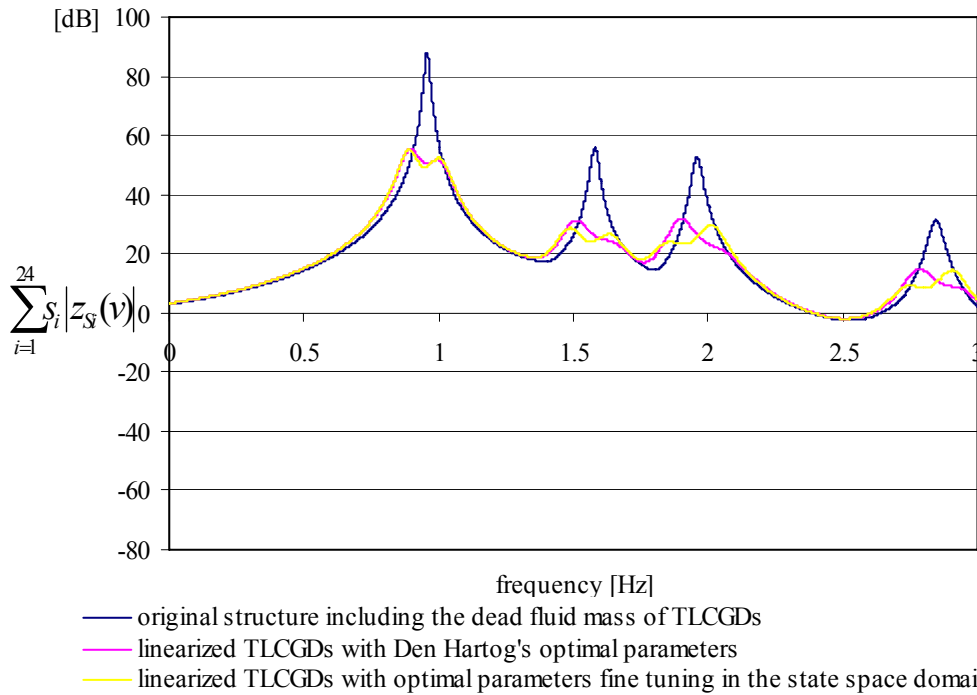


Fig. 4.62: Weighed sum of amplitude response functions for the 12-DOF linearized, four-storey, moderately asymmetric space frame, with four linearized TLCGDs attached (TLCGD4 on the fourth floor) and without the TLCGDs (angle of attack of the time-harmonic base acceleration $\alpha = 2\pi/3$), maximum gain 33dB.

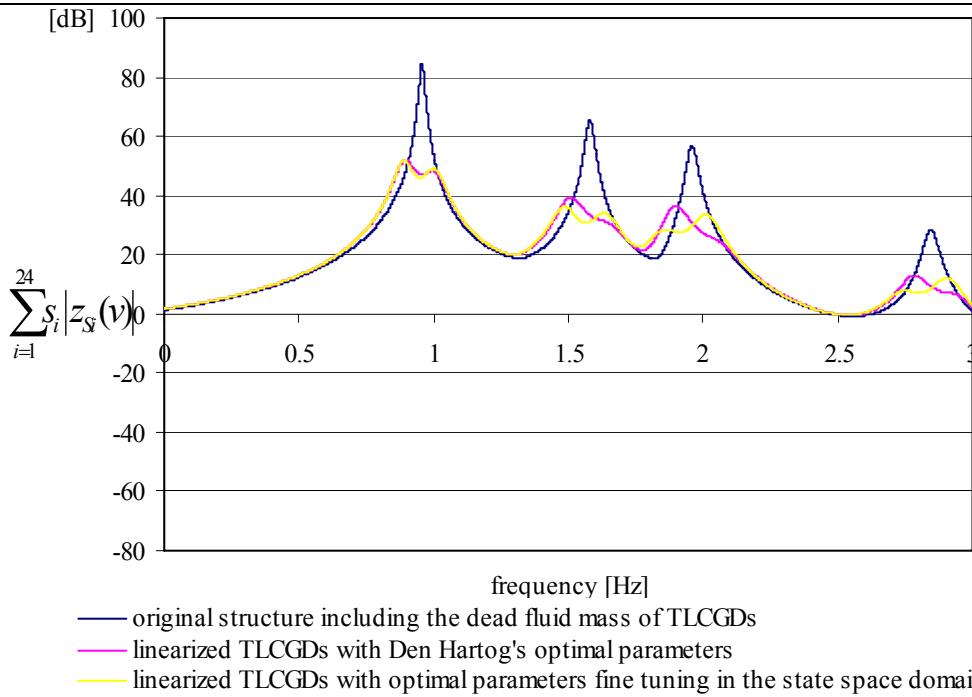


Fig. 4.63: Weighed sum of amplitude response functions for the 12-DOF linearized, four-storey, moderately asymmetric space frame, with four linearized TLCGDs attached (TLCGD4 on the fourth floor) and without the TLCGDs (angle of attack of the time-harmonic base acceleration $\alpha = 3\pi/4$), maximum gain 32.7dB.

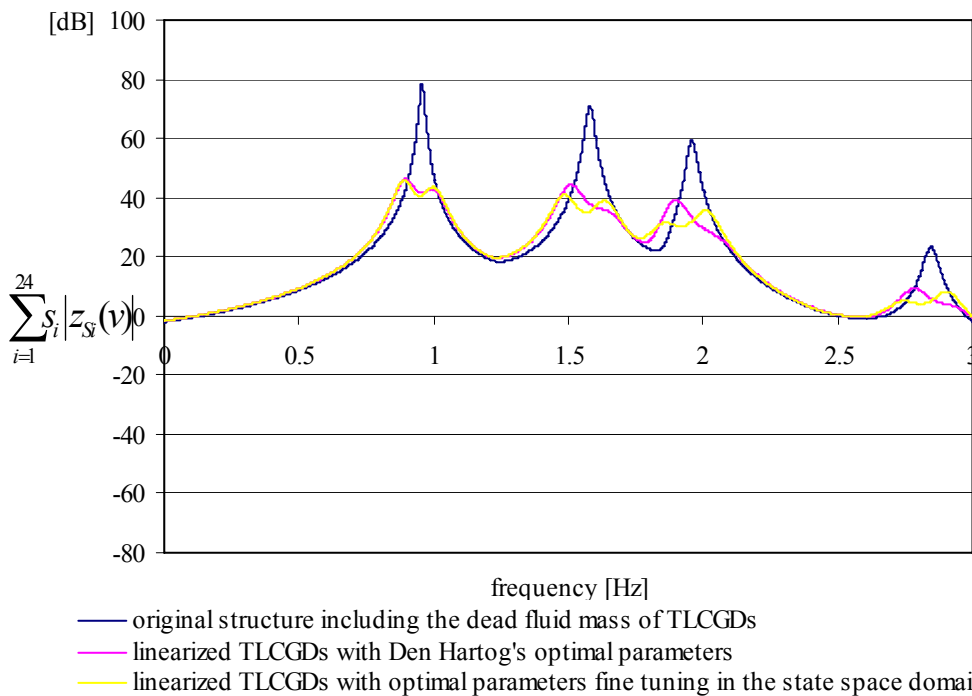


Fig. 4.64: Weighed sum of amplitude response functions for the 12-DOF linearized, four-storey, moderately asymmetric space frame, with four linearized TLCGDs attached (TLCGD4 on the fourth floor) and without the TLCGDs (angle of attack of the time-harmonic base acceleration $\alpha = 5\pi/6$), maximum gain 32.3dB.

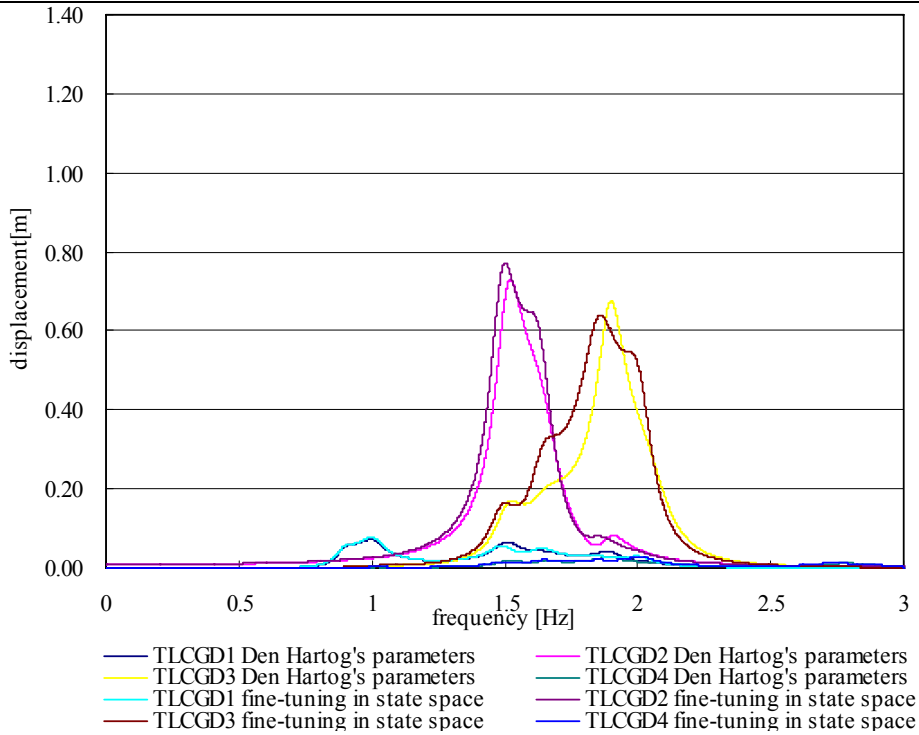


Fig. 4.65: Amplitude response curves of fluid displacement $|u|$ of four linearized TLCGDs attached to the 12-DOF space frame (TLCGD4 on the fourth floor). TLCGDs either with Den Hartog's optimal parameters or those resulting from fine-tuning in state space ($\alpha = 0$).

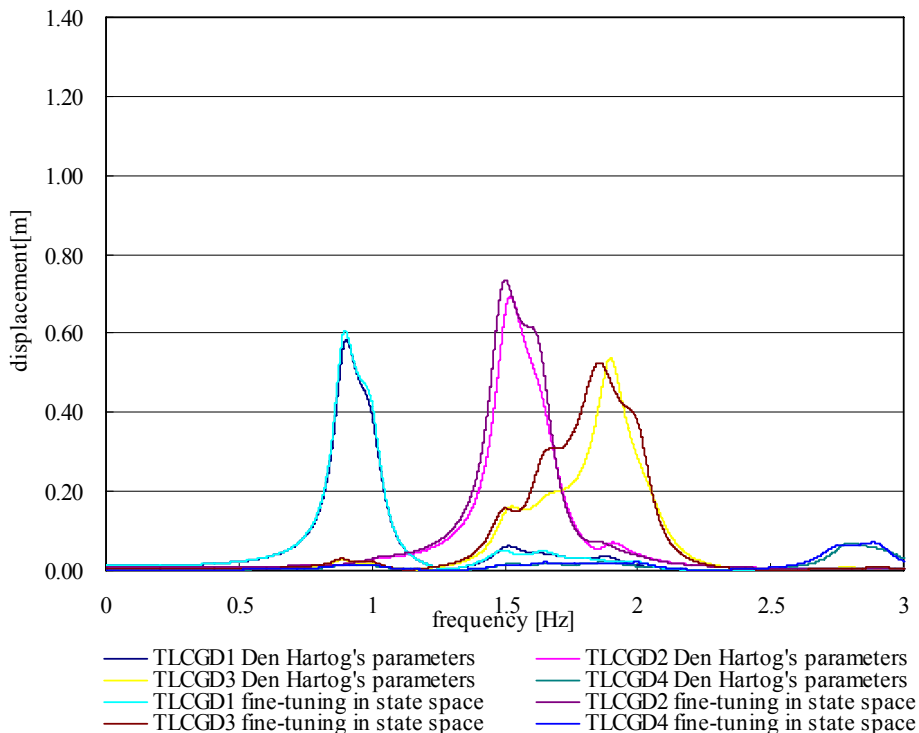


Fig. 4.66: Amplitude response curves of fluid displacement $|u|$ of four linearized TLCGDs attached to the 12-DOF space frame (TLCGD4 on the fourth floor). TLCGDs either with Den Hartog's optimal parameters or those resulting from fine-tuning in state space ($\alpha = \pi/6$).

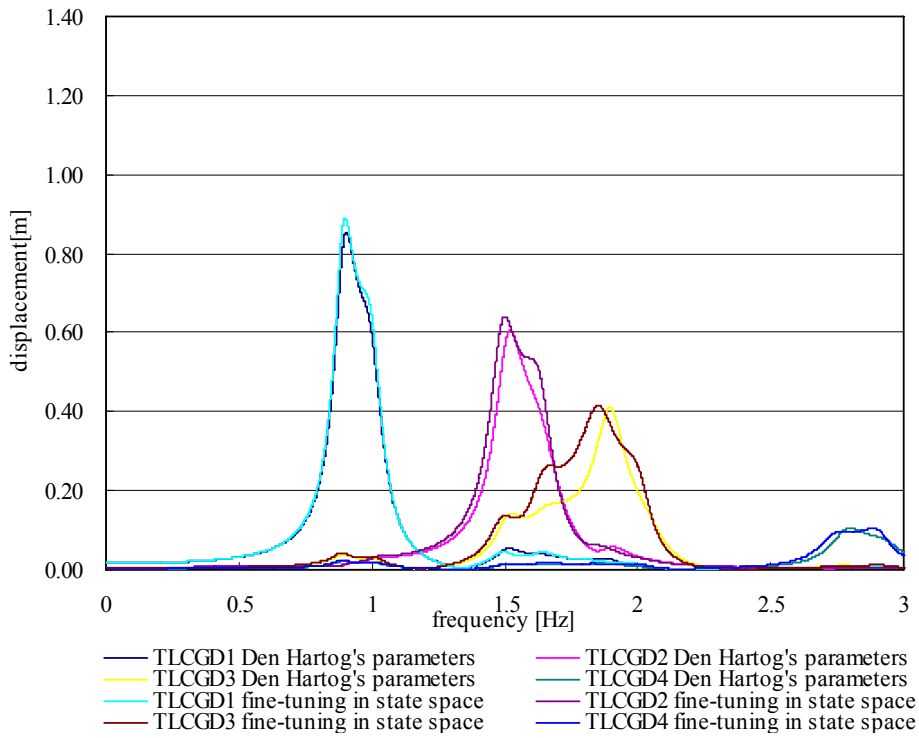


Fig. 4.67: Amplitude response curves of fluid displacement $|u|$ of four linearized TLCDGs attached to the 12-DOF space frame (TLCDG4 on the fourth floor). TLCDGs either with Den Hartog's optimal parameters or those resulting from fine-tuning in state space ($\alpha = \pi/4$).

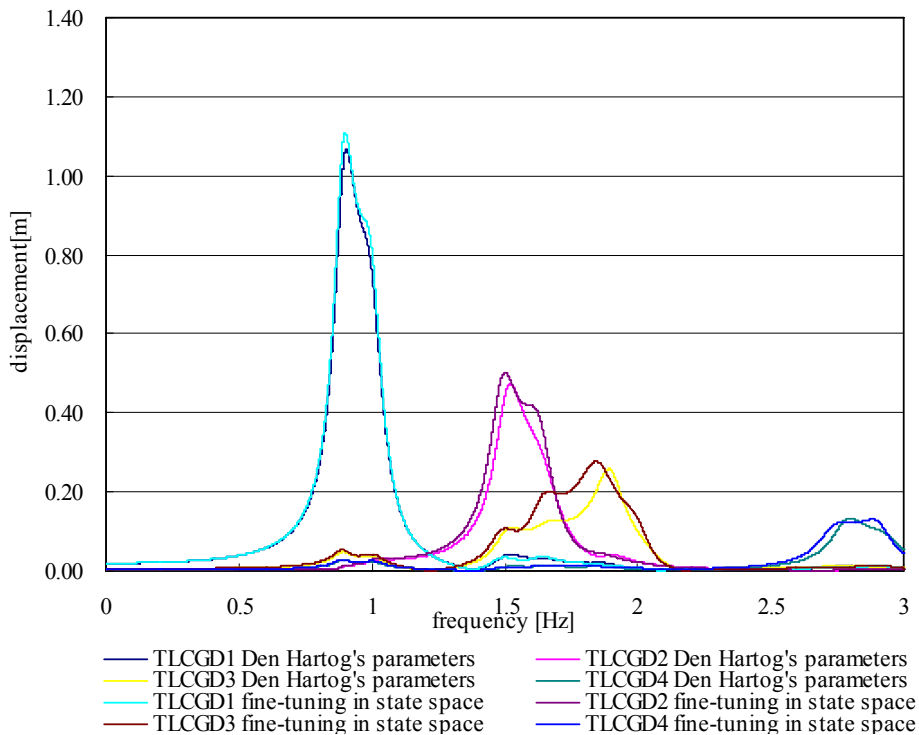


Fig. 4.68: Amplitude response curves of fluid displacement $|u|$ of four linearized TLCDGs attached to the 12-DOF space frame (TLCDG4 on the fourth floor). TLCDGs either with Den Hartog's optimal parameters or those resulting from fine-tuning in state space ($\alpha = \pi/3$).

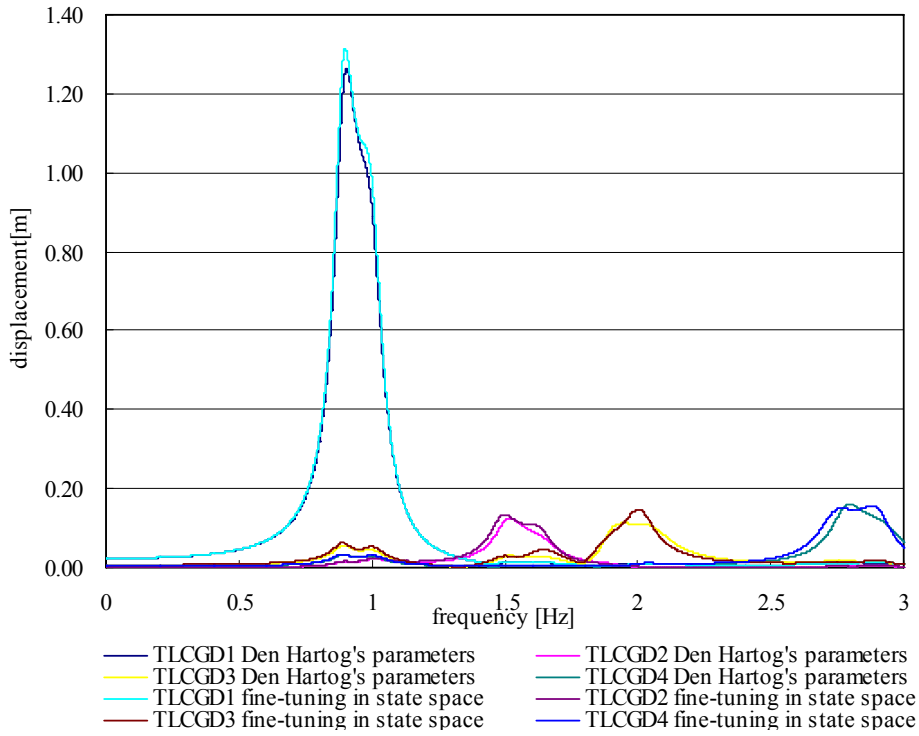


Fig. 4.69: Amplitude response curves of fluid displacement $|u|$ of four linearized TLCGDs attached to the 12-DOF space frame (TLCGD4 on the fourth floor). TLCGDs either with Den Hartog's optimal parameters or those resulting from fine-tuning in state space ($\alpha = \pi/2$).

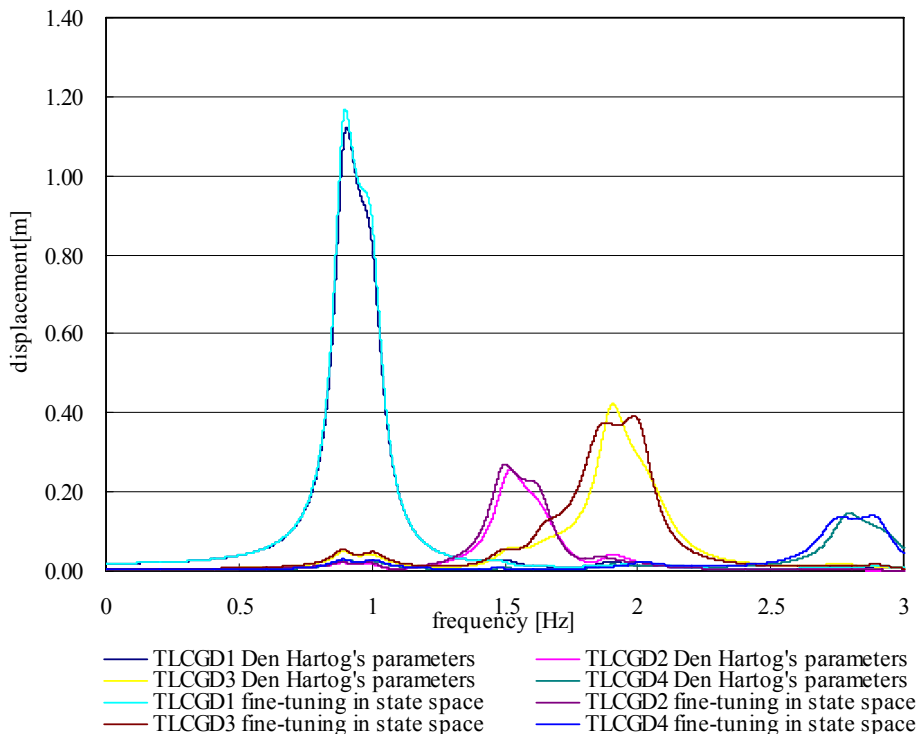


Fig. 4.70: Amplitude response curves of fluid displacement $|u|$ of four linearized TLCGDs attached to the 12-DOF space frame (TLCGD4 on the fourth floor). TLCGDs either with Den Hartog's optimal parameters or those resulting from fine-tuning in state space ($\alpha = 2\pi/3$).

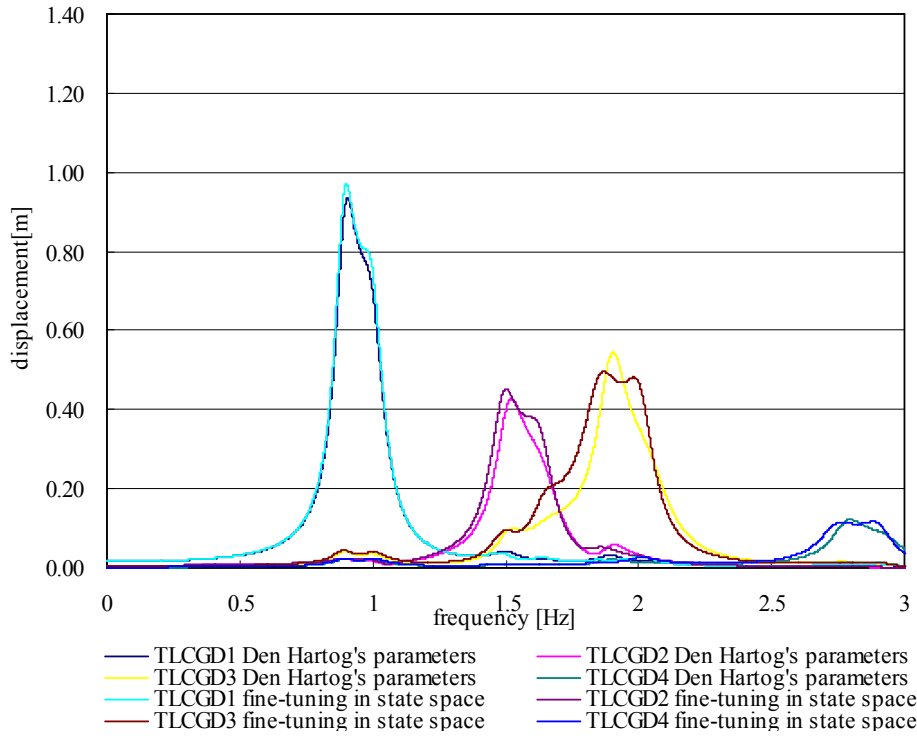


Fig. 4.71: Amplitude response curves of fluid displacement $|u|$ of four linearized TLCGDs attached to the 12-DOF space frame (TLCGD4 on the fourth floor). TLCGDs either with Den Hartog's optimal parameters or those resulting from fine-tuning in state space ($\alpha = 3\pi/4$).

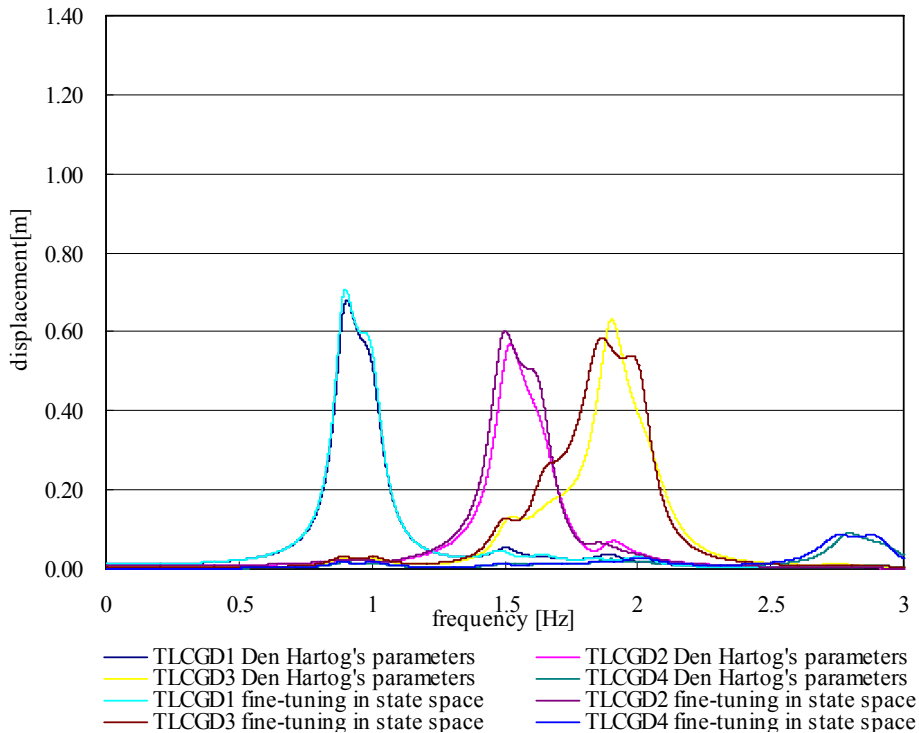


Fig. 4.72: Amplitude response curves of fluid displacement $|u|$ of four linearized TLCGDs attached to the 12-DOF space frame (TLCGD4 on the fourth floor). TLCGDs either with Den Hartog's optimal parameters or those resulting from fine-tuning in state space ($\alpha = 5\pi/6$).

The wall thickness and the estimated dead mass of the piping system are listed in Table 4.12 for the four absorbers, designed according to Table 4.10.

	TLCGD1	TLCGD2	TLCGD3	TLCGD4
h_0 [m]	56.28	69.72	86.88	88.08
H_a [m]	4	2.36	2.08	1.25
$10^{-5} p_{(D)}$ [N/m ²] Eq.(2.128)	25.19	31.33	39.27	39.76
pipe diameter $2r$ [mm]	575.4	422.2	247.2	334.7
t [mm] Eq.(2.124)	5.2	4.7	3.5	4.8
m_p [kg] Eq.(2.130)	1152.9	513.91	209.31	272.90
dead fluid-mass[kg]	665.03	212.32	58.16	50.31
$10^{-5} \bar{p}_{(D)}$ [N/m ²] Eq.(2.129)	1.35	1.91	2.63	2.68

Table 4.12: Dimensioning of circular steel pipes.

The gauge pressure under expansion conditions turns out to be positive as listed in Table 4.12. The final dimensions of circular steel pipes must be changed according to their commercial availability.

4.6.6 TLCGD4 alternatively installed on the second floor

Since the same fluid weight of TLCGD4 is considered, the mass ratio is $\mu_4 = 0.51\%$. The optimal parameters of TLCGD4 are $\delta_{opt4} = 0.996$, $\zeta_{opt4} = 4.08\%$. The optimal frequency is $f_{A4} = 2.86\text{Hz}$.

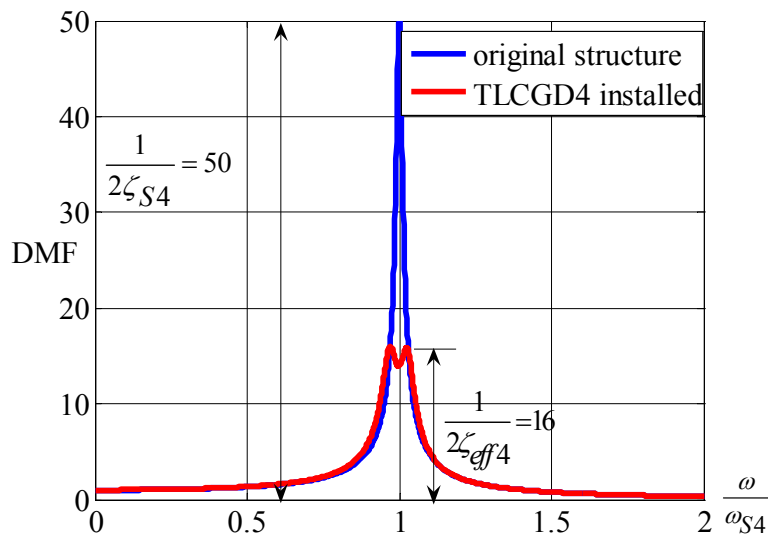


Fig.4.73: Frequency response curves of the fourth mode without and with linearized TLCGD4 attached, TLCGD4 with Den Hartog's optimal parameters.

The effective modal damping coefficient of the system is $\zeta_{eff4} = 3.1\%$, the gain is slightly lower when compared to TLCGD4 oriented on the fourth floor.

Forcing direction	structure						TLCD4	
	v_2 [mm]	w_2 [mm]	$u_{T2} = r_{S2}\theta_2$ [mm]	v_4 [mm]	w_4 [mm]	$u_{T4} = r_{S4}\theta_4$ [mm]		
$\alpha = 0$	C _{M2}	0	-1	0	0	1	0	9
	A	0	-1					
$\alpha = \pi/6$	C _{M2}	0	-8	-1	0	8	0	74
	A	0	-7					
$\alpha = \pi/4$	C _{M2}	1	-11	-2	-1	11	2	110
	A	0	-10					
$\alpha = \pi/3$	C _{M2}	1	-14	-2	-1	14	3	137
	A	0	-13					
$\alpha = \pi/2$	C _{M2}	1	-17	-3	-1	17	4	163
	A	0	-16					
$\alpha = 2\pi/3$	C _{M2}	1	-15	-2	-1	15	3	146
	A	0	-14					
$\alpha = 3\pi/4$	C _{M2}	1	-12	-2	-1	12	3	122
	A	0	-12					
$\alpha = 5\pi/6$	C _{M2}	1	-9	-1	0	9	2	89
	A	0	-9					

Table 4.10: Maximum displacements of four-storey structure in the fourth mode from time-harmonic excitation in α -directions, $a_0=0.1g$, $r_{S1} = 2.97m$, $r_{S2} = 2.98m$, $r_{S3} = 2.97m$, $r_{S4} = 2.97m$.

The optimal natural frequencies and damping ratios are found to be $f_{A1} = 0.941Hz$, $f_{A2} = 1.552Hz$, $f_{A3} = 1.893Hz$, $f_{A4} = 2.87Hz$, $\zeta_{A1} = 7.81\%$, $\zeta_{A2} = 5.75\%$, $\zeta_{A3} = 5.81\%$, $\zeta_{A4} = 3.62\%$. The equilibrium pressure head h_0 of four TLCDs are 52.91, 64.41, 77.10 and 87.59m. The Figures 4.74-4.81 show the frequency response of the weighed sum $\sum_{i=1}^{24} s_i |z_{Si}(\nu)|$ of the building states for the original and the optimized system, in the logarithmic decibel scale within the relevant frequency window $0 \leq f \leq 3Hz$. The resonance curves with fine-tuning optimal parameters also have broader peaks. From inspection of these figures 4.82-4.89 it is apparent that the maximum relative fluid displacements for all cases are well within the acceptable limits. The maximum fluid velocities of four TLCDs are calculated by Eq. (2.35) 7.69, 7.61, 7.61 and 3.25m/s and are also within the acceptable speed limit.

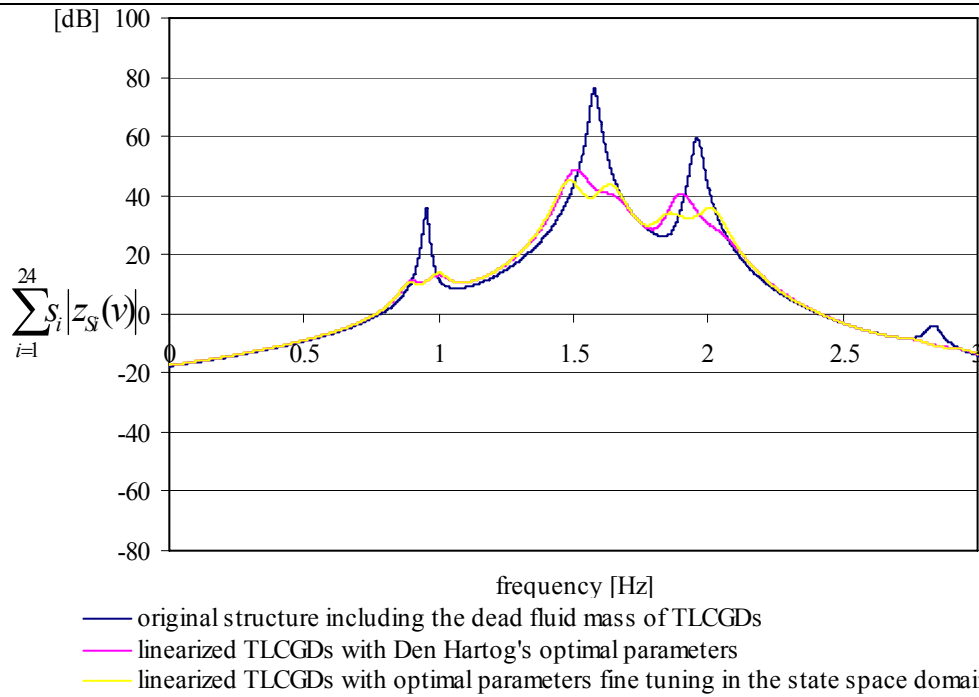


Fig. 4.74: Weighed sum of amplitude response functions for the 12-DOF linearized, four-storey, moderately asymmetric space frame, with four linearized TLCGDs attached (TLCGD4 on the second floor) and without the TLCGDs (angle of attack of the time-harmonic base acceleration $\alpha = 0$), maximum gain 30.8dB.

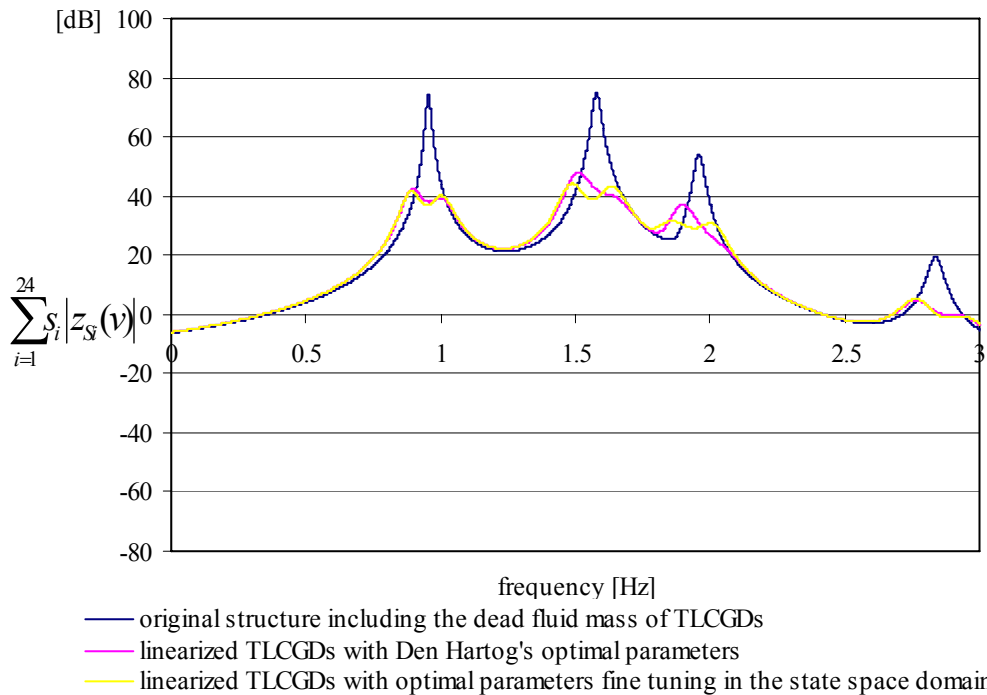


Fig. 4.75: Weighed sum of amplitude response functions for the 12-DOF linearized, four-storey, moderately asymmetric space frame, with four linearized TLCGDs attached (TLCGD4 on the second floor) and without the TLCGDs (angle of attack of the time-harmonic base acceleration $\alpha = \pi/6$), maximum gain 30.7dB.

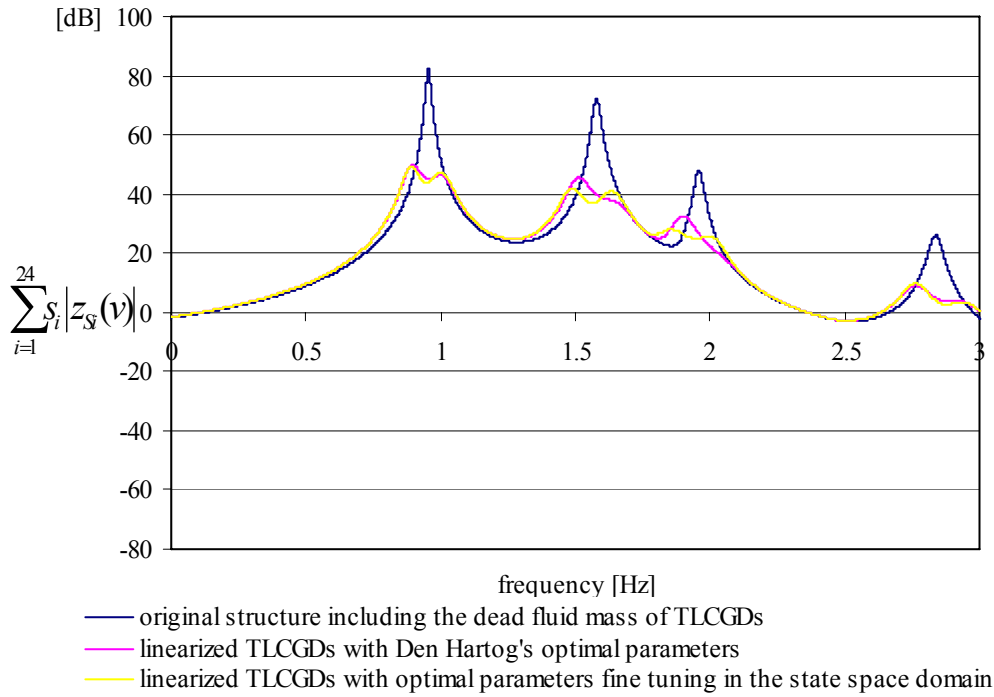


Fig. 4.76: Weighed sum of amplitude response functions for the 12-DOF linearized, four-storey, moderately asymmetric space frame, with four linearized TLCGDs attached (TLCGD4 on the second floor) and without the TLCGDs (angle of attack of the time-harmonic base acceleration $\alpha = \pi/4$), maximum gain 33.1dB.

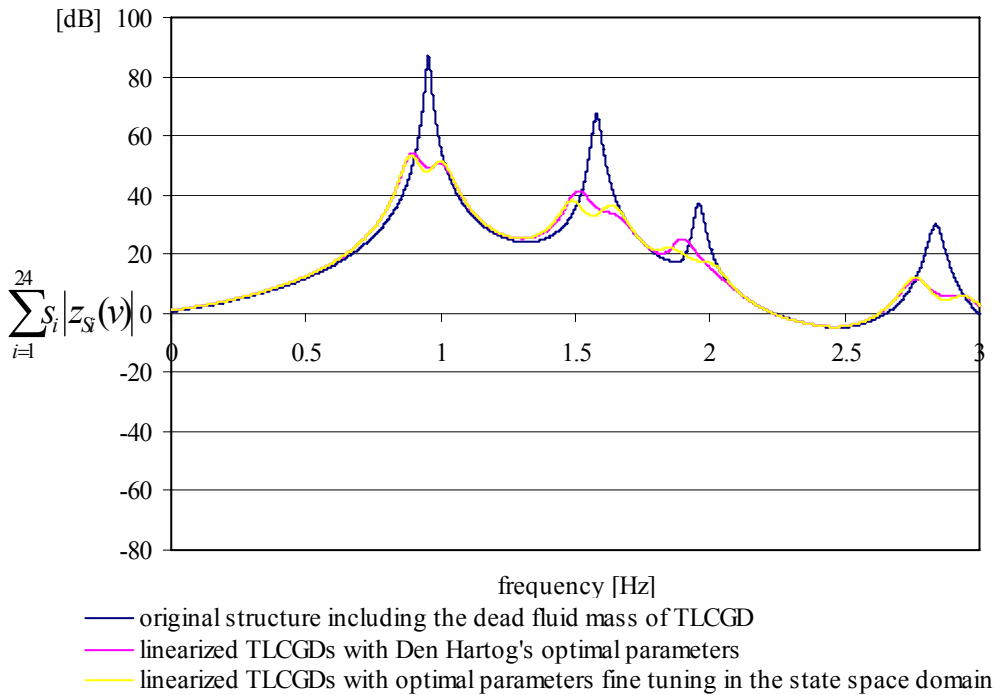


Fig. 4.77: Weighed sum of amplitude response functions for the 12-DOF linearized, four-storey, moderately asymmetric space frame, with four linearized TLCGDs attached (TLCGD4 on the second floor) and without the TLCGDs (angle of attack of the time-harmonic base acceleration $\alpha = \pi/3$), maximum gain 33.3dB.

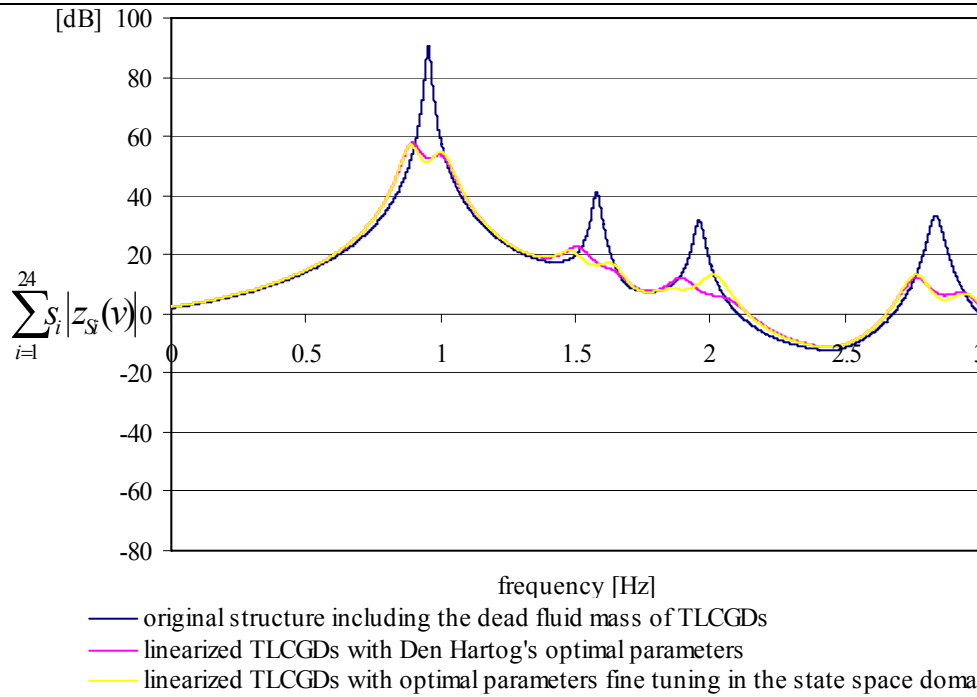


Fig. 4.78: Weighed sum of amplitude response functions for the 12-DOF linearized, four-storey, moderately asymmetric space frame, with four linearized TLCGDs attached (TLCGD4 on the second floor) and without the TLCGDs (angle of attack of the time-harmonic base acceleration $\alpha = \pi/2$), maximum gain 33.2dB.

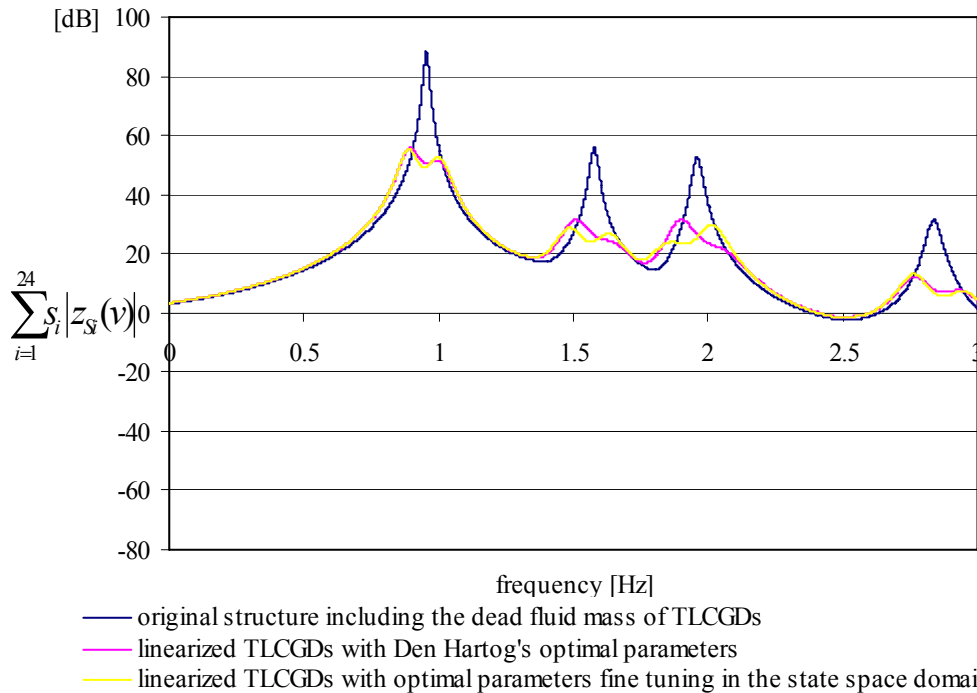


Fig. 4.79: Weighed sum of amplitude response functions for the 12-DOF linearized, four-storey, moderately asymmetric space frame, with four linearized TLCGDs attached (TLCGD4 on the second floor) and without the TLCGDs (angle of attack of the time-harmonic base acceleration $\alpha = 2\pi/3$), maximum gain 33dB.

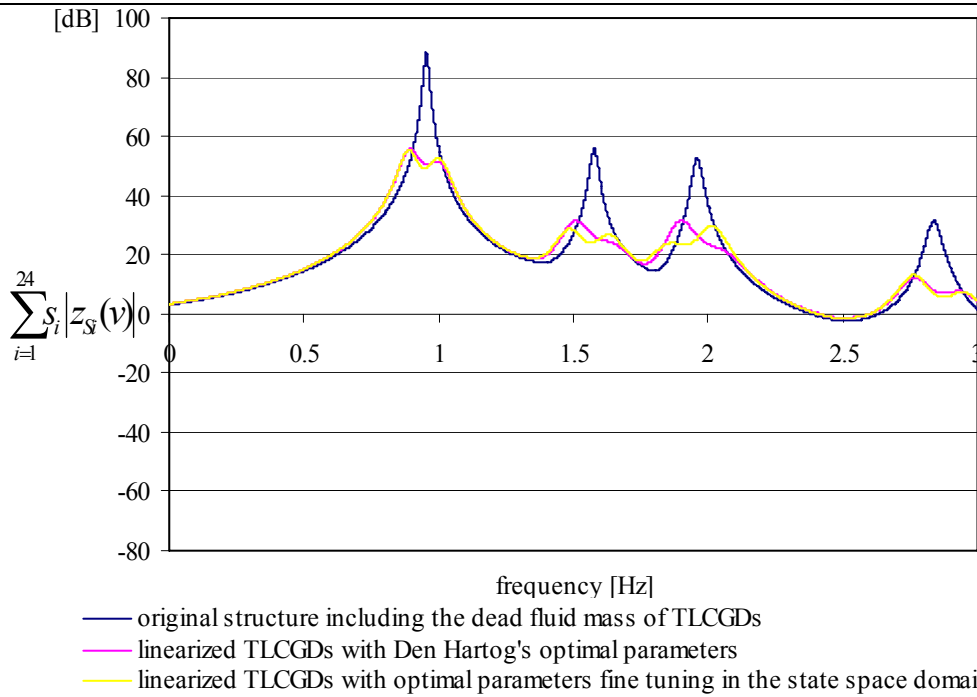


Fig. 4.80: Weighed sum of amplitude response functions for the 12-DOF linearized, four-storey, moderately asymmetric space frame, with four linearized TLCGDs attached (TLCGD4 on the second floor) and without the TLCGDs (angle of attack of the time-harmonic base acceleration $\alpha = 3\pi/4$), maximum gain 32.7dB.

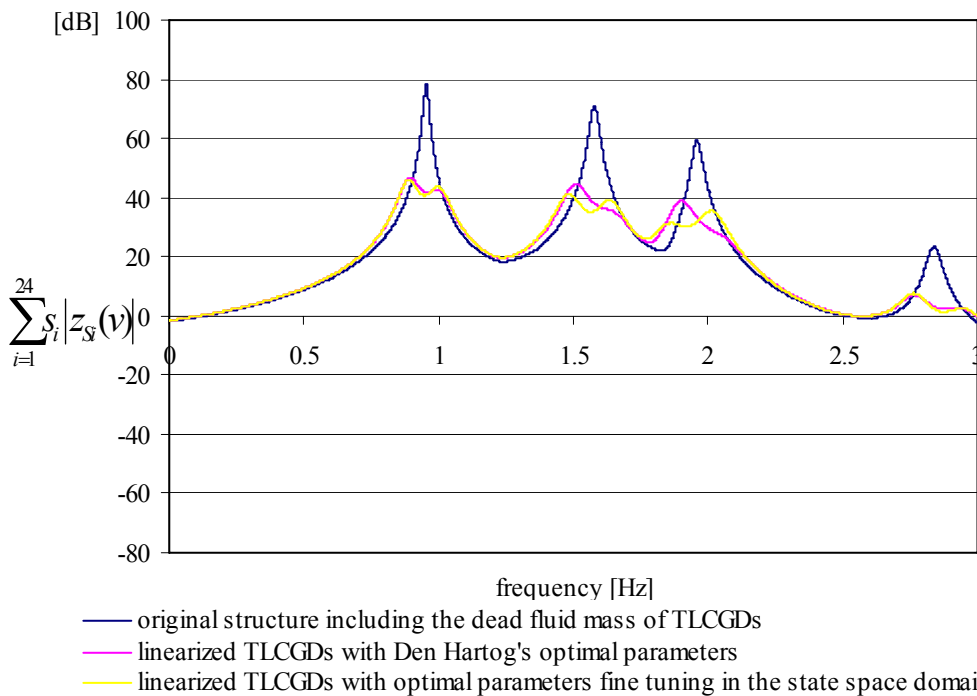


Fig. 4.81: Weighed sum of amplitude response functions for the 12-DOF linearized, four-storey, moderately asymmetric space frame, with four linearized TLCGDs attached (TLCGD4 on the second floor) and without the TLCGDs (angle of attack of the time-harmonic base acceleration $\alpha = 5\pi/6$), maximum gain 32.3dB.

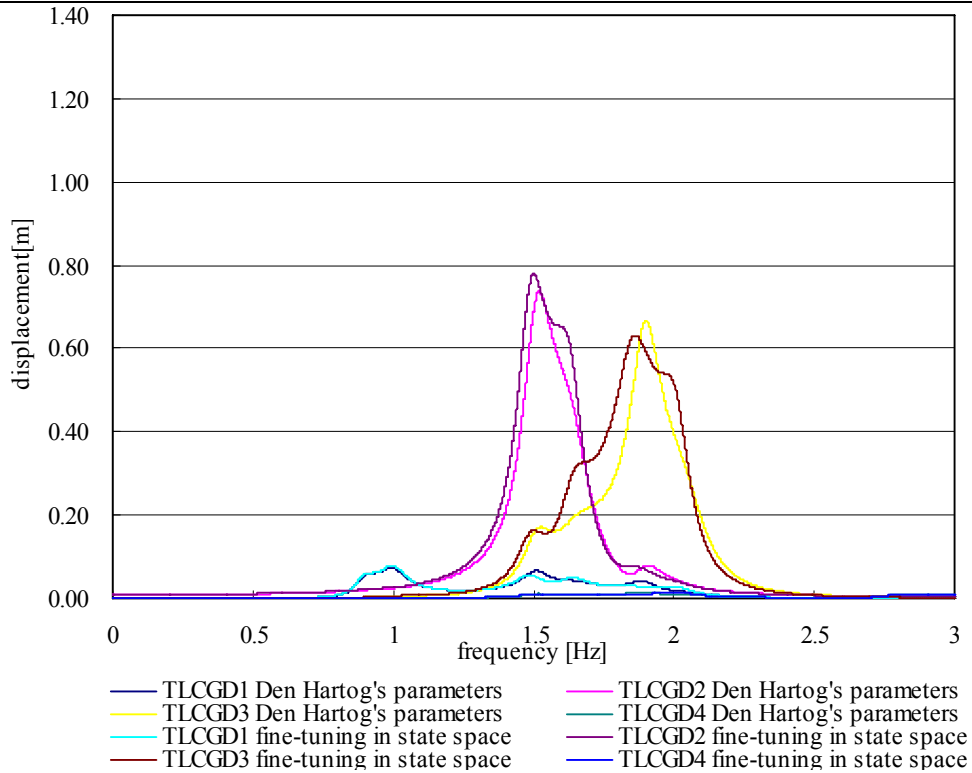


Fig. 4.82: Amplitude response curves of fluid displacement $|u|$ of four linearized TLCGDs attached to the 12-DOF space frame (TLCGD4 on the second floor). TLCGD either with Den Hartog's optimal parameters or those resulting from fine-tuning in state space ($\alpha = 0$).

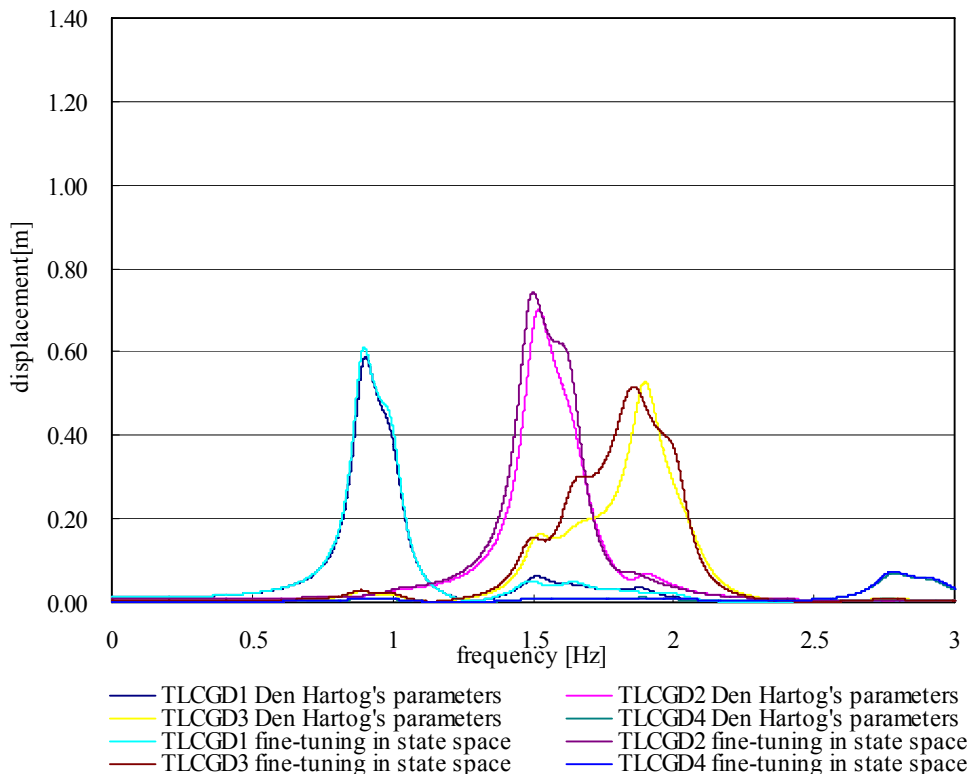


Fig. 4.83: Amplitude response curves of fluid displacement $|u|$ of four linearized TLCGDs attached to the 12-DOF space frame (TLCGD4 on the second floor). TLCGD either with Den Hartog's optimal parameters or those resulting from fine-tuning in state space ($\alpha = \pi/6$).

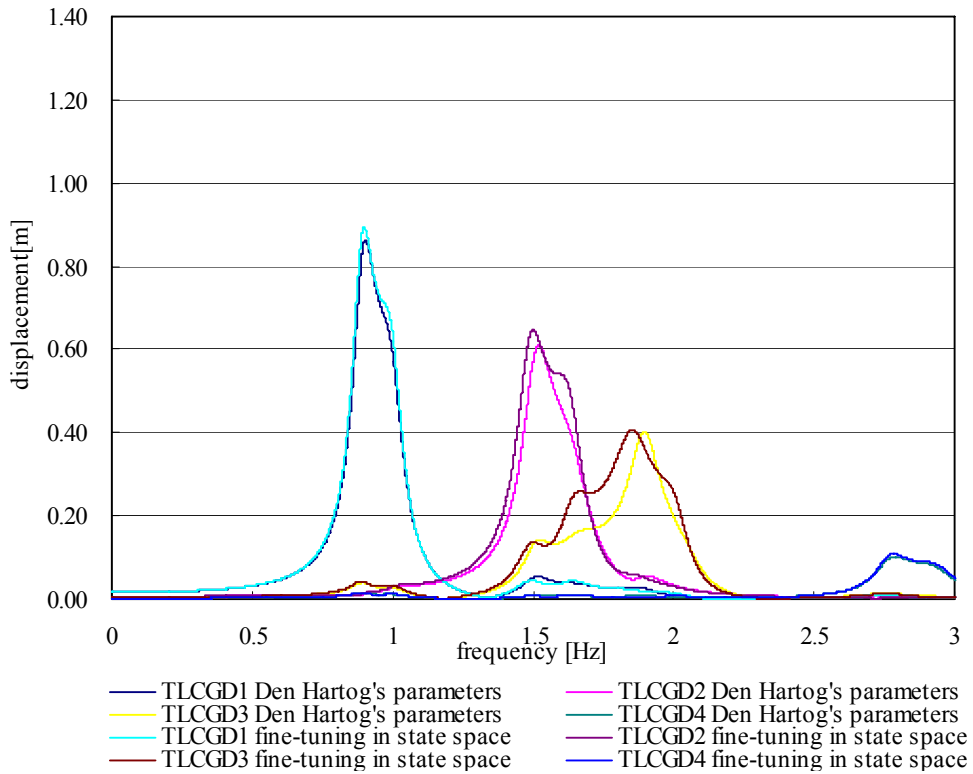


Fig. 4.84: Amplitude response curves of fluid displacement $|u|$ of four linearized TLCGDs attached to the 12-DOF space frame (TLCGD4 on the second floor). TLCGD either with Den Hartog's optimal parameters or those resulting from fine-tuning in state space ($\alpha = \pi/4$).

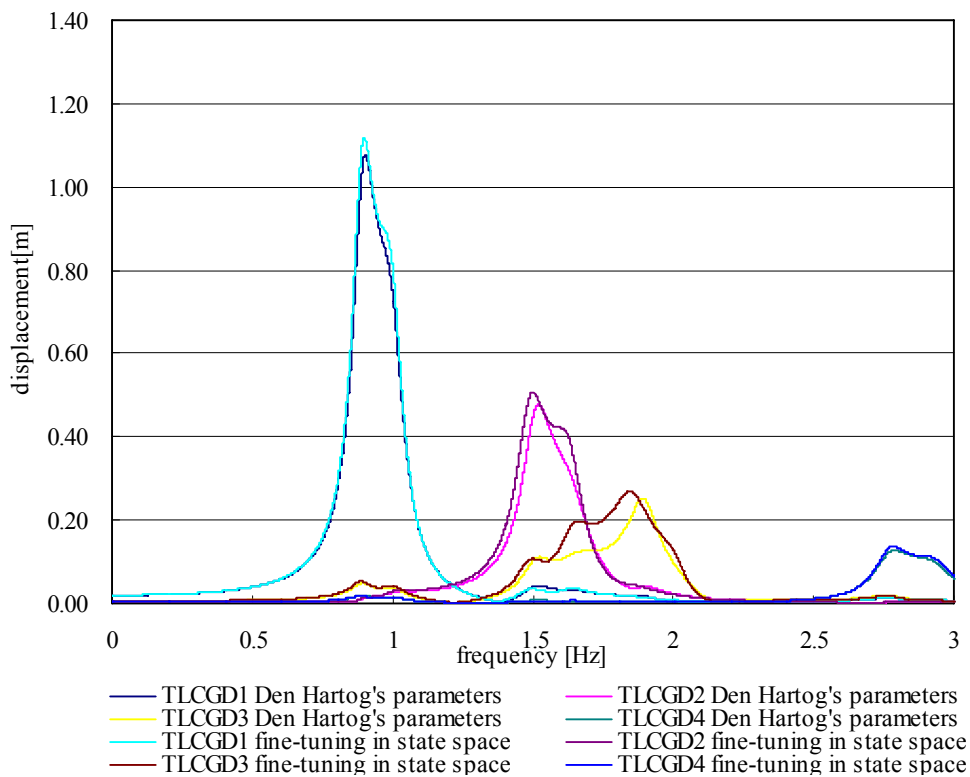


Fig. 4.85: Amplitude response curves of fluid displacement $|u|$ of four linearized TLCGDs attached to the 12-DOF space frame (TLCGD4 on the second floor). TLCGD either with Den Hartog's optimal parameters or those resulting from fine-tuning in state space ($\alpha = \pi/3$).

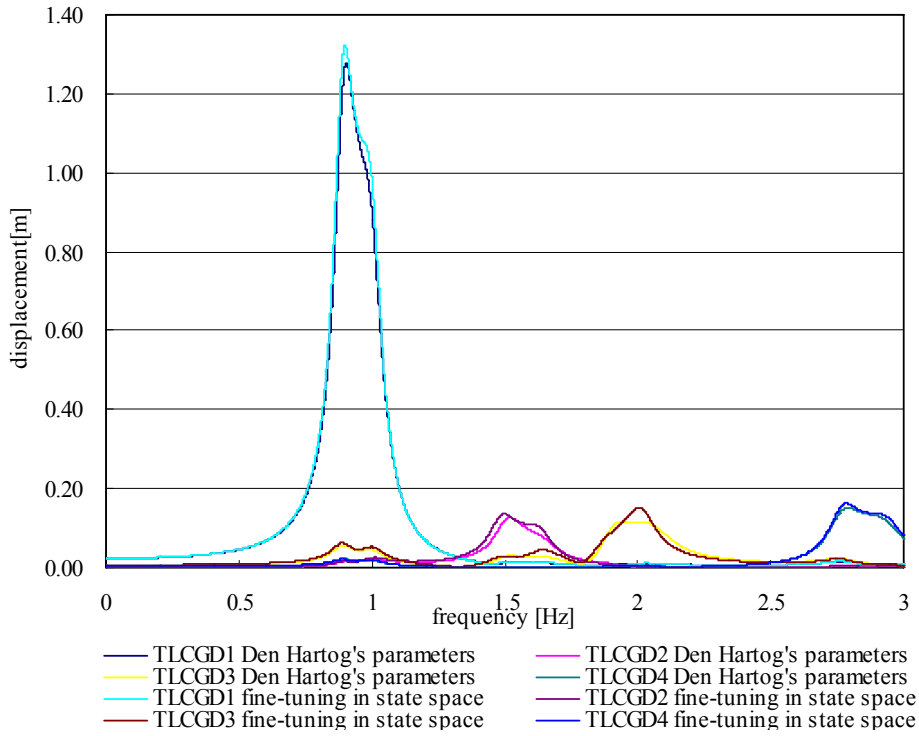


Fig. 4.86: Amplitude response curves of fluid displacement $|u|$ of four linearized TLCGDs attached to the 12-DOF space frame (TLCGD4 on the second floor). TLCGD either with Den Hartog's optimal parameters or those resulting from fine-tuning in state space ($\alpha = \pi/2$).

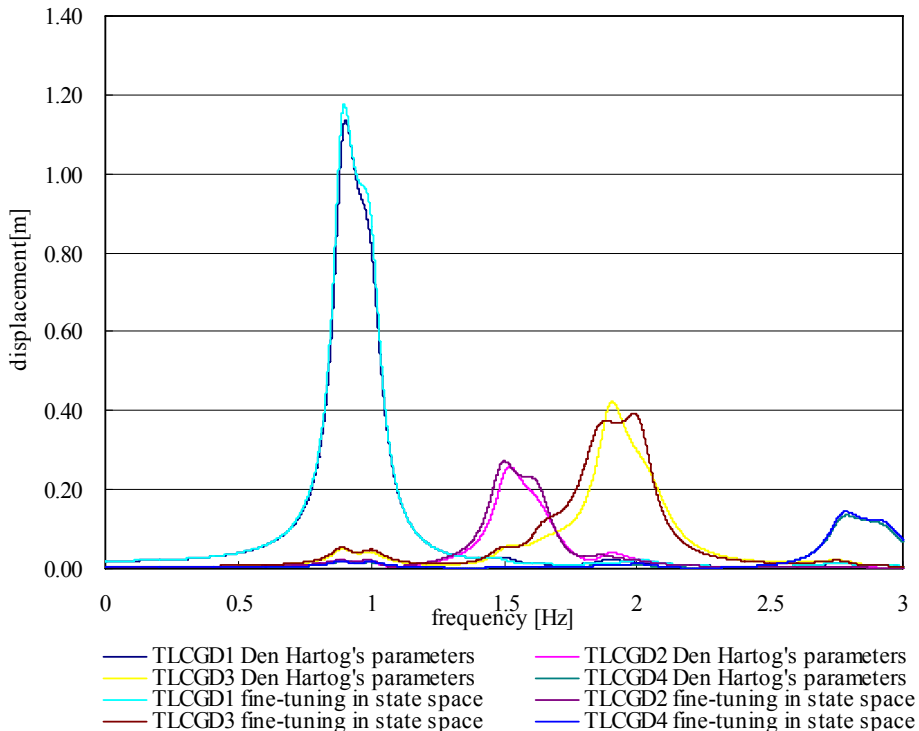


Fig. 4.87: Amplitude response curves of fluid displacement $|u|$ of four linearized TLCGDs attached to the 12-DOF space frame (TLCGD4 on the second floor). TLCGD either with Den Hartog's optimal parameters or those resulting from fine-tuning in state space ($\alpha = 2\pi/3$).

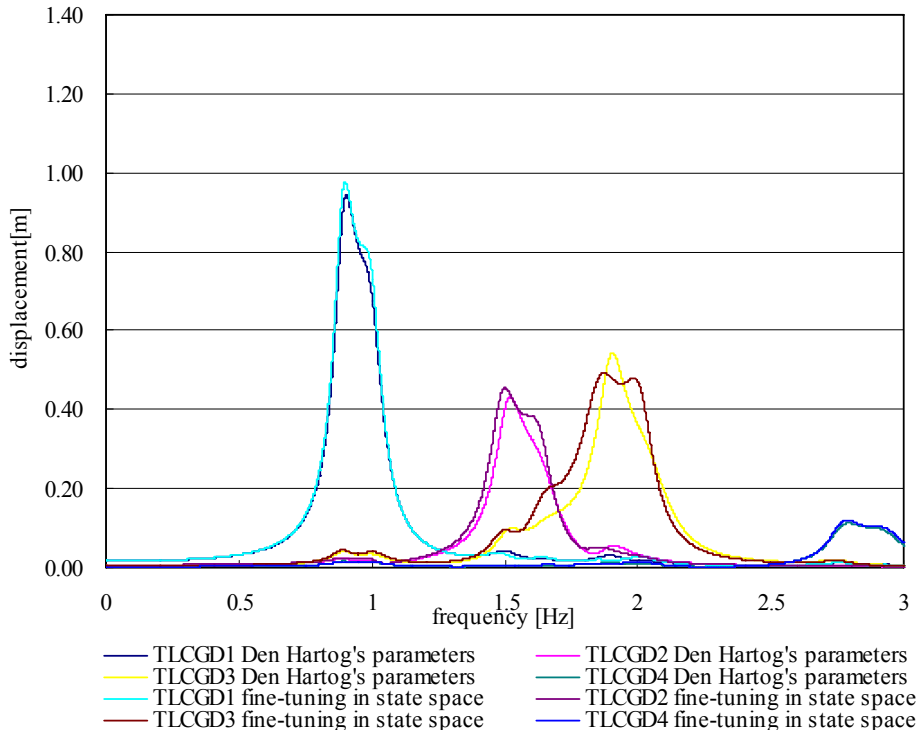


Fig. 4.88: Amplitude response curves of fluid displacement $|u|$ of four linearized TLCGDs attached to the 12-DOF space frame (TLCGD4 on the second floor). TLCGD either with Den Hartog's optimal parameters or those resulting from fine-tuning in state space ($\alpha = 3\pi/4$).

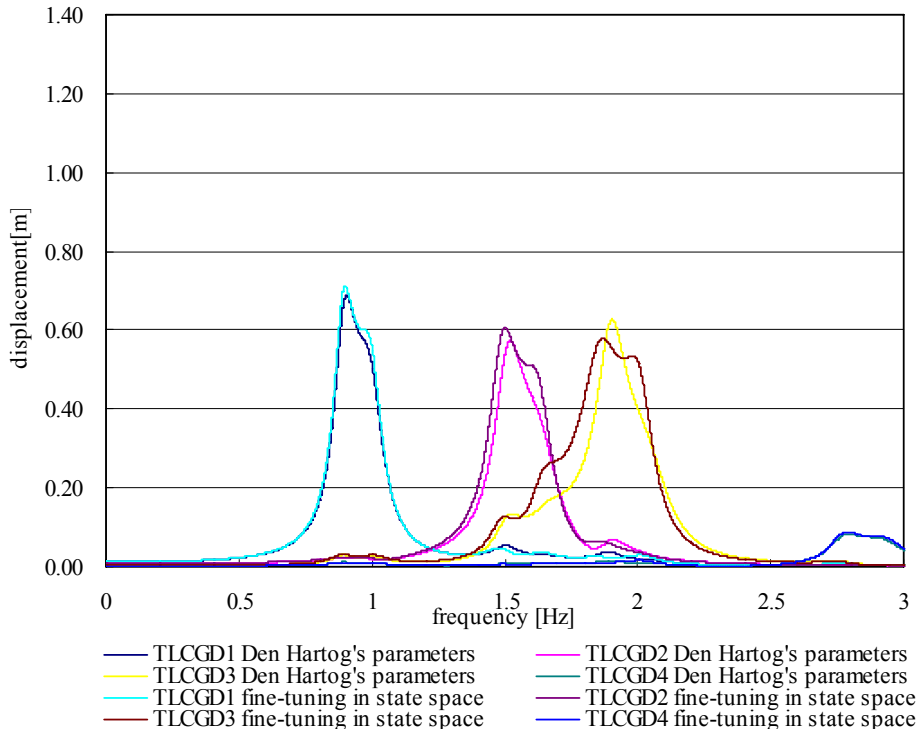


Fig. 4.89: Amplitude response curves of fluid displacement $|u|$ of four linearized TLCGDs attached to the 12-DOF space frame (TLCGD4 on the second floor). TLCGD either with Den Hartog's optimal parameters or those resulting from fine-tuning in state space ($\alpha = 5\pi/6$).

Comparing the results of the two cases all four TLCGDs on top and alternatively TLCGD4 placed on the second floor, the latter arrangement achieves a somewhat better result in the vibration reduction.

4.6.7 Forcing by the NS-EI Centro seismogram under varying angles of attack

The maximum acceleration of the NS-EI Centro earthquake record is set as $0.35g$. Varying the angle of attack refers to the effect of bidirectional forcing of the four-storey moderately asymmetric space frame. Four TLCGDs are installed to counteract the first four natural modes and TLCGD 4 is installed on the second floor. The results are presented graphically in Fig. 4.90-Fig. 4.97, where the relative floor displacements with respect to the base and the relative floor accelerations for the root mean square (RMS) responses¹ are displayed. The RMS value is given by

$$RMS = \sqrt{\frac{1}{T} \int_0^T i^2 dt}, \quad T = 20s. \quad (4.26)$$

where T is the strong motion phase of the NS-EI Centro earthquake record. The rotation displacement about x-axis is $u_{Ti} = \theta_i r_{Si}$, where $r_{S1} = 2.97m$, $r_{S2} = 2.98m$, $r_{S3} = 2.97m$, $r_{S4} = 2.97m$.

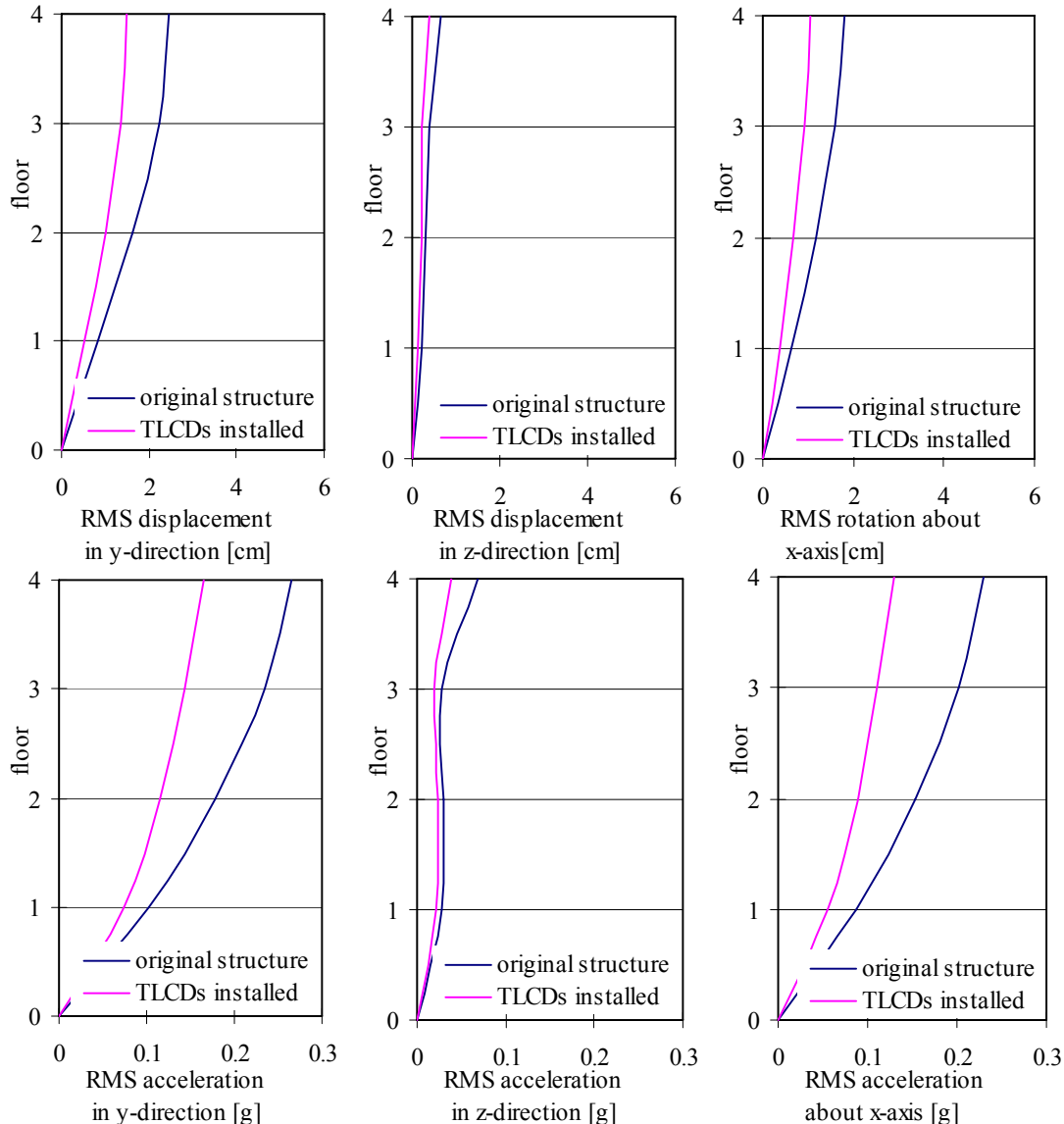


Fig. 4.90: RMS responses for floor displacement and acceleration of the four-storey moderately asymmetric building (El Centro $0.35g$, angle of attack $\alpha = 0$).

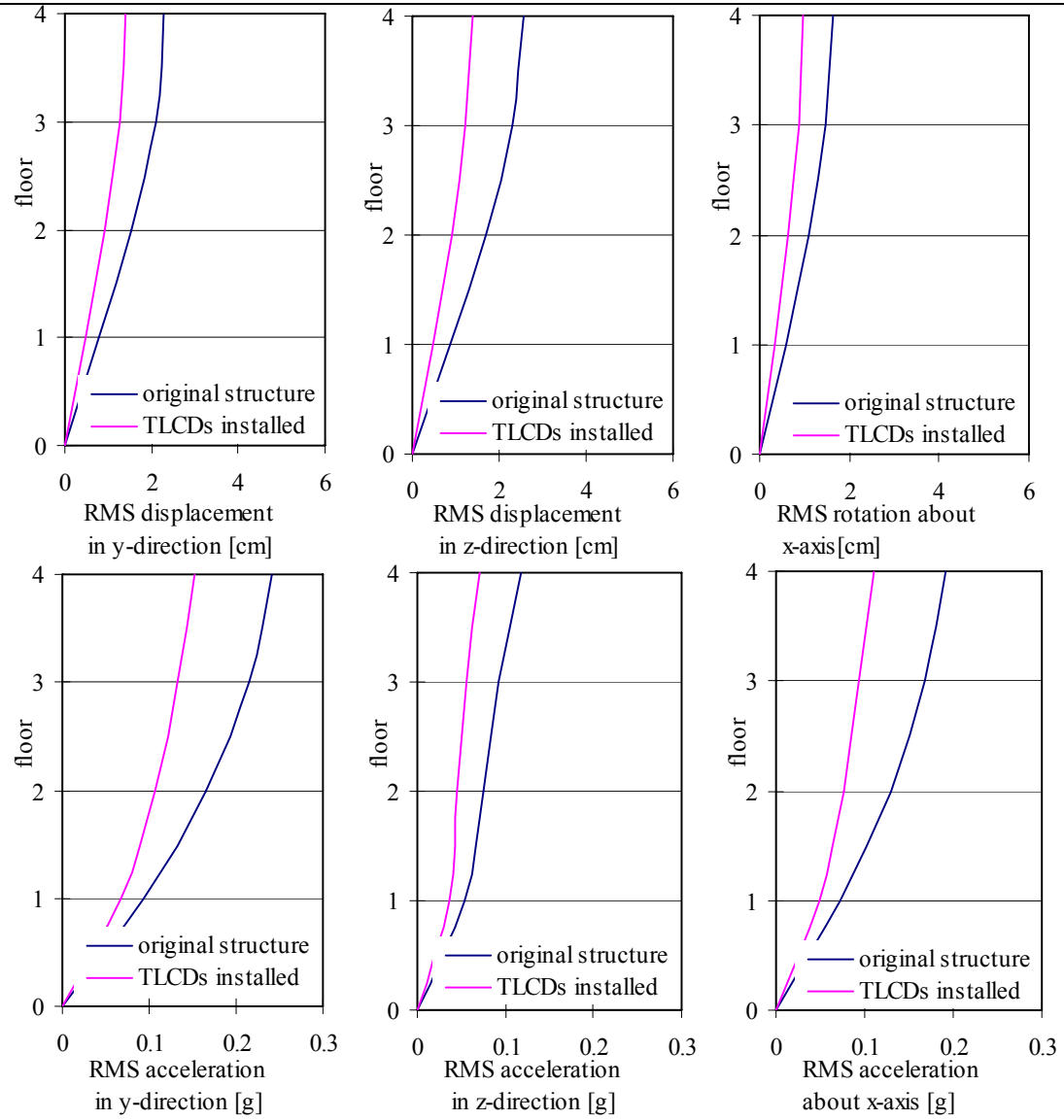
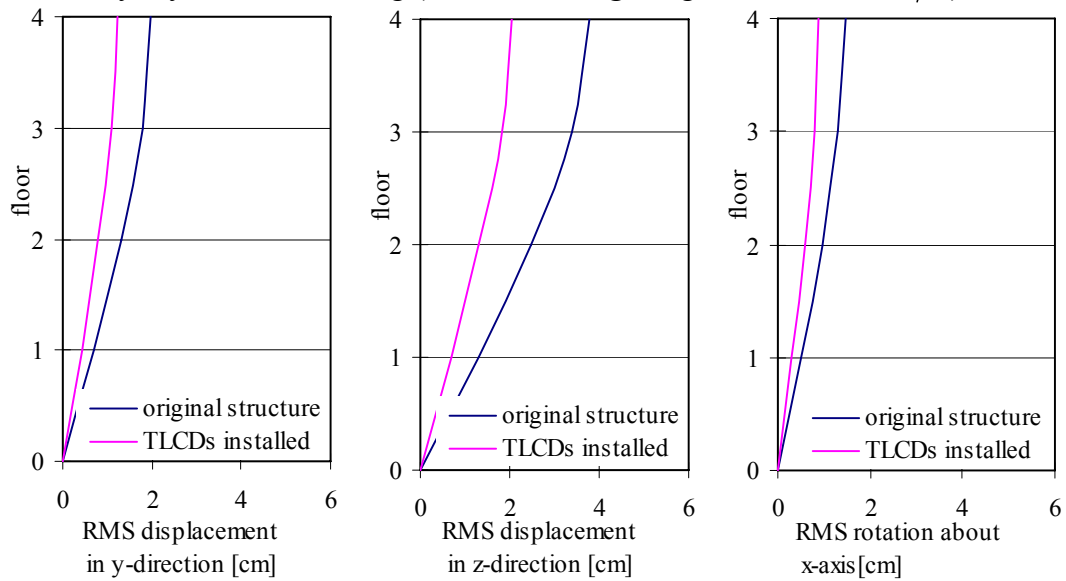


Fig. 4.91: RMS responses for floor displacement and acceleration of the four-storey moderately asymmetric building (El Centro 0.35g , angle of attack $\alpha = \pi/6$).



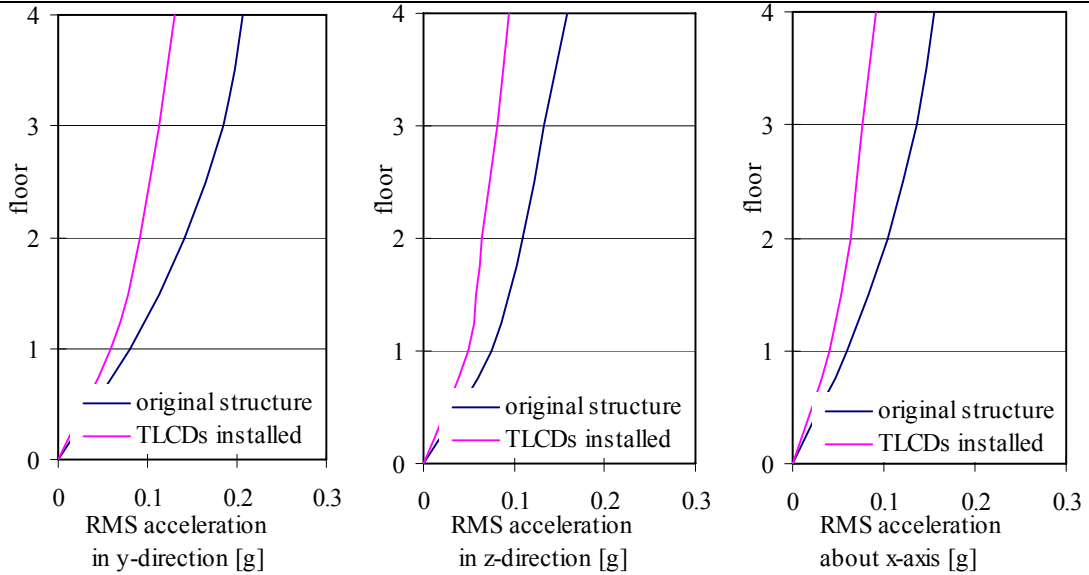


Fig. 4.92: RMS responses for floor displacement and acceleration of the four-storey moderately asymmetric building (El Centro 0.35g , angle of attack $\alpha = \pi/4$).

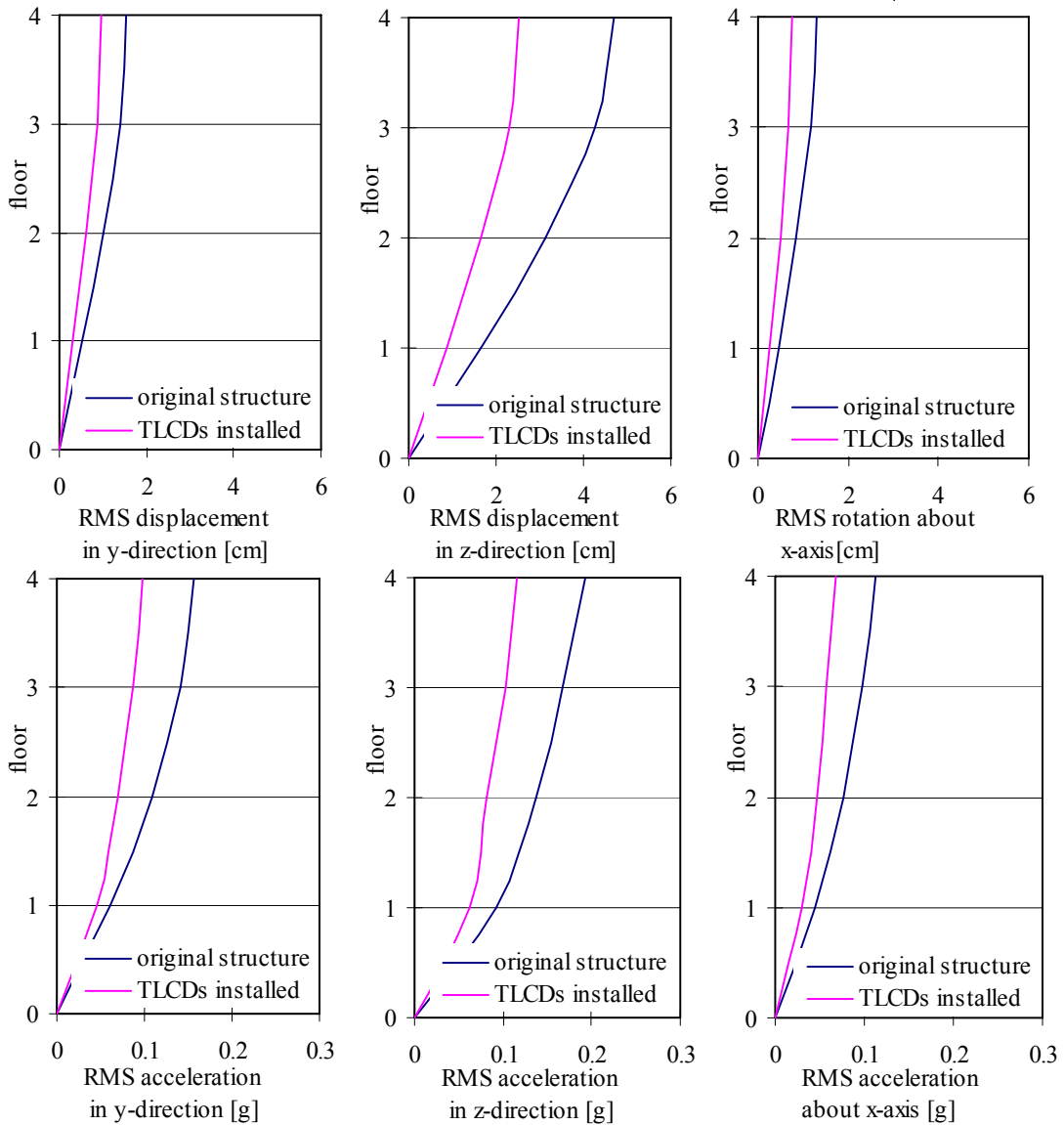


Fig. 4.93: RMS responses for floor displacement and acceleration of the four-storey moderately asymmetric building (El Centro 0.35g , angle of attack $\alpha = \pi/3$).

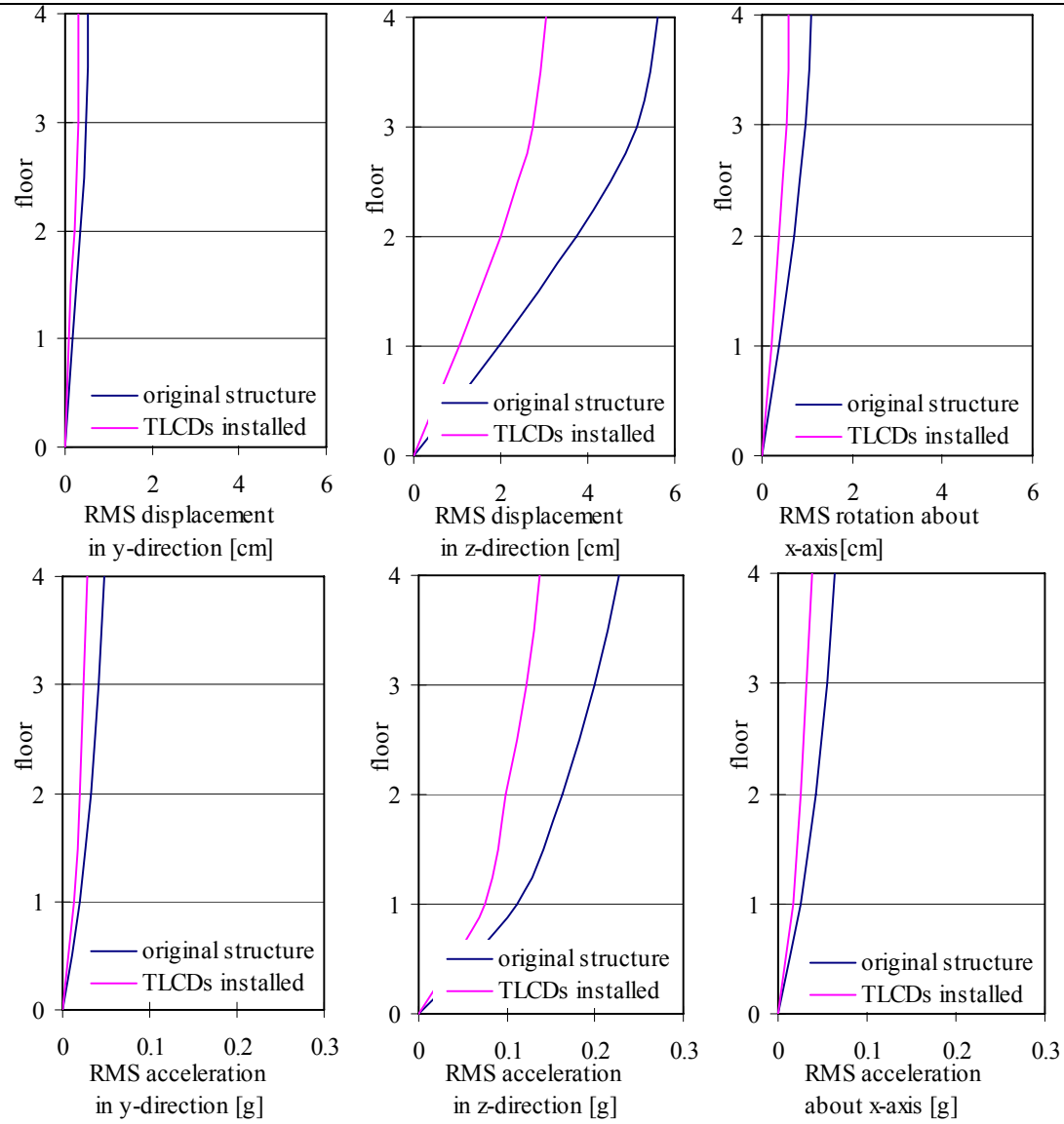
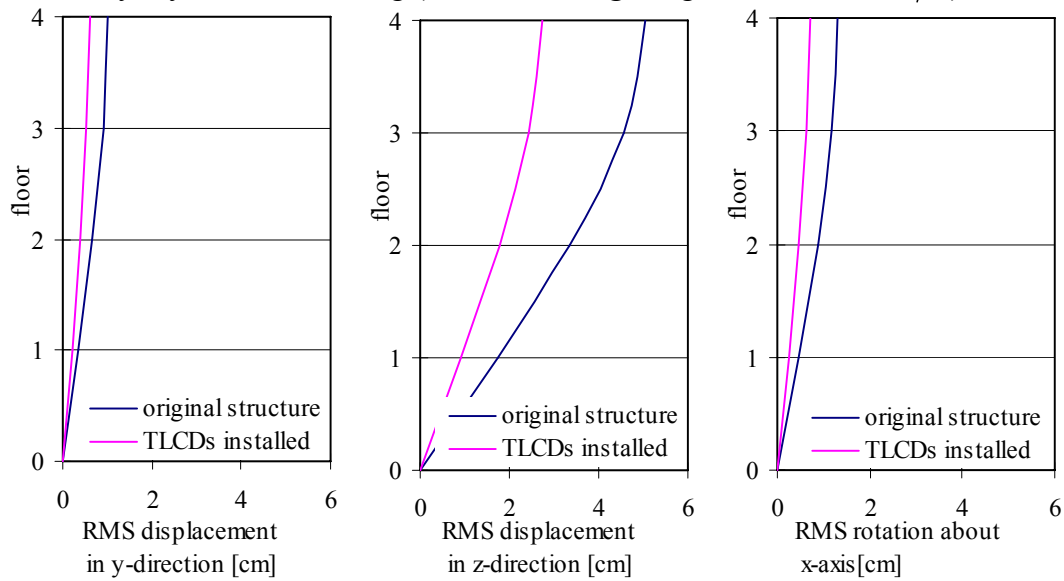


Fig. 4.94: RMS responses for floor displacement and acceleration of the four-storey moderately asymmetric building (El Centro 0.35g , angle of attack $\alpha = \pi/2$).



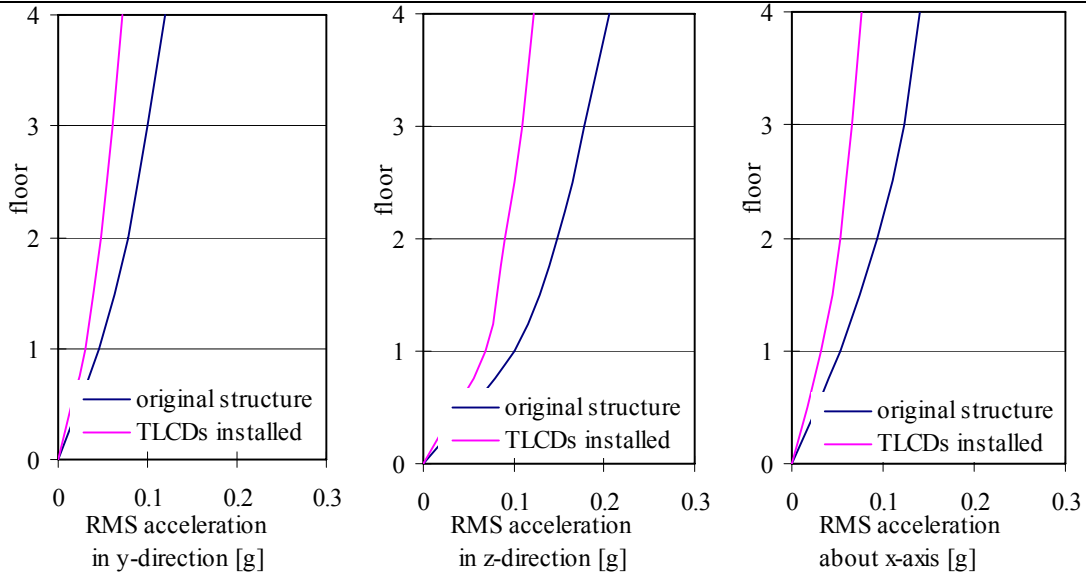


Fig. 4.95: RMS responses for floor displacement and acceleration of the four-storey moderately asymmetric building (El Centro 0.35g , angle of attack $\alpha = 2\pi/3$).

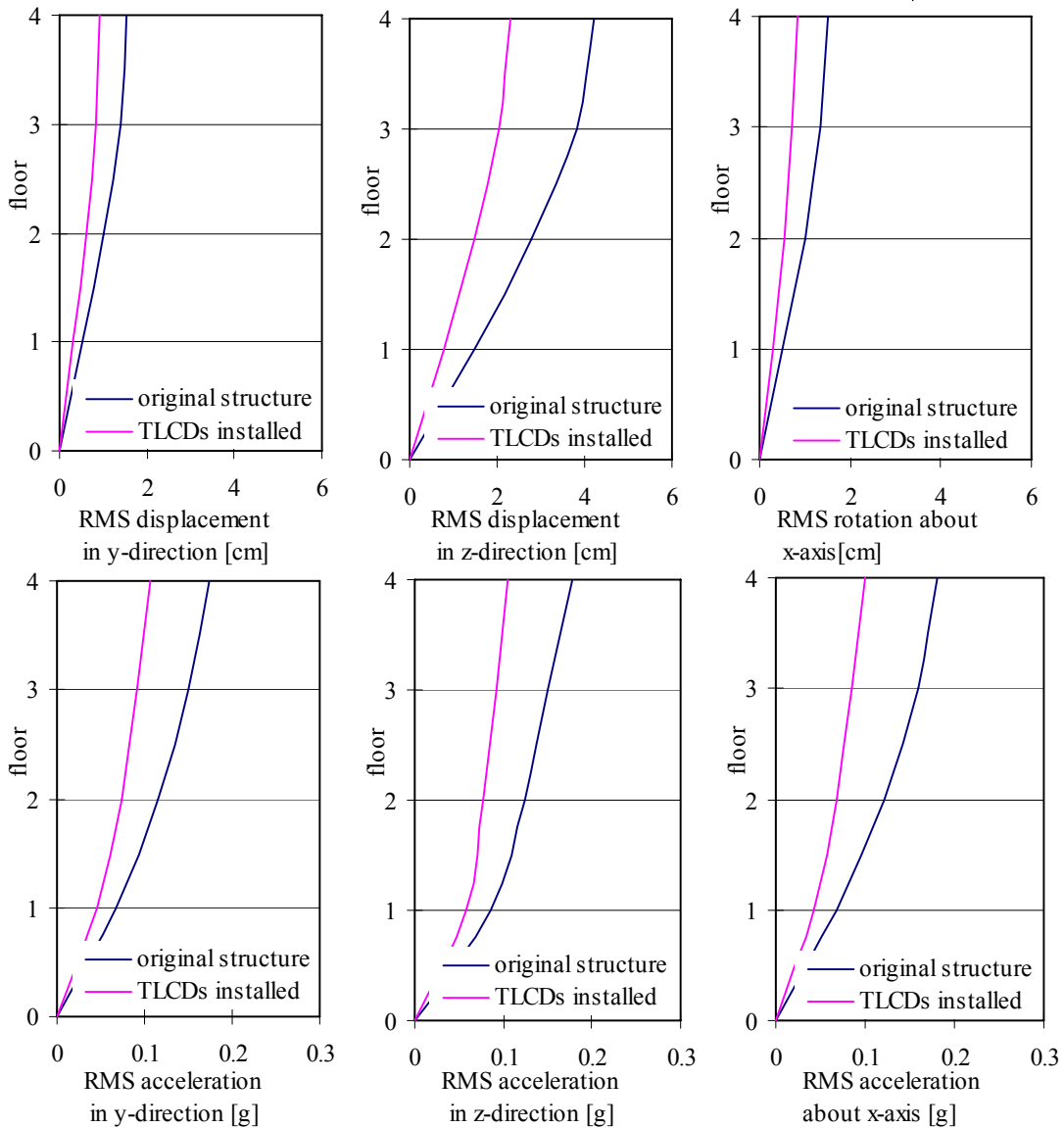


Fig. 4.96: RMS responses for floor displacement and acceleration of the four-storey moderately asymmetric building (El Centro 0.35g , angle of attack $\alpha = 3\pi/4$).

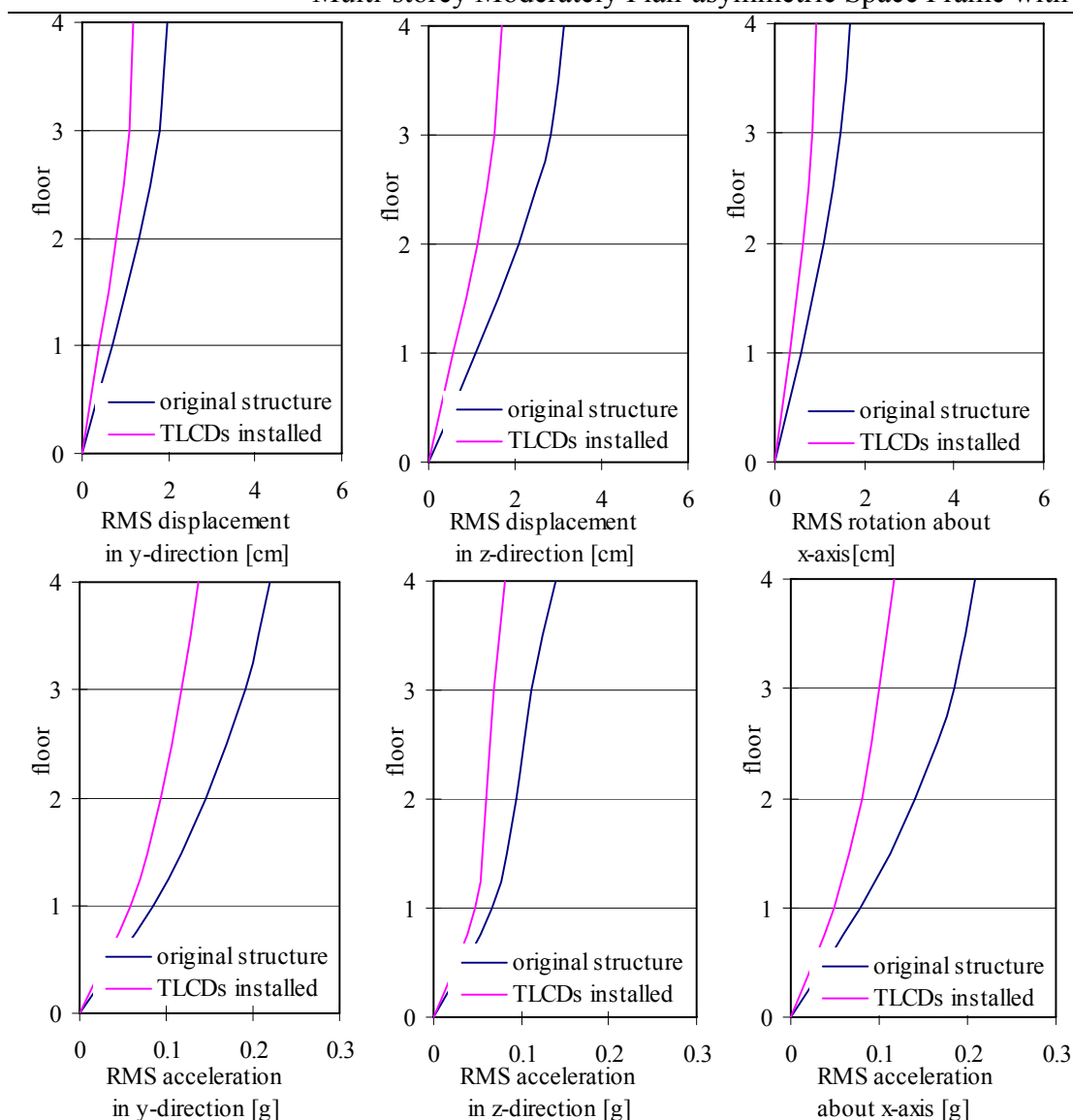


Fig. 4.97: RMS responses for floor displacement and acceleration of the four-storey moderately asymmetric building (El Centro $0.35g$, angle of attack $\alpha = 5\pi/6$).

It is seen that all RMS response are reduced for earthquake excitation from any angle of incidence. Thus, it is concluded that the optimal TLCDs are adequate for asymmetric buildings in seismic active zones.

References

- [1] Chopra A.K., Dynamics of Structures, Prentice-Hall, New Jersey, 1995.
- [2] MATLAB, User Guide, Control Toolbox. MathWorks Inc., Version 6.5.1, 2002.
- [3] Li H.N., Huo L.S., TLCD semi-active control of eccentric structures using neural networks, 15th ASCE Engineering Mechanics Conference June 2-5, 2003, Columbia University, New York, NY.
- [4] Huo L.S., Li H.N., Sun L., Parameter study of TLCD control system excited by multi-dimensional ground motions, Earthquake engineering and engineering vibration. 2001; 21, 4, 147-153.
- [5] Xue S.D., Torsional vibration control of suspension bridge decks using tuned liquid column damper. Dissertation (in English), the Hong Kong Polytechnic University, 1999.
- [6] Lin J.L., Tsai K.C., Simplified seismic analysis of asymmetric building systems, Earthquake Engineering and Structural Dynamics. 2007; 36, 4, 459-479.
- [7] Ziegler F., Chuan Fu, Effective vibration damping of plan-asymmetric buildings. In: Proc. of the 8th Int. Conf. on Multi-purpose High-rise Towers and Tall Buildings, Eds.: A.-R.R. Sabouni, K.M. El-Sawy. The International Federation of High-Rise Structures, CD-Rom Paper ID IFHS-039, Abu Dhabi, 2007, 1-13. (www.acevents.ae/online_documents/ifhs2007+ifhs2007dxb_TB-28.pdf).

5 Multi-storey Strongly Plan-asymmetric Space Frame with TTLCGDs and TLCGDs

5.1 Introduction

In Chapter 3, torsional TLCGD=TTLCGD is described as an effective damper to reduce the coupled lateral and torsional vibration in the case where the center of velocity is located in the floor-plan according to the results derived for the single-storey model when subjected to horizontal seismic excitation. In this chapter such results should be re-checked for multi-storey strongly asymmetric buildings. Based on the equation of motion for the TTLCGD-structure system, the optimal control parameters of TTLCGD are given using the analogy to TTMD-tuning with the properly transformed Den Hartog's optimal parameters, and subsequently, in a state space optimization with the Den Hartog parameters as starting values. The performance of TTLCGD ($\beta = \pi/2$) is studied numerically using 2-storey, 3-storey and 4-storey building models with asymmetric stiffness distribution.

5.2 Equation of motion for multi-storey strongly asymmetric space frame

The equation of motion of the undamped multi-storey asymmetric space frame is described in Section 4.2.2, see Eq. (4.9). The mass matrix is the same in Eq. (4.10). However, the symmetric stiffness matrix \mathbb{K} of the system with asymmetric stiffness distribution, derived by the direct method becomes, cf. Eqs. (4.12)- (4.15),

$$\mathbb{k}_{i(i-1)} = \begin{bmatrix} -4k_{yi} - k'_{yi} & 0 & k'_{yi}e_z/r_S \\ 0 & -4k_{zi} - k'_{zi} & -k'_{zi}e_y/r_S \\ k'_{yi}e_z/r_S & -k'_{zi}e_y/r_S & k_{\theta i \theta i-1} \end{bmatrix}, (i=2-N) \quad (5.1)$$

$$\mathbb{k}_{ii} = \begin{bmatrix} 4(k_{yi} + k_{yi+1}) + (k'_{yi} + k'_{yi+1}) & 0 & -(k'_{yi} + k'_{yi+1})e_z/r_S \\ 0 & 4(k_{zi} + k_{zi+1}) + (k'_{zi} + k'_{zi+1}) & (k'_{zi} + k'_{zi+1})e_y/r_S \\ -(k'_{yi} + k'_{yi+1})e_z/r_S & (k'_{zi} + k'_{zi+1})e_y/r_S & k_{\theta i \theta i} \end{bmatrix}, (i=1-N-1) \quad (5.2)$$

$$\mathbb{k}_{ii} = \begin{bmatrix} 4k_{yi} + k'_{yi} & 0 & -k'_{yi}e_z/r_S \\ 0 & 4k_{zi} + k'_{zi} & k'_{zi}e_y/r_S \\ -k'_{yi}e_z/r_S & k'_{zi}e_y/r_S & k_{\theta i \theta i} \end{bmatrix}, (i=N) \quad (5.3)$$

$$\mathbb{k}_{i(i+1)} = \begin{bmatrix} -4k_{yi+1} - k'_{yi+1} & 0 & k'_{yi+1}e_z/r_S \\ 0 & -4k_{zi+1} - k'_{zi+1} & -k'_{zi+1}e_y/r_S \\ k'_{yi+1}e_z/r_S & -k'_{zi+1}e_y/r_S & k_{\theta i \theta i+1} \end{bmatrix}, (i=1-N-1) \quad (5.4)$$

where,

$$k_{\theta i \theta i} = \left[(k_{yi} + k_{yi+1})b^2 + (k_{zi} + k_{zi+1})a^2 + (k'_{yi} + k'_{yi+1})e_z^2 + (k'_{zi} + k'_{zi+1})e_y^2 \right] / r_S^2, (i=1-N-1)$$

$$k_{\theta i \theta i} = (k_{yi}b^2 + k_{zi}a^2 + k'_{yi}e_z^2 + k'_{zi}e_y^2) / r_S^2, (i=N)$$

$$k_{\theta i \theta i+1} = \left(-k_{y_{i+1}} b^2 - k_{z_{i+1}} a^2 - k'_{y_{i+1}} e_z^2 - k'_{z_{i+1}} e_y^2 \right) / r_S^2, \quad (i=1-N-1)$$

$$k_{\theta i \theta i-1} = \left(-k_{y_i} b^2 - k_{z_i} a^2 - k'_{y_i} e_z^2 - k'_{z_i} e_y^2 \right) / r_S^2, \quad (i=2-N)$$

5.3 Control of N-storey strongly plan-asymmetric space frame by a single TTLCGD ($\beta = \pi/2$) when compared to an equivalent TTMD

5.3.1 TTMD attached to space frame

The analogy between an equivalent TTMD and TTLCGD for single-storey structure is presented in Section 3.5. Here a single TTMD is installed on the i -th floor of the N-storey strongly plan-asymmetric space frame. The equation of motion for the coupled undamped main-system can be given in hypermatrix form, cf. Eq. (2.88),

$$\underline{\mathbf{M}}^* \ddot{\underline{\mathbf{x}}} + \underline{\mathbf{K}}^* \underline{\mathbf{x}} = -\underline{\mathbf{M}}^* \ddot{\underline{\mathbf{x}}}_{gN} + \underline{\mathbf{P}}^*, \quad \underline{\mathbf{M}}^* = \text{diag} \left[\underline{\mathbf{M}}_1^* \cdots \underline{\mathbf{M}}_i^* \cdots \underline{\mathbf{M}}_N^* \right], \quad \underline{\mathbf{x}}^T = \left[\underline{\mathbf{x}}_1^T \cdots \underline{\mathbf{x}}_i^T \cdots \underline{\mathbf{x}}_N^T \right],$$

$$\underline{\mathbf{x}}_i^T = \left[v_i \quad w_i \quad u_{Ti} \right], \quad \ddot{\underline{\mathbf{x}}}_{gN} = \underline{\mathbf{E}}_N \ddot{\underline{\mathbf{x}}}_g, \quad \ddot{\underline{\mathbf{x}}}_g^T = \left[\ddot{v}_g \quad \ddot{w}_g \quad 0 \right],$$

$$\underline{\mathbf{E}}_N = \begin{bmatrix} 1 & 0 & 0 & 1 & 0 & 0 & 1 & \cdots \\ 0 & 1 & 0 & 0 & 1 & 0 & 0 & \cdots \\ 0 & 0 & 0 & 0 & 0 & 0 & 0 & \cdots \end{bmatrix}^T, \quad \underline{\mathbf{P}}^{*T} = -\left[0, \cdots, F_{C_M i y}^*, F_{C_M i z}^*, M_{C_M i x}^* / r_{Si}, \cdots, 0 \right],$$

$$F_{C_M i y}^* = m_{Aj}^* (\ddot{v}_g + \ddot{v}_i), \quad F_{C_M i z}^* = m_{Aj}^* (\ddot{w}_g + \ddot{w}_i), \quad M_{C_M i x}^* = \bar{I}_{C_M i x}^* (\ddot{u}_{TTi}^* + \ddot{u}^*) / r_{Ai}^*. \quad (5.5)$$

The equation of the N-storey space frame with a single TTMD attached to the i -th floor are approximated by the selected mode, cf. Eq. (3.57) and subscript the floor number i ,

$$\left(1 + \mu_j^* \right) \ddot{q}_j + \omega_{Sj}^{*2} q_j + \frac{m_{Aj}^*}{m_j^*} \lambda_{ij}^* \ddot{u}^* = -\frac{1}{m_j^*} \left(\sum_{n=1}^N m_{Sn}^* + m_{Aj}^* \right) \phi_{j(3i-2)} \ddot{v}_g - \frac{1}{m_j^*} \left(\sum_{n=1}^N m_{Sn}^* + m_{Aj}^* \right) \phi_{j(3i-1)} \ddot{w}_g,$$

$$\mu_j^* = \frac{m_{Aj}^*}{m_j^*} v_{Tij}^{*2}, \quad v_{Tij}^{*2} = \phi_{j(3i-2)}^2 + \phi_{j(3i-1)}^2 + \left(\phi_{j3i} r_{Aij}^* / r_{Si} \right)^2, \quad \lambda_{ij}^* = \frac{r_{Aij}^*}{r_{Si}^*} \phi_{j3i}^*. \quad (5.6)$$

The approximated equation of motion of TTMD renders, cf. Eq. (3.58) with floor number I considered,

$$\ddot{u}^* + 2\zeta_A \omega_A \dot{u}^* + \omega_A^2 u^* = -\lambda_{ij}^* \ddot{q}_j. \quad (5.7)$$

With light structural damping of the main system added, the coupled approximated equations of motion of the main system with TTMD attached, in matrix notation become, cf. Eq. (3.59),

$$\begin{bmatrix} 1 + \mu_j^* & \lambda_{ij}^* m_{Aj}^* / m_j^* \\ \lambda_{ij}^* & 1 \end{bmatrix} \begin{bmatrix} \ddot{q}_j \\ \ddot{u}^* \end{bmatrix} + \begin{bmatrix} 2\zeta_{Sj}^* \omega_{Sj}^* & 0 \\ 0 & 2\zeta_{Aj}^* \omega_{Aj}^* \end{bmatrix} \begin{bmatrix} \dot{q}_j \\ \dot{u}^* \end{bmatrix} + \begin{bmatrix} \omega_{Sj}^{*2} & 0 \\ 0 & \omega_{Aj}^{*2} \end{bmatrix} \begin{bmatrix} q_j \\ u^* \end{bmatrix} = -\begin{bmatrix} \bar{L}_{Tj}^{*T} / m_j^* \\ \bar{0}^T \end{bmatrix} \ddot{\underline{\mathbf{x}}}_g, \quad (5.8)$$

where the generalized participation factors are

$$\bar{L}_{Tj}^{*T} = \begin{bmatrix} L_{Tjy}^* & L_{Tjz}^* & 0 \end{bmatrix}, \quad L_{Tjy}^* = \left(\sum_{n=1}^N m_{Sn}^* + m_{Aj}^* \right) \phi_{j(3i-2)}, \quad L_{Tjz}^* = \left(\sum_{n=1}^N m_{Sn}^* + m_{Aj}^* \right) \phi_{j(3i-1)}.$$

5.3.2 TTLCGD attached to space frame (the vertical segment, $\mathbf{A}(\mathbf{y}_A, \mathbf{z}_A, \mathbf{0})$, $\beta = \pi/2$)

A single TTLCGD is installed on the i -th floor of N -storey moderately plan-asymmetric space frame, the equation of motion for the coupled undamped main-system can be given in matrix form, cf. Eq. (2.94),

$$\begin{aligned} \underline{M}\ddot{\bar{\mathbf{x}}} + \underline{K}\bar{\mathbf{x}} &= -\underline{M}\ddot{\bar{\mathbf{x}}}_{gN} + \bar{\mathbf{P}}, \quad \bar{\mathbf{P}}^T = -\left[0, \dots, F_{C_Miy}, F_{C_Miz}, M_{C_Mix}/r_{Si}, \dots, 0 \right], \\ F_{C_Miy} &= m_{ff} \left(\ddot{v}_g + \ddot{v}_i - \bar{\kappa}_{T3} \ddot{u}_{TTi} z_{Ai}/r_{fi} \right), \quad F_{C_Miz} = m_{ff} \left(\ddot{w}_g + \ddot{w}_i + \bar{\kappa}_{T3} \ddot{u}_{TTi} y_{Ai}/r_{fi} \right), \\ M_{C_Mix} &= m_{ff} r_{fi} \left(\ddot{u}_{TTi} + \frac{\bar{\kappa}_{T3} y_{Ai}}{r_{fi}} a_z - \frac{\bar{\kappa}_{T3} z_{Ai}}{r_{fi}} a_y \right) + m_{ff} r_{fi} \bar{\kappa}_{T0} \ddot{u}. \end{aligned} \quad (5.9)$$

The equation of a N -storey space frame with a single TTLCGD are approximated by the selected mode, cf. Eq. (3.60),

$$\begin{aligned} (1 + \mu_j) \ddot{q}_j + \omega_{Sj}^2 q_j + \frac{m_{ff}}{m_j} \bar{\lambda}_{ij} \ddot{u} &= -\frac{1}{m_j} \left[\sum_{n=1}^N m_{Sn} \phi_{j(3i-2)} + m_{ff} \left(\phi_{j(3i-2)} - \bar{\kappa}_{T3} \phi_{j3i} z_{Aij}/r_{Si} \right) \right] \ddot{v}_g \\ &\quad - \frac{1}{m_j} \left[\sum_{n=1}^N m_{Sn} \phi_{j(3i-1)} + m_{ff} \left(\phi_{j(3i-1)} + \bar{\kappa}_{T3} \phi_{j3i} y_{Aij}/r_{Si} \right) \right] \ddot{w}_g, \\ \mu_j &= \frac{m_{ff}}{m_j} V_{Tij}^2, \quad V_{Tij}^2 = v_{Tij}^2 + 2\phi_{j3i} \bar{\kappa}_{T3} \left(y_{Aij} \phi_{j(3i-1)} - z_{Aij} \phi_{j(3i-2)} \right) / r_{Si}, \quad \lambda_{ij} = \kappa_{T0} \phi_{j3i} r_{fij} / r_{Si}, \\ v_{Tij}^2 &= \phi_{j(3i-2)}^2 + \phi_{j(3i-1)}^2 + \left(\phi_{j3i} r_{fij} / r_{Si} \right)^2, \quad \bar{\lambda}_{ij} = \lambda_{ij} L_{eff} / L_1. \end{aligned} \quad (5.10)$$

Light structural modal damping of the main system is added and the equation of motion of TTLCGD is approximated by the selected mode cf. Eq. (3.61)

$$\ddot{u} + 2\zeta_{Aj} \omega_{Aj} \dot{u} + \omega_{Aj}^2 u = -\lambda_{ij} \ddot{q}_j. \quad (5.11)$$

In matrix form the linearized coupled approximated system of equations of the main system with TTLCGD attached becomes, cf. Eq. (3.62)

$$\begin{bmatrix} 1 + \mu_j & \bar{\lambda}_{ij} m_{ff} / m_j \\ \lambda_{ij} & 1 \end{bmatrix} \begin{bmatrix} \ddot{q}_j \\ \ddot{u} \end{bmatrix} + \begin{bmatrix} 2\zeta_{Sj} \omega_{Sj} & 0 \\ 0 & 2\zeta_{Aj} \omega_{Aj} \end{bmatrix} \begin{bmatrix} \dot{q}_j \\ \dot{u} \end{bmatrix} + \begin{bmatrix} \omega_{Sj}^2 & 0 \\ 0 & \omega_{Aj}^2 \end{bmatrix} \begin{bmatrix} q_j \\ u \end{bmatrix} = - \begin{bmatrix} \bar{L}_{Tj}^T / m_j \\ \bar{\mathbf{0}}^T \end{bmatrix} \ddot{\bar{\mathbf{x}}}_g. \quad (5.12)$$

The participation factors are formally still given by Eq. (4.25), however, before their substitution, the modal displacements of Eq. (4.18) have to be altered by the substitutions,

$$v_{Ai,j} \rightarrow \phi_{j(3i-2)} - \bar{\kappa}_{T3} \phi_{j3i} z_{Aij} / r_{Si}, \quad w_{Ai,j} \rightarrow \phi_{j(3i-1)} + \bar{\kappa}_{T3} \phi_{j3i} y_{Aij} / r_{Si}.$$

5.3.3 Analogy between TTMD and TTLCGD when attached to N-storey space frame

Comparing the approximated equations of motion for coupled system consisting of a N-storey structure, see Section 3.6.3 for the single-storey space frame, the result about the relationship of modal mass ratios μ_j^* and μ_j , the optimal absorber tuning ratio δ_{jopt} and the damping ratio are exactly the same as in the single-storey structure discussed, Eqs.(3.66)-(3.68) still hold true for a well separated mode. The analogy between TTMD and TTLCGD ($\pi/4 \leq \beta < \pi/2$) has the same result, Eqs. (3.82)- (3.84).

5.4 Two-storey strongly asymmetric space frame: numerical example

The two-storey stiffness asymmetric structure is considered as a first numerical example. The homogenous distributed mass of each floor is $m_s=16 \times 10^3 \text{kg}$. The common stiffness of columns in y- and z-directions of each storey are $k_{yi}=594.17 \text{kN/m}$ and $k_{zi}=216.56 \text{kN/m}$. The anisotropic stiffness of the additional column of each storey is $k'_{yi}=6.54 \times 10^3 \text{kN/m}$ and $k'_{zi}=2.38 \times 10^3 \text{kN/m}$, the eccentricity of the column with respect to $C_M=O$ is assumed $e_y=e_z=1 \text{m}$. The mass moment of inertia about the vertical x-axis of each floor is calculated: $I_{xi}=106.67 \times 10^3 \text{kg} \cdot \text{m}^2$, $r_{si}=2.58 \text{m}$.

5.4.1 Static dimensioning and a static safety criterion of the columns

The critical load of a steel profile HEB-140 length 4m, is calculated $F_c = -711.74 \text{kN}$. The combined load without TLCGD in column of first floor is $F = -201.948 \text{kN}$, thus $\frac{F}{F_c} = \frac{-201.948}{-711.74} = 0.28 < \frac{1}{3}$. Consequently, a geometric correction of the stiffness is applicable.

The corrected stiffness of column in y-direction becomes:

$$\bar{k}_y = \begin{bmatrix} 1127.8 & -563.88 \\ -563.88 & 563.88 \end{bmatrix} \text{kN/m}.$$

The corrected stiffness of column in z-direction becomes:

$$\bar{k}_z = \begin{bmatrix} 372.54 & -186.27 \\ -186.27 & 186.27 \end{bmatrix} \text{kN/m}.$$

5.4.2 Natural modes of the main structure

The computed natural frequencies by means of Matlab 7.0¹ become 1.2, 1.57, 2.46, 3.13, 4.1 and 6.44 Hz, prestress of the column considered and extra column comes no weight of the floors. The orthonormalized modal matrix of the undamped main system with respect to \underline{M} is the output of Matlab 7.0¹.

$$\tilde{\phi} = 10^{-2} \begin{bmatrix} -0.101130 & 0.146810 & 0.375450 & -0.163630 & -0.237550 & 0.607490 \\ 0.310810 & 0.274910 & -0.023778 & 0.502900 & -0.444820 & -0.038474 \\ -0.256740 & 0.274980 & -0.176680 & -0.415410 & -0.444930 & -0.285870 \\ -0.163630 & 0.237550 & 0.607490 & 0.101130 & 0.146810 & -0.375450 \\ 0.502900 & 0.444820 & -0.038474 & -0.310810 & 0.274910 & 0.023778 \\ -0.415410 & 0.444930 & -0.285870 & 0.256740 & 0.274980 & 0.176680 \end{bmatrix}$$

Correction of this output of orthonormalized eigenvectors might become necessary with respect to orthogonality, also see section 2.9.2. However, test calculations render sufficient accuracy,

$$\begin{aligned} \delta_{11} &= 1, & \delta_{12} &= 3.3 \times 10^{-16}, & \delta_{13} &= 2.8 \times 10^{-17}, & \delta_{14} &= -1.1 \times 10^{-16}, & \delta_{15} &= 6.4 \times 10^{-16}, \\ \delta_{16} &= 3.2 \times 10^{-16}, & \delta_{21} &= 3.9 \times 10^{-16}, & \delta_{22} &= 1, & \delta_{23} &= 5.6 \times 10^{-17}, & \delta_{24} &= -1.7 \times 10^{-16}, \\ \delta_{25} &= 3.6 \times 10^{-16}, & \delta_{26} &= -2.8 \times 10^{-17}, & \delta_{31} &= -2.8 \times 10^{-17}, & \delta_{32} &= 5.6 \times 10^{-17}, & \delta_{33} &= 1, \\ \delta_{34} &= 2.5 \times 10^{-16}, & \delta_{35} &= 3.9 \times 10^{-16}, & \delta_{36} &= -3.2 \times 10^{-16}, & \delta_{41} &= -1.1 \times 10^{-16}, & \delta_{42} &= -1.1 \times 10^{-16}, \\ \delta_{43} &= 2.2 \times 10^{-16}, & \delta_{44} &= 1, & \delta_{45} &= -2.9 \times 10^{-16}, & \delta_{46} &= -8.3 \times 10^{-17}, & \delta_{51} &= 6.1 \times 10^{-16}, \\ \delta_{52} &= 3.6 \times 10^{-16}, & \delta_{53} &= 3.9 \times 10^{-16}, & \delta_{54} &= -3.2 \times 10^{-16}, & \delta_{55} &= 1, & \delta_{56} &= 2.9 \times 10^{-16}, \\ \delta_{61} &= 3.5 \times 10^{-16}, & \delta_{62} &= 0, & \delta_{63} &= -3.2 \times 10^{-16}, & \delta_{64} &= -1.1 \times 10^{-16}, & \delta_{65} &= 2.6 \times 10^{-16}, & \delta_{66} &= 1. \end{aligned}$$

5.4.3 Position of the modal centers of velocity C_V

The coordinates of the modal centers of velocity C_V with corrected column stiffness taken into account are defined by Eq. (2.12).

mode	1	2	3	4	5	6
Floor 1	(3.13,1.02)	(-2.58,1.38)	(-0.35,-5.49)	(3.13,1.02)	(-2.58,1.38)	(-0.35,-5.49)
Floor 2	(3.13,1.02)	(-2.58,1.38)	(-0.35,-5.49)	(3.13,1.02)	(-2.58,1.38)	(-0.35,-5.49)

Table 5.1: The coordinates of the centers of velocity C_V for 6 modes.

C_{V1} and C_{V2} are inside the floor plan, C_{V3} lies outside. Consequently, two TTLCGDs and one plane TLCGD parallel to y-axis are positioned on the top floor. The installation of absorbers is the same as in the section 3.8.3.

5.4.4 TTLCGD and TLCGD design, Den Hartog' optimization

The fluid mass $m_{f1} = 700kg$, $m_{f2} = 700kg$ and $m_{f3} = 300kg$ of water is chosen. Dimensions of three absorbers tuned first by means of the TMD analogy applying Den Hartog's formulas, Eqs. (3.66)- (3.68) for TTLCGDs ($\beta = \pi/2$) and Eqs. (2.102)- (2.04) for TLCGD ($\beta = \pi/4$) are summarized in Table 5.2. The dynamic magnification factor (DMF) calculated with Matlab 7.0¹, linearized damping of the absorbers considered, is illustrated in Figure 5. 1.

The effective modal damping coefficients of the system are increased from 1% to $\zeta_{eff1} = 4.85\%$, $\zeta_{eff2} = 4.73\%$, $\zeta_{eff3} = 5.32\%$. From Table 5.3a-c it follows that all maximum fluid displacements resulting for various angles of attack, are within the acceptable limits, $u_0 < H_a/3$ (of linearized gas compression) and $u_0 < H/2$. The maximum fluid velocities of three absorbers are calculated by Eq. (2.35) 5.18, 3.55 and 4.15m/s and are within the acceptable speed limit.

Multi-storey Strongly Plan-asymmetric Space Frame with TTLCGDs and TLCGDs

	TTLCGD1	TTLCGD2	TLCGD3
Horizontal length of the liquid column B [m]	24.00	24.00	2.50
Length of the upright liquid column H [m]	1.50	0.90	0.60
Cross-sectional area of the pipe [m ²] $A_H=A_B$	0.0260	0.0270	0.0810
Effective length $L_{eff} = L_1 = 2H + B$ [m], Eq. (2.34a)	27.00	25.80	3.70
Angle of the inclined pipe section β [rad]	$\pi/2$	$\pi/2$	$\pi/4$
Equivalent mathematical pendulum length L_0 [m] Eq. (2.37)	0.17	0.10	0.04
Geometry factor $\kappa = \bar{\kappa}$ or $\kappa_{T0} = \bar{\kappa}_{T0}$, Eqs. (2.34a), (2.44),(3.14a),(3.44)	0.66	0.70	0.91
Equilibrium pressure head h_0 [m], $n=1.2$, Eq. (2.34a)	161	152.9	45.26
Gas volume $V_0 = A_H H_a$ [m ³], Eq. (2.38)	0.055000	0.033000	0.080000
The mass ratio of the TLCGD-main system μ , Eqs. (2.97), (3.60)	4.88%	4.77%	2.1%
The mass ratio of the equivalent TMD-main system μ^* , Eqs. (2.102), (3.66)	1.82%	2.10%	1.69%
Natural frequency $f_{A,opt}$ [Hz] Eq. (2.104), (2.112)	1.16	1.51	2.41
Optimal linear damping %, Eq. (2.113)	8.18	8.78	7.88

Table 5.2: Layout of the modally tuned absorbers, gas volume and gas equilibrium pressure assigned, note the rather high gas pressure in TTLCGD.

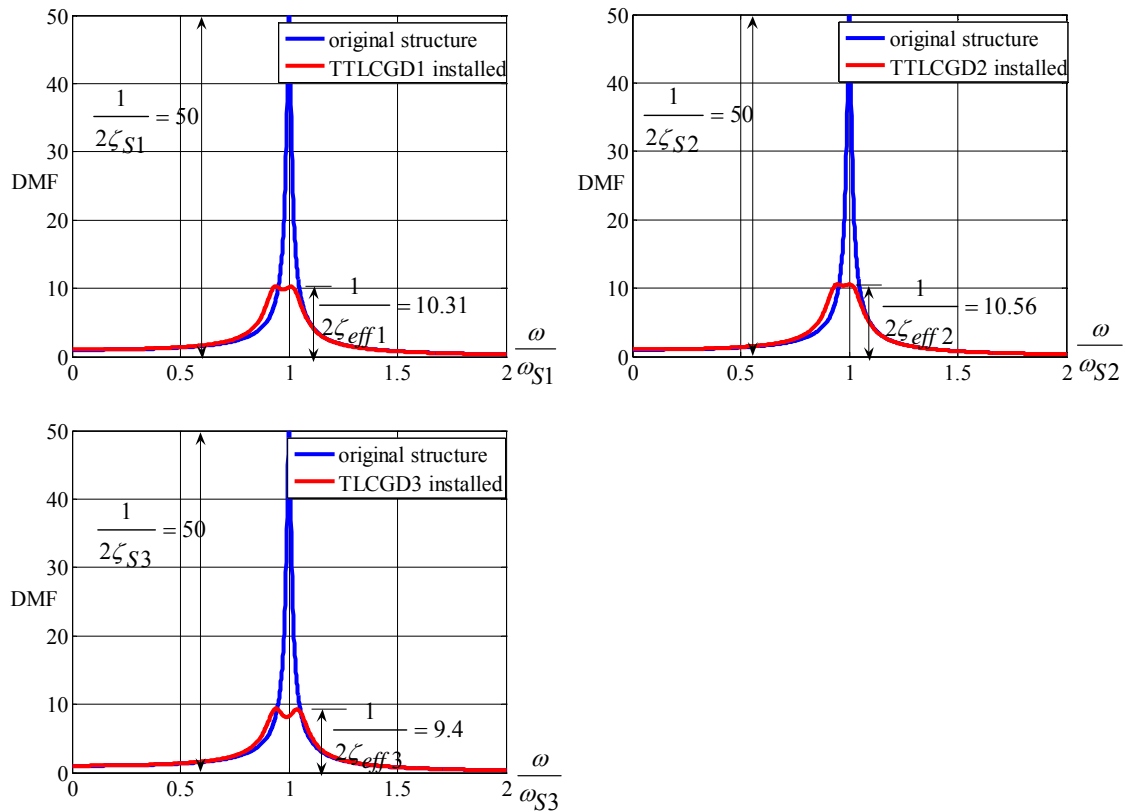


Fig. 5.1: Individual frequency response curves without and with linearized absorbers attached with Den Hartog's optimal parameter.

Forcing direction	structure							TTLCGD1
	v_1 [mm]	w_1 [mm]	$u_{T1} = r_{S1}\theta_1$ [mm]	v_2 [mm]	w_2 [mm]	$u_{T2} = r_{S2}\theta_2$ [mm]	u_0 [mm]	
$\alpha = 0$	C_{Mi}	-10	30	-25	-16	49	-40	225
$\alpha = \pi/6$	C_{Mi}	-7	20	-17	-11	33	-27	150
$\alpha = \pi/4$	C_{Mi}	-14	44	-36	-23	71	-59	329
$\alpha = \pi/3$	C_{Mi}	-21	65	-54	-34	105	-87	486
$\alpha = \pi/2$	C_{Mi}	-30	92	-76	-49	149	-123	691
$\alpha = 2\pi/3$	C_{Mi}	-31	95	-78	-50	154	-127	711
$\alpha = 3\pi/4$	C_{Mi}	-28	87	-71	-46	140	-116	648
$\alpha = 5\pi/6$	C_{Mi}	-23	72	-60	-38	117	-96	541

Table 5.3a: Maximum displacements of two-storey structure in the first mode from time-harmonic excitation in α -directions, $a_0=0.1g$, $r_{Si} = 2.58m$.

Forcing direction	structure							TTLCGD2
	v_1 [mm]	w_1 [mm]	$u_{T1} = r_{S1}\theta_1$ [mm]	v_2 [mm]	w_2 [mm]	$u_{T2} = r_{S2}\theta_2$ [mm]	u_0 [mm]	
$\alpha = 0$	C_{Mi}	11	20	20	17	32	32	176
$\alpha = \pi/6$	C_{Mi}	19	36	36	31	58	58	317
$\alpha = \pi/4$	C_{Mi}	22	41	41	35	66	66	358
$\alpha = \pi/3$	C_{Mi}	23	42	42	37	69	69	374
$\alpha = \pi/2$	C_{Mi}	20	37	37	32	61	61	330
$\alpha = 2\pi/3$	C_{Mi}	12	22	22	19	36	36	198
$\alpha = 3\pi/4$	C_{Mi}	7	12	12	11	20	20	109
$\alpha = 5\pi/6$	C_{Mi}	1	1	1	1	2	2	12

Table 5.3b: Maximum displacements of two-storey structure in the second mode from time-harmonic excitation in α -directions, $a_0=0.1g$, $r_{Si} = 2.58m$.

Forcing direction	structure							TLCGD3
	v_1 [mm]	w_1 [mm]	$u_{T1} = r_{S1}\theta_1$ [mm]	v_2 [mm]	w_2 [mm]	$u_{T2} = r_{S2}\theta_2$ [mm]	u_0 [mm]	
$\alpha = 0$	24	-2	-11	C_{M2}	39	-2	-18	274
				A	53	-2		
$\alpha = \pi/6$	20	-1	-9	C_{M2}	32	-2	-15	229
				A	44	-2		
$\alpha = \pi/4$	16	-1	-7	C_{M2}	26	-2	-12	182
				A	35	-2		
$\alpha = \pi/3$	11	-1	-5	C_{M2}	17	-1	-8	123
				A	24	-1		
$\alpha = \pi/2$	1	0	-1	C_{M2}	2	0	-1	16
				A	3	0		
$\alpha = 2\pi/3$	13	-1	-6	C_{M2}	21	-1	-10	151
				A	29	-1		
$\alpha = 3\pi/4$	18	-1	-8	C_{M2}	29	-2	-14	205
				A	40	-2		
$\alpha = 5\pi/6$	21	-1	-10	C_{M2}	35	-2	-16	246
				A	47	-2		

Table 5.3c: Maximum displacements of two-storey structure in the third mode from time-harmonic excitation in α -directions, $a_0=0.1g$, $r_{Si} = 2.58m$.

5.4.5 Optimization of the TTLCGD-, TLCGD-structure system in the state space domain

The fine tuned optimal natural frequencies and damping ratios by calling the function *fminsearch* of the performance index J , Eq. (2.123), are found to be $f_{A1} = 1.15Hz$, $f_{A2} = 1.47Hz$, $f_{A3} = 2.35Hz$, $\zeta_{A1} = 5.97\%$, $\zeta_{A2} = 7\%$, $\zeta_{A3} = 6.49\%$. Frequency fine tuning is achieved by adjusting the equilibrium gas pressure: 149.12, 134.91 and 41.33m .Figs.

5.2-5.9 illustrate the weighed sum of the frequency response function $\sum_{i=1}^{12} s_i |z_{Si}(\nu)|$, $\zeta = \text{diag}$

(10,10,10,10,10,10,1,1,1,1,1,1) of the building states for the original and the optimized system under various angles of attack, in the logarithmic decibel scale in the relevant frequency window $0 \leq f \leq 3Hz$. The resonance curves with fine-tuning optimal parameters have broader peaks. The maximum fluid displacement amplitudes of three absorbers in Figs. 5.9-5.16 are well within the acceptable limits. The maximum fluid velocities of three absorbers are calculated by Eq. (2.35) 5.64, 3.79 and 5.17m/s and are also within the acceptable speed limit.

The wall thickness and the estimated dead mass of the piping system are listed in Table 5.4 for the three absorbers, designed according to Table 5.2.

	TTLCGD1	TTLCGD2	TLCGD3
h_0 [m]	161	152.9	45.26
H_a [m]	2.12	1.22	1.00
$10^{-5} p_{(D)}$ [N/m ²] Eq.(2.128)	73.54	69.75	20
pipe diameter $2r$ [mm]	181.9	185.4	321.1
t [mm] Eq.(2.124)	4.8	4.6	2.3
m_p [kg] Eq.(2.130)	665.4	592.74	102.28
dead fluid-mass[kg]	395.08	357	51.57
$10^{-5} \bar{p}_{(D)}$ [N/m ²] Eq.(2.129)	5.72	5.39	0.89

Table 5.4: Dimensioning of circular steel pipes.

The gauge pressure under expansion conditions turns out to be positive as listed in Table 5.4. The final dimensions of circular steel pipes must be changed according to their commercial availability.

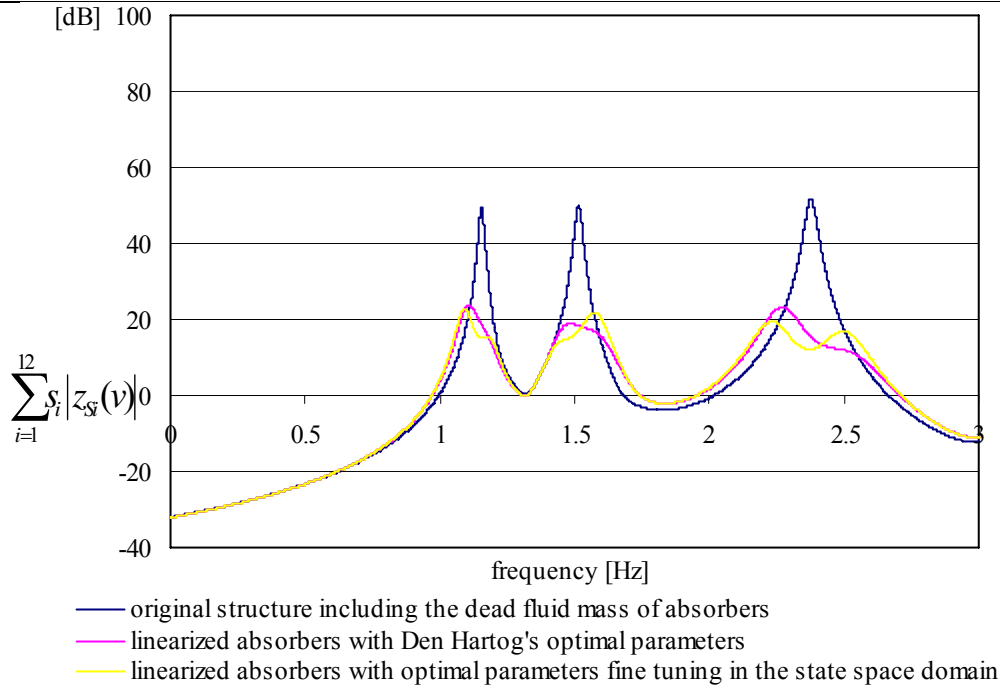


Fig. 5.2: Weighed sum of amplitude response functions for the 6-DOF linearized, two-storey, strongly asymmetric space frame with three linearized absorbers attached and without the absorbers (angle of attack of the time-harmonic base acceleration $\alpha = 0$), maximum gain 28.96dB.

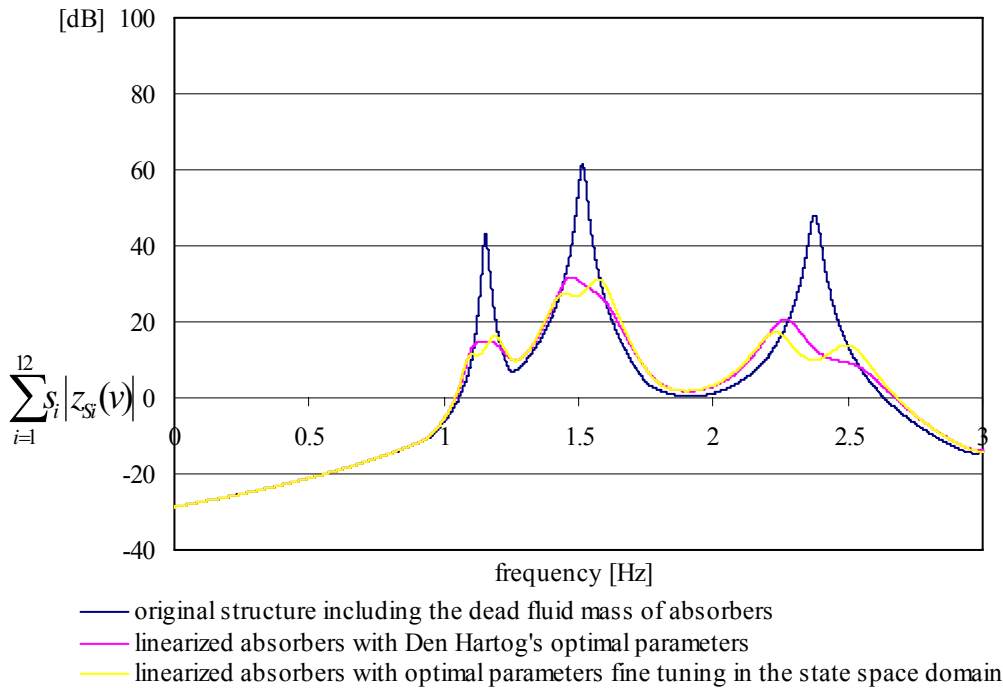


Fig. 5.3: Weighed sum of amplitude response functions for the 6-DOF linearized, two-storey, strongly asymmetric space frame with three linearized absorbers attached and without the absorbers (angle of attack of the time-harmonic base acceleration $\alpha = \pi/6$), maximum gain 30.32dB.

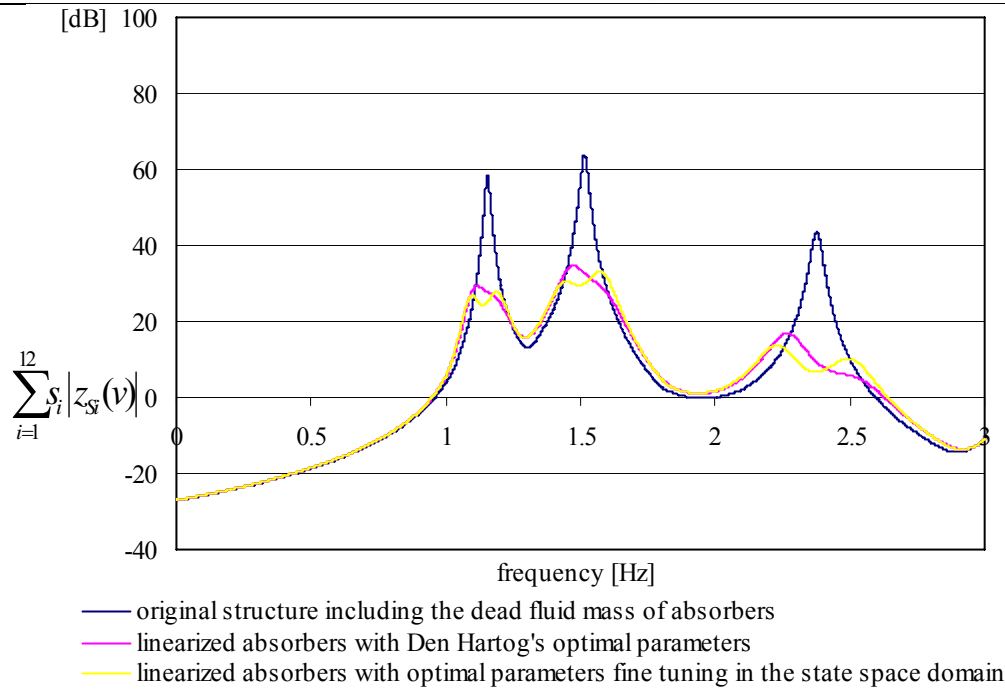


Fig. 5.4: Weighed sum of amplitude response functions for the 6-DOF linearized, two-storey, strongly asymmetric space frame with three linearized absorbers attached and without the absorbers (angle of attack of the time-harmonic base acceleration $\alpha = \pi/4$), maximum gain 30.77dB.

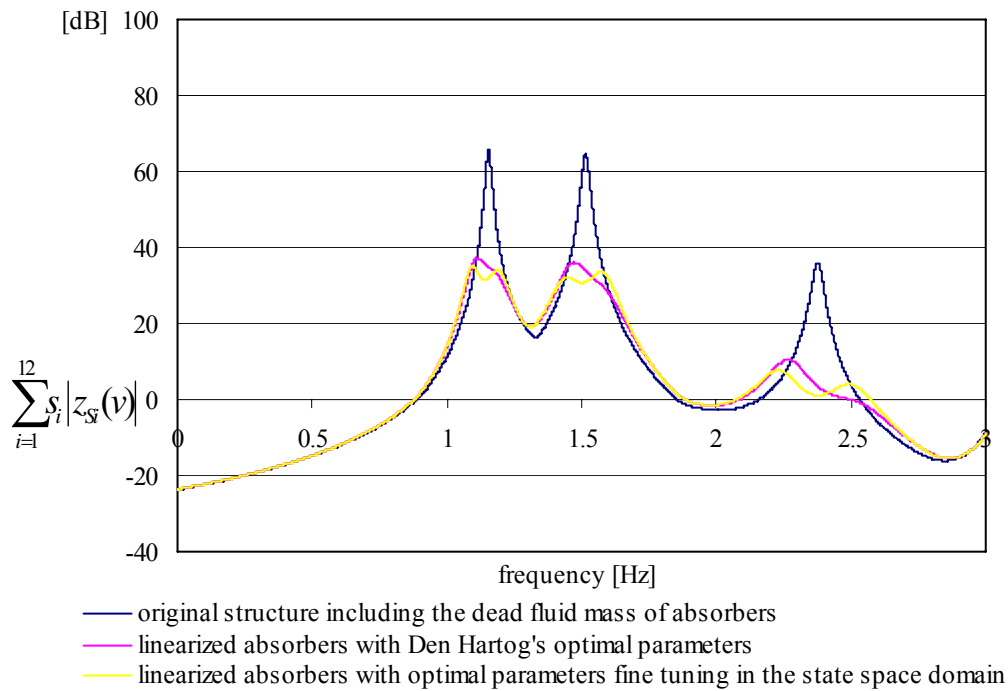


Fig. 5.5: Weighed sum of amplitude response functions for the 6-DOF linearized, two-storey, strongly asymmetric space frame with three linearized absorbers attached and without the absorbers (angle of attack of the time-harmonic base acceleration $\alpha = \pi/3$), maximum gain 30.78dB.

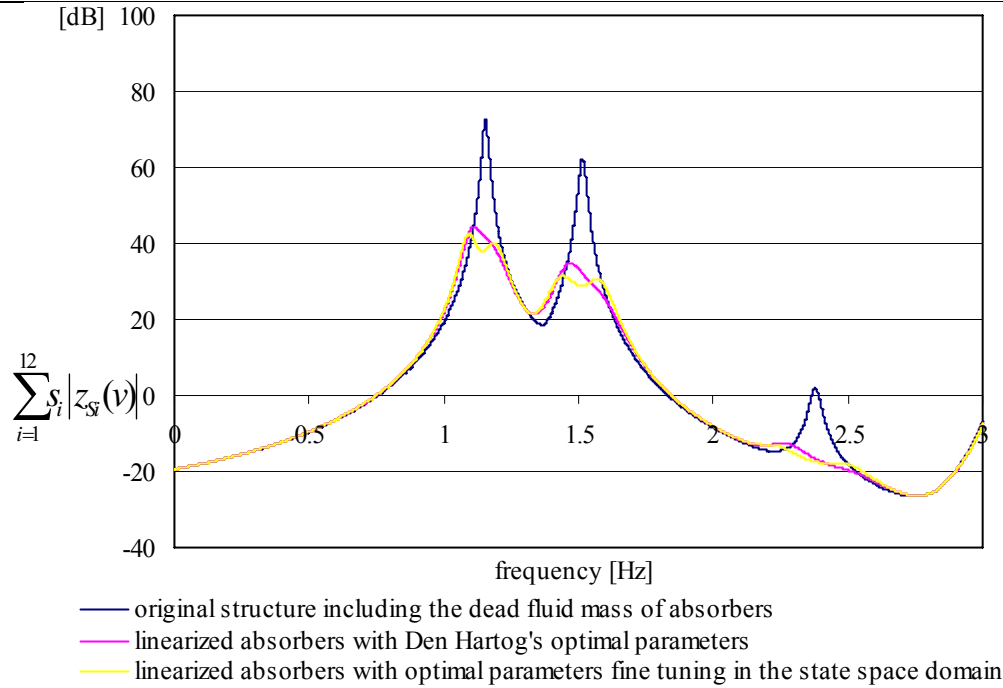


Fig. 5.6: Weighed sum of amplitude response functions for the 6-DOF linearized, two-storey, strongly asymmetric space frame with three linearized absorbers attached and without the absorbers (angle of attack of the time-harmonic base acceleration $\alpha = \pi/2$), maximum gain 30.16dB.

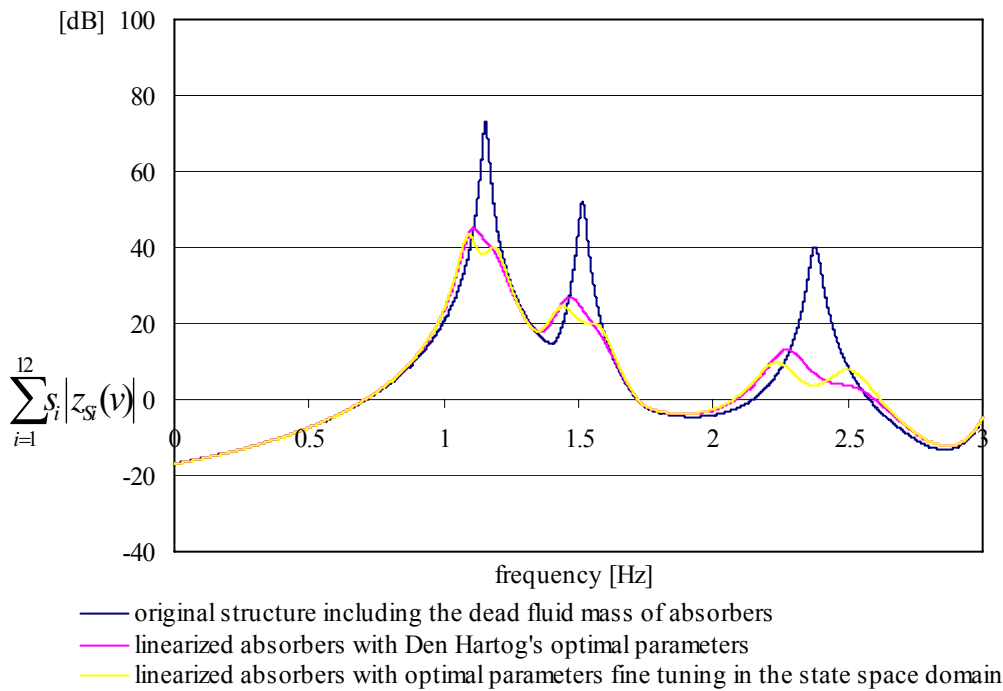


Fig. 5.7: Weighed sum of amplitude response functions for the 6-DOF linearized, two-storey, strongly asymmetric space frame with three linearized absorbers attached and without the absorbers (angle of attack of the time-harmonic base acceleration $\alpha = 2\pi/3$), maximum gain 29.68dB.

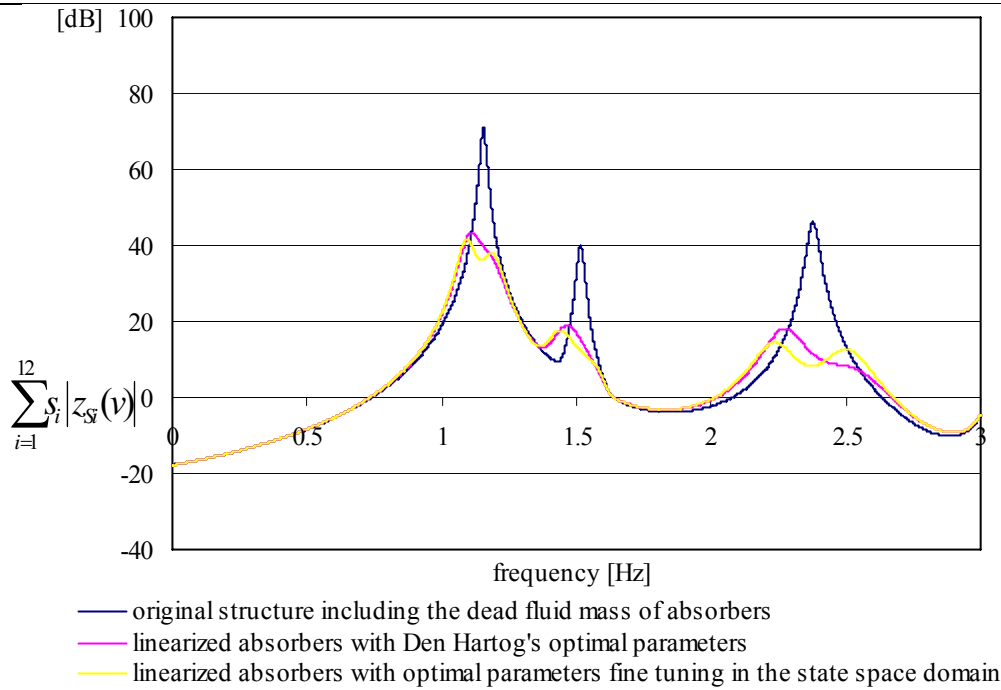


Fig. 5.8: Weighed sum of amplitude response functions for the 6-DOF linearized, two-storey, strongly asymmetric space frame with three linearized absorbers attached and without the absorbers (angle of attack of the time-harmonic base acceleration $\alpha = 3\pi/4$), maximum gain 29.41dB.

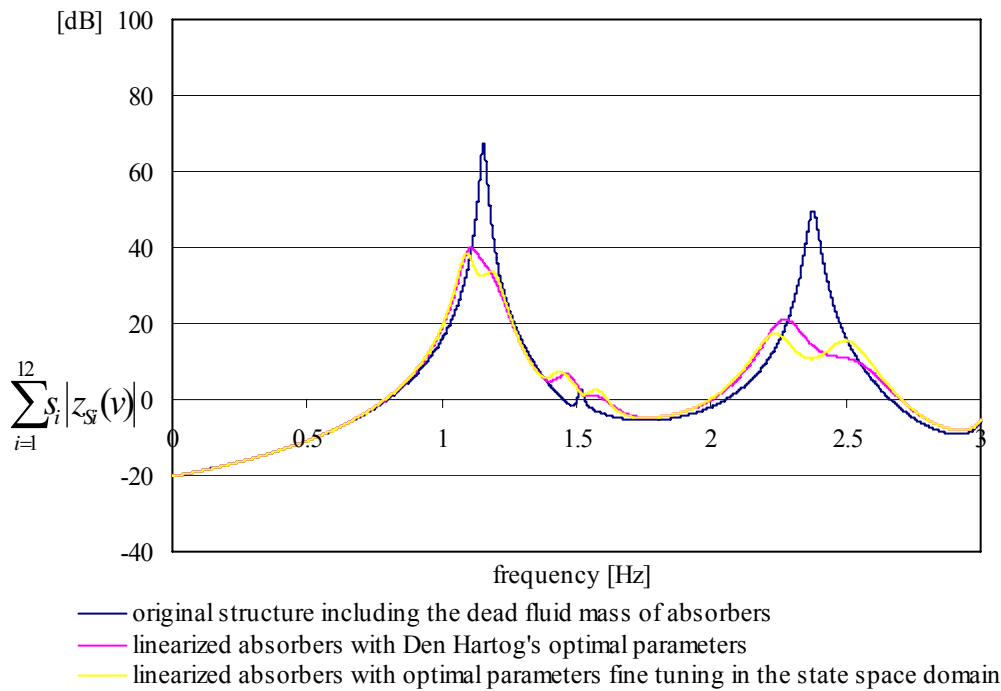


Fig. 5.9: Weighed sum of amplitude response functions for the 6-DOF linearized, two-storey, strongly asymmetric space frame with three linearized absorbers attached and without the absorbers (angle of attack of the time-harmonic base acceleration $\alpha = 5\pi/6$), maximum gain 29.03dB.

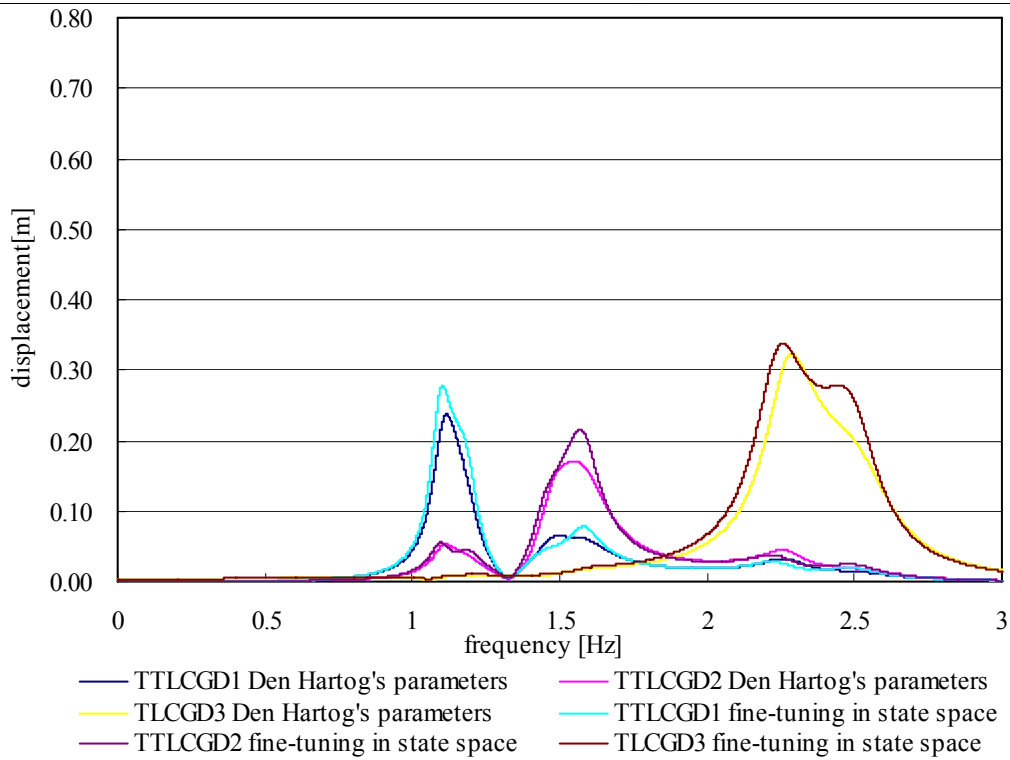


Fig. 5.10: Amplitude response curves of fluid displacement $|u|$ of three linearized absorbers attached to the two-storey strongly asymmetric space frame. Absorbers either with Den Hartog's optimal parameters or those resulting from fine-tuning in state space ($\alpha = 0$).

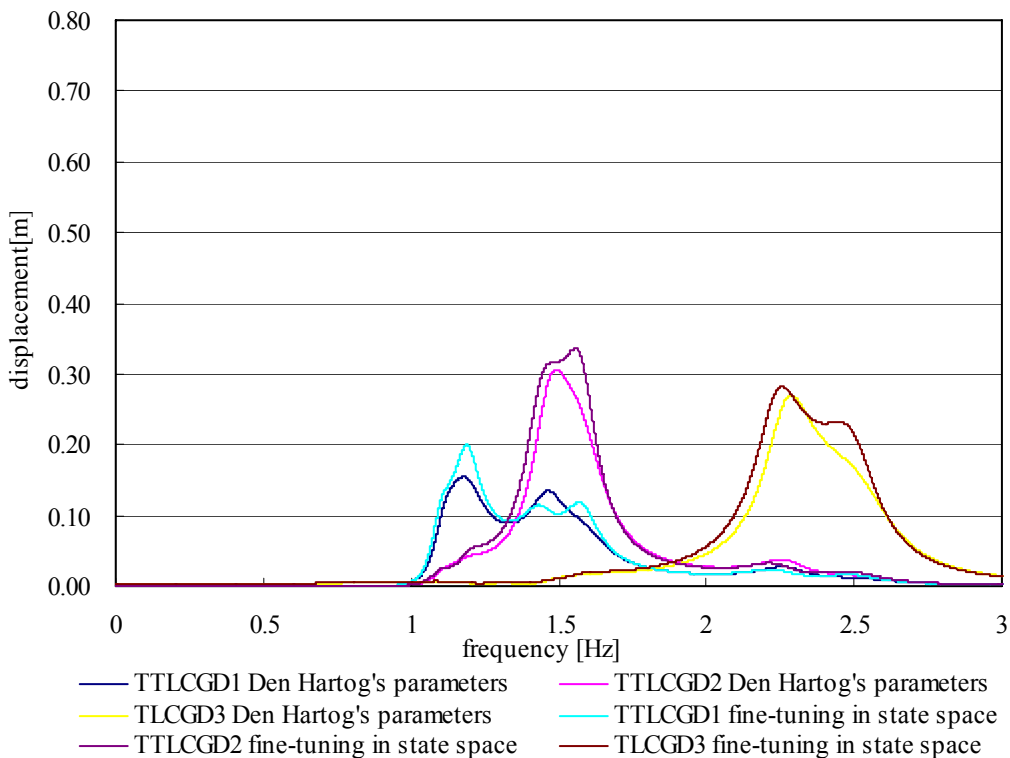


Fig. 5.11: Amplitude response curves of fluid displacement $|u|$ of three linearized absorbers attached to the two-storey strongly asymmetric space frame. Absorbers either with Den Hartog's optimal parameters or those resulting from fine-tuning in state space ($\alpha = \pi/6$).

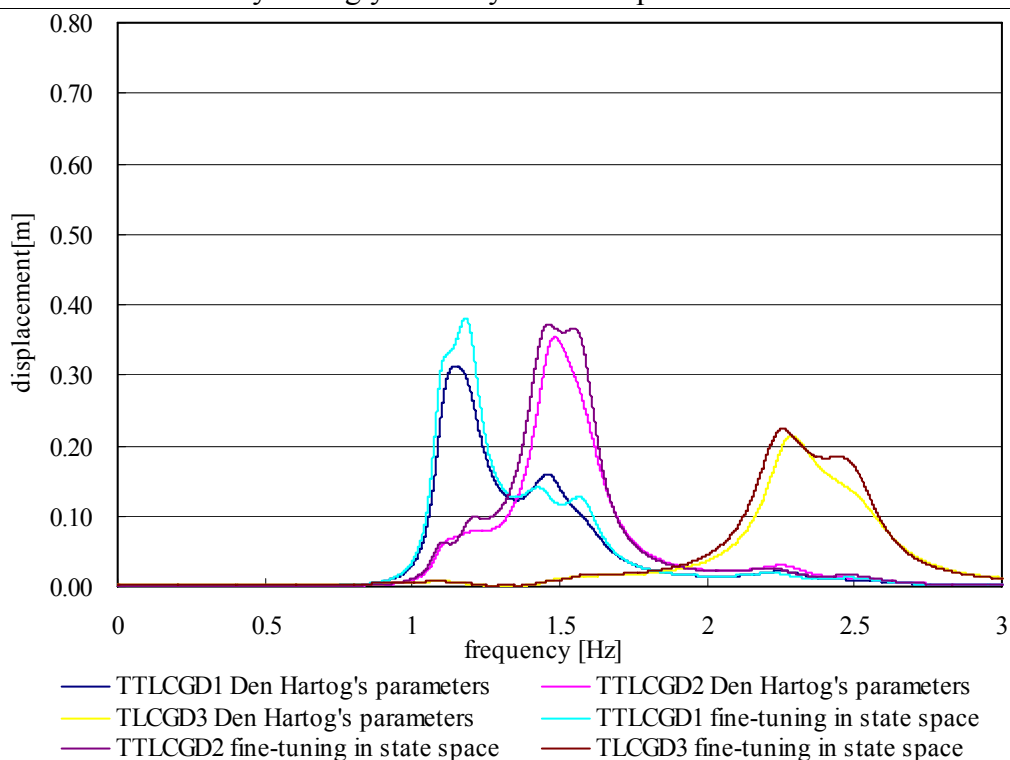


Fig. 5.12: Amplitude response curves of fluid displacement $|u|$ of three linearized absorbers attached to the two-storey strongly asymmetric space frame. Absorbers either with Den Hartog's optimal parameters or those resulting from fine-tuning in state space ($\alpha = \pi/4$).

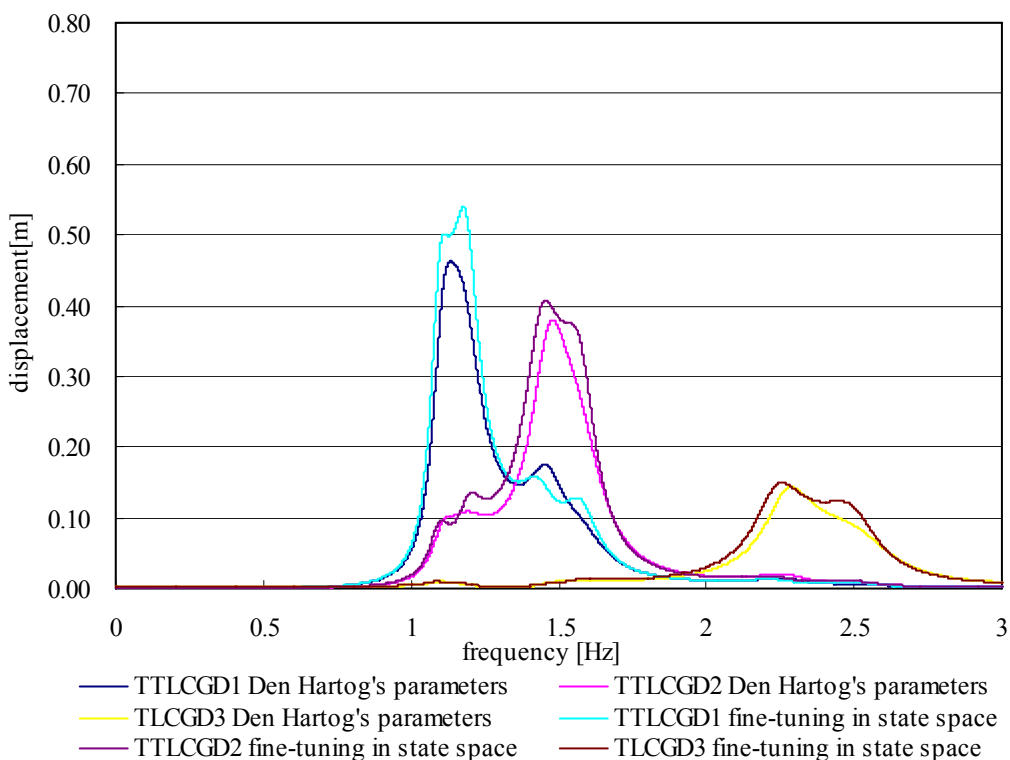


Fig. 5.13: Amplitude response curves of fluid displacement $|u|$ of three linearized absorbers attached to the two-storey strongly asymmetric space frame. Absorbers either with Den Hartog's optimal parameters or those resulting from fine-tuning in state space ($\alpha = \pi/3$).

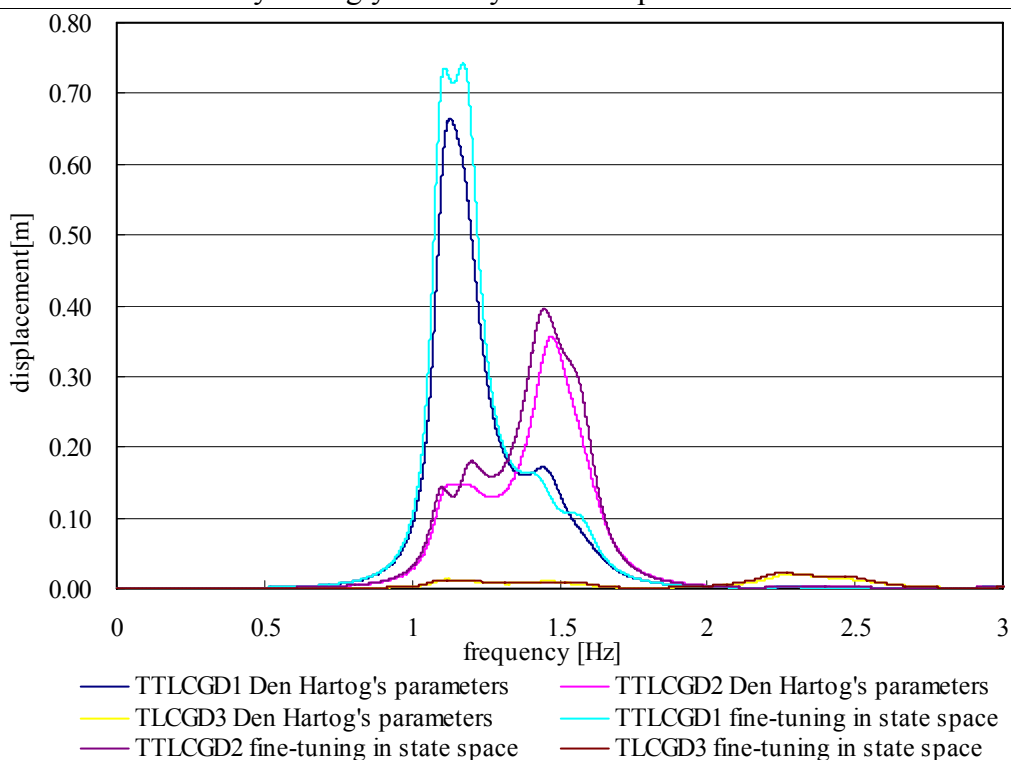


Fig. 5.14: Amplitude response curves of fluid displacement $|u|$ of three linearized absorbers attached to the two-storey strongly asymmetric space frame. Absorbers either with Den Hartog's optimal parameters or those resulting from fine-tuning in state space ($\alpha = \pi/2$).

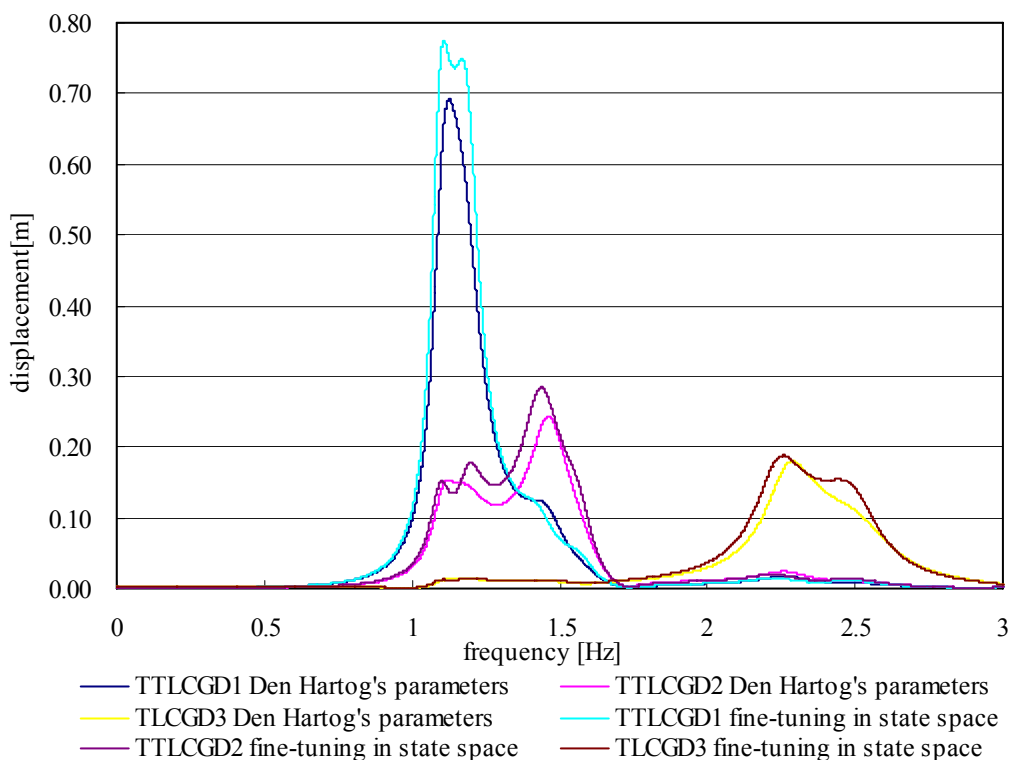


Fig. 5.15: Amplitude response curves of fluid displacement $|u|$ of three linearized absorbers attached to the two-storey strongly asymmetric space frame. Absorbers either with Den Hartog's optimal parameters or those resulting from fine-tuning in state space ($\alpha = 2\pi/3$).

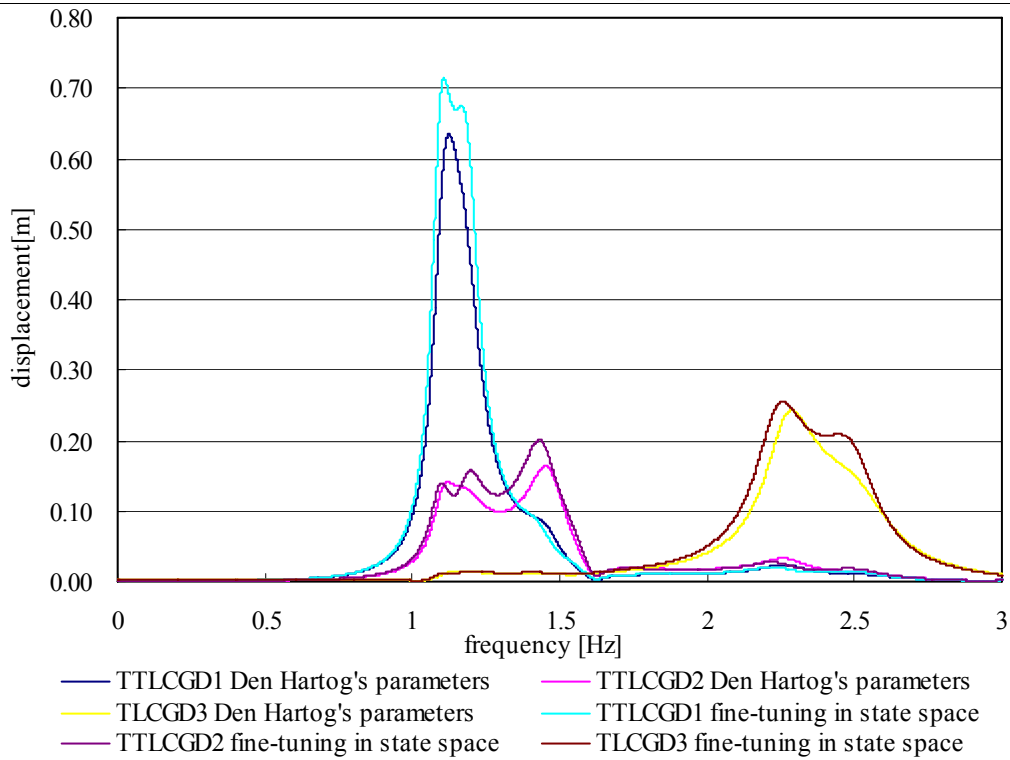


Fig. 5.16: Amplitude response curves of fluid displacement $|u|$ of three linearized absorbers attached to the two-storey strongly asymmetric space frame. Absorbers either with Den Hartog's optimal parameters or those resulting from fine-tuning in state space ($\alpha = 3\pi/4$).

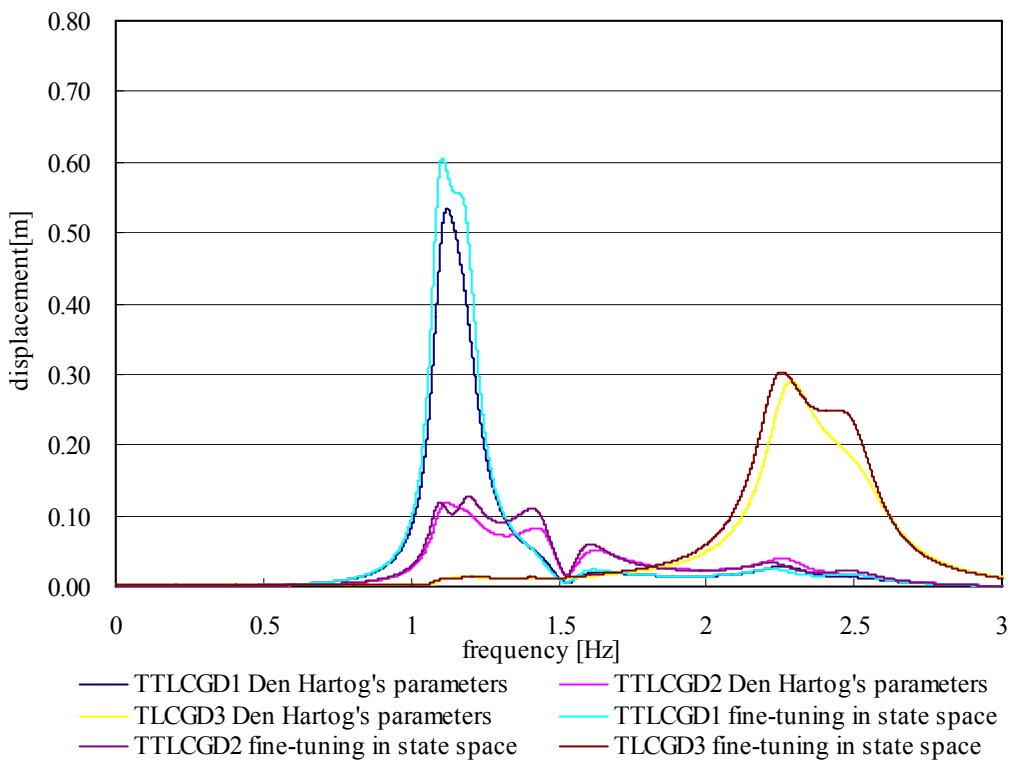


Fig. 5.17: Amplitude response curves of fluid displacement $|u|$ of three linearized absorbers attached to the two-storey strongly asymmetric space frame. Absorbers either with Den Hartog's optimal parameters or those resulting from fine-tuning in state space ($\alpha = 5\pi/6$).

5.5 Three-storey strongly asymmetric space frame: numerical example

The three-storey stiffness asymmetric structure serves as another numerical example. The common stiffness of columns in y - and z -directions of each storey are increased to $k_{yi}=981.23\text{kN/m}$ and $k_{zi}=350.04\text{kN/m}$. The anisotropic stiffness of an extra column of each storey are $k'_{yi}=11.78\times 10^3\text{kN/m}$ and $k'_{zi}=4.2\times 10^3\text{kN/m}$. The other properties of building are listed in Section 5.4.

5.5.1 Static dimensioning and a static safety criterion of the columns

The critical load of a steel profile HEB-160 length 4m, is calculated $F_c = -1150.43\text{kN}$. The combined load without TLCGD in column of first floor is $F = -302.92\text{kN}$, thus

$$\frac{F}{F_c} = \frac{-302.92}{-1150.43} = 0.26 < \frac{1}{3}.$$

The corrected stiffness in y -direction becomes:

$$\bar{k}_y = \begin{bmatrix} 1901.9 & -950.93 & 0 \\ -950.93 & 1901.9 & -950.93 \\ 0 & -950.93 & 950.93 \end{bmatrix} \text{ kN/m}.$$

The corrected stiffness in z -direction becomes:

$$\bar{k}_z = \begin{bmatrix} 639.5 & -319.75 & 0 \\ -319.75 & 639.5 & -319.75 \\ 0 & -319.75 & 319.75 \end{bmatrix} \text{ kN/m}.$$

5.5.2 Natural modes of the main structure

The computed natural frequencies are 1.13, 1.49, 2.36, 3.17, 4.16, 4.57, 6.01, 6.61 and 9.55 Hz, prestress of the column considered and extra column comes no weight of the floors. The orthonormalized modal matrix of the undamped main system with respect to \bar{M} is the output of Matlab 7.0.

$$\begin{aligned} \bar{\phi}_1 &= \begin{bmatrix} \bar{\phi}_{1,1} \\ \bar{\phi}_{1,2} \\ \bar{\phi}_{1,3} \end{bmatrix}, \quad \bar{\phi}_{1,1} = 10^{-2} \begin{bmatrix} 0.065177 \\ -0.18953 \\ 0.16452 \end{bmatrix}, \quad \bar{\phi}_{1,2} = 10^{-2} \begin{bmatrix} 0.11744 \\ -0.34151 \\ 0.29645 \end{bmatrix}, \quad \bar{\phi}_{1,3} = 10^{-2} \begin{bmatrix} 0.14645 \\ -0.42586 \\ 0.36967 \end{bmatrix}; \\ \bar{\phi}_2 &= \begin{bmatrix} \bar{\phi}_{2,1} \\ \bar{\phi}_{2,2} \\ \bar{\phi}_{2,3} \end{bmatrix}, \quad \bar{\phi}_{2,1} = 10^{-2} \begin{bmatrix} -0.089444 \\ -0.17636 \\ -0.16773 \end{bmatrix}, \quad \bar{\phi}_{2,2} = 10^{-2} \begin{bmatrix} -0.16117 \\ -0.31778 \\ -0.30223 \end{bmatrix}, \quad \bar{\phi}_{2,3} = 10^{-2} \begin{bmatrix} -0.20098 \\ -0.39627 \\ -0.37688 \end{bmatrix}; \\ \bar{\phi}_3 &= \begin{bmatrix} \bar{\phi}_{3,1} \\ \bar{\phi}_{3,2} \\ \bar{\phi}_{3,3} \end{bmatrix}, \quad \bar{\phi}_{3,1} = 10^{-2} \begin{bmatrix} -0.23449 \\ 0.01459 \\ 0.10971 \end{bmatrix}, \quad \bar{\phi}_{3,2} = 10^{-2} \begin{bmatrix} -0.42254 \\ 0.026291 \\ 0.19768 \end{bmatrix}, \quad \bar{\phi}_{3,3} = 10^{-2} \begin{bmatrix} -0.5269 \\ 0.032784 \\ 0.24651 \end{bmatrix}; \end{aligned}$$

$$\begin{aligned}
 \vec{\phi}_4 &= \begin{bmatrix} \vec{\phi}_{4,1} \\ \vec{\phi}_{4,2} \\ \vec{\phi}_{4,3} \end{bmatrix}, \quad \vec{\phi}_{4,1} = 10^{-2} \begin{bmatrix} 0.14645 \\ -0.42586 \\ 0.36967 \end{bmatrix}, \quad \vec{\phi}_{4,2} = 10^{-2} \begin{bmatrix} 0.065177 \\ -0.18953 \\ 0.16452 \end{bmatrix}, \quad \vec{\phi}_{4,3} = 10^{-2} \begin{bmatrix} -0.11744 \\ 0.34151 \\ -0.29645 \end{bmatrix}; \\
 \vec{\phi}_5 &= \begin{bmatrix} \vec{\phi}_{5,1} \\ \vec{\phi}_{5,2} \\ \vec{\phi}_{5,3} \end{bmatrix}, \quad \vec{\phi}_{5,1} = 10^{-2} \begin{bmatrix} -0.20098 \\ -0.39627 \\ -0.37688 \end{bmatrix}, \quad \vec{\phi}_{5,2} = 10^{-2} \begin{bmatrix} -0.089444 \\ -0.17636 \\ -0.16773 \end{bmatrix}, \quad \vec{\phi}_{5,3} = 10^{-2} \begin{bmatrix} 0.16117 \\ 0.31778 \\ 0.30223 \end{bmatrix}; \\
 \vec{\phi}_6 &= \begin{bmatrix} \vec{\phi}_{6,1} \\ \vec{\phi}_{6,2} \\ \vec{\phi}_{6,3} \end{bmatrix}, \quad \vec{\phi}_{6,1} = 10^{-2} \begin{bmatrix} -0.11744 \\ 0.34151 \\ -0.29645 \end{bmatrix}, \quad \vec{\phi}_{6,2} = 10^{-2} \begin{bmatrix} 0.14645 \\ -0.42586 \\ 0.36967 \end{bmatrix}, \quad \vec{\phi}_{6,3} = 10^{-2} \begin{bmatrix} -0.065177 \\ 0.18953 \\ -0.16452 \end{bmatrix}; \\
 \vec{\phi}_7 &= \begin{bmatrix} \vec{\phi}_{7,1} \\ \vec{\phi}_{7,2} \\ \vec{\phi}_{7,3} \end{bmatrix}, \quad \vec{\phi}_{7,1} = 10^{-2} \begin{bmatrix} 0.16117 \\ 0.31778 \\ 0.30223 \end{bmatrix}, \quad \vec{\phi}_{7,2} = 10^{-2} \begin{bmatrix} -0.20098 \\ -0.39627 \\ -0.37688 \end{bmatrix}, \quad \vec{\phi}_{7,3} = 10^{-2} \begin{bmatrix} 0.089444 \\ 0.17636 \\ 0.16773 \end{bmatrix}; \\
 \vec{\phi}_8 &= \begin{bmatrix} \vec{\phi}_{8,1} \\ \vec{\phi}_{8,2} \\ \vec{\phi}_{8,3} \end{bmatrix}, \quad \vec{\phi}_{8,1} = 10^{-2} \begin{bmatrix} 0.5269 \\ -0.032784 \\ -0.24651 \end{bmatrix}, \quad \vec{\phi}_{8,2} = 10^{-2} \begin{bmatrix} 0.23449 \\ -0.01459 \\ -0.10971 \end{bmatrix}, \quad \vec{\phi}_{8,3} = 10^{-2} \begin{bmatrix} -0.42254 \\ 0.026291 \\ 0.19768 \end{bmatrix}; \\
 \vec{\phi}_9 &= \begin{bmatrix} \vec{\phi}_{9,1} \\ \vec{\phi}_{9,2} \\ \vec{\phi}_{9,3} \end{bmatrix}, \quad \vec{\phi}_{9,1} = 10^{-2} \begin{bmatrix} -0.42254 \\ 0.026291 \\ 0.19768 \end{bmatrix}, \quad \vec{\phi}_{9,2} = 10^{-2} \begin{bmatrix} 0.5269 \\ -0.032784 \\ -0.24651 \end{bmatrix}, \quad \vec{\phi}_{9,3} = 10^{-2} \begin{bmatrix} -0.23449 \\ 0.01459 \\ 0.10971 \end{bmatrix}.
 \end{aligned}$$

5.5.3 Position of the modal centers of velocity C_V

The coordinates of the modal centers of velocity C_V with corrected column stiffness considered are listed in Table 5.5 for the first three relevant modes. Two TTLCGDs tuned to the first two (mainly torsional) modes and one plane TLCGD parallel to y-axis tuned to the mainly translational third mode are located on the top floor.

mode	1	2	3
Floor 1	(2.97,1.02)	(-2.71,1.38)	(-0.34,-5.52)
Floor 2	(2.97,1.02)	(-2.71,1.38)	(-0.34,-5.52)
Floor 3	(2.97,1.02)	(-2.71,1.38)	(-0.34,-5.52)

Table 5.5: The coordinates of the centers of velocity C_V for 3 relevant modes.

5.5.4 TTLCGD and TLCGD design, Den Hartog' optimization

The fluid mass is chosen $m_{f1} = 1100\text{kg}$, $m_{f2} = 1100\text{kg}$ and $m_{f3} = 500\text{kg}$ of water. Dimensions of three absorbers tuned first by means of the TMD analogy applying Den Hartog's formulas, Eqs. (3.66)- (3.68) for TTLCGDs ($\beta = \pi/2$) and Eqs. (2.102)- (2.104) for TLCGD ($\beta = \pi/4$) are summarized in Table 5.6. The dynamic magnification factor (DMF) calculated with Matlab 7.0¹, linearized damping of the absorbers considered, is illustrated in Figure 5. 18. The effective modal damping coefficients of the system are increased from 1% to $\zeta_{eff1} = 5.45\%$, $\zeta_{eff2} = 5.23\%$, $\zeta_{eff3} = 5.85\%$. From Table 5.7a-c it follows that all maximum fluid displacements occurring for various angles of attack, are within the acceptable limits, $u_0 < H_a/3$ (of linearized gas compression) and $u_0 < H/2$. The maximum fluid velocities of

three absorbers are calculated by Eq. (2.35) 4.81, 3.48 and 3.71m/s and are within the acceptable speed limit.

	TTLCGD1	TTLCGD2	TLCGD3
Horizontal length of the liquid column B [m]	24.00	24.00	2.50
Length of the upright liquid column H [m]	1.40	0.80	0.60
Cross-sectional area of the pipe [m ²] $A_H=A_B$	0.0410	0.0430	0.1350
Effective length $L_{eff} = L_1 = 2H + B$ [m], Eq. (2.34a)	26.80	25.60	3.70
Angle of the inclined pipe section β [rad]	$\pi/2$	$\pi/2$	$\pi/4$
Equivalent mathematical pendulum length L_0 [m] Eq. (2.37)	0.19	0.11	0.04
Geometry factor $\kappa = \bar{\kappa}$ or $\kappa_{T0} = \bar{\kappa}_{T0}$, Eqs. (2.34a), (2.44),(3.14a),(3.44)	0.67	0.71	0.91
Equilibrium pressure head h_0 [m], $n=1.2$, Eq. (2.34a)	146.79	134.56	36.70
Gas volume $V_0 = A_H H_a$ [m ³], Eq. (2.38)	0.089000	0.050000	0.120000
The mass ratio of the TLCGD-main system μ , Eqs. (2.97), (3.60)	5.78%	5.50%	2.63%
The mass ratio of the equivalent TMD-main system μ^* , Eqs. (2.102), (3.66)	2.20%	2.48%	2.10%
Natural frequency $f_{A,opt}$ [Hz] Eq. (2.104), (2.112)	1.09	1.43	2.3
Optimal linear damping %, Eq. (2.113)	8.98	9.52	8.79

Table 5.6: Layout of the modally tuned absorbers, gas volume and gas equilibrium pressure assigned, note again the rather high gad pressure in TTLCGD.

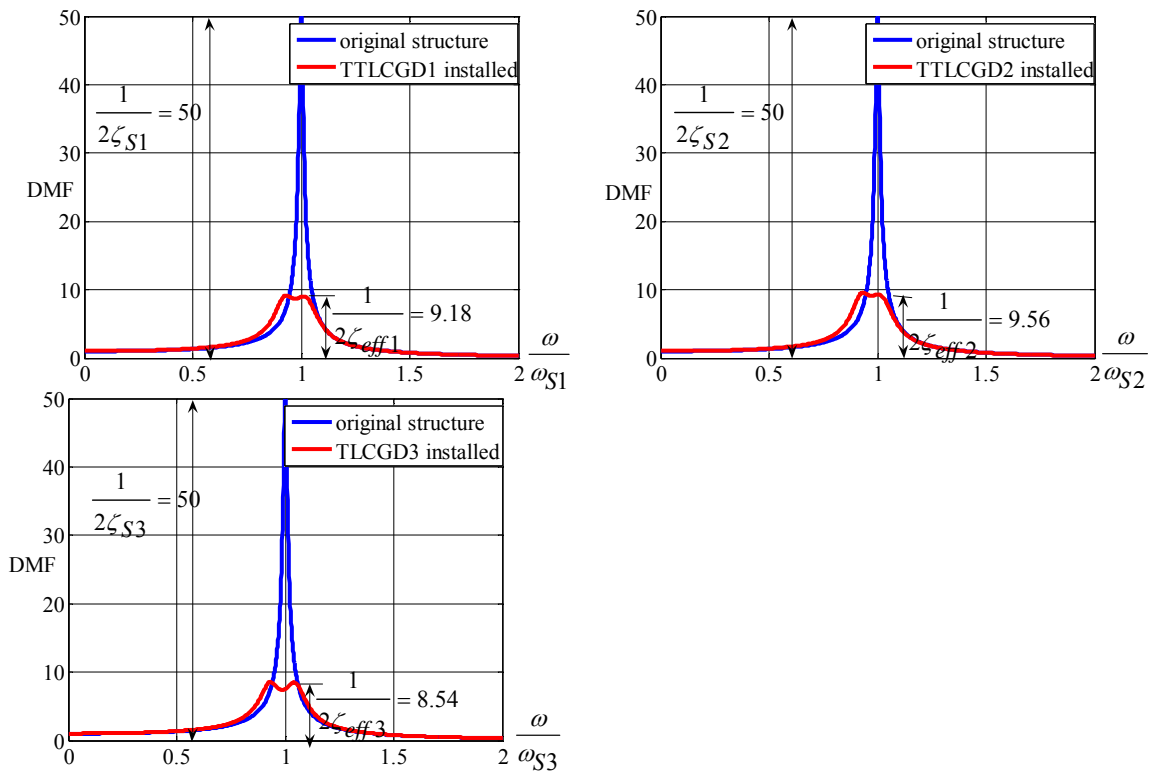


Fig. 5.18: Individual frequency response curves without and with linearized absorbers attached, with Den Hartog's optimal parameter.

Forcing direction	structure			TTLCGD1
	v_3 [mm]	w_3 [mm]	$u_{T3} = r_{S3}\theta_3$ [mm]	u_0 [mm]
$\alpha = 0$	C_{M3} 18	-52	45	233
$\alpha = \pi/6$	C_{M3} 11	-31	27	136
$\alpha = \pi/4$	C_{M3} 24	-70	61	314
$\alpha = \pi/3$	C_{M3} 36	-105	91	469
$\alpha = \pi/2$	C_{M3} 52	-152	132	677
$\alpha = 2\pi/3$	C_{M3} 54	-158	137	702
$\alpha = 3\pi/4$	C_{M3} 50	-144	125	643
$\alpha = 5\pi/6$	C_{M3} 42	-121	105	540

Table 5.7a: Maximum displacements of three-storey structure in the first mode from time-harmonic excitation in α -directions, $a_0=0.1g$, $r_{Si} = 2.58m$.

Forcing direction	structure			TTLCGD2
	v_3 [mm]	w_3 [mm]	$u_{T3} = r_{S3}\theta_3$ [mm]	u_0 [mm]
$\alpha = 0$	C_{M3} -18	-36	-35	175
$\alpha = \pi/6$	C_{M3} -34	-67	-64	325
$\alpha = \pi/4$	C_{M3} -39	-76	-73	368
$\alpha = \pi/3$	C_{M3} -41	-80	-76	387
$\alpha = \pi/2$	C_{M3} -36	-72	-68	346
$\alpha = 2\pi/3$	C_{M3} -22	-44	-42	212
$\alpha = 3\pi/4$	C_{M3} -13	-25	-24	120
$\alpha = 5\pi/6$	C_{M3} -2	-4	-4	21

Table 5.7b: Maximum displacements of three-storey structure in the second mode from time-harmonic excitation in α -directions, $a_0=0.1g$, $r_{Si} = 2.58m$.

Forcing direction	structure			TLCGD3
	v_3 [mm]	w_3 [mm]	$u_{T3} = r_{S3}\theta_3$ [mm]	u_0 [mm]
$\alpha = 0$	C_{M3} -40	3	19	257
	A -55	3		
$\alpha = \pi/6$	C_{M3} -34	2	16	215
	A -46	2		
$\alpha = \pi/4$	C_{M3} -27	2	13	171
	A -36	2		
$\alpha = \pi/3$	C_{M3} -18	1	8	115
	A -25	1		
$\alpha = \pi/2$	C_{M3} -2	0	1	15
	A -3	0		
$\alpha = 2\pi/3$	C_{M3} -22	1	10	141
	A -30	1		
$\alpha = 3\pi/4$	C_{M3} -30	2	14	192
	A -41	2		
$\alpha = 5\pi/6$	C_{M3} -36	2	17	230
	A -49	2		

Table 5.7c: Maximum displacements of three-storey structure in the third mode from time-harmonic excitation in α -directions, $a_0=0.1g$, $r_{Si} = 2.58m$.

5.5.5 Optimization of the TTLCGD-, TLCGD-structure system in the state space domain

The fine tuned optimal natural circular frequencies and damping ratios by calling the function *fminsearch* of the performance index J , Eq. (2.123), are found to be $f_{A1} = 1.08\text{Hz}$, $f_{A2} = 1.38\text{Hz}$, $f_{A3} = 2.23\text{Hz}$, $\zeta_{A1} = 7.55\%$, $\zeta_{A2} = 8.89\%$, $\zeta_{A3} = 7.77\%$. Tuning is achieved by properly adjusting the equilibrium gas pressure: 134, 115.82 and 32.93m. The

Figures 5.19-5.26 show the weighed sum of the frequency responses $\sum_{i=1}^{18} s_i |z_{Si}(\nu)|$, $\mathfrak{S} = \text{diag}$

(10,10,10,10,10,10,10,10,10,10,1,1,1,1,1,1,1,1) of the building states for the original and the optimized system, in the logarithmic decibel scale in the relevant frequency window $0 \leq f \leq 3\text{Hz}$. The resonance curves with fine-tuning optimal parameters have broader peaks. The maximum fluid displacement amplitudes of three absorbers in Figs. 5.27-5.34 are well within the acceptable limits. The maximum fluid velocities of three absorbers are calculated by Eq. (2.35) 4.89, 3.47 and 4.20m/s and are also within the acceptable speed limit.

The wall thickness and the estimated dead mass of the piping system are listed in Table 5.8 for the three absorbers, designed according to Table 5.6.

	TTLCGD1	TTLCGD2	TLCGD3
h_0 [m]	146.79	134.56	36.70
H_a [m]	2.17	1.16	0.89
$10^{-5} p_{(D)}$ [N/m ²] Eq.(2.128)	66.96	61.27	16.01
pipe diameter $2r$ [mm]	228.5	234.0	414.6
t [mm] Eq.(2.124)	5.5	5.1	2.4
m_p [kg] Eq.(2.130)	952.71	819.79	131.92
dead fluid-mass[kg]	606.21	545.49	85.95
$10^{-5} \bar{p}_{(D)}$ [N/m ²] Eq.(2.129)	5.13	4.62	0.53

Table 5.8: Dimensioning of circular steel pipes.

The gauge pressure under expansion conditions turns out to be positive as listed in Table 5.8. The final dimensions of circular steel pipes must be changed according to their commercial availability.

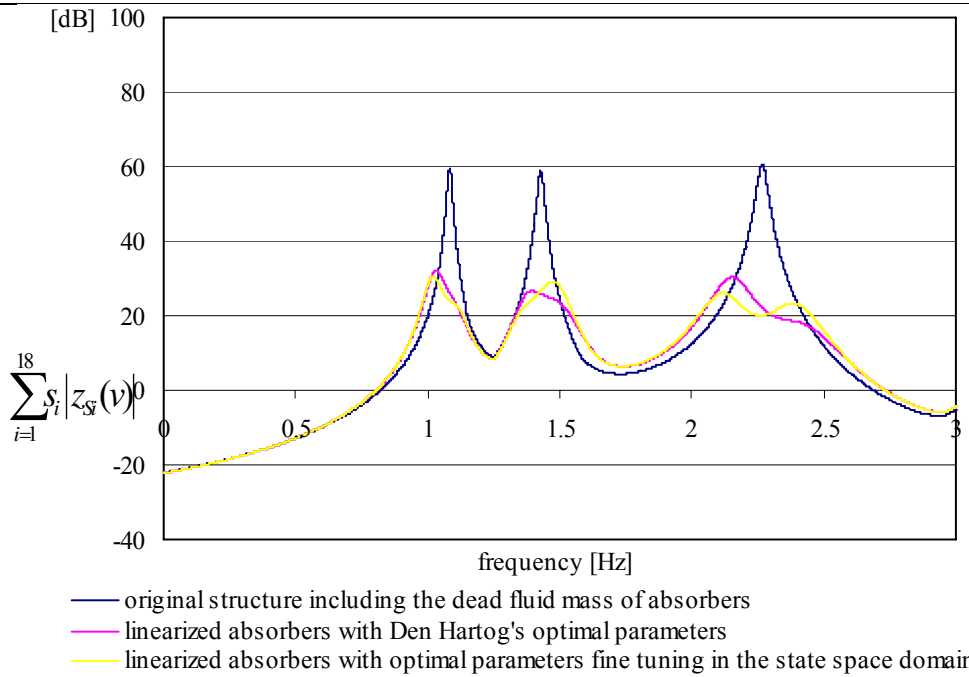


Fig. 5.19: Weighed sum of amplitude response functions for the 9-DOF linearized, three-storey, strongly asymmetric space frame with three linearized absorbers attached and without the absorbers (angle of attack of the time-harmonic base acceleration $\alpha = 0$), maximum gain 29.90dB.

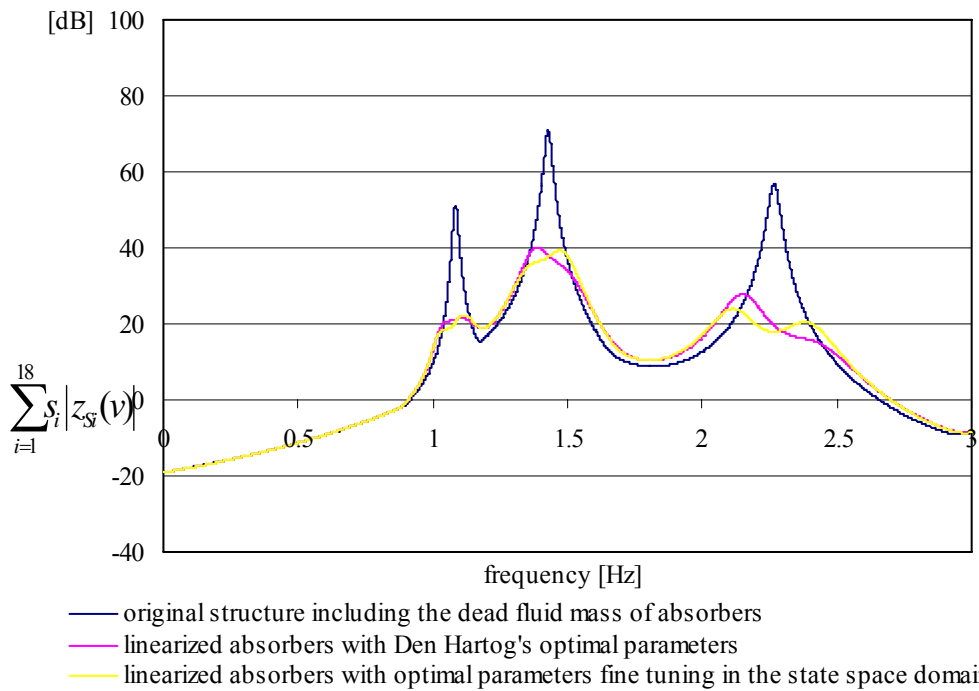


Fig. 5.20: Weighed sum of amplitude response functions for the 9-DOF linearized, three-storey, strongly plan asymmetric space frame with three linearized absorbers attached and without the absorbers (angle of attack of the time-harmonic base acceleration $\alpha = \pi/6$), maximum gain 31.50dB.

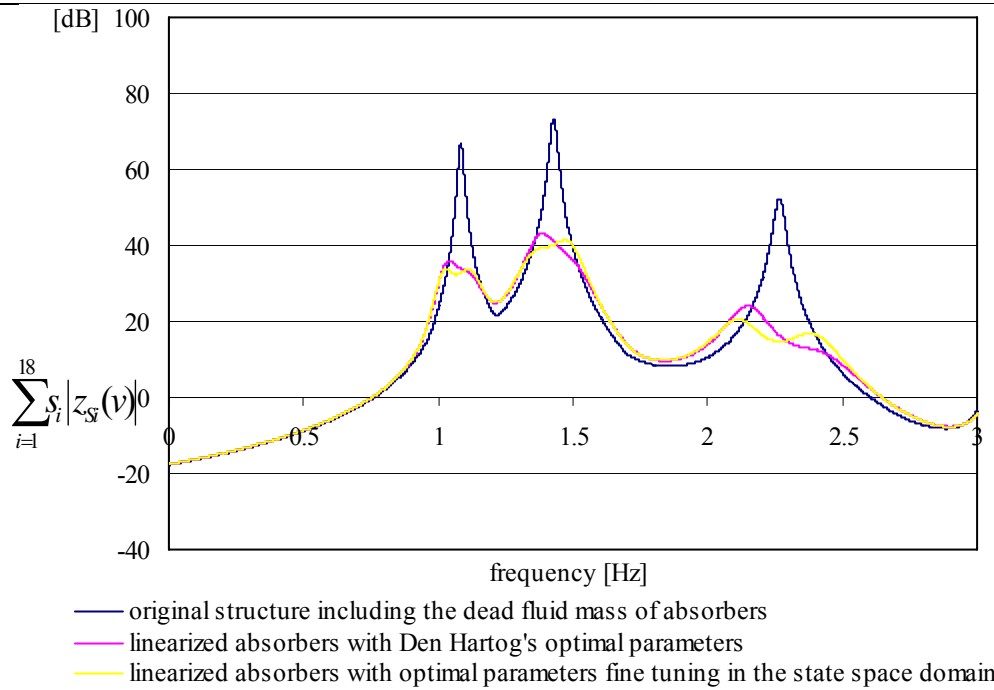


Fig. 5.21: Weighed sum of amplitude response functions for the 9-DOF linearized, three-storey, strongly asymmetric space frame with three linearized absorbers attached and without the absorbers (angle of attack of the time-harmonic base acceleration $\alpha = \pi/4$), maximum gain 31.82dB.

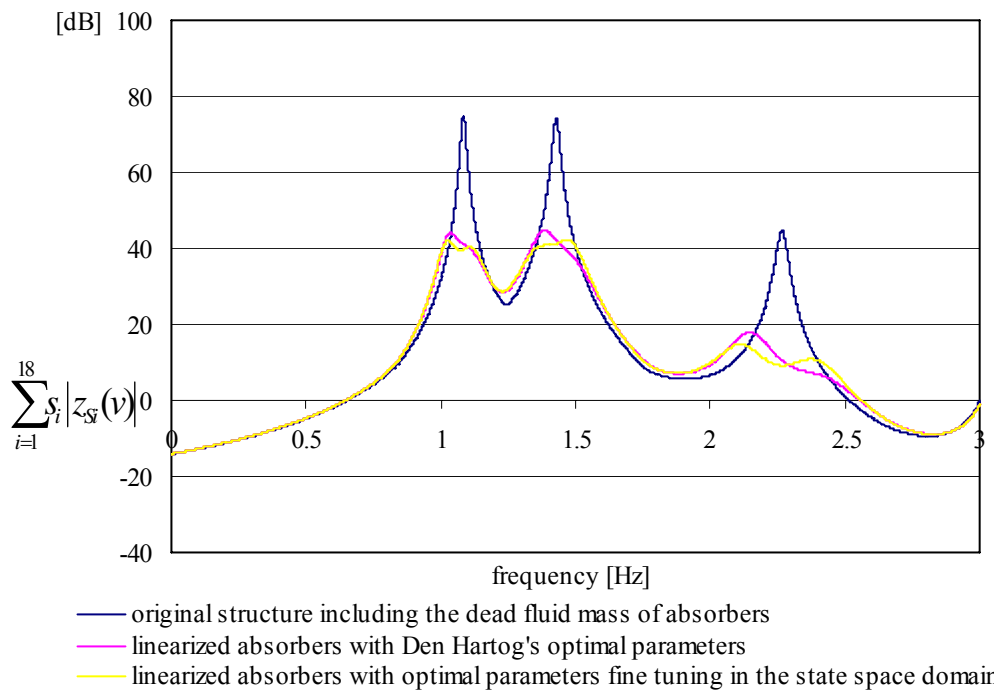


Fig. 5.22: Weighed sum of amplitude response functions for the 9-DOF linearized, three-storey, strongly asymmetric space frame with three linearized absorbers attached and without the absorbers (angle of attack of the time-harmonic base acceleration $\alpha = \pi/3$), maximum gain 32.47dB.

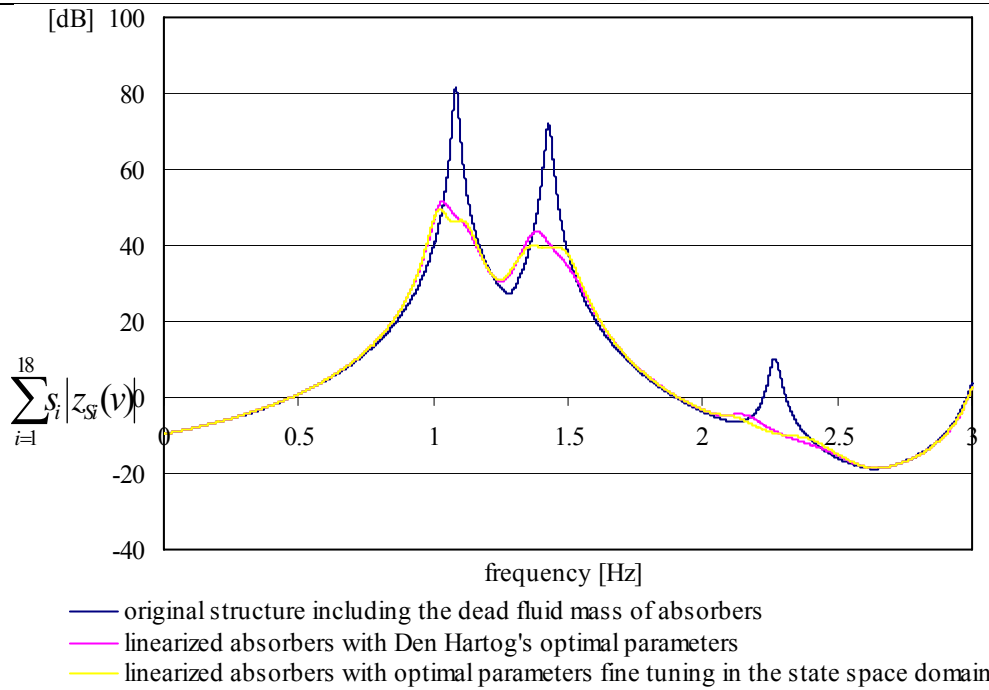


Fig. 5.23: Weighed sum of amplitude response functions for the 9-DOF linearized, three-storey, strongly asymmetric space frame with three linearized absorbers attached and without the absorbers (angle of attack of the time-harmonic base acceleration $\alpha = \pi/2$), maximum gain 32.23dB.

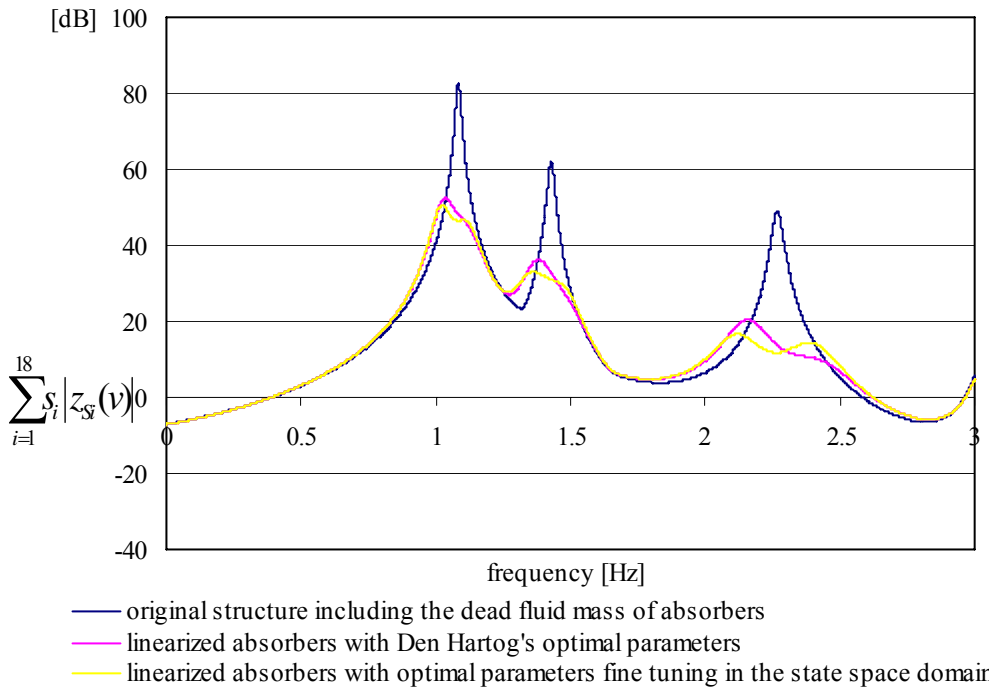


Fig. 5.24: Weighed sum of amplitude response functions for the 9-DOF linearized, three-storey, strongly asymmetric space frame with three linearized absorbers attached and without the absorbers (angle of attack of the time-harmonic base acceleration $\alpha = 2\pi/3$), maximum gain 31.79dB.

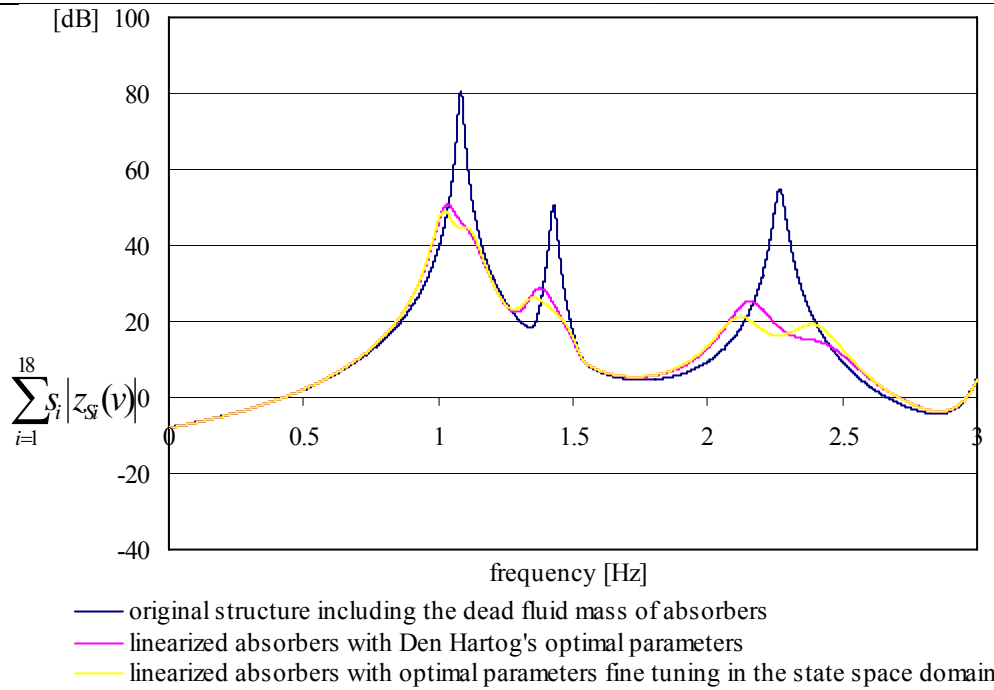


Fig. 5.25: Weighed sum of amplitude response functions for the 9-DOF linearized, three-storey, strongly asymmetric space frame with three linearized absorbers attached and without the absorbers (angle of attack of the time-harmonic base acceleration $\alpha = 3\pi/4$), maximum gain 31.53dB.

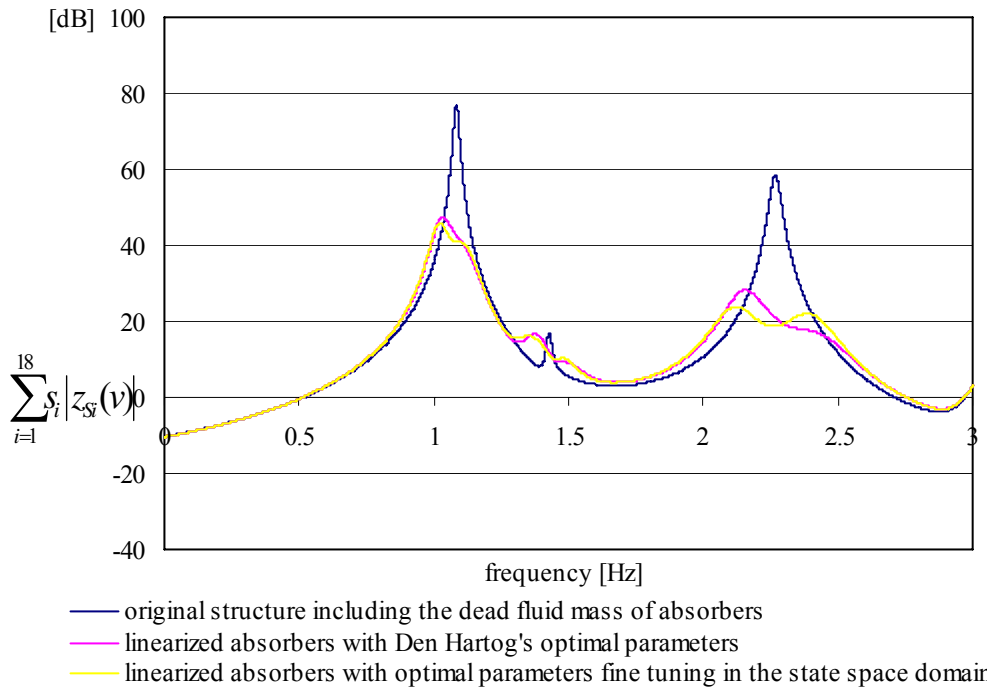


Fig. 5.26: Weighed sum of amplitude response functions for the 9-DOF linearized, three-storey, strongly asymmetric space frame with three linearized absorbers attached and without the absorbers (angle of attack of the time-harmonic base acceleration $\alpha = 5\pi/6$), maximum gain 31.17dB.

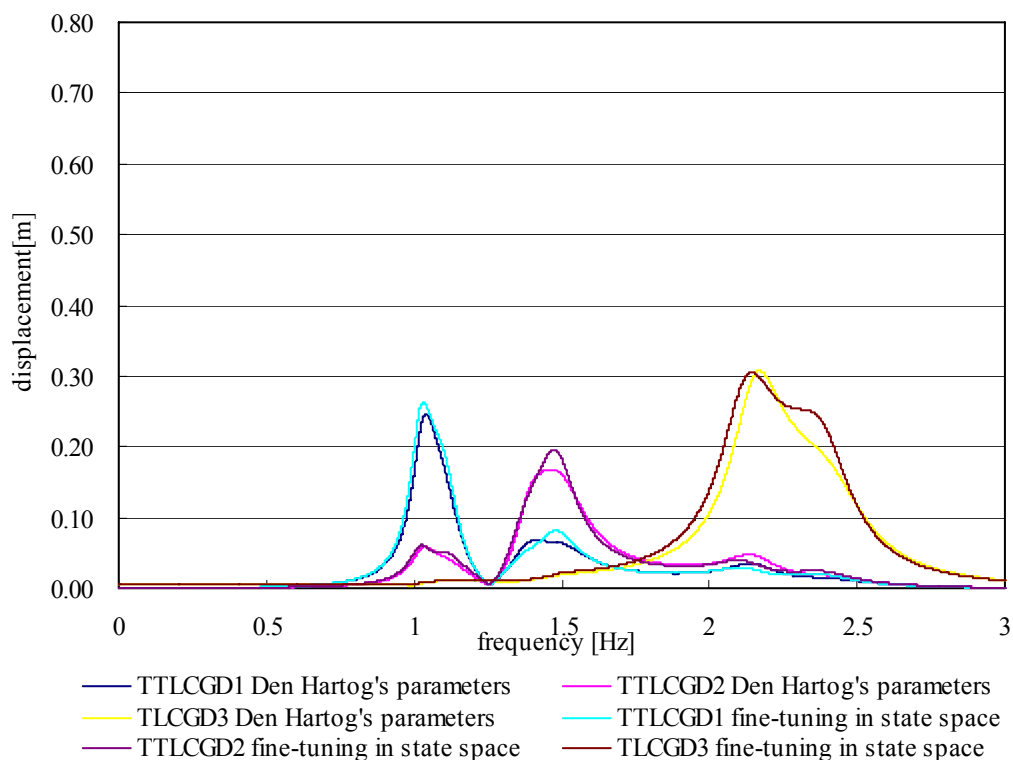


Fig. 5.27: Amplitude response curves of fluid displacement $|u|$ of three linearized absorbers attached to the three-storey strongly asymmetric space frame. Absorbers either with Den Hartog's optimal parameters or those resulting from fine-tuning in state space ($\alpha = 0$).

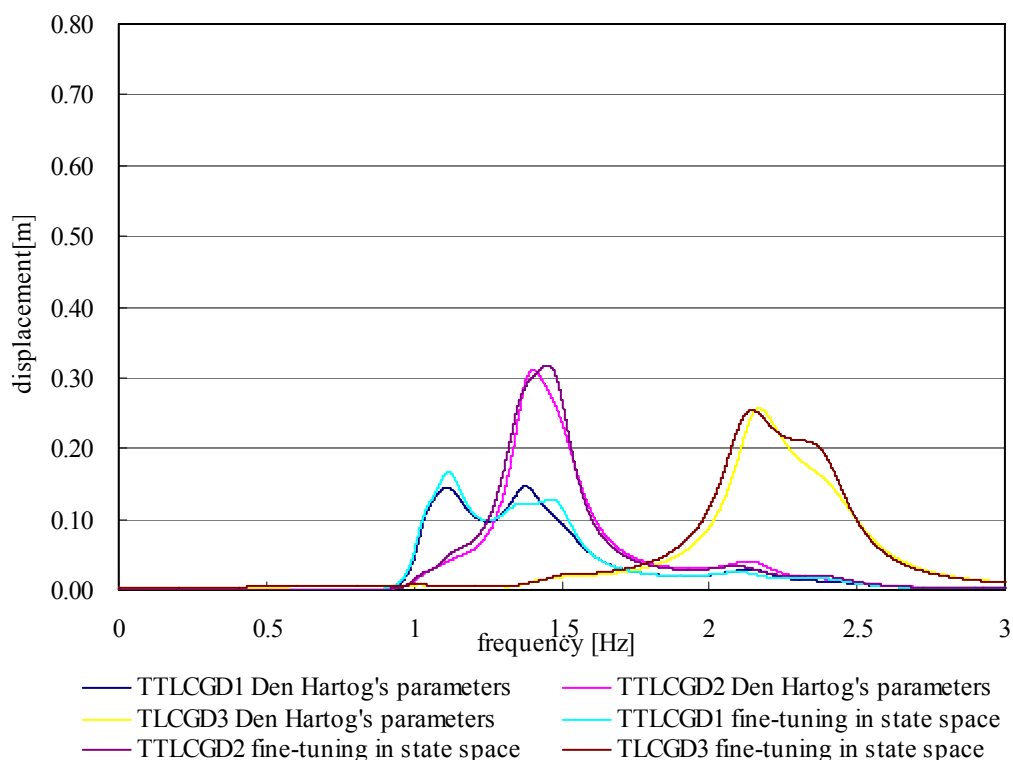


Fig. 5.28: Amplitude response curves of fluid displacement $|u|$ of three linearized absorbers attached to the three-storey strongly asymmetric space frame. Absorbers either with Den Hartog's optimal parameters or those resulting from fine-tuning in state space ($\alpha = \pi/6$).

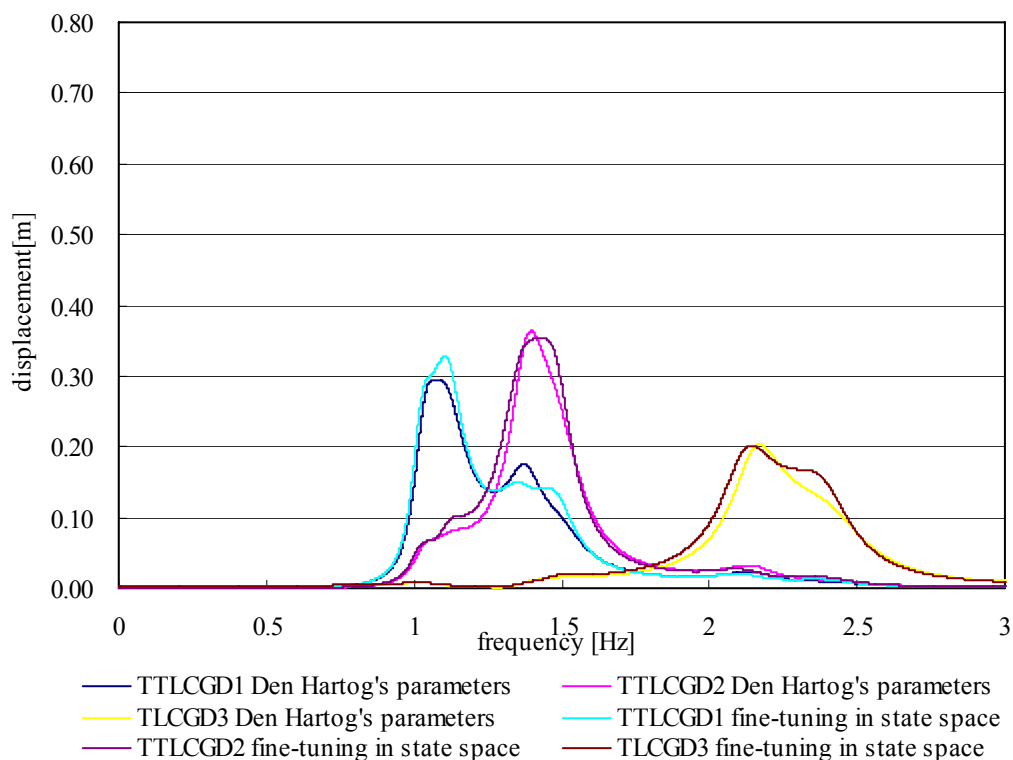


Fig. 5.29: Amplitude response curves of fluid displacement $|u|$ of three linearized absorbers attached to the three-storey strongly asymmetric space frame. Absorbers either with Den Hartog's optimal parameters or those resulting from fine-tuning in state space ($\alpha = \pi/4$).

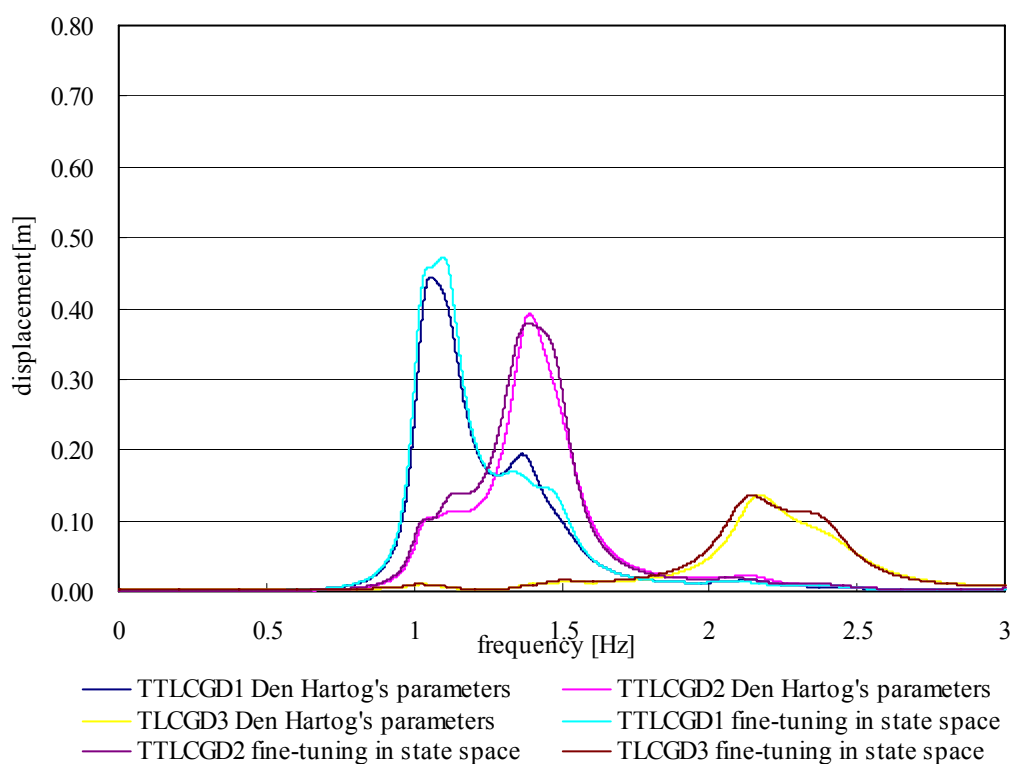


Fig. 5.30: Amplitude response curves of fluid displacement $|u|$ of three linearized absorbers attached to the three-storey strongly asymmetric space frame. Absorbers either with Den Hartog's optimal parameters or those resulting from fine-tuning in state space ($\alpha = \pi/3$).

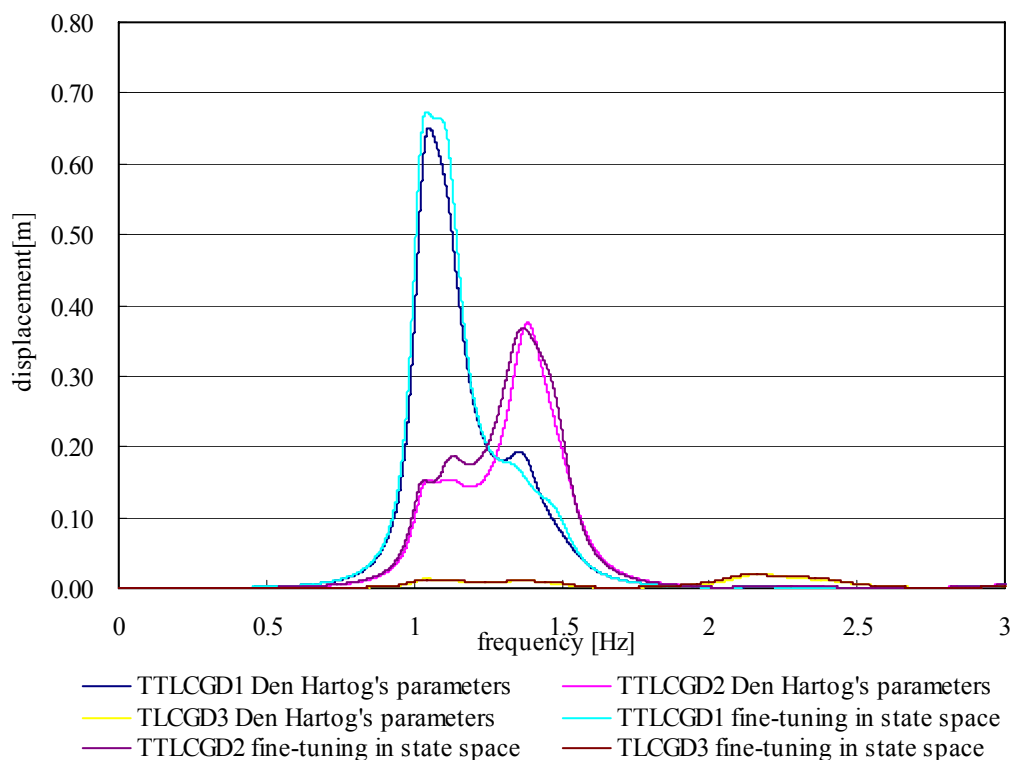


Fig. 5.31: Amplitude response curves of fluid displacement $|u|$ of three linearized absorbers attached to the three-storey strongly asymmetric space frame. Absorbers either with Den Hartog's optimal parameters or those resulting from fine-tuning in state space ($\alpha = \pi/2$).

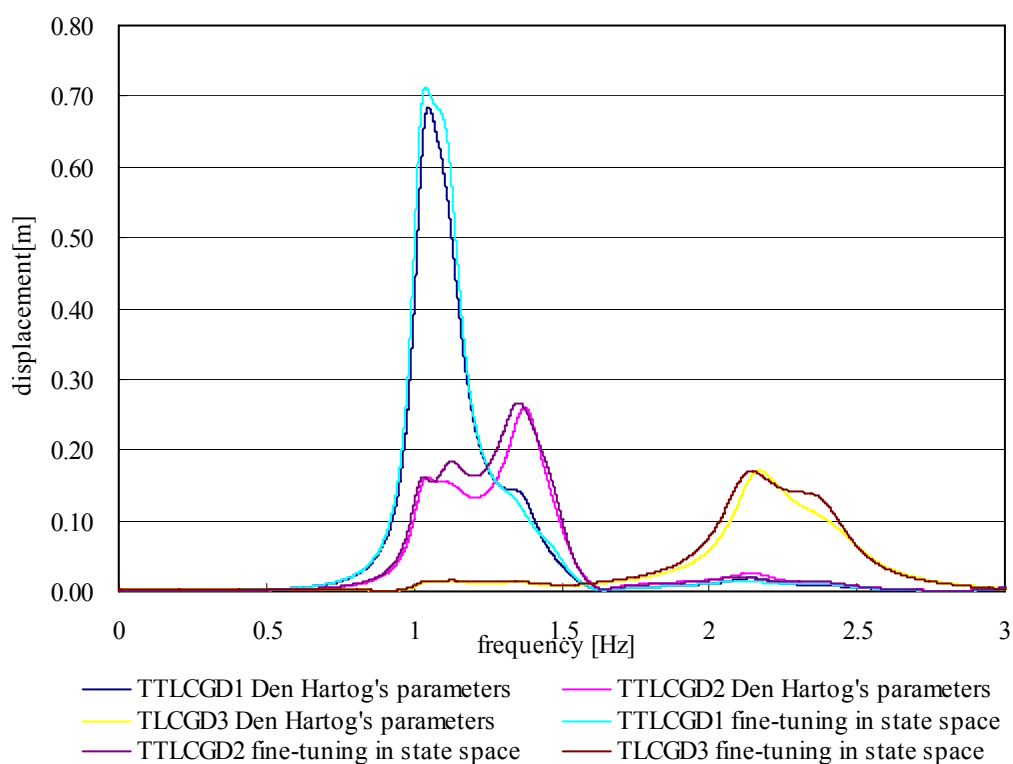


Fig. 5.32: Amplitude response curves of fluid displacement $|u|$ of three linearized absorbers attached to the three-storey strongly asymmetric space frame. Absorbers either with Den Hartog's optimal parameters or those resulting from fine-tuning in state space ($\alpha = 2\pi/3$).

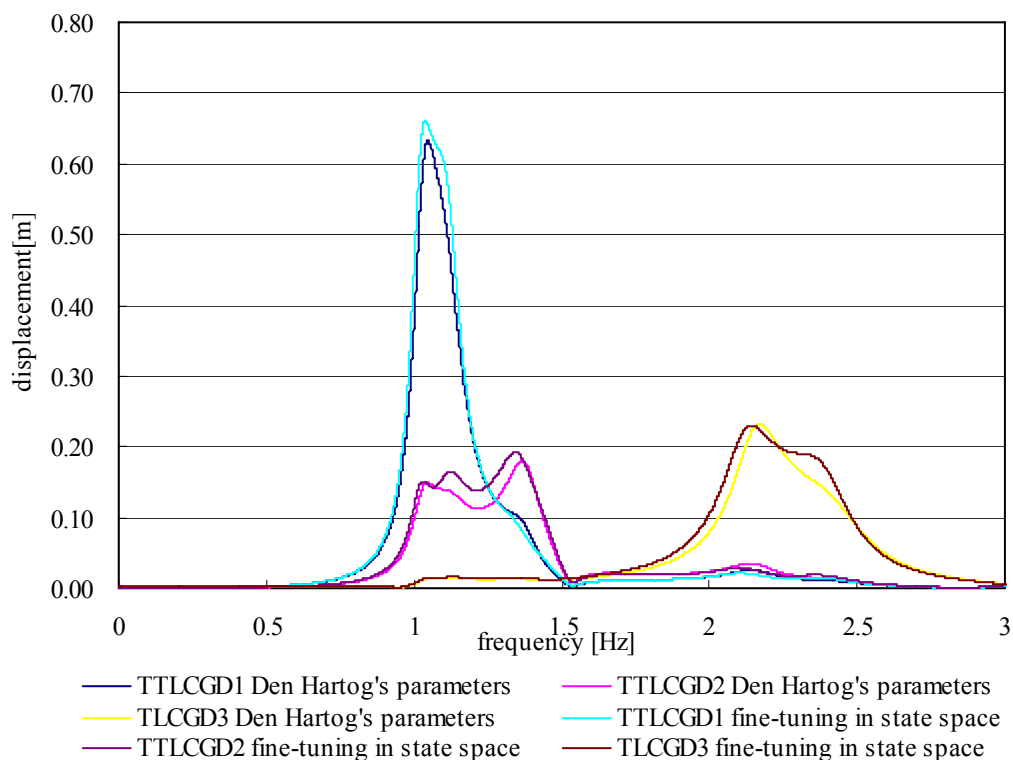


Fig. 5.33: Amplitude response curves of fluid displacement $|u|$ of three linearized absorbers attached to the three-storey strongly asymmetric space frame. Absorbers either with Den Hartog's optimal parameters or those resulting from fine-tuning in state space ($\alpha = 3\pi/4$).

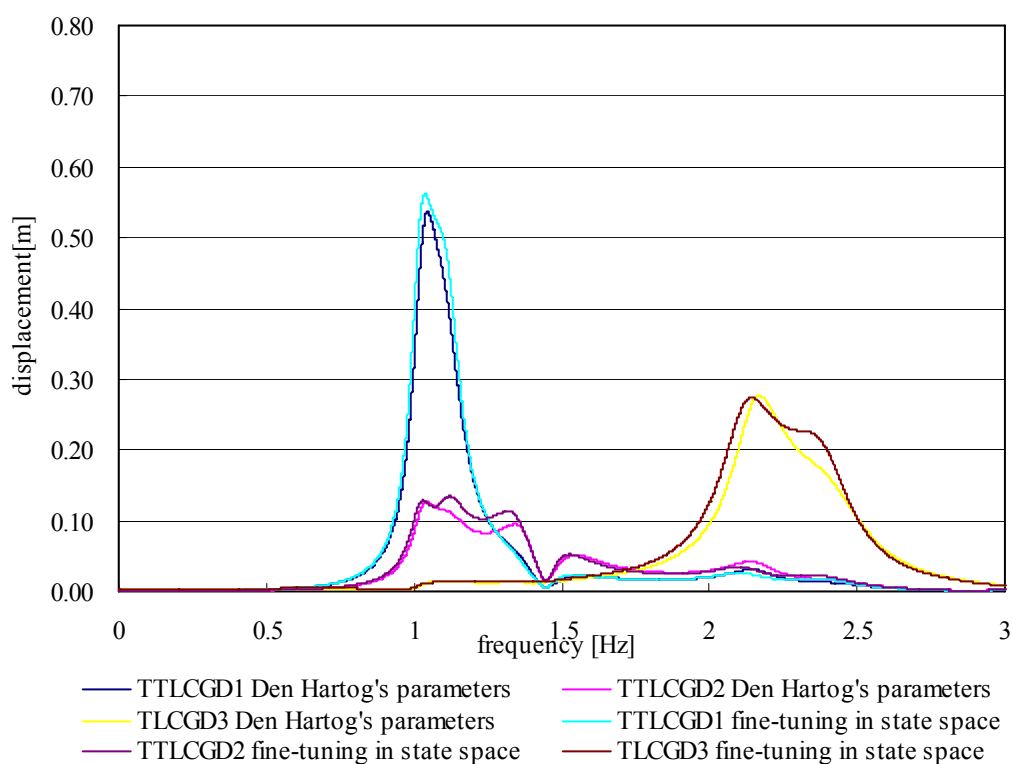


Fig. 5.34: Amplitude response curves of fluid displacement $|u|$ of three linearized absorbers attached to the three-storey strongly asymmetric space frame. Absorbers either with Den Hartog's optimal parameters or those resulting from fine-tuning in state space ($\alpha = 5\pi/6$).

5.6 Four-storey strongly asymmetric space frame: numerical example

The properties of building are: stiffness of corner cc-columns of each storey in y - and z -directions $k_{yi}=1508.5\text{kN/m}$ and $k_{zi}=536.68\text{kN/m}$, stiffness of an additional cc-column of each storey $k'_{yi}=18.10\times 10^3\text{kN/m}$ and $k'_{zi}=6.44\times 10^3\text{kN/m}$. The eccentricity is $e_y=e_z=1\text{m}$. Floor mass unchanged, $m_s=16\times 10^3\text{kg}$.

5.6.1 Static dimensioning and a static safety criterion of the columns

The critical load of a steel profile HEB-180 length 4m, is calculated $F_c = -1763.82\text{kN}$. The combined load without TLCD in column of first floor is $F = -403.896\text{kN}$, thus $\frac{F}{F_c} = \frac{-403.896}{-1763.82} = 0.23 < \frac{1}{3}$.

The corrected stiffness of column in y -direction becomes:

$$\bar{k}_y = \begin{bmatrix} 2956.3 & -1478.2 & 0 & 0 \\ -1478.2 & 2956.3 & -1478.2 & 0 \\ 0 & -1478.2 & 2956.3 & -1478.2 \\ 0 & 0 & -1478.2 & 1478.2 \end{bmatrix} \text{ kN/m.}$$

The corrected stiffness of column in z -direction becomes:

$$\bar{k}_z = \begin{bmatrix} 1012.8 & -506.39 & 0 & 0 \\ -506.39 & 1012.8 & -506.39 & 0 \\ 0 & -506.39 & 1012.8 & -506.39 \\ 0 & 0 & -506.39 & 506.39 \end{bmatrix} \text{ kN/m.}$$

5.6.2 Natural modes of the main structure

The computed natural frequencies are 1.10, 1.44, 2.28, 3.17, 4.16, 4.85, 5.97, 6.37, 6.58, 7.81, 10.08, 12.36 Hz, prestress of the column considered and extra column comes no weight of the floors. The natural vibration modes, which have been orthonormalized to obtain

$$\bar{\phi}_j^T \bar{M} \bar{\phi}_i = \delta_{ij} = \begin{cases} 0, & i \neq j \\ 1, & i = j \end{cases}, \text{ are } \bar{\phi}_i = [\bar{\phi}_{i,1} \quad \bar{\phi}_{i,2} \quad \bar{\phi}_{i,3} \quad \bar{\phi}_{i,4}]^T,$$

$$\bar{\phi}_{1,1} = 10^{-2} [0.044763 \quad -0.13334 \quad 0.112740]^T, \quad \bar{\phi}_{1,2} = 10^{-2} [0.084127 \quad -0.25059 \quad 0.211890]^T,$$

$$\bar{\phi}_{1,3} = 10^{-2} [0.113340 \quad -0.33763 \quad 0.285470]^T, \quad \bar{\phi}_{1,4} = 10^{-2} [0.128890 \quad -0.38393 \quad 0.324630]^T;$$

$$\bar{\phi}_{2,1} = 10^{-2} [0.063041 \quad 0.120880 \quad 0.117930]^T, \quad \bar{\phi}_{2,2} = 10^{-2} [0.118480 \quad 0.227180 \quad 0.221640]^T,$$

$$\bar{\phi}_{2,3} = 10^{-2} [0.159630 \quad 0.306080 \quad 0.298610]^T, \quad \bar{\phi}_{2,4} = 10^{-2} [0.181520 \quad 0.348060 \quad 0.339570]^T;$$

$$\bar{\phi}_{3,1} = 10^{-2} [0.1628400 \quad -0.010143 \quad -0.076649]^T, \quad \bar{\phi}_{3,2} = 10^{-2} [0.3060300 \quad -0.019063 \quad -0.144050]^T,$$

$$\bar{\phi}_{3,3} = 10^{-2} [0.4123200 \quad -0.025683 \quad -0.194080]^T, \quad \bar{\phi}_{3,4} = 10^{-2} [0.4688700 \quad -0.029206 \quad -0.220700]^T;$$

$$\bar{\phi}_{4,1} = 10^{-2} [-0.11334 \quad 0.337630 \quad -0.28547]^T, \quad \bar{\phi}_{4,2} = 10^{-2} [-0.11334 \quad 0.337630 \quad -0.28547]^T,$$

$$\bar{\phi}_{4,3} = 10^{-2} [0 \quad 0 \quad 0]^T, \quad \bar{\phi}_{4,4} = 10^{-2} [0.113340 \quad -0.33763 \quad 0.285470]^T;$$

$$\bar{\phi}_{5,1} = 10^{-2} [0.15963 \quad 0.30608 \quad 0.29861]^T, \quad \bar{\phi}_{5,2} = 10^{-2} [0.15963 \quad 0.30608 \quad 0.29861]^T,$$

$$\begin{aligned} \vec{\phi}_{5,3} &= 10^{-2} [0 \ 0 \ 0]^T, \quad \vec{\phi}_{5,4} = 10^{-2} [-0.15963 \ -0.30608 \ -0.29861]^T; \\ \vec{\phi}_{6,1} &= 10^{-2} [0.12889 \ -0.38393 \ 0.32463]^T, \quad \vec{\phi}_{6,2} = 10^{-2} [-0.044763 \ 0.13334 \ -0.11274]^T, \\ \vec{\phi}_{6,3} &= 10^{-2} [-0.11334 \ 0.33763 \ -0.28547]^T, \quad \vec{\phi}_{6,4} = 10^{-2} [0.084127 \ -0.25059 \ 0.21189]^T; \\ \vec{\phi}_{7,1} &= 10^{-2} [0.084127 \ -0.25059 \ 0.21189]^T, \quad \vec{\phi}_{7,2} = 10^{-2} [-0.12889 \ 0.38393 \ -0.32463]^T, \\ \vec{\phi}_{7,3} &= 10^{-2} [0.11334 \ -0.33763 \ 0.28547]^T, \quad \vec{\phi}_{7,4} = 10^{-2} [-0.044763 \ 0.13334 \ -0.11274]^T; \\ \vec{\phi}_{8,1} &= 10^{-2} [0.18152 \ 0.34806 \ 0.33957]^T, \quad \vec{\phi}_{8,2} = 10^{-2} [0.063041 \ -0.12088 \ -0.11793]^T, \\ \vec{\phi}_{8,3} &= 10^{-2} [-0.15963 \ -0.30608 \ -0.29861]^T, \quad \vec{\phi}_{8,4} = 10^{-2} [0.11848 \ 0.22718 \ 0.22164]^T; \\ \vec{\phi}_{9,1} &= 10^{-2} [-0.41232 \ 0.025683 \ 0.19408]^T, \quad \vec{\phi}_{9,2} = 10^{-2} [-0.41232 \ 0.025683 \ 0.19408]^T, \\ \vec{\phi}_{9,3} &= 10^{-2} [0 \ 0 \ 0]^T, \quad \vec{\phi}_{9,4} = 10^{-2} [0.41232 \ -0.025683 \ -0.19408]^T; \\ \vec{\phi}_{10,1} &= 10^{-2} [-0.11848 \ -0.22718 \ -0.22164]^T, \quad \vec{\phi}_{10,2} = 10^{-2} [0.18152 \ 0.34806 \ 0.33957]^T, \\ \vec{\phi}_{10,3} &= 10^{-2} [-0.15963 \ -0.30608 \ -0.29861]^T, \quad \vec{\phi}_{10,4} = 10^{-2} [0.063041 \ 0.12088 \ 0.11793]^T; \\ \vec{\phi}_{11,1} &= 10^{-2} [-0.46887 \ 0.029206 \ 0.2207]^T, \quad \vec{\phi}_{11,2} = 10^{-2} [0.16284 \ -0.010143 \ -0.076649]^T, \\ \vec{\phi}_{11,3} &= 10^{-2} [0.41232 \ -0.025683 \ -0.19408]^T, \quad \vec{\phi}_{11,4} = 10^{-2} [-0.30603 \ 0.019063 \ 0.14405]^T; \\ \vec{\phi}_{12,1} &= 10^{-2} [0.30603 \ -0.019063 \ -0.14405]^T, \quad \vec{\phi}_{12,2} = 10^{-2} [-0.46887 \ 0.029206 \ 0.2207]^T, \\ \vec{\phi}_{12,3} &= 10^{-2} [0.41232 \ -0.025683 \ -0.19408]^T, \quad \vec{\phi}_{12,4} = 10^{-2} [-0.16284 \ 0.010143 \ 0.076649]^T. \end{aligned}$$

5.6.3 Position of the modal centers of velocity

The coordinates of the modal centers of velocity C_V with corrected column stiffness are shown in Table 5.9 for the relevant first four modes subjected to effective damping.

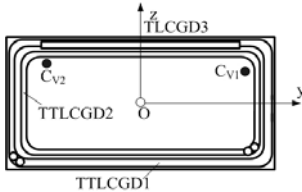
mode	1	2	3	4
floor 1	(3.05,1.03)	(-2.65,1.38)	(-0.34,-5.49)	(3.05,1.03)
floor 2	(3.05,1.03)	(-2.65,1.38)	(-0.34,-5.49)	(3.05,1.03)
floor 3	(3.05,1.03)	(-2.65,1.38)	(-0.34,-5.49)	(2.03,-0.77)
floor 4	(3.05,1.03)	(-2.65,1.38)	(-0.34,-5.49)	(3.05,1.03)

Table 5.9: The coordinates of the centers of velocity C_V for 4 modes.

(i) Installation of the absorbers

With the first four modal centers of velocity considered, two TTLCGDs to suppress the first and second mode, one plane TLCGD on the long side tuned to the third mode are positioned on the top floor. With respected to the fourth mode one TLCGD is installed along the short side on the second floor.

Fourth floor:



Second floor:

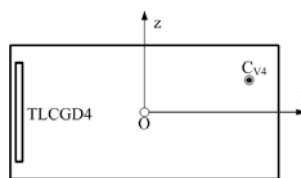


Fig. 5.35: Installation of absorbers, ● the centers of velocity of second floor, ● the centers of velocity of fourth floor.

Multi-storey Strongly Plan-asymmetric Space Frame with TTLCGDs and TLCGDs

	TTLCGD1	TTLCGD2	TLCGD3	TLCGD4
Horizontal length of the liquid column B [m]	24.00	24.00	2.50	3.00
Length of the upright liquid column H [m]	1.50	1.00	0.80	0.50
Cross-sectional area of the pipe [m ²] $A_H=A_B$	0.0520	0.0540	0.1700	0.0380
Effective length $L_{eff} = L_1 = 2H + B$ [m], Eq. (2.34a)	27.00	26.00	4.10	4.09
Angle of the inclined pipe section β [rad]	$\pi/2$	$\pi/2$	$\pi/4$	$\pi/4$
Equivalent mathematical pendulum length L_0 [m] Eq. (2.37)	0.20	0.12	0.05	0.02
Geometry factor $\kappa = \bar{\kappa}$ or $\kappa_{T0} = \bar{\kappa}_{T0}$, Eqs. (2.34a), (2.44),(3.14a),(3.44)	0.66	0.69	0.89	0.93
Equilibrium pressure head h_0 [m], $n=1.2$, Eq. (2.34a)	146.79	159.00	51.38	57.49
Gas volume $V_0 = A_H H_a$ [m ³], Eq. (2.38)	0.120000	0.080000	0.200000	0.030000
The mass ratio of the TLCGD-main system μ , Eqs. (2.97), (3.60)	5.85%	5.71%	2.94%	0.95%
The mass ratio of the equivalent TMD-main system μ^* , Eqs. (2.102), (3.66)	2.17%	2.43%	2.24%	0.80%
Natural frequency $f_{A,opt}$ [Hz] Eq. (2.104), (2.112)	1.06	1.39	2.23	3.15
Optimal linear damping %, Eq. (2.113)	8.92	9.42	9.06	5.45

Table 5.10: Layout of the modally tuned absorbers, gas volume and gas equilibrium pressure assigned, note the rather high gas pressure in TTLCGD.

5.6.4 TTLCGD and TLCGD design, Den Hartog’ optimization

The fluid mass is chosen $m_{f1}=1400kg$, $m_{f2}=1400kg$, $m_{f3}=700kg$ and $m_{f4}=150kg$ of water. Dimensions of four absorbers tuned first by means of the TMD analogy applying Den Hartog’s formulas, Eqs. (3.66)- (3.68) for TTLCGDs ($\beta = \pi/2$) and Eqs. (2.102)- (2.104) for TLCGDs ($\beta = \pi/4$) are summarized in Table 5.10.

Forcing direction	structure							TTLCGD1
	v_2 [mm]	w_2 [mm]	$u_{T2} = r_{S2}\theta_2$ [mm]	v_4 [mm]	w_4 [mm]	$u_{T4} = r_{S4}\theta_4$ [mm]	u_0 [mm]	
$\alpha = 0$	C_{Mi}	12	-37	31	19	-57	48	248
$\alpha = \pi/6$	C_{Mi}	8	-23	20	12	-35	30	154
$\alpha = \pi/4$	C_{Mi}	17	-52	44	27	-80	67	345
$\alpha = \pi/3$	C_{Mi}	26	-77	65	40	-118	100	514
$\alpha = \pi/2$	C_{Mi}	37	-111	94	57	-170	143	736
$\alpha = 2\pi/3$	C_{Mi}	38	-114	97	59	-175	148	761
$\alpha = 3\pi/4$	C_{Mi}	35	-104	88	54	-160	135	696
$\alpha = 5\pi/6$	C_{Mi}	29	-88	74	45	-134	113	583

Table 5.11a: Maximum displacements of four-storey structure in the first mode from time-harmonic excitation in α -directions, $a_0=0.1g$, $r_{Si} = 2.58m$.

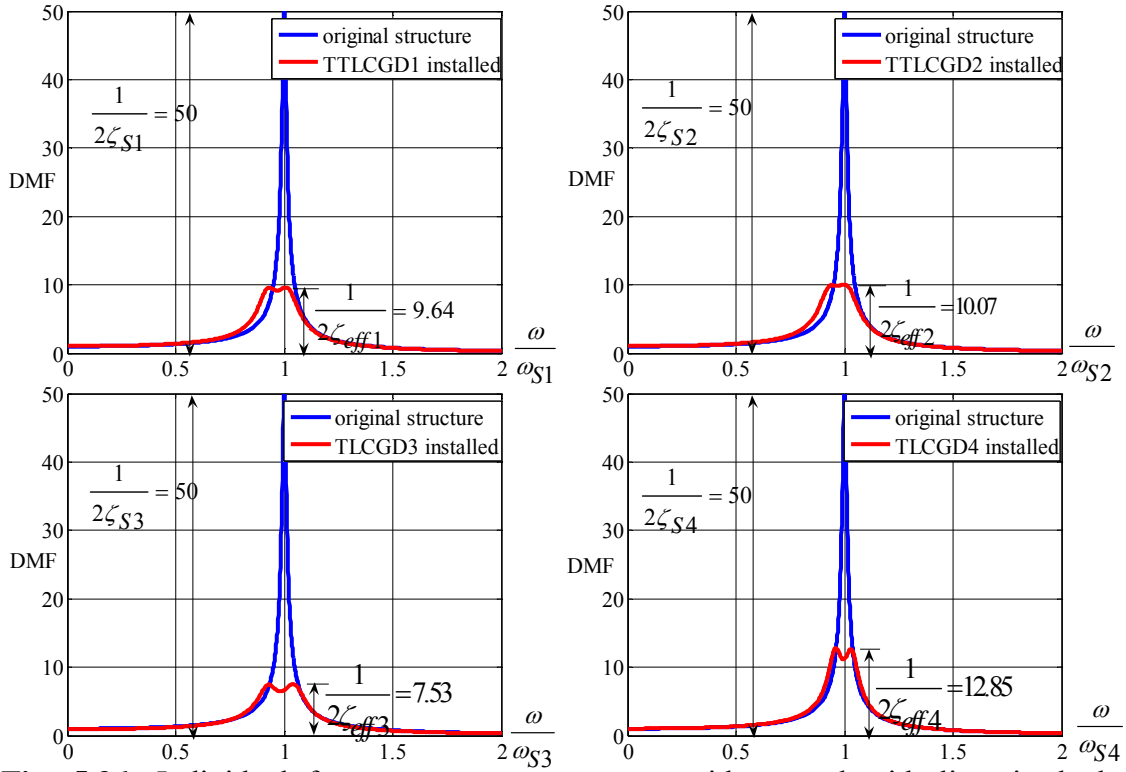


Fig. 5.36: Individual frequency response curves without and with linearized absorbers attached, with Den Hartog's optimal parameters.

The dynamic magnification factor (DMF) calculated with Matlab 7.0¹, linearized damping of the absorbers considered, is illustrated in Figure 5. 36. The effective modal damping coefficients of the system are increased from 1% to $\zeta_{eff1} = 5.19\%$, $\zeta_{eff2} = 4.97\%$, $\zeta_{eff3} = 6.64\%$ and $\zeta_{eff4} = 3.9\%$, illustrated in Fig. 5.36. From Table 5.11a-d it follows that all maximum fluid displacements occurring for various angles of attack, are within the acceptable limits, $u_0 < H_a/3$ (of linearized gas compression) and $u_0 < H/2$. The maximum fluid velocities of four absorbers are calculated by Eq. (2.35) 5.07, 3.61, 3.62 and 2.30m/s and are within the acceptable speed limit.

Forcing direction	Structure							TTLCGD2
	v_2 [mm]	w_2 [mm]	$u_{T2} = r_{S2}\theta_2$ [mm]	v_4 [mm]	w_4 [mm]	$u_{T4} = r_{S4}\theta_4$ [mm]	u_0 [mm]	
$\alpha = 0$	C_{Mi}	13	25	25	20	39	38	191
$\alpha = \pi/6$	C_{Mi}	24	46	45	37	71	69	349
$\alpha = \pi/4$	C_{Mi}	27	52	51	42	80	78	394
$\alpha = \pi/3$	C_{Mi}	29	55	54	44	84	82	413
$\alpha = \pi/2$	C_{Mi}	25	49	48	39	75	73	366
$\alpha = 2\pi/3$	C_{Mi}	15	29	29	24	45	44	222
$\alpha = 3\pi/4$	C_{Mi}	9	16	16	13	25	25	124
$\alpha = 5\pi/6$	C_{Mi}	1	2	2	2	4	4	18

Table 5.11b: Maximum displacements of four-storey structure in the second mode from time-harmonic excitation in α -directions, $a_0=0.1g$, $r_{Si} = 2.58m$.

Forcing direction	Structure						TLCGD3	
	v_2 [mm]	w_2 [mm]	$u_{T2} = r_{S2}\theta_2$ [mm]	v_4 [mm]	w_4 [mm]	$u_{T4} = r_{S4}\theta_4$ [mm]	u_0 [mm]	
$\alpha = 0$	28	-2	-13	C_{M4}	42	-3	-20	258
				A	58	-3		
$\alpha = \pi/6$	23	-1	-11	C_{M4}	36	-2	-17	216
				A	48	-2		
$\alpha = \pi/4$	18	-1	-9	C_{M4}	28	-2	-13	172
				A	39	-2		
$\alpha = \pi/3$	12	-1	-6	C_{M4}	19	-1	-9	116
				A	26	-1		
$\alpha = \pi/2$	2	0	-1	C_{M4}	3	0	-1	150
				A	3	0		
$\alpha = 2\pi/3$	15	-1	-7	C_{M4}	23	-1	-11	142
				A	32	-1		
$\alpha = 3\pi/4$	21	-1	-10	C_{M4}	32	-2	-15	193
				A	43	-2		
$\alpha = 5\pi/6$	25	-2	-12	C_{M4}	38	-2	-18	231
				A	52	-2		

Table 5.11c: Maximum displacements of four-storey structure in the third mode from time-harmonic excitation in α -directions, $a_0=0.1g$, $r_{Si} = 2.58m$.

Forcing direction	Structure						TLCGD4	
	v_2 [mm]	w_2 [mm]	$u_{T2} = r_{S2}\theta_2$ [mm]	v_4 [mm]	w_4 [mm]	$u_{T4} = r_{S4}\theta_4$ [mm]	u_0 [mm]	
$\alpha = 0$	C_{M2}	-1	2	-2	1	-2	2	34
	A	-1	4					
$\alpha = \pi/6$	C_{M2}	-1	1.49	-1	1	-1	1	29
	A	-1	3.45					
$\alpha = \pi/4$	C_{M2}	-1	3.10	-3	1	-3	3	58
	A	-1	7.15					
$\alpha = \pi/3$	C_{M2}	-2	4.49	-4	2	-4	4	83
	A	-2	10.38					
$\alpha = \pi/2$	C_{M2}	-2	6.30	-5	2	-6	5	114
	A	-2	14.55					
$\alpha = 2\pi/3$	C_{M2}	-2	6.42	-5	2	-6	5	116
	A	-2	14.83					
$\alpha = 3\pi/4$	C_{M2}	-2	5.82	-5	2	-6	5	104
	A	-2	13.44					
$\alpha = 5\pi/6$	C_{M2}	-2	4.82	-4	2	-5	4	86
	A	-2	11.14					

Table 5.11d: Maximum displacements of four-storey structure in the fourth mode from time-harmonic excitation in α -directions, $a_0=0.1g$, $r_{Si} = 2.58m$.

5.6.5 Optimization of the TTLCGD-, TLCGD-mainstructure system in the state space domain

The fine tuned optimal natural frequencies and damping ratios by calling the function *fminsearch* of the performance index J , Eq. (2.123), of the Matlab Optimization Toolbox are found to be $f_{A1}=1.05Hz$, $f_{A2}=1.34Hz$, $f_{A3}=2.16Hz$, $f_{A3}=3.09Hz$, $\zeta_{A1}=7.35\%$, $\zeta_{A2}=8.65\%$, $\zeta_{A3}=8.39\%$, $\zeta_{A3}=5.41\%$. Fine tuning requires the equilibrium gas pressure adjusted to 132.80, 136.80, 45.77 and 54.85m. Figs. 5.37-5.44 illustrate the weighed sum of the

frequency response functions $\sum_{i=1}^{24} s_i |z_{Si}(v)|$, $\mathfrak{S} = \text{diag}(10,10,10,10,10,10,10,10,10,10,10,10,1,1,$

1,1,1,1,1,1,1,1,1,1) of the building states for the original and the optimized system under various angles of attack, in the logarithmic decibel scale in the relevant frequency window $0 \leq f \leq 3.5 \text{ Hz}$. The resonance curves with fine-tuning optimal parameters have broader peaks.

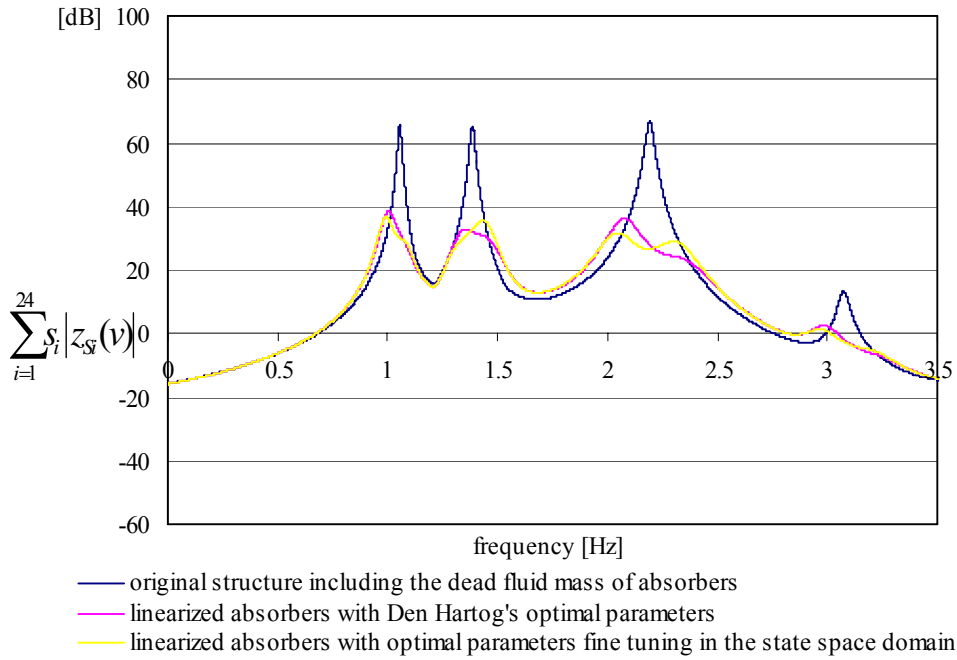


Fig. 5.37: Weighed sum of amplitude response functions for the 12 DOF linearized, four-storey, strongly asymmetric space frame with four linearized absorbers attached and without the absorbers (angle of attack of the time-harmonic base acceleration $\alpha = 0$), maximum gain 30.17dB.

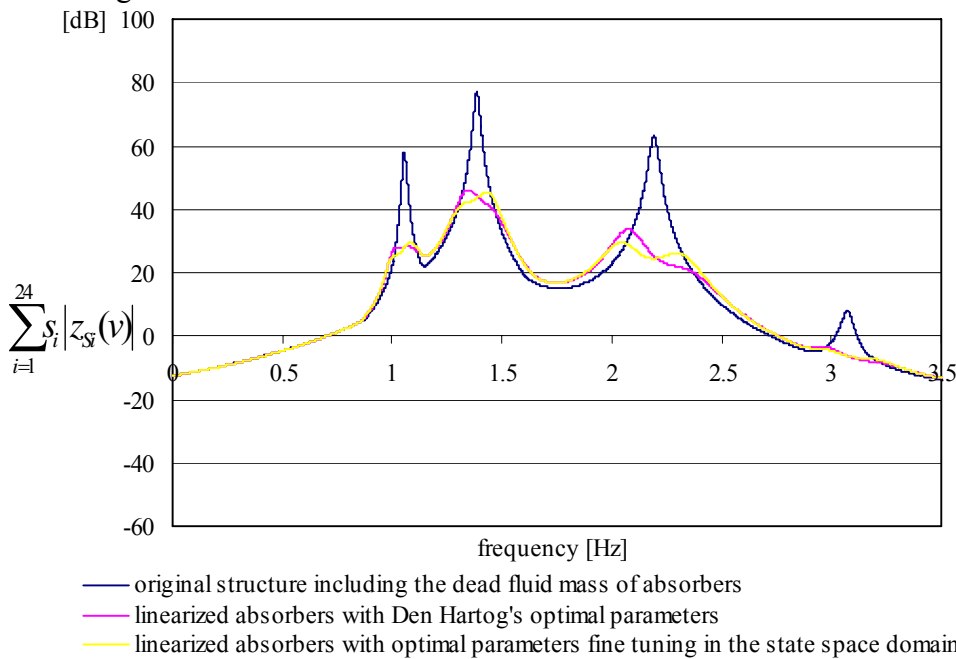


Fig. 5.38: Weighed sum of amplitude response functions for the 12 DOF linearized, four-storey, strongly asymmetric space frame with four linearized absorbers attached and without the absorbers (angle of attack of the time-harmonic base acceleration $\alpha = \pi/6$), maximum gain 31.50dB.

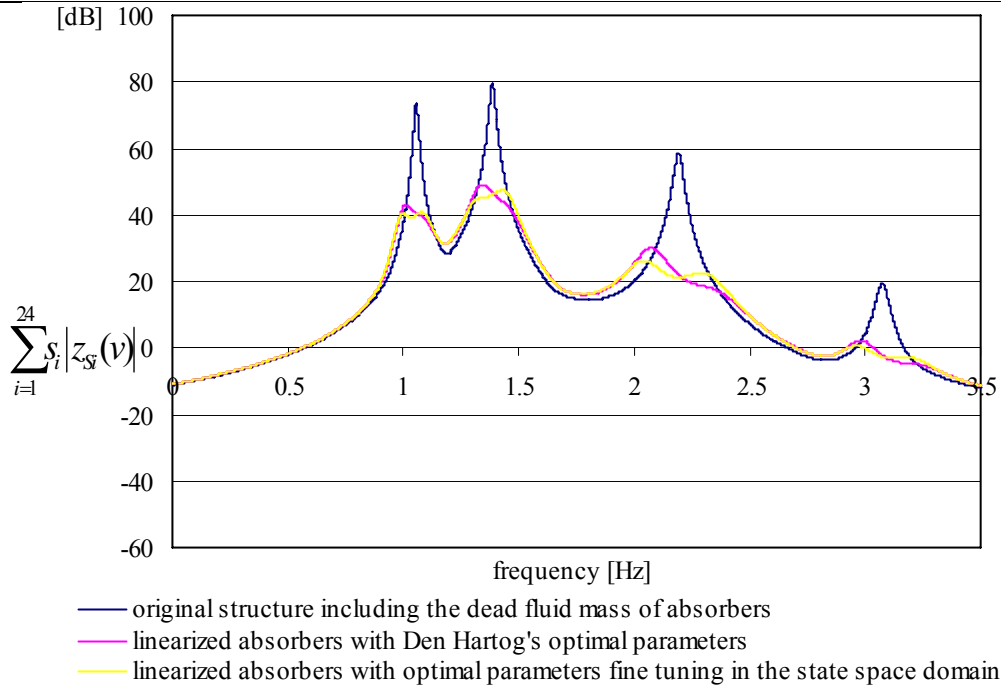


Fig. 5.39: Weighed sum of amplitude response functions for the 12 DOF linearized, four-storey, strongly asymmetric space frame with four linearized absorbers attached and without the absorbers (angle of attack of the time-harmonic base acceleration $\alpha = \pi/4$), maximum gain 31.83dB.

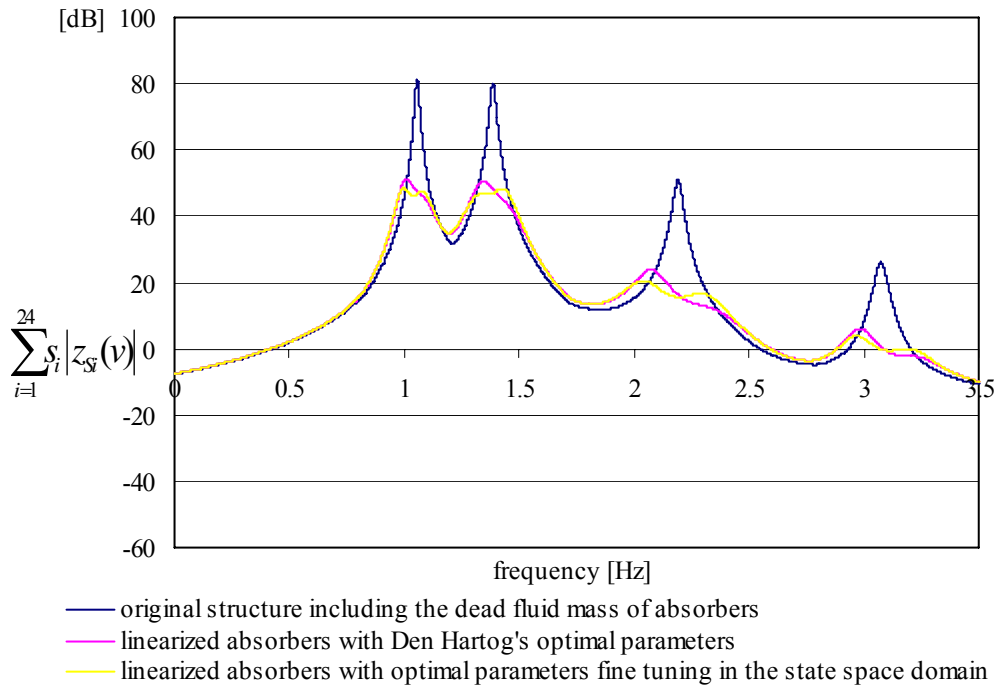


Fig. 5.40: Weighed sum of amplitude response functions for the 12 DOF linearized, four-storey, strongly asymmetric space frame with four linearized absorbers attached and without the absorbers (angle of attack of the time-harmonic base acceleration $\alpha = \pi/3$), maximum gain 32.65dB.

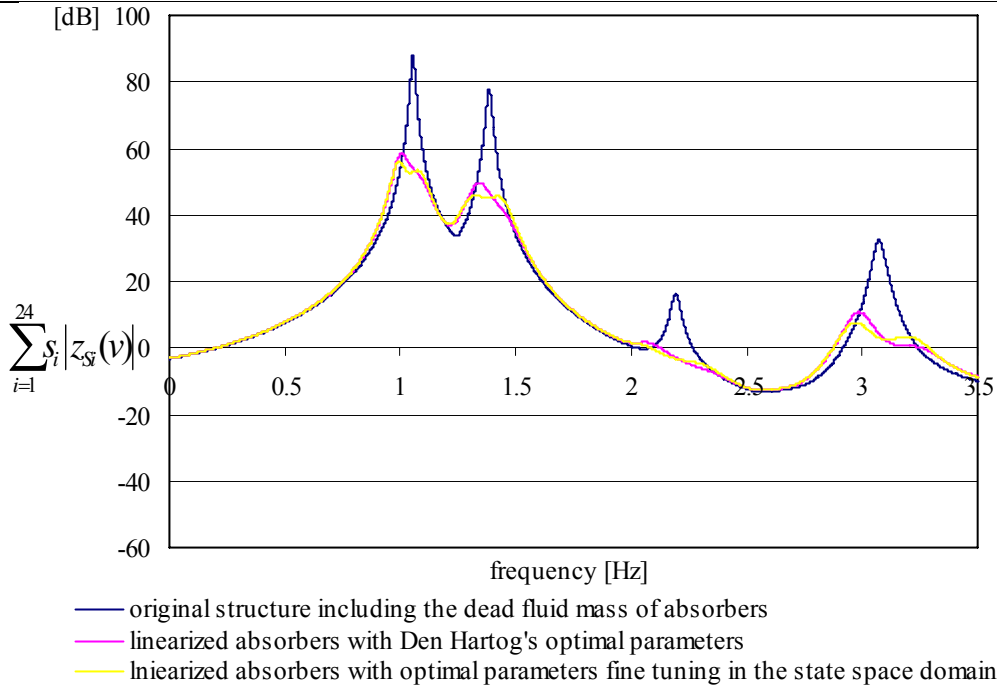


Fig. 5.41: Weighed sum of amplitude response functions for the 12 DOF linearized four-storey, strongly asymmetric space frame with four linearized absorbers attached and without the absorbers (angle of attack of the time-harmonic base acceleration $\alpha = \pi/2$), maximum gain 32.11dB.

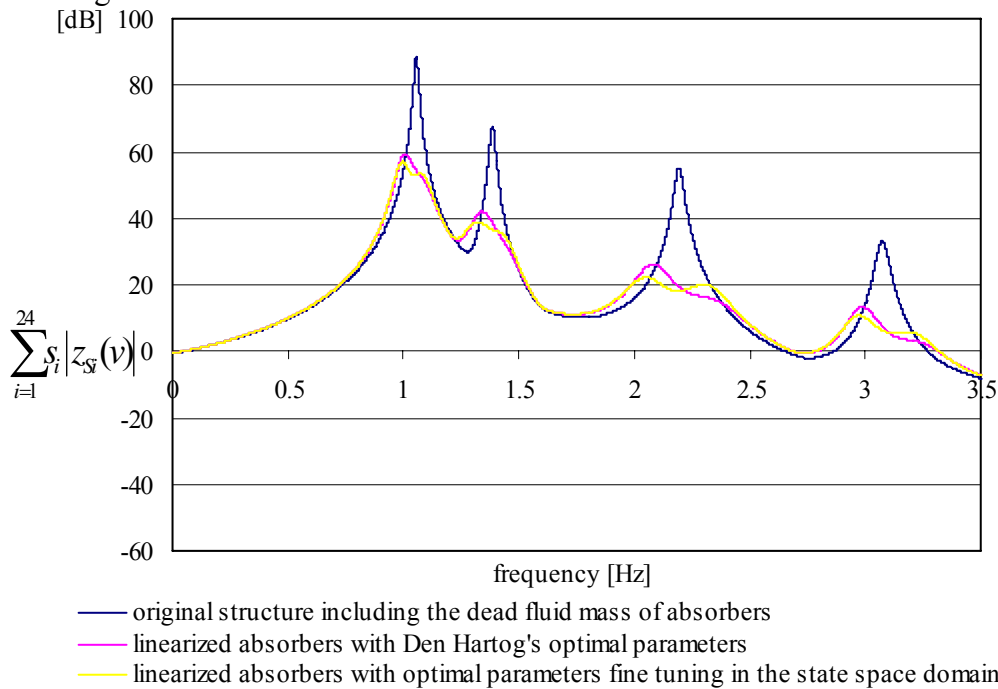


Fig. 5.42: Weighed sum of amplitude response functions for the 12 DOF linearized, four-storey, strongly asymmetric space frame with four linearized absorbers attached and without the absorbers (angle of attack of the time-harmonic base acceleration $\alpha = 2\pi/3$), maximum gain 31.68dB.

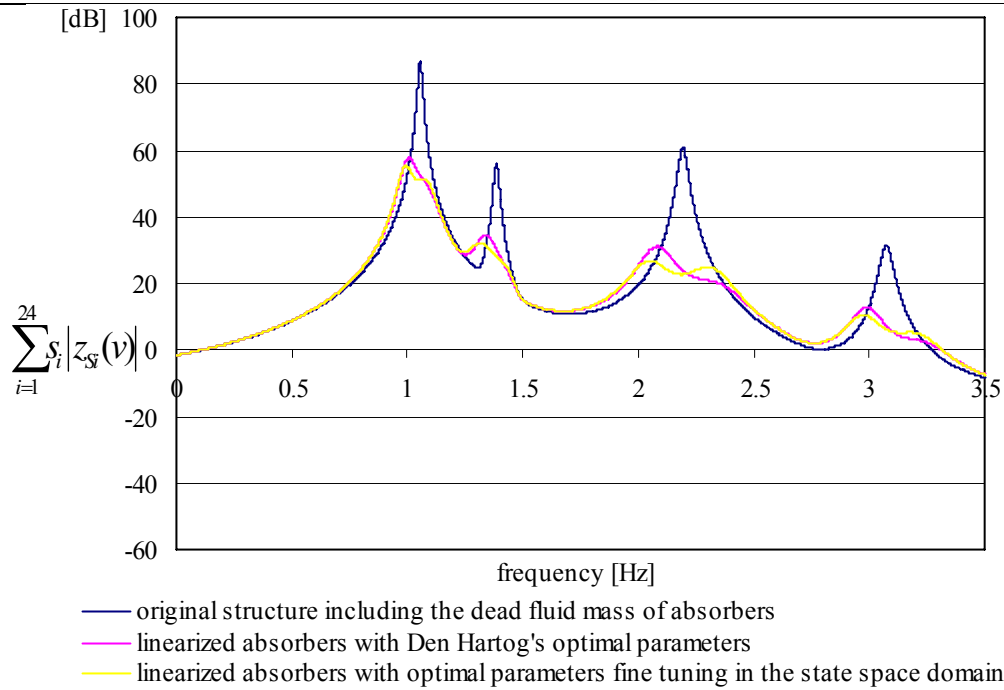


Fig. 5.43: Weighed sum of amplitude response functions for the 12 DOF linearized, four-storey, strongly asymmetric space frame with four linearized absorbers attached and without the absorbers (angle of attack of the time-harmonic base acceleration $\alpha = 3\pi/4$), maximum gain 31.43dB.

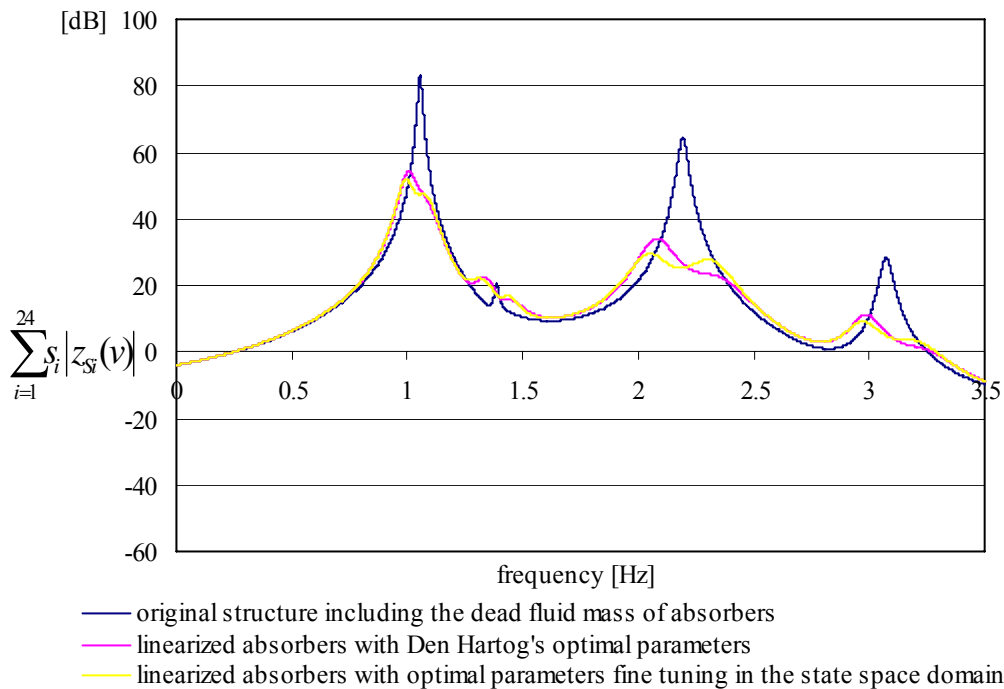


Fig. 5.44: Weighed sum of amplitude response functions for the 12 DOF linearized, four-storey, strongly asymmetric space frame with four linearized absorbers attached and without the absorbers (angle of attack of the time-harmonic base acceleration $\alpha = 5\pi/6$), maximum gain 31.08dB.

The maximum fluid displacement amplitudes of three absorbers in Figs.5.45-5.52 are well within the acceptable limits. The maximum fluid velocities of four absorbers are calculated by Eq. (2.35) 5.15, 3.45, 4.07 and 1.94m/s and are also within the acceptable speed limit.

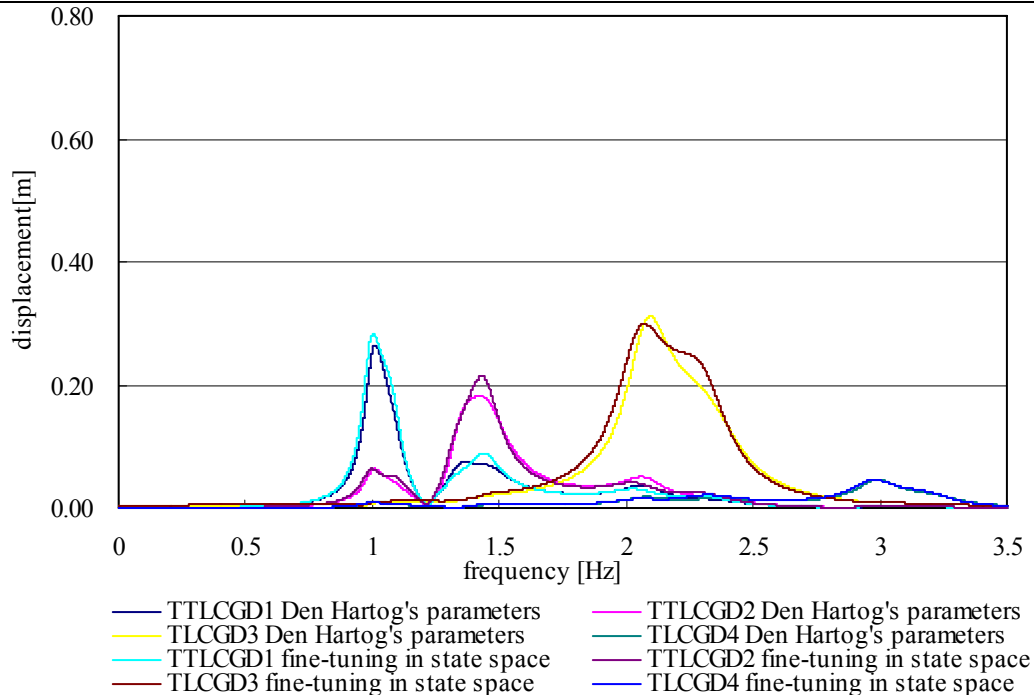


Fig. 5.45: Amplitude response curves of fluid displacement $|u|$ of four linearized absorbers attached to the four-storey strongly asymmetric space frame. Absorbers either with Den Hartog's optimal parameters or those resulting from fine-tuning in state space ($\alpha = 0$).

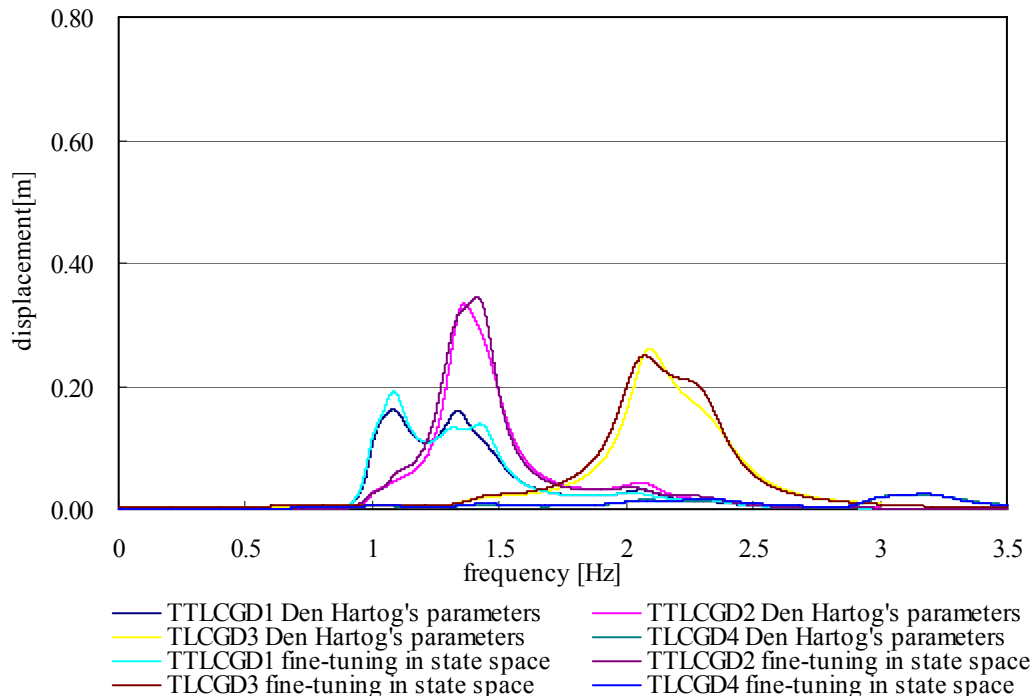


Fig. 5.46: Amplitude response curves of fluid displacement $|u|$ of four linearized absorbers attached to the four-storey strongly asymmetric space frame. Absorbers either with Den Hartog's optimal parameters or those resulting from fine-tuning in state space ($\alpha = \pi/6$).

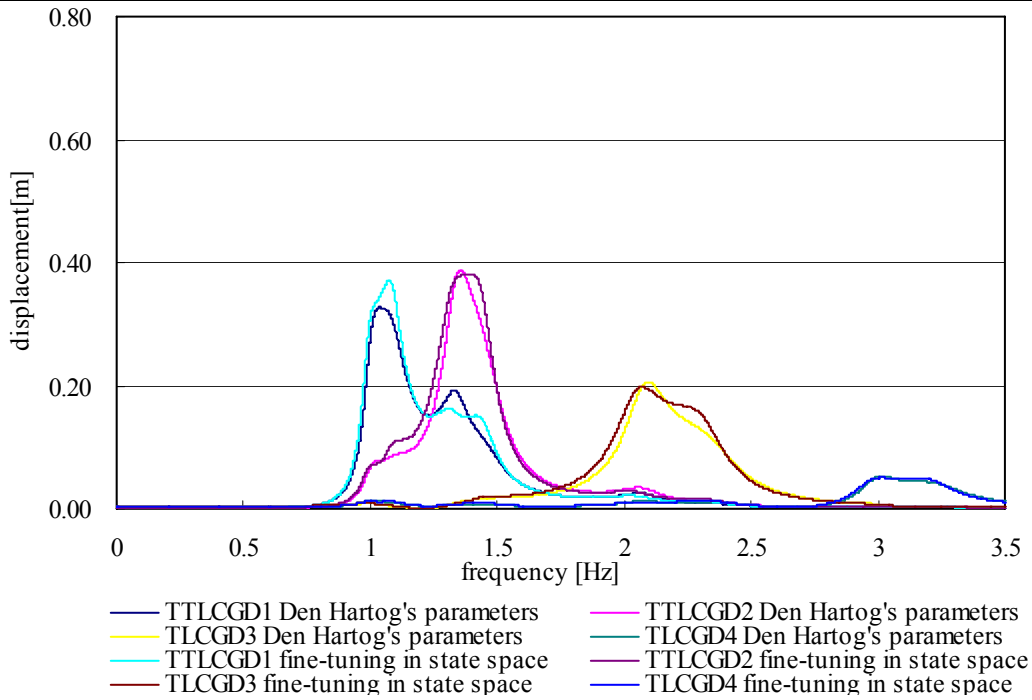


Fig. 5.47: Amplitude response curves of fluid displacement $|u|$ of four linearized absorbers attached to the four-storey strongly asymmetric space frame. Absorbers either with Den Hartog's optimal parameters or those resulting from fine-tuning in state space ($\alpha = \pi/4$).

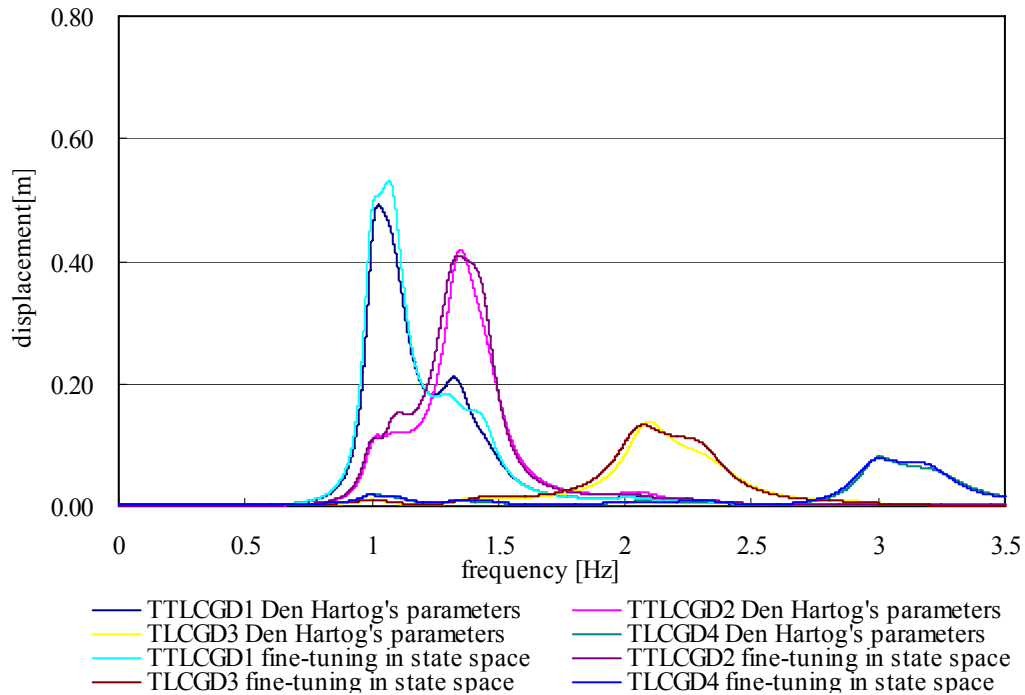


Fig. 5.48: Amplitude response curves of fluid displacement $|u|$ of four linearized absorbers attached to the four-storey strongly asymmetric space frame. Absorbers either with Den Hartog's optimal parameters or those resulting from fine-tuning in state space ($\alpha = \pi/3$).

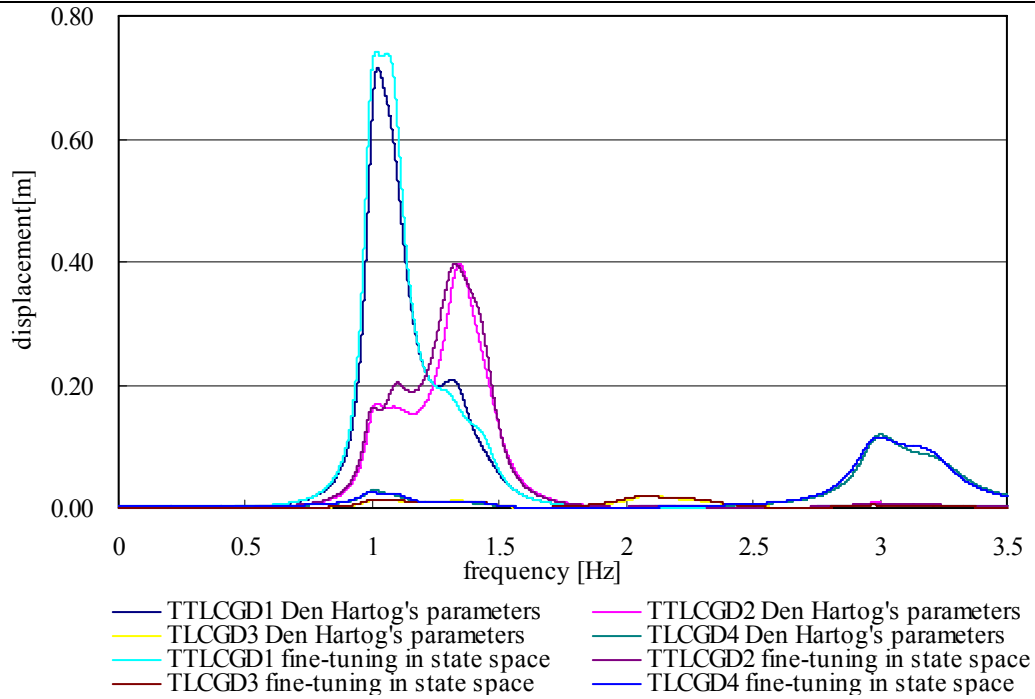


Fig. 5.49: Amplitude response curves of fluid displacement $|u|$ of four linearized absorbers attached to the four-storey strongly asymmetric space frame. Absorbers either with Den Hartog's optimal parameters or those resulting from fine-tuning in state space ($\alpha = \pi/2$).

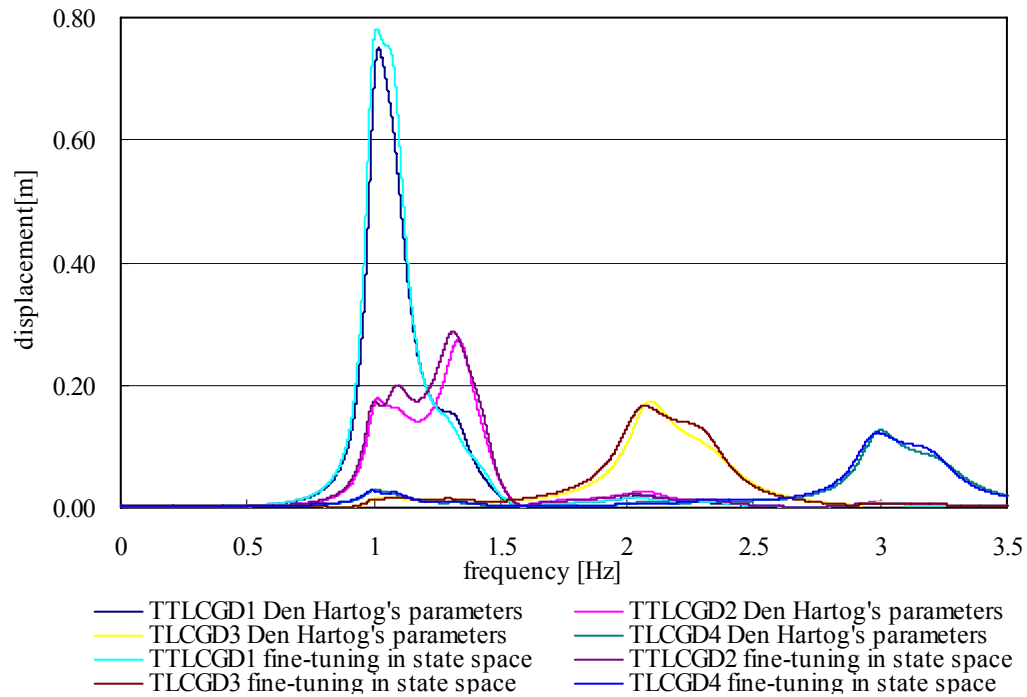


Fig. 5.50: Amplitude response curves of fluid displacement $|u|$ of four linearized absorbers attached to the four-storey strongly asymmetric space frame. Absorbers either with Den Hartog's optimal parameters or those resulting from fine-tuning in state space ($\alpha = 2\pi/3$).

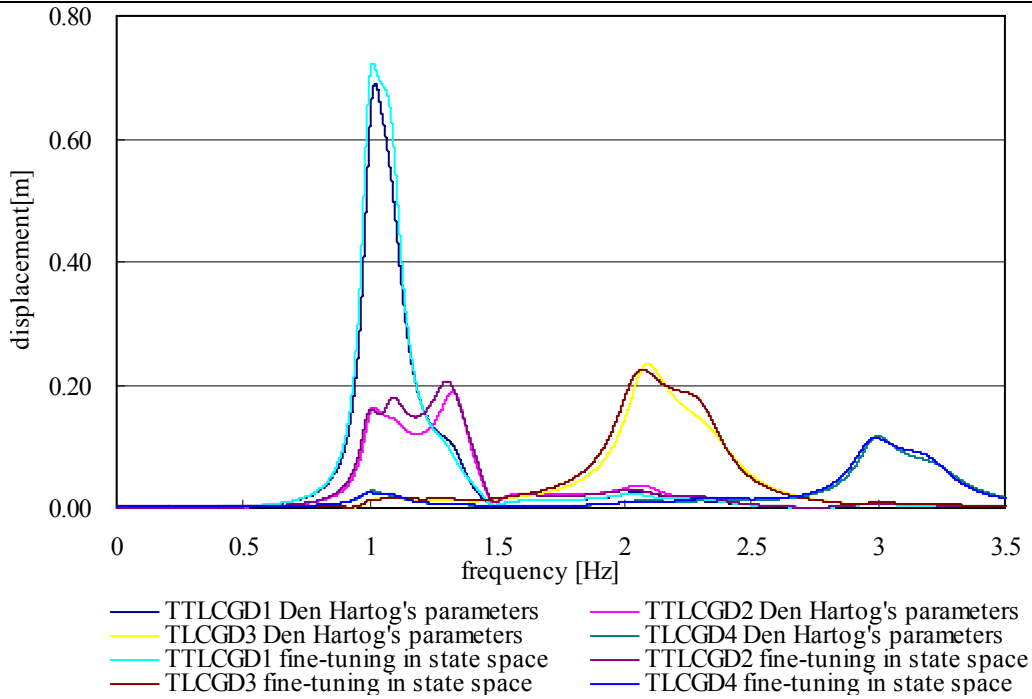


Fig. 5.51: Amplitude response curves of fluid displacement $|u|$ of four linearized absorbers attached to the four-storey strongly asymmetric space frame. Absorbers either with Den Hartog's optimal parameters or those resulting from fine-tuning in state space ($\alpha = 3\pi/4$).

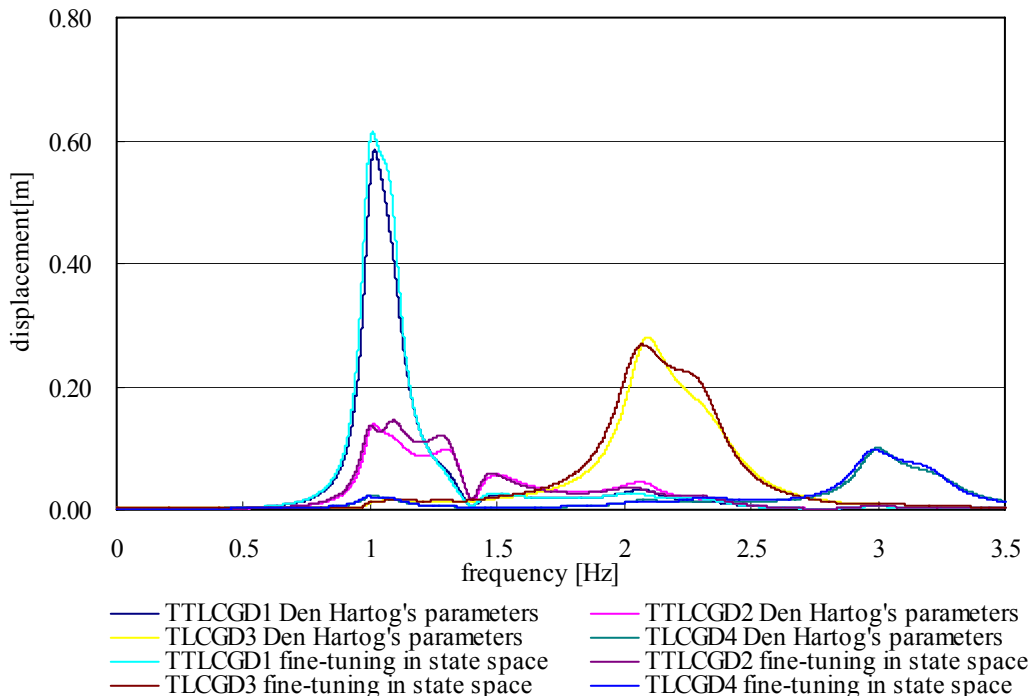


Fig. 5.52: Amplitude response curves of fluid displacement $|u|$ of four linearized absorbers attached to the four-storey strongly asymmetric space frame. Absorbers either with Den Hartog's optimal parameters or those resulting from fine-tuning in state space ($\alpha = 5\pi/6$).

The wall thickness and the dead mass of the piping system are listed in Table 5.12 for the four absorbers, designed according to Table 5.10. The gauge pressure under expansion conditions turns out to be positive as listed in Table 5.12. The final dimensions of circular steel pipes must be changed according to their commercial availability.

	TLCGD1	TLCGD2	TLCGD3	TLCGD4
h_0 [m]	146.79	159.00	51.38	57.49
H_a [m]	2.31	1.48	1.18	0.80
$10^{-5} p_{(D)}$ [N/m ²] Eq.(2.128)	66.97	72.58	22.81	25.62
pipe diameter $2r$ [mm]	257.3	262.2	465.2	220
t [mm] Eq.(2.124)	6.2	6.8	3.8	2.0
m_p [kg] Eq.(2.130)	1226.8	1265	278.83	60.51
dead fluid-mass[kg]	790.16	733.46	145.53	20.27
$10^{-5} \bar{p}_{(D)}$ [N/m ²] Eq.(2.129)	5.13	5.64	1.15	1.40

Table 5.12: Dimensioning of circular steel pipes.

5.6.6 Forcing by the NS-El Centro seismogram under varying angles of attack

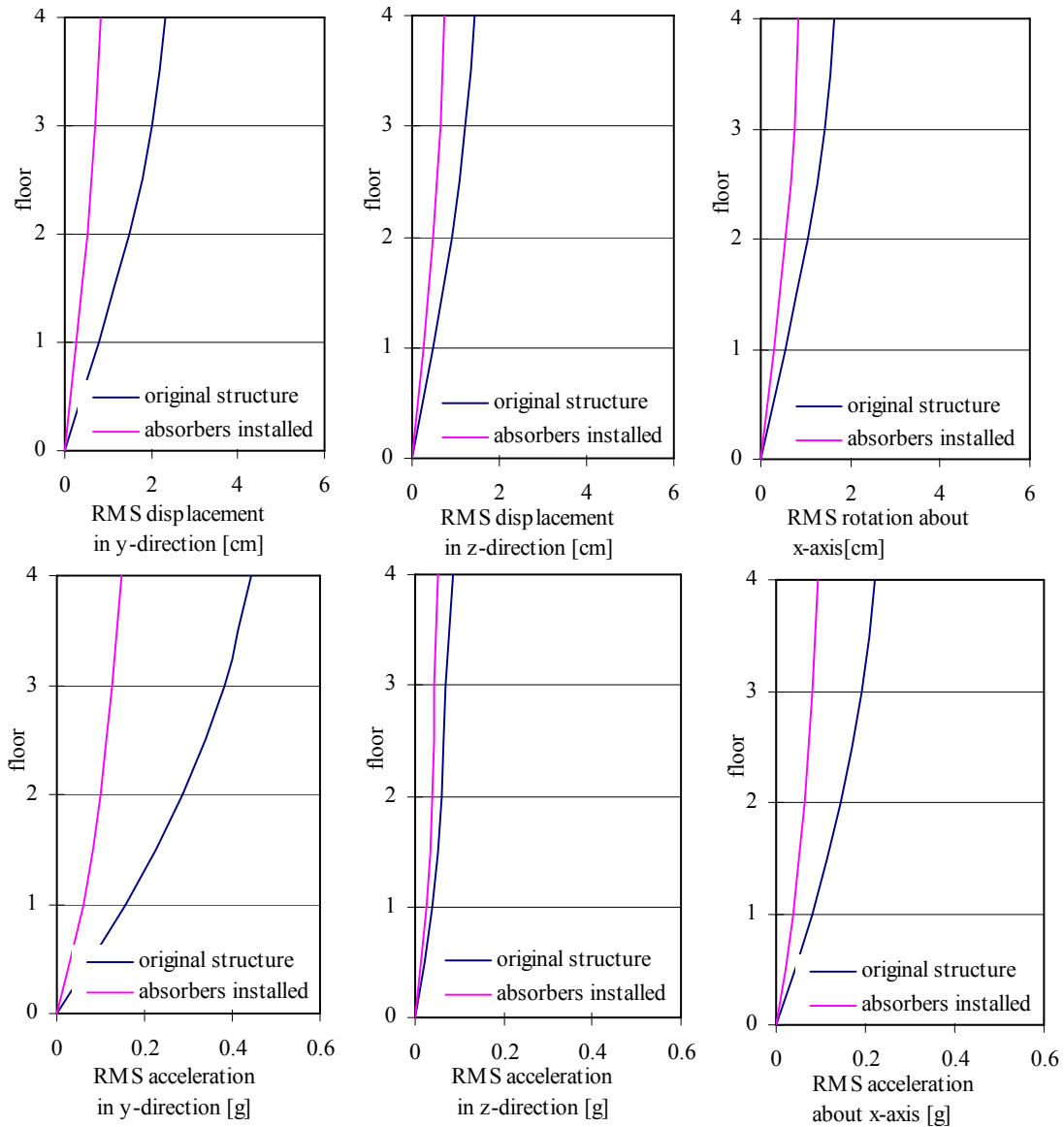


Fig. 5.53: RMS responses for floor displacement and acceleration of four-storey strongly asymmetric building (El Centro 0.35g, angle of attack $\alpha = 0$, $r_{Si} = 2.58m$).

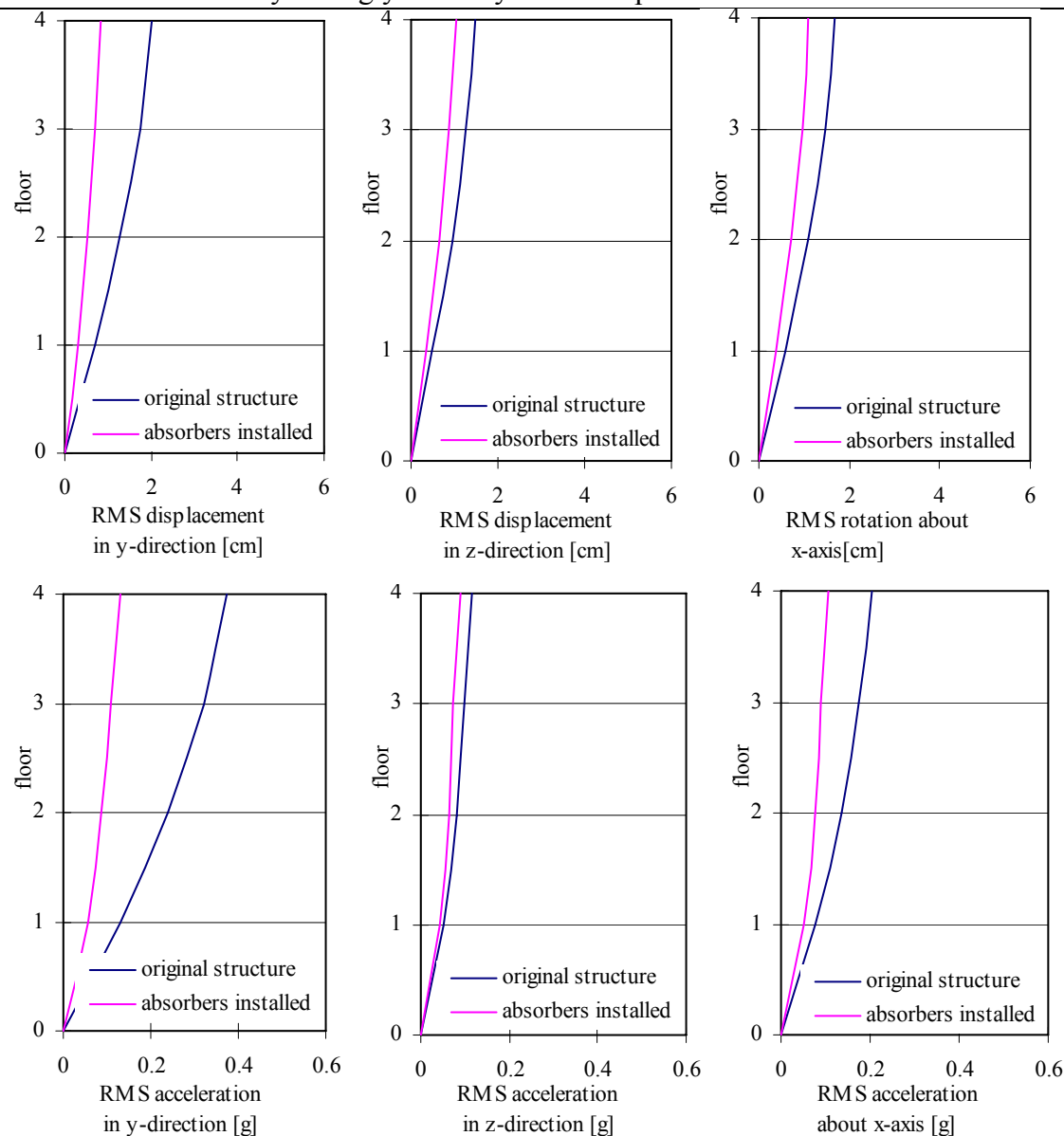
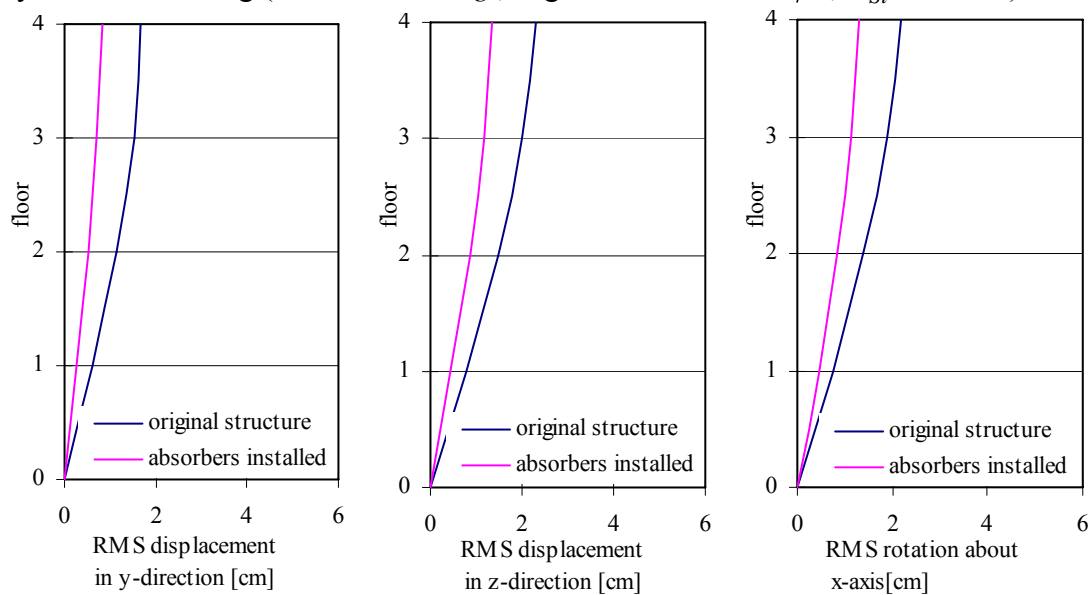


Fig. 5.54: RMS responses for floor displacement and acceleration of four-storey strongly asymmetric building (El Centro 0.35g, angle of attack $\alpha = \pi/6$, $r_{Si} = 2.58m$).



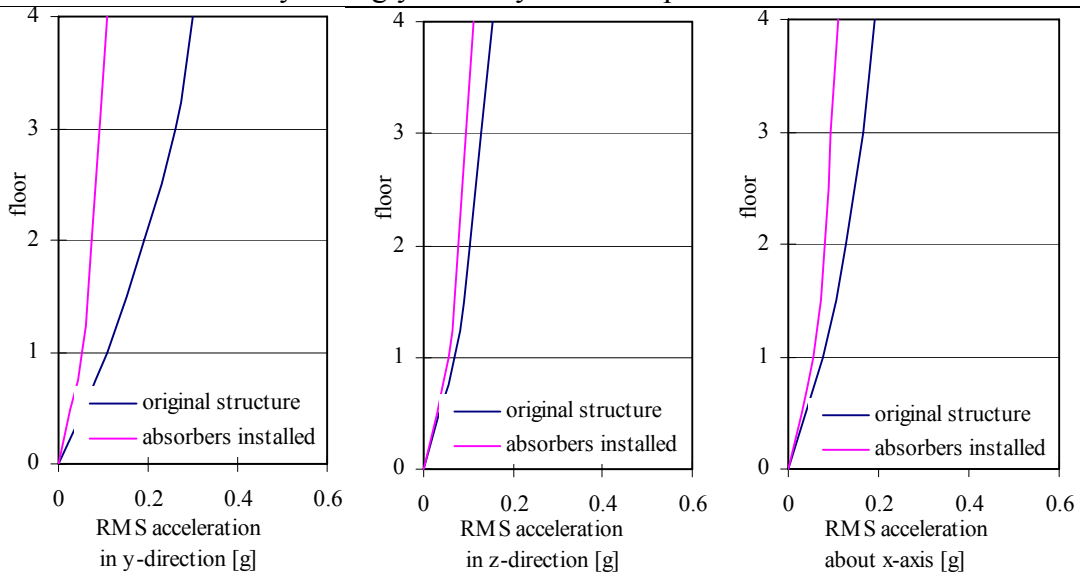


Fig. 5.55: RMS responses for floor displacement and acceleration of four-storey strongly asymmetric building (El Centro $0.35g$, angle of attack $\alpha = \pi/4$, $r_{Si} = 2.58m$).

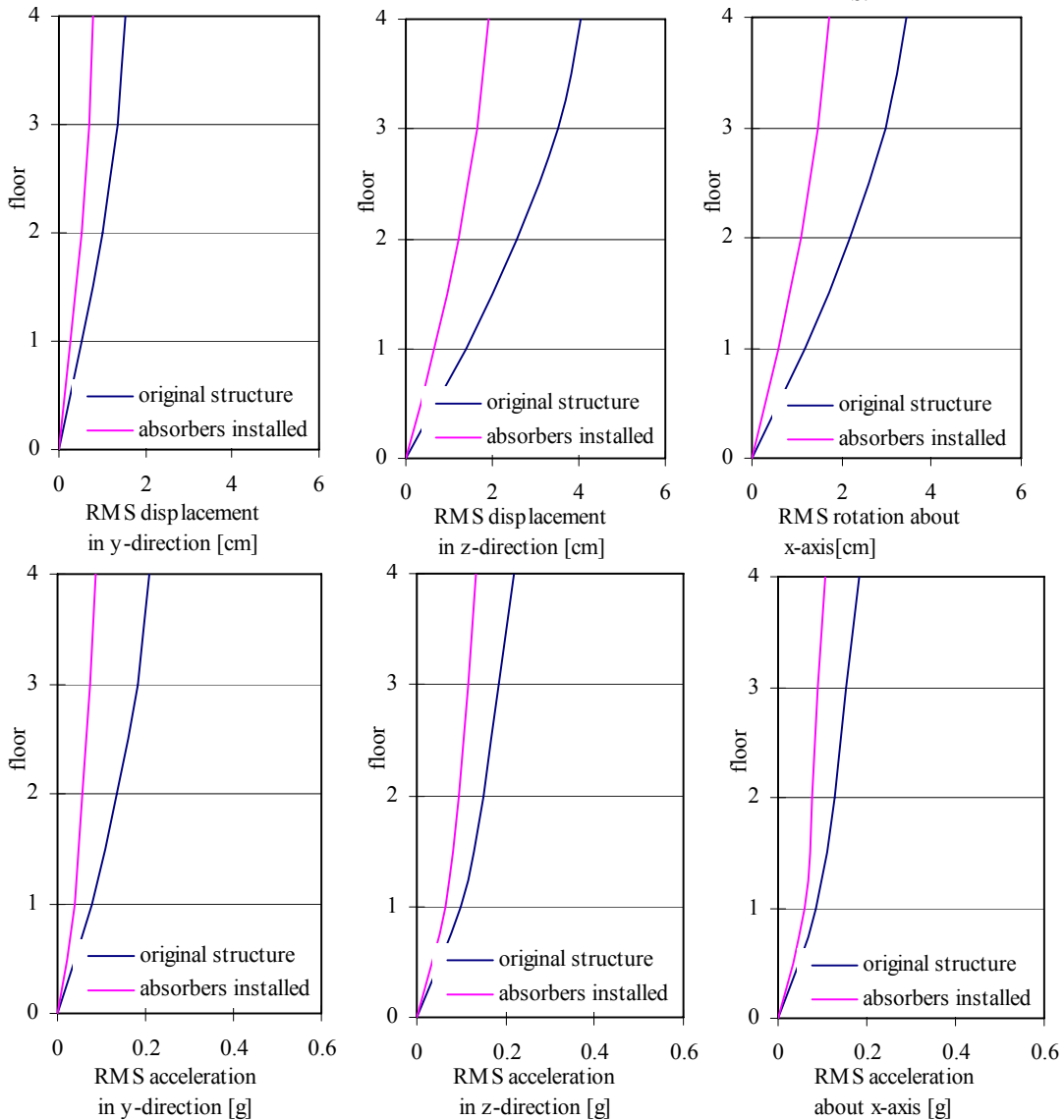


Fig. 5.56: RMS responses for floor displacement and acceleration of four-storey strongly asymmetric building (El Centro $0.35g$, angle of attack $\alpha = \pi/3$, $r_{Si} = 2.58m$).

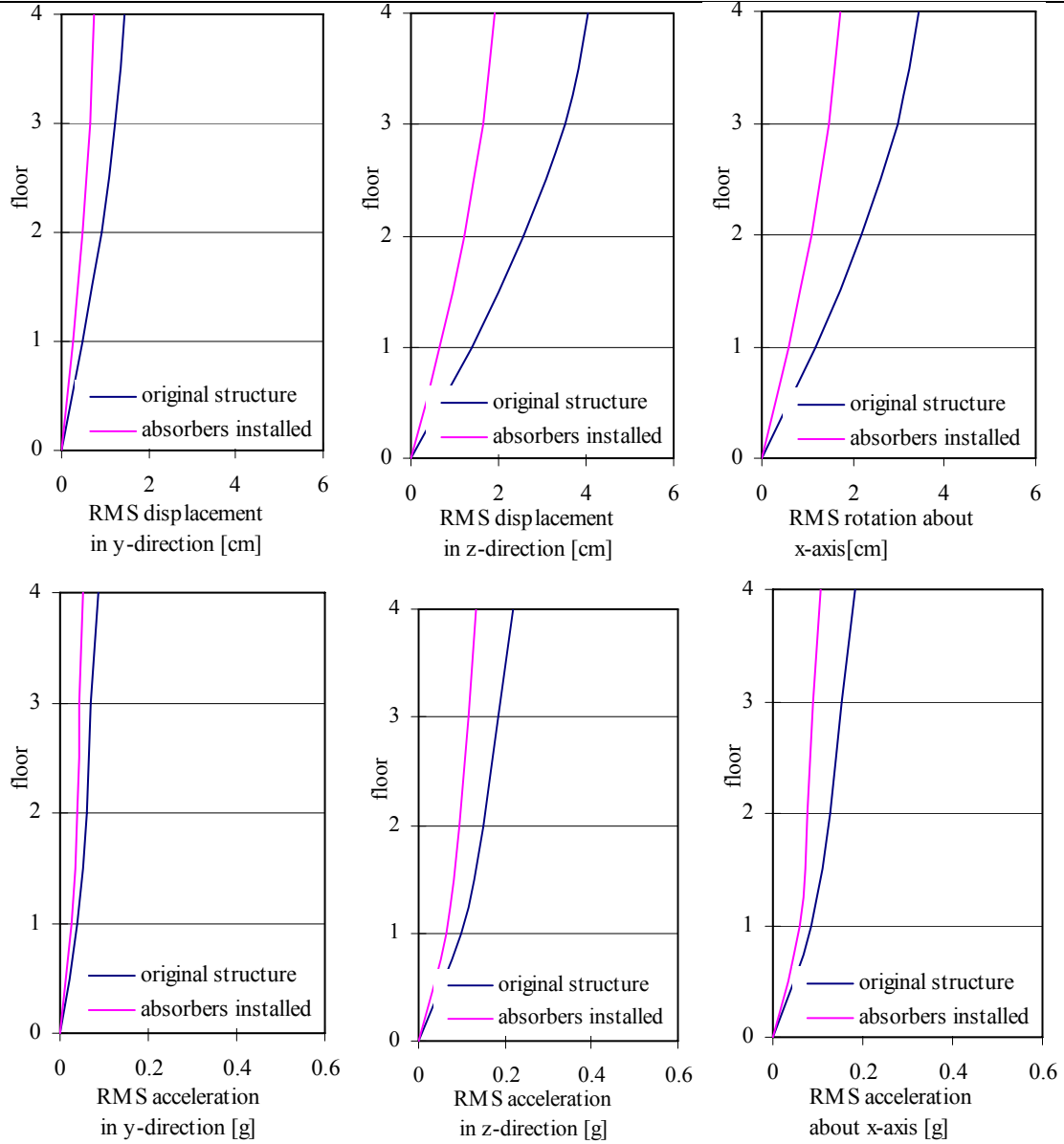
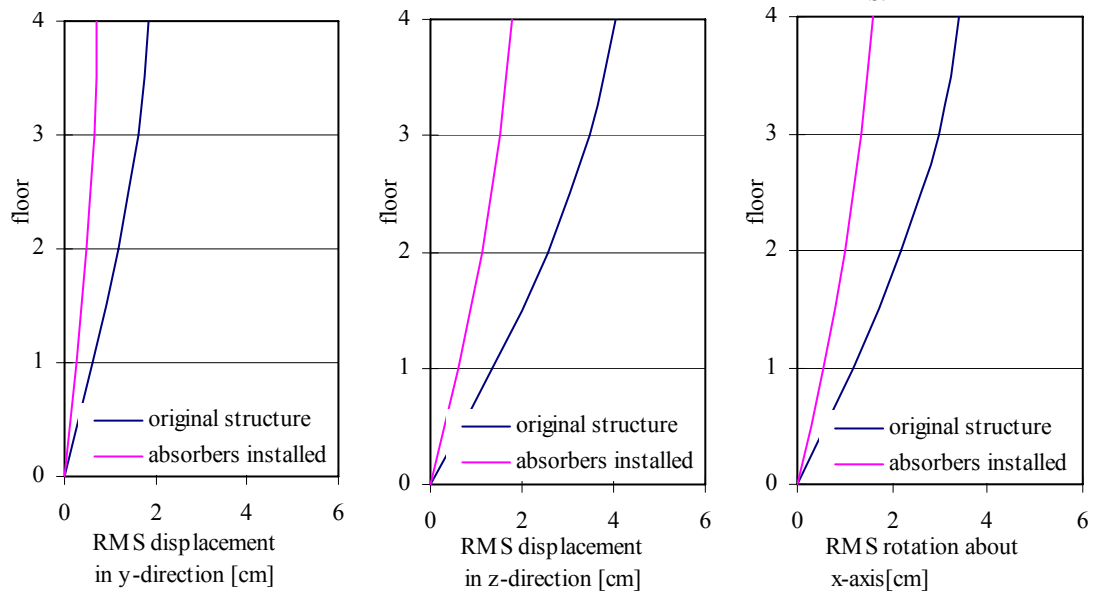


Fig. 5.57: RMS responses for floor displacement and acceleration of four-storey strongly asymmetric building (El Centro $0.35g$, angle of attack $\alpha = \pi/2$, $r_{Si} = 2.58m$).



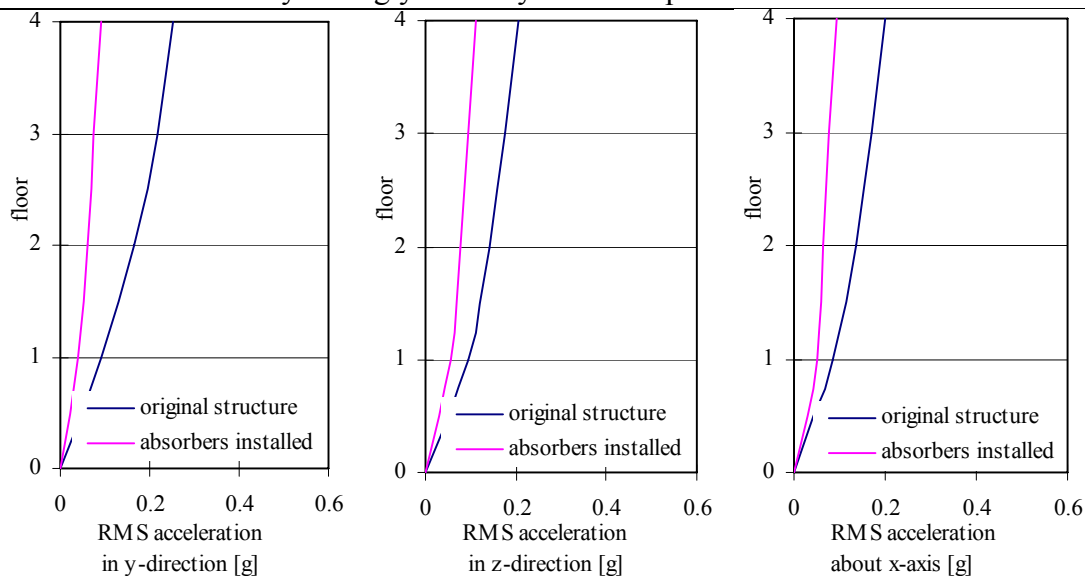


Fig. 5.58: RMS responses for floor displacement and acceleration of four-storey strongly asymmetric building (El Centro $0.35g$, angle of attack $\alpha = 2\pi/3$, $r_{Si} = 2.58m$).

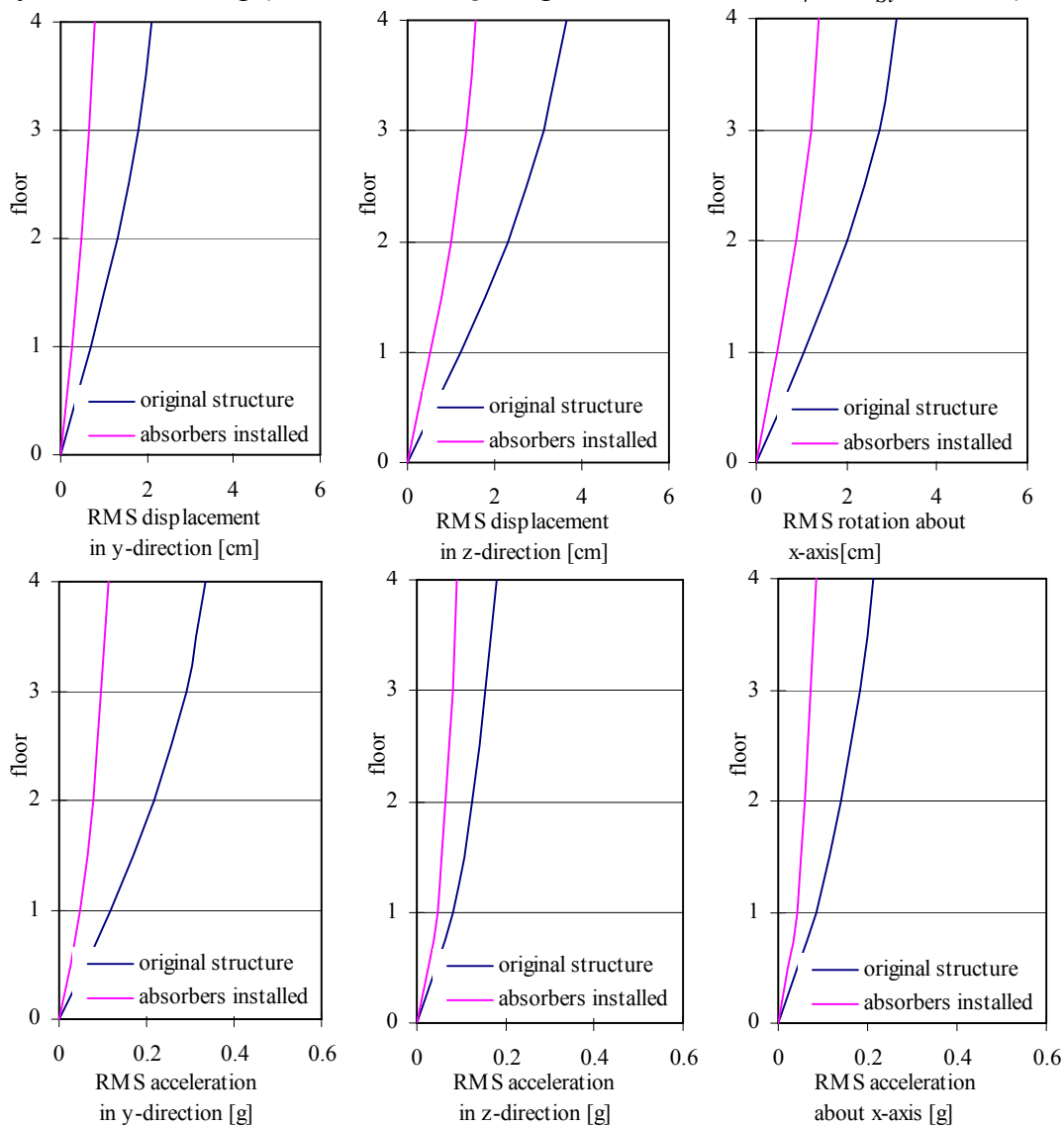


Fig. 5.59: RMS responses for floor displacement and acceleration of four-storey strongly asymmetric building (El Centro $0.35g$, angle of attack $\alpha = 3\pi/4$, $r_{Si} = 2.58m$).

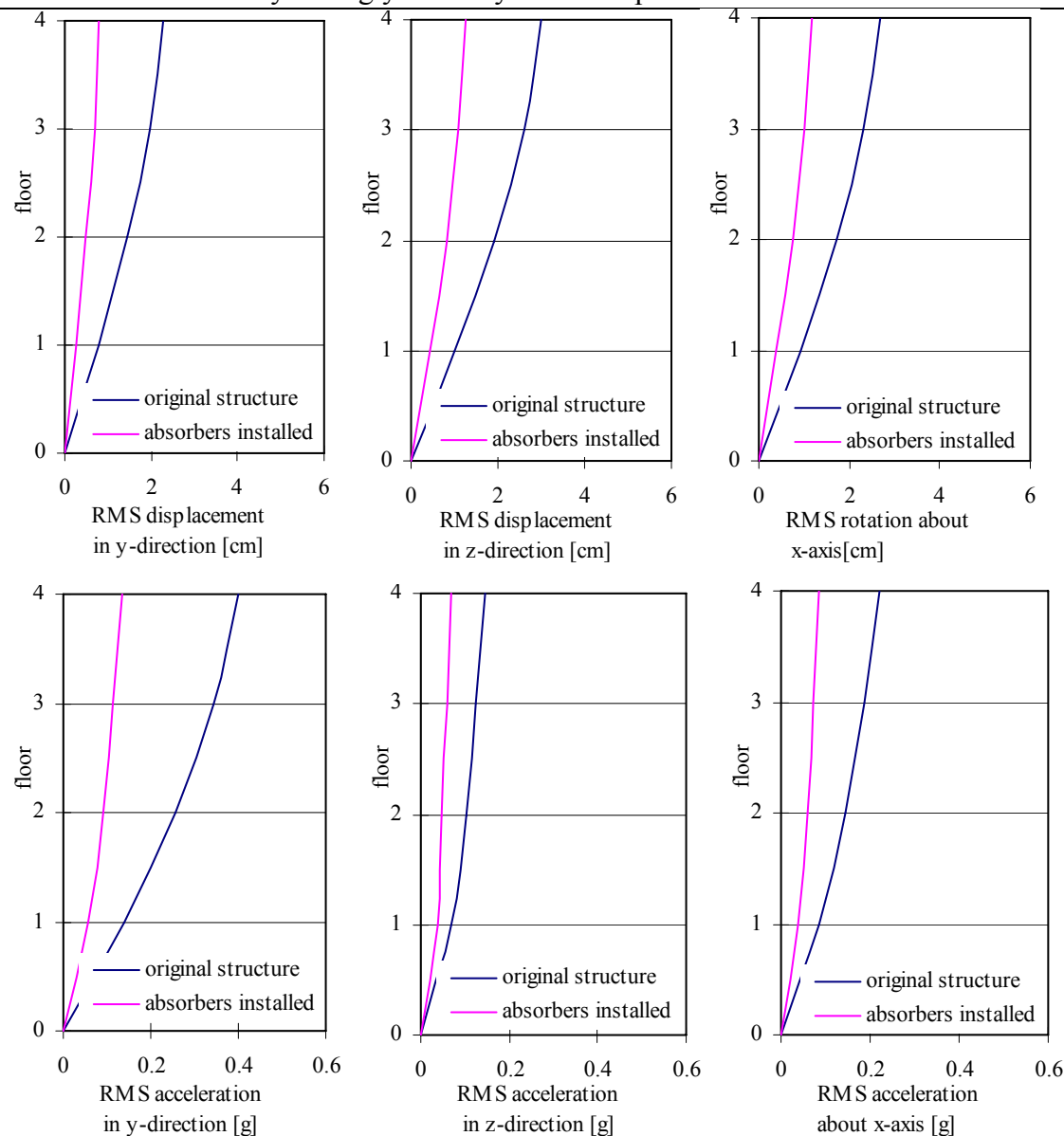


Fig. 5.60: RMS responses for floor displacement and acceleration of four-storey strongly asymmetric building (El Centro $0.35g$, angle of attack $\alpha = 5\pi/6$, $r_{Si} = 2.58m$).

This Section illustrates the vibration control effectiveness of TLCGDs for the four-storey strongly asymmetric building under bi-directional horizontal NS-El Centro earthquake. Figs. 5.53-5.82 show the displacements and accelerations for the root mean square (RMS) responses² of structure with and without absorbers for four floors. The RMS value is defined in Eq. (4.26).

References

- [1] MATLAB, User Guide, Control Toolbox. MathWorks Inc., Version 6.5.1, 2002.
- [2] Chopra A.k., Dynamics of Structures, Prentice-Hall, New Jersey, 1995.
- [3] Liang S.G., Experiment study of torsionally structure vibration control using circular tuned liquid column dampers [J], Special structures. 1996; 13, 3, 33-35.
- [4] Ziegler F., Chuan Fu, Effective vibration damping of plan-asymmetric buildings. In: Proc. of the 8th Int. Conf. on Multi-purpose High-rise Towers and Tall Buildings, Eds.: A.-R.R. Sabouni, K.M. El-Sawy. The International Federation of High-Rise Structures, CD-Rom Paper ID IFHS-039, Abu Dhabi, 2007, 1-13. ([www.acevents.ae/online documents'_ifhs2007+ifhs2007dxb_TB-28.pdf](http://www.acevents.ae/online_documents/ifhs2007+ifhs2007dxb_TB-28.pdf)).

6 Thirty-storey Moderately Asymmetric Structure

A 30-storey high-rise asymmetric structure is analysed using passive TLCGD control. The building data were obtained by Huo L.S.¹. The homogeneously distributed mass of each storey is $384 \times 10^3 \text{ kg}$, the moment of inertia with respect to the mass center of each storey is $5.96 \times 10^6 \text{ kg} \cdot \text{m}^2$, resulting shear stiffness in y and z direction is $k_y = 8.64 \times 10^5 \text{ kN/m}$ and $k_z = 7.8 \times 10^5 \text{ kN/m}$, respectively. The torsional stiffness of a storey is $k_t = 1.38 \times 10^8 \text{ kN} \cdot \text{m/rad}$. The eccentric distance of the center of shear from the mass center is $e_y = 4 \text{ m}$ and $e_z = 3 \text{ m}$. Since every storey has three degrees of freedom assigned, the structure is described by 90 DOF. The first 12 (undamped) natural frequencies are 0.348, 0.384, 1.042, 1.151, 1.343, 1.734, 1.915, 2.421, 2.673, 3.102, 3.425 and 3.774 Hz, respectively.

6.1 Installation of the TLCGD

The first three mode shapes are exaggerated and plotted in Figs. 6.1-6.3.

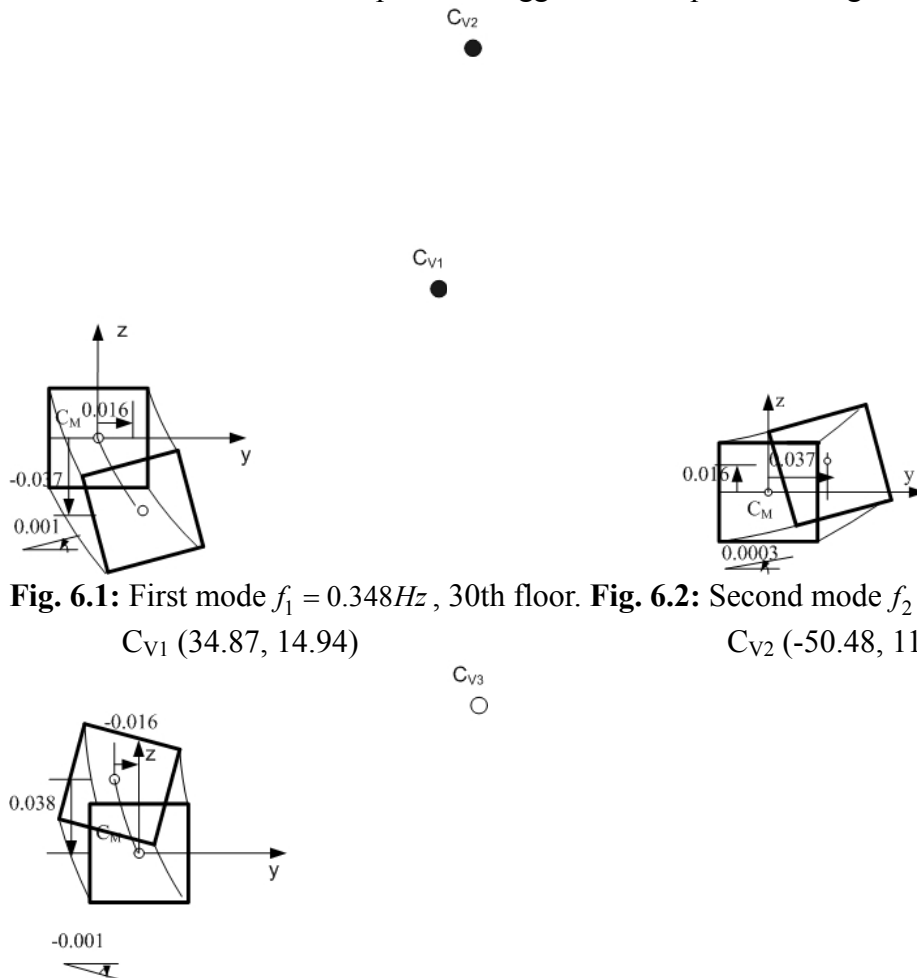


Fig. 6.1: First mode $f_1 = 0.348 \text{ Hz}$, 30th floor. **Fig. 6.2:** Second mode $f_2 = 0.384 \text{ Hz}$, 30th floor.

$C_{V1} (34.87, 14.94)$

$C_{V2} (-50.48, 116.78)$

Fig. 6.3: Third mode $f_3 = 1.042 \text{ Hz}$, 10th floor. $C_{V3} (34.87, 14.94)$.

Three modal centers of velocity fall outside the floor plan, the structure is considered to be moderately asymmetric. Two TLCGDs are installed on top of the structure to mitigate the fundamental and second vibration mode. TLCGD1 is installed z-parallel in the left side.

TLCGD2 can be installed y -parallel at the lower edge. TLCGD3 is installed at floor level ten and z -parallel in the left side, as illustrated in Figure 6.4. A model reduction from 90 to 12 degrees of freedom using the method of modal truncation is generated by keeping the first 12 vibration modes, see Clough-Penzien², page 158. The relevant first three mode shapes are calculated and given by Eq. (2.18).

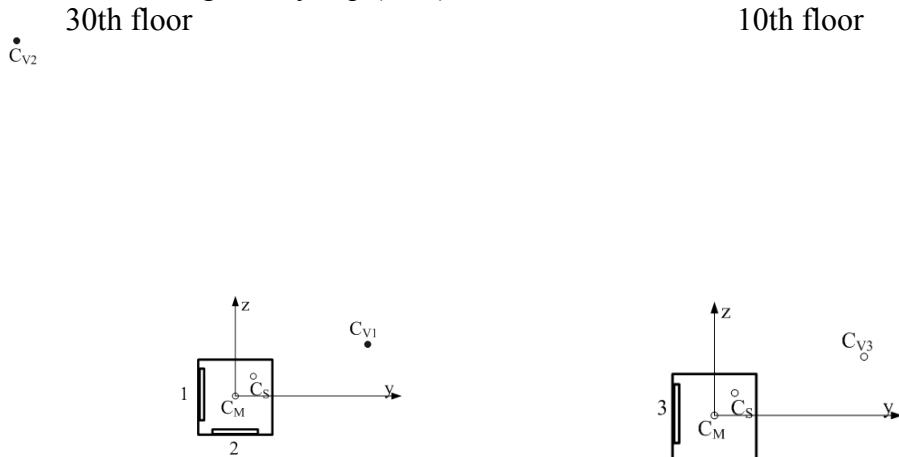


Fig. 6.4: Installation of TLCGD1, 2, 3, ○ the modal centers of velocity of 10th floor, ● the modal centers of velocity of 30th floor.

6.2 TLCGD design, Den Hartog's optimization

The fluid mass is chosen as $m_{f1} = 270 \times 10^3 \text{ kg}$, $m_{f2} = 250 \times 10^3 \text{ kg}$ and $m_{f3} = 50 \times 10^3 \text{ kg}$ of water. Dimensions of the three TLCGDs tuned first by means of the TMD analogy Eqs. (2.102)- (2.104) applying Den Hartog's formulas are summarized in Table 6.1. The modal dynamic magnification factor (DMF) calculated with Matlab 7.0³, equivalently linearized damping of the TLCGD considered, is illustrated in Figure 6.5.

	TLCGD1	TLCGD2	TLCGD3
Horizontal length of the liquid column B [m]	10.00	10.00	3.00
Inclined length of the liquid column H [m]	5.40	5.00	1.00
Cross-sectional area of the pipe [m ²] $A_H=A_B$	12.98	12.50	10.00
Effective length $L_{eff} = L_1 = 2H + B$ [m], Eq. (2.34a)	20.80	20.00	5.00
Angle of the inclined pipe section β [rad]	$\pi/4$	$\pi/4$	$\pi/4$
Equivalent mathematical pendulum length L_0 [m], Eq. (2.37)	2.06	1.69	0.23
Geometry factor $\kappa = \bar{\kappa}$, Eqs. (2.34a), (2.44)	0.85	0.85	0.88
Geometry factor $\bar{\kappa}_3$, Eq. (2.59)	1.00	1.10	1.84
Equilibrium pressure head h_0 [m], $n=1.2$, Eq. (2.34a)	35.47	39.14	30.00
Gas volume $V_0 = A_H H_a$ [m ³], Eq. (2.38)	105.88	93.75	30.10
The mass ratio of the TLCGD-main system μ , Eq. (2.97)	5.84%	4.58%	1.06%
The mass ratio of the equivalent TMD-main system μ^* , Eq. (2.102)	4.12%	3.29%	1.23%
Natural frequency $f_{A,opt}$ [Hz] Eq. (2.104), (2.112)	0.33	0.37	1.03
Optimal linear damping %, Eq. (2.113)	12.09	10.93	5.55

Table 6.1: Layout of the modally tuned TLCGDs, gas volume and gas equilibrium pressure assigned, cf. Fig. (6.4).

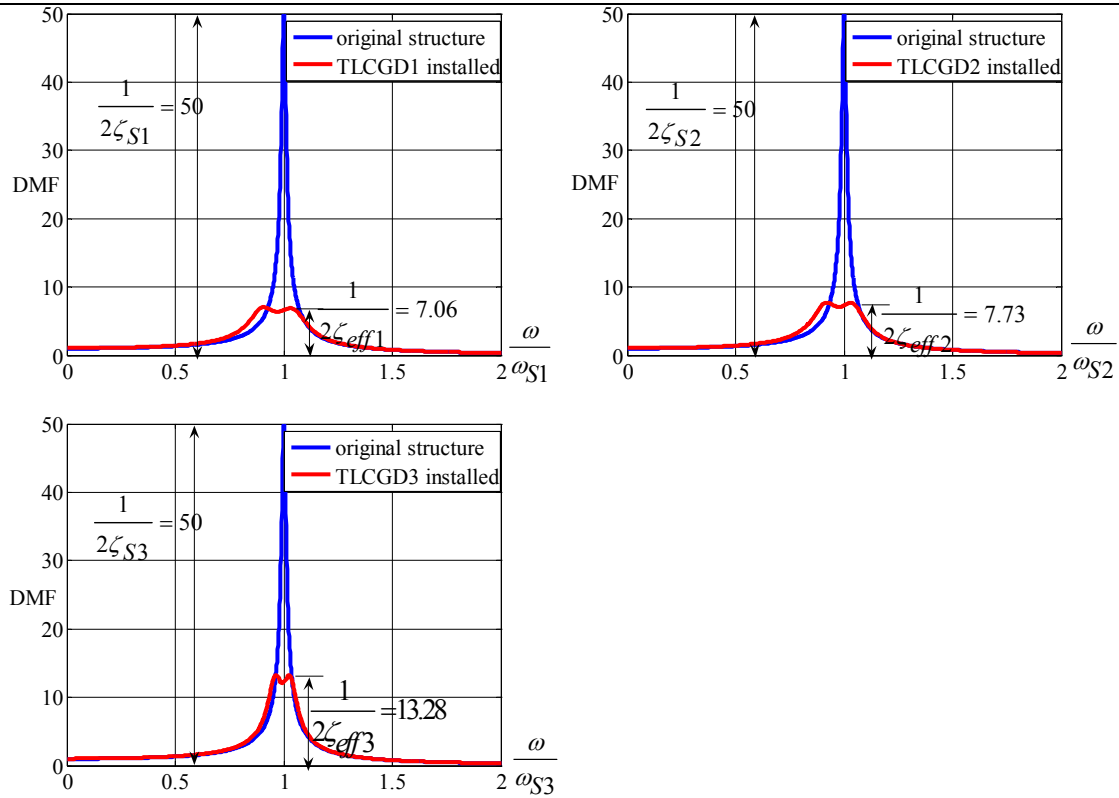


Fig. 6.5: Modal frequency response curves without and with linearized TLCGDs attached, Eqs. (2.106) and (2.110), TLCGDs with Den Hartog's optimal parameters.

The TLCGD in its passive mode considerably reduces steady state vibrations of lightly damped structures similarly to an increase of the effective structural damping. The effective modal damping coefficients of the system in each mode are increased from $\zeta_{Sj} = 1\%$ to $\zeta_{eff1} = 7.08\%$, $\zeta_{eff2} = 6.47\%$ and $\zeta_{eff3} = 3.77\%$.

Forcing direction	structure			TLCGD1	
	v_{30} [mm]	w_{30} [mm]	$u_T = r_S \theta_{30}$ [mm]		u_0 [mm]
$\alpha = 0$	C_M	113	-263	30	979
	A	113	-301		
$\alpha = \pi/6$	C_M	42	-98	11	421
	A	42	-112		
$\alpha = \pi/4$	C_M	116	-271	31	1080
	A	116	-309		
$\alpha = \pi/3$	C_M	183	-427	48	1673
	A	183	-488		
$\alpha = \pi/2$	C_M	276	-644	73	2488
	A	276	-736		
$\alpha = 2\pi/3$	C_M	295	-688	78	2639
	A	295	-787		
$\alpha = 3\pi/4$	C_M	274	-640	72	2445
	A	274	-732		
$\alpha = 5\pi/6$	C_M	235	-549	62	2085
	A	235	-627		

Table 6.2a: Maximum displacements in the first mode from time-harmonic excitation in α -directions, $a_0 = 0.04g$, $r_S = 3.94m$.

Thirty-storey Moderately Asymmetric Structure

Forcing direction	structure			TLCGD2	
	v_{30} [mm]	w_{30} [mm]	$u_T = r_S \theta_{30}$ [mm]	u_0 [mm]	
$\alpha = 0$	C_M	584	252	20	2294
	A	609	252		
$\alpha = \pi/6$	C_M	626	271	21	2442
	A	653	271		
$\alpha = \pi/4$	C_M	583	252	20	2267
	A	608	252		
$\alpha = \pi/3$	C_M	501	216	17	1937
	A	522	216		
$\alpha = \pi/2$	C_M	242	105	8	920
	A	252	105		
$\alpha = 2\pi/3$	C_M	85	-37	3	374
	A	89	37		
$\alpha = 3\pi/4$	C_M	243	105	8	984
	A	253	105		
$\alpha = 5\pi/6$	C_M	385	166	13	1534
	A	402	166		

Table 6.2b: Maximum displacements in the second mode from time-harmonic excitation in α -directions, $a_0=0.04g$, $r_S = 3.94m$.

Forcing direction	structure			TLCGD3	
	v_{10} [mm]	w_{10} [mm]	$u_T = r_S \theta_{10}$ [mm]	u_0 [mm]	
$\alpha = 0$	C_M	-8	18	-2	154
	A	-8	21		
$\alpha = \pi/6$	C_M	-3	7	-1	73
	A	-3	8		
$\alpha = \pi/4$	C_M	-8	19	-2	178
	A	-8	23		
$\alpha = \pi/3$	C_M	-13	31	-3	272
	A	-13	35		
$\alpha = \pi/2$	C_M	-20	46	-5	401
	A	-20	53		
$\alpha = 2\pi/3$	C_M	-21	49	-6	423
	A	-21	56		
$\alpha = 3\pi/4$	C_M	-20	46	-5	390
	A	-20	52		
$\alpha = 5\pi/6$	C_M	-17	39	-4	332
	A	-17	45		

Table 6.2c: Maximum displacements in the third mode from time-harmonic excitation in α -directions, $a_0=0.04g$, $r_S = 3.94m$.

From Table 6.2a-c it follows that all of the maximum fluid displacements for varying angles of attack of the time harmonic excitation, are within the acceptable limits, $u_0 < H_a/3$ (of linearized gas compression) and $u_0 < H/2$. The maximum fluid velocities of three TLCGDs are calculated by Eq. (2.35) 5.47, 5.68 and 2.74m/s and are within the acceptable speed limit.

	TLCGD1					
	1	2	3	4	5	6
f_i [Hz]	0.383	0.361	0.329	0.306	0.309	0.340
ζ_i [%]	14.85	9.39	5.75	5.61	15.09	11.06
h_0 [m]	44.38	38.65	31.11	26.06	26.81	33.67
	TLCGD2					
	1	2	3	4	5	6
f_i [Hz]	0.360	0.362	0.381	0.332	0.370	0.425
ζ_i [%]	15.62	11.11	14.14	5.77	4.60	5.89
h_0 [m]	33.85	34.20	38.51	27.96	36.03	49.14
	TLCGD3					
	1	2	3	4		
f_i [Hz]	1.088	1.117	1.028	0.990		
ζ_i [%]	2.71	1.30	1.86	1.80		
h_0 [m]	33.72	35.66	29.87	27.55		

Table 6.4: Fine tuned optimal parameters and the equilibrium pressure head of TLCGDs.

It is obvious that the parameter optimization reduced the vibration amplitude at the resonant peaks tremendously.

6.4 Forcing of the 30 storey moderately asymmetric building by the NS-EI Centro seismogram under varying angles of attack

The maximum acceleration of the NS-EI Centro earthquake record is set to $0.35g$. Varying the angle of attack refers to the effect of bidirectional forcing of the thirty-storey moderately asymmetric space frame without and with 16 small TLCGD-units. The results are presented graphically in Figs. 6.14- 6.21, where the relative floor displacements with respect to the base and the relative floor accelerations for the root mean square (RMS) response⁴ are displayed. The RMS value is defined in Eq. (4.26).

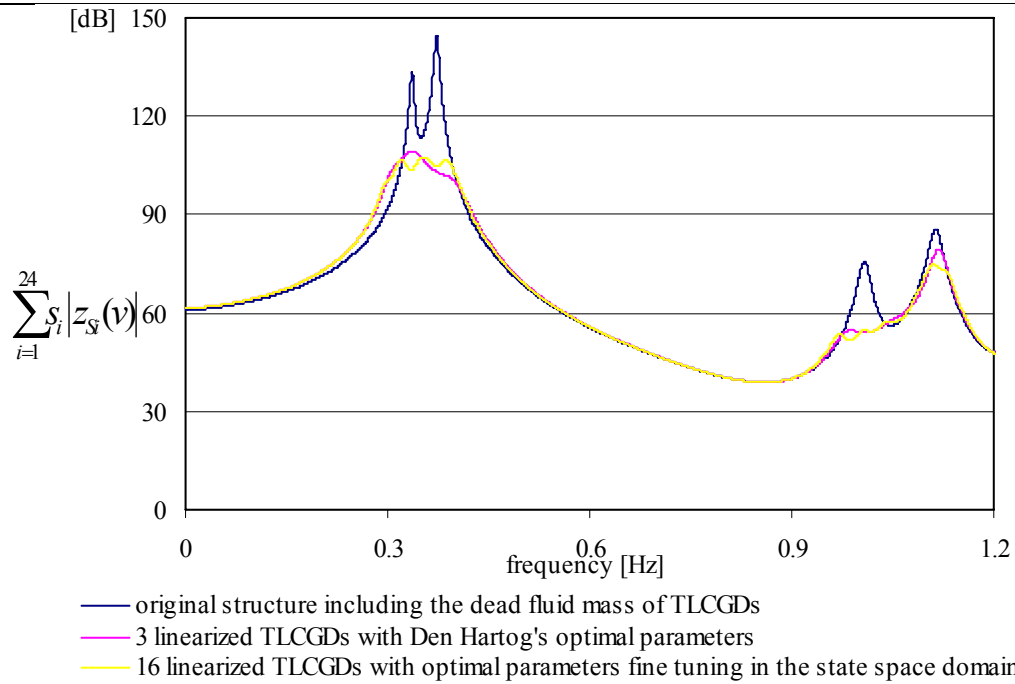


Fig. 6.6: Weighed sum of amplitude response functions for the 90-DOF linearized, thirty-storey asymmetric space frame, with linearized TLCGDs attached and without the TLCGDs (angle of attack of the time-harmonic base acceleration $\alpha = 0$), maximum gain 34.89dB.

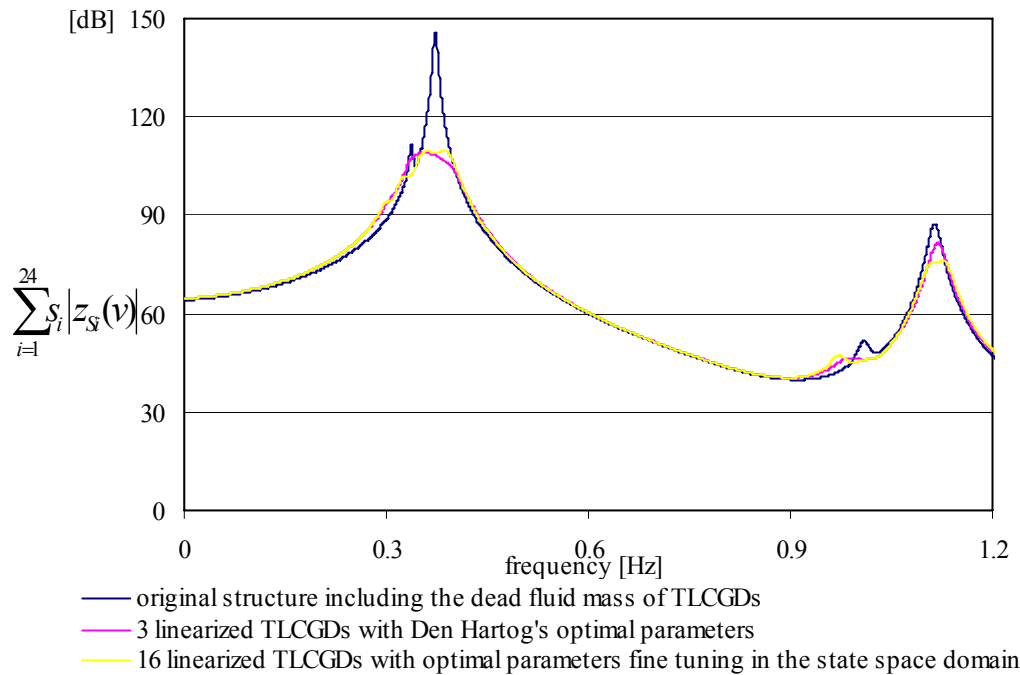


Fig. 6.7: Weighed sum of amplitude response functions for the 90-DOF linearized, thirty-storey asymmetric space frame, with linearized TLCGDs attached and without the TLCGDs (angle of attack of the time-harmonic base acceleration $\alpha = \pi/6$), maximum gain 37.10dB.

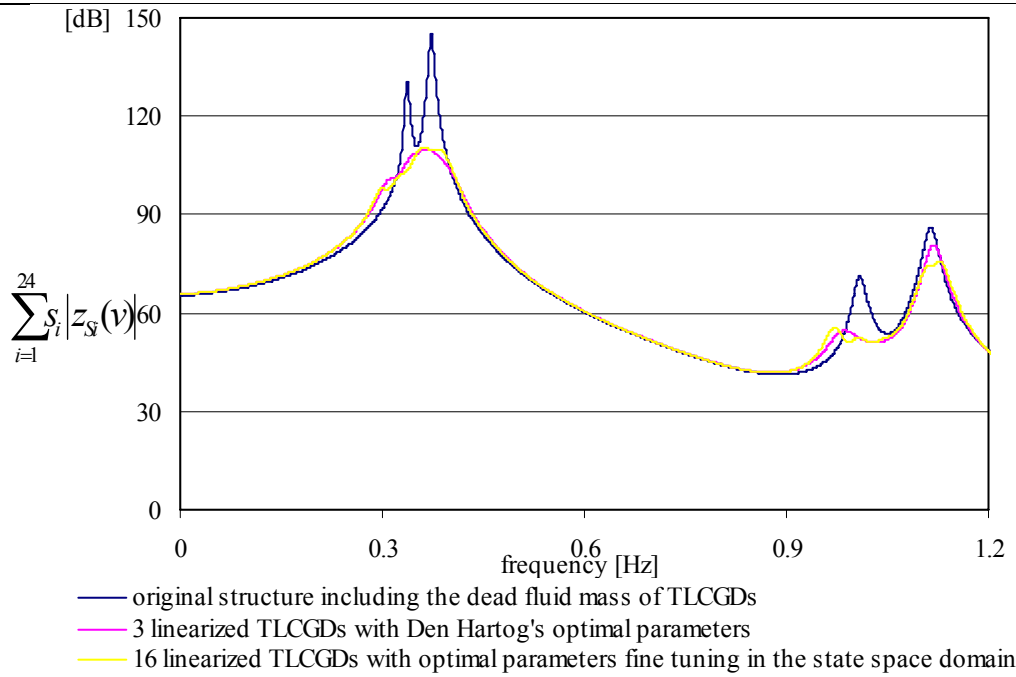


Fig. 6.8: Weighed sum of amplitude response functions for the 90-DOF linearized, thirty-storey asymmetric space frame, with linearized TLCGDs attached and without the TLCGDs (angle of attack of the time-harmonic base acceleration $\alpha = \pi/4$), maximum gain 34.86dB.

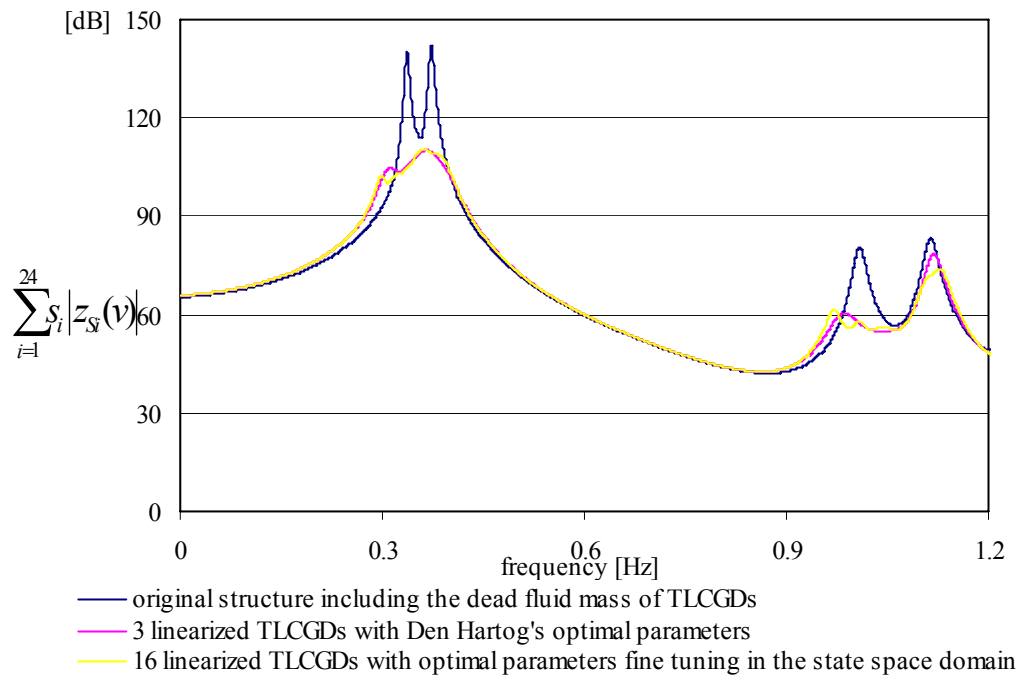


Fig. 6.9: Weighed sum of amplitude response functions for the 90-DOF linearized, thirty-storey asymmetric space frame, with linearized TLCGDs attached and without the TLCGDs (angle of attack of the time-harmonic base acceleration $\alpha = \pi/3$), maximum gain 32.01dB.

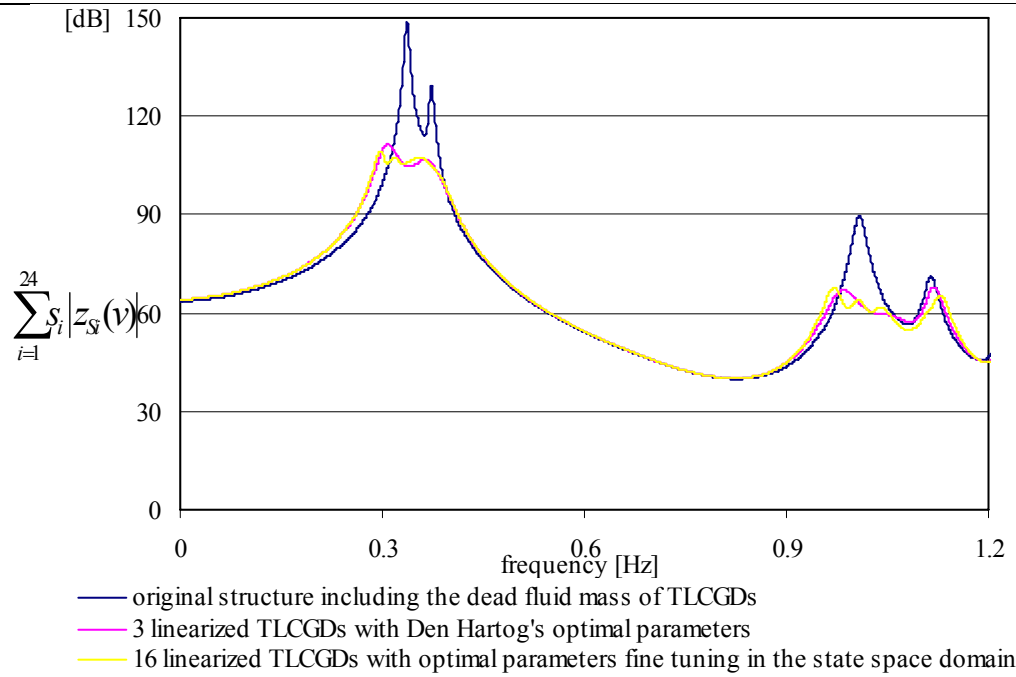


Fig. 6.10: Weighed sum of amplitude response functions for the 90-DOF linearized, thirty-storey asymmetric space frame, with linearized TLCGDs attached and without the TLCGDs (angle of attack of the time-harmonic base acceleration $\alpha = \pi/2$), maximum gain 37.46dB.

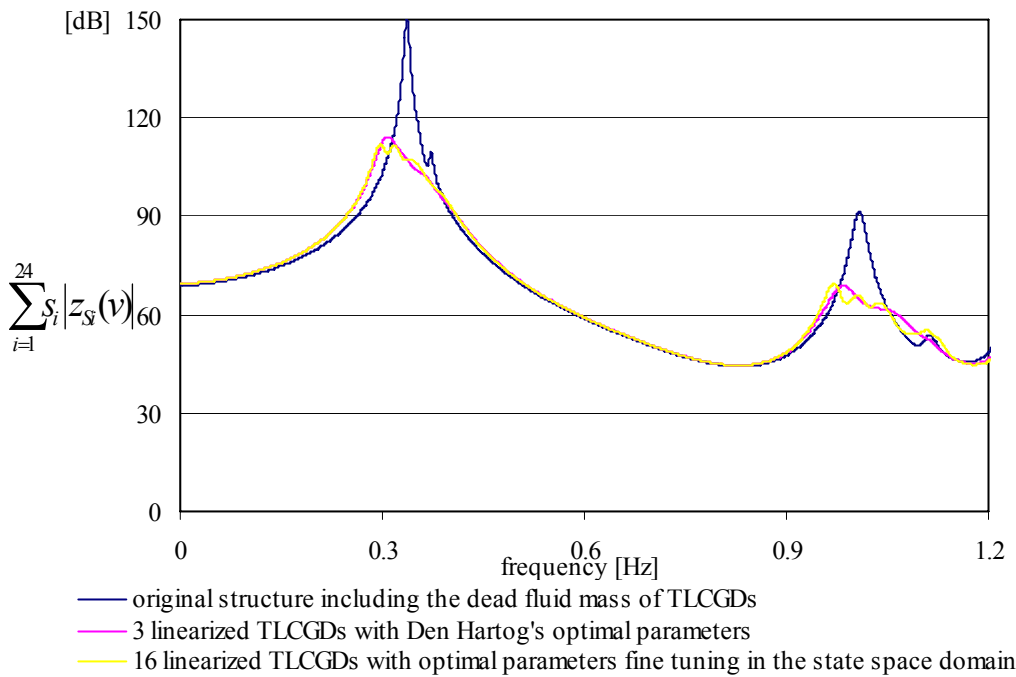


Fig. 6.11: Weighed sum of amplitude response functions for the 90-DOF linearized, thirty-storey asymmetric space frame, with linearized TLCGDs attached and without the TLCGDs (angle of attack of the time-harmonic base acceleration $\alpha = 2\pi/3$), maximum gain 36.26dB.

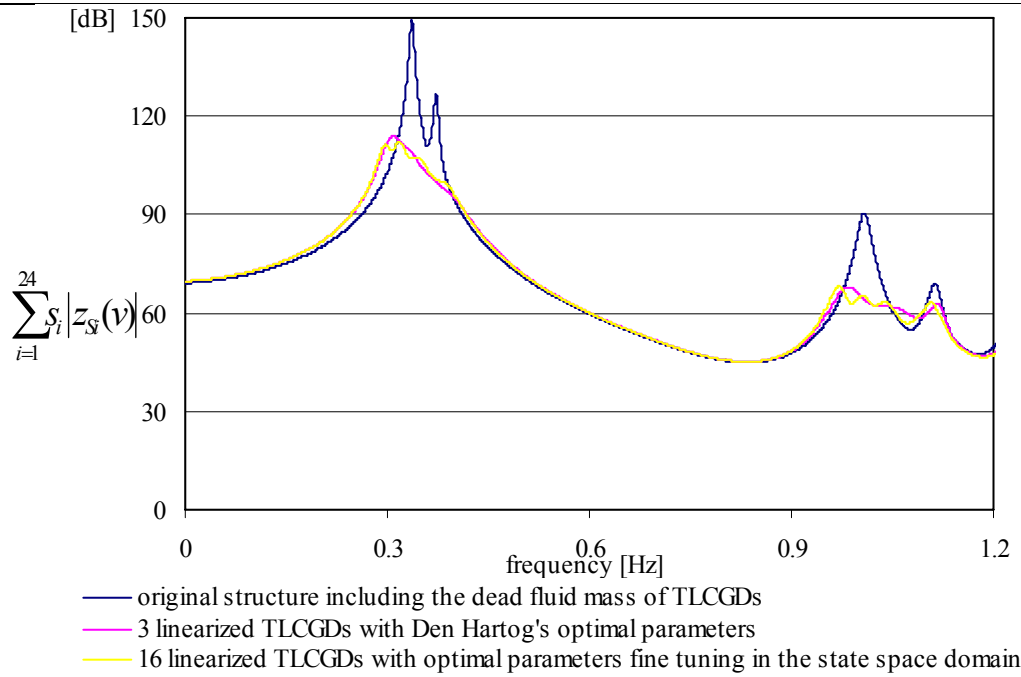


Fig. 6.12: Weighed sum of amplitude response functions for the 90-DOF linearized, thirty-storey asymmetric space frame, with linearized TLCGDs attached and without the TLCGDs (angle of attack of the time-harmonic base acceleration $\alpha = 3\pi/4$), maximum gain 35.36dB.

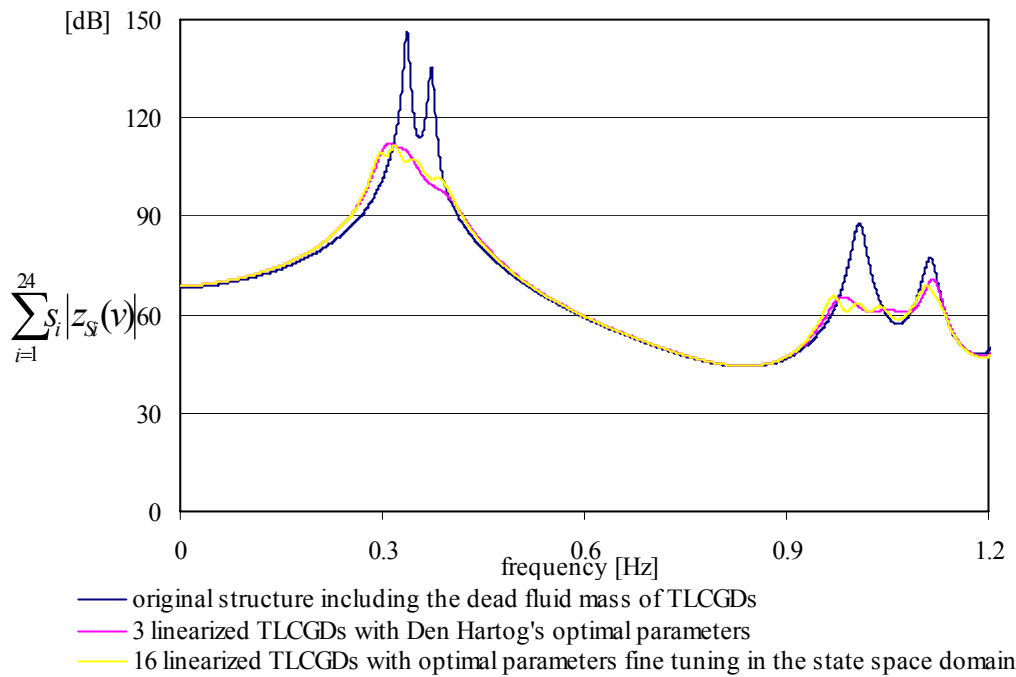


Fig. 6.13: Weighed sum of amplitude response functions for the 90-DOF linearized, thirty-storey asymmetric space frame, with linearized TLCGDs attached and without the TLCGDs (angle of attack of the time-harmonic base acceleration $\alpha = 5\pi/6$), maximum gain 34.15dB.

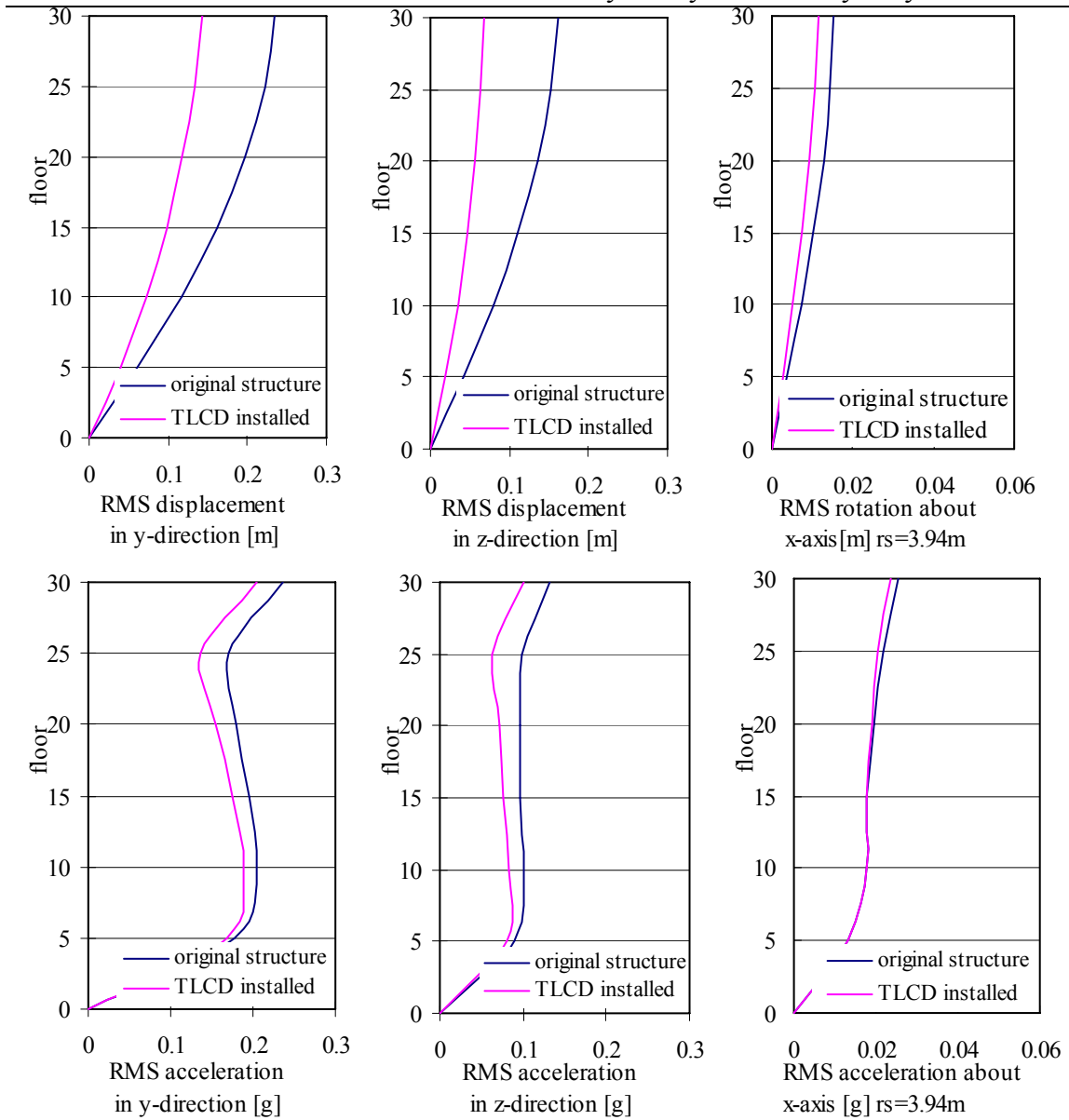
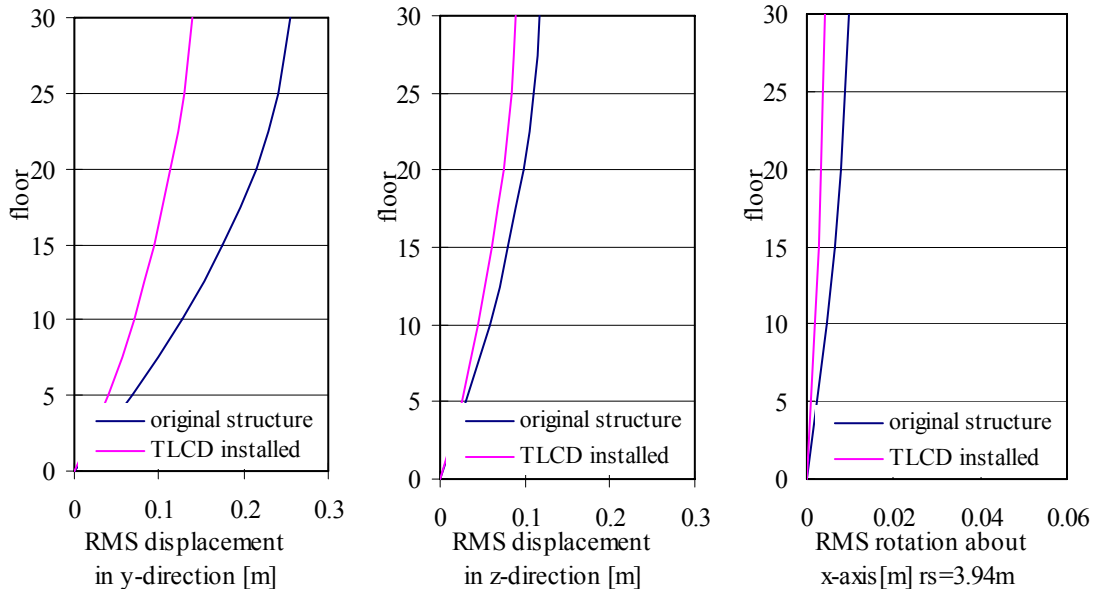


Fig. 6.14: RMS responses for floor displacement and acceleration of the thirty-storey asymmetric building (El Centro 0.35g, angle of attack $\alpha = 0$).



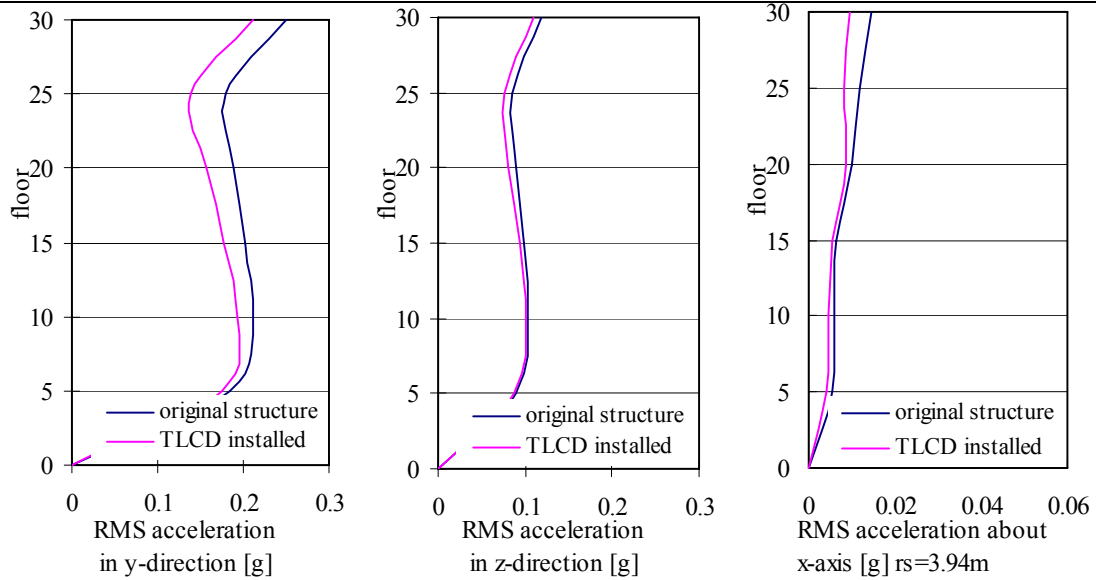


Fig. 6.15: RMS responses for floor displacement and acceleration of the thirty-storey asymmetric building (El Centro $0.35g$, angle of attack $\alpha = \pi/6$).

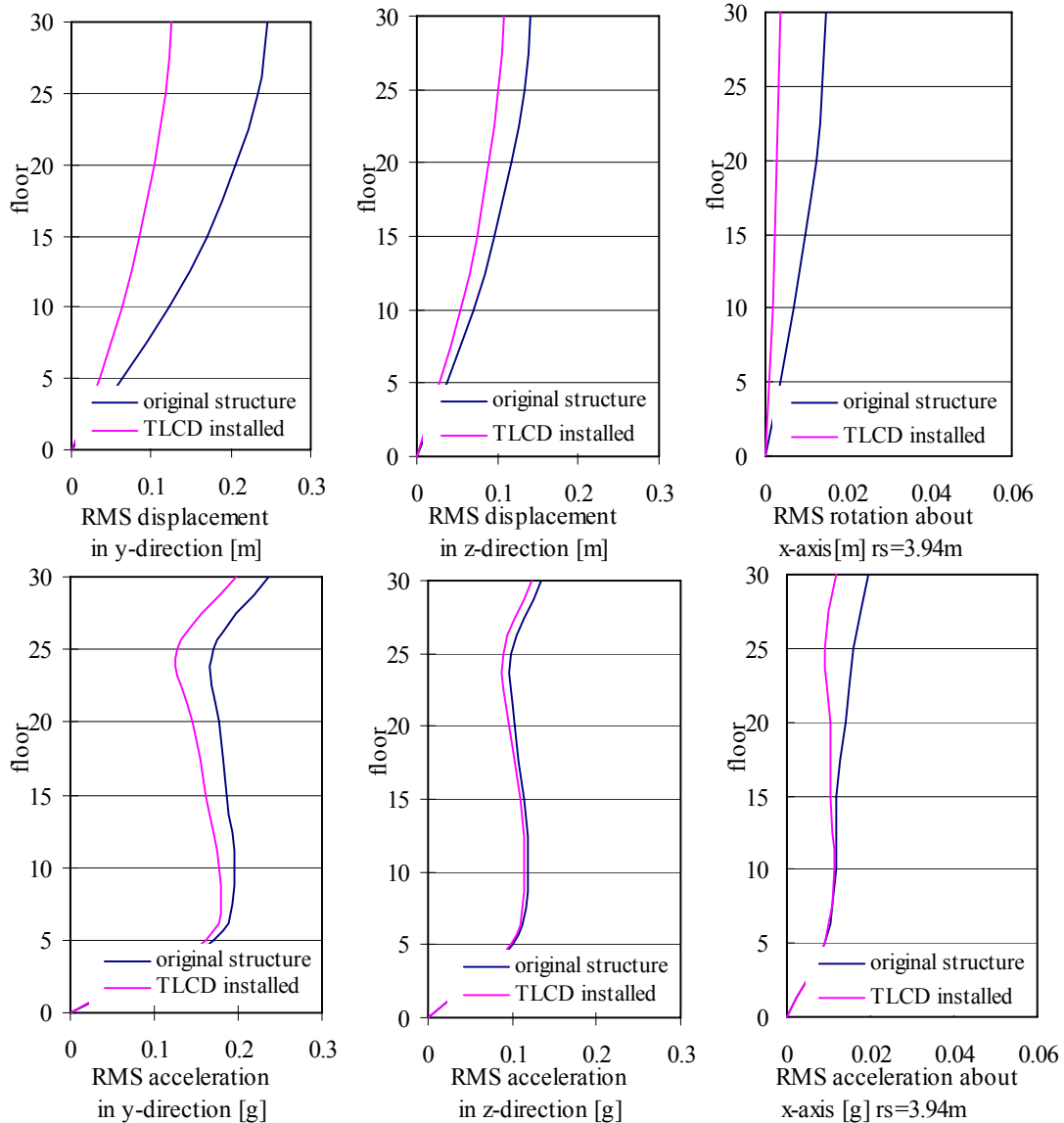


Fig. 6.16: RMS responses for floor displacement and acceleration of the thirty-storey asymmetric building (El Centro $0.35g$, angle of attack $\alpha = \pi/4$).

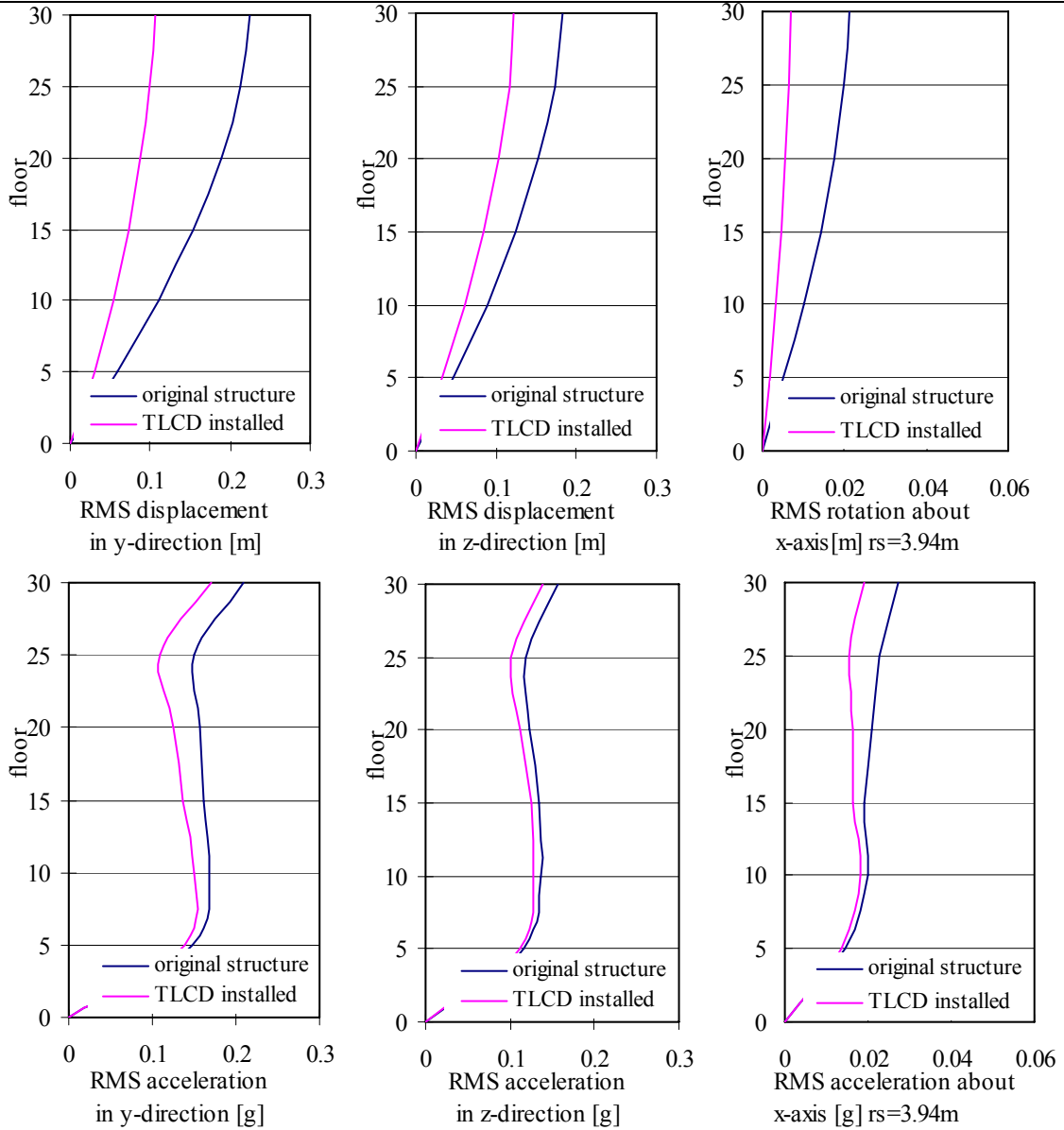
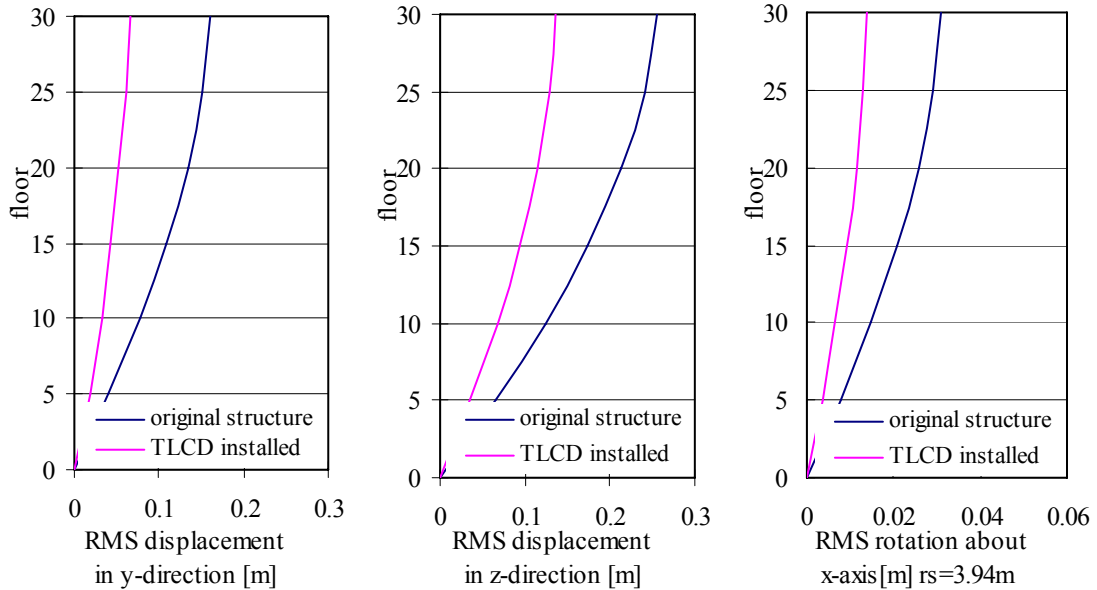


Fig. 6.17: RMS responses for floor displacement and acceleration of the thirty-storey asymmetric building (El Centro $0.35g$, angle of attack $\alpha = \pi/3$).



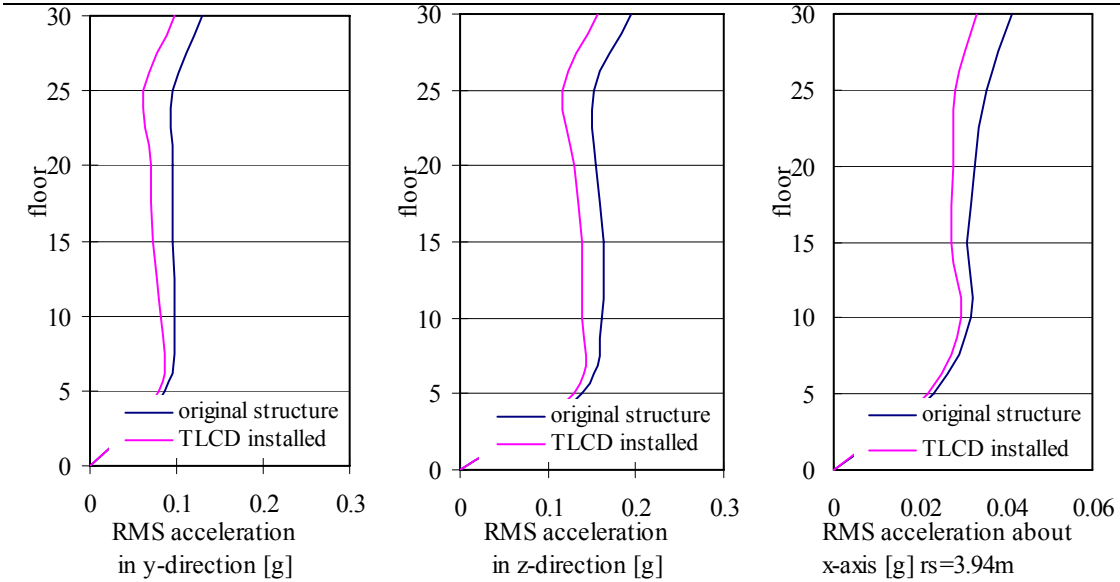


Fig. 6.18: RMS responses for floor displacement and acceleration of the thirty-storey asymmetric building (El Centro $0.35g$, angle of attack $\alpha = \pi/2$).

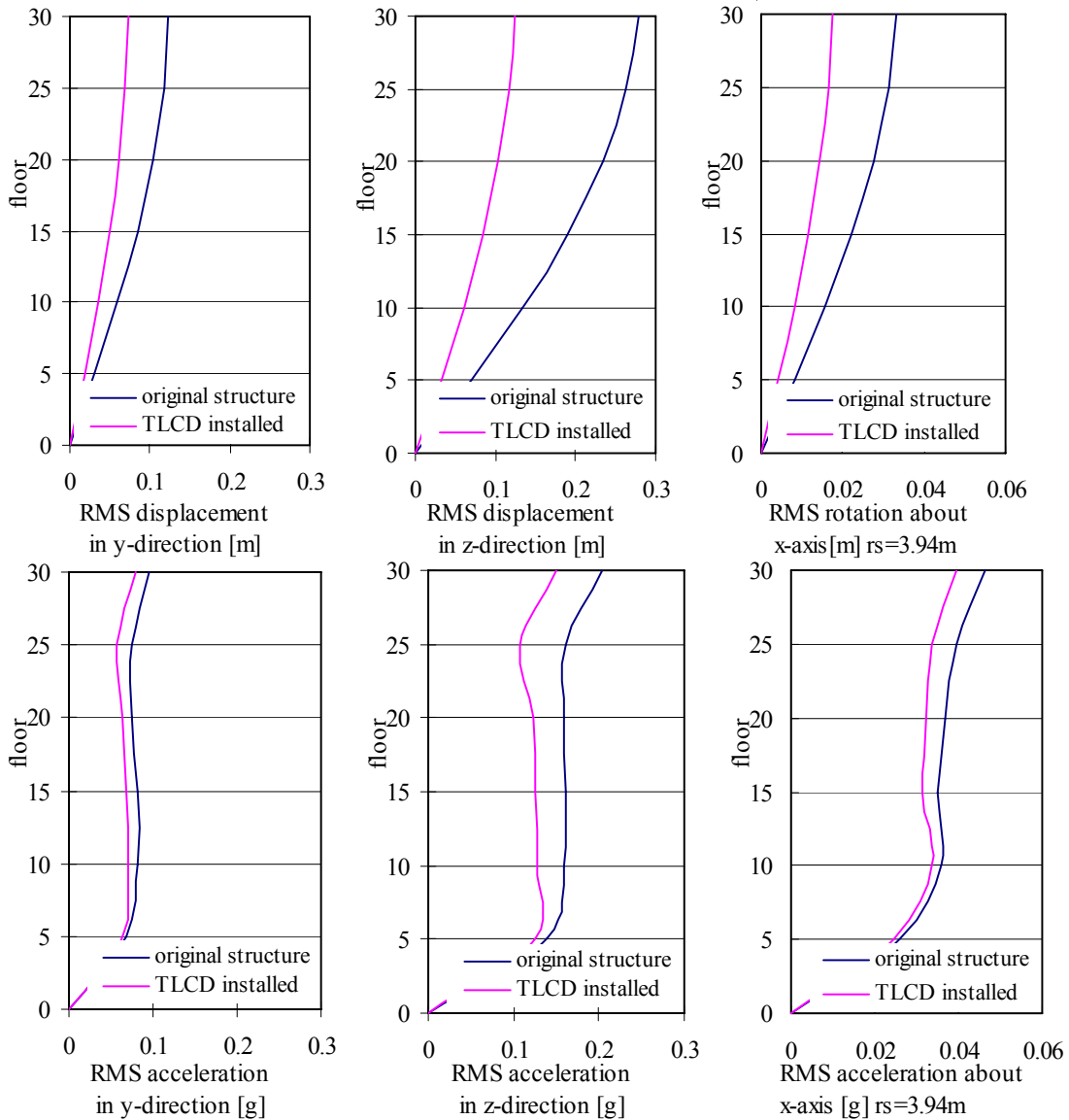


Fig. 6.19: RMS responses for floor displacement and acceleration of the thirty-storey asymmetric building (El Centro $0.35g$, angle of attack $\alpha = 2\pi/3$).

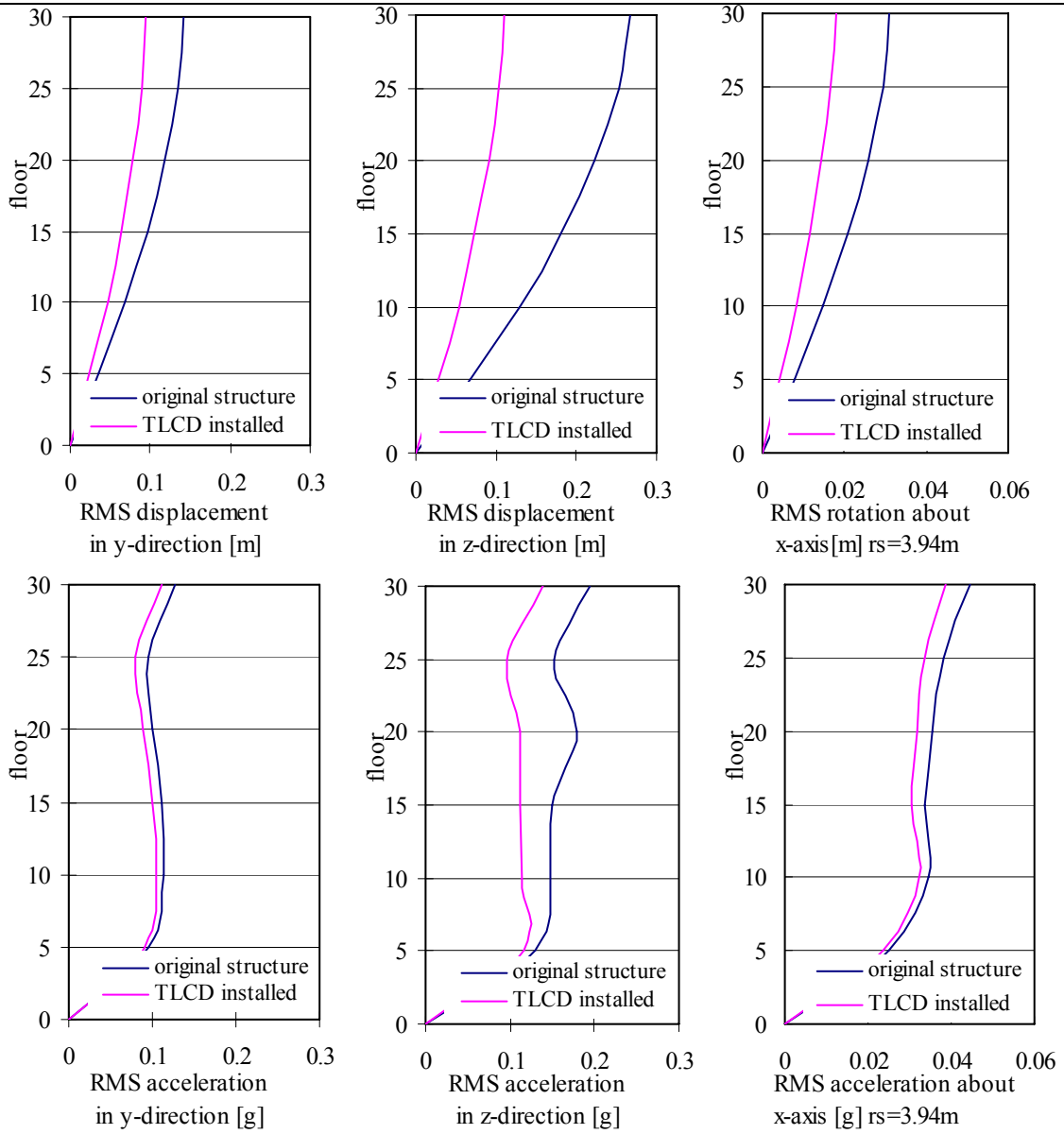
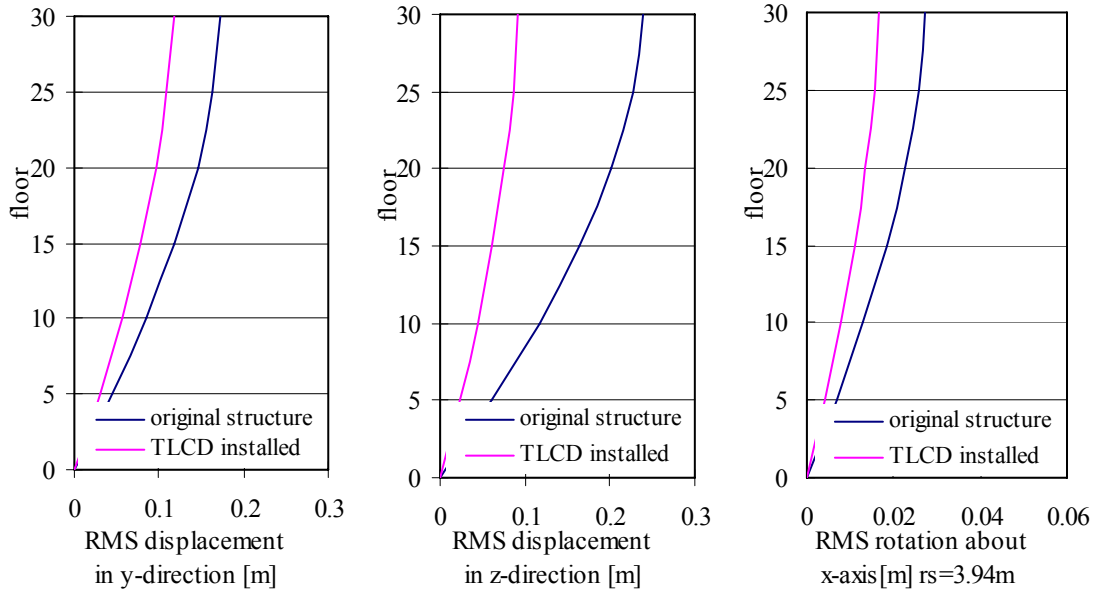


Fig. 6.20: RMS responses for floor displacement and acceleration of the thirty-storey asymmetric building (El Centro $0.35g$, angle of attack $\alpha = 3\pi/4$).



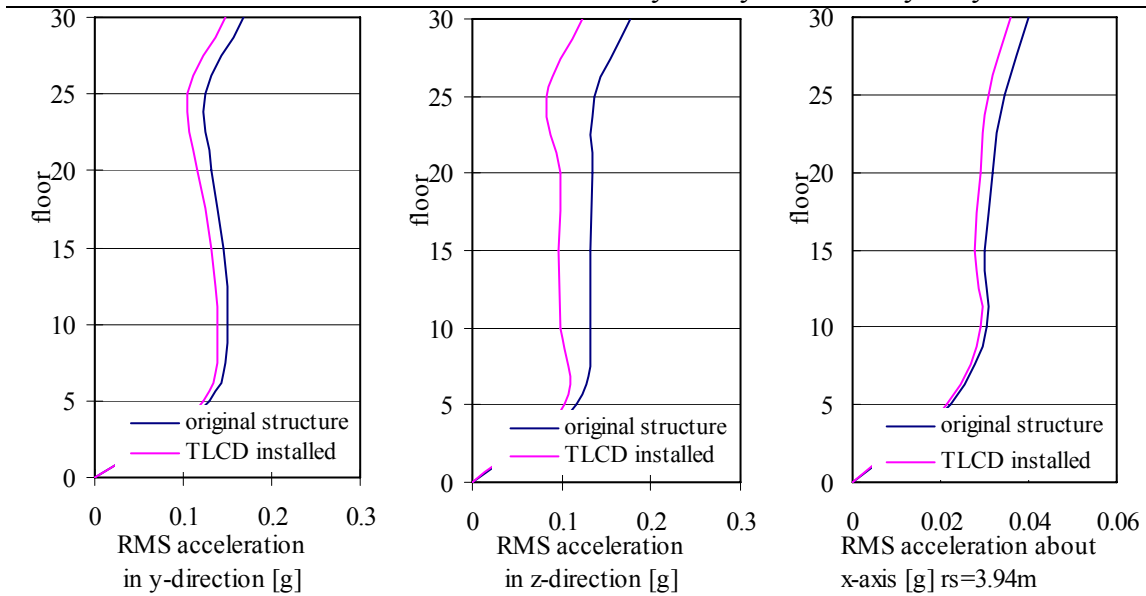


Fig. 6.21: RMS responses for floor displacement and acceleration of the thirty-storey asymmetric building (El Centro $0.35g$, angle of attack $\alpha = 5\pi/6$).

From these numerical results, TLCGDs installed and tuned to the structural frequency can effectively reduce the translational and torsional response of structures.

Comparing the time histories of structural seismic response with those given by Huo L.S.¹, namely the top floor displacements are illustrated in Fig.6.22, achieved in this section, ground action of El Centro $0.35g$ and angle of attack $\alpha = \pi/3$. The figure clearly indicates the superiority of the fine tuned 16 TLCGDs, effective damping is much larger.

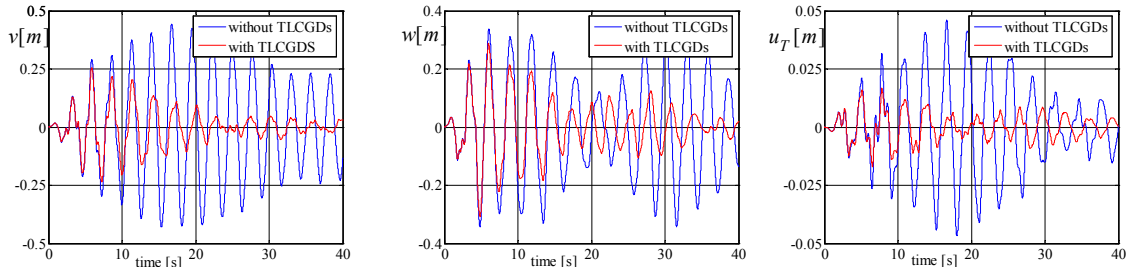


Fig. 6.22: Relative top floor displacements of center of mass, v , w and rotation $u_T=r_S\theta$ without and with TLCGDs attached, $r_S = 3.94m$.

References

- [1] Huo L.S., Li H.N., Sun L., Parameter study of TLCD control system excited by multi-dimensional ground motions. Earthquake Engineering and engineering vibration, 2001, 21, 4, 147-153.
- [2] Clough R.W., Penzien J., Dynamics of Structures, 2nd edition, McGraw-Hill, 1993.
- [3] MATLAB, User Guide, Control Toolbox. MathWorks Inc., Version 6.5.1, 2002.
- [4] Chopra A.K., Dynamics of Structures, Prentice/Hall, New Jersey, 1995.
- [5] Hochrainer M.J., Control of vibrations of civil engineering structures with special emphasis on tall buildings. Dissertation (in English), TU-Wien, A-1040 Vienna, Austria, 2001.

7 Conclusions

In this dissertation, a detailed investigation of the coupled torsional vibration control of asymmetric structures by using tuned liquid column gas damper (TLCGD) and torsional tuned liquid column gas damper (TTLCGD) has been performed. Theoretical studies and computer simulations have been carried out to investigate the control performance and effectiveness of these absorbers. Many useful conclusions were obtained within the dissertation, which may be considered as guidelines for future applications of the damper. The main contributions and conclusions made in this dissertation are summarized as follows:

1. We define moderate asymmetry if the modal centers of velocity fall outside of the floor plan. The ideal position of the trace midplane of the U-shaped TLCGD requires its normal distance to the center of velocity maximum. For a strongly asymmetric building, the velocity centers of several modes fall inside the floor plan. The novel TTLCGD with its horizontal curved piping section enclosing the center for best efficiency becomes superior.
2. The equations of relative fluid motion in TLCGD and TTLCGD are derived using a generalized Bernoulli equation of relative streamlines in a moving frame. The interaction forces between the moving supporting floor and damper are determined for structural synthesis in the dynamic analysis.
3. The general analogy between TMD and TLCGD, TTMD and TTLCGD when attached to main single storey- and multi storey structures under the horizontal base acceleration has been established the first time in this dissertation. Thus, the classical tuning procedure can be applied. Adjusting the equilibrium gas pressure allows easy frequency tuning and makes final tuning possible in a most simple way.
4. It is concluded from the numerical studies that TLCGD is very promising in the moderately asymmetric structure and TTLCGD can be used in the strongly asymmetric structure to mitigate translational and torsional vibration. The frequency limit of application of these absorbers is discussed in connection with the maximum fluid stroke to keep the fluid-gas interface intact and the piston theory applicable.

References

- Adrian Y.J.W., Performance assessment of tuned liquid column damper under random seismic loading, *J. Non-linear Mechanics*. 1997; 32, 4, 745-758. [2]75
- Alexandros A., Optimal design and performance of liquid column mass dampers for rotational vibration control of structures under white noise excitation, *Engineering Structures*. 2005; 27, 4, 524-534. [2]75
- Chang C.C., Mass dampers and their optimal designs for building vibration control, *Engineering Structures*. 1999; 21, 5, 454-463. [2]75
- Chopra A.K., *Dynamics of Structures*, Prentice-Hall, New Jersey, 1995. [2]74,[4]191,[5]244,[6]263
- Clough R.W., Penzien J., *Dynamics of Structures*, 2nd edition, McGraw-Hill, 1993. [2]74,[6]263
- DenHartog J.P., *Mechanical vibrations*. 4th edn, McGraw-Hill, New York, 1956. [1]4,[2]74
- Fujina Y., Sun L.M., Vibration control by multiple tuned liquid dampers (MTLDs), *ASCE J. of Structural Engineering*. 1993; 119, 12, 3482-3502. [2]75
- Giuseppe C.M., Probabilistic seismic response and reliability assessment of isolated bridges, *Earthquake engineering and engineering vibration*. 2005; 4, 1, 95-106. [2]74
- H.Gao, K.S.C. Kwok, B. Samali, Characteristics of multiple tuned liquid column dampers in suppressing structural vibration, *Engineering Structures*. 1993; 21, 1, 216-331. [1]5
- Haroun M.A., Pires J.A., Won A.Y.J., Suppression of environmentally-induced vibrations in tall buildings by hybrid liquid column dampers, *The Structural Design of Tall Buildings*. 1996; 5, 1, 45-54. [1]5
- Hochrainer M.J., Control of vibrations of civil engineering structures with special emphasis on tall buildings. Dissertation (in English), TU-Wien, A-1040 Vienna, Austria, 2001. [1]4,[2]74,[3]118,[6]263
- Hochrainer M.J., Ziegler F., Control of tall building vibrations by sealed tuned liquid column dampers, *Structural Control and Health Monitoring*. 2006; 6, 13, 980-1002. [1]4,[2]74,
- Hochrainer M.J., Adam C, Ziegler F., Application of tuned liquid column dampers for passive structural control. Proceeding of the 7th ICSV, CD ROM paper, Garmisch-Partenkirchen, Germany, 2000. [3]118
- Höllinger F., *Bebeneregte Schwingungen elastischer Sperrenkonstruktionen*. Dissertation (in German), TU-Wien, A-1040 Vienna, Austria, 1982. [2]74
- Höllinger F., Ziegler F., Instationäre Zufallsschwingungen einer elastischen Gewichtsmauer bei beliebig geformtem Becken, *ZAMM*. 1983; 63, 1, 49-54. [2]74
- Huo L.S., Li H.N., Sun L., Parameter study of TLCD control system excited by multi-dimensional ground motions, *Earthquake engineering and engineering vibration*. 2001; 21, 4, 147-153. [1]5,[6]263
- Huo L.S., Li H.N., Torsionally coupled response control of offshore platform structures using circular tuned liquid column dampers, *China Ocean Engineering*. 2004; 18, 2, 173-183. [1]5,[3]118
- Huo, L.S., Li. H.N., Torsion-coupled response control of structure using circular tuned liquid column dampers. *Engineering mechanics*, 2005; 22, 2, 124-131. [3]118
- Kanai K., Semi-empirical formula for the seismic characteristics of the ground, *Bulletin of the earthquake research institute. University of Tokyo*. 1957; 35, 2, 309-325. [2]74
- Kwok K.C.S., Xu Y.L., Samali B., Control of wind-induced vibrations of tall structures by optimized tuned liquid column dampers, *Computational mechanics*. 1991, 249-254. [1]5
- Li H.N., Huo L.S., TLCD semi-active control of eccentric structures using neural networks, 15th ASCE Engineering Mechanics Conference June 2-5, 2003, Columbia University, New York, NY. [1]5,[4]191
- Liang S.G., Experiment study of torsionally structure vibration control using circular tuned liquid column dampers [J], *Special structures*. 1996; 13, 3, 33-35. [3]118,[5]244
- Lin C.C., Ueng J.M., Huang T.C., Seismic response reduction of irregular building using passive tuned mass dampers, *Engineering Structures*. 2000; 22, 5, 513-524. [2]74
- Lin J.L., Tsai K.C., Simplified seismic analysis of asymmetric building systems, *Earthquake Engineering and Structural Dynamics*. 2007; 36, 4, 459-479. [4]191
- Lindner-Silvester T., Schneider W., The moving contact line with weak viscosity effects-an application and evaluation of Shikhmurzaev's model, *Acta Mechanica*. 2005, 176, 3, 245-258. [2]74
- MATLAB, User Guide, Control Toolbox. MathWorks Inc., Version 6.5.1, 2002. [2]74,[3]118,[4]191,[5]244, [6]263
- Matlab, Simulink Version 3.0.1, The MathWorks Inc., 1984-2001, campus licence TU-Wien. [2]74,[3]118
- Matlab, Signal Processing Toolbox, The MathWorks Inc., 1984-2001, campus licence TU-Wien. [2]74,[3]118
- Ni Y.Q., Ying Z.G., Wang J.Y., Ko J.M., Spencer B.F., Stochastic optimal control of wind-excited tall buildings using semi-active MR-TLCDs, *Probabilistic Engineering Mechanics*. 2004; 19, 3, 269-277. [1]5
- Ou J.P., Random earthquake ground motion model and its parameter determination used in seismic design, *Earthquake engineering and engineering vibration*. 1991; 11, 3, 45-54. [2]74
- Reiterer M., Damping of vibration-prone civil engineering structures with emphasis on bridges. Dissertation (in German), TU-Wien, A-1040 Vienna, Austria, 2004. [1]4,[2]74
- Reiterer M., Ziegler F., Control of pedestrian-induced vibrations of long-span bridges, *Structural Control and Health Monitoring*. 2006; 13, 6, 1003-1027. [1]4,[2]74
- Robert K., *Bautabellen*, Wien, Verl.Jugend&Volk, 2002. [2]74

- Sakai F., Takaeda S., Tamaki T., Tuned liquid column damper-new type device for suppression of building vibration. In: Proc. Int. Conf. on High-rise Buildings, Nanjing, China, 1989, 926-931. [1]4
- Shum K.M., Xu Y.L., Multiple-tuned liquid column dampers for torsional vibration control of structures: experimental investigation, *Earthquake Engineering and Structural Dynamics*. 2002; 31, 4, 977-991. [1]5
- Shum K.M., Xu Y.L., Multiple-tuned liquid column dampers for torsional vibration control of structures: theoretical investigation, *Earthquake Engineering and Structural Dynamics*. 2003; 32, 2, 309-328. [1]5
- Shum K.M., Xu Y.L., Multiple tuned liquid column dampers for reducing coupled lateral and torsional vibration of structures, *Engineering structures*. 2004; 26, 6, 745-758. [3]118
- Xue S.D., Ko J.M., Xu Y.L., Tuned liquid column dampers for suppressing pitching motion of structures, *Engineering Structures*. 2000; 22, 11, 1538-1551. [1]5
- Xue S.D., Torsional vibration control of suspension bridge decks using tuned liquid column damper. Dissertation (in English), the Hong Kong Polytechnic University, 1999. [2]74,[4]191
- Ying Z.G., Ni Y.Q., Semi-active optimal control of linearized systems with multi-degree of freedom and application, *Journal of sound and vibration*. 2005; 279, 1-2, 373-388. [3]118
- Zhang Z.Y., Sun B.T. and Song T. S., Study on the parameters of seismic power spectrum model based on the new seismic code, *World information on earthquake engineering*. 2000; 16, 3, 33-38. [2]74
- Ziegler F., *Mechanics of Solids and Fluids*, correct reprint of second edition, Springer, New York, 1998. [1]5, [2]74,[3]118
- Ziegler F., The tuned liquid column damper as the cost-effective alternative of the mechanical damper in civil engineering structures, *International Journal of Acoustics and Vibration*. 2007; 12, 1, 25-39. [2]74
- Ziegler F., *Structural dynamics, lecture notes*, TU-Wien, 1979. [2]74
- Ziegler F., Special design of tuned liquid column-gas dampers for the control of spatial structural vibrations, *Acta Mechanica*. 2008, ISSN 0001-5970. [2]74
- Ziegler F., Chuan Fu, Effective vibration damping of plan-asymmetric buildings. In: Proc. of the 8th Int. Conf. on Multi-purpose High-rise Towers and Tall Buildings, Eds.: A.-R.R. Sabouni, K.M. El-Sawy. The International Federation of High-Rise Structures, CD-Rom Paper ID IFHS-039, Abu Dhabi, 2007, 1-13. (www.acevents.ae 'online documents' _ifhs2007+ifhs2007dxb _TB-28.pdf). [4]192,[5]244

Curriculum Vitae

General information:

Name: FU chuan
Sex: female
Address: Pfeilgasse 4-6, 1080 Vienna, Austria
Date of birth: September 23, 1979
Birthplace: Yi Yang, Hunan province
Citizenship: P.R. China

Education:

09,1994-06,1997 Yi Yang No.1 middle school, P.R.China

09,1997-06,2001 bachelor degree, Department of civil engineering, Hunan University, P.R.China. Graduate design: one-storey industry steel buildings

10,2002-03,2005 master degree, Department of civil engineering, building construction and technology, Vienna University of Technology, Austria. Thesis: Horizontale Aussteifung von Hochhäusern in Stahlbauweise und wirtschaftliche Untersuchung einer Verbunddecke, in german language.

03,2005-present: Ph.D. Candidate, Department of civil engineering, building construction and technology, Vienna University of Technology, Austria. Thesis: Effective Damping of Vibrations of Plan-asymmetric Buildings, in English language.

Professional experience:

07,2003-09,2003 Hunan university, P.R.China, Visiting Scholar, research on composite floor with the headed stud shear connectors and shank nails.

07,2006-09,2006 Tongji university, P.R.China, Visiting Scholar, research on mitigating vibration of asymmetric building under dynamic loads by means of computer simulations.